CHOLESTEROL AUTOXIDATION REVISITED

&

MECHANISTIC INSIGHTS INTO HYDROGEN ATOM TRANSFER REACTIONS TO PEROXYL RADICALS

Zosia Anna Marie Zielinski

A thesis submitted to the University of Ottawa

in partial fulfillment of the requirements for the

Doctorate in Philosophy degree in Chemistry

Department of Chemistry and Biomolecular Sciences

Faculty of Science

University of Ottawa

Abstract

Oxygen causes the degradation of virtually all hydrocarbons over time through a process called autoxidation: it's the reason engine oil breaks down, plastics get brittle over time, and butter turns rancid. Autoxidation, in many ways, is what causes humans to degrade as well; the process has been linked to aging, cancer, cardiovascular disease, asthma, macular degeneration, and neurodegenerative conditions like Alzheimer's, Parkinson's, and multiple sclerosis. Unsurprisingly, the body has many natural antioxidant defences to combat oxidative stress, and many so-called "superfoods" are dense in antioxidants such as: vitamins A, C, and E, found in fruits and vegetables like leafy greens, citrus, and avocado; the (poly)phenolic compounds found in berries, green tea, and red wine; and the organosulfur compounds found in garlic and onions. As such, there has been significant interest in this area of research. Our understanding of the kinetics and mechanisms of autoxidation, and the antioxidants that slow the process, has advanced significantly over the past few decades; however, some questions remain unanswered, and some widely-accepted beliefs warrant revisitation.

One such widely-accepted belief was that the autoxidation of cholesterol yields only a single regiosomeric hydroperoxide product (the cholesterol 7-hydroperoxide). We have shown, as outlined in Chapters 2 and 3, that the mechanism of cholesterol autoxidation is far more complex than previously appreciated. Indeed, cholesterol 4-, 6-, and 7-hydroperoxides are produced in the free-radical process, and an additional regiosomeric product, cholesterol 5-hydroperoxide, is produced when autoxidation occurs in the presence of a good H-atom donor. We have also demonstrated that the pathogenic secosterol compounds linked to a number of degenerative diseases can arise from the Hock fragmentation of cholesterol 5- or 6-hydroperoxide, and heretofore uncharacterized secosterols may arise from a similar transformation in cholesterol 4- and 7-hydroperoxide. This, taken together with the well characterized pathogenic potential of such cholesterol-derived electrophiles, is excellent

evidence for a link between cholesterol autoxidation and degenerative disease, without invoking high-energy oxidants like singlet oxygen or ozone.

Our mechanistic study of cholesterol autoxidation also led to the discovery of some surprising stereoelectronic and quantum mechanical effects. In Chapter 3, we show that cholesteryl acetate, a model for the esterified cholesterol particularly abundant in lipoproteins (e.g. LDL and HDL), autoxidizes at 4 times the rate of free cholesterol, which is more abundant in lipid bilayers. We also characterized the pathway of peroxyl radical addition to cholesterol, resulting in cholesterol epoxides. This pathway could be favoured by deuterating the allylic positions in cholesterol to suppress H-atom abstraction by the peroxyl radical, resulting in a deuterium kinetic isotope effect of 20. This evidence of quantum mechanical tunnelling in the H-atom transfer pathway, along with some recent reports of such an effect in other lipids, led us to further explore the impact of tunnelling on H-atom transfer reactions more generally. Using a series of computational model systems, as well as an experimental model for the simplest unsaturated lipid, oleic acid, we demonstrated that tunnelling in C-H abstractions by peroxyl radials is likely significant across the board, so long as the barriers to such reactions are sufficiently high. We also suggest that oleate-derived epoxides may have been overlooked as (minor) products of its autoxidation, and the epoxides derived from plasmalogen lipids may be even more significant than the corresponding hydroperoxide products.

Throughout our work, we have supplemented experimental evidence with computational investigations. A common theme to the computations has been the influence of secondary orbital interactions in H-atom transfers to peroxyl radicals, when the substrate has a secondary orbital donor (lone pair or π-system) adjacent the position bearing the labile H-atom, which can interact with the internal peroxyl oxygen atom. Our work comparing such an effect in sulfenic and selenenic acids (RSOH vs. RSeOH), as outlined in Chapter 5, is some of the best experimental evidence for the influence of secondary orbital interactions. The hindered triptyceneselenenic acid reacted only 18-fold more slowly with peroxyl radicals than the corresponding triptycenesulfenic acid, despite its O-H

bond being 9 kcal/mol stronger! Furthermore, we show that the reaction of peroxyl radicals with unhindered selenenic acids is predicted to be over an order of magnitude faster than their sulfenic acid counterparts, owing to the influence of proper geometrical alignment on the secondary orbital interaction, which is hindered with the bulky substituent. The influence of secondary orbital interactions is further explored in Chapter 6, where we evaluate the feasibility of quantifying or predicting the effects thereof on H-atom transfer reactivity across more diverse classes of compounds. While the many confounding stereoelectronic factors present in these transition states makes such an endeavour difficult, this work has underscored the significance of computations in helping to explain seemingly anomalous experimental evidence.

Acknowledgement

Thank you to: my supervisor, Prof. Derek A. Pratt, for everything you've taught me; the entire Pratt Group, for your endless support and entertainment; the University of Ottawa, for funding and resources; the Natural Sciences and Engineering Research Council (NSERC) of Canada, for a Canada Graduate Scholarships; and my friends and family, for your patience.

"I was taught that the way of progress was neither swift nor easy."

– Marie Curie

Statement of Originality

I hereby certify that all of the work described in this thesis is the original work of the author, with exceptions for work performed by collaborators noted in the preface to each chapter. The work in this thesis draws upon a great deal of published research. Any published (or unpublished) work by others is cited and fully acknowledged within the references.

Zosia Zielinski

Table of Contents

List of Schemes

List of Figures

List of Tables

List of Abbreviations

$^1O_2$	singlet oxygen
$^3O_2$	triplet (or molecular) oxygen
4-HNE	4-hydroxynonenal
7-DHC	7-dehydrocholesterol
AH	antioxidant
AMP	antioxidant-mediated peroxidation
APCI	atmospheric pressure chemical ionization
BDE	bond dissociation enthalpy
BDMP	4-*tert*-butyl-2,6-dimethylphenol
BSA	N,O-bis(trimethylsilyl)acetamide
CBS-QB3	a complete basis set approach (quantum chemistry composite method) developed by Petersson and coworkers
chol	cholesterol
chol OAc	cholesteryl acetate
DNPH	2,4-dinitrophenylhydrazine
DTBN	di-*tert*-butyl hyponitrite
E_a	activation energy
EPR	electron paramegnetic resonance
ESI	electrospray ionization
FID	flame ionization detection
GC	gas chromatography
GPx	glutathione peroxidase
HAT	hydrogen-atom transfer
HDL	high-density lipoprotein

HOMO	highest (fully) occupied molecular orbital
HPLC	high performance liquid chromatography
KIE	kinetic isotope effect
LDL	low-density lipoprotein
MDA	malondialdehyde
MeOAMVN	2,2'-Azobis (4-methoxy-2,4-dimethylvaleronitrile)
MS	mass spectrometry
MS/MS	tandem mass spectrometry
PCET	proton-coupled electron transfer
PMC	2,2,5,7,8-pentamethyl-6-chromanol
PUFA	polyunsaturated fatty acid
ROS	reactive oxygen species
S_Hi	intramolecular homolytic substitution
SLOS	Smith-Lemli-Opitz syndrome
SOD	superoxide dismutase
SOMO	singly occupied molecular orbital
TS	transition state
UPLC	ultra performance liquid chromatography
α-TOH	α -tocopherol
$\Delta G^{\ddagger}$	free energy of activation, or reaction barrier

Chapter 1: Introduction*

1.1 Autoxidation

Earth's oxygen-rich environment is necessary to support life as we know it, but it is not without its consequences. Oxygen is responsible for the degradation of virtually all petroleum-derived products, from lubricants and polymers to commodity and specialty chemicals. This process, termed *autoxidation* (Figure 1.1A), also takes place in biological contexts; in fact, many of the polyunsaturated fatty acids and sterols (Figure 1.1B) that are essential to life are among the most susceptible hydrocarbons. Lipid oxidation products have been associated with a myriad of pathophysiological conditions,[1-3] and their accumulation has been linked to ferroptosis, a recently characterized mode of regulated necrosis that may link lipid peroxidation and disease.[4,5] As such, significant effort has been directed at understanding the potential for antioxidants to slow lipid autoxidation,[6] as well as imaging lipid peroxidation products in cells and tissues, and the effect of antioxidants on the rate of their formation.[7]

1.1.1 Mechanism

Autoxidation is the archetype free radical chain reaction (Eq. 1.1-1.6).[1,2,8,9] It is both initiated by – and produces – hydroperoxides, and can therefore be considered an autocatalytic process. The spontaneous homolysis of the hydroperoxide O-O bond (Eq. 1.1a), or its one electron reduction (Eq. 1.1b, e.g. by Fe^{2+}), produces highly reactive alkoxyl and/or hydroxyl radicals. The subsequent

---

* This chapter is reproduced in part with permission from Zielinski, Z.A.M.; Pratt, D.A. *J. Org. Chem.* **2017**, *82*, 2817. Copyright 2017 American Chemical Society. For greater clarity:

- a portion of the section "Understanding product distributions", as published, is removed from Section 1.3.1, as the discussion therein overlapped with the results and discussion on cholesterol autoxidation, presented in greater detail in Chapters 2 and 3;
- Sections 1.1.2, 1.1.3, 1.1.4, and 1.5 did not appear in the published article, but are added here for further context.

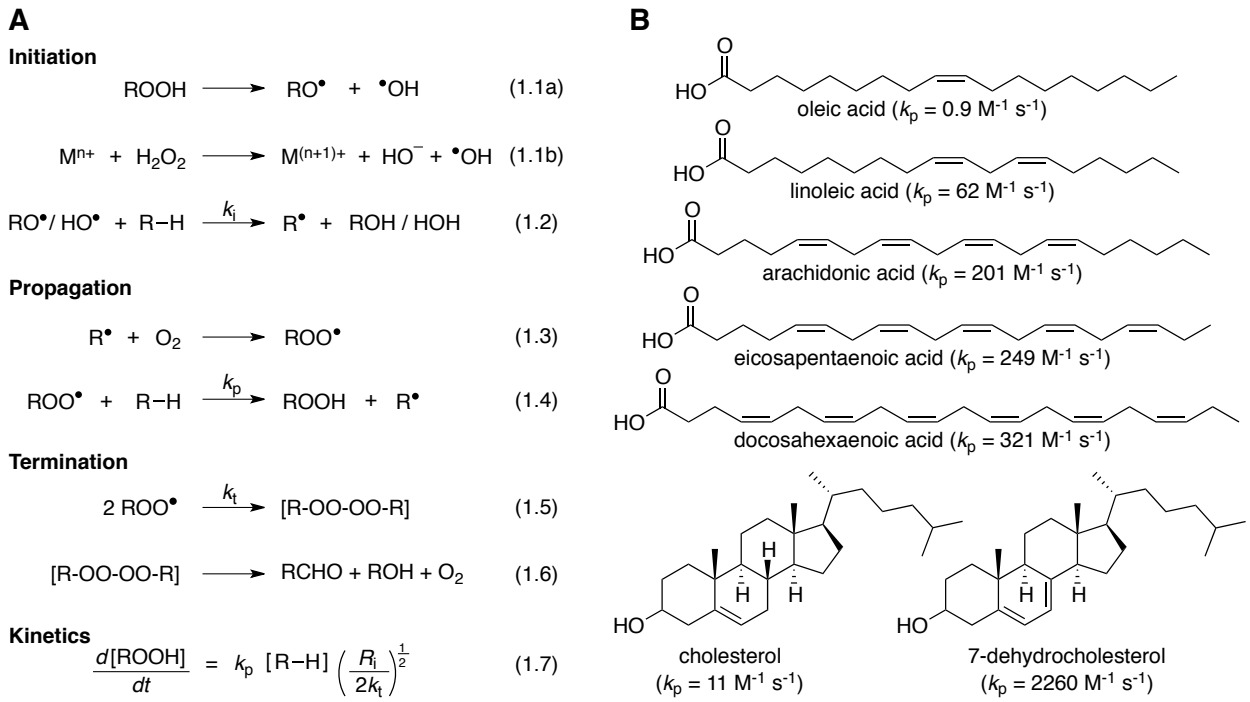

Figure 1.1. A) Free radical chain mechanism of hydrocarbon autoxidation, and B) structures of representative lipids and their associated propagation rate constants.[14]

abstraction of a labile hydrogen atom from the hydrocarbon substrate initiates the chain reaction (Eq. 1.2). The alkyl radical so formed reacts with oxygen at near the diffusion-controlled rate to give the chain-carrying peroxyl radical (Eq. 1.3). The rate-limiting propagation step involves H-atom transfer (HAT) from the hydrocarbon substrate to a peroxyl radical, characterized by the key propagation rate constant, k_p (Eq. 1.4). Propagation competes with termination of the radical chain reaction (Eq. 1.5), which generally takes place by the reaction of two peroxyl radicals, given the low concentration of alkyl radicals under aerobic conditions. Recent computations suggest that termination occurs by the asymmetric cleavage of the tetroxide intermediate, loss of O_2, and in-cage disproportionation of the two alkoxyl radicals.[10] In a biological context, the rate of autoxidation (Eq. 1.7) is exacerbated in cell membranes and lipoproteins, where the effective concentration of the substrate (lipid) is very high. It

should be noted that lipid hydroperoxides can also be formed in enzyme-mediated processes (e.g. by lipoxygenases[12] and cyclooxygenases)[11,12] or through lipid oxidation by singlet oxygen ($^1O_2$).[13]

1.1.2 Kinetics

The rate of autoxidation is presented in Eq 1.7. For further clarity, the derivation of this expression is presented here. Inititiating radicals can be produced in a number of ways, *vide infra*, one of which being the homolysis of a hydroperoxide (Eq. 1.1a), which may be generalized as in Eq 1.8:

$$\mathrm{In{-}In} \xrightarrow{k_d} 2\ \mathrm{In}^{\bullet} \qquad (1.8).$$

The rate of initiation, R_i, is therefore expressed in Eq. 1.9:

$$R_i = 2ek_d[\text{In-In}] \qquad (1.9)$$

where the term *e* represents the efficiency of cage escape, or the likelihood the two radicals diffuse away from one another as compared to recombining, which is exacerbated in viscous solvents.

The kinetics of propagation can be derived using the steady state approximation, accounting for the intermediate initiating radical in Eq. 1.10:

$$\frac{d[\mathrm{In}^{\bullet}]}{dt} = 2ek_d[\text{In-In}] - k_i[\mathrm{In}^{\bullet}][\mathrm{RH}] \qquad (1.10)$$

and accounting for the fates of the substrate-derived intermediate radical in Eq. 1.11:

$$\frac{d[\mathrm{R}^{\bullet}]}{dt} = k_i[\mathrm{In}^{\bullet}][\mathrm{RH}] - k_p[\mathrm{ROO}^{\bullet}][\mathrm{RH}] + k_p[\mathrm{ROO}^{\bullet}][\mathrm{RH}] - 2k_t[\mathrm{ROO}^{\bullet}]^2 \qquad (1.11)$$

where the addition of molecular oxygen ($^3O_2$) to the alkyl radical during propagation (Eq. 1.3) is presumed to be sufficiently fast to be ignored in the rate equation, as it approaches the diffusion limit in solution (~10^9 $M^{-1}s^{-1}$). Thus the third term effectively represents the production of $R^{\bullet}$, and the equation can be simplified in Eq. 1.12:

$$\therefore \frac{d[\mathrm{R}^{\bullet}]}{dt} = k_i[\mathrm{In}^{\bullet}][\mathrm{RH}] - 2k_t[\mathrm{ROO}^{\bullet}]^2 \qquad (1.12).$$

The steady state approximation for initiation results in Eq. 1.14 as follows:

$$\frac{d[\mathrm{In}^{\bullet}]_{SSA}}{dt} = 0 \qquad (1.13)$$

$$\therefore 2ek_d[\text{In-In}] = k_i[\mathrm{In}^{\bullet}]_{SSA}[\mathrm{RH}] \qquad (1.14),$$

and the steady state approximation for propagation results in the Eq. 1.16 as follows:

$$\frac{d[R^{\bullet}]_{SSA}}{dt} = 0 \qquad (1.15)$$

$$\therefore k_i[\mathrm{In}^{\bullet}]_{SSA}[\mathrm{RH}] = 2k_t[\mathrm{ROO}^{\bullet}]^2_{SSA} \qquad (1.16).$$

Combining the two equations provides the below approximation for the concentration of peroxyl radicals (Eq. 1.18):

$$2ek_d[\text{In-In}] = 2k_t[\mathrm{ROO}^{\bullet}]^2_{SSA} \qquad (1.17)$$

$$\therefore [\mathrm{ROO}^{\bullet}]_{SSA} = \sqrt{\frac{ek_d[\text{In-In}]}{k_t}} \qquad (1.18).$$

The overall rate of autoxidation (R_{O_2}) may be represented as the production of ROOH (as in Eq. 1.7) or by consumption of the starting materials (RH and O_2):

$$R_{\mathrm{O}_2} = -\frac{d[\mathrm{RH}]}{dt} = -\frac{d[\mathrm{O}_2]}{dt} = k_i[\mathrm{In}^{\bullet}][\mathrm{RH}] + k_p[\mathrm{ROO}^{\bullet}][\mathrm{RH}] \qquad (1.19),$$

which can be simplified by assuming the autoxidation involves suitably long chain lengths, where the first term <<< the second term, resulting in Eq. 1.20:

$$R_{\mathrm{O}_2} = k_p[ROO^{\bullet}]_{SSA}[\mathrm{RH}] \qquad (1.20).$$

Eq. 1.20 may be substituted with the steady state approximation-derived term for the concentration of peroxyl radicals (Eq. 1.18), to give the rate equation Eq. 1.21:

$$R_{O_2} = k_p[\text{RH}]\sqrt{\frac{ek_d[\text{In-In}]}{k_t}} \qquad (1.21).$$

This equation can be further simplified by inserting the rate of initiation Eq. 1.22 into Eq. 1.21 to give Eq. 1.23 as follows:

$$R_i = 2ek_d[\text{In-In}] \qquad (1.22)$$

$$\therefore R_{O_2} = k_p[\text{RH}]\sqrt{\frac{R_i}{2k_t}} \qquad (1.23).$$

Another important equation when studing autoxidation is the chain length (x), which may be determined by Eq. 1.24, relating the production of hydroperoxide over time, divided by the rate of initiation:

$$x = \frac{[\text{ROOH}]/t}{R_i} \qquad (1.24).$$

The kinetics of autoxidaton are further complicated by the presence of antioxidants, which slow the process, *vide infra.*

1.1.3 Consequences

Oxidative stress is generally considered to be the imbalance between the production of reactive oxygen species (ROS) and their detoxification by antioxidants. Superoxide ($O_2^{\bullet-}$) is a key reactive oxygen species, produced in significant quantities *in vivo* by the one electron reduction of molecular oxygen (cf. Scheme 1.1). Its production occurs, for example, as a side product of one electron redox chemistry of coenzyme Q10 (ubiquinol) in the mitochondria as a consequence of cellular respiration.

It is estimated that a human produces on the order of kilograms of superoxide per year from this so-called "electron leakage".[15,16] Superoxide itself is not nefarious, but it may lead to other, more reactive radicals through a number of pathways presented in Scheme 1.1. The pKa of the hydroperoxyl radical is 4.8 in water,[17] therefore protonation of superoxide at physiological pH is highly reversible. The reaction of two radicals such as two hydroperoxyl radicals is diffusion-controlled; thus hydrogen peroxide may be produced from superoxide, albeit with an unfavourable pre-equilibrium. As shown in Eq. 1.1b, hydrogen peroxide undergoes a one electron reduction (Fenton reaction) to produce a highly reactive hydroxyl radical. Hydroxyl radicals can also be produced from the reaction of hydrogen peroxide and chlorine, via hypochlorous acid as an intermediate (Scheme 1.1).

Scheme 1.1. Production of reactive oxygen (and nitrogen) species in vivo.

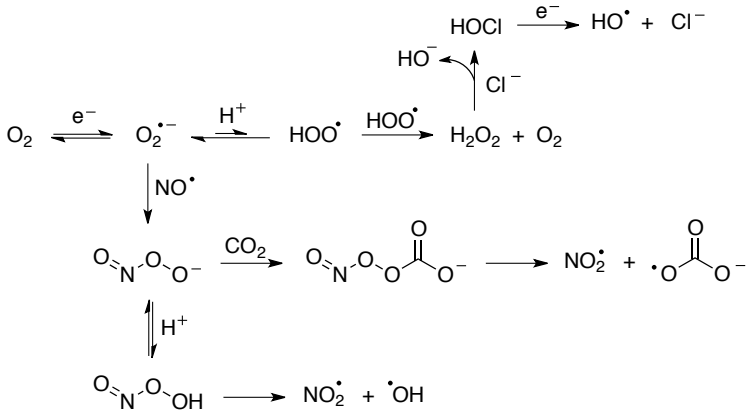

Initiating radicals can also form when superoxide combines with a nitric oxide radical to form peroxynitrite. Peroxynitrite is a powerful oxidant and nitrating agent that can also react with CO_2 to form nitrogen dioxide and a carbonate radical. Alternatively, peroxynitrite may be protonated (pKa 6.8)[18] and homolyzed to form nitrogen dioxide and a hydroxyl radical. Because of the strong O-H

bond in water (bond dissociation entalpy, BDE, of nearly 120 kcal),[19] the hydroxyl radical is highly reactive and is likely to abstract a hydrogen atom from essentially the first molecule it intercepts. The downstream reactive oxygen (and nitrogen) species produced from superoxide are capable of reacting directly with biological targets (e.g. damaging DNA or proteins), or initiating free radical chain reactions such as the autoxidation of lipids. This is exacerbated if the initiating event occurs within lipid-rich environments like lipid bilayer membranes or in lipoproteins where lipids are packed densely, facilitating propagation. The effects of superoxide are not all deleterious to health, though. Superoxide is also produced in inflammatory response by NADPH oxidaze, which is over-expressed in phagocytes. Phagocytes, such as white blood cells, trigger superoxide production as a part of the cascade to destroy engulfed particles, such as bacterial cells.[15]

Superoxide generation as a consequence of cellular respiration is not the only source of initiating raticals *in vivo*. As noted above, lipid hydroperoxides can also be formed in enzyme-mediated processes (e.g. by lipoxygenases[12] and cyclooxygenases)[11,12] or through lipid oxidation by singlet oxygen ($^1O_2$).[13] The hydroperoxides so formed can, in turn, homolyze (either spontaneously, or though transition-metal catalysis) to initiate autoxidation and lead to further lipid peroxidation. Oxidized lipids are also present in dietary sources, in which peroxidation may be initiated and/or exacerbated by high temperature cooking. Natural and artificial pigments in foods can also act as photosensitizers for the generation of $^1O_2$, which generates lipid peroxides by a non-radical "ene" reaction (cf. Scheme 1.2).[20]

Scheme 1.2. Reaction of singlet oxygen and an alkene, to yield a hydroperoxide.

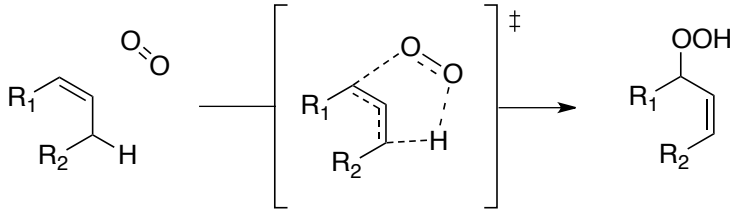

The ground state of molecular oxygen is the triplet state ($^3O_2$), whereas singlet oxygen ($^1O_2$) is 22 kcal/mol higher in energy. Singlet oxygen can be generated when a sensitizer (S, in Eq. 1.25) undergoes activation by light to the first excited state (^1S), followed by intersystem crossing to form a triplet state (^3S). The first excited state is short-lived and can alternatively return to the ground state (^0S) by emitting a photon or interacting with neighboring molecules such as solvent, rather than undergoing intersystem crossing. The triplet state, on the other hand, is longer-lived and can initiate photochemical reactions, like the conversion of triplet oxygen to singlet oxygen.[21]

$$^0S \xrightarrow{h\nu} {}^1S \longrightarrow {}^3S \xrightarrow{^3O_2} {}^0S + {}^1O_2 \qquad (1.25)$$

Photosensitizers present in human skin (e.g. porphyrins and flavins) and retinas (e.g. lipofuscin) can also convert $^3O_2$ to $^1O_2$ as a consequence of UV exposure.[20] Singlet oxygen is generated enzymatically as well, such as the myeloperoxidase-catalyzed production of $^1O_2$, as an antibacterial response in leukocytes.[22] Such endogenous production of $^1O_2$ was also implicated in the controversial[23-25] suggestion that ozone (O_3) is also produced endogenously.[26] Ozone is known to contribute to the respiratory toxicity of poluted air, due to its action on epithelial cells.[27,28] However, Wentworth and coworkers hypothesized that an antibody-catalyzed water-oxidation pathway, when in proximity to endogenous $^1O_2$ production, would yield ozone.[26] Our lab,[29] and others,[23-25] largely discredited the conclusions of this work. For example, Wentworth and coworkers used cholesterol ozonolysis products **1.1** and **1.2** as biomarkers to support their theory.

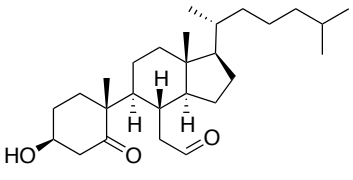

1.1

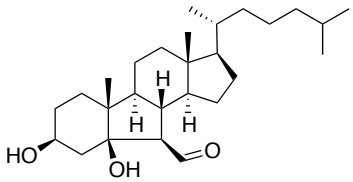

1.2

However, it was shown that these products could also be derived from the Hock fragmentation of cholesterol 5-hydroperoxide, the product of cholesterol and $^1O_2$ (recall, $^1O_2$ was an implicated

intermediate in the purported pathway to endogenous ozone production). This controversy, and alternative means of production of secosterols**,** will be further discussed in Chapters 2 and 3.

The secosterols **1.1** and **1.2** are also refered to as atheronals, as their presence was first confirmed *in vivo* in atheroscleratic plaques.[26] While their mechanism of production was the focus of the controversy, their pathogenic potential has only been further supported over time. Following Wentworth's report, the secosterols were subsequently implicated in the pathogenesis of Alzheimer's disease,[30] cardiovascular disease,[31] cancer,[32] Parkinson's disease,[33] and multiple sclerosis.[34] Indeed, lipid-derived electrophiles (aldehydes) are believed to be a link between lipid peroxidation and degenerative disease, as will be further discussed in section 1.3 in relation to the highly autoxidizable cholesterol precursor 7-dehydrocholesterol (7-DHC), as well as polyunsaturated fatty acids and the pathogenic compounds derived therefrom. As the consequences of oxidative stress link aging, cancer, and degenerative diseases to environmental factos such as UV exposure, pollutants, smoking, and diet, it follows that there is naturally considerable effort put toward slowing the process biologically, and significant interest in potential human interventions.

1.1.4 Inhibition

A schematic representation of hydrocarbon autoxidation is presented in Scheme 1.3. Autoxidation is inhibited in the presence of antioxidants, which may be classified as preventative or chain-breaking, depending upon their mechanism of action – the former slowing initiation (Eq. 1.1-1.2), and the latter slowing propagation (Eq. 1.4).

Scheme 1.3. Hydrocarbon autoxidation and inhibition thereof by antioxidants.

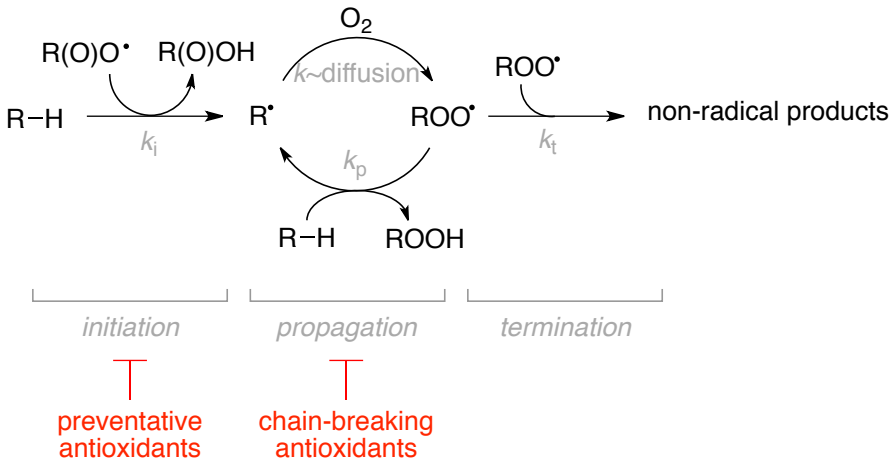

Superoxide dismutase (SOD) is a key biological defence against reactive oxygen species. It acts as a preventative antioxidant, catalyzing the disproportionation of superoxide to form hydrogen peroxide and oxygen (Eq. 1.25), and thereby preventing the formation of superoxide-derived initiating radicals (cf. Scheme 1.1).

$$2\ O_2^{\bullet -} + 2\ H^+ \xrightarrow{\text{SOD}} H_2O_2 + O_2 \qquad (1.25)$$

Another important preventative antioxidant is glutathione peroxidase (GPx), which reduces hydroperoxides to alcohols via the mechanism shown in Scheme 1.4. The active site selenocysteine residue results in an intermediate selenenic acid (RSeOH) – the redox chemistry of which will be explored in Chapter 5. Other preventative antioxidants include peroxide decomposers (e.g. catalase enzymes), metal chelators, UV absorbers (e.g. melanin), and $^1O_2$ quenchers – all of which, in some way, prevent radical formation or scavenge reactive oxygen species that can act as initiators. Many so-called "superfoods" are rich in antioxdants. For example, β-carotene, a form of vitamin A present in dark leafy greens and other fruits and vedetables, effectively quenches $^1O_2$, and phytic acid, found in many nuts, seeds, legumes, and grains, is a metal chelator.[35]

Scheme 1.4. Glutathione peroxidase reduction of hydroperoxide.

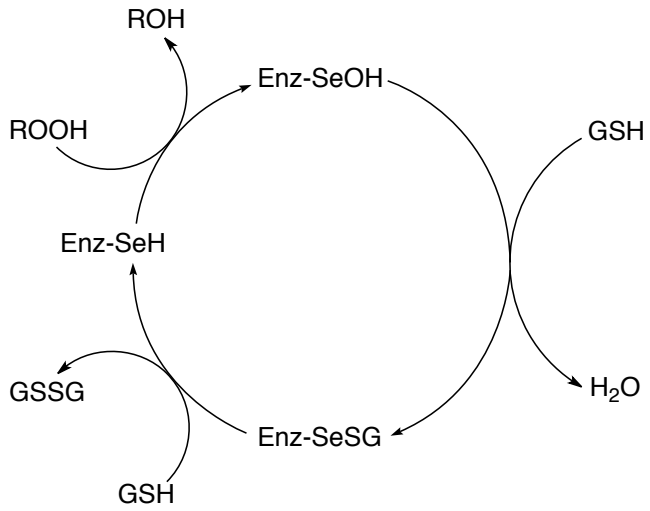

Chain-breaking antioxidants (or radical-trapping antioxidants, RTAs, or A-H in Scheme 1.4) instead slow propagation by intercepting chain-carrying peroxyl radicals, and must compete with the substrate to do so. Therefore, an effective chain-breaking antioxidant has k_{inh}[A-H] > k_p[R-H]; and more realistically k_{inh} >>> k_p, given that the relative amount of antioxidant compared to substrate is low, in practice (i.e. for effective antioxidants *in vivo*, or in other applications).

Scheme 1.5. Fates of peroxyl radicals: propagation vs. inhibition.

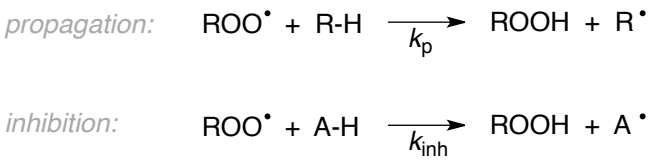

Furthermore, the antioxidant-derived radical A• should not propagate the chain reaction, such as by abstracting a labile H-atom to generate an alkyl radical. For example, the mechanism of phenolic antioxidants is well known, where the antioxidant-derived phenoxyl radical is persistent enough to

trap a second peroxyl radical, to form a non-radical product. This is demonstrated in Scheme 1.6 for α-tocopherol – the most bioactive form of Vitamin E and Nature's best chain-breaking antioxidant with k_{inh} of 3.2×10^6 $M^{-1}s^{-1}$.

Scheme 1.6. Radical-trapping antioxidant activity of α-tocopherol.

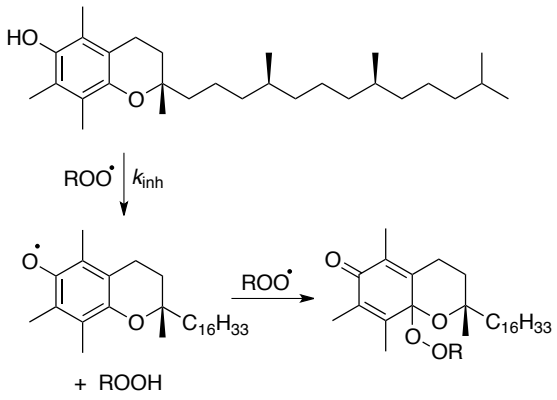

Again, many so-called "superfoods" are rich in (poly)phenolic antioxidants like anthocyanins (berries), catechins (green tea), resveratrol (red wine), and curcumin (turmeric). Organosulfur compounds are also natural antioxidants, such as the thiosulfinates derived from plants in the *Allium* genus, including garlic and onions (the sulfenic acids derived therefrom will be discussed further in Chapter 5, and the references cited therein). The antioxidant activity of ascorbic acid (vitamin C, abundant in citrus fruits) is mainly to act as a water-soluble reducing cofactor, for example, reducing the intermediate tocopheroxyl radical in Scheme 1.6 back to the corresponding phenol.[35] A discussion on other classes of synthetic and industrially-relevant radical-trapping antioxidants, such as pyridinols/pyrimidinols, arylamines, nitroxides, and organosulfur compounds may be found elsewhere.[35-37]

The kinetics of autoxidation in the presence of a chain-breaking antioxidant can be represented by the rate equation Eq. 1.26:

$$R_{\text{inh}} = \frac{k_p[\text{RH}]R_i}{n\,k_{inh}[AH]} \qquad (1.26)$$

where the stoichiometric factor, *n*, denotes the number of peroxyl radicals the antioxidant, AH, is able to trap (i.e. for the case of α-tocopherol in Scheme 1.6, *n* = 2), and k_{inh} is the rate at which AH transfers its H-atom to the chain-carrying peroxyl radical. It is worth noting that these reactions are susceptible to a kinetic solvent effect, akin to a pre-equilibrium – if the antioxidant (e.g. ArOH) participates in a H-bonding interation with the solvent, it is unable to have the participating H-atom abstracted by a peroxyl radical (cf. Scheme 1.7).

Scheme 1.7. Kinetic solvent effect in H-atom abstraction.

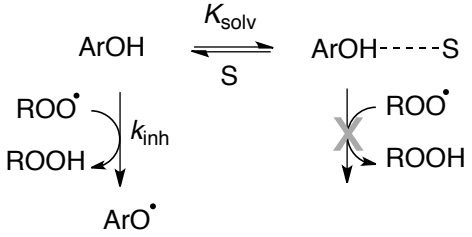

Thus, the effective rate constant in a given solvent can be represented by Eq. 1.27. Ingold and coworkers[38] found that the relationship in Eq. 1.28, using Abraham's parameters α_2^H, the solute H-bonding acidity, and β_2^H, the solvent H-bonding basicity, effectively reflects the solvent effect for H-atom abstraction from phenols.

$$k_{inh}^{solv} = \frac{k_{inh}^{o}}{1 + K_{solv}[S]} \qquad (1.27)$$

$$\log k_{inh}^{solv} = \log k_{inh}^{o} - 8.3\alpha_2^H\beta_2^H \qquad (1.28)$$

This work by Ingold helped to clarify the effect of solvent on H-atom transfer reactions. Again, the focus herein is on the biological context of autoxidation and lipid peroxidation, which occurs in lipid-

rich environments. These environments are non-polar, thus much of the *in vitro* models for lipid peroxidation are effectively carried out in non-polar solvents like chlorobenzene and hexanes. In other words, "biologically-relevant" need not always mean "buffered pH 7.4 aqueous solution". The factors influencing H-atom transfer reactivity with a peroxyl radical, which is the key step in both propagation and initiation of autoxidation, are introduced below in Section 1.2, and will be the subject of further discussion in Chapters 4-6.

1.2 What makes an (auto)oxidizable hydrocarbon?

Since the rate-limiting step in hydrocarbon autoxidation is generally a formal HAT from the substrate to a peroxyl radical (we will discuss the exception to this below), it follows that the strength of the C-H bond that is broken should determine the rate of autoxidation. Indeed, the difference in k_p values for oleic and linoleic acid (Figure 1.1B) is consistent with a bisallylic C-H being weaker than an allylic C-H (a pentadienyl radical is roughly 10 kcal/mol more stable than an allyl radical). Moreover, k_p values for the polyunsaturated lipids are correlated to the number of bis-allylic positions. As suggested by the Evans-Polanyi principle, the magnitude of the propagation rate constants (k_p) for a wide variety of (sterically unhindered) hydrocarbons generally correlate to the strength of their most labile C-H bonds (Figure 1.2A). However, several points are outliers to the correlation – with higher rate constants than would be predicted based on their C-H BDEs. This 'alternative' correlation features substrates wherein the C-H is abstracted from a position α to a heteroatom. Furthermore, when the plot is populated with data for other H-atom donors, e.g. phenolic antioxidants that slow lipid peroxidation (such as α-tocopherol, the most biologically active form of Vitamin E),[39] they are related by a different expression. Several explanations have been advanced for these differences, underscoring the fact that steric and stereoelectronic effects in the formal HAT transition state can be as important as the overall thermodynamics.[40]

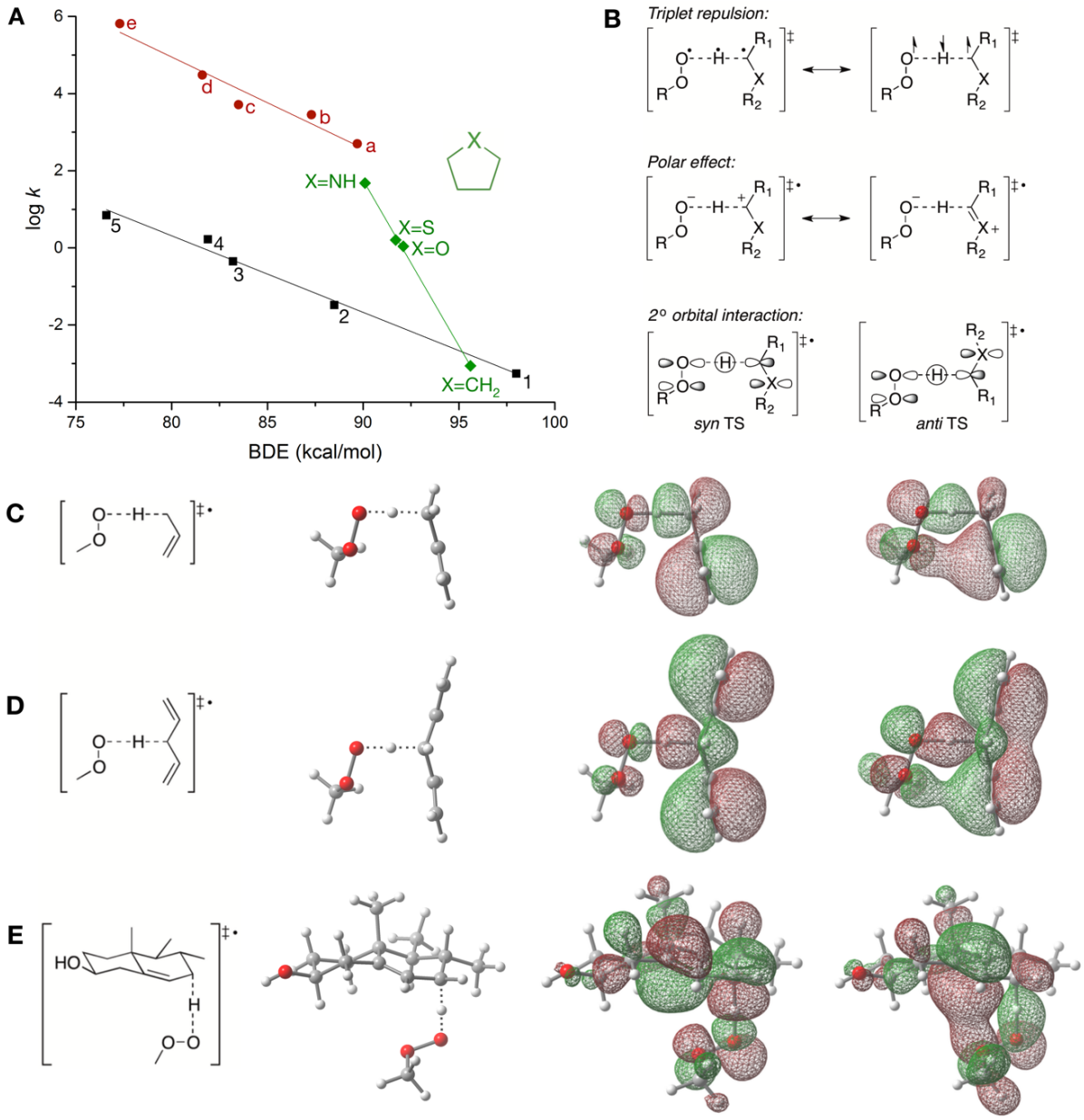

Figure 1.2. A) Evans-Polanyi correlation of experimental bond dissociation enthalpies (BDEs)[19] and hydrogen atom transfer (HAT) rate constants (k, M^{-1} s^{-1}) at 30°C[41] for C-H bonds in: hexene (1), toluene (2), cumene (3), cyclohexene (4) and penta-1,4-diene (5); for C-H bonds α to a heteroatom; and for Y-H bonds in aniline (a, Y=N), phenol (b, Y=O), thiophenol (c, Y=S), 2,6-di-*tert*-butyl-4-methylphenol (d, Y=O) and α-tocopherol (e, Y=O). B) Stereoelectronic factors affecting the HAT transition state. C-E) Transition state structures for H-atom abstraction from models of oleate (propene, C), linoleate (1,4-pentadiene, D) and cholesterol (E), by a methylperoxyl radical. The computed singly occupied molecular orbitals (SOMO) and highest (fully) occupied molecular orbitals (HOMO) are shown alongside.

A prominent concept used to explain the deviation in linearity in Evans-Polanyi correlations is triplet-repulsion,[42,43] which suggests that the barrier for HAT (Eq. 1.29) between X-H and Y is dictated by the electronegativity of X and Y. Repulsion between the unpaired electrons localized on X and Y, which necessarily have the same spin in the H-atom transfer transition state (Figure 1.2B), is greater among less electronegative X and Y. Thus, H-atom transfer between heteroatoms and oxygen occurs relatively more quickly than carbon and oxygen. However, if triplet-repulsion were a sufficient explanation, the Evans-Polanyi principle would hold true within a series of X-H bonds (provided X and Y are the same). One need only consider the aforementioned series of C-H abstractions α to a heteroatom to see that triplet-repulsion cannot fully explain these trends. Polar effects,[40,44,45] which are also related to the electronegativities of X and Y (or distal substituents), may be invoked to explain these deviations, as an α-heteroatom would serve to stabilize the dipole created in the HAT transition state.

$$X\text{–}H + {}^{\cdot}Y \rightarrow \left[X\text{--}H\text{--}Y\right]^{\ddagger\cdot} \rightarrow X^{\cdot} + H\text{–}Y \quad (1.29)$$

More recently, computational investigations have revealed the significance of secondary orbital interactions in these reactions. The first prominent example showed the lowest energy transition state structure for the hydrogen peroxide/hydroperoxyl radical couple (Eq. 1.30) has a *syn* disposition of the substituents on the oxygen atoms between which the H-atom is transferred. This geometry is initially counter-intuitive, as it would appear to maximize electron-electron repulsion between the two reacting groups. However, the computations demosntrate that orbital overlap in the highest (doubly) occupied molecular orbital (HOMO) compensates for this repulsion.[46] We have found that such secondary orbital interactions are also significant in the reaction of unsaturated fatty acids with peroxyl radicals.[47] For example, in allylic H-atom abstractions by peroxyl radicals, using propene as a model for oleic acid, a *syn* transition state is lower in enthalpy by 1.1 kcal/mol relative to the *anti* configuration due to a secondary orbital interaction between the π HOMO of propene and the π* singly occupied molecular orbital (SOMO) of the methylperoxyl radical (*cf.* Figure 1C). In penta-

1,3-diene, the *syn* transition state is even more preferential (1.5 kcal/mol relative to the *anti* configuration), as the conjugated system has a higher energy HOMO. Since penta-1,4-diene (a model for linoleic acid) is symmetrical, it is impossible to compare the *syn* and *anti* configurations; however, the lowest energy transition state is the one which maximizes secondary orbital interactions, and not one which minimizes steric repulsion (*cf.* Figure 1.2D).[47]

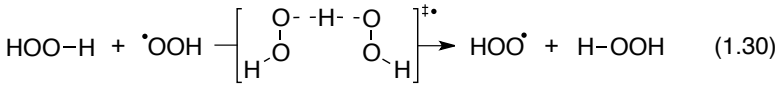

Corresponding interactions are evident in the transition states of HAT from the allylic positions in cholesterol by a peroxyl radical. In particular, abstraction from C7-H on the α-face of the sterol framework benefits from *syn* transition state geometry involving a secondary orbital interaction between the C5-C6 unsaturation and the peroxyl radical (*cf.* Figure 1.2E, and discussed in greater detail in Chapters 2 and 3), while abstraction from the β-face is less favourable due to a steric interaction with the C10-methyl group.[48] Secondary orbital interactions are even more important in other types of HAT reactions. For example, we found a remarkable interaction in the reaction of sulfenic (RSOH)[49] and selenenic (RSeOH)[50] acids with peroxyl radicals, the latter having surprisingly good H-atom donating ability despite its relatively strong O-H bond (as will be discussed in Chapters 5 and 6).[50]

A final consideration in rationalizing trends in bond strengths and the rate of HAT (k_p) is that these reactions do not necessarily obey classical behaviour (as will be discussed in Chapter 4). A recent study on the autoxidation of 11,11-d_2-linoleic acid found the deuterium kinetic isotope effect on its propagation rate constant to be *ca.* 13.[51] Even larger isotope effects have been observed in α-tocopherol–loaded autoxidations, where D-atom transfers to tocopheryl radicals from 11,11-d_2-linoleic acid,[52] 11,11,14,14-d_4-α-linolenic acid,[52] and 9,14-d_2-7-dehydrocholesterol[53] are reported to be 23-, 32-, and 21-fold slower than the corresponding HATs, respectively. These values are significantly greater than the classical limit for a deuterium kinetic isotope effect ($k_H/k_D \sim 7$ at room

temperature), implying that quantum mechanical tunnelling plays a significant role in lipid peroxidation. Interestingly, yeast and human kidney cells cultured in the presence of 11,11-d_2-linoleic acid were resistant to copper-induced toxicity[51] and ferroptotic cell death,[54] respectively, suggesting that the contribution of tunelling to lipid peroxidation translates beyond the test tube. Although tunnelling is well precedented for the transfer of hydrogen (H^+, $H^\bullet$ or H^-),[55,56] examples in the context of hydrocarbon autoxidation are scarce.[57]

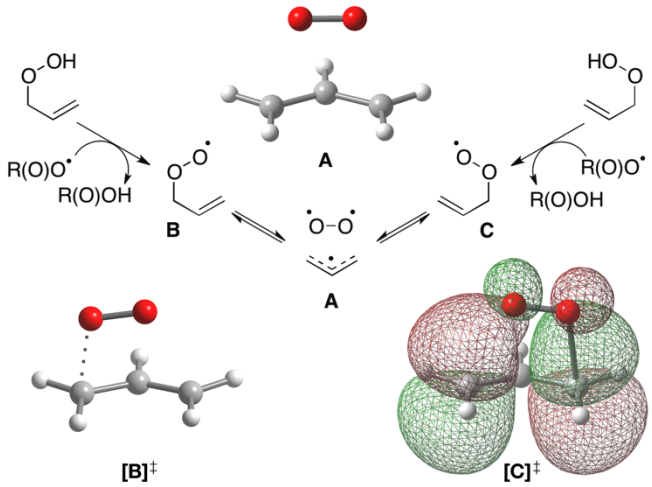

Figure 1.3. Schenck rearrangement mechanism for (reversible) oxygen addition to an allylic radical, where the computed structures are shown for the weakly bound allyl-O_2 moiety (A), the transition state (TS) for the *syn* addition of the allylic radical ([B]‡), and the analogous TS overlayed with the highest occupied molecular orbital (HOMO) showing the secondary orbital interaction ([C]‡).

Secondary orbital interactions are not unique to HAT to peroxyl radicals. Indeed, the (reversible) addition of oxygen to unsaturated lipids also benefits from this interaction. Calculations on the addition of oxygen to allyl and pentadienyl radicals indicate the *syn* transition state is most favourable for oxygen addition by 5.1 and 4.1 kcal/mol, respectively, relative to the *anti* configuration.[47] The transition states for the addition of oxygen at either end of the allyl radical are interconnected on the potential energy surface by a weakly bound allyl:O_2 complex (Figure 1.3). The step-wise mechanism for this rearrangement (sometimes referred to as the Schenck rearrangement) is calculated to be far more favourable than the concerted process,[47] and accounts for the suprafacial

stereoselectivity and retention of ^{18}O in rearrangments of isotopically labeled hydroperoxides under air.[58,59]

1.3 Lipid Peroxidation

1.3.1 Understanding Product Distributions

Lipid unsaturation promotes the rate of autoxidation, but also increases the complexity of the product distribution. This distribution can change based upon experimental conditions (or different environments *in vivo*) due to the reversibility of oxygen addition to the lipid-derived radicals and the presence of H-atom donors capable of trapping isomeric peroxyl radical intermediates. The propensity for oxygen to fragment from a peroxyl radical is reflected in the β-fragmentation rate constant, k_β, which is related to the C-OO$^\bullet$ bond strength. One might assume that the strength of this bond is determined solely by the stability of the resultant carbon-centered radical, but it has been shown that significant hyperconjugative interactions between the σ* orbital of the C-OO$^\bullet$ bond and neighbouring lone pairs or filled π-orbitals is also a significant determinant.[60,61]

Oleic acid (and its esters), with a single unsaturation spanning C9 and C10, autoxidizes to give six primary hydroperoxide products (Scheme 1.8A). HAT from either of the allylic positions, followed by oxygen addition on either end of the allylic radicals formed gives four possible kinetic products (**1a**, **1b**, **2a** and **2b**). The reversible addition of oxygen ($k_\beta \sim 0.5$ to 8 s^{-1}) enables formation of the thermodynamic *trans*-alkene products (**3a** and **3b**).[62] A slightly more complex product distribution can arise from the autoxidation of the doubly unsaturated linoleic acid and its esters (Scheme 1B), where HAT from the bis-allylic position yields a delocalized pentdienyl radical to which oxygen may add at each of the three positions that bear unpaired electron spin density (C9, C11 and C13). Addition at the 9- and 13-positions yields conjugated products with *cis,trans* configuations of the two

double bonds, as opposed to the *cis*,*cis* configurations of the non-conjugated double bonds formed upon addition to C11. Indeed, the 11-hydroperoxide (**4**) can only be trapped in the presence of a H-

Scheme 1.8. Product formation in the autoxidation of esters of oleate (A), linoleate (B) and arachidonate (C).

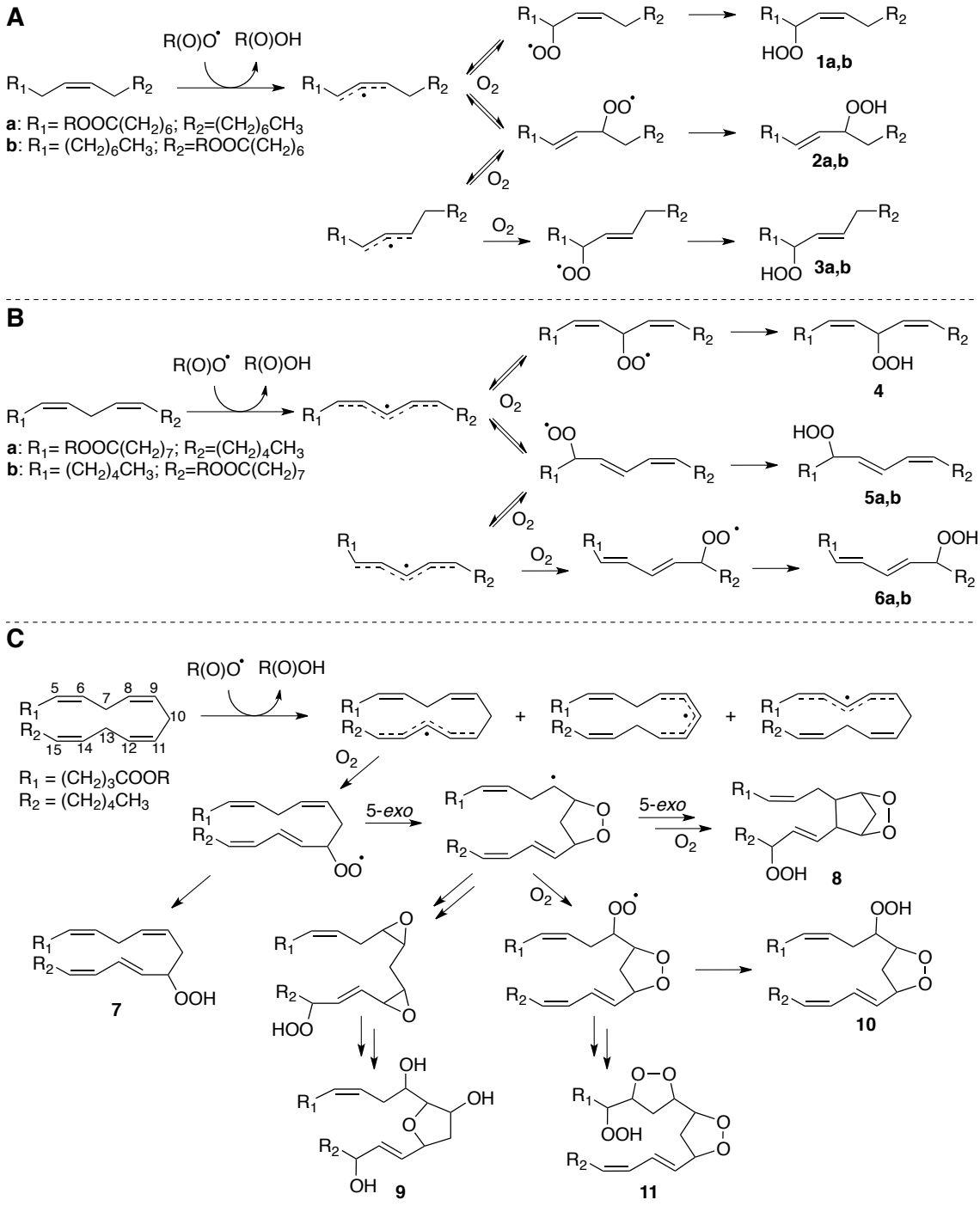

atom donor that can compete with the rapid β-fragmentation of the 11-peroxyl radical ($k_\beta = 1.9\times10^6$ s^{-1}).[63] The reversible addition of oxygen is also a competing factor, albeit with slower k_β, in the 9- and 13-peroxyl radicals (k_β = 690 s^{-1}).[64] Thus, the initially formed (kinetic) *cis,trans* products can rearrange to give (thermodynamic) *trans,trans* products (**6a** and **6b**).

Autoxidation product distributions become even more complex for higher polyunsaturated substrates. For example, initial H-atom abstraction from arachidonic acid (and its esters) can take place at any of the three bisallylic positions (Scheme 1.8C), and subsequent addition of oxygen may then take place at the (kinetic) 7-, 10- or 13-positions or the (thermodynamic) 5-, 8-, 9-, 11-, 12- or 15-positions, analogous to linoleate. However, the intermediate peroxyl radicals face several competing reaction pathways. In addition to H-atom abstraction (propagation) to give hydroperoxides (*e.g.* 11-hydroperoxyeicosatetraenoate **7**), the peroxyl radicals may also undergo 5-*exo* cyclization[65] with a rate constant of *ca.* 8×10^2 s^{-1}.[66] From the initially-formed endoperoxide, ring-opening, addition of oxygen or further cyclization pathways are accessible. These are just a few of the possible fates from initial oxygen addition at the 11-position, and some of the possible products include isoprostanes (e.g. **8**), isofurans (e.g. **9**) and mono- and polycyclic endoperoxides (e.g. **10** and **11**, respectively). A more detailed presentation of the various oxidation products that are observed in the autoxidation of arachidonic acid and its esters is available elsewhere.**

Similarly to the fatty acids, the introduction of further unsaturation in sterols leads to both increased oxidizability and ever more complicated product distributions.[2] 7-Dehydrocholesterol (7-DHC), a biosynthetic precursor to both cholesterol and vitamin D, builds up in patients with Smith-Lemli-Opitz syndrome (SLOS), and the formation of 7-DHC oxidation products has been linked to the pathogenesis of the disease.[1,9] 7-DHC is the most reactive lipid H-atom donor investigated to date with a k_p of 2260 M^{-1} s^{-1},[14b] and its autoxidation gives a complex mixture of oxysterol products

** The autoxidation of cholesterol is revisited in Chapters 2 and 3. Prior to this work, the consensus in the literature was that the major (if not, only) hydroperoxide product of cholesterol autoxidation was cholesterol 7-hydroperoxide (**15** in Scheme 1.9**).**

(Scheme 1.9B).[67] Similar to the aforementioned lipids, the autoxidation of 7-DHC begins with an initial H-atom abstraction at an allylic position (the 9-position being the most labile), and a subsequent addition of oxygen at the 5-, 7- or 9-positions. Analogous to arachidonate autoxidation, the products derived from oxygen addition at C7 are only observed in the presence of a good H-atom donor, due to β-fragmentation of the peroxyl radical.[68] The peroxyl radicals derived from C5- or C9-addition can subsequently undergo a 5-*exo* cyclization,[69] followed by either intramolecular homolytic substitution to give epoxide **16**, or a second addition of oxygen giving rise to the two major endoperoxide-hydroperoxide products (**17**).[67,68]

Scheme 1.9. Product formation in the autoxidation of cholesterol (A) and 7-dehydrocholesterol (B).

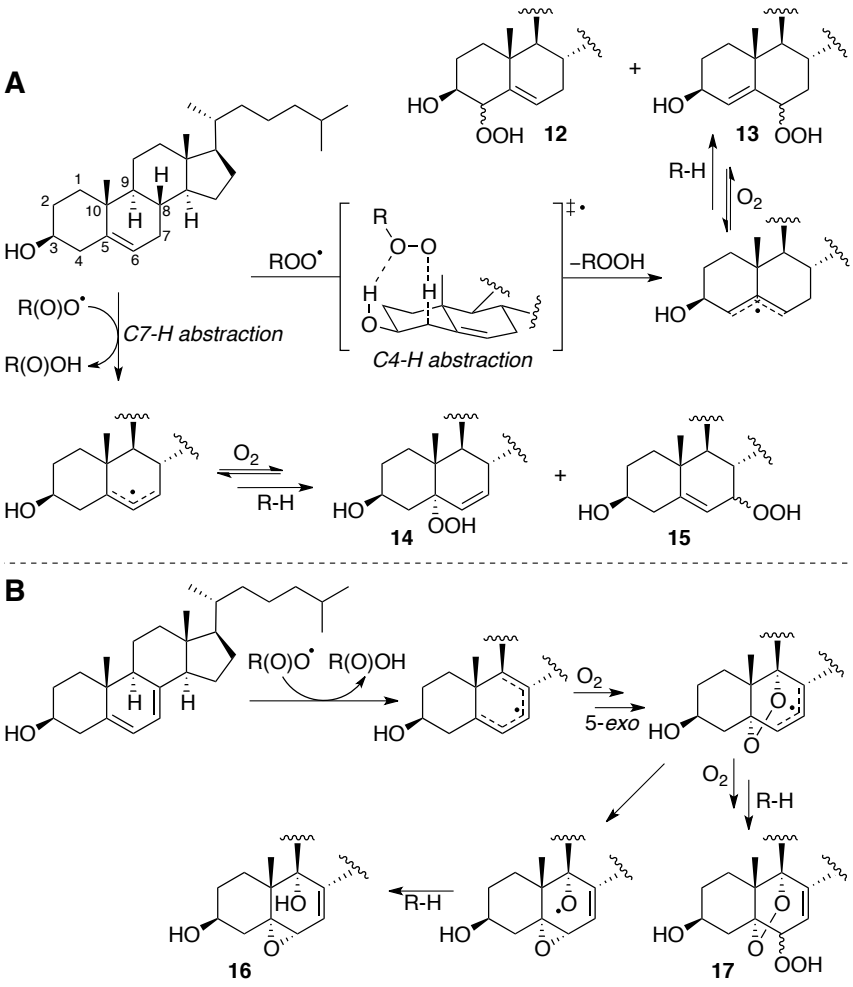

1.3.2 Peroxyl radical addition in lipid peroxidation

An alternative mechanism by which lipids autoxidize involves rate-determining addition of peroxyl radicals to the unsaturations in lipids (Scheme 1.10). Although this reaction is well known in the hydrocarbon autoxidation literature – best exemplified by the autoxidation of styrene, which results in oligomers of styrene and O_2 (Eq. 1.31) – it is far less prominent in the lipid peroxidation literature. It is known to take place in sterol autoxidation, resulting in sterol-5,6-epoxides from cholesterol via Eq. 1.32[2,70] or from 7-DHC via Eq. 1.33.[67] In contrast, comparatively few reports exist on peroxyl radical addition to fatty acids, which implies that HAT from polyunsaturated lipids is much faster than addition (this will be discussed in detail in Chapters 3 and 4). Interestingly, Stein and co-workers reported that epoxide products predominate over hydroperoxides when linoleic acid is autoxidaized in a monolayer adsorbed onto silica gel (though not in bulk solution).[71] To our knowledge, this is the only direct evidence for epoxide formation due to the autoxidation of a fatty acid. There have been some reports of various lipid-derived epoxides detected in humans and other mammals,[72-74] hinting that peroxyl radical addition may be able to compete with HAT under certain conditions, although an enzymatic origin for these compounds could not be excluded. Since peroxyl radical addition results – at least initially – in the formation of a carbon-centered radical, the stability of the radical formed should dictate the competition between the two pathways. Therefore, conjugated dienes (e.g. conjugated linoleic acid) may be expected to be better substrates for peroxyl radical addition than linoleic acid. Indeed, cardiolipin – a phospholipid containing four linoleate chains – once oxidized to a conjugated diene (e.g. **5** or **6** in Scheme 1.8), has been proposed to undergo intramolecular peroxyl radical addition by a peroxyl radical on another linoleate chain to yield several byproducts, including lipid epoxides and 4-hydroxynonenal (discussed below).[75]

Scheme 1.10. Examples of peroxyl radical addition reactions.

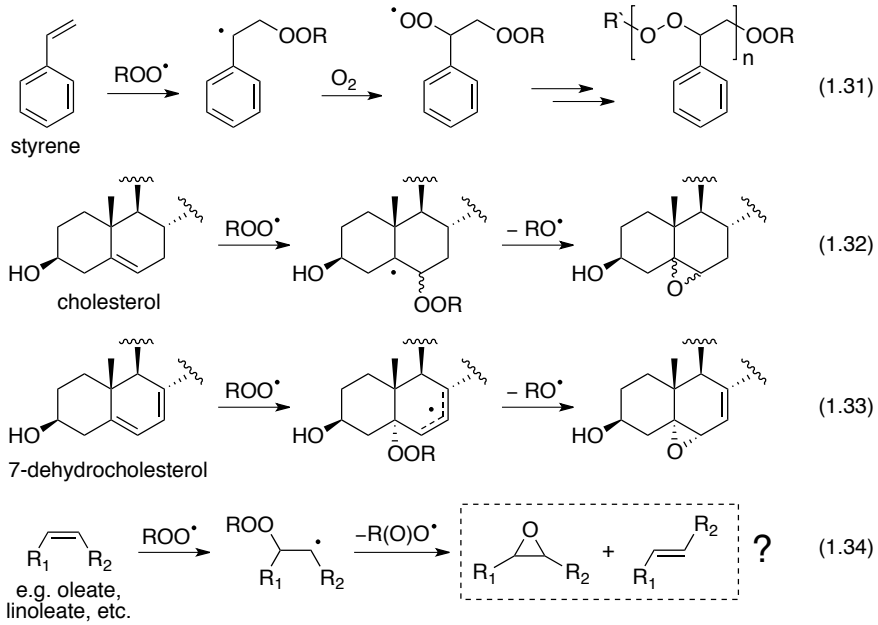

1.3.3 Fates of the Primary Products of Lipid Peroxidation

Although the aforementioned hydroperoxide products are the primary products of autoxidation, it is often compounds derived therefrom that are implicated in their cytotoxicity and/or pathogenicity. In particular, lipid-derived electrophiles (typically aldehydes) can form adducts with DNA, proteins and other nucleophilic biomolecules[76] – reactions that have been implicated in a number of degenerative conditions, including aging, cancer, atherosclerosis, macular degeneration, Alzheimer's and Parkinson's disease. Among the various fates of lipid hydroperoxides, the simplest is the formal dehydration of a secondary hydroperoxide to give the corresponding ketone (e.g. the conversion of **15** to 7-ketocholesterol, the commonly used biomarker for cholesterol autoxidation).[77-79] Various mechanisms can contribute to ketone formation (Scheme 1.11A), including H-atom abstraction from the carbon bearing the hydroperoxide and expulsion of a hydroxyl radical.[80] Peroxidic O-O bonds can also be cleaved by homolysis or one electron reduction (e.g. with Fe^{2+}) leading to carbonyls and chain scission products.[81] A related sequence of reactions is likely responsible for the formation of

malondialdehyde (MDA), a potent mutagen,[82,83] from isoprostanes (e.g. **8**).[84] A possible mechanism involves the initial (reversible) homolysis of the endoperoxide O-O bond, which would trigger two successive α-cleavage steps to form the dialdehyde (Scheme 1.11B).

Scheme 1.11. Fates of primary products of lipid autoxidation. A) Alcohol, ketone or aldehyde formation from a hydroperoxide. B) Formation of malondialdehyde (MDA) from a bicyclic endoperoxide derived from arachidonate autoxidation. C) Formation of 4-hydroxynonenal (4-HNE) from linoleate hydroperoxide **5a** by Hock fragmentation followed by further autoxidation. D) Formation of secosterols **18** and **19** by Hock fragmentation of cholesterol 5-hydroperoxide (**14**).

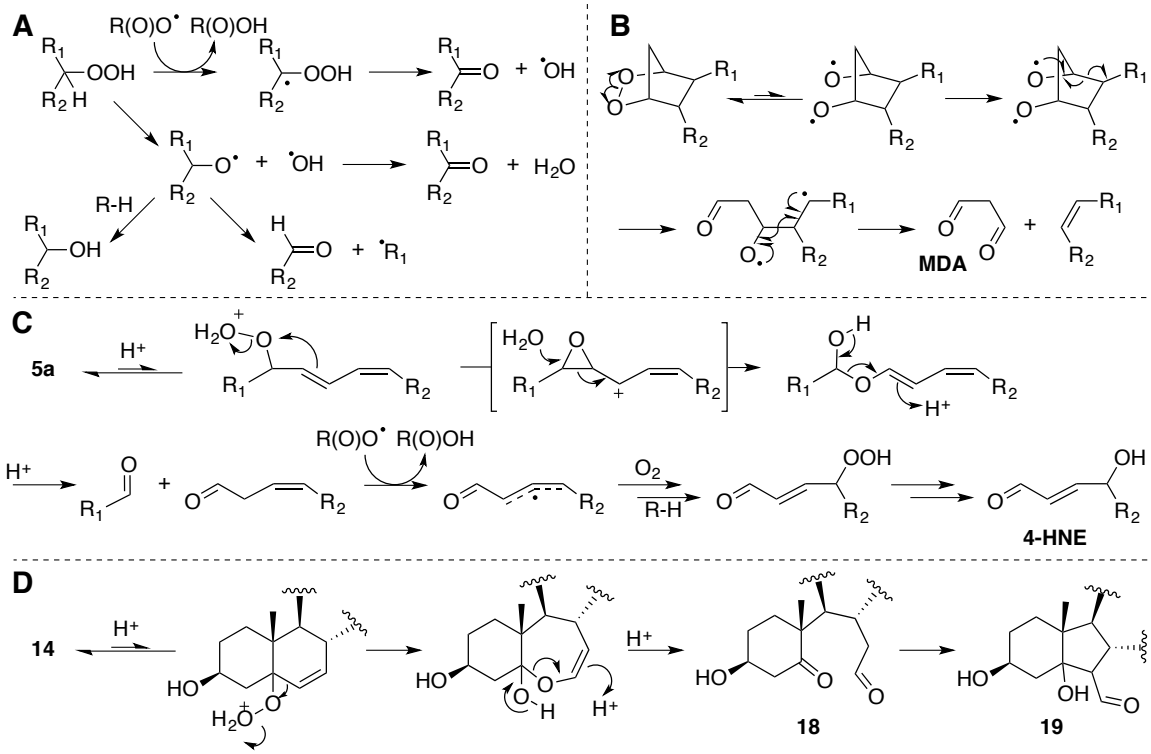

Hock fragmentation is another common fate of hydroperoxides, and is perhaps most well known for its role in the industrial synthesis of acetone and phenol following autoxidation of cumene to cumene hydroperoxide. Hock fragmentation may play an important role *in vivo* as well. An example involves the toxic electrophile 4-hydroxynonenal (4-HNE), which is known to adduct a variety of cellular nucleophiles.[85-87] 4-HNE formation (aside from the cardiolipin-derived 4-HNE

discussed above) is believed[88] to occur through either Hock fragmentation then further autoxidation of linoleate-derived hydroperoxide **5a** (*cf.* Scheme 1.11C) or *vice versa* of **5b**. Sterol-derived hydroperoxides undergo Hock fragmentation as well. Secosterols **18** and **19** have been linked to cardiovascular disease,[26,31] cancer,[32] and various forms of neurodegeneration.[30,33,34,89] Their formation *in vivo* is likely due to Hock fragmentation of cholesterol hydroperoxides, as we have demonstrated for both chol 5α-OOH[29] (*cf.* Scheme 1.11D) and 6β-OOH[48] (which will be discussed in detail in Chapter 2). It follows that similar transformations could take place from chol 4-OOH and chol 7-OOH – or hydroproxides derived from 7-DHC – which would give rise to unique secosterols, but this remains unexplored.

1.4 Summary

Our fundamental chemical understanding of lipid peroxidation has advanced considerably over the past 30 years; it is now possible to look at the structure of a given fatty acid or sterol and anticipate the rate at which it will autoxidize, and predict which products will form under different conditions (i.e. the presence or absence of radical-trapping antioxidants or other good H-atom donors). Nevertheless, some lingering questions remain, e.g. what are the structural requirements that make peroxyl radical addition to double bonds competitive with H-atom abstraction? And, given the massive kinetic isotope effects in the rate-limiting step of lipid peroxidation, how important is quantum mechanical tunnelling in this competition? In contrast to the basic chemistry, our understanding of the role of lipid peroxidation products in biology, and more specifically disease pathogenesis, still lags significantly behind. Although it is widely acknowledged that electrophiles derived from lipid hydroperoxides can adduct cellular nucleophiles, much remains to be learned of which electrophiles derive from which primary oxidation products, and what proteins they target in the cell. Since electrophilic fragmentation products with vastly different physical properties (e.g. solubility) can be formed (e.g. malondialdehyde *vs.* 4-hydroxynonenal *vs.* Secosterol A/B), it is likely

that they interact with distinct members of the proteome – differentially impacting cell growth, differentiation and death. For that matter, it is likely that many of the electrophiles that arise from fragmentation of lipid hydroperoxides are yet unidentified, and the mechanisms responsible for the formation of those that we do know about remain a matter of some debate. Although the accumulation of oxidized lipids has been linked to cell death through ferroptosis, it remains to be seen whether a link exists between this and pathophysiological events, such as in ischemic reperfusion injury or neurodegenerative disease. The field promises to remain a very exciting place to learn for some time!

1.5 Research Objectives

1.5.1 Cholesterol Autoxidation Revisited

Following the controversial reports that two so-called "atheronal" compounds (also called secosterols) were produced due to endogenous ozone production (discussed in section 1.1.3), we became interested in revisiting cholesterol autoxidation. The atheronals were first discovered *in vivo* in 27therosclerotic plaques[26] – hence their namesake – and the atheronals were subsequently implicated in the pathogenesis of various degenerative diseases.[30-34] Their presence *in vivo* and pathogenic potential were not the focus of the controversy, but rather their mechanism of production. Our group showed that the atheronal compounds could also be formed from the (acid catalyzed) Hock fragmentation of cholesterol 5-hydroperoxide.[29] Thus, the atheronals could be produced directly from cholesterol ozonolysis, or via the intermediacy of cholesterol 5-hydroperoxide which is the major product of cholesterol oxidation by singlet oxygen. Neither of these oxidants are abundant *in vivo*; therefore we considered whether there could be an alternative mechanism for their production. We wondered whether cholesterol 5-hydroperoxide could be produced from cholesterol autoxidation, even in minor amounts, in the presence of a good H-atom donor. Thus the objectives of this work (Chapters 2 and 3) were to:

1. Develop an analytical technique to study cholesterol autoxidation with sufficient sensitivity to detect minor products;

2. Characterize the product distribution of cholesterol autoxidation in the presence of increasing amounts of H-atom donor, to determine if cholesterol 5-hydroperoxide is produced; and

3. Support the experimental findings with theoretical calculations to garner mechanistic insight.

1.5.2 Tunnelling in H-Atom Abstractions by Peroxyl Radicals

Following the results of the study on cholesterol autoxidation, which revealed an even more complex mechanism than had been originally expected, we were interested in further exploring the significance of tunnelling in H-atom abstractions by peroxyl radicals. In particular, we were interested in exploring the significance of H-atom tunnelling and its impact on the mechanism of autoxidation of unsaturated substrates, which may also react via peroxyl radical addition to the double bond. In the intervening time, the publication of several accounts of tunnelling in hydrocarbon autoxidation (e.g. tetralin,[57] linoleate,[51,52] and 7-dehydrocholesterol[53]) further piqued our interest. The objectives of this work (Chapter 4) were to:

1. Study the H-atom transfer reactivity of broader classes of compounds computationally, to assess whether trends were easily predicted, and to benchmark computational approaches where complimentary experimental data existed;

2. Identify potential substrates where the experimental investigation of kinetic isotope effects (k_H/k_D) would be feasible analytically; and

3. Determine if tunnelling is more prevalent across H-atom abstractions by peroxyl radicals, or if the recent reports were somehow unique cases.

1.5.3 Redox Chemistry of Selenenic Acids

Previous work in our group had investigated the redox chemistry of sulfenic acids using the persistent (bulky) triptycenesulfenic acid (TrpSOH).[90] As selenenic acids are relevant both biologically (e.g. glutathione peroxidase) and in synthesis (e.g. syn elimination of alkyl selenoxides), but are typically not persistent enough to study, we wondered if a similar approach might be effective to study the redox properties of triptyceneselenenic acid (TrpSeOH). Furthermore, purely from the perspective of academic intrigue, we were interested in a fundamental comparison of the chalcogen series of ROOH vs. RSOH vs. RseOH. The objectives of this work (Chapter 5) were to:

1. Synthesize triptyceneselenenic aicd by modifying the literature procedure;

2. Study the redox properties of triptyceneselenenic acid, including its oxidation potential, O-H BDE, and the rate of H-atom transfer to peroxyl radicals;

3. Compare the redox properties of the selenenic acid to sulfenic acid and hydroperoxide, and explore the systems computationally to help explain experimental observations.

1.5.4 Secondary Orbital Interactions in H-Atom Abstractions by Peroxyl Radicals

Following the experimental support for a significant acceleration of HAT reactivity in RseOH as compared to RSOH due to a secondary orbital interaction, we were interested in further exploring this phenomenon. Guided mainly by academic intrigue, we set out to explore broader classes of compounds for H-atom transfer reactivity with peroxyl radicals, to gain more insight into the effect of secondary orbital interactions. The objectives of this work (Chapter 6) were to:

1. Determine a theoretical approach to calculate bond strengths and H-atom transfer transition states with sufficient accuracy, across a broad class of compounds;

2. Develop a library of computed BDEs and HAT rate constants, and explore deviations in linearity in Evans-Polanyi correlations (plot of BDE vs. log *k*), and outliers thereto; and

3. Determine whether the effect of secondary orbital interactions on the H-atom transfer rate constant can be quantified and/or predicted.

1.6 References

(1) Xu, L.; Porter, N. A. *Free Radic. Res.* **2015**, *49*, 835.

(2) Yin, H.; Xu, L.; Porter, N. A. *Chem. Rev.* **2011**, *111*, 5944.

(3) Niki, E. *Free Radic. Biol. Med.* **2009**, *47*, 469.

(4) Angeli, J.; Schneider, M.; Proneth, B.; Tyurina, Y. Y. *Nature Cell Biol.* **2014**, *16*, 1180.

(5) Dixon, S. J.; Lemberg, K. M.; Lamprecht, M. R.; Skouta, R.; Zaitsev, E. M.; Gleason, C. E.; Patel, D. N.; Bauer, A. J.; Cantley, A. M.; Yang, W. S.; Morrison, B., III; Stockwell, B. R. *Cell* **2012**, *149*, 1060.

(6) For example, see: (a) Valgimigli, L.; Pratt, D. A. *Acc. Chem. Res.* **2015**, *48*, 966, (b) Ingold, K. U.; Pratt, D. A. *Chem. Rev.* **2014**, *114*, 9022.

(7) For example, see: (a) Krumova, K.; Cosa, G. Fluorogenic probes for imaging reactive oxygen species. In *Photochemistry*; Royal Society of Chemistry: Cambridge, 2013; Vol. 41, pp 279, (b) Winterbourn, C. C. *Biochim. Biophys. Acta, Gen. Subj.* **2014**, *1840*, 730, (c) Li, B.; Pratt, D. A. *Free Radic. Biol. Med.* **2015**, *82*, 187.

(8) Pratt, D. A.; Tallman, K. A.; Porter, N. A. *Acc. Chem. Res.* **2011**, *44*, 458.

(9) Porter, N. A. *J. Org. Chem.* **2013**, *78*, 3511.

(10) Lee, R.; Gryn'ova, G.; Ingold, K. U.; Coote, M. L. *Phys. Chem. Chem. Phys.* **2016**, *18*, 23673.

(11) Haeggström, J. Z.; Funk, C. D. *Chem. Rev.* **2011**, *111*, 5866.

(12) Rouzer, C. A.; Marnett, L. J. *Chem. Rev.* **2011**, *111*, 5899.

(13) Pryor, W. A.; Houk, K. N.; Foote, C. S.; Fukuto, J. M.; Ignarro, L. J.; Squadrito, G. L.; Davies, K. J. A. *Am. J. Physiol. Regul. Integr. Comp. Physiol.* **2006**, *291*, R491.

(14) The k_p of oleate and linoleate were determined at 30°C, see: (a) Howard, J. A.; Ingold, K. U. *Can. J. Chem.* **1967**, *45*, 793. The rest were determined at 37°C, see: (b) Xu, L.; Davis, T. A.; Porter, N. A. *J. Am. Chem. Soc.* **2009**, *131*, 13037.

(15) Hayyan, M.; Hashim, M. A.; AlNashef, I. M. *Chem. Rev.* **2016**, *116*, 3029.

(16) Indo, H. P.; Yen, H.-C.; Nakanishi, I.; Matsumoto, K.-I.; Tamura, M.; Nagano, Y.; Matsui, H.; Gusev, O.; Cornette, R.; Okuda, T.; Minamiyama, Y.; Ichikawa, H.; Suenaga, S.; Oki, M.; Sato, T.; Ozawa, T.; Clair, D. K. S.; Majima, H. J. *J. Clin. Biochem. Nutr.* **2015**, *56*, 1.

(17) Bielski, B. H. J.; Cabelli, D. E.; Arudi, R. L.; Ross, A. B. *J. Phys. Chem. Ref. Data* **1985**, *14*, 1041.

(18) Pryor, W. A.; Squadrito, G. L. *Am. J. Physiol.* **1995**, *268*, L699.

(19) Luo, Y.-R. *Handbook of Bond Dissociation Energies in Organic Compounds*; CRC Press LLC: Boca Raton, 2009.

(20) Bäumler, W.; Regensburger, J.; Knak, A.; Felgenträger, A.; Maisch, T. *Photochem. Photobiol. Sci.* **2011**, *11*, 107.

(21) Kanner, J.; German, J. B.; Kinsella, J. E. *Crit. Rev. Food Sci. Nutr.* **1987**, *25*, 317.

(22) Onyango, A. N. *Oxid. Med. Cell. Longev.* **2016**, 1.

(23) Kettle, A. J.; Clark, B. M.; Winterbourn, C. C. *J. Biol. Chem.* **2004**, *279*, 18521.

(24) Smith, L. L. *Free Radic. Biol. Med.* **2004**, *37*, 318.

(25) Sies, H. *Angew. Chem. Int. Ed.* **2004**, *43*, 3514.

(26) Wentworth, P.; Nieva, J.; Takeuchi, C.; Galvé, R.; Wentworth, A.; Dilley, R. B.; DeLaria, G. A.; Saven, A.; Babior, B. M.; Janda, K. D.; Eschenmooser, A.; Lerner, R. A. *Science* **2003**, *302*, 1053.

(27) Pulfer, M. K.; Murphy, R. C. *J. Biol. Chem.* **2004**, *279*, 26331.

(28) Pryor, W. A.; Squadrito, G. L.; Friedman, M. *Free Radic. Biol. Med.* **1995**, *19*, 935.

(29) Brinkhorst, J.; Nara, S. J.; Pratt, D. A. *J. Am. Chem. Soc.* **2008**, *130*, 12224.

(30) Zhang, Q.; Powers, E. T.; Nieva, J.; Huff, M. E.; Dendle, M. A.; Bieschke, J.; Glabe, C. G.; Eschenmooser, A.; Wentworth, P., Jr.; Lerner, R. A.; Kelly, J. W. *Proc. Natl. Acad. Sci. USA* **2004**, *101*, 4752.

(31) Takeuchi, C.; Galvé, R.; Nieva, J.; Witter, D. P.; wentworth, A. D.; Troseth, R. P.; Lerner, R. A.; Wentworth, P. *Biochemistry* **2006**, *45*, 7162.

(32) Nieva, J.; Song, B.-D.; Rogel, J. K.; Kujawara, D.; Altobel, L., III; Izharrudin, A.; Boldt, G. E.; Grover, R. K.; wentworth, A. D.; Wentworth, P., Jr. *Chem. Biol.* **2011**, *18*, 920.

(33) Bosco, D. A.; Fowler, D. M.; Zhang, Q. H.; Nieva, J.; Powers, E. T.; Wentworth, P.; Lerner, R. A.; Kelly, J. W. *Nat. Chem. Biol.* **2006**, *2*, 249.

(34) Cygan, N. K.; Scheinost, J. C.; Butters, T. D.; Wentworth, P., Jr. *Biochemistry* **2011**, *50*, 2092.

(35) Valgimigli, L.; Pratt, D. A. *Antioxidants in Chemistry and Biology*; John Wiley & Sons, Ltd: Chichester, UK, 2011.

(36) Ingold, K. U.; Pratt, D. A. *Chem. Rev.* **2014**, *114*, 9022.

(37) Poon, J.-F.; Pratt, D. A. *Acc. Chem. Res.* **2018**, *51*, 1996.

(38) Litwinienko, G.; Ingold, K. U. *Acc. Chem. Res.* **2007**, *40*, 222.

(39) Burton, G. W.; Ingold, K. U. *Acc. Chem. Res.* **1986**, *19*, 194.

(40) Beckwith, A. L. J. *Chem. Soc. Rev.* **1993**, *22*, 143.

(41) Howard, J. A.; Scaiano, J. C. *Oxyl-, peroxyl- and related radicals*; Fischer, H., Ed.; Landolt-Bornstein New Series, Springer-Verlag: Berlin, 1984; Vol. 13 d.

(42) Zavitsas, A. A. *J. Am. Chem. Soc.* **1972**, *94*, 2779.

(43) Zavitsas, A. A.; Chatgilialoglu, C. *J. Am. Chem. Soc.* **1995**, *117*, 10645.

(44) Giese, B. *Angew. Chem. Int. Ed.* **1983**, *22*, 753.

(45) Kaushal, P.; Mok, P. L. H.; Roberts, B. P. *J. Chem. Soc., Perkin Trans. 2* **1990**, 1663.

(46) Isborn, C.; Hrovat, D. A.; Borden, W. T.; Mayer, J. M.; Carpenter, B. K. *J. Am. Chem. Soc.* **2005**, *127*, 5794.

(47) Hu, D.; Pratt, D. A. *Chem. Commun.* **2010**, *46*, 3711.

(48) Zielinski, Z. A. M.; Pratt, D. A. *J. Am. Chem. Soc.* **2016**, *138*, 6932.

(49) Vaidya, V.; Ingold, K. U.; Pratt, D. A. *Angew. Chem. Int. Ed.* **2008**, *48*, 157.

(50) Zielinski, Z.; Presseau, N.; Amorati, R.; Valgimigli, L.; Pratt, D. A. *J. Am. Chem. Soc.* **2014**, *136*, 1570.

(51) Hill, S.; Lamberson, C. R.; Xu, L.; To, R.; Tsui, H. S.; Shmanai, V. V.; Bekish, A. V.; Awad, A. M.; Marbois, B. N.; Cantor, C. R.; Porter, N. A.; Clarke, C. F.; Shchepinov, M. S. *Free Radic. Biol. Med.* **2012**, *53*, 893.

(52) Lamberson, C. R.; Xu, L.; Muchalski, H.; Montenegro-Burke, J. R.; Shmanai, V. V.; Bekish, A. V.; McLean, J. A.; Clarke, C. F.; Shchepinov, M. S.; Porter, N. A. *J. Am. Chem. Soc.* **2014**, *136*, 838.

(53) Muchalski, H.; Xu, L.; Porter, N. A. *Org. Biomol. Chem.* **2015**, *13*, 1249.

(54) Yang, W. S.; Kim, K. J.; Gaschler, M. M.; Patel, M.; Shchepinov, M. S.; Stockwell, B. R. *Proc. Natl. Acad. Sci. USA* **2016**, *113*, E4966.

(55) Bell, R. P. *Chem. Soc. Rev.* **1974**, *3*, 513.

(56) Ley, D.; Gerbig, D.; Schreiner, P. R. *Org. Biomol. Chem.* **2012**, *10*, 3769.

(57) For example, see: Muchalski, H.; Levonyak, A. J.; Xu, L.; Ingold, K. U.; Porter, N. A. *J. Am. Chem. Soc.* **2015**, *137*, 94 and the references discussed therein.

(58) Porter, N. A.; Wujek, J. S. *J. Org. Chem.* **1987**, *52*, 5085.

(59) Beckwith, A. L. J.; Davies, A. G.; Davison, I. G. E.; Maccoll, A.; Mruzek, M. H. *J. Chem. Soc., Perkin Trans. 2* **1989**, 815.

(60) Pratt, D. A.; Porter, N. A. *Org. Lett.* **2003**, *5*, 387.

(61) Pratt, D. A.; Mills, J. H.; Porter, N. A. *J. Am. Chem. Soc.* **2003**, *125*, 5801.

(62) Porter, N. A.; Mills, K. A.; Carter, R. L. *J. Am. Chem. Soc.* **1994**, *116*, 6690.

(63) Tallman, K. A.; Pratt, D. A.; Porter, N. A. *J. Am. Chem. Soc.* **2001**, *123*, 11827.

(64) Tallman, K. A.; Roschek, B.; Porter, N. A. *J. Am. Chem. Soc.* **2004**, *126*, 9240.

(65) Porter, N. A.; Funk, M. O.; Gilmore, D.; Isaac, R.; Nixon, J. *J. Am. Chem. Soc.* **1976**, *98*, 6000.

(66) Porter, N. A.; Lehman, L. S.; Weber, B. A. *J. Am. Chem. Soc.* **1981**, *103*, 6447.

(67) Xu, L.; Korade, Z.; Porter, N. A. *J. Am. Chem. Soc.* **2010**, *132*, 2222.

(68) Xu, L.; Porter, N. A. *J. Am. Chem. Soc.* **2014**, *136*, 5443.

(69) It was noted in Ref. 67 that the 5- and 9-peroxyl radicals could not be trapped even in the presence of 1.0 M α-tocopherol; therefore, the subsequent 5-*exo* cyclization is either exceptionally fast ($> 3.5\times10^6$ s^{-1}), or the addition/cyclization may be concerted. Given that secondary orbital interactions stabilize weakly bound substrate-O_2 complexes in the addition of oxygen to oleate- and linoleate-derived radicals (see Ref. 46), the analogous complex with the 7-DHC-derived pentadienyl radical may facilitate the concerted reaction.

(70) Smith, L. L. *Cholesterol Autoxidation*; Springer US: Boston, MA, 1981.

(71) Wu, G.-S.; Stein, R. A.; Mead, J. F. *Lipids* **1977**, *12*, 971.

(72) Sevanian, A.; Mead, J. F.; Stein, R. A. *Lipids* **1979**, *14*, 634.

(73) Tsikas, D.; Sawa, M.; Brunner, G.; Gutzki, F. M.; Meyer, H. H.; Frolich, J. C. *J. Chromatogr. B Analyt. Technol. Biomed. Life Sci.* **2003**, *784*, 351.

(74) Tsikas, D.; Mitschke, A.; Gutzki, F. M.; Meyer, H. H.; Frolich, J. C. *J. Chromatogr. B Analyt. Technol. Biomed. Life Sci.* **2004**, *804*, 403.

(75) Liu, W.; Porter, N. A.; Schneider, C.; Brash, A. R.; Yin, H. *Free Radic. Biol. Med.* **2011**, *50*, 166.

(76) Marnett, L. J.; Riggins, J. N.; West, J. D. *J. Clin. Invest.* **2003**, *111*, 583.

(77) Niki, E. *Biochim. Biophys. Acta, Gen. Subj.* **2014**, *1840*, 809.

(78) Lee, C.-Y. J.; Huang, S. H.; Jenner, A. M.; Halliwell, B. *Free Radic. Biol. Med.* **2008**, *44*, 1314.

(79) Iuliano, L.; Micheletta, F.; Natoli, S.; Ginanni Corradini, S.; Iappelli, M.; Elisei, W.; Giovannelli, L.; Violi, F.; Diczfalusy, U. *Anal. Biochem.* **2003**, *312*, 217.

(80) Frenette, M.; Scaiano, J. C. *J. Am. Chem. Soc.* **2008**, *130*, 9634.

(81) Girotti, A. W. *J. Lipid Res.* **1998**, *39*, 1529.

(82) Mukai, F. H.; Goldstein, B. D. *Science* **1976**, *191*, 868.

(83) Marnett, L. J. *Carcinogenesis* **2000**, *21*, 361.

(84) Pryor, W. A.; Stanley, J. P. *J. Org. Chem.* **1975**, *40*, 3615.

(85) Esterbauer, H.; Schaur, R. J.; Zollner, H. *Free Radic. Biol. Med.* **1991**, *11*, 81.

(86) Ullery, J. C.; Marnett, L. J. *Biochim. Biophys. Acta, Biomembr.* **2012**, *1818*, 2424.

(87) Codreanu, S. G.; Ullery, J. C.; Zhu, J.; Tallman, K. A.; Beavers, W. N.; Porter, N. A.; Marnett, L. J.; Zhang, B.; Liebler, D. C. *Mol. Cell. Proteomics* **2014**, *13*, 849.

(88) Schneider, C.; Tallman, K. A.; Porter, N. A.; Brash, A. R. *J. Biol. Chem.* **2001**, *276*, 20831.

(89) Usui, K.; Hulleman, J. D.; Paulsson, J. F.; Siegel, S. J.; Powers, E. T.; Kelly, J. W. *Proc. Natl. Acad. Sci. USA* **2009**, *106*, 18563.

(90) McGrath, A. J.; Garrett, G. E.; Valgimigli, L.; Pratt, D. A. *J. Am. Chem. Soc.* **2010**, *132*, 16759.

Chapter 2: Cholesterol Autoxidation Revisited: Debunking the Dogma Associated with the Most Vilified of Lipids*

2.1 Preface

The longstanding dogma that cholesterol (chol) autoxidation gives chol 7-hydroperoxide (7-OOH) as the sole primary product is shown to be invalid. In fact, the epimers of each of chol 4-OOH, 6-OOH, and 7-OOH are readily formed. Although the C4-H bond that must be cleaved to produce the chol 4-OOH and 6-OOH products is significantly stronger than the C7-H bond, H-atom abstraction from C4 is facilitated by H-bond formation between the attacking peroxyl radical and the 3β-OH. Chol 5α-OOH is also formed, but only in the presence of a good H-atom donor. Chol 5α-OOH and 6-OOH undergo Hock fragmentation to yield the secosterols implicated in cardiovascular and neurodegenerative diseases, suggesting that they are likely to arise simply from autoxidation and not from reactions with O_3 or $^1O_2$. This chapter is presented as it was published in the *Journal of the American Chemical Society* (Zielinski, Z.A.; Pratt, D.A. *J. Am. Chem. Soc.* **2016**, *138*, 6932), with the exception of Section 2.4, which adds a perspective in the context of this Thesis. Please note, this communication was followed by a full article (see Chapter 3) which clarified that the amount of chol 4-OOH reported in the current chapter was overestimated.

2.2 Introduction

Cholesterol (chol) constitutes up to 50% of all lipids present in the plasma membrane (on a molar basis).[1] Its levels, as esters of polyunsaturated fatty acids in circulating low-density lipoprotein (LDL), are an established risk determinant of cardiovascular disease.[2] Furthermore, chol-derived

* This chapter is reproduced with permission from Zielinski, Z.A.; Pratt, D.A. *J. Am. Chem. Soc.* **2016**, *138*, 6932. Copyright 2016 American Chemical Society.

oxidation products (and those of related sterols[3]) have been implicated in the pathogenesis of various degenerative diseases.[4] Of particular interest are the electrophilic secosterols **2.1** and **2.2**:

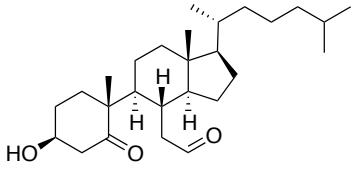

2.1

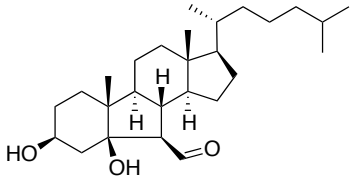

2.2

Secosterols **2.1** and **2.2** are known products of chol ozonolysis and may contribute to the respiratory toxicity of O_3 present in polluted air.[5] More recently, **2.1** and **2.2** were identified following acid-catalyzed derivatization of extracts of atherosclerotic heart tissue[6] and brain tissue of Alzheimer's patients[7] with 2,4-dinitrophenylhydrazine. These results have prompted studies of the pathogenic potential of **2.1** and **2.2** in cardiovascular disease,[8] cancer,[9] and neurodegeneration (including Alzheimer's,[10] Parkinson's[11] and multiple sclerosis[12]), and the highly controversial[13] suggestion that O_3 is formed endogenously.[6]

A short time ago, we demonstrated that the formation of **2.1** and **2.2** is not unique to ozonolysis. In fact, these products also arise upon (acid-catalyzed) Hock fragmentation of chol 5α-hydroperoxide (chol 5α-OOH)[14] – the product of the reaction of chol with $^1O_2$. Of course, if chol 5α-OOH were formed simply from chol autoxidation, no highly energetic oxidants (i.e. O_3 and $^1O_2$) would need to be implicated in the formation of **2.1** and **2.2**. Thus, **2.1** and **2.2** could be considered among the nefarious byproducts of lipid peroxidation, such as 4-hydroxynonenal or malondialdehyde – well known to derive from oxidized linoleic acid (linoleate) and arachidonic acid (arachidonate), respectively.[15] However, a survey of the vast literature on chol autoxidation reveals that the primary products are limited to the epimers of chol 7-OOH,[16] the immediate precursor to 7-hydroxycholesterol (chol 7-OH) and 7-ketocholesterol, frequently identified biomarkers of lipid oxidation.[17]

Scheme 2.1. The mechanism of cholesterol autoxidation.

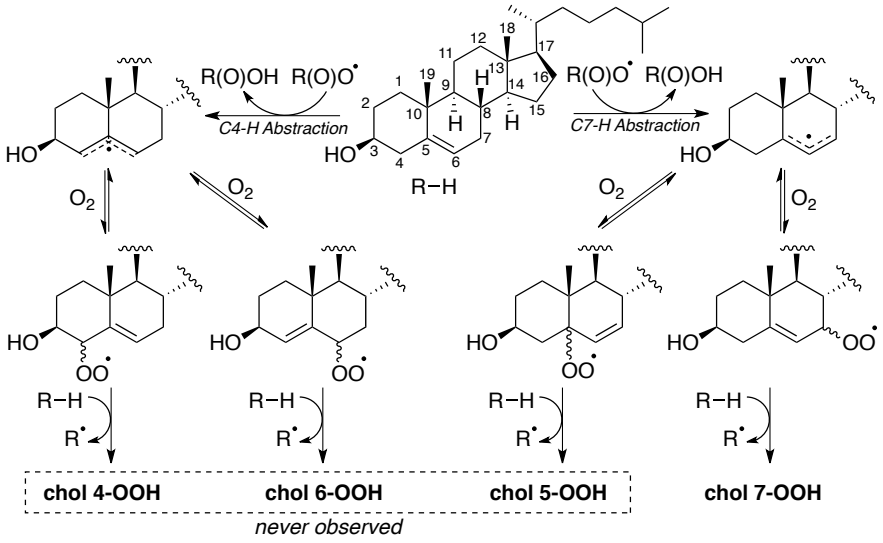

We were admittedly puzzled by this dogma, since Porter has shown that the autoxidation of other monounsaturated lipids, such as oleic acid (oleate), yields hydroperoxides derived from O_2 addition to both ends of the allylic radical intermediate.[18] In principle, chol autoxidation should give eight products (*cf.* Scheme 2.1) resulting from H-atom abstraction from either the C4 or C7 positions, followed by O_2 addition to either end of the respective allylic radical intermediates, on either the α- or β-face of the sterol framework. Since it has been demonstrated that the product distribution arising in autoxidations of polyunsaturated lipids is affected by the reversible addition of O_2 to intermediate radicals, and thus the concentration and identity of potential H-atom donors,[19] we elected to revisit the mechanism of chol autoxidation.

2.3 Results and Discussion

Chol autoxidations were carried out in aerated chlorobenzene (0.5 M) at 37°C for 16 hours, initiated by decomposition of the azo compound MeOAMVN (20 mM). The resultant mixtures were analyzed by normal phase HPLC with APCI-MS/MS detection. In each instance, the samples were first treated with PPh_3 to convert the hydroperoxide products to their corresponding alcohols, which are more

stable to chromatography and MS analysis. Somewhat surprisingly, we observed six primary products (Figure 2.1A). The compounds (chol 4α-OH, 4β-OH, 6α-OH, 6β-OH, 7α-OH and 7β-OH) were identified by comparison with authentic standards, synthesized according to literature precedent, and determined relative to a newly synthesized d_6-chol 5α-OH standard (see Supporting Information, section 2.5.1 for details).

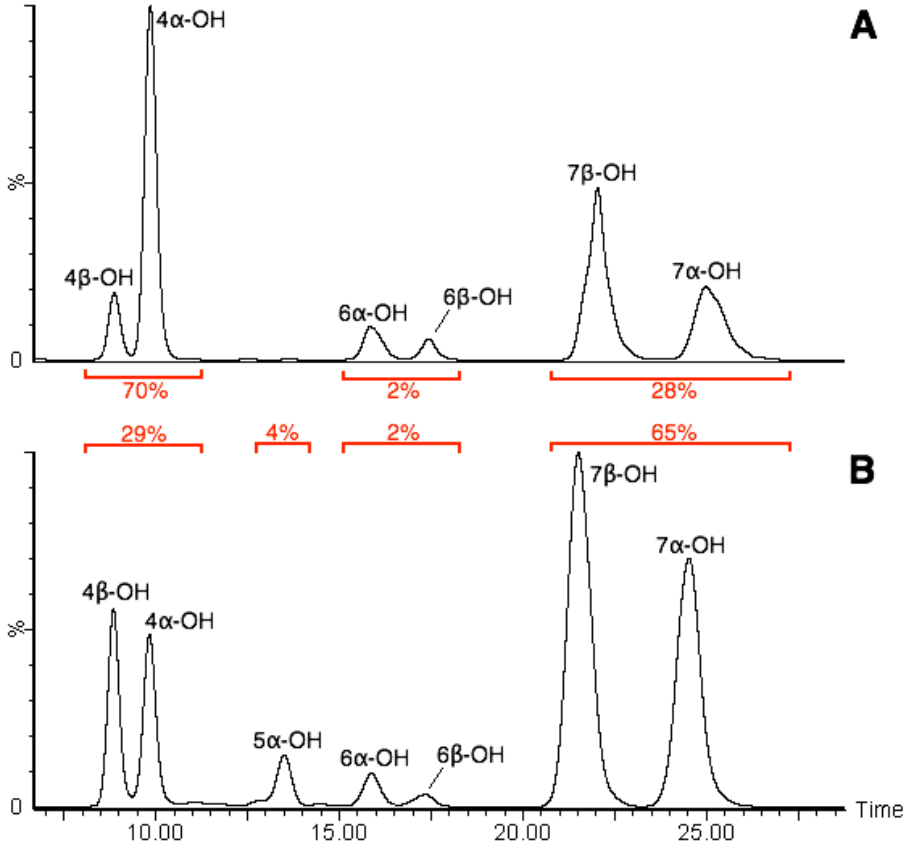

Figure 2.1. Product distributions from MeOAMVN-initiated autoxidations of chol in chlorobenzene at 37°C with no added antioxidant (A) and with 250 mM BDMP (B). Data were obtained by HPLC (95:5 hexane:*i*-PrOH, 1.5 mL/min) with APCI$^+$-MS/MS detection (*m/z* 385.35 → *m/z* 367.37). The alcohols are observed due to pre-treatment with PPh_3.

Based on the mechanism in Scheme 2.1, chol 4-OOH and 6-OOH presumably arise from initial H-atom abstraction from C4 – previously assumed to be an uncompetitive pathway. Indeed, high accuracy CBS-QB3[20] calculations on the A-B ring system of chol suggest that the C4-H bond is

ca. 6 kcal/mol stronger than the C7-H bond (89.0 and 83.2 kcal/mol respectively). However, given that the H-atom abstraction step is likely to be irreversible, the product ratio should be determined by kinetics. We therefore calculated the barriers for each pathway with MeOO• as a model chain-carrying peroxyl radical using the density functional theory step of the CBS-QB3 calculation (B3LYP/CBSB7).[21] α-H abstraction from C7 by MeOO• is predicted to be favoured over β-H abstraction due to steric hindrance imposed from the β-CH_3 at C10. More interestingly, H-atom abstraction from C4 by MeOO• is predicted to be competitive with abstraction from C7; the barrier to β-H abstraction from C4 being lowered by a hydrogen-bonding interaction between the internal oxygen atom of the peroxyl radical and the β-OH group at C3 (*cf.* Figure 2.2). This interaction is relatively unaffected by sterics (i.e. the same trend exists with cyclohexylperoxyl, see Supporting Information, section 2.5.3).

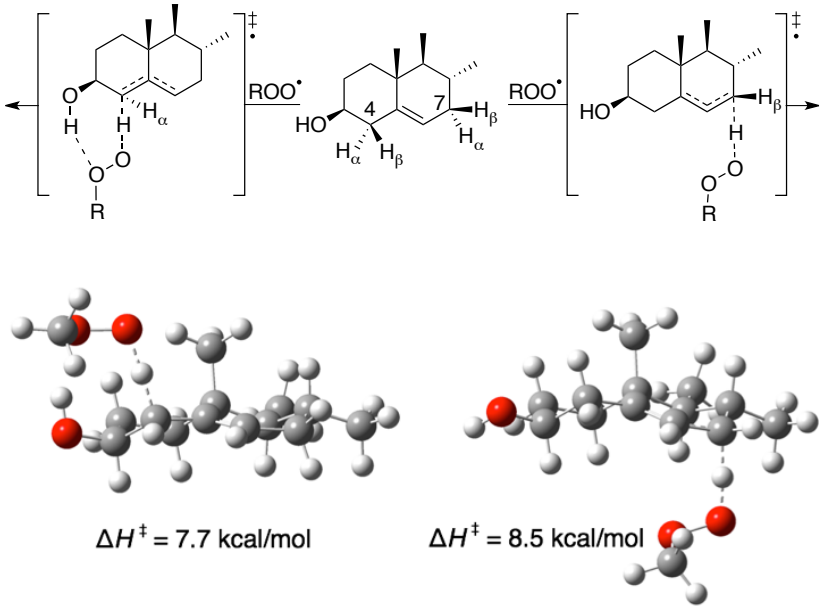

Figure 2.2. Lowest energy transition state structures and associated enthalpic barriers for H-atom abstraction from C4 and C7 (chol numbering) by a methylperoxyl radical.

The foregoing accounts for the observed products in Figure 2.1A, but it remains unclear why no chol 5-OOH products are observed. We wondered if the peroxyl radicals resulting from O_2 addition to C5 were particularly unstable. In fact, calculations suggest that the 5α- and 5β-peroxyl radicals are *ca.* 3 and 6 kcal/mol less stable, respectively, than the peroxyl radicals formed from O_2 addition at the 7-position. It is predicted that the 5β-peroxyl radical is particularly unstable due to a conformational change in the steroid backbone that accompanies O_2 addition (*cf.* Figure 2.3).

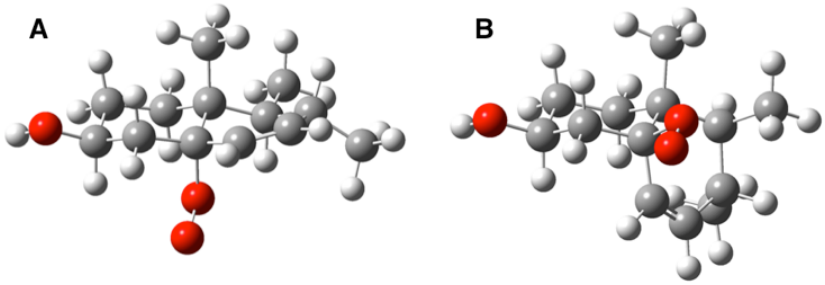

Figure 2.3. Calculated minimum energy structures of models of chol 5α- (A) and 5β- (B) peroxyl radicals.

The relative instability of the peroxyl radicals derived from addition at C5 suggests that they may undergo facile β-fragmentation under the autoxidation conditions to favour the C7 oxidation products at the expense of the C5 oxidations products – an accepted mechanism for the known rearrangement of chol 5α-OOH to 7α-OOH.[22] Thus, in the presence of a good H-atom donor, the C5 peroxyl radicals may be trapped to give chol 5-OOHs (*cf.* Scheme 2.2). It should be pointed out that chol autoxidations carried out *in vitro* typically depended on the H-atom donor being chol itself (k_H = 11 M^{-1} s^{-1});[23] however, chol autoxidation *in vivo* can occur in the presence of far better H-atom donors. For example, α-tocopherol (α-TOH), Nature's premier lipid soluble radical-trapping antioxidant, has $k_H = 3.2 \times 10^6$ $M^{-1}s^{-1}$,[24] and is present within cell membranes and chol-rich lipid rafts.

Hence, product distributions were determined in autoxidations of chol in the presence of 2,2,5,7,8-pentamethyl-6-chromanol (PMC), a truncated α-TOH.

Scheme 2.2. The kinetically-controlled autoxidation of chol enables determination of k_β for chol 5α-OO•.

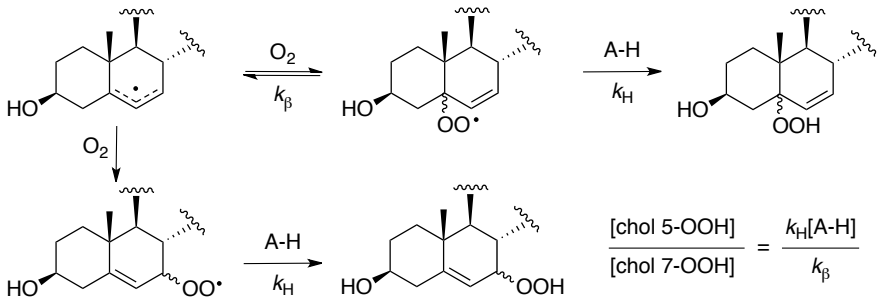

Chol autoxidations to which PMC (25 mM) was added (and analyzed as above) did indeed contain chol 5α-OH – in addition to 4α-OH, 4β-OH, 6α-OH, 6β-OH, 7α-OH and 7β-OH (see Figure 2.8). Since, in principle, a determination of the product distribution as a function of PMC concentration would reveal the rate constant at which the C5 peroxyl radical undergoes β-fragmentation (as in Scheme 2.2), we carried out further autoxidations at higher PMC concentrations. Unfortunately, too little products were formed to reliably quantify. Exchanging PMC for 4-*tert*-butyl-2,6-dimethylphenol (BDMP), a less reactive radical-trapping antioxidant (*vide infra*), chol 5α-OH was again observed (Figure 2.9), but in a lower amount than that observed at the same concentration of PMC. However, upon increasing [BDMP] (250 mM), the ratio of chol 5α-OH/7-OH increased as is shown in Figure 2.1B. Furthermore, the ratio of products was clearly linearly dependent on the concentration of BDMP (Figure 2.4) and from the simple expression in Scheme 2.2 we could obtain $k_\beta = (5.6 \pm 0.1) \times 10^5$ s^{-1} (using $k_H = (1.3 \pm 0.1) \times 10^5$ $M^{-1}s^{-1}$ for BDMP – determined by inhibited autoxidation of styrene,[25] see Supporting Information, section 2.5.1). Similarly, $k_\beta = (8.6 \pm 0.4) \times 10^3$

s^{-1} for chol 4β-OO• could be determined from the ratio of chol 4β-OH/4α-OH with varying BDMP (*cf.* Figure 2.17).

Interestingly, the ratio of products derived from H-atom abstraction from C4 and C7 was also dependent on BDMP concentration (also shown in Figure 2.4). Increasing the BDMP concentration lead to a marked decrease in 4-OH and 6-OH products relative to 5-OH and 7-OH products. This result reflects the increasing contribution of the antioxidant-mediated peroxidation (AMP) mechanism[26] in the autoxidation with increasing [BDMP]. That is, as the concentration of BDMP increases, the BDMP-derived phenoxyl radicals (BDMP•) become the prominent chain-carrying species. Since BDMP• lacks a good H-bond acceptor to interact with the β-OH group at C3, the barrier to abstraction of the C4 β-H is increased relative to that for abstraction at C7. Our calculations suggest that the difference is *ca.* 1.5 kcal/mol.

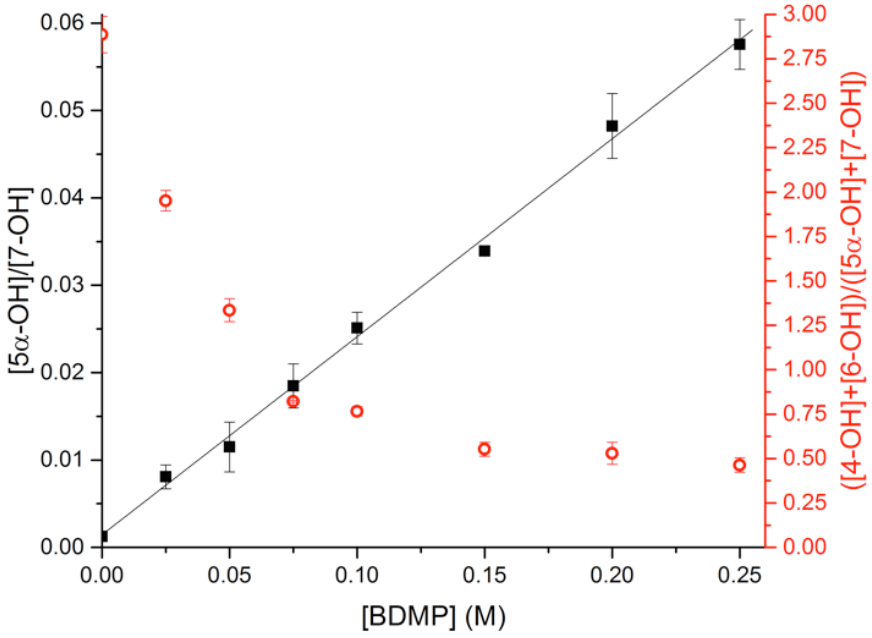

Figure 2.4. Dependence of chol 5α-OH to 7-OH ratio (■) and chol 4-OH and 6-OH to 5α-OH and 7-OH ratio (O) on 4-*tert*-butyl-2,6-dimethylphenol (BDMP) concentration.

The foregoing observations directly address the longstanding speculation about the C4-H abstraction pathway in chol autoxidation.[4] Although both epimers of chol 4-OH have been detected *in vitro*[27] and *in vivo,*[28,29] their formation was only tenuously tied to autoxidation by Diczfalusy and co-workers, who showed that ^{18}O was incorporated into chol 4α-OH and 4β-OH in low density lipoproteins oxidized in an $^{18}O_2$-enriched atmosphere.[29] Interestingly, the ratio of 4α-OH and 4β-OH observed in their experiments was *ca.* 1:1, consistent with the presence of a significant amount of antioxidant in the LDL (*cf.* Figure 2.1A and 2.1B). However, it is likely that free chol and the cholesterol esters that predominate in LDL give rise to different product distributions (arising from initial C7-H *vs.* C4-H abstraction). Indeed, the regiochemistry of H-atom abstraction is presumably influenced both by the identity of the abstracting radical and the possibility for H-bonding interactions with the medium, e.g. at the aqueous interface of a lipid bilayer or lipoprotein. This is currently under investigation.

It remains to reiterate that the observation of chol 5α-OOH in chol autoxidations offers a pathway to the secosterols **2.1** and **2.2** that does not require high-energy oxidants (i.e. O_3 or $^1O_2$). However, our elucidation of the complete set of products of chol autoxidations prompts the suggestion of an even more compelling pathway – the (acid-catalyzed) Hock fragmentation of chol 6-OOH:

Scheme 2.3. Proposed mechanism of the Hock fragmentation of chol 6-OOH.

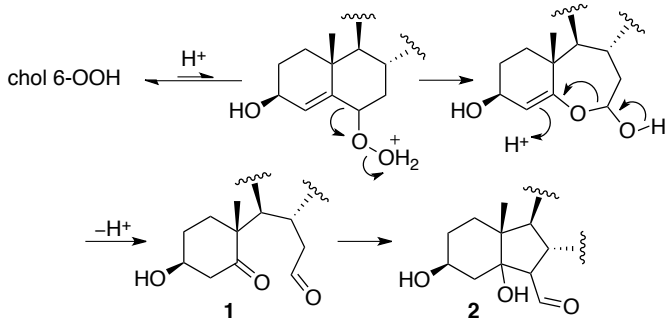

Although it is a minor product, chol 6-OOH arises from the autoxidation of chol in the absence of antioxidants. As expected from the transformation in Scheme 2.3, when authentic chol 6β-OOH was subjected to the same derivatization conditions used for the identification of **2.1** and **2.2** in human heart and brain tissue (2,4-dinitrophenylhydrazine-HCl),[6,7] the (derivatized) secosterols **2.1** and **2.2** were the only products observed (see Supporting Information, section 2.5.1 for details). Thus, formation of **2.1** and **2.2** can be linked directly to the ubiquitous process of lipid peroxidation by *two of the four possible autoxidation products*. However, since derivatization processes used to identify **2.1** and **2.2** from tissue samples employ acid as a catalyst,[6,7,11] it remains to determine unambiguously whether **2.1** and **2.2** are formed *in vivo* or *ex vivo*.

2.4 Perspective

The foregoing work was originally inspired by the controversial report of secosterols **2.1** and **2.2** in human heart and brain tissues derivatized with 2,4-dinitrophenylhydrazine-HCl, and the accompanying suggestion that the presence of the secosterols was due to *in vivo* production of ozone.[6,7] Subsequent work in The Pratt Group showed that secosterols **2.1** and **2.2** could also be formed from the (acid catalyzed) Hock fragmentation of chol 5α-OOH.[14] A seemingly simple question then arose – could we detect chol 5-OOH in chol autoxidations? This would offer a much more plausible explanation for the presence of the secosterols *in vivo*, even if produced in small amounts or under particular conditions. It was hypothesized that the addition of a H-atom donor – one that is not so effective as to shut down autoxidation entirely, but effective enough to trap the chol 5-peroxyl radical intermediate – may be the key to observing chol 5-OOH. At this point, it was hypothesized that the C-H BDE of the cholesterol C4-H bond was far too strong to ever observe chol 4-OOH or 6-OOH, as, to the best of our knowledge, the compounds had never been reported as autoxidation products. Thus the hypothesis was quite clear; however, studying the minor products of cholesterol autoxidation proved to be an analytical challenge.

A former graduate student, Philip Lynett, initially attempted to study cholesterol autoxidation using HPLC-UV. The absorption of cholesterol ($\pi \rightarrow \pi^*$ for C5=C6) is weak at the minimum wavelength of 210 nm for our UV detector, and Phil was unable to get clear chromatograms for the autoxidation products. However, some of the chromatograms Phil obtained had a small (albeit noisy) peak where chol 5α-OH was expected to elute, suggesting further study was warranted.

We therefore set out to expand upon Phil's preliminary study. We initially attempted tagging the C3-OH of chol with a benoyl group (Bz-chol), in an attempt to increase the absorption for HPLC-UV detection. However, while preparing an authentic standard of the Bz-chol-derived 5α-OOH through $^1O_2$ oxidation, it was observed that Bz-chol reacted significantly more slowly than chol (e.g. 10% conversion in 6 hours, vs. 60% conversion for chol under the same conditions). This was quite surprising to us, as the "substituent effect" was evidently perpetuated through the C3, C4, and C5 bonds (cf. Figure 2.5, and note that the C3-substituent effect is discussed in the context of autoxidation in Chapter 3). We briefly explored introducing a tag elsewhere on the sterol backbone (e.g. by derivatizing the C20-position of pregnenolone); however, we ultimately decided that the best way to study chol autoxidation was with chol itself rather than a derivative. Some attempts were made to measure the product distribution by NMR (500 MHz, inverse probe); however, given the low conversion for autoxidation, the chol starting material peak was far stronger than any of the products. This was so pronounced that the chol starting material peaks had satellite peaks which overlapped with regions where the characteristic product peaks were expected.

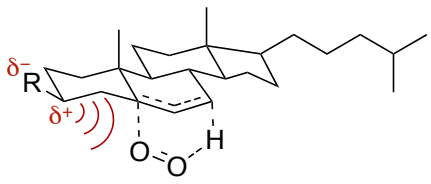

Figure 2.5. Substituent effect on the transition state for the $^1O_2$ oxidation of cholesterol.

We then turned our attention to LC-MS. The Pratt Group's UPLC-MS instrument (Waters Acquity UPLC H-Class System) was typically operated under reversed-phase conditions and using an electrospray ionization (ESI) probe. Due to cholesterol's poor solubility in (even moderately) polar solvents, reversed-phase conditions were not ideal, and neutral sterols do not effectively ionize by ESI. Thus we looked to atmospheric pressure chemical ionization (APCI), for which the UPLC-MS instrument was capable using a dual ESI-APCI probe. We observed weak, but measurable, ionization of the chol autoxidation products (chol X-OH) by APCI, and noted that there was a limit to the maximum temperature the dual ESI-APCI probe could go (~350°C). We therefore invested in a dedicated IonSABRE APCI probe, which is designed to operate at higher temperatures (~500°C) and offered much better ionization of chol X-OH.

When chol autoxidation samples were studied under the optimized conditions, we were surprised to see the product distribution was so complex (cf. Figure 2.1). We therefore prepared authenic standards for chol 4α-OH, 4β-OH, 5α-OH, 6α-OH, 6β-OH, 7α-OH and 7β-OH, and indeed each authentic standard corresponded to a peak in the chol autoxidation chromatogram (chol 5α-OH, only under conditions with added H-atom donor). As will be discussed in Chapter 3, however, we had not accounted for the cholesterol-5,6-epoxide products which derive from peroxyl radical addition to the C5=C6 bond. An expansion of this study, with a focus on the interplay between the H-atom abstraction and peroxyl radical addition pathways in cholesterol autoxidation, follows in Chapter 3.

2.5 References

(1) van Meer, G.; Voelker, D. R.; Feigenson, G. W. *Nat. Rev. Mol. Cell Biol.* **2008**, *9*, 112.

(2) (a) Epstein, F. H.; Steinberg, D.; Parthasarathy, S.; Carew, T. E.; Khoo, J. C.; Witztum, J. L. *N Engl J Med.* **1989**, *320,* 915, (b) Cleeman, J. I. *JAMA-J. Am. Med. Assoc.* **2001**, *285*, 2486.

(3) Perhaps the best example is that 7-dehydrocholesterol, a precursor to vitamin D_3 and chol, builds up in patients with Smith-Lemli-Opitz syndrome and oxidizes readily to form the oxysterols believed to be important in the pathogenesis of the disease. See: (a) Xu, L.; Porter, N. A. *J. Am. Chem. Soc.* **2014**, *136*, 5443, and (b) Xu, L.; Korade, Z.; Porter, N. A. *J. Am. Chem. Soc.* **2010**, *132*, 2222.

(4) For example, see: (a) Xu, L.; Porter, N. A. *Free Radic. Res.* **2015**, *49*, 835, (b) Yin, H.; Xu, L.; Porter, N. A. *Chem. Rev.* **2011**, *111*, 5944 and references cited therein.

(5) For example, see: (a) Pulfer, M. K.; Murphy, R. C. *J. Biol. Chem.* **2004**, *279*, 26331, and (b) Pryor, W. A.; Squadrito, G. L.; Friedman, M. *Free Radic. Biol. Med.* **1995**, *19*, 935.

(6) Wentworth, P.; Nieva, J.; Takeuchi, C.; Galvé, R.; Wentworth, A.; Dilley, R. B.; DeLaria, G. A.; Saven, A.; Babior, B. M.; Janda, K. D.; Eschenmooser, A.; Lerner, R. A. *Science* **2003**, *302*, 1053.

(7) Zhang, Q.; Powers, E. T.; Nieva, J.; Huff, M. E.; Dendle, M. A.; Bieschke, J.; Glabe, C. G.; Eschenmooser, A.; Wentworth, P.; Lerner, R. A.; Kelly, J. W. *Proc Natl Acad Sci USA* **2004**, *101*, 4752.

(8) Takeuchi, C.; Galvé, R.; Nieva, J.; Witter, D. P.; Wentworth, A. D.; Troseth, R. P.; Lerner, R. A.; Wentworth, P. *Biochemistry* **2006**, *45*, 7162.

(9) Nieva, J.; Song, B.D.; Rogel, J. K.; Kujawara, D.; Altobel, L.; Izharrudin, A.; Boldt, G. E.; Grover, R. K.; Wentworth, A. D.; Wentworth, P. *Chem. Biol.* **2011**, *18*, 920.

(10) Usui, K.; Hulleman, J. D.; Paulsson, J. F.; Siegel, S. J.; Powers, E. T.; Kelly, J. W. *Proc. Natl. Acad. Sci. USA* **2009**, *106*, 18563.

(11) Bosco, D. A.; Fowler, D. M.; Zhang, Q. H.; Nieva, J.; Powers, E. T.; Wentworth, P.; Lerner, R. A.; Kelly, J. W. *Nat. Chem. Biol.* **2006**, *2*, 249.

(12) Cygan, N. K.; Scheinost, J. C.; Butters, T. D.; Wentworth, P. *Biochemistry* **2011**, *50*, 2092.

(13) For example, see: (a) Kettle, A. J.; Clark, B. M.; Winterbourn, C. C. *J. Biol. Chem.* **2004**, *279*, 18521, Smith, L. L. *Free Radical Biol. Med.* **2004**, *37*, 318 and (b) Sies, H. *Angew. Chem. Intl. Ed.* **2004**, *43*, 3514.

(14) Brinkhorst, J.; Nara, S. J.; Pratt, D. A. *J. Am. Chem. Soc.* **2008**, *130*, 12224.

(15) For example, see: (a) Ullery, J. C.; Marnett, L. J. *BBA-Biomembranes* **2012**, *1818*, 2424, (b) Beavers, W. N.; Serwa, R.; Shimozu, Y.; Tallman, K. A.; Vaught, M.; Dalvie, E. D.; Marnett, L. J.; Porter, N. A. *J. Am. Chem. Soc.* **2014**, *136*, 11529 and references cited therein.

(16) For example, see: (a) Iuliano, L. *Chem. Phys. Lipids* **2011**, *164*, 457, (b) Murphy, R. C.; Johnson, K. M. *J. Biol. Chem.* **2008**, *283*, 15521, (c) Schroepfer, G. J. *Physiol. Rev.* **2000**, *80*, 361, and (d) Smith, L. L. Cholesterol Autoxidation; Springer US: Boston, MA, 1981 and references therein.

(17) For example, see: (a) Niki, E. *BBA-Gen. Subjects* **2014**, *1840*, 809, (b) Lee, C.-Y. J.; Huang, S. H.; Jenner, A. M.; Halliwell, B. *Free Radic Biol Med*. **2008**, *44,* 1314, and (c) Iuliano, L.; Micheletta, F.; Natoli, S.; Ginanni Corradini, S.; Iappelli, M.; Elisei, W.; Giovannelli, L.; Violi, F.; Diczfalusy, U. *Anal. Biochem.* **2003**, *312*, 217.

(18) Porter, N. A.; Mills, K. A.; Carter, R. L. *J. Am. Chem. Soc.* **1994**, *116*, 6690.

(19) (a) Pratt, D. A.; Tallman, K. A.; Porter, N. A. *Acc. Chem. Res.* **2011**, *44*, 458. (b) Tallman, K. A.; Pratt, D. A.; Porter, N. A. *J. Am. Chem. Soc.* **2001**, *123*, 11827.

(20) Montgomery, J. A.; Ochterski, J. W.; Petersson, G. A. *J. Chem. Phys.* **1994**, *101*, 5900.

(21) The B3LYP/CBSB7 step was used since the CBS-QB3 calculation is prohibitively intensive for these systems.

(22) Beckwith, A. L. J.; Davies, A. G.; Davison, I. G. E.; Maccoll, A.; Mruzek, M. H. *J. Chem. Soc., Perkin Trans. 2* **1989**, 815.

(23) Xu, L.; Davis, T. A.; Porter, N. A. *J. Am. Chem. Soc.* **2009**, *131*, 13037.

(24) Burton, G. W.; Ingold, K. U. *Acc. Chem. Res.* **1986**, *19*, 194. (25) Haidasz, E. A.; Van Kessel, A. T. M.; Pratt, D. A. *J. Org. Chem.* **2016**, *81*, 737.

(26) Bowry, V. W.; Ingold, K. U. *Acc. Chem. Res*. **1999**, *32*, 27.

(27) Ansari, G. A. S.; Walker, R. D.; Smart, V. B.; Smith, L. L. *Food Chem. Toxicol.* **1982**, *20*, 35.

(28) Breuer, O. *J. Lipid Res.* **1995**, *36*, 2275.

(29) Breuer, O.; Dzeletovic, S.; Lund, E.; Diczfalusy, U. *BBA-Lipid Lipid Met*. **1996**, *1302*, 145..

2.6 Supporting Information

Note: reference numbering starts anew for this section, and references can be found in section 2.5.4 Supplementary References.

2.6.1 Experimental Details

All chemicals and solvents were purchased from Sigma Aldrich Co. LLC and used as received, unless otherwise stated. Cholesterol (92%) was purified to >99% by the well precedented method of bromination/debromination to remove other sterol impurities.[1] The >99% cholesterol was then freshly recrystallized from methanol prior to each experiment to remove trace oxidation product impurities. 2,2'-Azobis (4-methoxy-2,4-dimethylvaleronitrile) (MeOAMVN)[2] was purchased from Wako Pure Chemical Industries, Ltd. And used as received. 2,6-di-*tert*-butyl-4-methylphenol (BHT) was recrystallized from hexane prior to use, and 2,4-dinitrophenylhydrazine was recrystallized from acetonitrile prior to use.

Cholesterol autoxidations: To 38 mg cholesterol (0.1 mmol) in a small vial was added 180 μL chlorobenzene and 20 μL of a 200 mM solution of MeOAMVN in benzene. The vial was capped loosely to allow air in, and incubated at 37°C for 16 hours. A 100 μL aliquot of the cholesterol autoxidation solution was quenched in a HPLC vial by adding 880 μL of a solution of 5.7 mM BHT and 5.7 mM PPh_3 in HPLC grade hexane, and 20 μL of a 1 mM solution of d_6-5α-hydroxycholesterol in chlorobenzene as an internal standard. Under these conditions, the amount of chol 4-OH and 7-OH products detected was above the concentration range used to make standard curves. To quantify them, an additional 10 μL aliquot of the cholesterol autoxidation solution was quenched in a HPLC vial by adding 970 μL of a solution of 5.7 mM BHT and 5.7 mM PPh_3 in HPLC grade hexane, and 20 μL of a 1 mM solution of d_6-5α-hydroxycholesterol in chlorobenzene as an internal standard.

Cholesterol autoxidations with H-atom donor: A 500 mM solution of H-atom donor (either PMC or BDMP) was prepared in chlorobenzene, and an aliquot was added to 38 mg

cholesterol (0.1 mmol) in a small vial (e.g. 25 μL was added for 25 mM H-atom donor, *etc.*). Enough chlorobenzene was added for a total volume of 180 μL, then 20 μL of a 200 mM solution of MeOAMVN in benzene was added. The vial was capped loosely to allow air in, and incubated at 37°C for 16 hours. A 100 μL aliquot of the cholesterol autoxidation solution was quenched in a HPLC vial by adding 880 μL of a solution of 5.7 mM BHT and 5.7 mM PPh_3 in HPLC grade hexane, and 20 μL of a 1 mM solution of d_6-5α-hydroxycholesterol in chlorobenzene as an internal standard.

Cholesterol blank: To 19 mg cholesterol (0.05 mmol) in a HPLC vial was added 100 μL of chlorobenzene, 880 μL of a solution of 5.7 mM BHT and 5.7 mM PPh_3 in HPLC grade hexane, and 20 μL of a 1 mM solution of d_6-5α-hydroxycholesterol in chlorobenzene as an internal standard.

HPLC-APCI-MS/MS analysis: For any of the autoxidation solutions prepared above, 10 μL was injected onto a normal phase HPLC column (Whatman Partisil 5 μm silica; 4.6 mm × 250 mm) and eluted with 95:5 hexane:*iso*-propanol (*i*-PrOH) at a flow rate of 1.5 mL/min. APCI-MS/MS detection in positive mode was used for the MS/MS transition 385.35 *m/z* → 367.37 *m/z*, which for any of the hydroxycholesterols corresponds to initial addition of a proton and loss of H_2O, followed by the loss of a second H_2O (*cf.* Scheme S1 and Figure S1). The same transition occurs with the internal standard d_6-5α-hydroxycholesterol, but due to the incorporation of 6 deuterium atoms, it was detected with the MS/MS transition 391.39 *m/z* → 373.37 *m/z*. The settings for mass spectral analysis were as follows: corona current 2 μA; cone voltage 25 V; source temperature 150°C; APCI probe temperature 500°C; desolvation gas flow 600 L/hr; cone gas flow 20 L/hr; collision gas flow 0.2 mL/min; collision energy 15 eV.

Scheme 2.4. The relevant APCI-MS transitions for chol 5α-OH and the deuterated d_6-chol 5α-OH internal standard. These transitions exist for any hydroxycholesterol studied herein, though only chol 5α-OH is shown as an example.

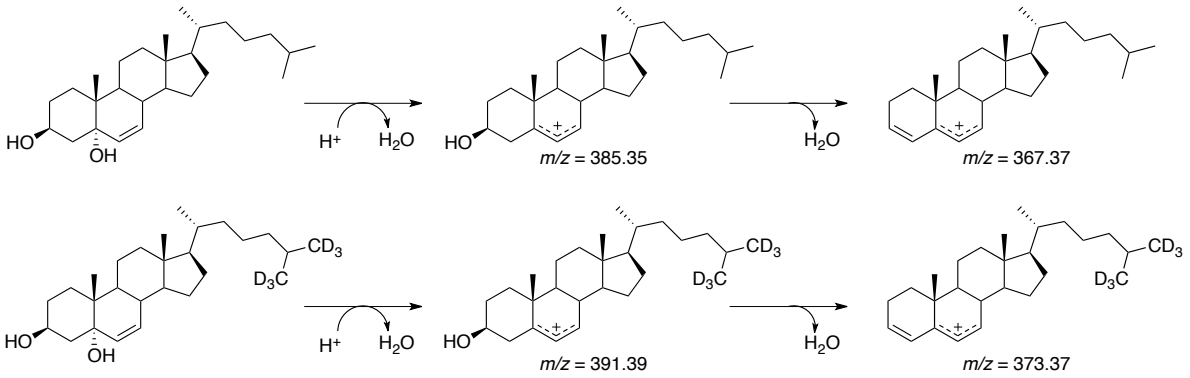

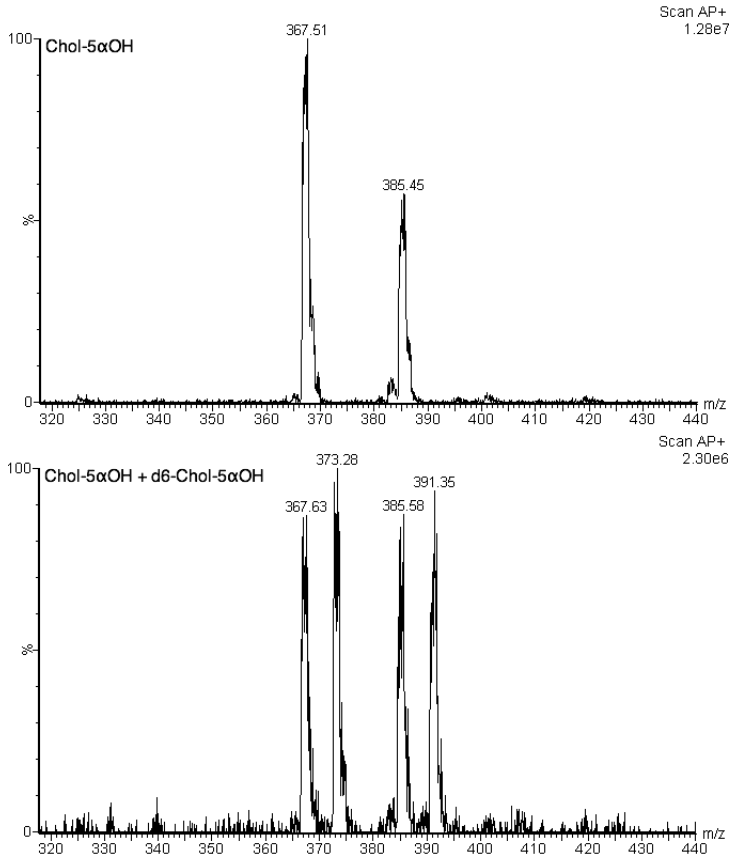

Figure 2.6. Direct infusion APCI-MS for chol 5α-OH (top) and a mixture of chol 5α-OH and d_6-chol 5α-OH (bottom).

HPLC-APCI+-MS/MS Chromatograms: An internal standard (d_6-chol 5α-OH, 20 μM) was present in each sample, but is not always shown as it is detected via a different MS/MS transition (391.39 *m/z* → 373.37 *m/z*); an example is shown in Figure 2.6A. While chol was freshly recrystallized prior to use, a small amount of chol 4β-OH was still present (*cf*. Figure 2.6B); therefore a blank was prepared (described above) for each set of experiments and the amount of chol 4β-OH was subtracted from autoxidation samples. Finally, it should be noted that the raw data for APCI chromatograms (*e.g*. Figure 2.6A-2.6C) were smoothed in all subsequent cases, which is conventional (*cf*. Figure 2.6D).

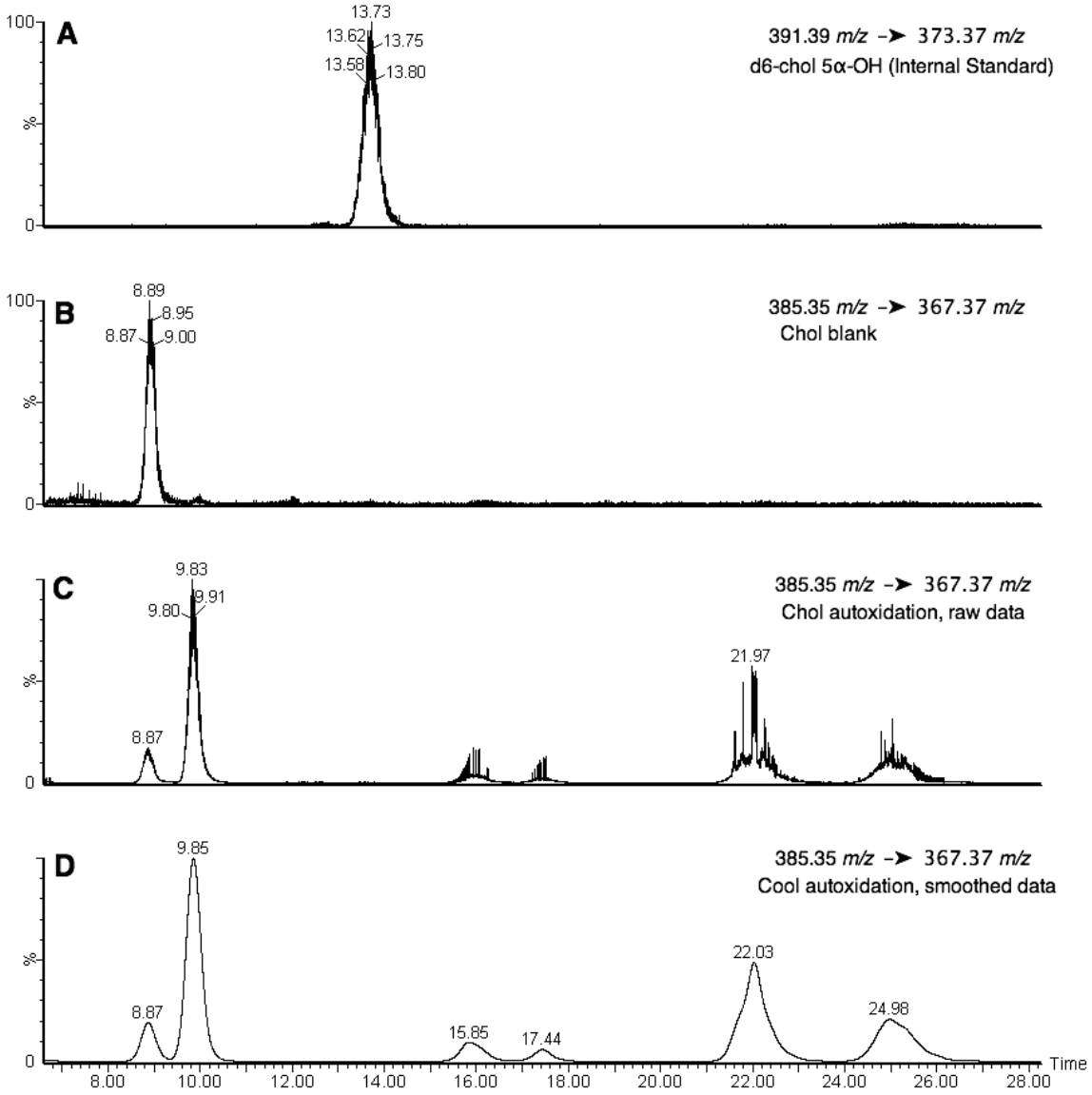

Figure 2.7. Chromatograms for d_6-chol 5α-OH, observed at the indicated MS/MS transition (A), a blank cholesterol sample (B), raw data for a chol autoxidation with no additive (C) and smoothed data (D, for the same data as in C). Data were obtained by HPLC (95:5 hexane:*i*-PrOH) with $APCI^+$-MS/MS detection for the transitions indicated on each panel.

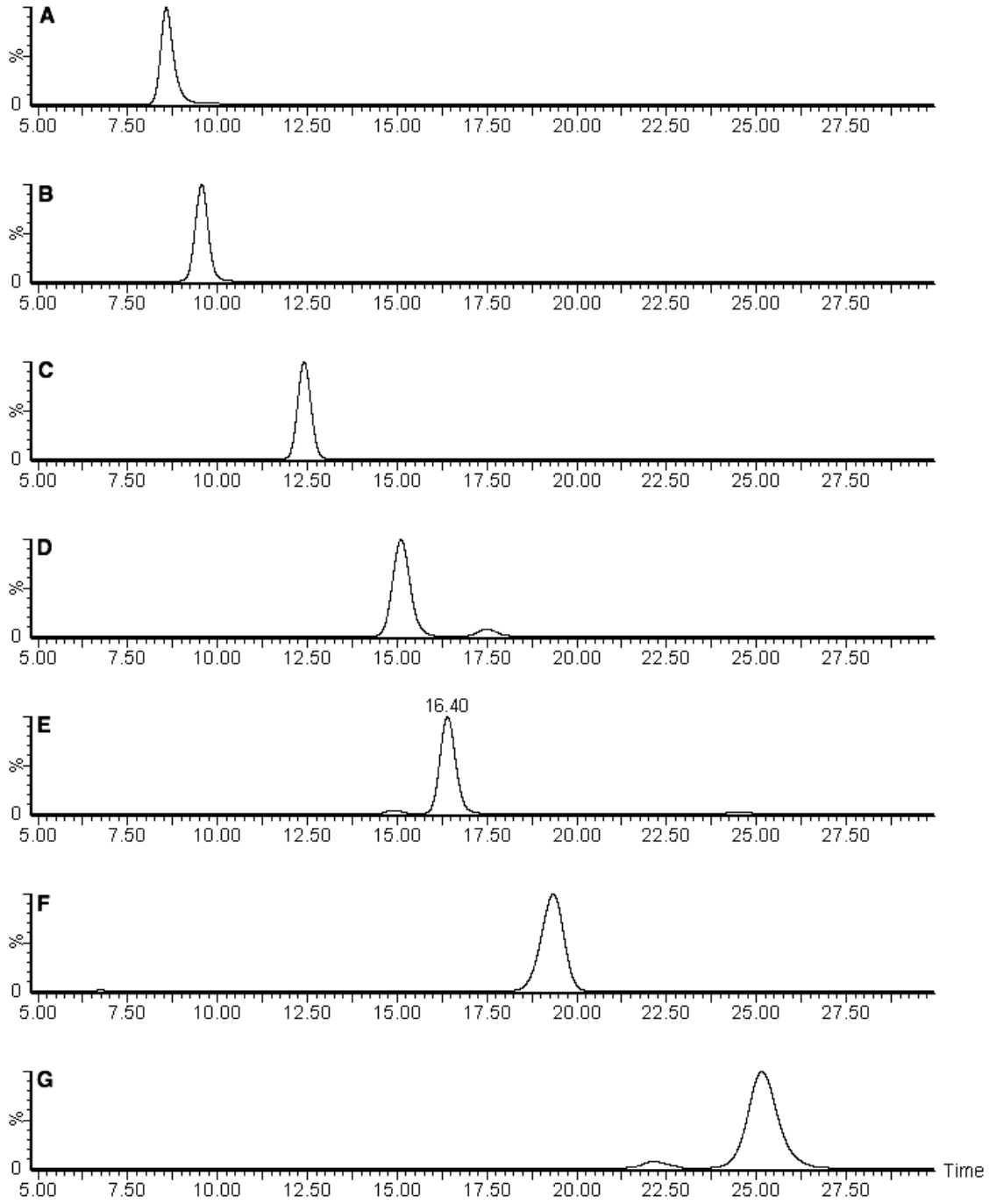

Figure 2.8. Chromatograms of authentic standards chol 4β-OH (A), chol 4α-OH (B), chol 5α-OH (C), chol 6α-OH (D) and chol 6β-OH (E) chol 7β-OH (F), and chol 7α-OH (G). Data were obtained by HPLC (95:5 hexane:*i*-PrOH) with $APCI^+$-MS/MS detection (*m/z* 385.35 → *m/z* 367.37).

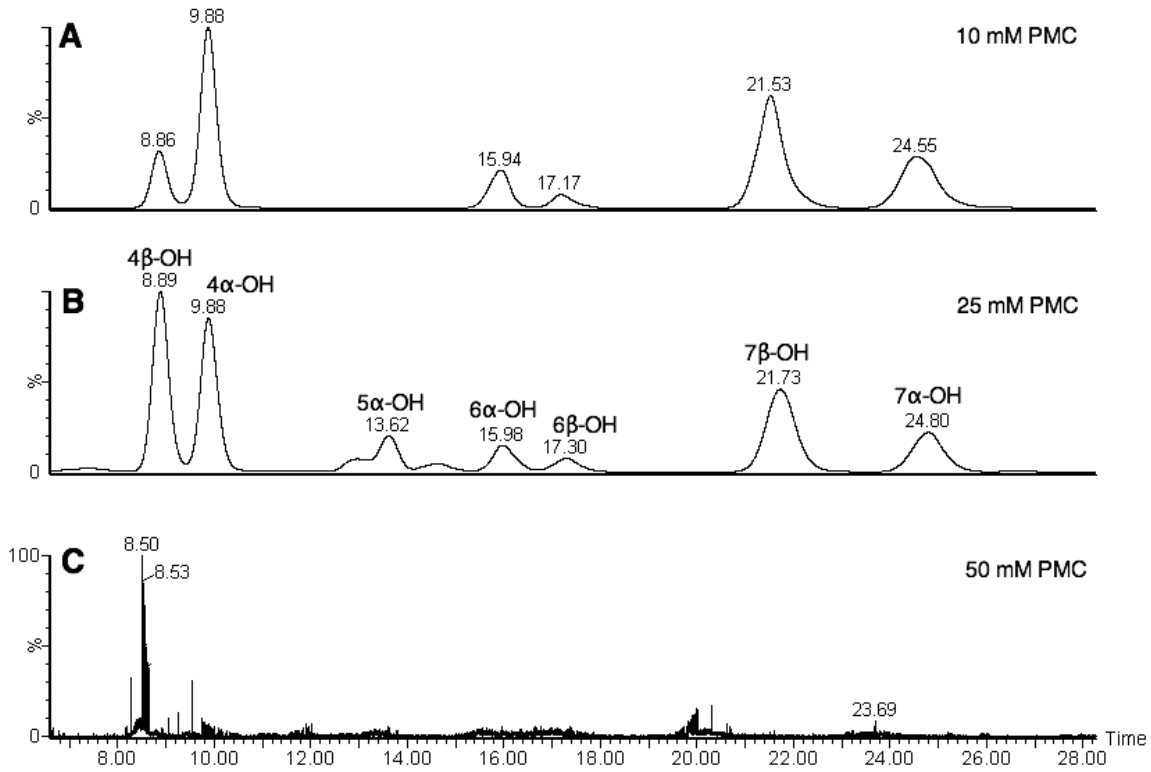

Figure 2.9. Product distributions from MeOAMVN-initiated autoxidations of chol in chlorobenzene at 37°C with 10 mM PMC (A), 25 mM PMC (B) and 50 mM PMC (C). Data were obtained by HPLC (95:5 hexane:*i*-PrOH) with $APCI^+$-MS/MS detection (*m/z* 385.35 → *m/z* 367.37). The alcohols are observed due to pre-treatment with PPh_3.

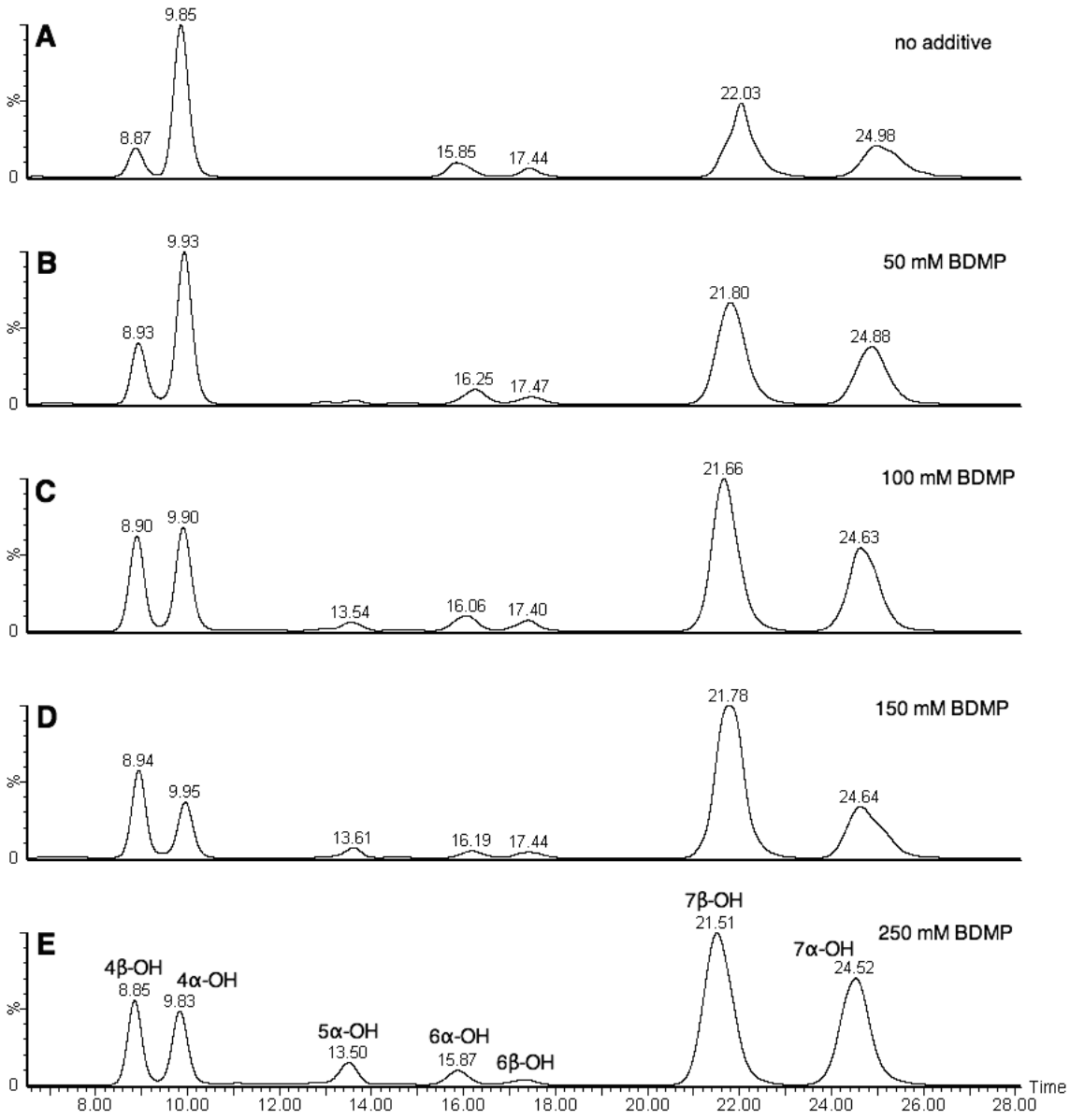

Figure 2.10. Product distributions from MeOAMVN-initiated autoxidations of chol in chlorobenzene at 37°C with no added antioxidant (A), and with 50 mM BDMP (B), 100 mM BDMP (C), 150 mM BDMP (D) and 250 mM BDMP (E). Data were obtained by HPLC (95:5 hexane:*i*-PrOH) with $APCI^+$-MS/MS detection (*m/z* 385.35 → *m/z* 367.37). The alcohols are observed due to pre-treatment with PPh_3.

Quantification of hydroxysterols: For the standard curves below (Figures 2.10-2.16), the apparent concentration (y-axis) is the integrated area of the standard compound divided by the integrated area of the internal standard (d_6-chol 5α-OH) multiplied by the concentration of the internal standard (20 μM):

$$\text{Apparent [chol XOH]} = \frac{\text{Area chol XOH}}{\text{Area } d_6\text{-chol 5α-OH}} \times [d_6\text{-chol 5α-OH}]$$

From the standard curves, the slope represents the response factor for each compound (*i.e.* how well the compound ionizes relative to the internal standard). These values, presented in Table 2.1, were used to quantify each compound in the autoxidation experiments.

Table 2.1. Response factors for authentic hydroxylcholesterols

	Response factor		Response factor
chol 4α-OH	0.461	chol 5α -OH	0.987
chol 4β -OH	0.740	chol 7α -OH	0.795
chol 6α-OH	3.14	chol 7β -OH	1.23
chol 6β -OH	1.84		

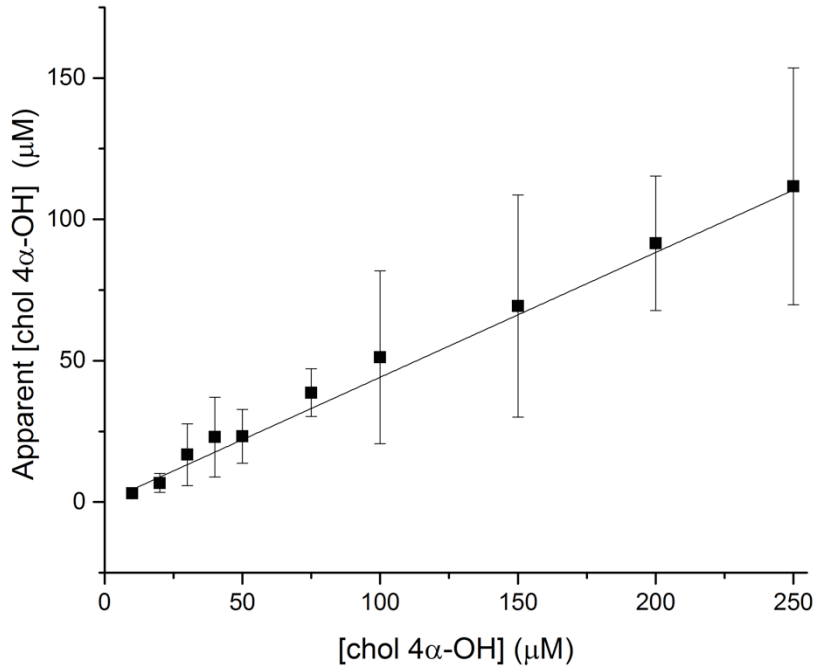

Figure 2.11. Standard curve for chol 4α-OH (y=0.4612x; R^2=0.997).

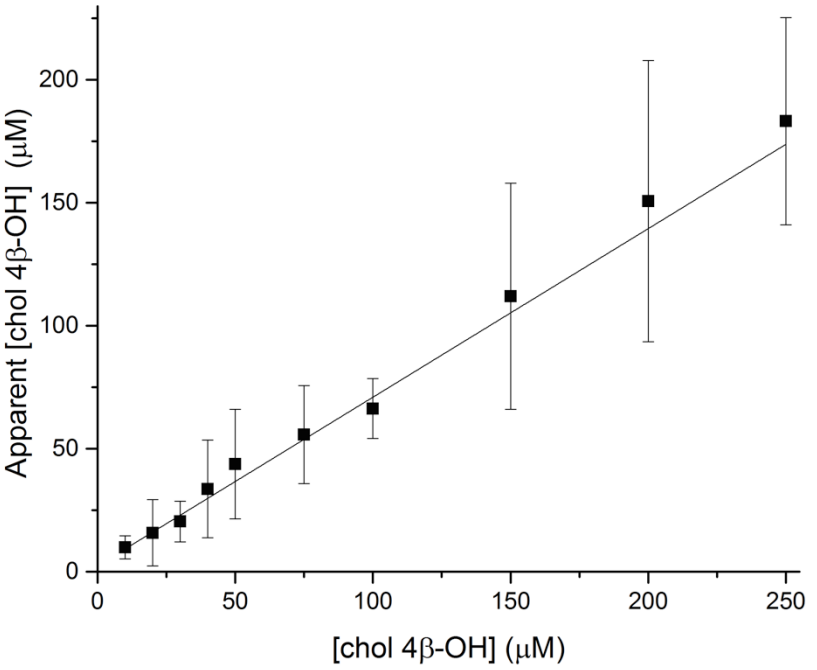

Figure 2.12. Standard curve for chol 4β-OH (y=0.7399x; R^2=0.9982).

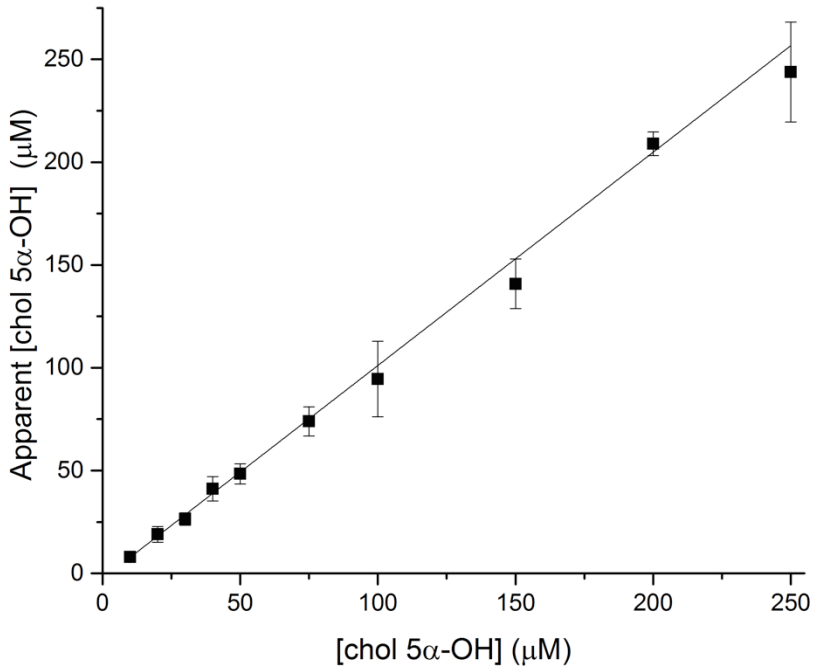

Figure 2.13. Standard curve for chol 5α-OH (y=0.9867x; R^2=0.9984).

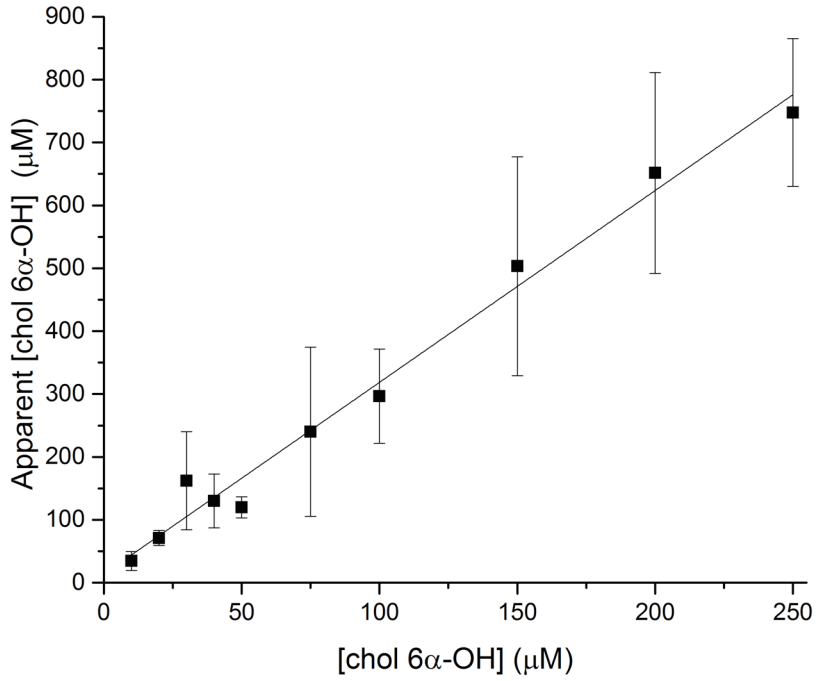

Figure 2.14. Standard curve for chol 6α-OH (y=3.1357x; R^2=0.9935).

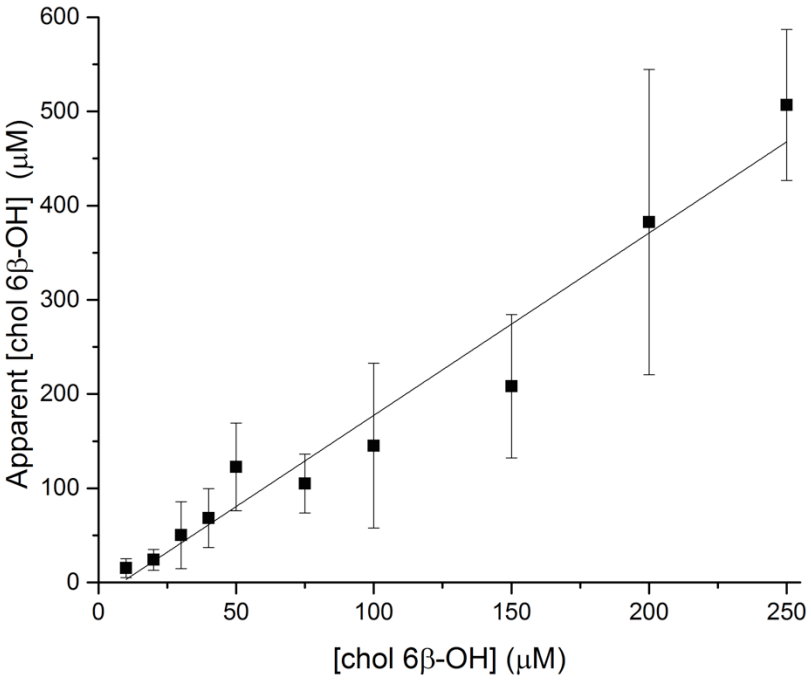

Figure 2.15. Standard curve for chol 6β-OH (y=1.8446x; R^2=0.9705).

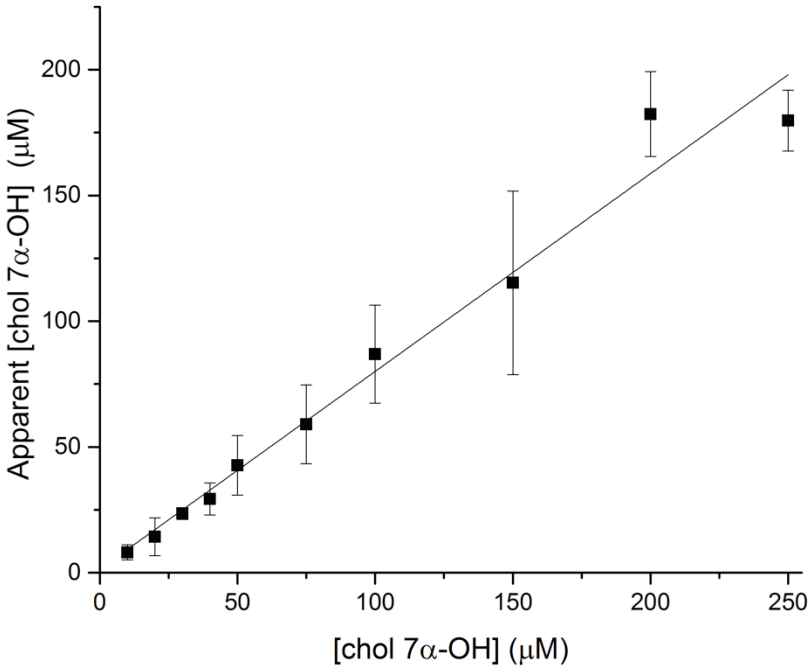

Figure 2.16. Standard curve for chol 7α-OH (y=0.7951x; R^2=0.9894).

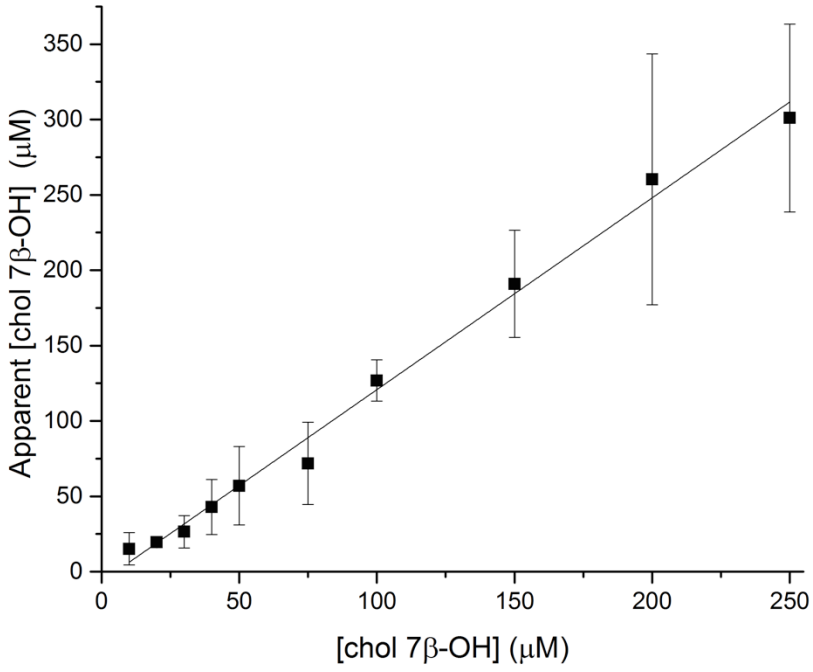

Figure 2.17. Standard curve for chol 7β-OH (y=1.2313x; R^2=0.9959).

Kinetics of O_2 addition at C4: Determination of rate constants required prior knowledge of the rate constant for the reaction of BDMP with secondary peroxyl radicals, which we determined to be (1.3±0.1)×10^5 $M^{-1}s^{-1}$ by co-autoxidations of cumene and STY-BODIPY by the spectrophotometric method we recently developed.[3]

To estimate k_β for chol 4β-OO• we were required to assume O_2 addition was exclusive to the 4-position over the 6-position. Given chol 6-OOH are minor products we believe this assumption to be reasonable. Note that since the chol 4α-OO• and 4β-OO• pathways are competitive, we cannot treat one as irreversible (as was the case in determining k_β for chol 5α-OO•), we therefore treated the kinetic scheme with an additional parameter (α, defined in Scheme 2.5).[4] The data were fit with nonlinear regression (*cf.* Figure 2.17A) using OriginPro software, and the (average) α = 0.41 and k_β/k_H = 0.0665 give k_β = (8.6±0.4)×10^3 s^{-1}. Note, when the data were linearized (*cf.* Figure 2.18B) the same values for α and k_β were obtained from the slope = 0.09559 and y-intercept = 1.437.

Scheme 2.5. The kinetically-controlled autoxidation of chol enables determination of k_β for chol 4β-OO•.

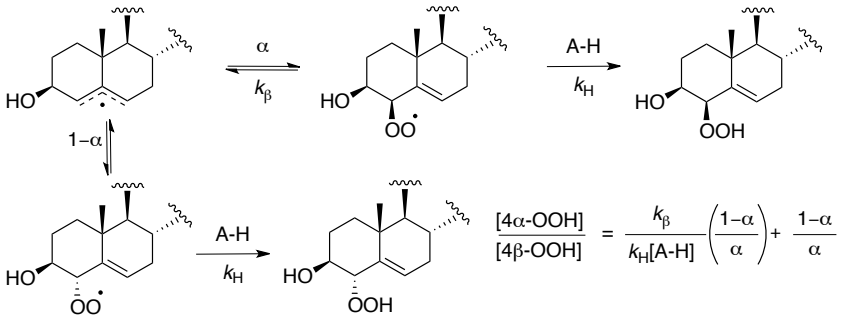

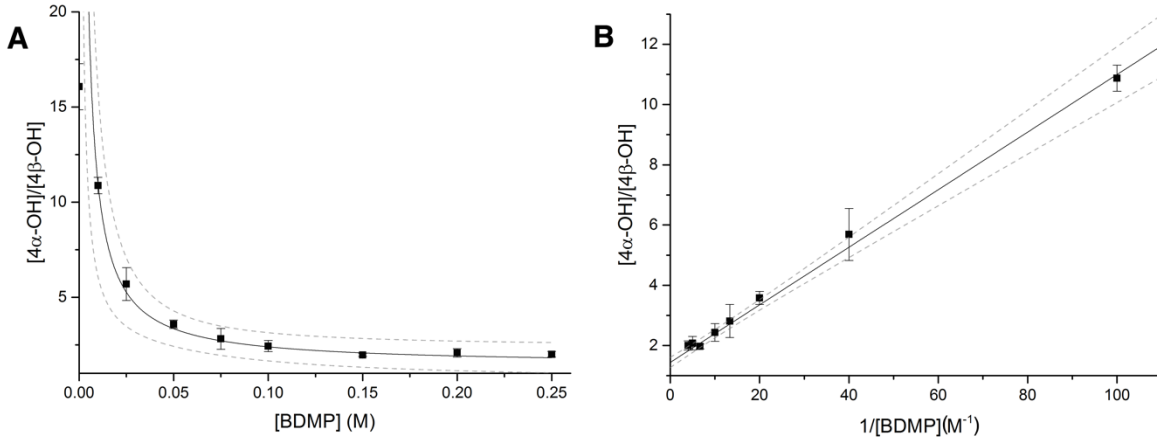

Figure 2.18. Dependence of [chol 4α-OH]/[chol 4β-OH] on BDMP concentration (A) and the inverse of BDMP concentration (B). 95% confidence intervals are indicated with dashed lines.

Acid-catalyzed Hock fragmentation and 2,4-dinitrophenylhydrazine (DNPH) derivatization: Cholesterol 6β-OOH (1 mg) was stirred in 1 mL ethanol containing 0.2 mM DNPH and 0.1 M HCl for 3 hours at room temperature under nitrogen. The solution was directly injected on HPLC under the conditions indicated in Figure 2.18. The authentic DNPH-derivatized secosterols **2.1** and **2.2** were synthesized and characterized as previously reported.[5]

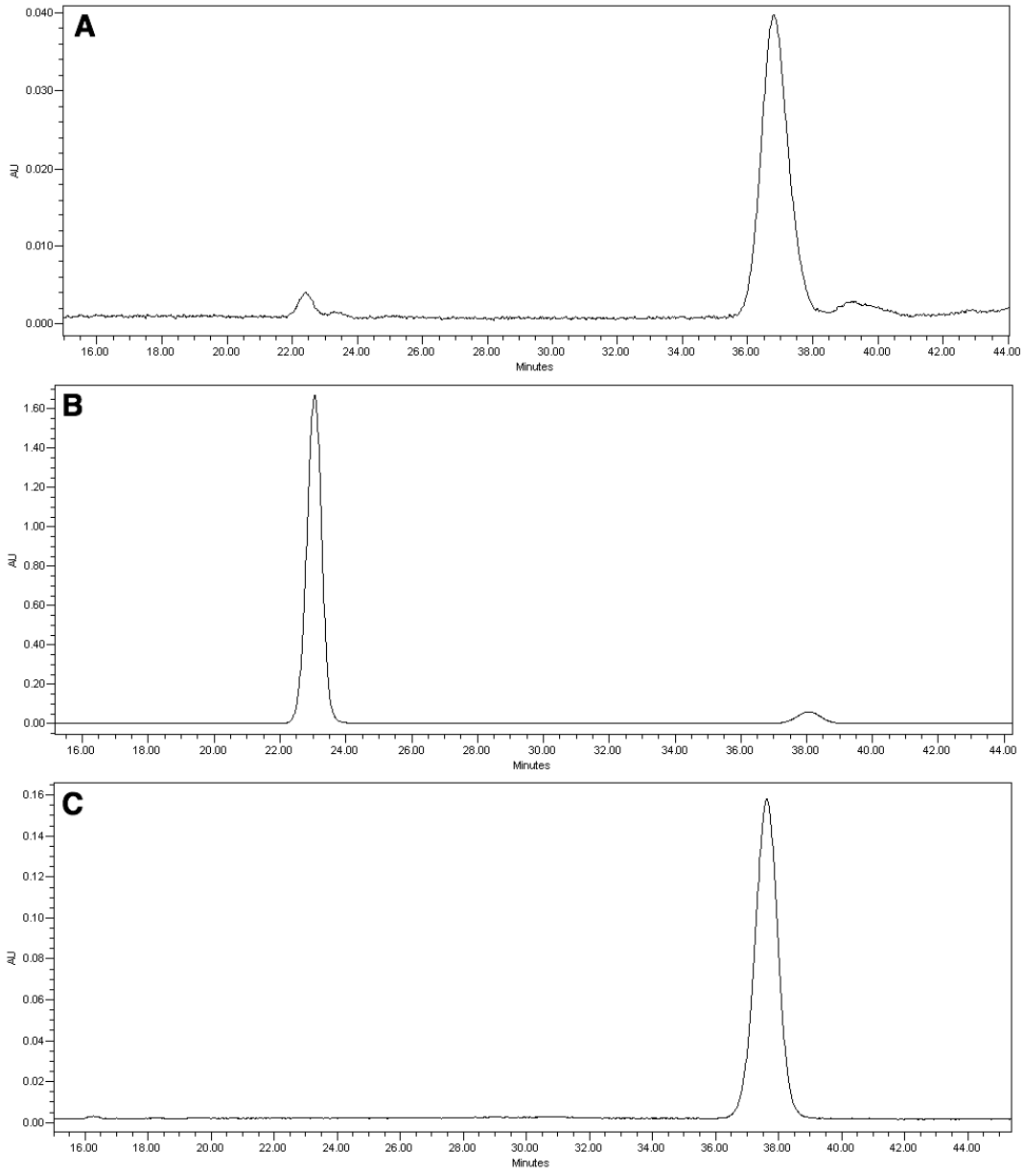

Figure 2.19. Acid-catalyzed Hock fragmentation and derivatization by 2,4-dinitrophenylhydrazine of chol 6β-OOH (A) gives two major products that match the authentic derivatized secosterols 1 (B) and 2 (C). Data were obtained by reverse phase HPLC (75:20:5 acetonitrile:methanol:water, 0.5 mL/min) with UV-vis detection at 365 nm.

Scheme 2.6. Synthesis of chol 4α-OH and chol 4β-OH, based on previous work.[6]

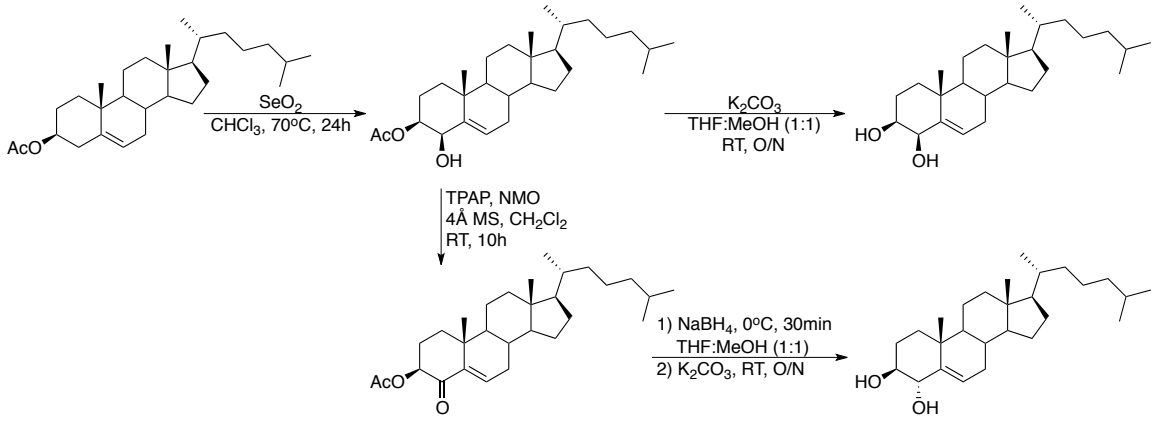

Scheme 2.7. Synthesis of chol 6α-OH and chol 6β-OH, based on previous work.[7,8]

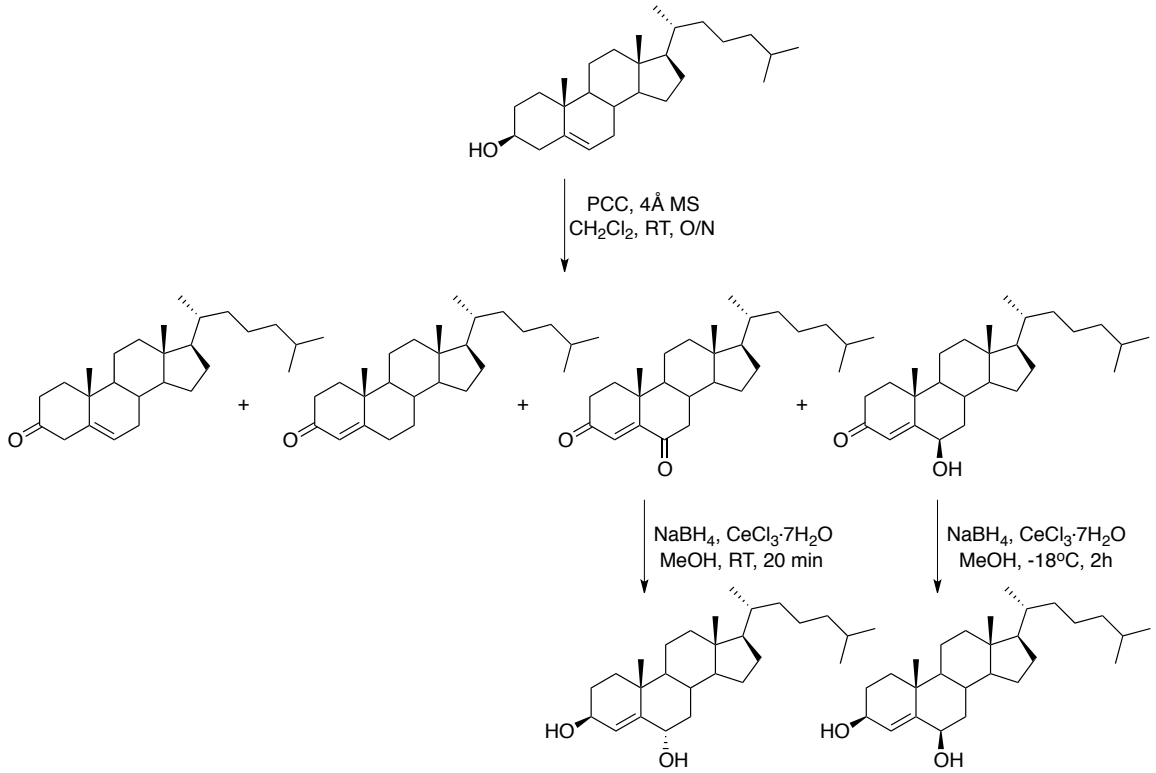

Scheme 2.8. Synthesis of chol 5α-OH and chol 7α-OH, based on previous work.[9]

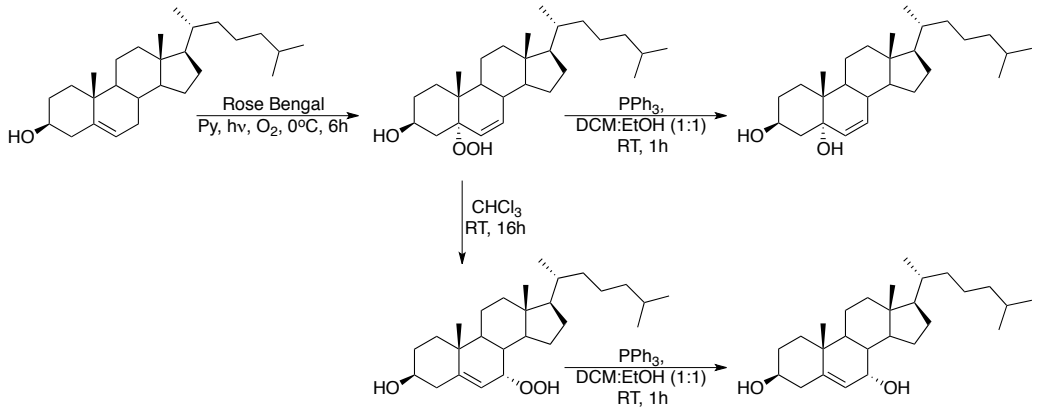

Scheme 2.9. Synthesis of chol 7α-OH and chol 7β-OH by autoxidation.

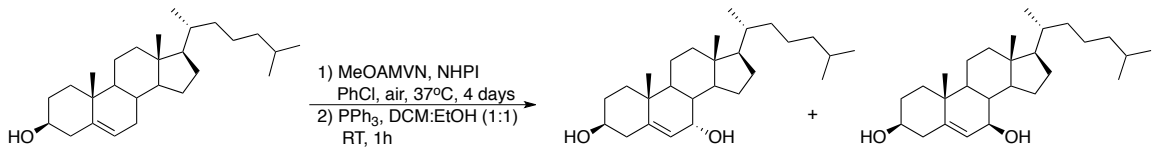

4α-hydroxycholesterol (chol 4α-OH). Prepared as previously reported[6] (*cf.* Scheme 2.6). Note that there appeared to be an inconsistency between the Experimental Methods section and the Supporting Information in the ^{1}H-NMR characterization by Lizard *et. al.*[6] for this compound. Our characterization matched the raw data found in the Supporting Information. White solid; ^{1}H-NMR (400 MHz; $CDCl_3$): δ 5.74 (dt, *J* = 5.4, 2.1 Hz, 1H), 4.06 (d, *J* = 7.4 Hz, 1H), 3.27 (td, *J* = 10.3, 4.5 Hz, 1H), 2.48 (br. S, 1H), 2.10 (dtd, *J* = 17.6, 5.3, 2.7 Hz, 1H), 2.02 (dt, *J* = 12.6, 3.4 Hz, 2H), 1.91-1.79 (m, 3H), 1.65-1.08 (m, 18H), 1.03 (s, 3H), 1.00-0.94 (m, 2H), 0.91 (d, *J* = 6.5 Hz, 3H), 0.86 (dd, *J* = 6.6, 1.8 Hz, 6H), 0.68 (s, 3H); ^{13}C-NMR (100 MHz; $CDCl_3$): δ 142.2, 118.0, 76.77, 75.3, 56.9, 56.3, 50.6, 42.4, 39.9, 39.7, 38.2, 36.8, 36.3, 35.9, 31.69, 31.57, 28.4, 28.20, 28.17, 24.4, 24.0, 23.0, 22.7, 21.1, 20.4, 18.9, 12.0; HRMS (EI): calculated for $C_{27}H_{46}O_2$ 402.3498, found 402.3517.

4β-hydroxycholesterol (chol 4β-OH). Prepared as previously reported[6] (*cf.* Scheme 2.6). Note that Lizard *et. al.*[6] claimed to have made a mixture of 3β-acetoxy-4β-hydroxycholesterol and 3β-acetoxy-6α-hydroxycholesterol (2:1 ratio) upon treatment of cholesterol with SeO_2; however, we found that upon deprotection, both products gave 4β-hydroxycholesterol. We believe that this reaction yields a mixture of 3β-acetoxy-4β-hydroxycholesterol and 4β-acetoxy-3β-hydroxycholesterol due to migration of the acetate group, and that Lizard *et. al.*[6] mis-identified the latter. We therefore used a different synthetic route to 6α-hydroxycholesterol (below). White solid; ^{1}H-NMR (400 MHz; $CDCl_3$): δ 5.68 (dd, *J* = 4.8, 1.7 Hz, 1H), 4.13 (d, *J* = 2.9 Hz, 1H), 3.55 (dt, *J* = 11.7, 4.1 Hz, 1H), 2.25-1.99 (m, 4H), 1.95-1.78 (m, 3H), 1.66-1.22 (m, 11H), 1.18 (s, 3H), 1.15-0.92 (m, 9H), 0.91 (d, *J* = 6.5 Hz, 3H), 0.86 (dd, *J* = 6.6, 1.8 Hz, 6H), 0.68 (s, 3H); ^{13}C-NMR (100 MHz; $CDCl_3$): δ 142.9, 128.9, 77.4, 72.6, 57.1, 56.3, 50.4, 42.5, 39.9, 39.7, 37.1, 36.3, 36.2, 35.9, 32.2, 32.0, 28.4, 28.2, 25.6, 24.4, 24.0, 23.0, 22.7, 21.2, 20.7, 18.9, 12.0; HRMS (EI): calculated for $C_{27}H_{46}O_2$ 402.3498, found 402.3501.

6α-hydroxycholesterol (chol 6α-OH). Prepared by reduction of cholest-4-ene-3,6-dione, which was prepared as previously reported.[7] Cholest-4-ene-3,6-dione (200 mg, 0.5 mmol) and $CeCl_3 \times 7H_2O$ (190 mg, 0.51 mmol) were dissolved in 30 mL methanol and $NaBH_4$ was added in portions over 10 minutes (60 mg, 1.6 mmol total). The reaction was quenched after an additional 10 minutes with 1M HCl and extracted with dichloromethane. The organic layer was washed with water twice, dried over $MgSO_4$ and concentrated *in vacuo*. The product was purified by silica gel flash column (60:40 hexanes:ethyl acetate) and compared to previously reported characterization[10] (*cf.* Scheme 2.7). White solid; 94% yield. ^{1}H-NMR (400 MHz; $CDCl_3$): δ 5.65 (q, *J* = 1.7 Hz, 1H), 4.25-4.16 (m, 2H), 2.08 (ddd, *J* = 11.6, 5.0, 3.6 Hz, 1H), 2.02-1.94 (m, 2H), 1.84 (dtd, *J* = 13.1, 9.4, 5.7 Hz, 1H), 1.71 (ddd, *J* = 13.1, 4.8, 2.4 Hz, 1H), 1.59-1.42 (m, 8H), 1.40-1.25 (m, 7H), 1.11 (td, *J* = 11.4, 6.1 Hz, 6H), 1.04 (s, 3H), 1.03-0.98 (m, 2H), 0.90 (d, *J* = 6.6 Hz, 3H), 0.86 (dd, *J* = 6.6, 1.8 Hz, 6H), 0.77-0.70 (m, 1H),

0.68 (s, 3H); ^{13}C-NMR (75 MHz; $CDCl_3$): δ 149.5, 119.9, 68.8, 68.1, 56.3, 55.9, 54.3, 42.7, 42.3, 39.81, 39.64, 38.1, 36.26, 36.10, 35.9, 34.5, 29.3, 28.29, 28.16, 24.3, 24.0, 23.0, 22.7, 21.1, 19.9, 18.8, 12.1; HRMS (EI): calculated for $C_{27}H_{46}O_2$ 402.3498, found 402.3495.

6β-hydroxycholesterol (chol 6β-OH). Prepared by reduction of 6β-hydroxycholest-4-ene-3-one, which was prepared as previously reported.[7] 6β-hydroxycholest-4-ene-3-one (360 mg, 0.9 mmol) and $CeCl_3 \times 7H_2O$ (402 mg, 1.08 mmol) were dissolved in 20 mL methanol and cooled to -18°C. $NaBH_4$ was added in 10 mg portions until no starting material remained by TLC (~50 mg). The reaction was quenched with saturated aqueous $NaHCO_3$ and extracted three times with dichloromethane. The combined organic layers were washed with brine, dried over $MgSO_4$ and concentrated *in vacuo*. (*cf.* Scheme 2.7) The product was recrystallized from dichloromethane and compared to full characterization,[11] as well as characterization for cholest-4-en-3β,6β-diol -24-one[12] and (22*R*,23*R*)-3β,6β,22,23-tetrahydroxystigmast-4-ene.[13] White solid; 89% yield. ^{1}H-NMR (400 MHz; $CDCl_3$): δ 5.54 (t, *J* = 1.7 Hz, 1H), 4.23 (t, *J* = 2.9 Hz, 1H), 4.18 (ddd, *J* = 10.2, 6.2, 1.8 Hz, 1H), 2.03-1.78 (m, 5H), 1.70 (dt, *J* = 13.6, 3.4 Hz, 1H), 1.62-1.32 (m, 13H), 1.26 (s, 3H), 1.15-1.07 (m, 7H), 1.02-0.95 (m, 2H), 0.91 (d, *J* = 6.6 Hz, 3H), 0.86 (dd, *J* = 6.6, 1.8 Hz, 6H), 0.76 (dd, *J* = 10.5, 4.9 Hz, 1H), 0.71 (s, 3H); ^{13}C-NMR (75 MHz; $CDCl_3$): δ 147.8, 128.8, 74.4, 68.2, 56.35, 56.27, 54.4, 42.7, 39.9, 39.6, 39.3, 36.99, 36.90, 36.3, 35.9, 30.4, 29.4, 28.34, 28.18, 24.3, 24.0, 23.0, 22.7, 21.7, 21.1, 18.8, 12.2; HRMS (EI): calculated for $C_{27}H_{46}O_2$ 402.3498, found 402.3480.

5α-hydroxycholesterol (chol 5α-OH). Prepared as previously reported[9] (*cf.* Scheme 2.8). White solid; ^{1}H-NMR (400 MHz; $CDCl_3$): δ 5.63 (dd, *J* = 9.8, 1.8 Hz, 1H), 5.56 (dd, *J* = 9.8, 2.6 Hz, 1H), 4.12 (tt, *J* = 10.9, 5.4 Hz, 1H), 2.04 (dt, *J* = 12.2, 2.9 Hz, 1H), 1.95-1.84 (m, 3H), 1.79 (ddd, *J* = 12.6, 5.2, 1.6 Hz, 1H), 1.66-1.11 (m, 22H), 1.02-0.95 (m, 1H), 0.915 (s, 3H), 0.913 (d, *J* = 6.5 Hz, 3H), 0.86 (dd, *J*

= 6.6, 1.7 Hz, 6H), 0.70 (s, 3H); ^{13}C-NMR (100 MHz; $CDCl_3$): δ 133.34, 133.31, 74.1, 67.3, 56.2, 54.0, 45.1, 43.8, 41.0, 40.2, 39.6, 38.6, 38.2, 36.3, 36.0, 30.7, 28.7, 28.5, 28.1, 24.00, 23.95, 23.0, 22.7, 21.2, 18.8, 14.8, 12.3; HRMS (EI): calculated for $C_{27}H_{46}O_2$ 402.3498, found 402.3472.

7α-hydroxycholesterol (chol 7α-OH). Prepared as previously reported[9] (*cf.* Scheme 2.8) and compared to full characterization[14]. White solid; ^{1}H-NMR (400 MHz; $CDCl_3$): δ 5.60 (dd, *J* = 5.3, 1.6 Hz, 1H), 3.85 (br. S, 1H), 3.59 (tt, *J* = 10.6, 5.1 Hz, 1H), 2.37-2.24 (m, 2H), 2.00 (dt, *J* = 12.6, 3.5 Hz, 1H), 1.92-1.83 (m, 3H), 1.74-1.66 (m, 1H), 1.58-1.08 (m, 22H), 0.99 (s, 3H), 0.92 (d, *J* = 6.5 Hz, 3H), 0.86 (dd, *J* = 6.6, 1.7 Hz, 6H), 0.68 (s, 3H); ^{13}C-NMR (100 MHz; CDCl3): δ 146.4, 124.0, 71.5, 65.5, 56.0, 49.6, 42.42, 42.30, 42.18, 39.7, 39.3, 37.67, 37.55, 37.2, 36.3, 35.9, 31.5, 28.4, 28.2, 24.4, 23.9, 23.0, 22.7, 20.9, 18.9, 18.4, 11.8; HRMS (EI): calculated for $C_{27}H_{46}O_2$ 402.3498, found 402.3503.

7β-hydroxycholesterol (chol 7β-OH). Cholesterol (350 mg, 0.65 mmol) was autoxidized in the presence of N-hydroxyphthalimide (21 mg, 0.13 mmol), initiated by MeOAMVN (20 mg, 0.065 mmol) in 3.2 mL chlorobenzene for 4 days at 40°C, open to air. The solvent was removed *in* vacuo, then the solid was taken up in 1:1 dichloromethane:*iso*-propanol (5 mL) and treated with triphenylphosphine (175 mg, 0.67 mmol). The solvent was removed *in vacuo* and the solid was purified by silica gel flash column (60:40 hexane:ethyl acetate) and was compared to full characterization[14]. White solid; 17% yield. ^{1}H-NMR (400 MHz; $CDCl_3$): δ 5.29 (t, *J* = 1.9 Hz, 1H), 3.84 (dt, *J* = 7.9, 1.9 Hz, 1H), 3.55 (tt, *J* = 11.2, 4.6 Hz, 1H), 2.34 (ddd, *J* = 13.2, 4.9, 1.8 Hz, 1H), 2.25 (tt, *J* = 12.2, 2.0 Hz, 1H), 2.02 (dt, *J* = 12.6, 3.4 Hz, 1H), 1.91-1.77 (m, 4H), 1.53-1.27 (m, 13H), 1.18-1.09 (m, 6H), 1.05 (s, 3H), 1.02-0.97 (m, 3H), 0.92 (d, *J* = 6.5 Hz, 3H), 0.86 (dd, *J* = 6.6, 1.8 Hz, 6H), 0.69 (s, 3H). ^{13}C-NMR (100 MHz; $CDCl_3$): δ 143.6, 125.6, 73.5, 71.6, 56.1, 55.6, 48.4, 43.1,

41.9, 41.1, 39.72, 39.65, 37.1, 36.6, 36.4, 35.9, 31.7, 28.7, 28.2, 26.5, 24.0, 23.0, 22.7, 21.2, 19.3, 18.9, 12.0. HRMS (EI): calculated for $C_{27}H_{46}O_2$ 402.3498, found 402.3472.

26,26,26,27,27,27-d_6-cholesterol (d_6-chol). Prepared as previously reported[15] (however, the compound is also commercially available). ^{1}H-NMR (400 MHz; $CDCl_3$): δ 5.35 (t, *J* = 2.7 Hz, 1H), 3.52 (tt, *J* = 10.7, 5.1 Hz, 1H), 2.32-2.20 (m, 2H), 2.04-1.94 (m, 2H), 1.86-1.78 (m, 3H), 1.49-1.05 (m, 17H), 1.01 (s, 3H), 0.97-0.88 (m, 4H), 0.83 (dd, *J* = 9.7, 6.6 Hz, 2H), 0.68 (s, 3H).

26,26,26,27,27,27-d_6-5α-hydroxycholesterol (d_6-chol 5α-OH). Prepared from d_6-chol as above for the transformation of chol to chol 5α-OH.[9] Note that there is a quartet in the ^{13}C-NMR corresponding to C26 and C27, as they are split by three D-atoms each. White solid; ^{1}H-NMR (400 MHz; $CDCl_3$): δ 5.63 (d, *J* = 11.0 Hz, 1H), 5.57 (dd, *J* = 9.9, 2.4 Hz, 1H), 4.12 (tt, *J* = 10.8, 5.4 Hz, 1H), 2.06-1.99 (m, 1H), 1.89 (dq, *J* = 21.0, 7.6 Hz, 3H), 1.79 (dd, *J* = 12.9, 4.6 Hz, 1H), 1.68-1.57 (m, 4H), 1.49-1.09 (m, 19H), 1.00-0.88 (m, 6H), 0.82 (q, *J* = 7.6 Hz, 2H), 0.70 (s, 3H); ^{13}C NMR (100 MHz; CDCl3): δ 133.35, 133.32, 74.1, 67.3, 56.2, 54.04, 45.2, 43.8, 41.0, 40.2, 39.5, 38.6, 38.2, 36.3, 35.96, 35.77, 35.4, 30.7, 28.7, 28.5, 27.7, 24.0 (q, 2C), 21.2, 18.8, 14.8, 12.3; HRMS (EI): calculated for $C_{27}H_{46}O_2$ 408.3874, found 408.3871.

4-(tert-butyl)-2,6-dimethylphenol (BDMP). 2,6-dimethylphenol (10.0 g, 81.9 mmol) was dissolved in 500 mL dry dichloromethane and 10.1 mL (90.1 mmol) 2-bromo-2-methylpropane was added. Aluminum chloride (12.0 g, 90.1 mmol) was slowly added and the mixture was stirred under nitrogen overnight, during which time the reaction solution turned from yellow to red. The reaction was quenched with water and the organic layer was separated, dried over $MgSO_4$ and concentrated *in vacuo*. The residue was purified by silica gel flash column (90:10 hexane:ethyl acetate) to give a

brown solid which was further purified by recrystallization from hexane. The characterization was consistent with a previous report.[16] Beige crystals; 76% yield. ^{1}H-NMR (400 MHz; $CDCl_3$): δ 7.00 (s, 2H), 4.46 (s, 1H), 2.25 (s, 6H), 1.29 (s, 9H); ^{13}C NMR (100 MHz; $CDCl_3$): δ 150.0, 143.0, 125.7, 122.4, 34.0, 31.7, 16.3.

6β-hydroperoxycholesterol (chol 6β-OOH). Prepared as previously reported.[17] ^{1}H-NMR (400 MHz; $CDCl_3$): δ 7.56 (s, 1H), 5.66 (s, 1H), 4.33 (t, J = 2.4 Hz, 1H), 4.23-4.16 (m, 1H), 2.06-1.99 (m, 3H), 1.87-1.60 (m, 3H), 1.48-1.25 (m, 10H), 1.19 (s, 3H), 1.17-0.94 (m, 9H), 0.90 (d, J = 6.5 Hz, 3H), 0.86 (dd, J = 6.5, 1.7 Hz, 6H), 0.79-0.71 (m, 2H), 0.68 (s, 3H).

2.6.2 NMR Spectra

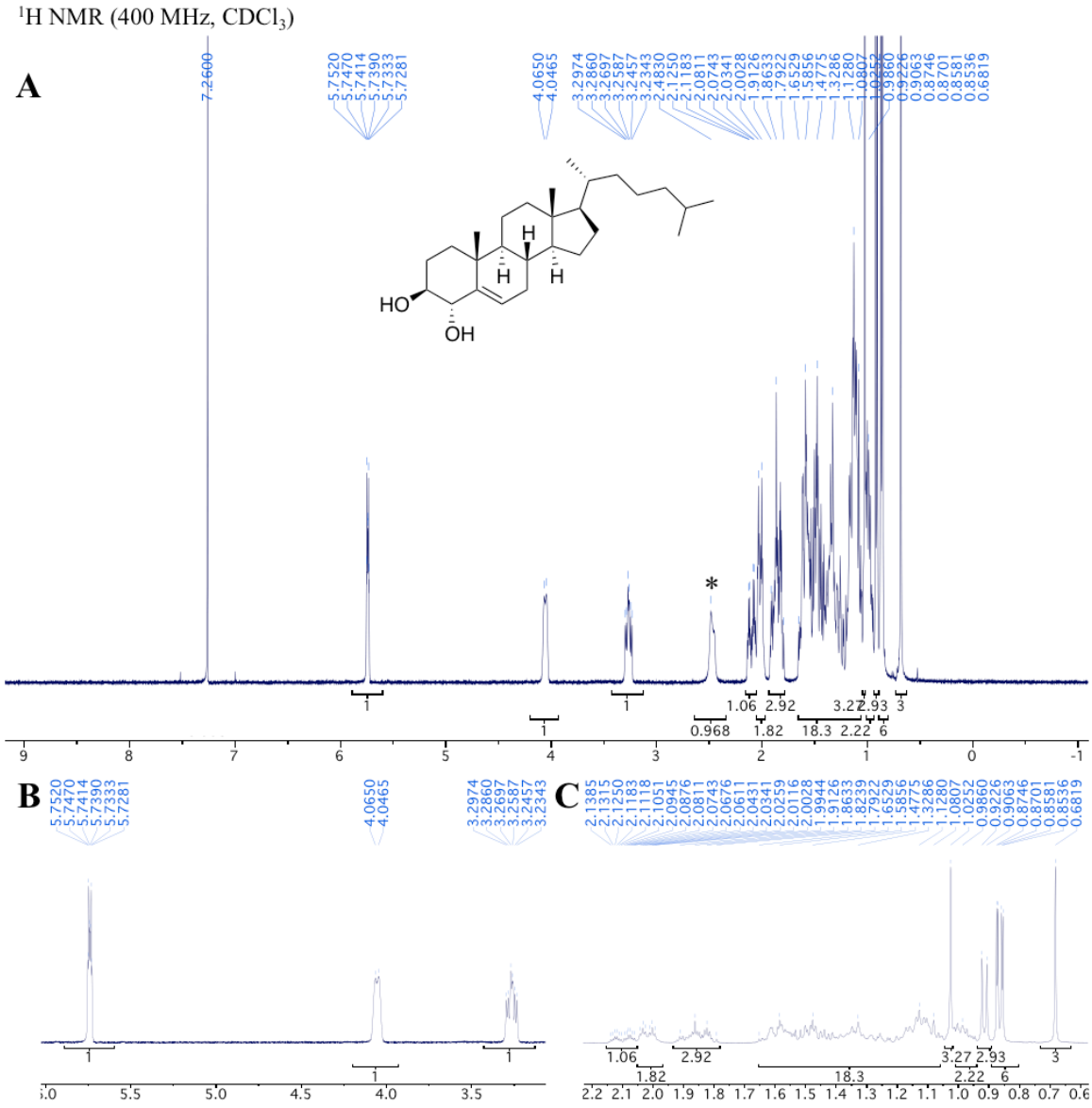

Figure 2.20. ^{1}H NMR spectrum of chol 4α-OH (A), and expansions of 6 – 3.2 ppm (B) and 2.2 – 0.6 ppm (C). The 73sterix (*) denotes a peak attributed to the (exchangeable) O-H protons, which is not always present (see Figure 2.20).

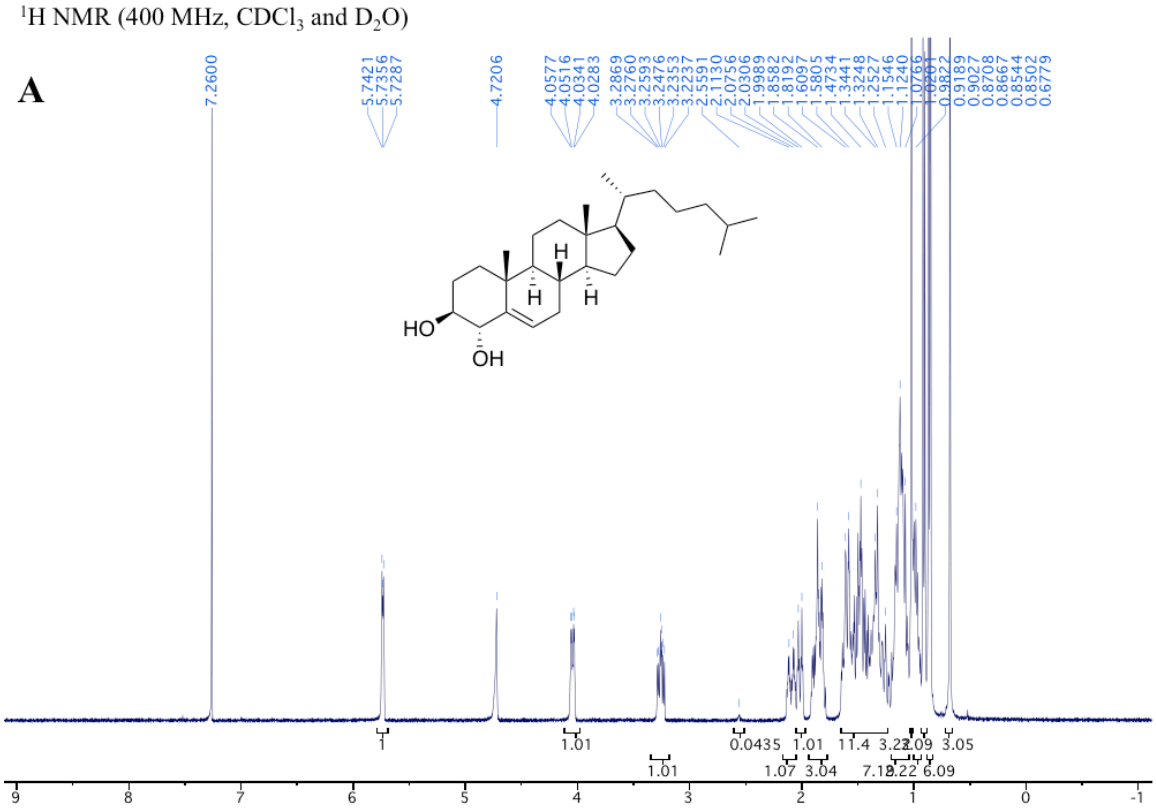

Figure 2.21. ^{1}H NMR spectrum of chol 4α-OH with a drop of D_2O added to the $CDCl_3$, where the peak attributed to the O-H protons (2.48 ppm) has exchanged almost completely, as compared to Figure 2.19.

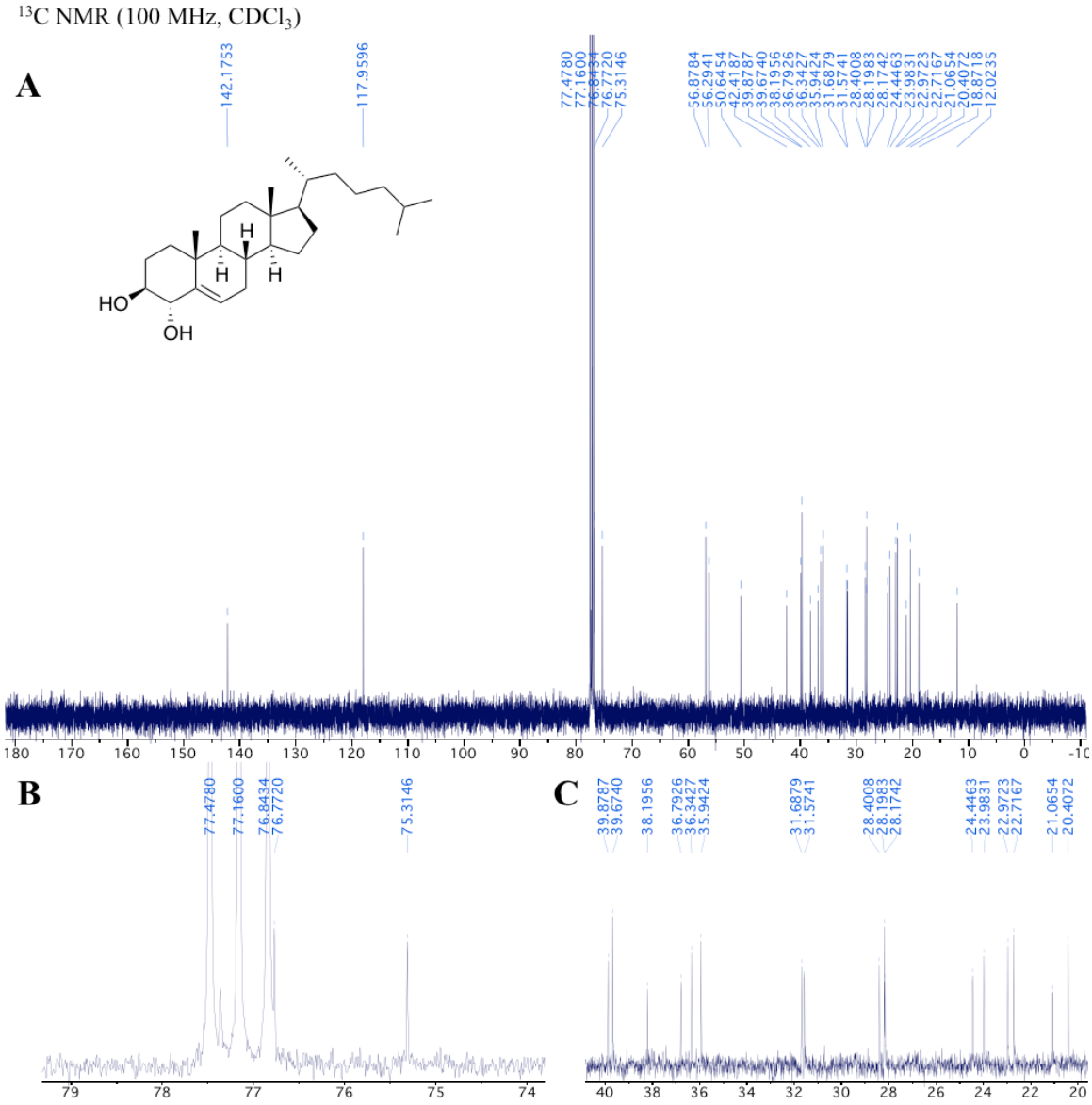

Figure 2.22. ^{13}C NMR spectrum of chol 4α-OH (A), expansion of 79 – 74 ppm, showing peak 76.77 adjacent to the $CDCl_3$ triplet (B) and expansion of 40 – 20 ppm (C).

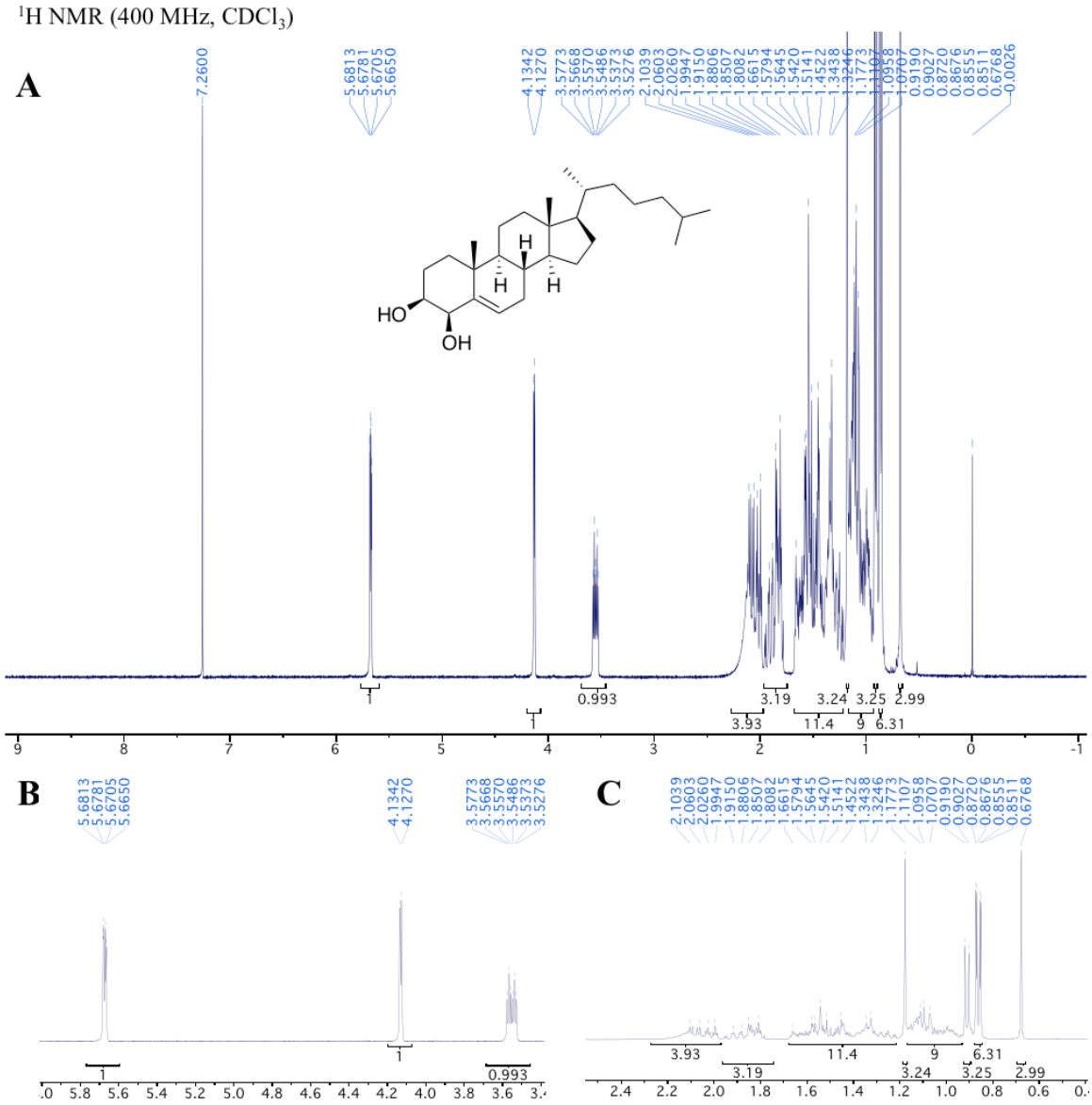

Figure 2.23. ^{1}H NMR spectrum of chol 4β-OH (A), and expansions of 6 – 3.5 ppm (B) and 2.5 – 0.5 ppm (C).

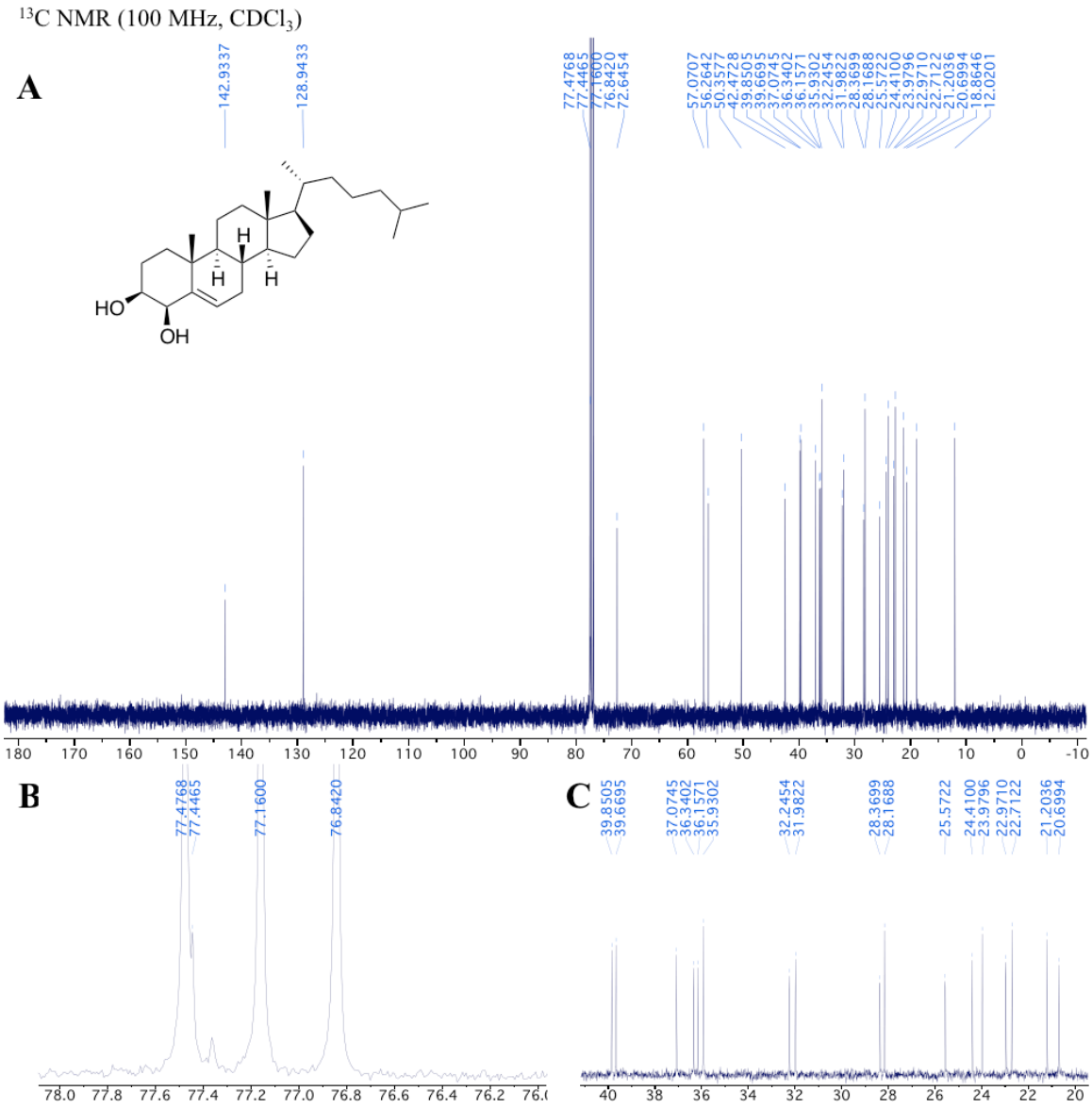

Figure 2.24. ^{13}C NMR spectrum of chol 4β-OH (A), expansion of 78 – 76 ppm, showing peak 77.45 adjacent to the $CDCl_3$ triplet (B) and expansion of 40 – 20 ppm (C).

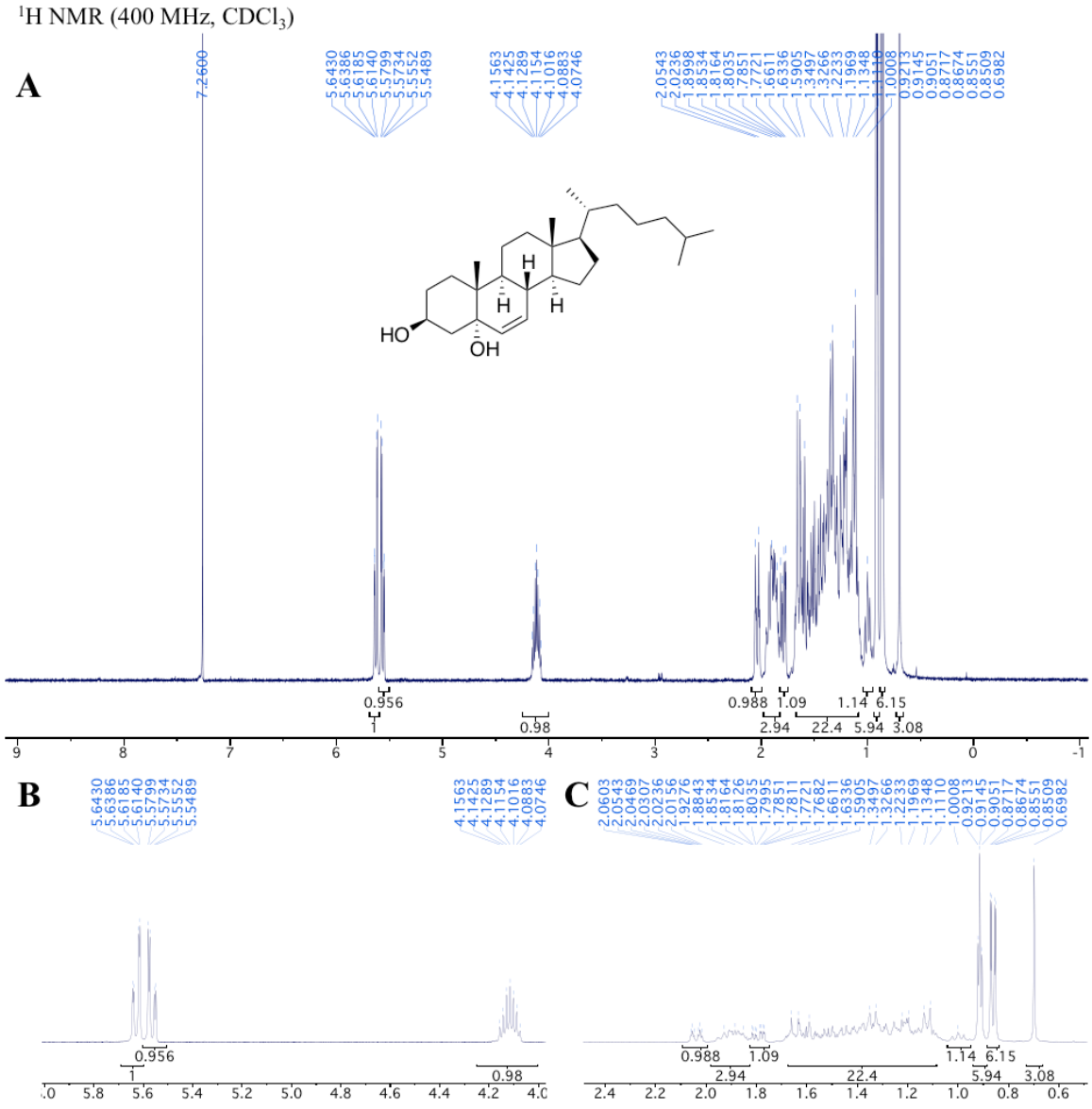

Figure 2.25. ^{1}H NMR spectrum of chol 5α-OH (A), and expansions of 6 – 4 ppm (B) and 2.4 – 0.5 ppm (C).

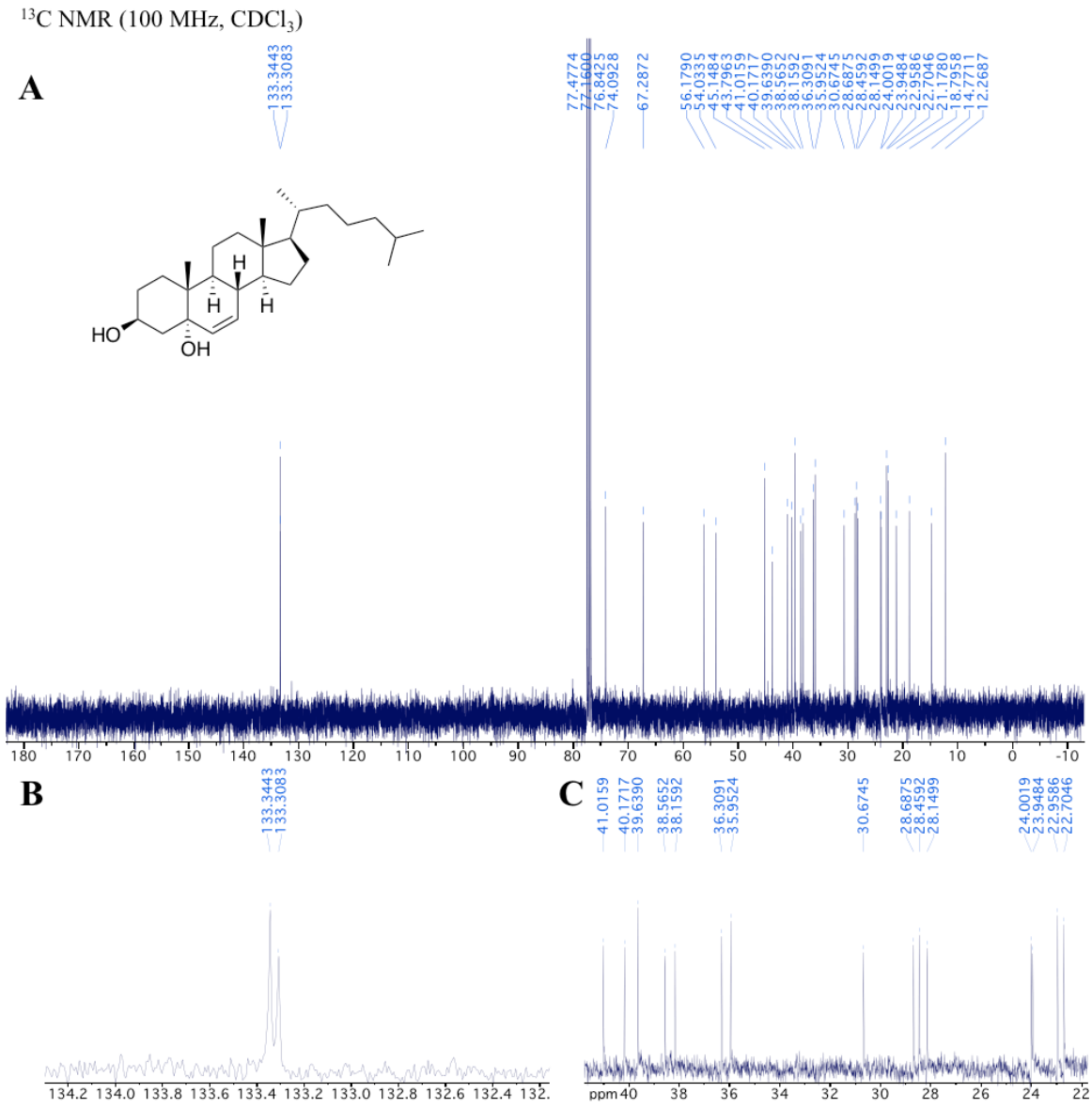

Figure 2.26. ^{13}C NMR spectrum of chol 5α-OH (A), and expansions of 134 – 132 ppm (B) and 42 – 22 ppm (C).

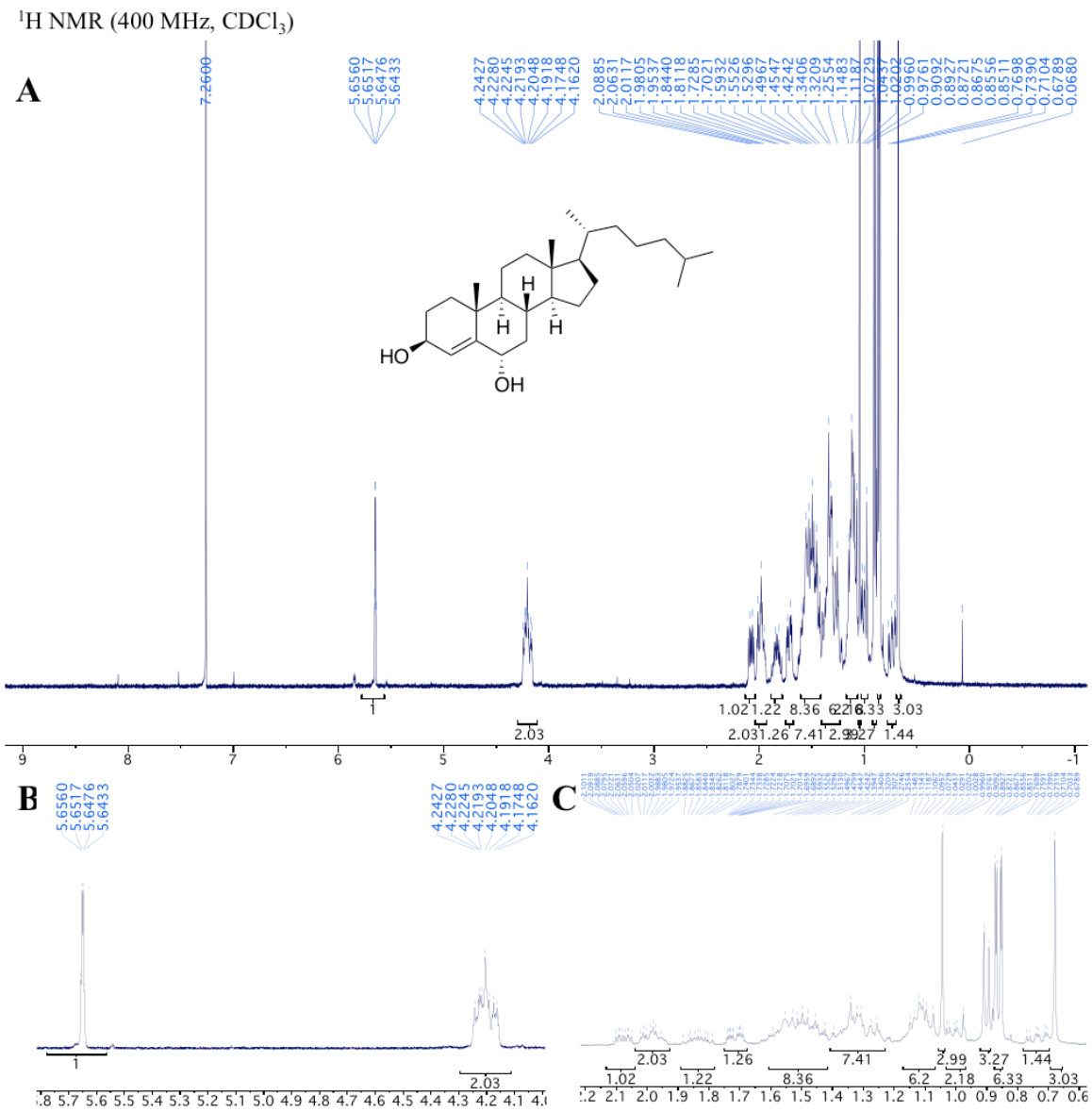

Figure 2.27. ^{1}H NMR spectrum of chol 6α-OH (A), and expansions of 6 – 4 ppm (B) and 2.2 – 0.6 ppm (C).

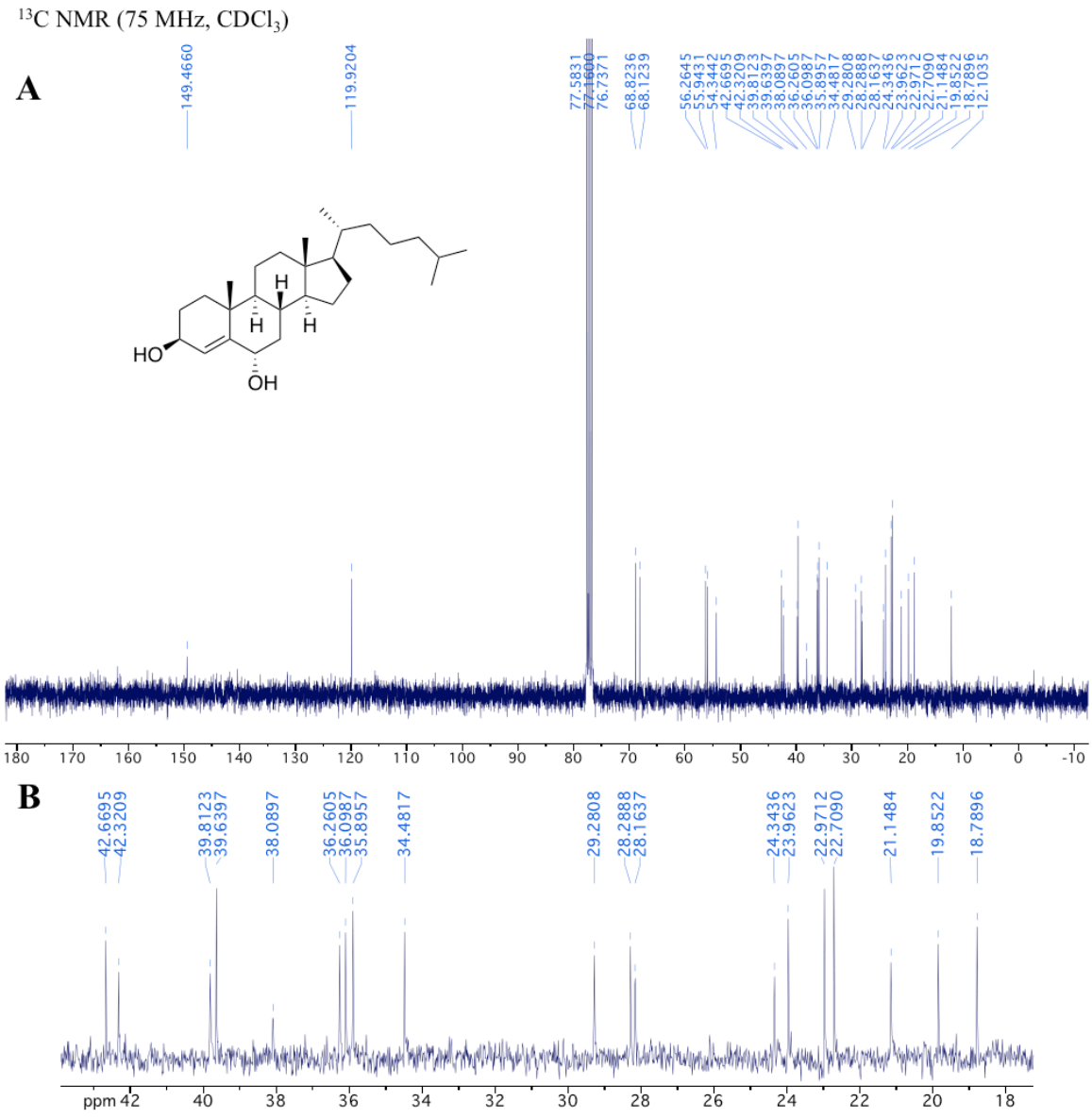

Figure 2.28. ^{13}C NMR spectrum of chol 6α-OH (A), and expansion of 43 – 18 ppm (B).

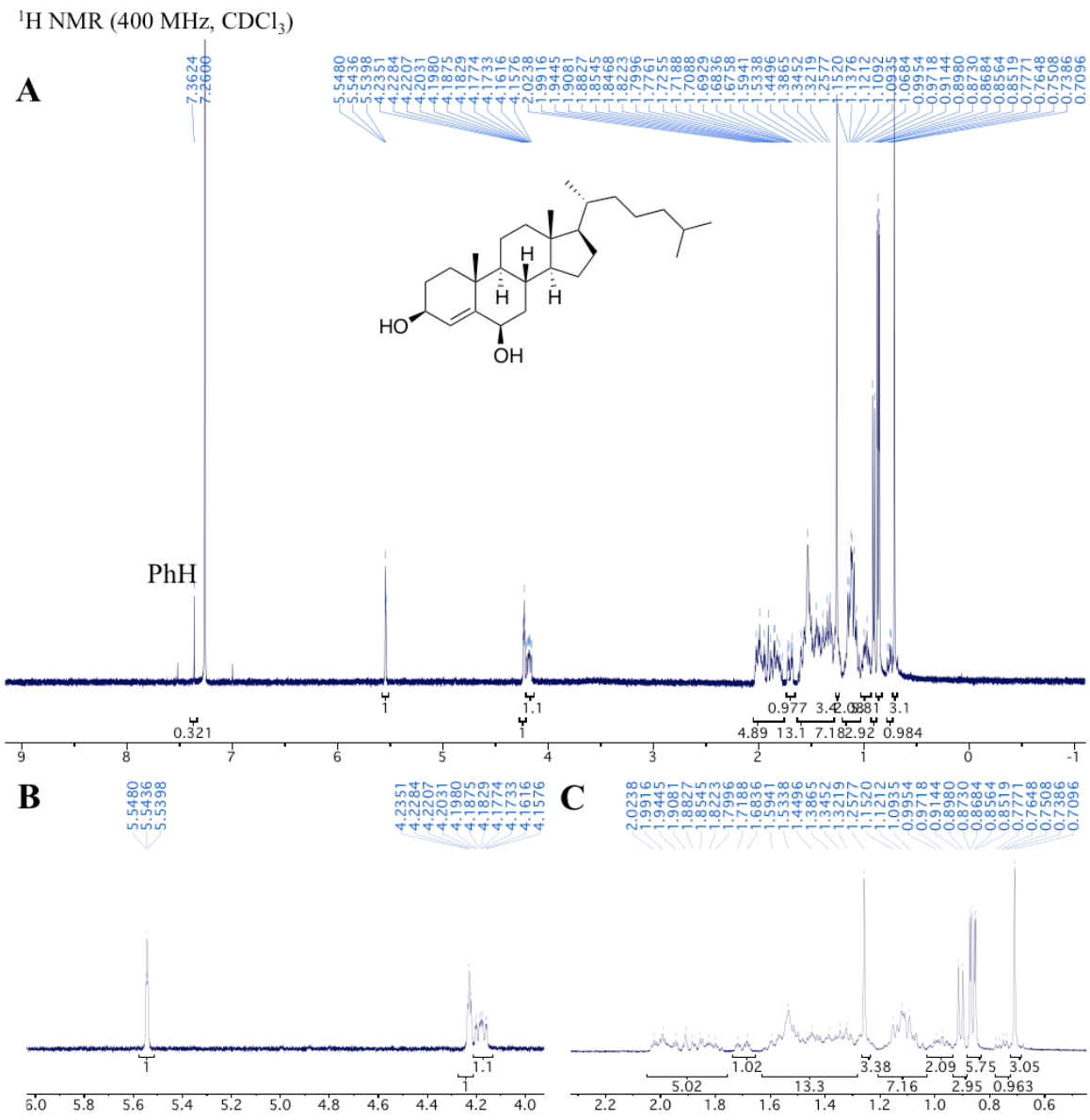

Figure 2.29. ^{1}H NMR spectrum of chol 6β-OH (A), and expansions of 6 – 4 ppm (B) and 2.3 – 0.5 ppm (C).

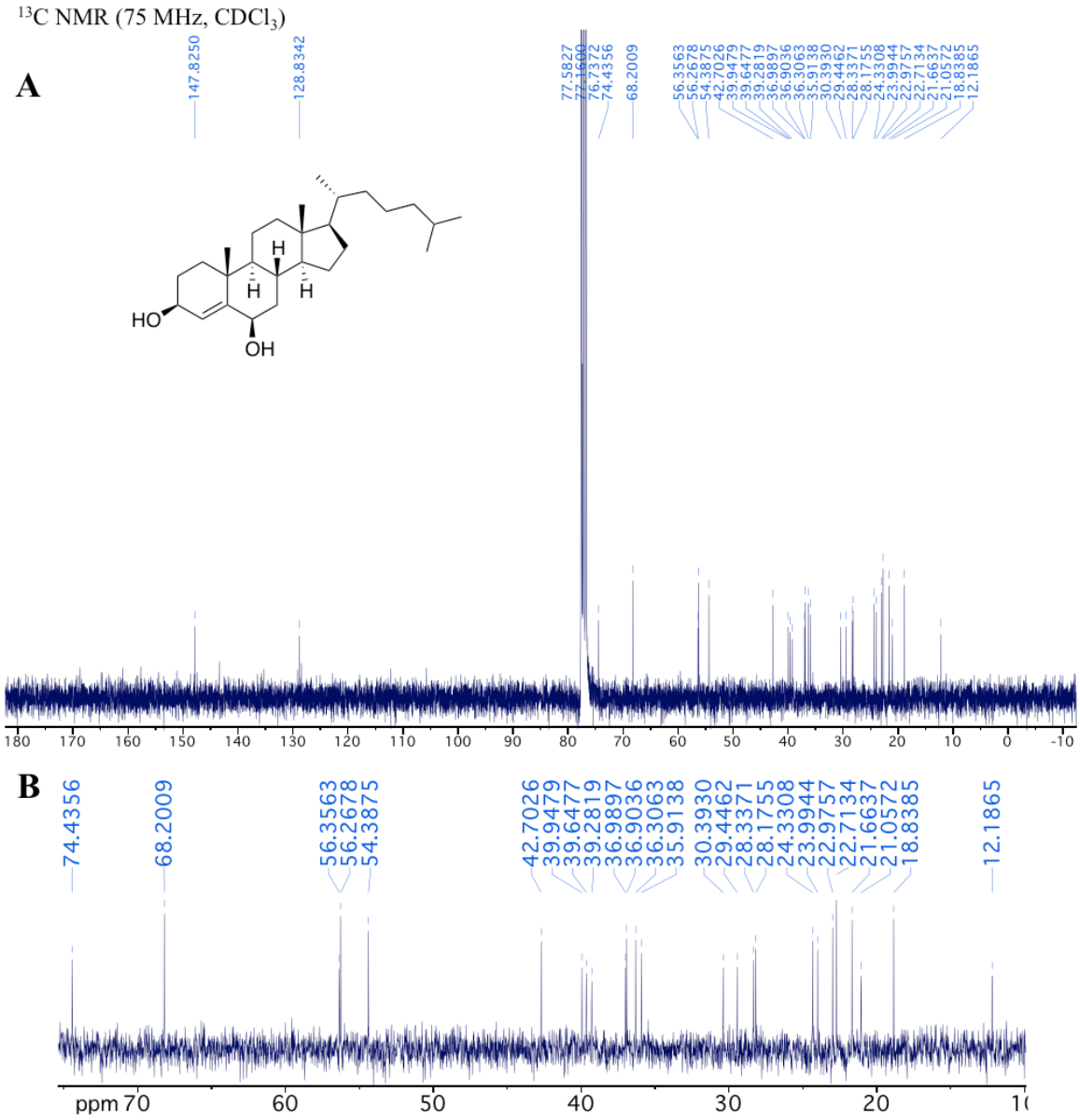

Figure 2.30. ^{13}C NMR spectrum of chol 6β-OH (A), and expansion of 75 – 10 ppm (B).

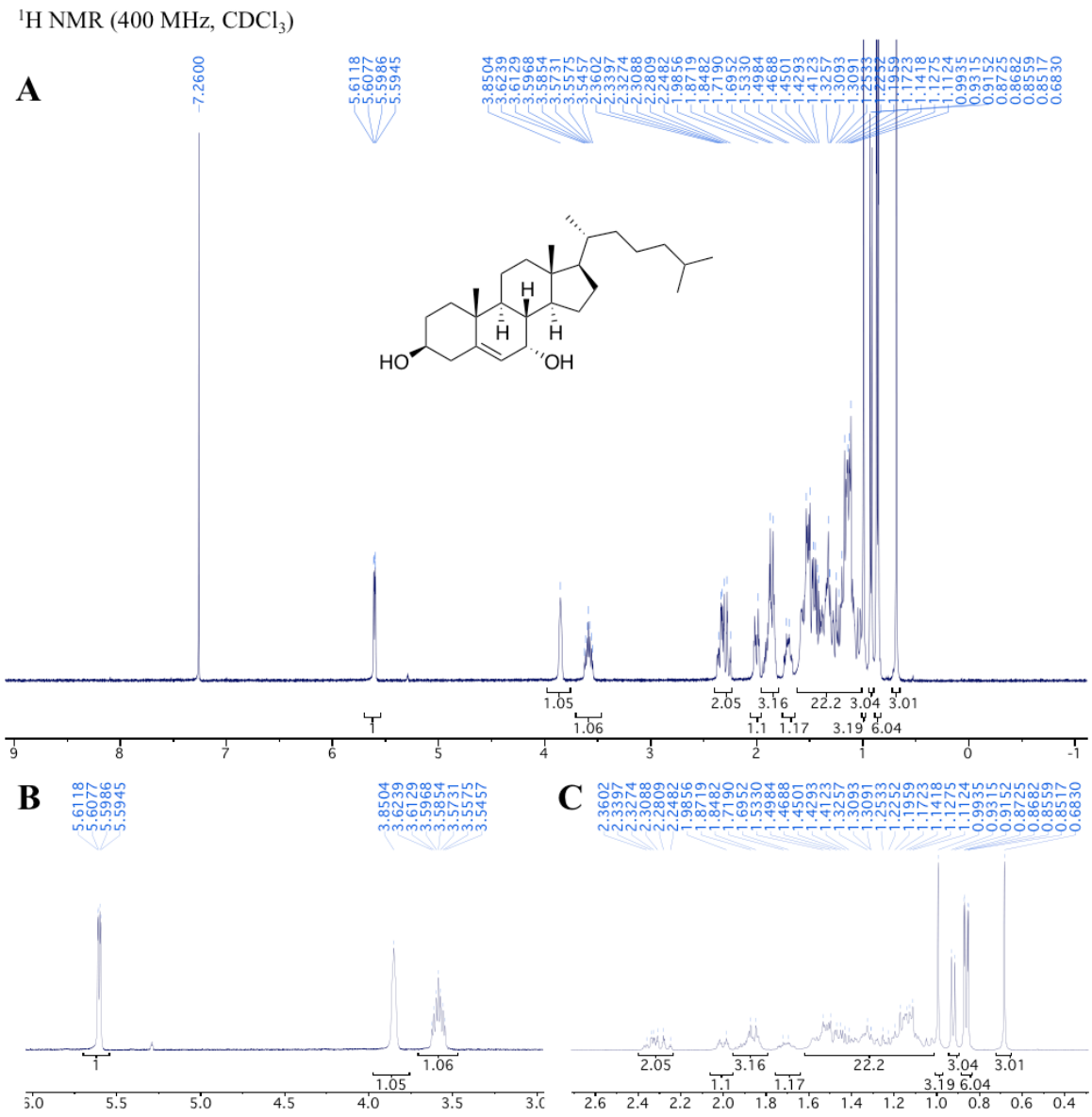

Figure 2.31. ^{1}H NMR spectrum of chol 7α-OH (A), and expansions of 6 – 3 ppm (B) and 2.7 – 0.3 ppm (C).

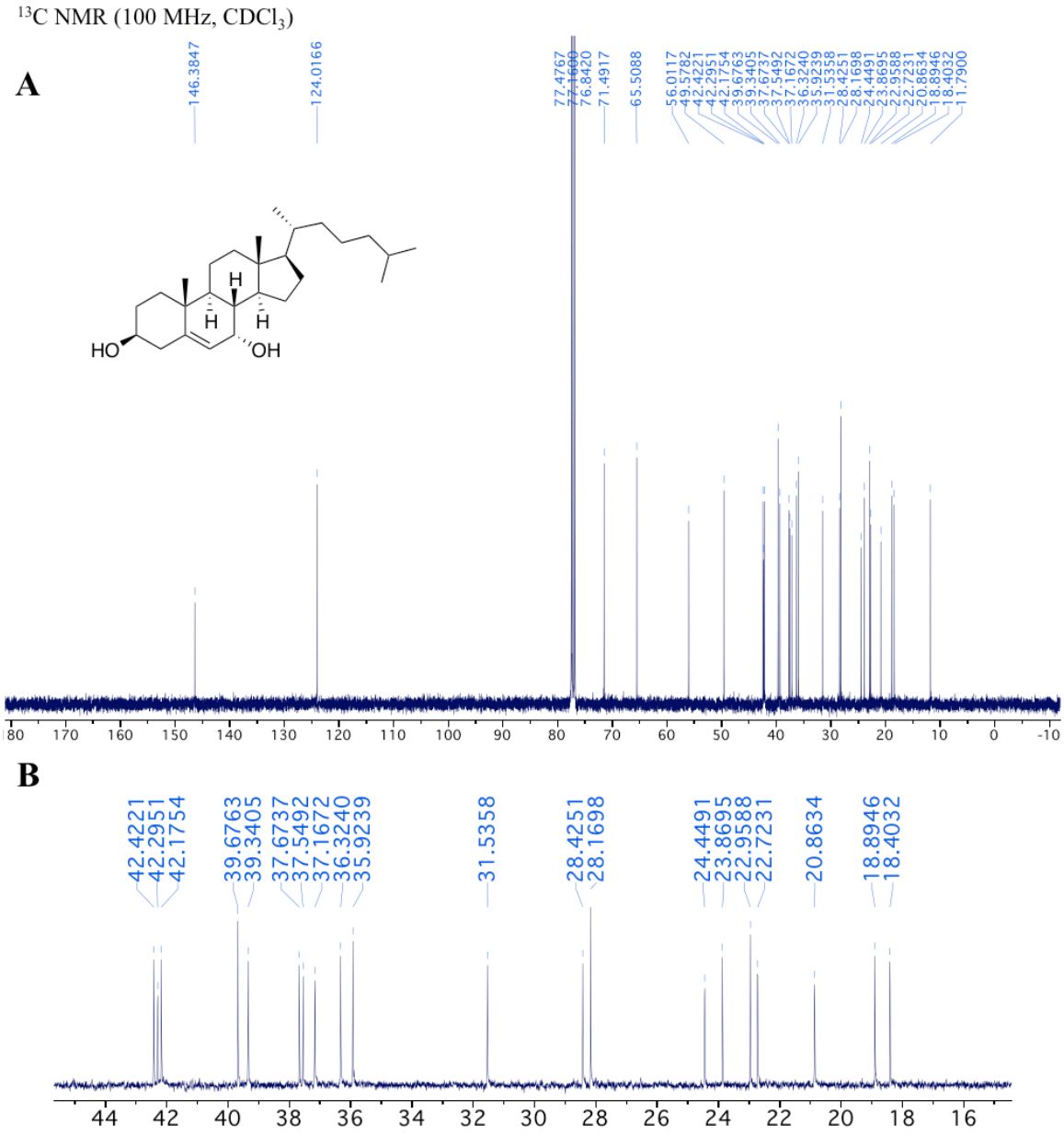

Figure 2.32. ^{13}C NMR spectrum of chol 7α-OH (A), and expansion of 45 – 15 ppm (B).

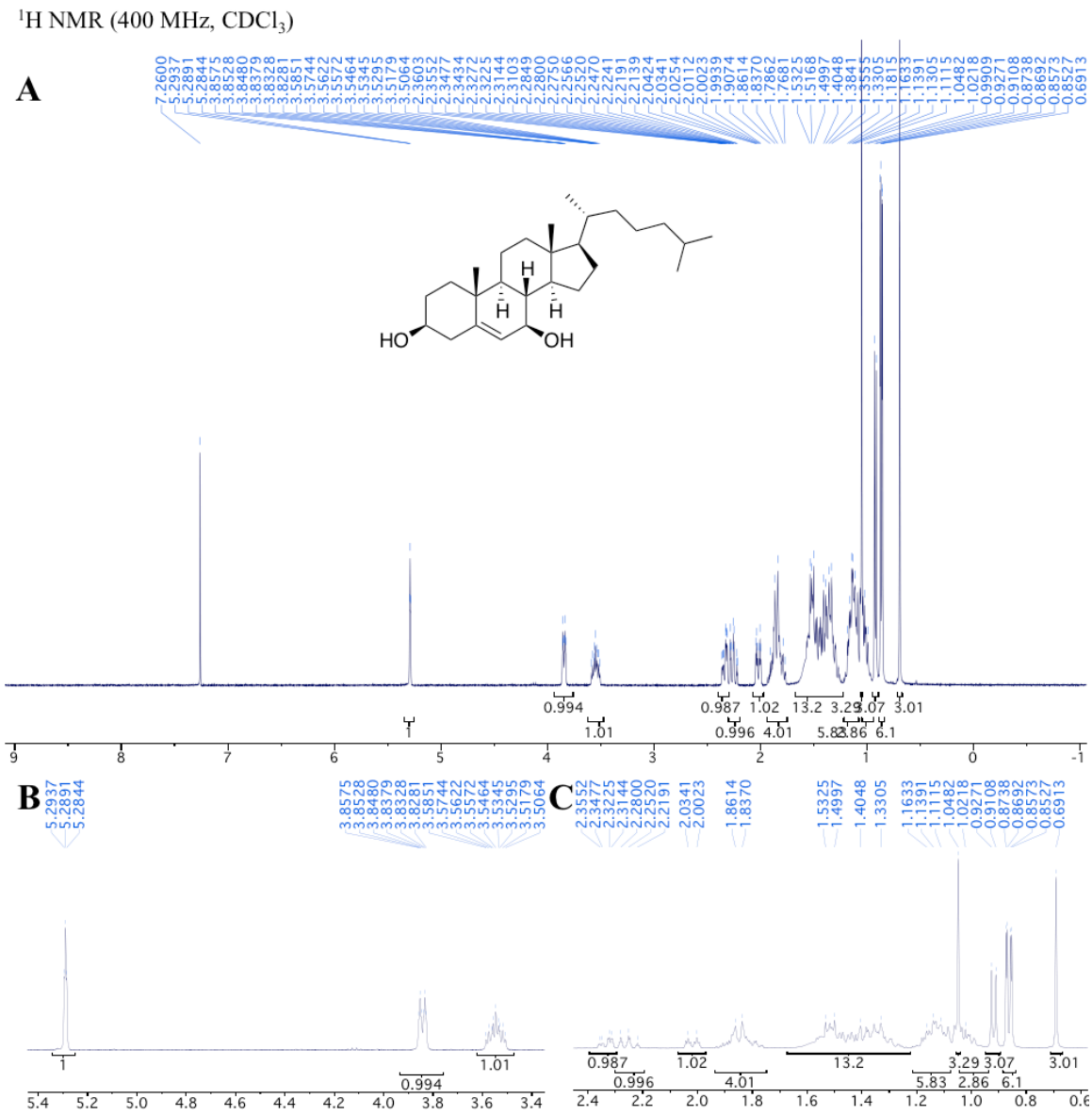

Figure 2.33. ^{1}H NMR spectrum of a chol 7β-OH (A), and expansions of 5.4 – 3.4 ppm (B) and 2.4 – 0.6 ppm (C).

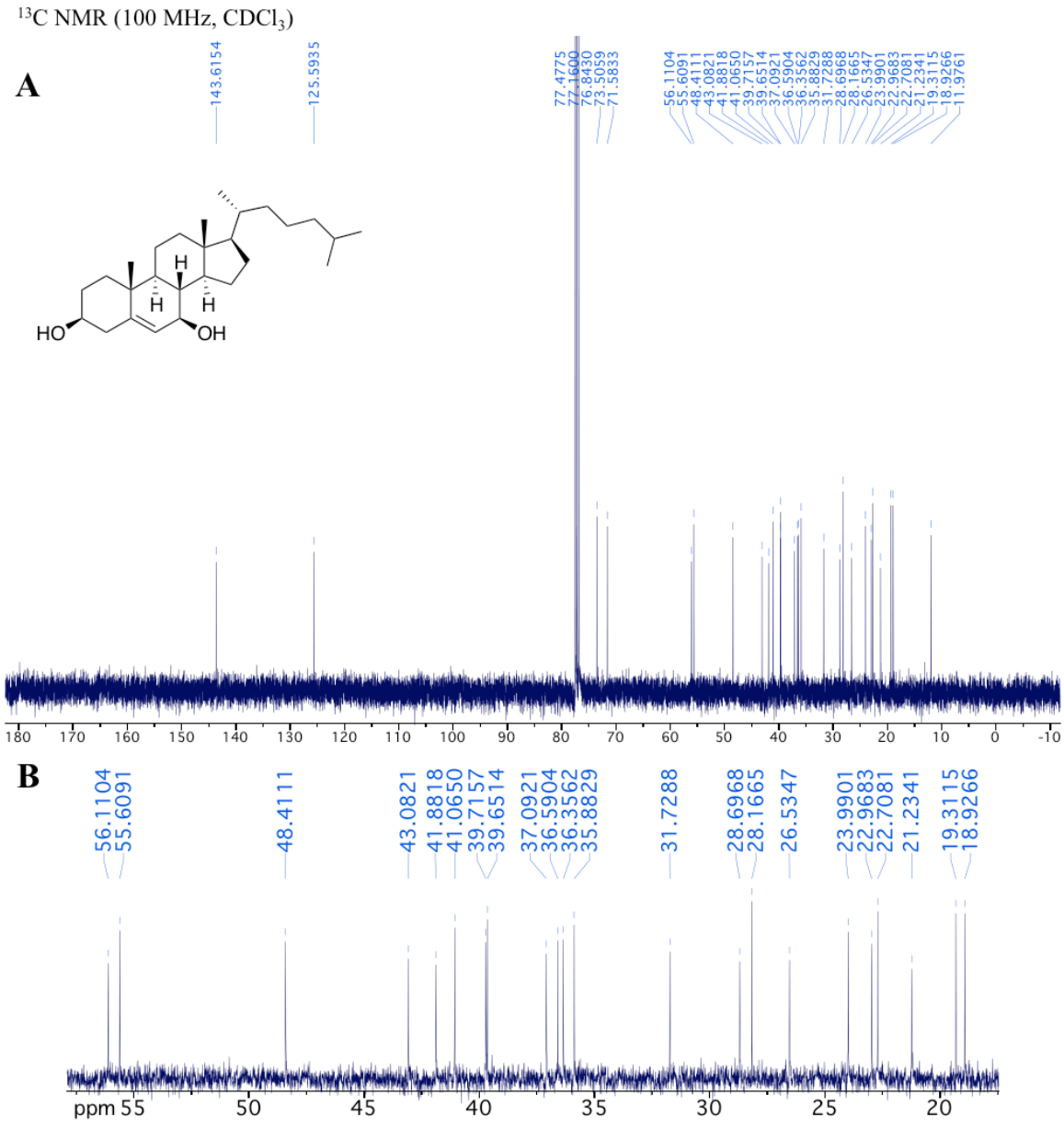

Figure 2.34. ^{13}C NMR spectrum of a chol 7β-OH (A), and expansion of 60 – 18 ppm (B).

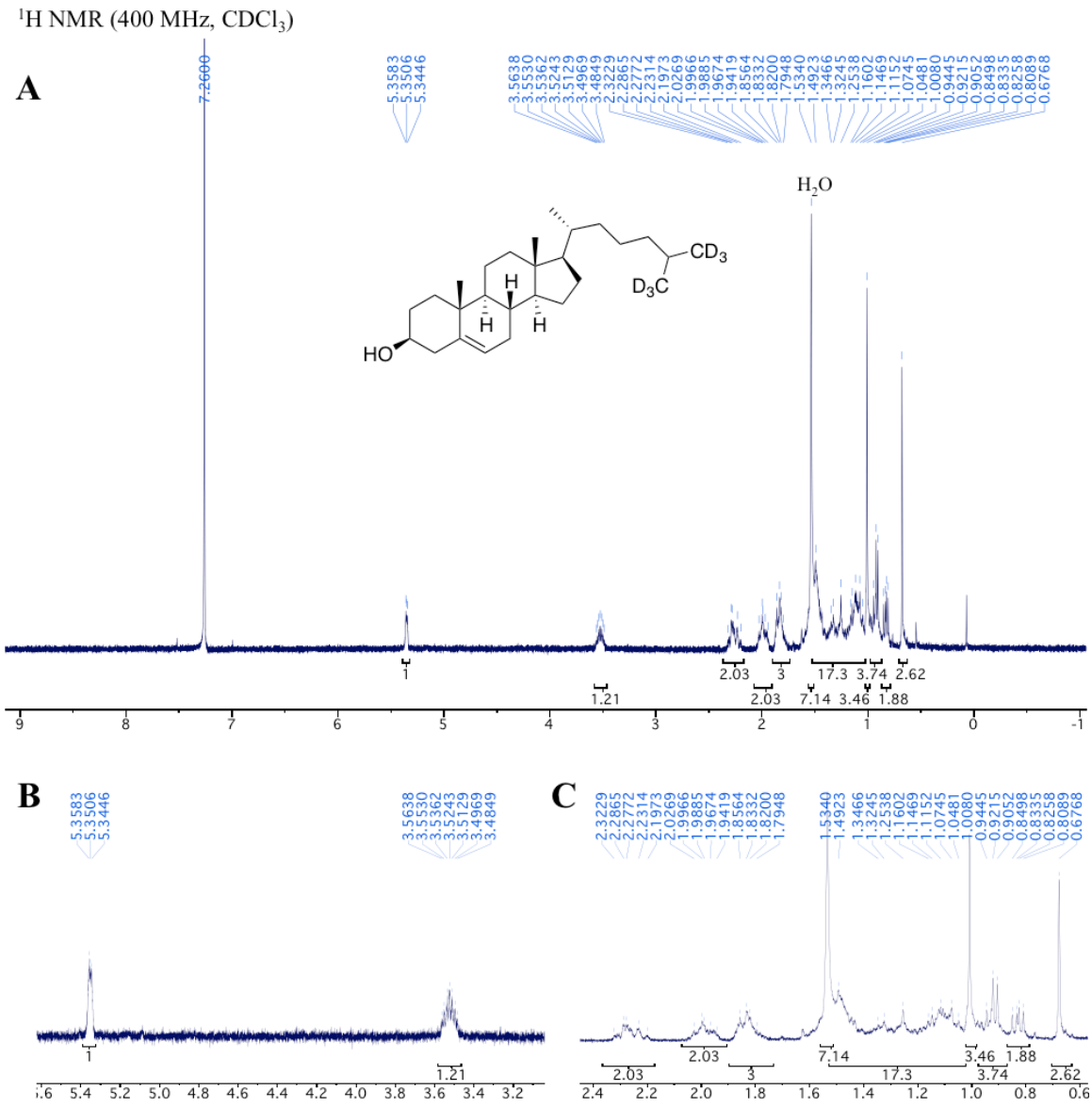

Figure 2.35. ^{1}H NMR spectrum of d_6-chol (A), and expansions of 5.5 – 3 ppm (B) and 2.4 – 0.6 ppm (C).

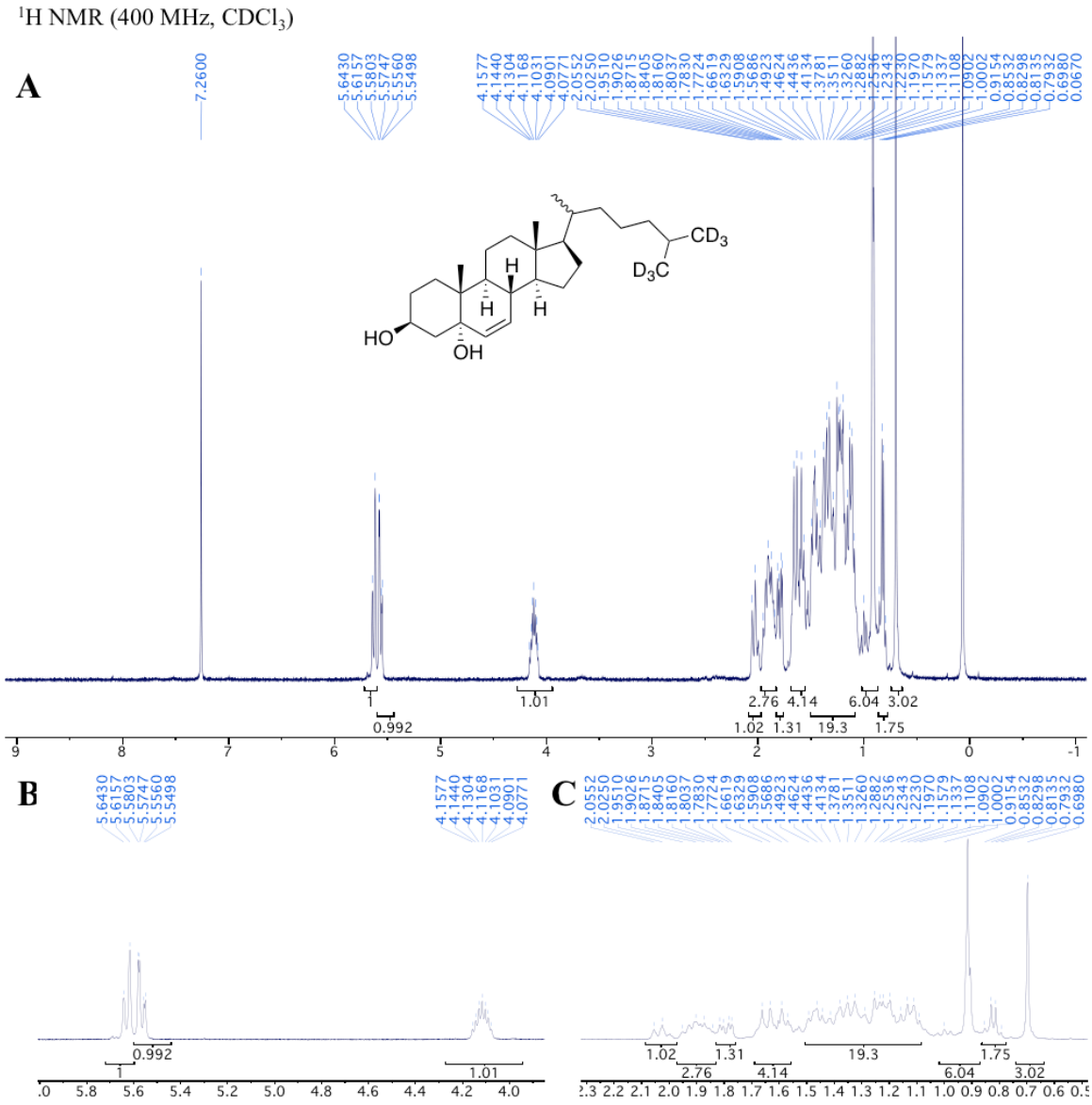

Figure 2.36. ^{1}H NMR spectrum of d_6-chol 5α-OH (A), and expansions of 6 – 4 ppm (B) and 2.3 – 0.5 ppm (C).

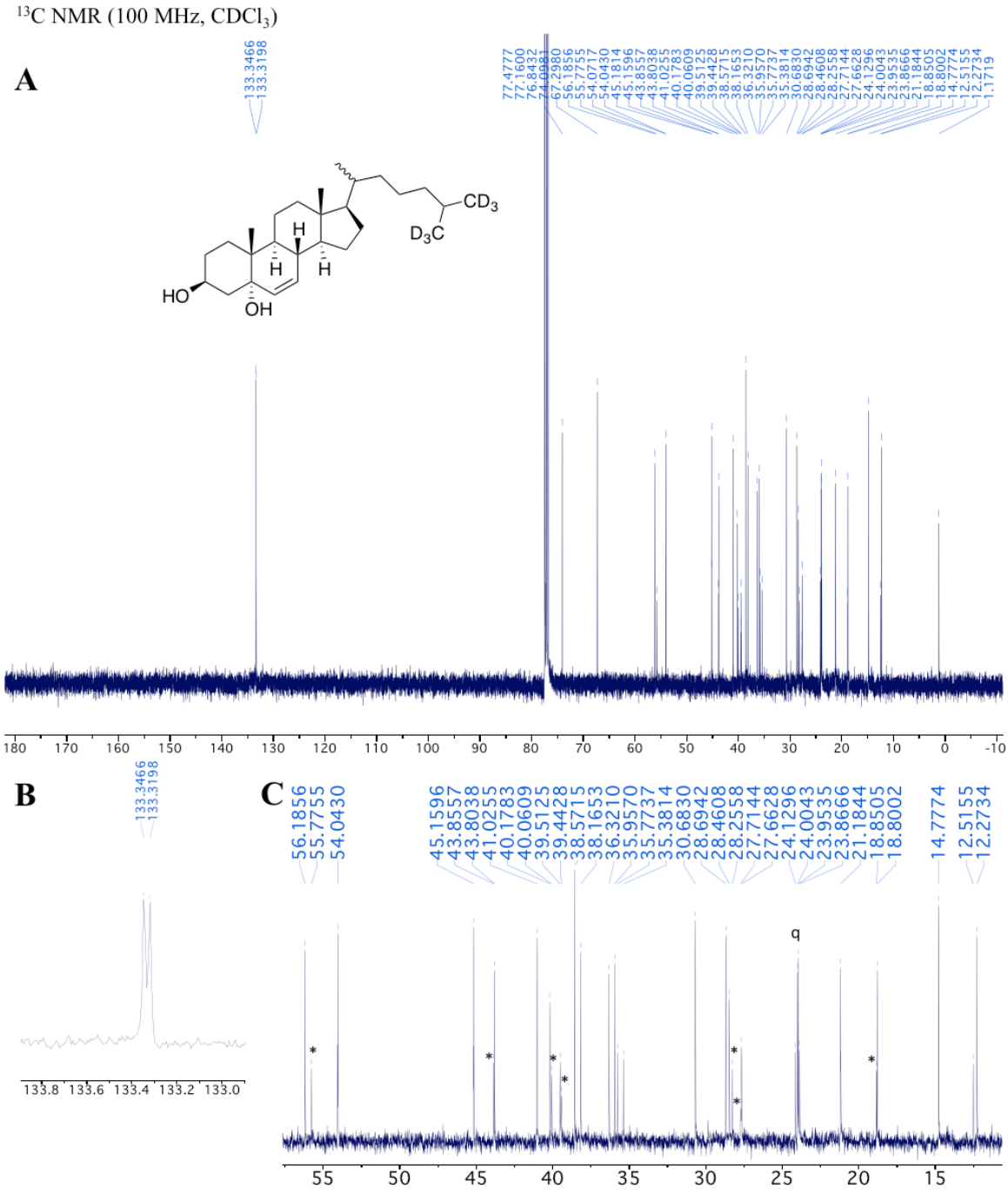

Figure 2.37. ^{13}C NMR spectrum of d_6-chol 5α-OH (A), and expansions of 134 – 133 ppm (B) and 60 – 10 ppm, where the peaks corresponding to the minor stereoisomer are indicated with asterisks and the quartet corresponding to the two CD_3 groups is marked with 'q' (C).

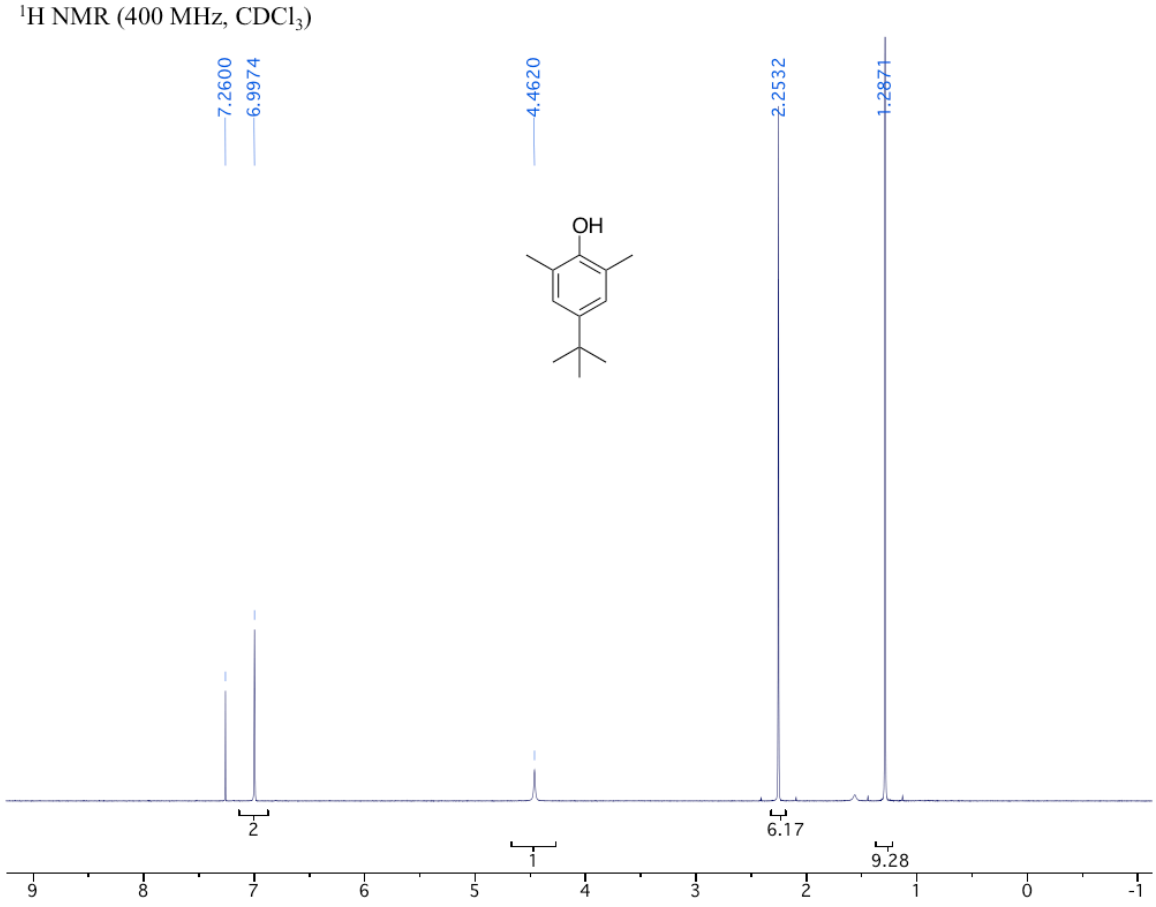

Figure 2.38. ^{1}H NMR spectrum of BDMP.

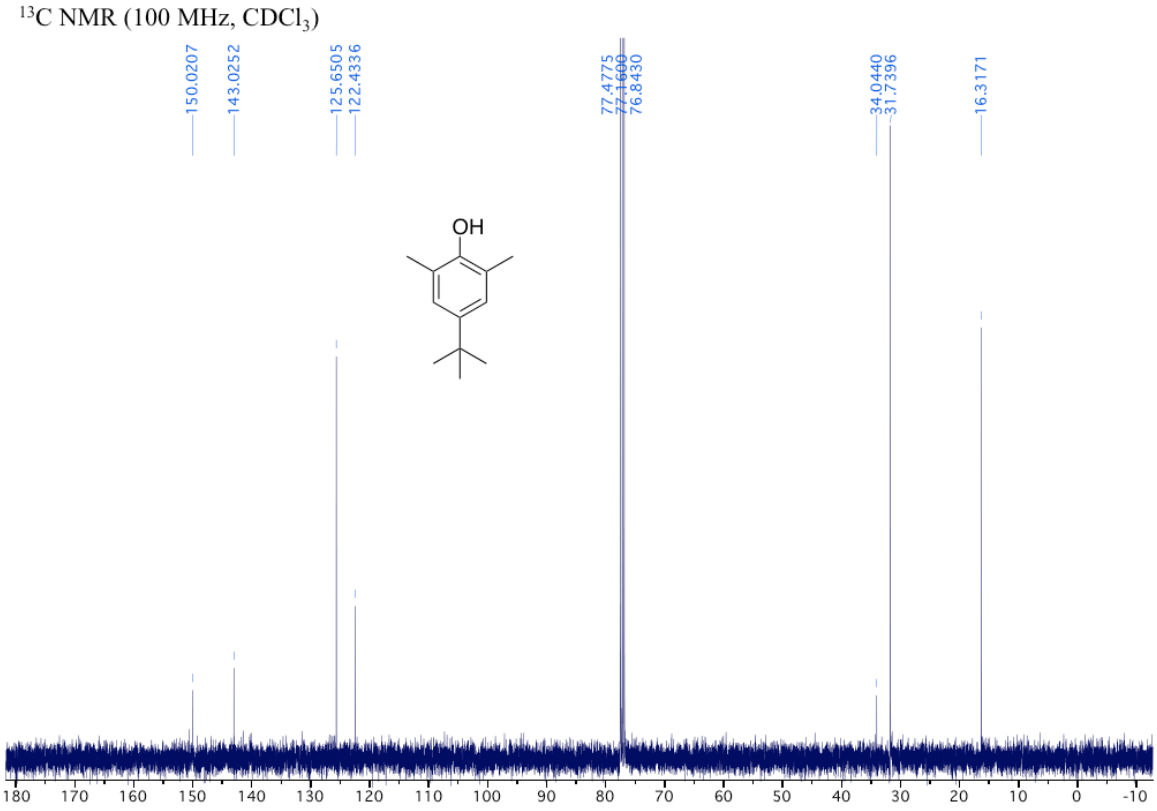

Figure 2.39. ^{13}C NMR spectrum of BDMP.

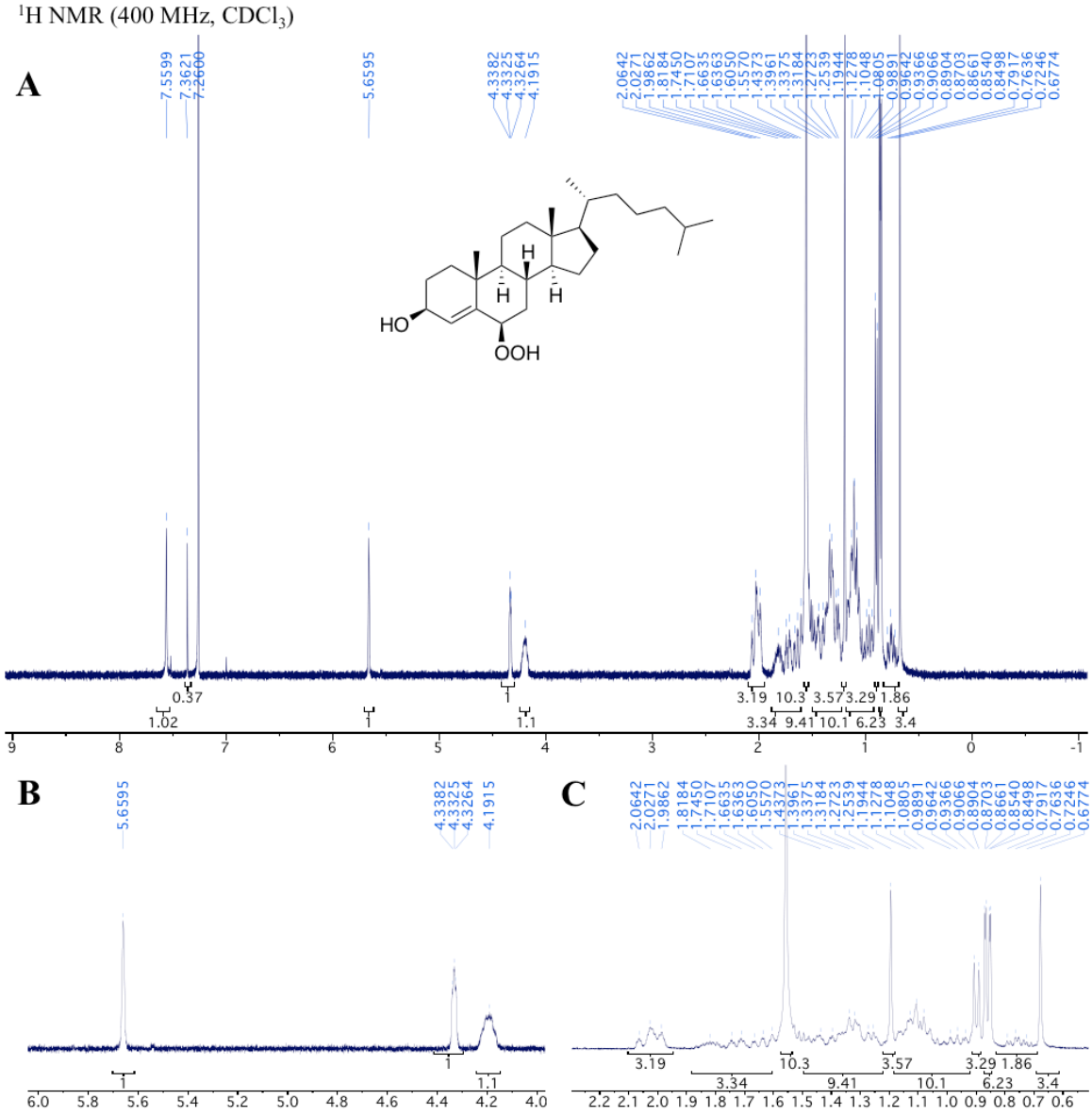

Figure 2.40. ^{1}H NMR spectrum of chol 6β-OOH (A), and expansions of 6 – 4 ppm (B) and 2.3 – 0.5 ppm (C). Note that the peaks at 7.36 and 1.56 are solvent impurities from benzene and water, respectively.

2.6.3 Computational Details

All calculations were carried out using the Gaussian 09 quantum chemistry package[18] using the CBS-QB3 complete basis set approach[19] where possible (for C-H bond strengths), or the density functional theory step of CBS-QB3 (B3LYP/CBSB7) in cases where the systems were too large to calculate with full CBS-QB3 (barriers to H-atom abstraction and C-OO bond strengths).

Table 2.2. Chol C4-H and C7-H bond dissociation enthalpies, calculated with CBS-QB3.

	C-H BDE (kcal/mol)
C4-H	89.0
C7-H	83.2

Table 2.3. Barriers (kcal/mol) to chol C-H abstraction from the four possible allylic hydrogen atoms with various abstracting raicals; methyl peroxyl (MeOO•), cyclohexyl peroxyl (CyOO•) or 2,4-dimethylphenoxyl radical (DMP•), calculated with B3LYP/CBSB7.

R =	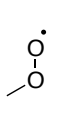 **MeOO•**	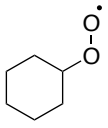 **CyOO•**	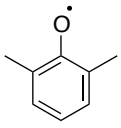 **DMP•**
C4α-H	14.7	15.9	22.1
C4β-H	7.7	8.4	16.1
C7α-H	8.5	9.6	14.6

C7β-H	10.3	11.4	15.6

Table 2.4. Cholesterol peroxyl radical C-OO bond dissociation enthalpies, calculated with B3LYP/CBSB7.

	C-OO BDE (kcal/mol)		C-OO BDE (kcal/mol)
chol 7β-OO•	13.4	chol 5β-OO•	6.5
chol 7α-OO•	12.9	chol 5α-OO•	9.7
chol 6β-OO•	16.6	chol 4β-OO•	15.4
chol 6α-OO•	15.6	chol 4α-OO•	15.6

2.6.4 Supplementary References

(1) Fieser, L. F. *J. Am. Chem. Soc.* **1953**, *75*, 5421.

(2) Noguchi, N.; Yamashita, H.; Gotoh, N.; Yamamoto, Y.; Numano, R.; Niki, E. *Free Radic. Biol. Med.* **1998**, *24*, 259.

(3) Haidasz, E. A.; Van Kessel, A. T. M.; Pratt, D. A. *J. Org. Chem.* **2016**, *81*, 737.

(4) Bill Roschek, Jr; Keri A Tallman; Christopher L Rector; Jason G Gillmore; Derek A Pratt; Carlo Punta, A.; Porter, N. A. *J. Org. Chem.* **2006**, *71*, 3527.

(5) Brinkhorst, J.; Nara, S. J.; Pratt, D. A. *J. Am. Chem. Soc.* **2008**, *130*, 12224.

(6) Nury, T.; Samadi, M.; Zarrouk, A.; Riedinger, J. M.; Lizard, G. *Eur. J. Med. Chem.* **2013**, *70*, 558.

(7) Korde, S. S.; Udasi, R. A.; Trivedi, G. K. *Synth. Commun.* **1997**, *27*, 3419.

(8) Luche, J. L. *J. Am. Chem. Soc.* **1978**, *100*, 2226.

(9) Beckwith, A. L. J.; Davies, A. G.; Davison, I. G. E.; Maccoll, A.; Mruzek, M. H. *J. Chem. Soc., Perkin Trans. 2* **1989**, *7*, 815.

(10) Zhang, W.; Wang, L.; Zhang, L.; Chen, W.; Chen, X.; Xie, M.; Yan, G.; Hu, X.; Xu, J.; Zhang, J. *Steroids* **2014**, *86*, 39.

(11) Sica, D.; Musumeci, D.; Zollo, F.; De Marino, S. *Eur. J. Org. Chem.* **2001**, *19*, 3731.

(12) Cui, J.; Zeng, L.; Su, J.; Lu, W. *Steroids* **2001**, *66*, 33.

(13) Drozdov, F. V.; Mekhtiev, A. P.; Morozevich, G. E. *Russ. J. Bioorganic Chem.* **2007**, *33*, 326.

(14) Li, S.; Pang, J.; Wilson, W. K.; Schroepfer, G. *J. Chem. Phys. Lipids* **1999**, *99*, 33.

(15) Holm, T.; Crossland, I. *J Label. Compd. Radiopharm.* **1996**, *38*, 803.

(16) Kamitori, Y.; Hojo, M.; Masuda, R.; Izumi, T.; Tsukamoto, S. *J. Org. Chem.* **1984**, *49*, 4161.

(17) Ronsein, G. E.; Prado, F. M.; Mansano, F. V.; Oliveira, M. C. B.; Medeiros, M. H. G.; Miyamoto, S.; Di Mascio, P. *Anal. Chem.* **2010**, *82*, 7293.

(18) Frisch, M. J.; Trucks, G. W.; Schlegel, H. B.; Scuseria, G. E.; Robb, M. A.; Cheeseman, J. R.; Scalmani, G.; Barone, V.; Mennucci, B.; Petersson, G. A.; Nakatsuji, H.; Caricato, M.; Li, X.; Hratchian, H. P.; Izmaylov, A. F.; Bloino, J.; Zheng, G.; Sonnenberg, J. L.; Hada, M.; Ehara, M.; Toyota, K.; Fukuda, R.; Hasegawa, J.; Ishida, M.; Nakajima, T.; Honda, Y.; Kitao, O.; Nakai, H.; Vreven, T.; Montgomery, J. A., Jr.; Peralta, J. E.; Ogliaro, F.; Bearpark, M.; Heyd, J. J.; Brothers, E.; Kudin, K. N.; Staroverov, V. N.; Keith, T.; Kobayashi, R.; Normand, J.;

Raghavachari, K.; Rendell, A.; Burant, J. C.; Iyengar, S. S.; Tomasi, J.; Cossi, M.; Rega, N.; Millam, J. M.; Klene, M.; Knox, J. E.; Cross, J. B.; Bakken, V.; Adamo, C.; Jaramillo, J.; Gomperts, R.; Stratmann, R. E.; Yazyev, O.; Austin, A. J.; Cammi, R.; Pomelli, C.; Ochterski, J. W.; Martin, R. L.; Morokuma, K.; Zakrzewski, V. G.; Voth, G. A.; Salvador, P.; Dannenberg, J. J.; Dapprich, S.; Daniels, A. D.; Farkas, O.; Foresman, J. B.; Ortiz, J. V.; Cioslowski, J.; Fox, D. J. *Gaussian 09, revision B.01*; Gaussian, Inc.: Wallingford CT, 2009.

(19) Montgomery, J. A.; Ochterski, J. W.; Petersson, G. A. *J. Chem. Phys.* **1994**, *101*, 5900.

Chapter 3: H-Atom Abstraction vs. Addition: Accounting for the Diverse Product Distribution in the Autoxidation of Cholesterol & its Esters*

3.1 Preface

The previous chapter outlined that the free radical-mediated oxidation (autoxidation) of cholesterol yields a more complex mixture of hydroperoxide products than previously appreciated. In addition to the epimers of the major product, cholesterol 7-hydroperoxide, the epimers of each of the regioisomeric 4- and 6-hydroperoxides are formed, as is the 5α-hydroperoxide in the presence of a good H-atom donor. Herein we determine the products resulting from competing peroxyl radical addition to cholesterol, the stereoisomeric cholesterol-5,6-epoxides, which account for 12% of the oxidation products, as well as electrophilic dehydration products of the cholesterol hydroperoxides, 4-, 6- and 7-ketocholesterol. Moreover, we interrogate how their distribution – and abundance relative to the H-atom abstraction products – changes in the presence of good H-atom donors, which has serious implications for how these oxysterols are used as biomarkers. The resolution and quantification of all autoxidation products by LC-MS/MS was greatly enabled by the synthesis of a new isotopically-labeled cholesterol standard and corresponding selected autoxidation products. The autoxidation of cholesteryl acetate was also investigated as a model for the cholesterol esters which abound *in vivo*. While esterification of cholesterol imparts measurable stereoelectronic effects – most importantly reflected in the fact that it autoxidizes at 4 times the rate of unesterified cholesterol – the product distribution is largely similar to cholesterol. Deuteration of the allylic positions in cholesterol suppresses autoxidation by H-atom transfer (HAT) in favour of addition, such that the epoxides become the major products. The corresponding kinetic isotope effect ($k_H/k_D \sim 20$) indicates that tunnelling underlies the preference for the HAT pathway. This chapter is presented as it was published in the *Journal of the American Chemical Society* (Zielinski, Z.A.; Pratt, D.A. *J. Am. Chem.*

Soc. **2019**, *141*, 3037), with the exception of Section 3.6, which adds a perspective in the context of this Thesis.

3.2 Introduction

Lipid autoxidation (peroxidation) has been linked to a myriad of degenerative diseases and conditions. The initial products of the free radical chain mechanism are usually hydroperoxides, and downstream products include electrophilic species containing ketones or aldehydes, including the pathogenic compounds malondialdehyde, derived from arachidonate, and 4-hydroxynonenal, derived from omega-6 polyunsaturated fatty acids (PUFAs), in general.[1] Sterol autoxidation has received comparatively less attention than PUFA autoxidation, presumably because sterols are typically less reactive, reflected in their lower propagation rate constants (k_p) (*cf.* Eq. 3.1 and Table 3.1). The exception to this is 7-dehydrocholesterol (7-DHC), the highly autoxidizable precursor to vitamin D_3 and cholesterol (chol). It has been shown that 7-DHC builds up in patients with Smith-Lemli-Opitz syndrome, and its oxidation is believed to be involved in the pathogenesis of the disease.[2,3]

$$ROO^{\bullet} + RH \xrightarrow{k_p} ROOH + R^{\bullet} \qquad (3.1)$$

Table 3.1. Propagation rate constants for selected lipids.[4]

PUFA	k_p ($M^{-1}s^{-1}$)	sterol	k_p ($M^{-1}s^{-1}$)
linoleate	62	cholesterol	11
arachidonate	201	7-DHC	2260

While chol is less reactive to autoxidation than any of the aforementioned lipids, it is considerably more abundant, constituting up to 50 mol% of the lipids in cell membranes.[5] In addition, the brain contains more cholesterol than any other organ, and essentially all of the brain's cholesterol is synthesized locally – of which an estimated 70% is contained in myelin.[6] Chol autoxidation

products have been reported to be in the vicinity of 1 μg/mL in human serum and LDL,[7-9] and elevated levels have been associated with many degenerative diseases,[10] though it remains unclear whether their role is causative or consequential – a debate that continues to garner interest.[10-13] The exception to this has been the secosterols **3.1** and **3.2**, which have been implicated in cardiovascular disease,[11] cancer,[12] and neurodegeneration (including Alzheimer's[13] and Parkinson's[14]). These compounds have been proposed to arise *in vivo* from ozonolysis of chol,[15] or more likely, Hock fragmentation of chol 5-hydroperoxide (chol 5-OOH) formed by oxidation with $^1O_2$.[16]

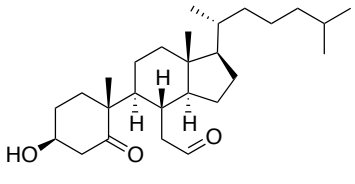

3.1

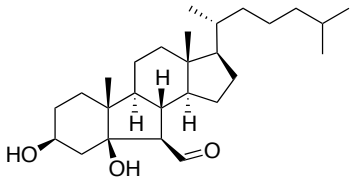

3.2

We recently showed[17] that chol autoxidation yields a more complex mixture of hydroperoxide products than previously understood (*cf.* Figure 3.1B). In addition to chol 7-hydroperoxide (7-OOH), both epimers of 4-OOH and 6-OOH were formed in chol autoxidations carried out in aerated chlorobenzene due to the C4-H abstraction pathway previously deemed uncompetitive with C7-H abstraction (*cf.* Figure 3.1A). Furthermore, 5α-OOH was formed in the presence of phenolic antioxidants, which are significantly more reactive H-atom donors than chol itself and are able to trap the 5α-OO$^\bullet$ intermediate faster than the β-fragmentation of O_2 (the reverse of oxygen addition) occurs. These observations provide an alternative explanation for the origin of the secosterols. Moreover, we found that chol 6-OOH also underwent Hock fragmentation to produce **3.1** and **3.2**, suggesting chol autoxidation may have a larger role in disease pathogenesis than previously believed.

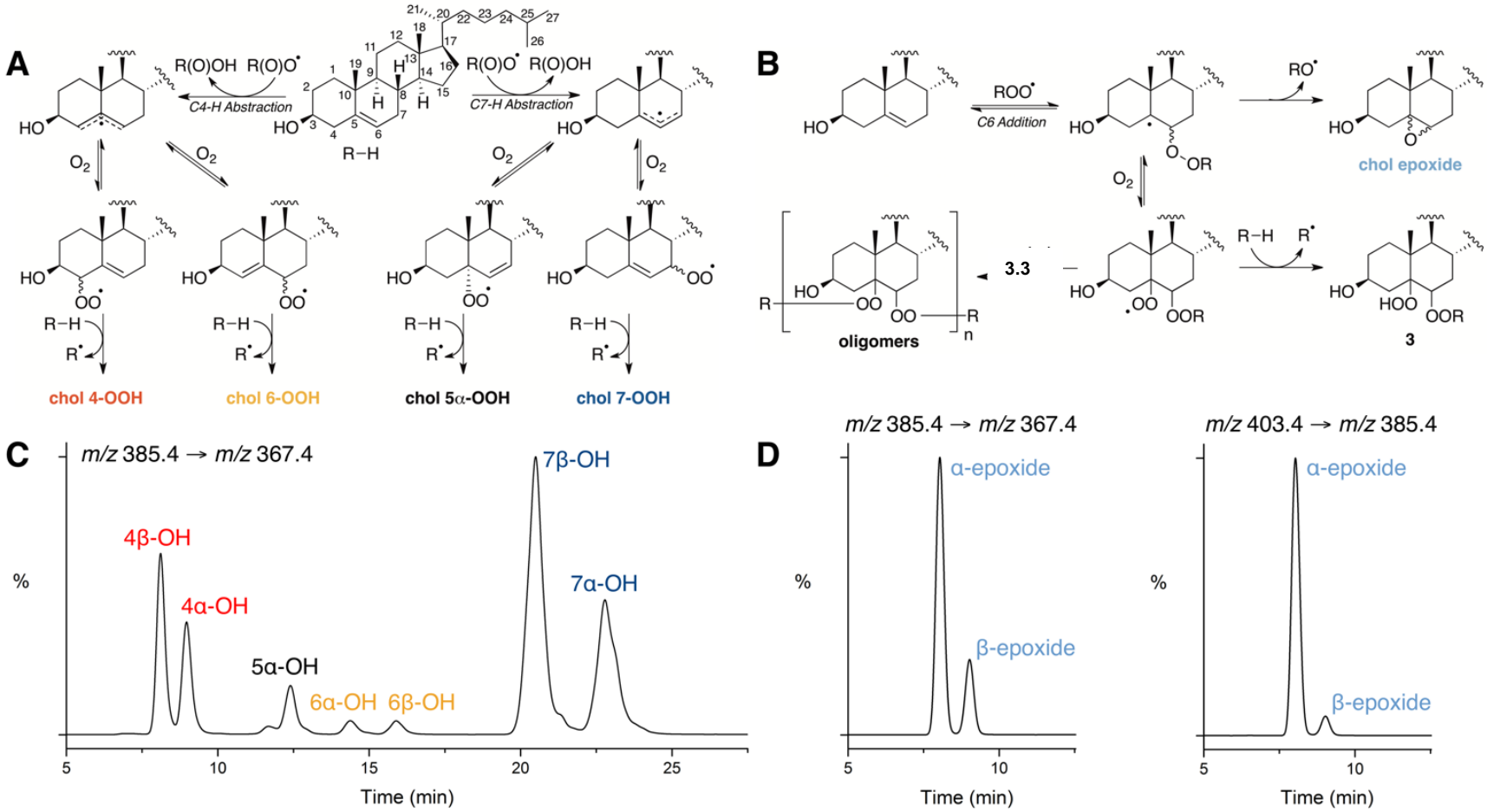

Figure 3.1. The competing pathways in cholesterol (chol) autoxidation: H-atom abstraction resulting in regioisomeric hydroperoxide formation (A) and peroxyl radical addition yielding epoxides and peroxides (B). The associated product distribution from MeOAMVN-initiated autoxidations of chol in chlorobenzene at 37°C in the presence of 4-*tert*-butyl-2,6-dimethylphenol (BDMP), where the alcohols are detected due to pre-treatment with PPh_3 (C).[17] Authentic chol epoxides have the same retention times as chol 4-Ohs (D). Data in panels C and D were obtained by HPLC (95:5 hexane:*i*-PrOH, 1.5 mL/min) with $APCI^+$-MS/MS detection for the *m/z* → *m/z* transitions indicated.

While these developments contributed to a more thorough understanding of chol autoxidation, the complete mechanism is even more nuanced. Herein, we report on our investigations of the interplay between H-atom abstraction by peroxyl radicals and their addition as propagation steps in cholesterol autoxidation (*cf.* Figures 3.1A and 3.1B, respectively). The intermediate radical formed upon addition can undergo intramolecular homolytic substitution (S_Hi) to yield 5α,6α-epoxycholesterol (chol α-epoxide) or 5β,6β-epoxycholesterol (chol β-epoxide) and an alkoxyl radical. The alkoxyl radical can then abstract an H-atom from another molecule of chol to propagate the radical chain reaction. Although chol epoxides are known products of chol autoxidation, their quantification in relation to chol hydroperoxides has been complicated by the fact that they are also believed to be formed by enzymes and/or other oxidants (e.g. O_3, inhaled in polluted air).[9,18,19] The α:β ratio is considered to be an indication of the origin of the epoxides; for example, the autoxidation ratio is reported to be *ca.* 1:3, whereas epoxides from enzymatic origin are almost exclusively the α-isomer.[18] We were therefore interested in studying the interplay between the H-atom abstraction and peroxyl radical addition pathways. Since the distribution of hydroperoxide products was affected by the addition of H-atom donors, we wondered if the ratio of epoxides, or the pathway preference, might also be affected. Furthermore, we surmised that O_2 could (reversibly) add to the alkyl radical formed upon peroxyl radical addition, yielding yet another class of compounds, and that this distribution could also be sensitive to H-atom donors (*cf.* Figure 3.1C). Inclusion of this manifold of reactivity provides a comprehensive view of cholesterol autoxidation chemistry which provides crucial insights on their use as biomarkers and implications in disease pathogenesis.

3.3 Results

3.3.1 Cholesterol Autoxidation Revisited.

Standards of the cholesterol-derived α- and β-epoxides were prepared by mCPBA oxidation as a mixture, and analyzed using the same HPLC-APCI$^+$-MS/MS technique used in our previous work

(see Experimental Section 3.6 for details).[17] To our surprise, not only did the epoxides ionize efficiently with the same MS/MS transition (*m/z* 385.4 → *m/z* 367.4), but they also eluted at the same retention time as chol 4α-OH and 4β-OH (*cf.* Figure 3.1D). Attempts to identify conditions that afforded clean separation of chol β-epoxide and chol 4α-OH were unsuccessful. The epoxides did, however, have a unique MS/MS transition (*m/z* 403.4 → *m/z* 385.4, *cf.* Section 3.8.1), enabling their quantification and deduction of the amount of chol 4α-OH (from MS/MS chromatograms corresponding to the shared transition of both of the products, i.e. *m/z* 385.4 → *m/z* 367.4).

Isotopically-labeled standards were required for precise quantification of chol 4α-OH and the epoxides, which were prepared from the newly synthesized 17,20,21,21,21,22-d_6-chol (**3.8**). We had previously used 26,26,26,27,27,27-d_6-chol to prepare our standards, which was synthesized using the method of Holm and Crossland,[20] with a (optimal) 7% yield over 9 steps. To our knowledge, the only other synthesis of chol-26,26,26,27,27,27-d_6 uses an expensive desmosterol starting material.[21,22] We therefore opted to develop a synthesis of 17,20,21,21,21,22-d_6-chol (**3.8**), which was achieved in 6 steps from pregnenolone with an overall yield of 34% (Scheme 3.1).

Briefly, the 3-OH of pregnenolone was silylated with TIPS-Cl and the product deuterated based on the method of De Miranda et. al.,[23] resulting in the quantitative formation of **3.5**. While attempts to couple **3.5** and 1-bromo-4-methylpentane by Wittig chemistry resulted in partial D/H exchange, the analogous Grignard reaction proceeded without loss of D. The subsequent elimination resulted in a mixture of three alkenes (purported to be 55% $\Delta^{20(22)}$, 25% $\Delta^{20(21)}$ and 20% $\Delta^{17(20)}$ when carried out on a similar substrate).[24] Carrying forward the mixture would have undoubtedly increased the overall yield, but would have led to a mixture of d_5- and d_6-chol in the final product. Thus, the desired $\Delta^{20(22)}$ alkene (**3.7**) was isolated from the mixture by silver-impregnated silica gel chromatography. Catalytic hydrogenation of **3.7** with D_2 installed the final two deuterium atoms, and fluoro-desilylation afforded 17,20,21,21,21,22-d_6-chol. From this novel d_6-chol, the desired internal

standards, d_6-chol 5α-OH and the d_6-chol epoxides (a mixture of α- and β-isomers) were prepared by known methods (see Experimental Section 3.6 for details).

Scheme 3.1. Synthesis of 17,20,21,21,21,22-d_6-cholesterol (**3.8**).

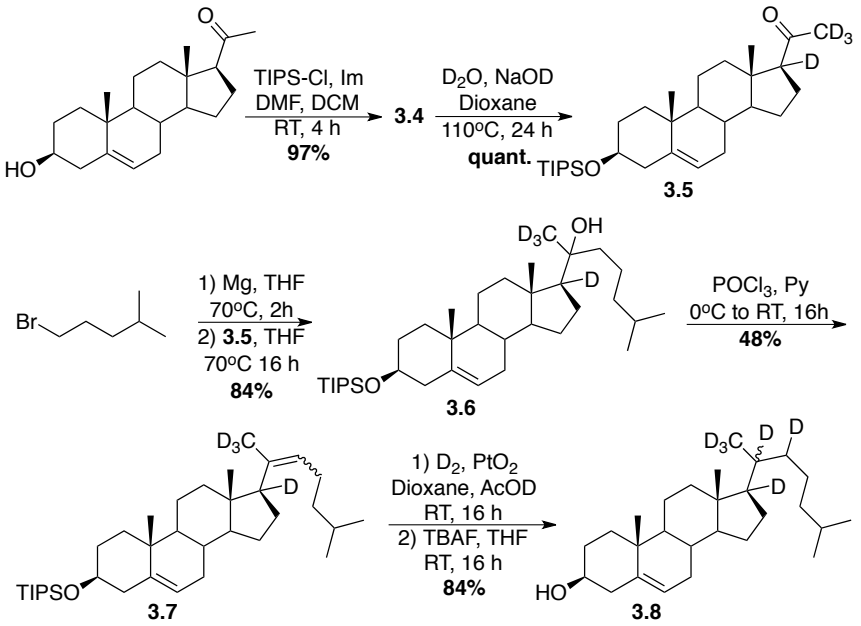

Cholesterol autoxidations were then carried out as described in Experimental Section 3.6. In each instance the samples were treated with PPh_3 to convert the hydroperoxide products to their corresponding alcohols, which are more stable toward chromatography and MS analysis.[25] Control experiments showed the chol epoxides to be stable under these conditions. In addition to the six primary products observed in our previous work (chol 4α-OH, 4β-OH, 6α-OH, 6β-OH, 7α-OH, and 7β-OH), the α- and β-epoxides were observed (Figure 3.2A), and found to constitute roughly 12% of the product distribution (Figure 3.2B).[26]

In addition to the primary hydroperoxide and epoxide products of autoxidation, we sought to determine whether significant amounts of secondary products were formed competitively in the early

stages of the autoxidations.[27] 7-Ketocholesterol (7-ketochol), the dehydration product of chol 7-OOH or termination product of chol-7OO$^{\bullet}$ and another peroxyl radical, is known to form *in vivo* and has been frequently used as a biomarker of lipid oxidation.[28-30] In theory, each of chol 4-OOH, 6-OOH and 7-OOH can dehydrate to give the corresponding ketones. Authentic standards for 4-, 6- and 7-ketochol were synthesized (see Supporting Information 3.8), and although they ionized well by APCI^{+}, the parent M+H^{+} ion (*m/z* 401.4) did not fragment to a significant extent, precluding MS/MS analysis. However, given their α,β-unsaturation, the ketones have absorption maxima at 234 nm, and could be quantified by UV detection. Indeed, measurable amounts of 6- and 7-ketochol were formed in the autoxidations. 4-Ketochol was surprisingly non-polar – presumably due to the C3-OH participating in a hydrogen bond with the ketone – and could not be separated from the solvent front. Since the ketochols could also be detected by APCI-MS, select autoxidation samples were analyzed this way, but 4-ketochol was not detected.

Chol autoxidations were also carried out in the presence of the radical-trapping antioxidant BDMP to explore the kinetic product distribution, where β-fragmentation of intermediate peroxyl radicals is minimized. Expectedly, the total amount of oxidation products decreased with increasing [BDMP] (*cf.* Figure 3.28). However, upon comparing the relative amounts of each oxidation product, it is clear that the reversibility of O_2 addition is a contributing factor to the overall product distribution. The products derived from C4-H abstraction (chol 4-OOH and 6-OOH) and peroxyl radical addition (chol α- and β-epoxide) decreased relative to chol 7-OOH with increasing BDMP concentration, albeit after an initial surge in epoxide concentration (Figure 3.2C). Conversely, the proportion of chol 5α-OOH increased with added BDMP. This dependence was used to determine the β-fragmentation rate constant for 5α-OO$^{\bullet}$ $k_{\beta} = (3.8 \pm 0.9) \times 10^{5}$ s^{-1} (*cf.* Figure 3.29). [31] The initial increase in epoxide was intriguing, and in addition to influencing the amount of epoxides formed compared to hydroperoxides, the ratio of α- to β-epoxide was also influenced by added BDMP (*cf.* Figure 3.2D).

Chol autoxidations were also carried out in the presence of PMC, an analogue of α-tocopherol, the most bioactive form of Vitamin E. As a more potent H-atom donor than BDMP (compare $k_{inh} = 3.8 \times 10^6$ $M^{-1}s^{-1}$ for PMC[32] with 1.3×10^5 M^{-1} s^{-1} for BDMP[17]) less autoxidation takes place in the presence of comparable amounts of PMC. Nevertheless, the trends observed in the PMC-loaded autoxidations are fully consistent with those observed in the presence of BDMP. It is noteworthy that in the presence of PMC, chol 5α-OH increased to a maximum of 15 mol% of the product distribution. Analogous to the BDMP-loaded autoxidations, there was an initial surge in epoxide concentration as the PMC concentration was increased, reaching a maximum at roughly the same amount (ca. 30 mol%) before decreasing.[33] The ratio of α-epoxide to β-epoxide, on the other hand, increased roughly two-fold past the BDMP maximum at higher [PMC] (*cf*. Figure 3.34).

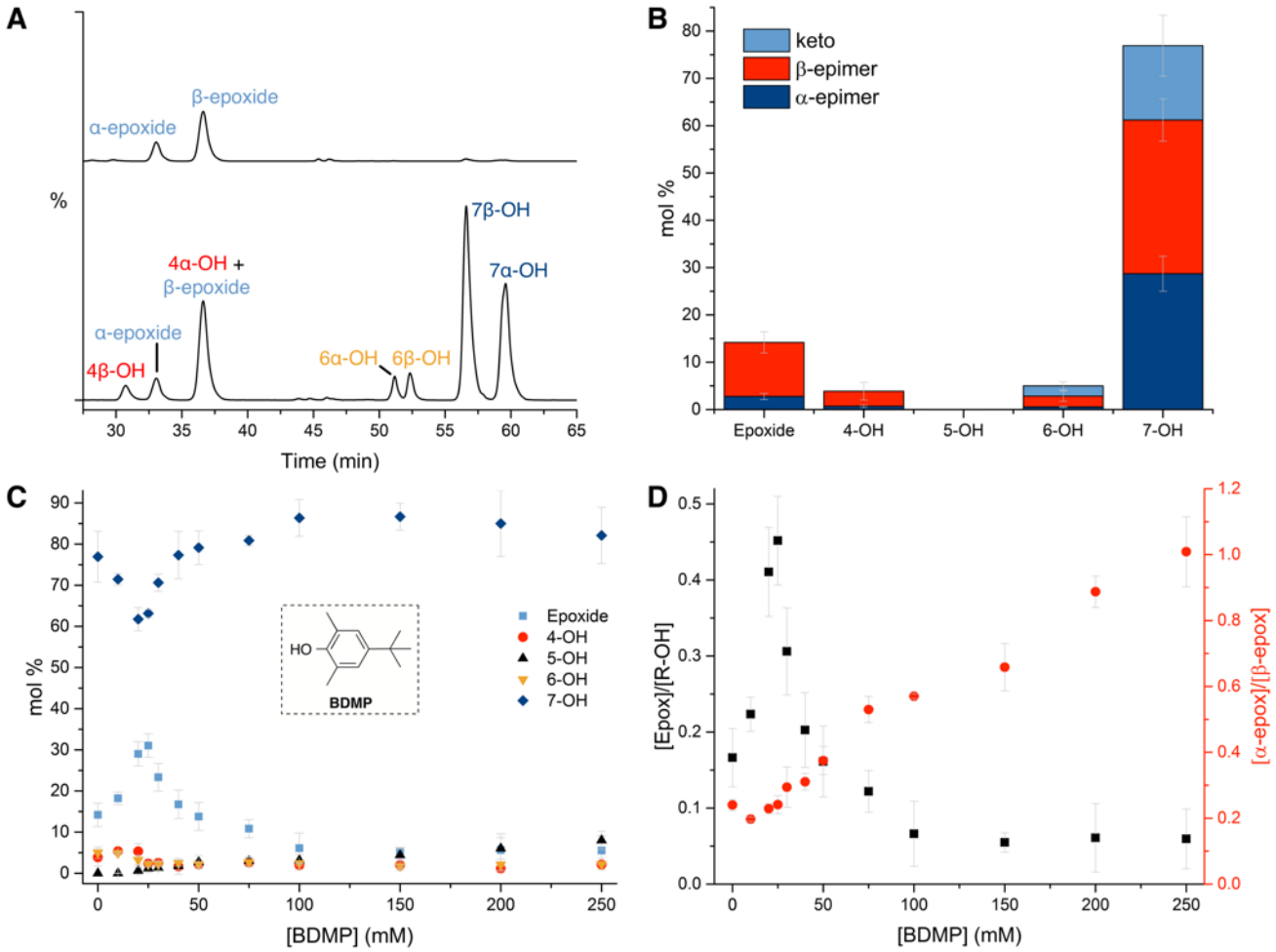

Figure 3.2. Product distribution from MeOAMVN-initiated autoxidation of chol in chlorobenzene at 37°C. (A) Chromatograms (conditions in experimental section) from HPLC/APCI$^+$-MS/MS analysis with *m/z* 403.4 → *m/z* 385.4 (top) and *m/z* 385.4 → *m/z* 367.4 (bottom), where the hydroperoxide-derived alcohols are detected following pretreatment of samples with PPh_3. (B) Distribution of α- and β-epimers, as well as dehydration products (keto). (C) Product distribution as a function of added BDMP. (D) Ratio of chol epoxides to chol OH (■), and ratio of α-epoxide to β-epoxide (●) as a function of added [BDMP].

3.3.2 Computational Insights on the Origins of Chemo- and Regioselectivity in Cholesterol Autoxidation.

To help rationalize the chemo- and regioselectivity observed in the cholesterol autoxidations, electronic structure calculations were carried out to determine the transition state structures for both H- atom abstraction from, and addition to, chol by a model peroxyl radical (methylperoxyl). For computational expediency, the calculations employed a simplified model of chol which included only the A and B rings at which the relevant chemistry occurs. In our preliminary report,[17] we reported that the C4-H and C7-H bond dissociation enthalpies – determined by the high-accuracy CBS-QB3 compound method – were 89.0 and 83.2 kcal/mol, respectively. The origin of the difference is clear when looking at the spin density distributions in the allylic radicals formed from C4-H and C7-H abstraction (*cf.* Figure 3.3); the latter benefits from having its spin density localized on both a tertiary and a secondary position, compared to the two secondary positions in the former. Moreover, the radical derived from C4-H abstraction is delocalized across both A and B rings, and the concomitant planarity causes each ring to distort from their optimal chair conformations. Nevertheless, the difference in BDEs does not alone govern the ratio of C4-H to C7-H abstraction. Given that H-atom abstraction is followed by the near diffusion-controlled addition of O_2 to the so-formed alkyl radicals, this kinetically controlled step is instead dictated by the barrier of H-atom transfer. We had previously calculated the barriers for the key transition states (TSs) for the C7-H and C4-H abstraction pathways with density functional theory, but herein the results of corresponding CBS-QB3 calculations are presented.

Conventional wisdom has been that the C7-H oxidation pathway operates more or less exclusively, as chol 7-OOH, chol 7-OH and 7-ketochol have been reported to be the vastly dominant products in liposomes, low density lipoprotein (LDL) and *in vivo*. Indeed, H-atom abstraction from the C7α-H has a relatively low enthalpic barrier (A1 in Figure 3.3A), benefitting from a secondary orbital interaction between the contribution of the internal peroxyl oxygen atom to the nominally

singly occupied π* and the electron-rich C5-C6 π bond. This (*syn*) TS structure is 1.4 kcal/mol lower in free energy than the corresponding *anti* TS structure (A2 in Figure 3.3A). H-atom abstraction from the C7β-H is slightly higher in energy, presumably due to the steric hindrance imposed by the C10-methyl group and the equatorial β-H requiring more reorganization of the B-ring to achieve the transition state.[34] However, the *syn* geometry that benefits from the secondary orbital interaction is still preferred over the *anti* geometry, despite the steric interaction (A3 and A4, respectively, in Figure 3.3A).

The proximity of the 3-OH group introduces a competing interaction in the C4-H abstraction TS. In fact, the preferred geometry for HAT from C4β-H involves a H-bonding interaction between the internal peroxyl oxygen atom and the C3-OH group (B1 in Figure 3.3B). In contrast, the *syn* geometry for C4β-H (B2 in Figure 3.3B) abstraction is less favourable by 1.1 kcal/mol. The H-bonding interaction lowers the barrier to within 2 kcal/mol of the most optimal C7-H abstraction TSs. The computed TSs for C4α-H abstraction, which are much higher in energy, are devoid of H-bonding interactions between the peroxyl radical and the C3-OH, presumably due to its equatorial position in the A-ring chair structure. Furthermore, C4α-H abstraction benefits from a secondary orbital interaction only if the A-ring is flipped to a boat geometry (B3 in Figure 3.3B), which lowers the barrier slightly relative to H-atom abstraction perpendicular to the framework (B4 in Figure 3.3B).

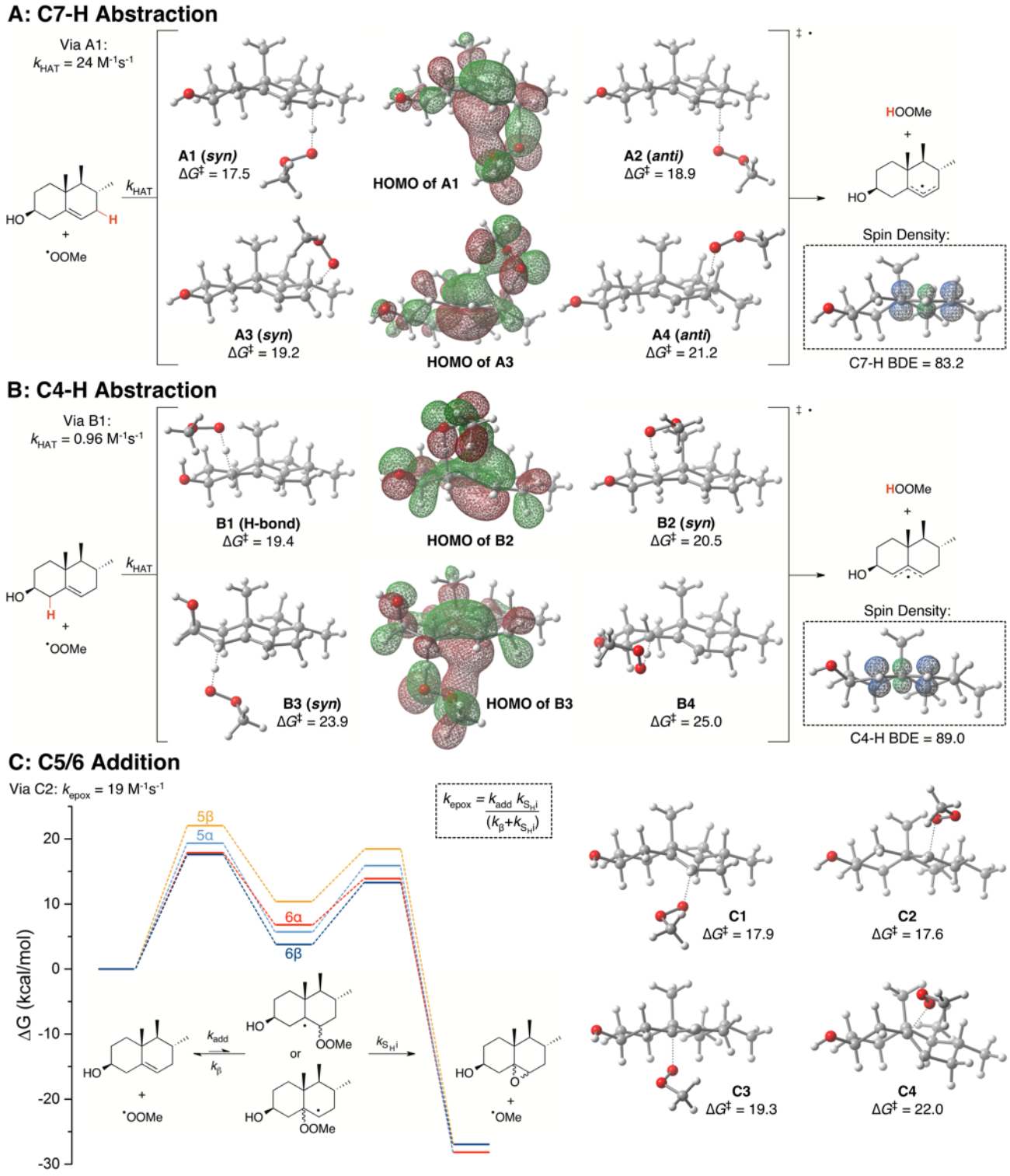

Figure 3.3. (A) H-atom abstraction from chol by a methylperoxyl radical at C7-H with transition state (TS) structures: C7α-H with a *syn* geometry and secondary orbital interaction (A1) or with an *anti* geometry (A2); or from C7β-H with a *syn* geometry and secondary orbital interaction (A3) or with an *anti* geometry (A4); as well as spin density distribution for the allylic radical formed therefrom

(right). (B) H-atom abstraction from chol by a methylperoxyl radical at C4-H with TS structures: C4β-H with a H-bonding interaction with the C3-OH (B1) or a *syn* geometry and secondary orbital interaction (B2); or from C4α-H with a *syn* geometry and secondary orbital interaction (B3) or no secondary interaction (B4); as well as spin density distribution for the allylic radical formed therefrom (right). Highest occupied molecular orbitals (HOMOs) are shown for TS structures in A and B that benefit from a secondary orbital interaction. (C) Reaction coordinate for the epoxidation pathway (left) and TS structures for addition to chol by a methylperoxyl radical at: C6 α-face (C1), C6 β-face (C2), C5 α-face (C3), or C5 β-face (C4), on the right. All structures were computed with CBS-QB3, energies are reported in kcal/mol, and TS structures are accompanied by the associated barriers.

To explore the peroxyl radical addition pathway, we calculated the barriers to peroxyl radical addition at C6 from the α- or β-face of the sterol framework (C1 or C2, respectively, in Figure 3.3C), or at C5 from the α- or β-face (C3 or C4, respectively, in Figure 3.3C). It appears that two factors affect additions at these four positions. First, C5 addition yields a secondary alkyl radical, whereas the C6 addition yields a more stable tertiary alkyl radical. However, despite any steric hindrance imposed by the C10 methyl group, C6 addition is preferred on the β-face, and C5 addition on the α-face. This is due to the resultant alkyl radicals adopting chair conformations, while C6 addition on the α-face and C5 addition on the β-face force the B-ring into a twist boat conformation. The interplay of these two factors are likely why both C5 addition pathways have higher barriers, but the intermediate formed from C5α addition is more stable than the one formed from C6α addition (*cf.* Figure 3.3C).

Since peroxyl radical addition is a reversible process, we also calculated the subsequent S_Hi reaction to form an epoxide and an alkoxyl radical, which had enthalpic barriers of 7.3 and 9.9 kcal/mol for the 6α- and 6β-peroxides, respectively, corresponding to unimolecular rate constants of 3.8×10^7 and 6.6×10^5 s^{-1}, respectively. Taken together, the overall rate of epoxide formation is fastest for initial C6β addition, with a computed k_{epox} of 19 $M^{-1}s^{-1}$ (*cf.* Figure 3.3C). Interestingly, this is predicted to be almost as fast as H-atom abstraction from C7-H (k_{HAT} = 24 $M^{-1}s^{-1}$), and significantly faster than abstraction of C4-H (k_{HAT} = 0.96 $M^{-1}s^{-1}$), in good agreement with the experimental observations.

3.3.3 Cholesteryl Acetate Autoxidation.

Given that the H-bonding interaction between the C3-OH of chol and the peroxyl radical in the C4-H abstraction TS seemed to be a reasonable explanation for the observation of chol 4-OOH and 6-OOH in autoxidations, we sought to further probe this experimentally. We therefore carried out cholesteryl acetate (chol OAc) autoxidations, as described in the Experimental Section 3.6. In each instance, the samples were treated with PPh_3 to convert the hydroperoxide products to their corresponding alcohols. The mixtures were further treated with 1M KOH in MeOH to convert the chol OAc-derived oxidation products to the corresponding chol-derived products, as the chol OAc products were not resolvable by normal phase HPLC. Control experiments were conducted to ensure quantitative deprotection of chol OAc and recovery of the oxidation products under these conditions.

Somewhat surprisingly, the amount of 4-OOH and 6-OOH only decreased by about half, and the product distribution was otherwise similar to chol autoxidations (*cf.* Figure 3.4A). The presence of chol 4-OOH and 6-OOH, albeit in a slightly lesser amount than in the chol autoxidations, indicated that the absence of the H-bonding interaction was not enough to fully suppress C4-H abstraction. On the other hand, the trends involving the epoxides were different – there was no initial surge in epoxide concentration relative to the other products, and the ratio of α- to β-epoxide was unaffected by [BDMP]. Otherwise, the outcomes of chol and chol OAc autoxidations were largely the same. The k_β of the 5α-peroxyl derived from chol OAc was 2-fold higher than with chol (*vide supra)*, as it was determined to be $(6.7 \pm 0.5) \times 10^5\ s^{-1}$ (*cf.* Figure 3.36). Similarly, the amounts of ketochol products were consistent with chol autoxidations, where 7-ketochol was ca. 10% of the mixture, 6-ketochol was a minor component and no 4-ketochol was detected.

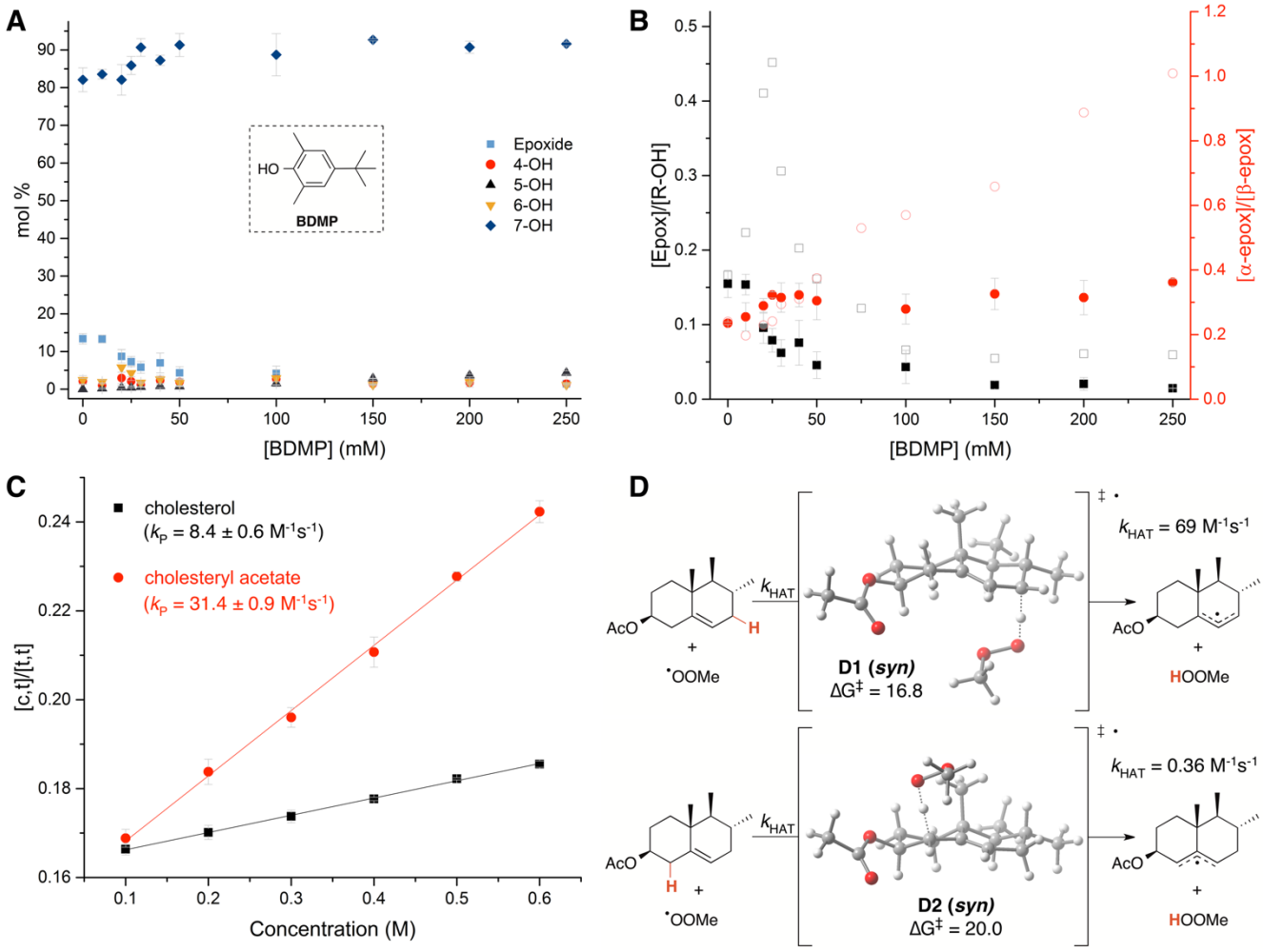

Figure 3.4. (A) Product distribution from MeOAMVN-initiated autoxidation of cholesteryl acetate (chol OAc) in chlorobenzene at 37°C as a function of added BDMP. The hydroperoxide-derived alcohols were quantified following pretreatment of samples with PPh_3. (B) Ratio of epoxides derived from chol OAc to alcohols (hydroperoxides) derived from chol OAc (■), and ratio of α-epoxide to β-epoxide (●) as a function of added [BDMP] (empty data points are the corresponding data for chol autoxidations, presented for comparison). (C) Propagation rate constants (k_p) for chol (■) and chol OAc (●) as determined from the *c*,*t*/*t*,*t* ratio of conjugated hydroperoxides arising from autoxidation of methyl linoleate in the presence of chol and chol OAc (see Experimental Section 3.6). (D) CBS-QB3 computed lowest energy transition states for H-atom abstraction from a model of chol OAc by a model peroxyl radical at C7α-H (top) or C4β-H (bottom) and the associated barriers in kcal/mol.

Once again, computations were carried out to enable rationalization of our observations. The CBS-QB3-predicted C-H BDEs are not significantly affected when chol is esterified – they were computed to be 88.6 and 83.1 kcal/mol for C4-H and C7-H, respectively, using CBS-QB3. Thus, the

C4-H bond is weakened by ca. 0.4 kcal/mol relative to chol, but is still 5 kcal/mol stronger than the C7-H. TSs were calculated for H-atom abstraction at the C4-H and C7-H positions. Analogous to chol, the preferred C7α-H abstraction geometry benefits from a secondary orbital interaction (*cf.* Figure 3.4D). This TS again was lower in energy than the C7β-H abstraction TS, which is subject to steric hindrance from the C10-methyl. For C4-H abstraction, no H-bonding interaction was possible between the peroxyl radical and the acetate group; however, the enthalpic barrier to C4β-H abstraction with a secondary orbital interaction was only 20.0 kcal/mol – 0.5 kcal lower than the same geometry in chol. This, again, was favoured relative to C4α-H abstraction, which required an A-ring flip to a boat conformation to benefit from the secondary orbital interaction.

To the best of our knowledge there are no reports that esterified chol autoxidizes more rapidly than chol, as our computations would suggest. We therefore determined the propagation rate constants (k_p) for chol and chol OAc using the peroxyl radical clock approach (*cf.* Figure 3.4C).[4] The k_p of chol OAc was almost four-fold higher than chol, at 31.4 ± 0.9 and 8.4 ± 0.6 M^{-1} s^{-1}, respectively.[35]

3.3.4 Isotopic Substitution Inverts Product Distribution in Cholesterol Autoxidation.

Given that the computed rates of H-atom abstraction from, and peroxyl radical addition to, chol were similar, we wondered whether tunnelling in the HAT pathway is responsible for the predominance of hydroperoxides over epoxides in cholesterol autoxidations. We therefore synthesized 2,2,4,4,7,7-d_6-cholesterol (**3.9**, 2,2,4,4,7,7-d_6-chol) by the method of Fujimoto et. al.[22] and carried out analogous autoxidations to those described above. Amazingly, the product distribution observed in the 2,2,4,4,7,7-d_6-chol autoxidations was completely inverted compared to that observed from chol, such that the epoxides accounted for over 75% of the product mixture. The ratio of hydroperoxide and epoxide products can be used to estimate a kinetic isotope effect (KIE) of $k_H/k_D = 20 \pm 1$ on H-atom

abstraction from chol by chain-propagating peroxyl radicals (*cf.* Figure 3.5). This value is significantly larger than the classical limit, supporting the contribution of tunnelling in the HAT pathway(s). It is noteworthy that the rate of autoxidation of 2,2,4,4,7,7-d_6-chol was significantly slower than of chol, yielding ca. 4-fold less oxidation products in total, but roughly the same amount of epoxide products. This suggests that deuteration affected only the H- atom abstraction pathway(s), and had a negligible effect on the rate of peroxyl radical addition.

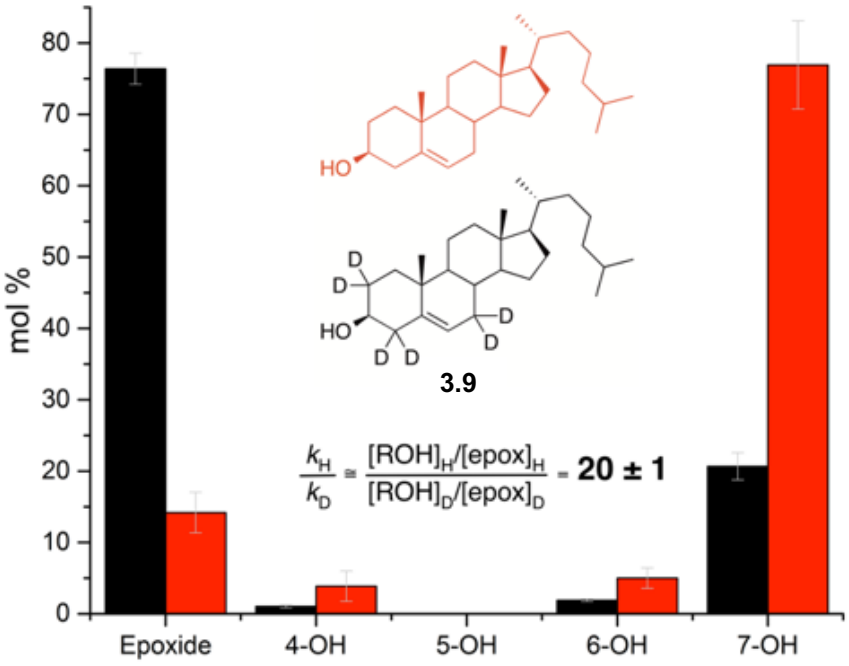

Figure 3.5. Product distributions in autoxidations of chol and 2,2,4,4,7,7-d_6-chol.

3.4 Discussion

Our preliminary study on chol autoxidation focused on the formation of the regioisomeric hydroperoxide products and the changes in their distribution upon addition of H-atom donors to the system (*cf.* Figure 3.1A). However, the mechanism of chol autoxidation is more complex, as peroxyl radicals also add to the C5-C6 unsaturation in competition with H-atom abstraction. The products of this addition pathway may, theoretically, include chol epoxides and peroxides (*cf.* Figure 3.1B).

Indeed, the epoxides are known autoxidation products of chol, but are also produced by other oxidants, which has complicated their quantification in the past. There has been significant interest in the bioactivity of chol epoxides, as they are reported to influence sterol synthesis and esterification, and have links to a number of diseases, including cancer.[9,18] While initial reports suggested chol epoxides may be alkylating agents, it was later shown that they have surprisingly weak electophilicity compared to other epoxides.[36] Their interaction with several enzymes (including topoisomerase-II, liver-X-receptors, cholesterol acyl transferases, and estrogen receptors) is more likely to be the reason for their pathogenesis. The epoxides are known to be metabolized to chol 3,5,6-triols by chol epoxide hydrolase enzymes (present in the liver, and to a lesser extent, the lungs), though the α-epoxide is significantly more susceptible to hydrolysis.[9,18] We therefore sought to quantify the product distribution of the H-atom abstraction and addition pathways simultaneously, as well as probe whether the addition of H-atom donors affects the distribution of products derived from the latter.

Using the modified HPLC-MS/MS protocol, the chol epoxides were quantified and found to constitute a significant amount of the product distribution in chol autoxidation, at *ca.* 15 mol% in the absence of H-atom donor. Meanwhile, the amount of chol 4-OOH accounted for *ca.* 5 mol% of the oxidation products – roughly equivalent to the amount of 6-OOH – and the remainder of the distribution belonged to 7-OOH. Upon addition of BDMP, a good H-atom donor, chol 5α-OOH was also observed. In our preliminary report, we proposed that this is due to the reversibility of the addition of O_2 to the allylic radical derived from C7-H abstraction. The addition of O_2 to allylic radicals is known to be reversible – the forward reaction is fast (approaching the diffusion limit),[37] while the rate of the reverse reaction, β-fragmentation, varies depending on the substrate. This has been demonstrated in other lipids, such as oleate[38] and linoleate[39] (*cf.* Scheme 3.2), whereby k_β is inversely proportional to the C-OO$^\bullet$ bond strength (i.e. the relative stability of the peroxyl radical, compared to the alkyl radical it derives from). In the context of autoxidation, peroxyl radicals with

large k_β may only be observed in the presence of an antioxidant (AH) that can compete with β-fragmentation (i.e., k_{inh} [AH] > k_β).

The β-fragmentation rate constant, k_β, for 5α-OO$^\bullet$ was determined to be $(3.8 \pm 0.9) \times 10^5$ s^{-1} (and *ca.* 2-fold higher for the chol OAc-derived peroxyl). We had previously estimated a value of k_β for 4β-OO$^\bullet$ to be $(8.6 \pm 0.4) \times 10^3$ s^{-1}, however, due to co-elution with the chol epoxides, the α/β ratio only appeared to be varying. It is now clear that 4β-OOH is the dominant product, regardless of [BDMP]. Furthermore, the ratio of [4-OH]/[6-OH] is unaffected by changing [BDMP], suggesting the 4-OO$^\bullet$ and 6-OO$^\bullet$ do not undergo measurable β-fragmentation under the reaction conditions. These results are consistent with computed C-O bond strengths in the 8 peroxyl radicals, since the C4-OO$^\bullet$ and C6-OO$^\bullet$ are both similar (26.0 and 24.1 kcal/mol, respectively, for the α-epimers, and 26.0 and 25.2 kcal/mol, respectively, for the β-epimers) and much stronger than for C5-OO$^\bullet$ and C7-OO$^\bullet$ (20.4 and 21.0 kcal/mol, respectively, for the α-epimers, and 17.1 and 21.2 kcal/mol, respectively, for the β-epimers).

Increasing [BDMP] also impacted the peroxyl radical addition pathway – initially increasing the amount of chol epoxides relative to the other products. An explanation for the increase involves a competition between S_Hi and O_2 addition to the alkyl radical initially formed from peroxyl radical addition to chol (*cf.* Scheme 3.3). The peroxyl radical formed could either propagate the radical chain, or it could be trapped as the corresponding hydroperoxide by a H-atom donor – a pathway that is more competitive at higher [BDMP] (or [PMC]). Since subsequent analysis reduced the hydroperoxide products to their corresponding alcohols, one could envision a displacement of the added peroxide fragment to yield an epoxide. Thus, an increase in the peroxide product (**3.3**) would lead to an artificial increase in the chol epoxide measured. The hydroperoxide in **3.3** could also be reduced to its corresponding alcohol by other means *in vivo* (i.e. glutathione peroxidase 4), suggesting that chol epoxides may not simply arise from S_Hi chemistry, as previously thought. Indeed, upon direct infusion of select chol autoxidation samples, we observed the *m/z* for the corresponding alcohol

of **3.3** wherein R is initiator-derived. Upon increasing [BDMP], this signal weakened, and the *m/z* for a corresponding BDMP-phenoxyl radical addition product was observed (cf. Figure 3.47).

Scheme 3.2. Reversible addition of O_2 to lipid-derived (bis)allylic radicals is key to the product distributions observed in autoxidations. B-Fragmentation rate constants are shown for key classes of lipid-derived peroxyl radicals.

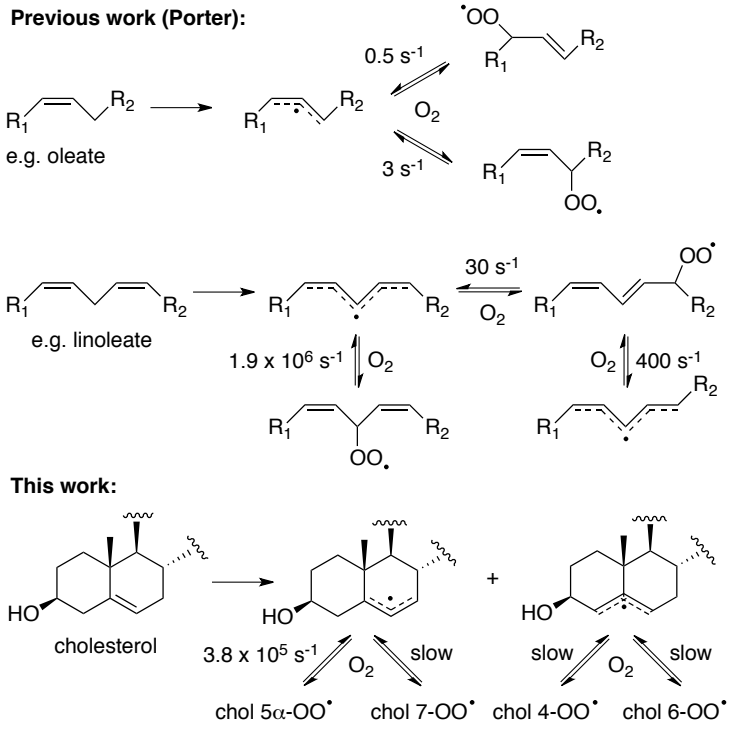

The fact that the α:β epoxide ratio varied with [BDMP] is also in line with the mechanism outlined in Scheme 3**.** Calculations predict that peroxyl radical addition to chol occurs at the C6 position on either the α- or β-face (with slight preference for the β-face), suggesting subsequent O_2 addition would yield two isomers of **3** (α,α or α,β). Upon reduction to the corresponding alcohols, the α,β-isomer is poised for displacement of the peroxide moiety, whereas the α,α-isomer is likely to be relatively stable. Therefore, the suggestion that increasing [BDMP] leads to a larger relative

amount of **3.3** is also consistent with an increase in the ratio of α:β epoxide, though this also implies the α,α-isomer was unaccounted for in this analysis.

Interestingly, the effect of increasing [BDMP] on the relative amount of epoxide and its stereochemistry differed in chol OAc autoxidations (*cf.* Figure 3.4B). However, since the workup required treatment with KOH to hydrolyze the acetate, any **3.3** formed would likely be cleaved by hydroxide to yield chol 3,5,6-triols (chol triol) rather than intramolecular displacement to yield chol epoxides. Indeed, we were able to detect an increased amount of chol triol in select chol OAc autoxidations relative to the analogous chol experiments.[27] Additionally, when chol autoxidations were treated with KOH, a similar amount of chol triol was present (*cf.* Figure 3.43), and the ratio of α:β epoxide (ca. 0.3) was unaffected by increasing [BDMP], supporting the fact that KOH could displace the peroxide in **3.3**. Unfortunately, attempts to cleave the peroxidic bond in **3.3** by other means (e.g. Zn or Mg) also lead to the hydrolysis of chol epoxides, complicating the product analysis.

Scheme 3.3. Simplified mechanism of cholesterol autoxidation (black) highlighting the competitive O_2 addition after initial peroxyl radical addition to chol (red).

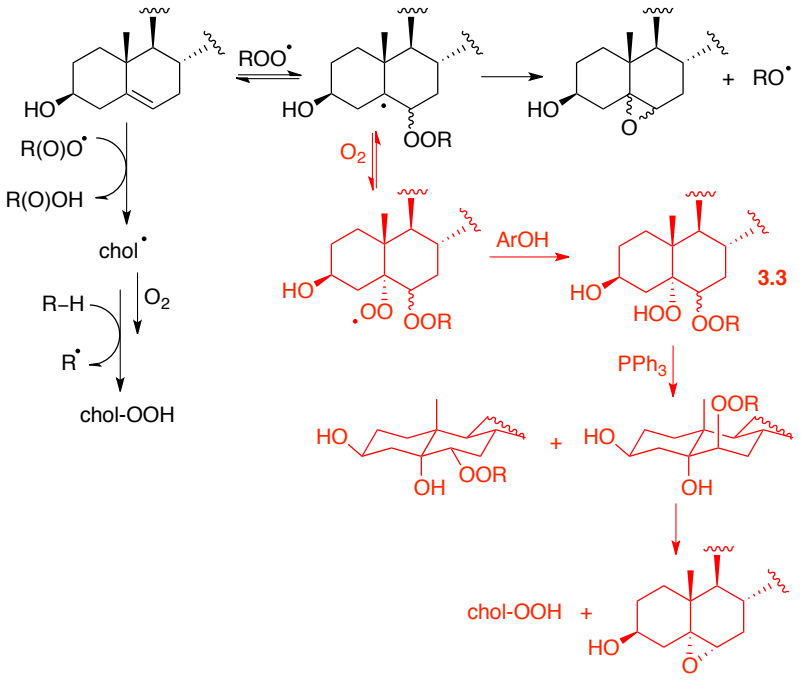

In chol and chol OAc autoxidations alike, the relative amount of chol epoxide in the product mixture decreased with increasing [BDMP] – after its initial surge in the former case. This is likely due to the increasing contribution of the antioxidant-mediated peroxidation mechanism, where at high [BDMP] the predominant chain-carrying radical is no longer the substrate-derived chol-OO$^{\bullet}$, but instead the antioxidant-derived phenoxyl radical (which was also suggested to be the reason for the decrease in 4- and 6-OOH, as previously discussed).[17] Phenoxyl radicals are unlikely to add to a double bond, as this would be both endothermic and highly reversible since S_Hi would not be possible. Therefore, at higher concentrations of BDMP the peroxyl radical addition pathway would give way to an increasing contribution from the C7-H abstraction pathway. Taken together, the foregoing discussion reiterates that mechanistic generalizations based on the amount or ratio of the stereoisomeric epoxides is tenuous at best, as they depend greatly on conditions.

A discussion of the interplay between the H-atom abstraction and peroxyl radical addition pathways in chol would not be complete without a comparison to other lipids. In particular, other monounsaturated lipids, such as oleate, are not reported to form epoxides through autoxidation at all.[40] Indeed, the secondary alkyl radical formed upon addition of the peroxyl radical is less stable than the tertiary one in chol, presumably so much so that its β-fragmentation is significantly faster than the S_Hi reaction (*cf.* Scheme 3.4). Instead, oleate is reported to form exclusively hydroperoxide products through the initial allylic H-atom abstraction. On the other hand, peroxyl radical addition to 7-DHC is known to occur, not at C6 as in cholesterol (to yield the stabilized tertiary alkyl radical), but instead at C5 – exclusively on the α-face – to yield a stabilized allylic radical.[3] The 5α,6α-epoxide so formed is known to be converted to 3β,5α-dihydroxycholest-7-en-6-one (DHCEO) *in vivo*, which has been used as a biomarker in Smith-Lemli-Opitz syndrome (SLOS). Interestingly, Porter and co-workers observed a decrease in DHCEO in a mouse model for SLOS upon administration of antioxidant (H-atom donor).[41] Surely the antioxidant would slow 7-DHC autoxidation in general; however, should the foregoing results for chol autoxidation translate to 7-DHC, one might assume the

H-atom abstraction and peroxyl radical addition pathways could be differentially impacted by the addition of H-atom donor.

Scheme 3.4. Peroxyl radical addition in select other hydrocarbons.

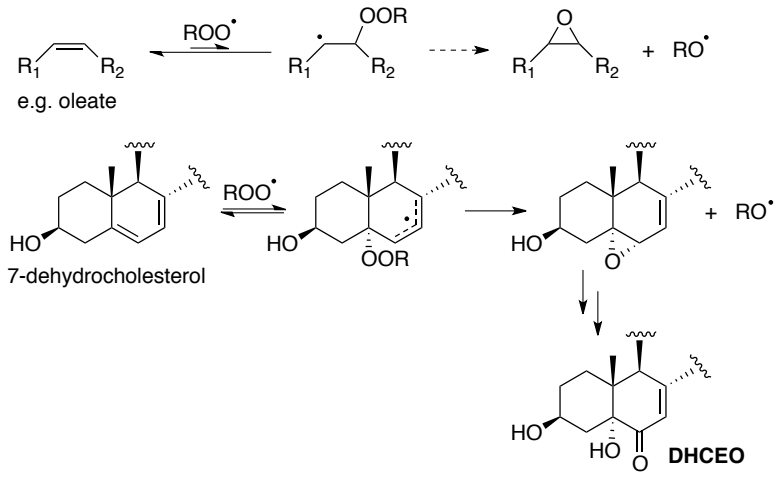

While we were able to identify chol 4-OOH, 6-OOH 7-OOH and 5,6-epoxides as the primary products of chol autoxidation (in addition to chol 5α-OOH in the presence of a good H-atom donor), much of the pathogenesis of lipid autoxidation is attributed to secondary (electrophilic) products. In our previous work we showed that secosterols **3.1** and **3.2** are formed upon Hock fragmentation of either chol 5α-OOH[16] or 6-OOH.[17] While they are likely less electrophilic, chol-derived ketones (ketochols) may also have pathogenic potential. In the course of the autoxidation, ketochols may arise from peroxyl-peroxyl termination, homolysis of hydroperoxides, or H-atom abstraction from the carbon of a hydroperoxide.[42] Interestingly, it appears the three secondary hydroperoxides form ketochols to differing extents – 4-ketochol was not observed under any conditions, suggesting 4-OOH is less prone to the aforementioned reactions. This could be due to H-bonding between the C3-OH and the hydroperoxide hindering ketone formation. Indeed, our computations suggested this type of interaction strengthens the C-OO• bond in the chol 4-peroxyl radical. Conversely, the 6-ketochol was

measurable only at low [BDMP] where the amount formed was above the threshold of UV detection. Without additive, the amount of 6-ketochol was *ca.* 1:1 relative to the amount of 6-OH. This was significantly more than the 7-ketochol, which was only ca. 1:5 relative to 7-OH in the timeframe of our autoxidations. It has been a great surprise that we detect measurable quantities of chol 4-OOH and 6-OOH, while the former had only been tenuously tied to chol autoxidation in the past,[43] and the latter has not been detected *in vivo,* to our knowledge. While analytical challenges surely contribute, the susceptibility of chol 6-OOH to Hock fragmentation and significant 6-ketochol formation could mean the concentration of chol 6-O(O)H *in vivo* is fleeting. However, the products so formed are likely significantly more insidious, suggesting the contribution of the C4-H abstraction pathway may be significant contributors to the pathological potential of chol oxidation products.

The presence of chol 4-OOH and 6-OOH in chol autoxidations was initially rationalized on the basis of a H-bonding interaction in the H-atom abstraction transition state (*cf.* Figure 3.3B). We therefore expected the C4-H abstraction pathway to be insignificant in chol OAc autoxidations, as this interaction would no longer exist; however, measurable amounts of 4-OOH and 6-OOH were nonetheless present. This led us to consider if another interaction was affecting the analogous transition state with chol OAc. Interestingly, the two key TSs for H-atom abstraction from chol OAc were abstraction of the C7α-H or C4β-H with *syn* TSs that benefit from secondary orbital interactions (*cf.* Figure 3.4D), and both were lowered by *ca.* 1 kcal/mol relative to the analogous TSs in chol. While this was consistent with the slightly weakened C4-H BDE in the chol OAc computations, we were perplexed by this substituent effect. One might expect the C3-OAc to be more inductively withdrawing than the C3-OH, which would both strengthen the C4-H bond and lower the C5=C6 HOMO, thus *slowing* HAT. To the best of our knowledge there are no reports of differing reactivity between chol and chol OAc. We were therefore surprised to find that the computational prediction was consistent with experimental evidence – the measured k_p was *ca*. 4-fold higher for chol OAc than for chol. This implies areas rich in esterified chol, such as low density lipoprotein (LDL) particles,

may be more susceptible to autoxidation than those enriched in free chol, such as the cell membrane. It also suggests that when esterified, chol is about half as reactive as linoleate!

In light of the k_p values determined in the peroxyl radical clock experiments, it is interesting that the total amount of oxidation products detected in our chol and chol OAc autoxidations were similar. We believe this could be due to steric hindrance in the propagation between two sterol molecules in chol and chol OAc autoxidations (*cf.* Figure 3.6). For example, the chain length in our chol and chol OAc autoxidations was ~1 in the absence of BDMP, and significantly lower (<0.1) in its presence (*cf.* Section 3.8.8). This suggests propagation is indeed inefficient in our system, and that the peroxyl radical species abstracting (or adding) is instead an (unhindered) initiator-derived radical. On the contrary, a chol-doped methyl linoleate autoxidation involves propagation between a sterol and a significantly less-hindered PUFA. We believe the latter to be more biologically relevant, indicating the reactivity difference between chol and cholOAc is likely to exist *in vivo*.

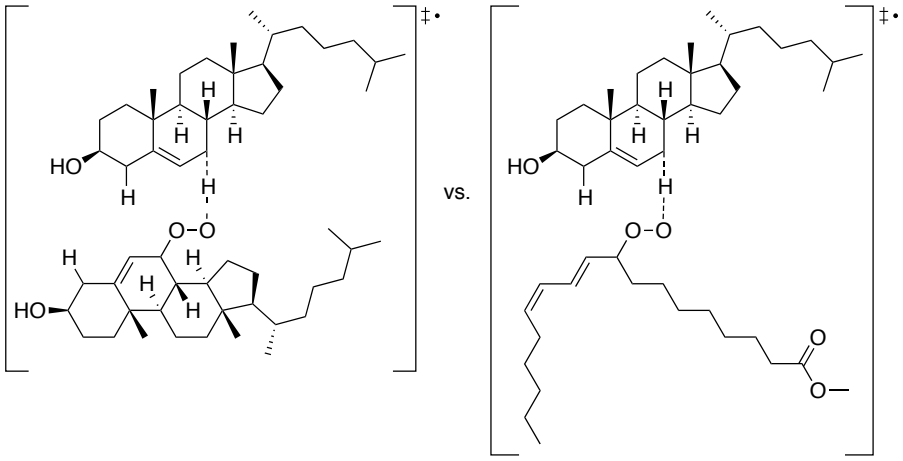

Figure 3.6. The steric hindrance is suggested to be greater in the H-atom abstraction of chol by a chol-derived peroxyl (left) as opposed to a linoleate-derived peroxyl (right). C7-H abstraction is shown for example.

We were intrigued by the fact that the computed rate constants for the C7-H-atom abstraction and C6-addition pathways were similar (e.g. 24 and 19 $M^{-1}s^{-1}$, respectively, for chol). Based on these results, one might expect the experimental chol hydroperoxide/epoxide ratio to be roughly 1:1. However, the experimentally determined ratio (in the absence of H-atom donor) was *ca.* 6:1. Recent reports of tunnelling in hydrocarbon autoxidation prompted us to consider whether this might underlie the observed preference for H-atom abstraction from chol. For example, the propagation rate constants in the autoxidation of linoleic acid[44] and tetralin[45] are reported to have a k_H/k_D of 13 and 16, respectively. Furthermore, the α-tocopherol-loaded autoxidation of 7-dehydrocholesterol has an isotope effect of 21 for H or D transfer to the chain-carrying tocopheroxyl radical.[46] The same experiment yielded values of 23 and 32 for linoleic acid, α-linolenic acid, respectively.[47] We were able to use the distribution of H-atom transfer vs. peroxyl radical addition products in chol and 2,2,4,4,7,7-d_6-chol autoxidations to estimate the k_H/k_D for HAT to a peroxyl radical to be 20 ± 1. Inclusion of corresponding deuterium atoms in our computational model, and application of Skodje-Truhlar tunnelling corrections, the k_H/k_D were predicted to be 29.9, 45.7, and 0.992, for C7 H-atom abstraction, C4-H atom abstraction and addition to the C5-C6 double bond, respectively. This is fully consistent with our experimental results, including the fact that the 4-OOH and 6-OOH products were more abundant than their (classical) reaction barriers had predicted; the greater contribution from tunnelling evidently enables products derived from C4-H abstraction to contribute.

The aforementioned large k_H/k_D values in PUFA autoxidation are the basis of the surprising protection afforded by the treatment of cells with deuterated-PUFAs. For example, Shchepinov and co-workers have demonstrated that the incorportation of 11,11-d_2-linoleate can protect yeast from lipid autoxidation-induced cell death, and surprisingly only 20% deuterated linoleate incorporation is required to achieve it.[44] This protective effect was also observed upon administration of deuterated-PUFAs in a mouse model for Parkinson's disease.[48] To the best of our knowledge, deuterated sterols have not been the subject of analogous investigations. Such an investigation would be interesting, as

it may also shed light on the overall importance of chol oxidation and whether HAT or addition pathways are more or less damaging to cell membranes.

3.5 Conclusions

We have demonstrated that the products of chol autoxidation include chol 4-OOH, chol 6-OOH, chol 7-OOH, chol 5,6-epoxides, 6-ketochol and 7-ketochhol whether cholesterol is esterified or not. Furthermore, in the presence of a good H-atom donor, chol 5α-OOH is formed. This product distribution is far more complex than previously reported, and is influenced by factors including: the presence of good H-atom donors, the esterification of the C3-OH, and the contribution of quantum mechanical tunnelling in the H-atom abstraction pathways. Furthermore, the pathogenesis of chol-derived oxysterols has, to date, focused on secosterols **3.1** and **3.2**, products purported to be derived from high energy oxidants like $^1O_2$ and O_3. While we have already demonstrated that chol 5-OOH and 6-OOH undergo Hock fragmentation to yield **3.1** and **3.2**, the complex product distribution of chol autoxidation presented herein begs the question whether there are other hitherto unidentified pathogenic compounds that may derive from, for example, chol 4-OOH or 7-OOH. While the epoxides were previously known to be autoxidation products, their quantification has been complicated by the fact that they are not unique to autoxidation. Others have advocated for the use of the α:β ratio of epoxides as an indicator of the oxidant they were derived from; however, we have shown that the presence of H-atom donors in the autoxidation medium can affect this ratio, suggested that this practice should be avoided, or at the very least, that interpretations of these data be made with caution.

3.6 Perspective

For the initial study of chol autoxidation by LC-MS presented in Chapter 2, we utilized the previously reported synthetic route to 26,26,26,27,27,27-d_6-cholesterol to prepare 26,26,26,27,27,27-d_6-5α-hydroxycholesterol for use as an internal standard. When faced with the issue of co-elution of the chol 4-OH and chol epoxide products, we felt having internal standards to elute therewith would increase the accuracy of our analysis. However, the synthesis of 26,26,26,27,27,27-d_6-cholesterol was challenging and low-yielding. Thus we were interested in exploring the synthesis of an alternative d_6-chol, and a significant amount of time and effort was required to optimize the synthetic route outlined in Scheme 3.1.

What began as a simple hypothesis (could chol 5-OOH be formed in chol autoxidations with added H-atom donor?) turned into a much larger study on the mechanism of chol autoxidation. We discovered that chol reacts with peroxyl radicals, not only through abstraction of the C7-H bond, but also through abstraction at the C4-position, and peroxyl radical addition to the C5=C6 bond. We have observed that the substituent at the C3-position has an impact on the kinetics of autoxidation, and that tunnelling contributed to accelerating H-atom abstraction relative to peroxyl radical addition. This complex mechanism is a significant departure from the previously accepted concept that chol autoxidation yields chol 7-OOH (and consequently, chol 7-OH and 7-ketochol) as the sole hydroperoxide product, and also produces chol epoxides to some extent (not properly quantified). Evidently, the analytical approaches used to study chol autoxidation in the past were insufficient to capture the complete product distribution.

Given the complexity of chol autoxidation, compared to what was previously understood, we wondered whether a more thorough study of other common lipids would yield similar results. In particular, we wondered whether the peroxyl radical addition pathway is somehow unique to cholesterol, or if lipid-derived epoxides may be more prevalent that previously understood. We therefore wished to conduct a similar study on another monounsaturated system, to see if the peroxyl

radical addition pathway would be competitive with H-atom abstractions under standard conditions, or if the substrate would have to be deuterated, in the positions α to the double bond, to observe epoxide products. We were also intrigued by the contribution of tunnelling in the H-atom abstraction of chol by peroxyl radicals, and wondered if tunnelling has a role in the autoxidation of lipids/hydrocarbons in a broader sense. These questions are addressed in Chapter 4.

3.7 Experimental Section

All chemicals and solvents were purchased from Sigma Aldrich Co. LLC and used as received, unless otherwise stated. Cholesterol (92%) was purified to >99% (NMR purity) by Fieser's bromination method to remove other sterol impurities.[49] The >99% cholesterol was then freshly recrystallized from methanol prior to each experiment to remove trace oxidation product impurities. 2,2'-Azobis (4-methoxy-2,4-dimethylvaleronitrile) (MeOAMVN)[50] was purchased from Wako Pure Chemical Industries, Ltd. And used as received. 2,6-Di-*tert*-butyl-4-methylphenol (BHT) was recrystallized from hexane prior to use. 3-Chloroperbenzoic acid (mCPBA, ≤77%) was recrystallized from CH_2Cl_2 prior to use.

Synthesis. 4α-Hydroxycholesterol (chol 4α-OH), 4β-hydroxycholesterol (chol 4β-OH), 5α-hydroxycholesterol (chol 5α-OH), 6α-hydroxycholesterol (chol 6α-OH), 6β-hydroxycholesterol (chol 6β-OH), and 7α-hydroxycholesterol (chol 7α-OH), 7β-hydroxycholesterol (chol 7β-OH), and 4-(tert-butyl)-2,6-dimethylphenol (BDMP) were prepared as previously reported.[17]

Cholesterol-5α,6α-epoxide (chol α-epoxide) and cholesterol 5β,6β-epoxide (chol β-epoxide). mCPBA (485 mg, 2.8 mmol) was added to 1.0 g cholesterol (2.6 mmol) in 25 mL dry CH_2Cl_2 and stirred for 6 hours under nitrogen. Aqueous, saturated $NaHCO_3$ (25 mL) was added and the mixture was stirred for 10 minutes. The organic layer was washed with water then brine, dried over $MgSO_4$ and concentrated *in vacuo*. The crude solid was purified by flash column on silica gel (7:3

hexanes:EtOAc) to give a mixture of chol α- and β-epoxide, with a ratio of 1:0.3, as a white solid; 94% yield. Spectroscopic characterization was consistent with literature precedent.[51]

3β-((Triisopropylsilyl)oxy)-pregn-5-en-20-one (**3.4**). Pregn-5-en-3β-ol-20-one (pregnenolone, 1.5 g, 4.7 mmol) was dissolved in 40 mL dimethylformamide and 10 mL dichloromethane, and imidazole (1.2 g, 17.6 mmol) and chlorotriisopropylsilane (1.7 mL, 7.8 mmol) were added. The reaction was stirred at room temperature under nitrogen for 4 hours. The reaction was taken up in ethyl acetate (50 mL) and washed with $NaHCO_3$ (aqueous, saturated, 2 x 50 mL) then brine (50 mL), dried over $MgSO_4$ and concentrated in vacuo. The resultant oil was purified by flash column on silica gel (9:1 hexanes:ethyl acetate) to yield a white waxy solid; 97% yield. ^{1}H-NMR (400 MHz; $CDCl_3$): δ 5.31 (d, *J* = 5.2 Hz, 1H), 3.56 (tdd, *J* = 10.3, 6.1, 4.2 Hz, 1H), 2.53 (t, *J* = 9.0 Hz, 1H), 2.28-2.16 (m, 3H), 2.12 (s, 3H), 2.06-1.96 (m, 2H), 1.84-1.79 (m, 2H), 1.72-1.44 (m, 9H), 1.28-1.13 (m, 2H), 1.06-1.05 (m, 21H), 1.00 (s, 3H), 0.98-0.89 (m, 1H), 0.63 (s, 3H); ^{13}C-NMR (100 MHz; $CDCl_3$): δ 209.7, 141.8, 120.9, 72.6, 63.9, 57.1, 50.2, 44.2, 43.2, 39.0, 37.6, 36.7, 32.5, 32.05, 31.98, 31.7, 24.7, 23.0, 21.2, 19.6, 18.3, 17.9, 13.4, 12.5; HRMS (EI): calculated for (loss of isopropyl from TIPS) $C_{30}H_{52}O_2Si$ 429.31833, found 429.32169.

3β-((Triisopropylsilyl)oxy)-pregn-5-en-20-one-17,21,21,21-d$_4$ (**3.5**). To **3.4** (2.0 g, 4.65 mmol) in 100 mL dry dioxane was added 7.5 mL D_2O and 2.5 mL sodium deuteroxide (40% solution in D_2O) in a flask fitted with a reflux condenser. The reaction was heated to 110°C for 24 hours under nitrogen, then cooled to room temperature. The solvent was removed in vacuo, and the residue taken up in ether (100 mL). The solution was washed successively with 100 mL each of H_2O, 1M HCl, $NaHCO_3$ (aqueous, saturated), and then brine. The organic layer was dried over $MgSO_4$ and concentrated in vacuo. The product was used without further purification. White waxy solid; 99% yield. ^{1}H-NMR (400 MHz; $CDCl_3$): δ 5.30 (d, *J* = 5.2 Hz, 1H), 3.55 (tdd, *J* = 10.3, 6.1, 4.1 Hz, 1H), 2.28-2.25 (m, 2H), 2.19-2.13 (m, 1H), 2.04-1.97 (m, 2H), 1.83-1.79 (m, 2H), 1.69-1.43 (m, 9H), 1.27-1.12 (m, 2H), 1.05-1.04 (m, 21H), 1.02 (s, 3H), 0.98-0.89 (m, 1H), 0.62 (s, 3H); ^{13}C-NMR (100 MHz;

$CDCl_3$): δ 209.9, 141.8, 120.9, 72.5, 57.1, 50.2, 44.1, 43.2, 39.0, 37.6, 36.7, 32.5, 32.21, 32.02, 31.96, 24.7, 22.8, 21.2, 19.6, 18.2, 17.8, 13.4, 12.5; HRMS (EI): calculated for (loss of isopropyl from TIPS) $C_{27}H_{41}D_4O_2Si^+$ 433.34344, found 433.34469.

3β-((Triisopropylsilyl)oxy)-cholest-5-en-20-ol-17,21,21,21-d₄ (**3.6**). Magnesium powder (306 mg, 12.6 mmol) was taken up in 5 mL dry THF in a round bottom flask fitted with a reflux condenser. A few drops of anhydrous HCl (4.0 M in dioxane) were added and the mixture was heated to 70ºC. The magnesium was activated by adding a solution (~10 mg/mL) of iodine in dry THF in three 300μL portions. 1-bromo-4-methylpentane (920 μL, 6.3 mmol) was then added dropwise in 5 mL dry THF at room temperature, and the mixture was refluxed for 2 hours then cooled to room temperature. **3.5** (500 mg, 1.05 mmol) was taken up in 5 mL dry THF and the Grignard reagent was added dropwise at room temperature. The reaction was refluxed overnight, then cooled to room temperature. 15 mL of NH_4Cl (aqueous, saturated) was added and the mixture was stirred for 30 minutes, then extracted with 3 × 15 mL EtOAc. The combined organic extracts were washed with brine, then dried over $MgSO_4$ and concentrated *in vacuo*. The resultant oil was purified by flash column on silica gel (9:1 hexanes:ethyl acetate) to yield a clear oil; 84% yield. ^{1}H-NMR (400 MHz; $CDCl_3$): δ 5.31 (d, J = 5.0 Hz, 1H), 3.56 (tdd, J = 10.3, 6.1, 4.1 Hz, 1H), 2.31-2.21 (m, 2H), 2.08 (dt, J = 12.4, 3.4 Hz, 1H), 2.00-1.93 (m, 1H), 1.83-1.42 (m, 13H), 1.33-1.11 (m, 9H), 1.05 (s, 21H), 1.01 (s, 3H), 0.89-0.86 (m, 9H); ^{13}C-NMR (100 MHz; $CDCl_3$): δ 141.8, 121.1, 75.2, 72.6, 57.1, 50.3, 44.2, 43.2, 42.7, 40.2, 39.8, 37.6, 36.7, 32.5, 32.0, 31.5, 28.20, 28.09, 24.0, 22.88, 22.72, 22.4, 22.1, 21.1, 19.6, 18.3, 13.7, 12.5; HRMS (EI): calculated for (loss of isopropyl from TIPS) $C_{33}H_{55}D_4O_2Si^+$ 519.45299, found 519.45353.

3β-((Triisopropylsilyl)oxy)-cholesta-5,20-diene-17,21,21,21-d₄ (**3.7**). Compound **3.6** (400 mg, 0.72 mmol) was dissolved in 20 mL dry pyridine and cooled to 0ºC. $POCl_3$ (110 μL, 1.2 mmol) was added dropwise, and the reaction was allowed to come to room temperature and stirred for 2 hours. Additional portions of $POCl_3$ (110 μL) were added at 0ºC until no starting material remained

by TLC (19:1 hexanes:ethyl acetate, where the R_f of **3.6** and **3.7** were 0.2 and 0.9, respectively). The reaction was quenched at 0ºC by dropwise addition of methanol (2 mL), then water (20 mL), then extracted twice with 50 mL ether. The combined ether extracts were washed twice with 0.1 M HCl (50 mL), then with 50 mL $NaHCO_3$ (aqueous, saturated), then 50 mL brine, dried over $MgSO_4$ and concentrated *in vacuo*. This reaction is known to give a mixture of three elimination products (purported to be 55% $\Delta^{20(22)}$, 25% Δ^{20} and 20% $\Delta^{17(20)}$ when carried out on a similar substrate),[24] therefore, the resultant oil was purified by flash column on silica gel impregnated with 10% silver nitrate (10:1 hexanes:toluene) to yield the $\Delta^{20(22)}$ product **7** as a clear oil; 48% yield. ^{1}H-NMR (400 MHz; $CDCl_3$): δ 5.32 (d, *J* = 5.1 Hz, 1H), 5.17 (t, *J* = 7.0 Hz, 1H), 3.56 (tdd, *J* = 10.4, 6.0, 4.3 Hz, 1H), 2.32-2.22 (m, 2H), 2.05-1.95 (m, 3H), 1.84-1.77 (m, 4H), 1.70-1.38 (m, 9H), 1.25-1.12 (m, 5H), 1.06 (s, 21H), 1.01 (s, 3H), 0.88 (d, *J* = 6.6 Hz, 6H), 0.54 (s, 3H); ^{13}C-NMR (100 MHz; $CDCl_3$): δ 141.9, 134.0, 125.9, 121.2, 77.2, 72.6, 56.5, 50.6, 43.5, 43.3, 39.4, 38.8, 37.6, 36.8, 32.53, 32.37, 32.1, 27.9, 26.1, 24.7, 24.5, 22.78, 22.73, 21.2, 19.7, 18.3, 13.0, 12.5; HRMS (EI): calculated for (loss of isopropyl from TIPS) $C_{33}H_{53}D_4OSi^+$ 501.44243, found 501.44429.

Cholesterol-17,20,21,21,21,22-d_6 (**3.8**). Compound **7** (300 mg, 0.6 mmol) was dissolved in 15 mL dry dioxane and 0.3 mL AcOD, and platinum oxide (25 mg, 0.09 mmol) was added. The flask was briefly placed under vacuum, then affixed with a balloon containing approximately 30 mL D_2. The reaction was stirred at room temperature overnight, passed through a pad of celite, then concentrated *in vacuo*. Crude ^{1}H NMR showed disappearance of the methylene proton at 5.17 ppm. The resultant clear oil was taken up in 15 mL THF and TBAF (1 M in THF) was added in 1 mL portions until the starting material was consumed by TLC. The mixture was taken up in ether (50 mL), washed with 50 mL water, then 50 mL brine, dried over $MgSO_4$, and concentrated *in vacuo*. The crude solid was purified by flash column on silica gel (9:1 hexanes:ethyl acetate) to yield a white solid; 84% yield. Note that in the ^{13}C NMR, D-bearing carbons (55.4, 35.9, 35.1, and 17.8 ppm) are barely visible due to D-coupling, and are therefore not reported. ^{1}H-NMR (400 MHz; $CDCl_3$): δ 5.34

(d, *J* = 5.2 Hz, 1H), 3.51 (tt, *J* = 10.6, 5.1 Hz, 1H), 2.31-2.20 (m, 2H), 2.02-1.93 (m, 2H), 1.85-1.77 (m, 3H), 1.70 (s, 1H) 1.55-1.43 (m, 7H), 1.25-1.11 (m, 8H), 1.00 (s, 3H), 0.95-0.89 (m, 2H), 0.86 (dd, *J* = 6.6, 1.9 Hz, 6H), 0.57 (s, 3H); ^{13}C-NMR (100 MHz; $CDCl_3$): δ 140.9, 121.8, 71.9, 56.9, 50.3, 42.4, 42.3, 39.8, 39.6, 37.4, 36.6, 32.05, 32.03, 31.8, 28.2, 28.0, 24.4, 23.9, 23.0, 22.7, 21.2, 19.5, 12.0; HRMS (EI): calculated for $C_{27}H_{40}D_6O$ 392.39253, found 392.39493.

5α-Hydroxycholesterol-17,20,21,21,21,22-d$_6$. The title compound was prepared from **3.8** in a manner analogous to the previously reported[52] synthesis of chol 5α-OH from chol: A solution of **3.8** (30 mg, 0.08 mmol) and Rose Bengal (1 mg, 0.001 mmol) in 2 mL pyridine was irradiated with a 400 W Na lamp at a distance of 5 cm at 0°C with constant O_2 bubbling for 6 hours. The pyridine was removed *in vacuo* and the residue taken up in 2 mL EtOH. PPh_3 (22 mg, 0.08 mmol) was added and the solution was stirred for 2 hours, then concentrated *in vacuo*. The residue was purified by flash column on silica gel (7:3 hexanes:ethyl acetate) to yield a white solid; 73% yield. ^{1}H-NMR (600 MHz; $CDCl_3$): δ 5.63 (dd, *J* = 9.83, 1.83 Hz, 1H), 5.57 (dd, *J* = 9.82, 2.70 Hz, 1H), 4.12 (m, 1H), 2.02 (m, 1H), 1.94-1.78 (m, 4H), 1.65-1.56 (m, 3H), 1.51-0.97 (m, 17 H), 0.92 (s, 3H), 0.86 (dt, *J* = 4.30, 2.34 Hz, 6H), 0.70 (s, 3H); ^{13}C-NMR (150 MHz; $CDCl_3$): δ 133.34, 133.32, 74.1, 67.3, 54.0, 45.2, 43.7, 41.0, 40.1, 39.6, 38.6, 38.2, 30.7, 28.7, 28.3, 28.2, 23.95, 23.86, 23.0, 22.90, 22.7, 21.2, 14.8, 12.3; HRMS (EI): calculated for $C_{27}H_{40}D_6O_2$ 408.38744, found 408.38674.

Cholesterol-5,6-epoxide-17,20,21,21,21,22-d$_6$. The title compound was prepared from **3.8** (50 mg, 0.13 mmol scale) using the same procedure as detailed above for the synthesis of the chol epoxides to give a mixture of d_6-chol α- and β-epoxide, in a ratio of 4:1, as a white solid; 89% yield. Characterization was consistent with that previously reported[51] for the protiated analogues (chol epoxides). *Cholesterol-5α,6α-epoxide-17,20,21,21,21,22-d$_6$*: ^{1}H-NMR (400 MHz; $CDCl_3$): δ 3.91 (tt, *J* = 10.9, 5.3 Hz, 1H), 2.90 (d, *J* = 4.7 Hz, 1H), 2.07 (t, *J* = 12.0 Hz, 1H), 1.95-1.87 (m, 3H), 1.82-1.10 (m, 23H), 1.06 (s, 3H), 1.02-0.92 (m, 3H), 0.86 (d, *J* = 6.6 Hz, 6H), 0.60 (s, 3H); ^{13}C-NMR (75 MHz; $CDCl_3$): δ 68.9, 65.8, 59.4, 57.0, 42.7, 42.4, 40.0, 39.48, 39.42, 35.0, 32.5, 31.3, 30.0, 29.0,

28.2, 28.1, 24.2, 24.1, 23.0, 22.7, 20.8, 16.1, 12.0; HRMS (EI): calculated for $C_{27}H_{40}D_6O_2$ 408.38744, found 408.38852. *Cholesterol-5β,6β-epoxide-17,20,21,21,21,22-d₆*: 3.70 (tt, *J* = 10.7, 5.3 Hz, 1H), 3.06 (d, *J* = 2.5 Hz, 1H), 2.07 (t, *J* = 12.0 Hz, 1H), 1.95-1.87 (m, 3H), 1.82-1.10 (m, 23H), 1.06 (s, 3H), 1.02-0.92 (m, 3H), 0.86 (d, *J* = 6.6 Hz, 6H), 0.63 (s, 3H); ^{13}C-NMR (75 MHz; $CDCl_3$): δ 69.6, 63.9, 63.1, 56.4, 51.5, 42.7, 42.4, 39.6, 39.5, 37.4, 35.0, 32.8, 31.2, 29.9, 28.2, 27.9, 24.0, 23.9, 22.9, 22.8, 22.2, 17.2, 11.9; HRMS (EI): calculated for $C_{27}H_{40}D_6O_2$ 408.38744, found 408.38852.

4-Ketocholesterol. To a solution of 4-ketocholesteryl acetate (150 mg, 0.34 mmol, prepared as previously reported)[17,53] in 6 mL MeOH was added KOH (340 mg, 6 mmol), and the mixture was stirred for 3 hours. CH_2Cl_2 (6 mL) was added, and the organic layer separated and washed with 1M HCl, then $NaHCO_3$ (aq. sat.), then brine, dried over $MgSO_4$ and concentrated *in vacuo*. The crude solid was purified by silica gel flash column (hexanes), and portions were further purified by preparative TLC (hexanes); white solid, 78% yield, based on the isolated inseparable mixture of 4-ketocholesterol and 4-hydroxycholest-4-en-3-one (characterization of the latter has been reported[54]). *4-Ketocholesterol*: ^{1}H-NMR (600 MHz; $CDCl_3$): δ 6.91 (dd, *J* = 5.2, 2.7 Hz, 1H), 6.07 (br, 1H), 6.03 (dd, J = 6.8, 2.8 Hz, 1H), 2.55-2.41 (m, 1H), 2.33-2.26 (m, 1H), 2.07-1.96 (m, 2H), 1.90-1.78 (m, 2H), 1.68-1.59 (m, 2H), 1.58-1.46 (m, 4H), 1.42-1.21 (m, 8H), 1.12 (s, 3H), 1.09-0.93 (m, 6H), 0.91 (dd, *J* = 10.5, 6.6 Hz, 3H), 0.86 (dt, *J* = 4.3, 2.3 Hz, 6H), 0.69 (s, 3H); ^{13}C-NMR (150 MHz; $CDCl_3$): δ 184.5, 146.4, 137.2, 115.4, 56.6, 56.2, 49.3, 42.5, 39.64, 39.64, 39.61, 37.9, 36.3, 35.9, 32.2, 31.2, 28.3, 28.2, 28.2, 24.3, 24.0, 23.0, 22.7, 21.9, 20.9, 18.9, 12.0; HRMS (EI): calculated for $C_{27}H_{44}O_2$ 400.33413, found 400.33523.

6-Ketocholesterol. Cholest-4-en-3,6-dione (100 mg, 0.25 mmol, prepared as previously reported)[17,55] was taken up in 2 mL dry THF and 1 mL dry EtOH, and $CeCl_3x7H_2O$ (100 mg, 0.27 mmol) was added. The mixture was cooled to 0°C and $NaBH_4$ (3.2 mg, 0.085 mmol) was added. The reaction was allowed to reach room temperature, then stirred for 1 hour and quenched with 2 mL water. The mixture was extracted with ether, washed with brine, dried over $MgSO_4$, and concentrated

in vacuo. The crude solid was purified by flash column on silica gel (7:3 hexanes:ethyl acetate); white solid, 45% yield. The compound matched previous characterization,[56,57] though we report ^{13}C NMR and a more complete ^{1}H NMR here: ^{1}H-NMR (400 MHz; $CDCl_3$): δ 6.17 (d, *J* = 1.24 Hz, 1H), 4.32 (dt, *J* = 10.8, 5.2 Hz, 1H), 2.46-2.30 (m, 2H), 2.17 (ddd, *J* = 11.9, 5.6, 3.4 Hz, 1H), 2.06-1.96 (m, 3H), 1.89-1.46 (m, 7H), 1.43-1.24 (m, 7H), 1.18 (s, 3H), 1.13-1.00 (m, 7H), 0.91 (d, *J* = 6.6 Hz, 3H), 0.86 (dd, *J* = 6.6, 1.9 Hz, 6H), 0.70 (s, 3H); ^{13}C-NMR (100 MHz; $CDCl_3$): δ 199.7, 171.9, 119.8, 68.8, 56.2, 55.7, 53.9, 42.6, 41.6, 39.62, 39.61, 39.2, 36.4, 36.2, 35.9, 34.3, 33.9, 28.3, 28.2, 24.3, 23.9, 23.0, 22.7, 21.2, 18.8, 18.4, 12.1.

7-Ketocholesterol. Cholesterol (500 mg, 1.3 mmol) and N-hydroxyphthalimide (30 mg, 0.2 mmol) were dissolved in PhCl (25 mL) and azobisisobutyronitrile (20 mg, 0.1 mmol) was added. The reaction was stirred open to air at 60°C for 72 hours, then PPh_3 (250 mg, 1 mmol) was added. The crude mixture was concentrated *in vacuo* and purified by silica gel flash column (gradient from 9:1 to 7:3 hexanes:ethyl actate) to yield a white solid; 13% yield. Spectroscopic characterization was consistent with literature precedent.[58]

Cholestane-3β,5α,6β-triol (chol triol). Cholesterol epoxide (200 mg, 0.5 mmol) was dissolved in 7 mL of acetone:water (10:1) in an ice bath and 60 μL of 70% perchloric acid was added. The reaction was warmed to room temperature and stirred for 2 hours. NaOH (50%, aqueous) was added until the pH was neutral, and the acetone was removed *in vacuo*. The crude mixture was taken up in 10 mL ether, washed with brine (3 x 10 mL), dried over $MgSO_4$ and concentrated in vacuo. The crude solid was purified by flash column on silica gel (gradient from 1:1 EtOAc:hexanes to EtOAc) to give a white solid; 86% yield. Spectroscopic characterization was consistent with literature precedent.[59]

Cholestane-3β,5α,6β-triol-17,20,21,21,21,22-d_6. The title compound was prepared from cholesterol-5,6-epoxide-17,20,21,21,21,22-d_6 (10 mg, 0.025 mmol scale) using the same procedure as

above for chol triol; white solid, 91% yield. ^{1}H-NMR (600 MHz; $CDCl_3$): δ 4.10 (tt, *J* = 10.9, 5.5 Hz, 1H), 3.54 (t, *J* = 2.9 Hz, 1H), 2.08 (dd, J = 12.9, 11.2 Hz, 1H), 2.00-1.94 (m, 1H), 1.87-1.69 (m, 3H), 1.63-1.48 (m, 7H), 1.43-1.22 (m, 8H), 1.18 (s, 3H), 1.15-0.95 (m, 6H), 0.86 (dd, *J* = 6.6, 2.6 Hz, 6H), 0.67 (s, 3H) ; ^{13}C-NMR (150 MHz; $CDCl_3$): δ 76.3, 76.2, 67.8, 56.1, 46.1, 42.8, 40.9, 40.0, 39.6, 38.5, 34.7, 32.5, 31.0, 30.3, 28.2, 28.0, 24.3, 23.9, 23.0, 22.7, 21.3, 17.1, 12.3; HRMS (EI): calculated for (M^+-H_2O) $C_{27}H_{41}D_6O_2^+$ 409.39472, found 408.39340.

Cholesterol-5,6-epoxide-2,2,4,4,7,7-d$_6$. The title compound was prepared from cholesterol-2,2,4,4,7,7-d_6 (prepared as previously reported)[22] (20 mg, 0.05 mmol scale) using the same procedure as above for the chol epoxides, to give a mixture of d_6-chol α- and β-epoxide, with a ratio of 4:1, as a white solid; 86% yield. Spectroscopic characterization was consistent with literature precedent for the protiated analogues (chol epoxides).[51] *Cholesterol-5α,6α-epoxide-2,2,4,4,7,7-d$_6$*: ^{1}H-NMR (600 MHz; $CDCl_3$): δ 3.89 (s, 1H), 2.89 (s, 1H), 1.96-1.93 (m, 1H), 1.84-1.77 (m, 1H), 1.67 (d, *J* = 13.52, 1H), H (br, 1H), 1.57-1.48 (m, 3H), 1.38-1.28 (m, 6H), 1.25-1.20 (m, 3H), 1.14-1.06 (m, 4H), 1.05 (s, 3H), 1.0-0.93 (m, 3H), 0.88 (d, *J* = 6.6 Hz, 3H), 0.85 (dd, *J* = 6.6, 3.0 Hz, 6H), 0.60 (s, 3H); ^{13}C-NMR (150 MHz; $CDCl_3$): δ 68.7, 65.7, 59.3, 56.9, 56.0, 42.6, 42.5, 39.63, 39.56, 36.3, 35.9, 34.9, 32.4, 29.8, 28.2, 28.1, 24.2, 24.0, 23.0, 22.7, 20.8, 18.8, 16.1, 12.0; HRMS (EI): calculated for $C_{27}H_{40}D_6O_2$ 408.38744, found 408.38675. *Cholesterol-5β,6β-epoxide-2,2,4,4,7,7-d$_6$*: ^{1}H-NMR (600 MHz; $CDCl_3$): δ 3.68 (s, 1H), 3.04 (s, 1H), 1.96-1.93 (m, 1H), 1.84-1.77 (m, 1H), 1.67 (d, *J* = 13.52, 1H), H (br, 1H), 1.57-1.48 (m, 3H), 1.38-1.28 (m, 6H), 1.25-1.20 (m, 3H), 1.14-1.06 (m, 4H), 1.05 (s, 3H), 1.0-0.93 (m, 3H), 0.88 (d, *J* = 6.6 Hz, 3H), 0.85 (dd, *J* = 6.6, 3.0 Hz, 6H), 0.63 (s, 3H); ^{13}C-NMR (150 MHz; $CDCl_3$): δ 69.4, 63.7, 63.0, 56.3, 56.3, 51.4, 42.4, 40.0, 39.6, 37.2, 36.3, 35.9, 34.9, 29.7, 28.3, 28.1, 24.3, 24.0, 23.0, 22.7, 22.1, 18.8, 17.2, 11.9; HRMS (EI): calculated for $C_{27}H_{40}D_6O_2$ 408.38744, found 408.38675.

Autoxidations. *Cholesterol autoxidations.* To 19 mg cholesterol (0.05 mmol) in a HPLC vial was added H-atom donor (BDMP or PMC) in a stock solution, and enough chlorobenzene to make up

the volume to 90 μL. MeOAMVN (10 μL of a 200 mM solution in benzene) was added. The vial was capped with a preslit HPLC cap, and incubated at 37°C for 16 hours. The solution was quenched by adding 760 μL of a solution of 6.5 mM BHT and 6.5 mM PPh_3 in HPLC grade hexane, and the following internal standards were added as 1 mM solutions in chlorobenzene: 20 μL of d_6-5α-hydroxycholesterol, 20 μL of d_6-cholesterol-5,6-epoxide, and 100 μL of 4-nitrophenol.

Cholesteryl acetate autoxidations. To 22 mg cholesteryl acetate (0.05 mmol) in a vial was added BDMP in a stock solution, and enough chlorobenzene to make up the volume to 90 μL. MeOAMVN (10 μL of a 200 mM solution in benzene) was added. The vial was capped loosely, and incubated at 37°C for 16 hours. The solution was quenched by adding 100 μL of 0.2 M BHT and PPh_3 in PhCl, then 2 mL of 1.0 M KOH in MeOH was added and the vial was shaken occasionally over 3 hours. 6 mL CH_2Cl_2 was added and the mixture was washed twice with 6 mL H_2O, dried over $MgSO_4$, concentrated *in vacuo*. The residue was taken up in 860 μL of HPLC grade hexane, and the following internal standards were added as 1 mM solutions in chlorobenzene: 20 μL of d_6-5α-hydroxycholesterol, 20 μL of d_6-cholesterol-5,6-epoxide, and 100 μL of 4-nitrophenol.

Cholesterol-2,2,4,4,7,7-d_6 autoxidations. Cholesterol-d_6 (20 mg) was treated as in the cholesterol autoxidation above, without additive, and 5α-hydroxycholesterol and cholesterol-5,6-epoxide were used as internal standards rather than the d_6-analogues.

HPLC-APCI-MS/MS Analyses. From each autoxidation (unless otherwise noted), 10 μL of the sample was injected onto a normal phase HPLC column (SunFire 5 μm silica; 4.6 mm × 250 mm) and eluted with the following gradient of hexane:*iso*-propanol (*i*-PrOH) at a flow rate of 1.5 mL/min: 99:1 to 98:2 over 30 minutes, 98:2 from 30 to 40 minutes, 98:2 to 95:5 from 40 to 41 minutes, 95:5 from 41 to 49 minutes, 95:5 to 99:1 from 49 to 50 minutes, and 99:1 from 50 to 60 minutes. APCI-MS/MS detection in positive ion mode was used for the MS/MS transitions: 403.4 *m/z* → 385.4 *m/z* and 385.4 *m/z* → 367.4 *m/z*, for chol epoxides and alcohols, respectively; as well as 409.4 *m/z* → 391.4 *m/z* and 391.4 *m/z* → 373.4 *m/z*, for d_6-chol epoxides and alcohols, respectively. The settings

for mass spectral analysis were as follows: corona current 2 μA; cone voltage 25 V; source temperature 150°C; APCI probe temperature 500°C; desolvation gas flow 600 L/hr; cone gas flow 20 L/hr; collision gas flow 0.2 mL/min; collision energy 15 eV. Simultaneous UV detection was carried out by photodiode array, and the 6- and 7-ketochols were detected at 234 nm relative to 4-nitrophenol as internal standard.

3.8 References

(1) Ullery, J. C.; Marnett, L. J. Protein modification by oxidized phospholipids and hydrolytically released lipid electrophiles: Investigating cellular responses. *Biochim. Biophys. Acta, Biomembr.* **2012**, *1818*, 2424.

(2) Xu, L.; Porter, N. A. Reactivities and Products of Free Radical Oxidation of Cholestadienols. *J. Am. Chem. Soc.* **2014**, *136*, 5443.

(3) Xu, L.; Korade, Z.; Porter, N. A. Oxysterols from Free Radical Chain Oxidation of 7-Dehydrocholesterol: Product and Mechanistic Studies. *J. Am. Chem. Soc.* **2010**, *132*, 2222.

(4) Xu, L.; Davis, T. A.; Porter, N. A. Rate Constants for Peroxidation of Polyunsaturated Fatty Acids and Sterols in Solution and in Liposomes. *J. Am. Chem. Soc.* **2009**, *131*, 13037.

(5) van Meer, G.; Voelker, D. R.; Feigenson, G. W. Membrane lipids: where they are and how they behave. *Nat. Rev. Mol. Cell Biol.* **2008**, *9*, 112.

(6) Björkhem, I.; Meaney, S. Brain Cholesterol: Long Secret Life Behind a Barrier. *Arterioscler. Thromb. Vasc. Biol.* **2004**, *24*, 806.

(7) Stiles, A. R.; Kozlitina, J.; Thompson, B. M.; McDonald, J. G.; King, K. S.; Russell, D. W. Genetic, anatomic, and clinical determinants of human serum sterol and vitamin D levels. *Proc. Natl. Acad. Sci. USA* **2014**, *111*, E4006.

(8) Dzeletovic, S.; Breuer, O.; Lund, E.; Diczfalusy, U. Determination of Cholesterol Oxidation Products in Human Plasma by Isotope Dilution-Mass Spectrometry. *Anal. Biochem.* **1995**, *225*, 73.

(9) Schroepfer, G. J. Oxysterols: Modulators of Cholesterol Metabolism and Other Processes. *Physiol. Rev.* **2000**, *80*, 361.

(10) For example see: (a) Porter, F. D.; Scherrer, D. E.; Lanier, M. H.; Langmade, S. J.; Molugu, V.; Gale, S. E.; Olzeski, D.; Sidhu, R.; Dietzen, D. J.; Fu, R.; Wassif, C. A.; Yanjanin, N. M.; Marso, S. P.; House, J.; Vite, C.; Schaffer, J. E.; Ory, D. S. Cholesterol Oxidation Products Are Sensitive and Specific Blood-Based Biomarkers for Niemann-Pick C1 Disease. *Sci. Transl. Med.* **2010**, *2*, 1; (b) Luu, W.; Sharpe, L. J.; Capell-Hattam, I.; Gelissen, I. C.; Brown, A. J. Oxysterols: Old Tale, New Twists. *Annu. Rev. Pharmacol. Toxicol.* **2016**, *56*, 447; (c) Guillemot-Legris, O.; Mutemberezi, V.; Muccioli, G. G. Oxysterols in Metabolic Syndrome: From Bystander Molecules to Bioactive Lipids. *Trends Mol. Med.* **2016**, *22*, 594; (d) Mutemberezi, V.; Guillemot-Legris, O.; Muccioli, G. G. Oxysterols: From cholesterol metabolites to key mediators. *Prog. Lipid Res.* **2016**, *64*, 152; (e) Doria, M.; Maugest, L.; Moreau, T.; Lizard, G.; Vejux, A. Contribution of cholesterol and oxysterols to the pathophysiology of Parkinson's disease. *Free Radic. Biol. Med.* **2016**, *101*, 393; (f) Kloudova, A.; Guengerich, F. P.; Soucek, P. The Role of Oxysterols in Human Cancer. *Trends Endocrinol. Metab.* **2017**, *28*, 485; (g) Gargiulo, S.; Testa, G.; Gamba, P.; Staurenghi, E.; Poli, G.; Leonarduzzi, G. Oxysterols and 4-hydroxy-2-nonenal contribute to atherosclerotic plaque destabilization. *Free Radic. Biol. Med.* **2017**, *111*, 140; (h) Mutemberezi, V.; Buisseret, B.; Masquelier, J.; Guillemot-Legris, O.; Alhouayek, M.; Muccioli, G. G. Oxysterol levels and metabolism in the course of neuroinflammation: insights from in vitro and in vivo models. *J. Neuroinflammation* **2018**, *15*, 74; (i) Testa, G.; Rossin, D.; Poli, G.; Biasi, F.; Leonarduzzi, G. Implication of oxysterols in chronic inflammatory human diseases. *Biochimie* **2018**, *153*, 220; (j) Bezine, M.; Namsi, A.; Sghaier, R.; Ben Khalifa, R.; Hamdouni, H.; Brahmi, F.; Badreddine, I.; Mihoubi, W.; Nury, T.; Vejux, A.; Zarrouk, A.; de Sèze,

J.; Moreau, T.; Nasser, B.; Lizard, G. The effect of oxysterols on nerve impulses. *Biochimie* **2018**, *153*, 46; and references cited therein.

(11) Takeuchi, C.; Galvé, R.; Nieva, J.; Witter, D. P.; Wentworth, A. D.; Troseth, R. P.; Lerner, R. A.; Wentworth, P., Jr. Proatherogenic Effects of the Cholesterol Ozonolysis Products, Atheronal-A and Atheronal-B. *Biochemistry* **2006**, *45*, 7162.

(12) Nieva, J.; Song, B.-D.; Rogel, J. K.; Kujawara, D.; Altobel, L., III; Izharrudin, A.; Boldt, G. E.; Grover, R. K.; Wentworth, A. D.; Wentworth, P., Jr. Cholesterol Secosterol Aldehydes Induce Amyloidogenesis and Dysfunction of Wild-Type Tumor Protein p53. *Chem. Biol.* **2011**, *18*, 920.

(13) Usui, K.; Hulleman, J. D.; Paulsson, J. F.; Siegel, S. J.; Powers, E. T.; Kelly, J. W. Site-specific modification of Alzheimer's peptides by cholesterol oxidation products enhances aggregation energetics and neurotoxicity. *Proc. Natl. Acad. Sci. USA* **2009**, *106*, 18563.

(14) Bosco, D. A.; Fowler, D. M.; Zhang, Q. H.; Nieva, J.; Powers, E. T.; Wentworth, P., Jr.; Lerner, R. A.; Kelly, J. W. Elevated levels of oxidized cholesterol metabolites in Lewy body disease brains accelerate a-synuclein fibrilization. *Nat. Chem. Biol.* **2006**, *2*, 249.

(15) Wentworth, P.; Nieva, J.; Takeuchi, C.; Galve, R.; Wentworth, A.; Dilley, R. B.; DeLaria, G. A.; Saven, A.; Babior, B. M.; Janda, K. D.; Eschenmooser, A.; Lerner, R. A. Evidence for Ozone Formation in Human Atherosclerotic Arteries. *Science* **2003**, *302*, 1053.

(16) Brinkhorst, J.; Nara, S. J.; Pratt, D. A. Hock Cleavage of Cholesterol 5r-Hydroperoxide: An Ozone-Free Pathway to the Cholesterol Ozonolysis Products Identified in Arterial Plaque and Brain Tissue. *J. Am. Chem. Soc.* **2008**, *130*, 12224.

(17) Zielinski, Z. A. M.; Pratt, D. A. Cholesterol Autoxidation Revisited: Debunking the Dogma Associated with the Most Vilified of Lipids. *J. Am. Chem. Soc.* **2016**, *138*, 6932.

(18) Poirot, M.; Silvente-Poirot, S. Cholesterol-5,6-epoxides: Chemistry, biochemistry, metabolic fate and cancer. *Biochimie* **2013**, *95*, 622.

(19) Speen, A. M.; Kim, H.-Y. H.; Bauer, R. N.; Meyer, M.; Gowdy, K. M.; Fessler, M. B.; Duncan, K. E.; Liu, W.; Porter, N. A.; Jaspers, I. Ozone-derived Oxysterols Affect Liver X Receptor (LXR) Signaling. *J. Biol. Chem.* **2016**, *291*, 25192.

(20) Holm, T.; Crossland, I. A Simple Preparation of Hexadeuteriocholesterol. *J. Label. Compd. Radiopharm.* **1996**, *38*, 803.

(21) Kirk, D. N.; Varley, M. J.; Makin, H. L. J.; Trafford, D. J. H. Synthesis of [26,27-$^{2}H_6$]Cholesterol and Derivatives substituted in the Side chain. *J. Chem. Soc., Perkin Trans. 1* **1983**, 2563.

(22) Chol A/B ring deuteration is precedented (e.g. 2,2,4,4,7,7-d_6-chol), however its conversion to the epoxide and 5α-OH standards would yield the former as d_6-labelled and the latter as d_5-labelled – and still requires 8 steps. See: Fujimoto, Y.; Maeda, I.; Ohyama, K.; Hikiba, J.; Kataoka, H. Biosynthesis of 20-hydroxyecdysone in plants: 3β-Hydroxy-5β-cholestan-6-one as an intermediate immediately after cholesterol in *Ajuga* hairy roots. *Phytochemistry* **2015**, *111*, 59.

(23) De Miranda, M. G.; Albert, A. L. M.; Cardoso, J. N.; Lopes, R. S. C.; Lopes, C. C. Straightforward Synthesis of 2,2,4,4,5,7,7-d_7-Cholestane: A New Deuterated Standard in Petroleum Analysis. *Quim. Nova* **2013**, *36*, 1160.

(24) Giner, J.-L.; Faraldos, J. A. A Biomimetic Approach to the Synthesis of an Antiviral Marine Steroidal Orthoester. *J. Org. Chem.* **2002**, *67*, 2717.

(25) We note that such hydroxycholesterols (chol XOH) and ketocholesterols may also form from peroxyl radical termination reactions and from further autoxidation or decomposition of the initially-

formed hydroperoxides.[42] A control experiment in the absence of PPh_3 showed the contribution of those pathways is relatively minor (<20%) in chol autoxidations without additive (cf. Section 3.8.7).

(26) The amount of chol 4-OH accounted for only 5% of the product distribution, indicating the amount previously reported[17] had been overestimated due to co-elution with the chol epoxides.

(27) Both chol epoxides may be hydrolyzed to give 5α,6β-dihydroxycholesterol[18] (chol triol), and the authentic chol triol was found to have a MS/MS transitions corresponding to $M+H^+-H_2O$ → $M+H^+-2H_2O$ (*m/z* 403.4 → *m/z* 385.4) as well as a second transition of $M+H^+-2H_2O$ → $M+H^+-3H_2O$ (*m/z* 385.4 → *m/z* 367.4). The chol triol was formed only in trace amounts (< 0.5 mol% of the products) during the 16-hour autoxidation (*cf.* Figure 3.27), which is not surprising given that harsh acidic or basic conditions were required to hydrolyze the epoxides synthetically (see 3.6 Experimental Section for details).

(28) Niki, E. Biomarkers of lipid peroxidation in clinical material. *Biochim. Biophys. Acta, Gen. Subj.* **2014**, 1840, 809.

(29) Lee, C.-Y. J.; Huang, S. H.; Jenner, A. M.; Halliwell, B. Measurement of F_2-isoprostanes, hydroxyeicosatetraenoic products, and oxysterols from a single plasma sample. *Free Radic. Biol. Med.* **2008**, *44*, 1314.

(30) Iuliano, L.; Micheletta, F.; Natoli, S.; Ginanni Corradini, S.; Iappelli, M.; Elisei, W.; Giovannelli, L.; Violi, F.; Diczfalusy, U. Measurement of oxysterols and a-tocopherol in plasma and tissue samples as indices of oxidant stress status. *Anal. Biochem.* **2003**, *312*, 217.

(31) This was a slight decrease from our previously reported value.[17]

(32) Haidasz, E. A.; Van Kessel, A. T. M.; Pratt, D. A. A Continuous Visible Light Spectrophotometric Approach To Accurately Determine the Reactivity of Radical-Trapping Antioxidants. *J. Org. Chem.* **2016**, *81*, 737.

(33) (a) Interestingly, the 30 mol% maximum in epoxide concentration occurs at higher [PMC] than [BDMP] (cf. Figures 3.32 and 3.2C, respectively). We suggest that the interplay between the H-atom donating ability of the two phenols (PMC being ~10-fold more potent), and the concentration of antioxidant at which the contribution of antioxidant-mediated peroxidation (AMP) becomes significant, dictates the maximum epoxide concentration. AMP is expected to be more efficient for BDMP than for PMC since the aryloxyl radical derived from BDMP is expected to be both less stable (O-H BDE for the former should be roughly 4 kcal/mol higher than for the latter, and similar to that in cholesterol) and more persistent owing to the *t*-butyl group on the (*para)* position. While the self-termination rate constant for the BDMP-derived phenoxyl radical has not been reported, the reported difference of 86,000-fold[33b] in k_t between 2,6-di-*tert*-butyl-4-methylphenoxyl radical and the 2,4,6-tri-*tert*-butylphenoxyl radical enables an estimate from the value of k_t for 2,4,6-trimethylphenol (4.5×10^7)[33b] of ~500 $M^{-1}s^{-1}$ – smaller than for PMC (α-tocopherol), for which 3000 $M^{-1}s^{-1}$ has been determined.[33b] (b) Burton, G. W.; Doba, T.; Gabe, E.; Hughes, L.; Lee, F. L.; Prasad, L.; Ingold, K. U. Autoxidation of Biological Molecules. 4. Maximizing the Antioxidant Activity of Phenols. *J. Am. Chem. Soc.* **1985**, *107*, 7053.

(34) Xu, L.; Porter, N. A. Free radical oxidation of cholesterol and its precursors: Implications in cholesterol biosynthesis disorders. *Free Radic. Res.* **2015**, *49*, 835.

(35) The k_p for chol was slightly lower in our hands than the literature value of 11 ± 2 M^{-1} s^{-1}.[4] In contrast to autoxidation, we have found that $^1O_2$ reacts more slowly with chol OAc than chol (unpublished results). Furthermore, the substituent has the opposite effect on peroxyl radical addition, where k_{epox} is slowed slightly to 7.8 and 13 $M^{-1}s^{-1}$ for addition to chol OAc at 6α and 6β, respectively. The origins of these differences are unclear and remain under active investigation in our labortatories.

(36) Paillasse, M. R.; Saffon, N.; Gornitzka, H.; Silvente-Poirot, S.; Poirot, M.; de Medina, P. Surprising unreactivity of cholesterol-5,6-epoxides towards nucleophiles. *J. Lipid Res.* **2012**, *53*, 718.

(37) Maillard, B.; Ingold, K. U.; Scaiano, J. C. Rate Constants for the Reactions of Free Radicals with Oxygen in Solution. *J. Am. Chem. Soc.* **1983**, *105*, 5095.

(38) Porter, N. A.; Mills, K. A.; Carter, R. L. A Mechanistic Study of Oleate Autoxidation: Competing Peroxyl H-Atom Abstraction and Rearrangement. *J. Am. Chem. Soc.* **1994**, *116*, 6690.

(39) Tallman, K. A.; Pratt, D. A.; Porter, N. A. Kinetic Products of Linoleate Peroxidation: Rapid β-Fragmentation of Nonconjugated Peroxyls. *J. Am. Chem. Soc.* **2001**, *123*, 11827.

(40) Though a recent report showed arachidonate forms epoxyeicosatrienoic acids via peroxyl radical addition, see: Aliwarga, T.; Raccor, B. S.; Lemaitre, R. N.; Sotoodehnia, N.; Gharib, S. A.; Xu, L.; Totah, R. A. Enzymatic and free radical formation of cis- and trans- epoxyeicosatrienoic acids in vitro and in vivo. *Free Radic Biol Med* **2017**, *112*, 131.

(41) Xu, L.; Korade, Z.; Rosado, D. A.; Liu, W.; Lamberson, C. R.; Porter, N. A. An oxysterol biomarker for 7-dehydrocholesterol oxidation in cell/mouse models for Smith-Lemli-Opitz syndrome. *J. Lipid Res.* **2011**, *52*, 1222.

(42) Zielinski, Z. A. M.; Pratt, D. A. Lipid Peroxidation: Kinetics, Mechanisms, and Products. *J. Org. Chem.* **2017**, *82*, 2817.

(43) Breuer, O.; Dzeletovic, S.; Lund, E.; Diczfalusy, U. The oxysterols cholest-5-ene-3β,4α-diol, cholest-5-ene-3β,4β-diol and cholestane-3β,5α,6α-triol are formed during in vitro oxidation of low density lipoprotein, and are present in human atherosclerotic plaques. *Biochim. Biophys. Acta, Lipids Lipid Metab.* **1996**, *1302*, 145.

(44) Hill, S.; Lamberson, C. R.; Xu, L.; To, R.; Tsui, H. S.; Shmanai, V. V.; Bekish, A. V.; Awad, A. M.; Marbois, B. N.; Cantor, C. R.; Porter, N. A.; Clarke, C. F.; Shchepinov, M. S. Small amounts of isotope-reinforced polyunsaturated fatty acids suppress lipid autoxidation. *Free Radic. Biol. Med.* **2012**, *53*, 893.

(45) Muchalski, H.; Levonyak, A. J.; Xu, L.; Ingold, K. U.; Porter, N. A. Competition H(D) Kinetic Isotope Effects in the Autoxidation of Hydrocarbons. *J. Am. Chem. Soc.* **2015**, *137*, 94.

(46) Muchalski, H.; Xu, L.; Porter, N. A. Tunnelling in tocopherol-mediated peroxidation of 7-dehydrocholesterol. *Org. Biomol. Chem.* **2015**, *13*, 1249.

(47) Lamberson, C. R.; Xu, L.; Muchalski, H.; Montenegro-Burke, J. R.; Shmanai, V. V.; Bekish, A. V.; McLean, J. A.; Clarke, C. F.; Shchepinov, M. S.; Porter, N. A. Unusual Kinetic Isotope Effects of Deuterium Reinforced Polyunsaturated Fatty Acids in Tocopherol-Mediated Free Radical Chain Oxidations. *J. Am. Chem. Soc.* **2014**, *136*, 838.

(48) Shchepinov, M. S.; Chou, V. P.; Pollock, E.; Langston, J. W.; Cantor, C. R.; Molinari, R. J.; Manning-Boğ, A. B. Isotopic reinforcement of essential polyunsaturated fatty acids diminishes nigrostriatal degeneration in a mouse model of Parkinson's disease. *Toxicol. Lett.* **2011**, *207*, 97.

(49) Fieser, L. F. Cholesterol and Companions. VII. Steroid Dibromides. *J. Am. Chem. Soc.* **1953**, *75*, 5421.

(50) Noguchi, N.; Yamashita, H.; Gotoh, N.; Yamamoto, Y.; Numano, R.; Niki, E. 2,2`-Azobis (4-Methoxy-2,4-dimethylvaleronitrile), A New Lipid-Soluble Azo Initiator: Application to Oxidations of Lipids and Low-Density Lipoprotein in Solution and in Aqueous Dispersions. *Free Radic. Biol. Med.* **1998**, *24*, 259.

(51) Carvalho, J. F. S.; Cruz Silva, M. M.; Moreira, J. N.; Simões, S.; Sá E Melo, M. L. Efficient Chemoenzymatic Synthesis, Cytotoxic Evaluation, and SAR of Epoxysterols. *J. Med. Chem.* **2009**, *52*, 4007.

(52) Beckwith, A. L. J.; Davies, A. G.; Davison, I. G. E.; Maccoll, A.; Mruzek, M. H. The Mechanisms of the Rearrangements of Allylic Hydroperoxides: 5α-Hydroperoxy-3β-hydroxycholest-6-ene and *7*α-Hydroperoxy-3β-hydroxycholest-5-ene. *J. Chem. Soc., Perkin Trans. 2* **1989**, 815.

(53) Nury, T.; Samadi, M.; Zarrouk, A.; Riedinger, J. M.; Lizard, G. Improved synthesis and in vitro evaluation of the cytotoxic profile of oxysterols oxidized at C4 (4α- and 4β-hydroxycholesterol) and C7 (7-ketocholesterol, 7α- and 7β-hydroxycholesterol) on cells of the central nervous system. *Eur. J. Med. Chem.* **2013**, *70*, 558.

(54) Thomas, M. G.; Suckling, C. J.; Pitt, A. R.; Suckling, K. E. The synthesis of A- and B-ring fluorinated analogues of cholesterol. *J. Chem. Soc., Perkin Trans. 1* **1999**, 3191.

(55) Korde, S. S.; Udasi, R. A.; Trivedi, G. K. Oxidation of Steroidal 5-En-3β-ol with Pyridinium Chlorochromate: Isolation of Key Intermediate, Steroidal 6β-Hydroxy-4-en-3-one. *Synth. Commun.* **1997**, *27*, 3419.

(56) Cui, J.; Huang, L.; Fan, L.; Zhou, A. A facile and efficient synthesis of some (6*E*)-hydroximino-4-en-3-one steroids, steroidal oximes from *Cinachyrella* spp. Sponges. *Steroids* **2008**, *73*, 252.

(57) Shamsuzzaman; Ahmad, S.; Khan, B. Z.; Shafiullah. A Convenient Method for the Synthesis of 3β-Hydroxy 4-En-6-one Steroids. *J. Org. Chem.* **1991**, *56*, 1936.

(58) Li, S.; Pang, J.; Wilson, W. K.; Schroepfer, G. J. Sterol synthesis. Preparation and characterization of fluorinated and deuterated analogs of oxygenated derivatives of cholesterol. *Chem. Phys. Lipids* **1999**, *99*, 33.

(59) Carvalho, J. F. S.; Silva, M. M. C.; Melo, M. L. S. E. Efficient trans-diaxial hydroxylation of Δ^5-steroids. *Tetrahedron* **2010**, *66*, 2455.

3.9 Supporting Information

Note: reference numbering starts anew for this section, and references can be found in section 3.9.11 Supplementary References.

3.9.1 Analysis of Typical Chol Autoxidations

Chol-d_6 and internal standards: the novel cholesterol-17,20,21,21,21,22-d_6 (APCI$^+$-MS spectrum in Figure 3.7) was used to prepare the internal standards 5α-hydroxycholesterol-17,20,21,21,21,22-d_6 and cholesterol-5,6-epoxide-17,20,21,21,21,22-d_6 (as a mixture of α- and β-epoxides), as outlined in the experimental section.

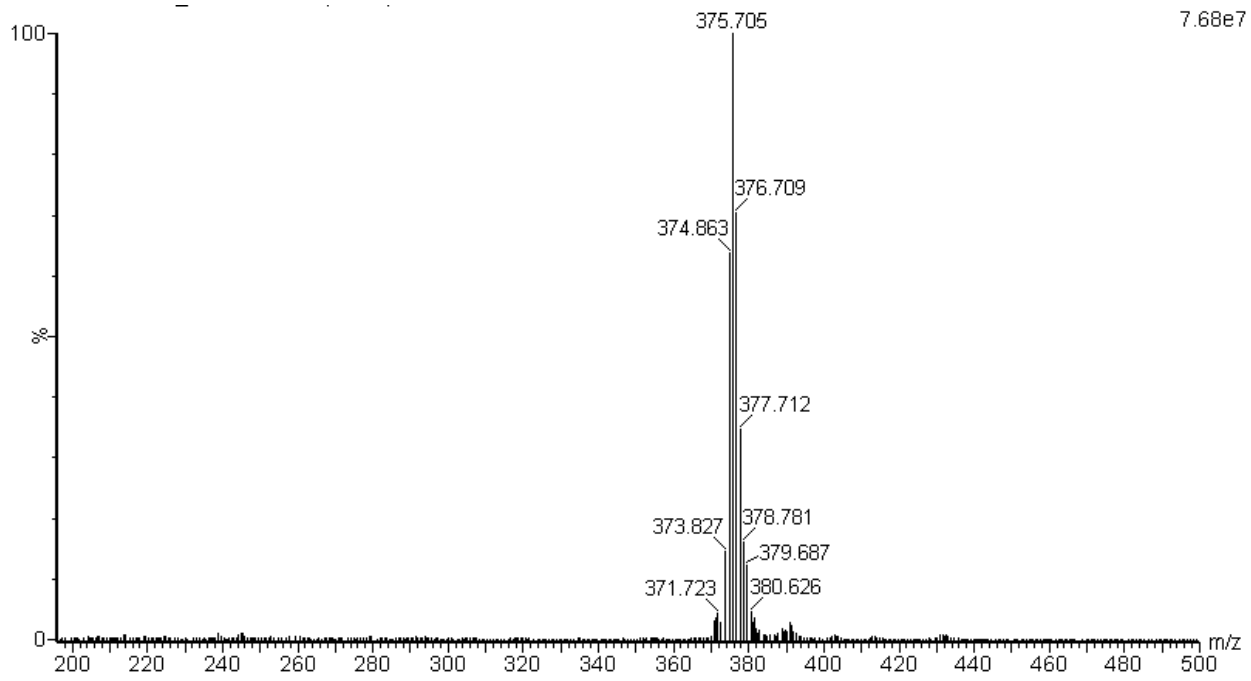

Figure 3.7. APCI$^+$-MS spectrum of cholesterol-17,20,21,21,21,22-d_6, showing the M+H$^+$-H_2O peak where the compound is predominantly d_6, with a tight distribution of other masses (d_2 to d_{11}).

Chol epoxides: We were initially surprised the chol epoxides showed the same MS/MS transition as the chol diols, which were detected by the MS/MS transition *m/z* 385.4 → *m/z* 367.4, corresponding to $M+H^+-H_2O$ → $M+H^+-2H_2O$. The $M+H^+$ ion (*m/z* 403) was not detectable for the diols, presumably due to the protonated alcohol rapidly dehydrating. Conversely, initial protonation of a chol epoxide is in resonance with the C5 carbocation and C6-OH (*cf.* Scheme 3.5). This ion, corresponding to $M+H^+$ or *m/z* = 403.4, is evidently longer lived than the corresponding $M+H^+$ for the chol diols. The subsequent dehydration of C3-OH or C6-OH (*m/z* = 385.4), followed by the second dehydration (*m/z* = 367.4), is analogous to the transitions of the chol diols. Indeed, when we computed $M+H^+$ of the epoxides, the C5-O bond was significantly lengthened to 1.9 Å, thus giving C5 carbocationic character (*cf.* Figure 3.8).

Scheme 3.5. Proposed $M+H^+$ ion formation for $APCI^+$ detection of chol epoxides.

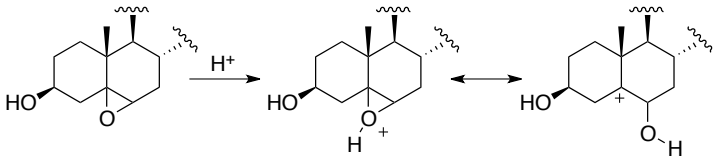

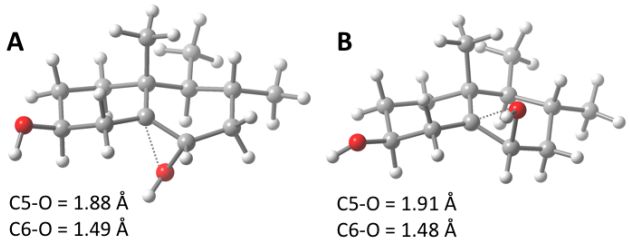

Figure 3.8. B3LYP/CBSB7 computed structure for protonated chol α-epoxide (A) and β-epoxide (B) and the associated epoxide C-O bond lengths.

HPLC analysis: As outlined in the experimental section 3.6, the autoxidations were analyzed by HPLC using simultaneous APCI-MS/MS and UV detection to quantify the compounds in Table 3.2. 4-ketochol and chol triol were detected using modified methods presented below. Shifts in retention time (up to ~3 min) were sometimes observed between runs; however, the internal standards were used to confirm peak assignments.

Table 3.2. HPLC retention times, detection methods, the internal standard each compound was compared to (including its concentration and detection method), and response factors (based on the standard curves below). Asterisk (*) indicates that the response factors previously determined[1] were used, as they were found to be unchanged with the modified mobile phase.

Compound	Retention time (min)	Detection method	Internal standard	Response factor
chol α-epoxide	35	APCI-MS/MS (403.4 *m/z* → 385.4 *m/z*)	d_6-chol α-epoxide (20 μM) APCI-MS/MS (409.4 *m/z* → 391.4 *m/z*)	1.0
chol β-epoxide	38	APCI-MS/MS (403.4 *m/z* → 385.4 *m/z*)	d_6-chol β-epoxide (5.6 μM) APCI-MS/MS (409.4 *m/z* → 391.4 *m/z*)	1.0
chol 4α-OH	38	APCI-MS/MS (385.4 *m/z* → 367.4 *m/z*)	d_6-chol β-epoxide (5.6 μM) APCI-MS/MS (409.4 *m/z* → 391.4 *m/z*)	7.11
chol 4β-OH	33	APCI-MS/MS (385.4 *m/z* → 367.4 *m/z*)	d_6-chol 5β-OH (20 μM) APCI-MS/MS (391.4 *m/z* → 373.4 *m/z*)	0.74*
chol 5α-OH	47	APCI-MS/MS (385.4 *m/z* → 367.4 *m/z*)	d_6-chol 5β-OH (20 μM) APCI-MS/MS (391.4 *m/z* → 373.4 *m/z*)	1.0*
chol 6α-OH	52	APCI-MS/MS (385.4 *m/z* → 367.4 *m/z*)	d_6-chol 5β-OH (20 μM) APCI-MS/MS (391.4 *m/z* → 373.4 *m/z*)	3.1*
chol 6β-OH	53	APCI-MS/MS (385.4 *m/z* → 367.4 *m/z*)	d_6-chol 5β-OH (20 μM) APCI-MS/MS (391.4 *m/z* → 373.4 *m/z*)	1.8*
chol 7α-OH	61	APCI-MS/MS (385.4 *m/z* → 367.4 *m/z*)	d_6-chol 5β-OH (20 μM) APCI-MS/MS (391.4 *m/z* → 373.4 *m/z*)	0.80*
chol 7β-OH	58	APCI-MS/MS (385.4 *m/z* → 367.4 *m/z*)	d_6-chol 5β-OH (20 μM) APCI-MS/MS (391.4 *m/z* → 373.4 *m/z*)	1.2*
6-ketochol	32	UV (234 nm)	4-nitrophenol (100 μM) UV (234 nm)	2.8
7-ketochol	45	UV (234 nm)	4-nitrophenol (100 μM) UV (234 nm)	2.9

HPLC-APCI-MS/MS Chromatograms

Figure 3.9 shows the chromatogram for the authentic standards of chol 4β-OH, 5α-OH, 6α-OH, 6β-OH, 7α-OH, and 7β-OH. These six compounds were all standardized and quantified against 5α-hydroxycholesterol-17,20,21,21,21,22-d_6 (d_6-chol 5α-OH). While they were quantified in the 385.4 *m/z* → 367.4 *m/z* channel, note that there is a slight signal for each compound in the 403.4 *m/z* → 385.4 *m/z* channel, particularly for chol 4β-OH. This can also be seen in the chromatograms for chol autoxidations, but does not affect the quantification of any compound, *vide infra*.

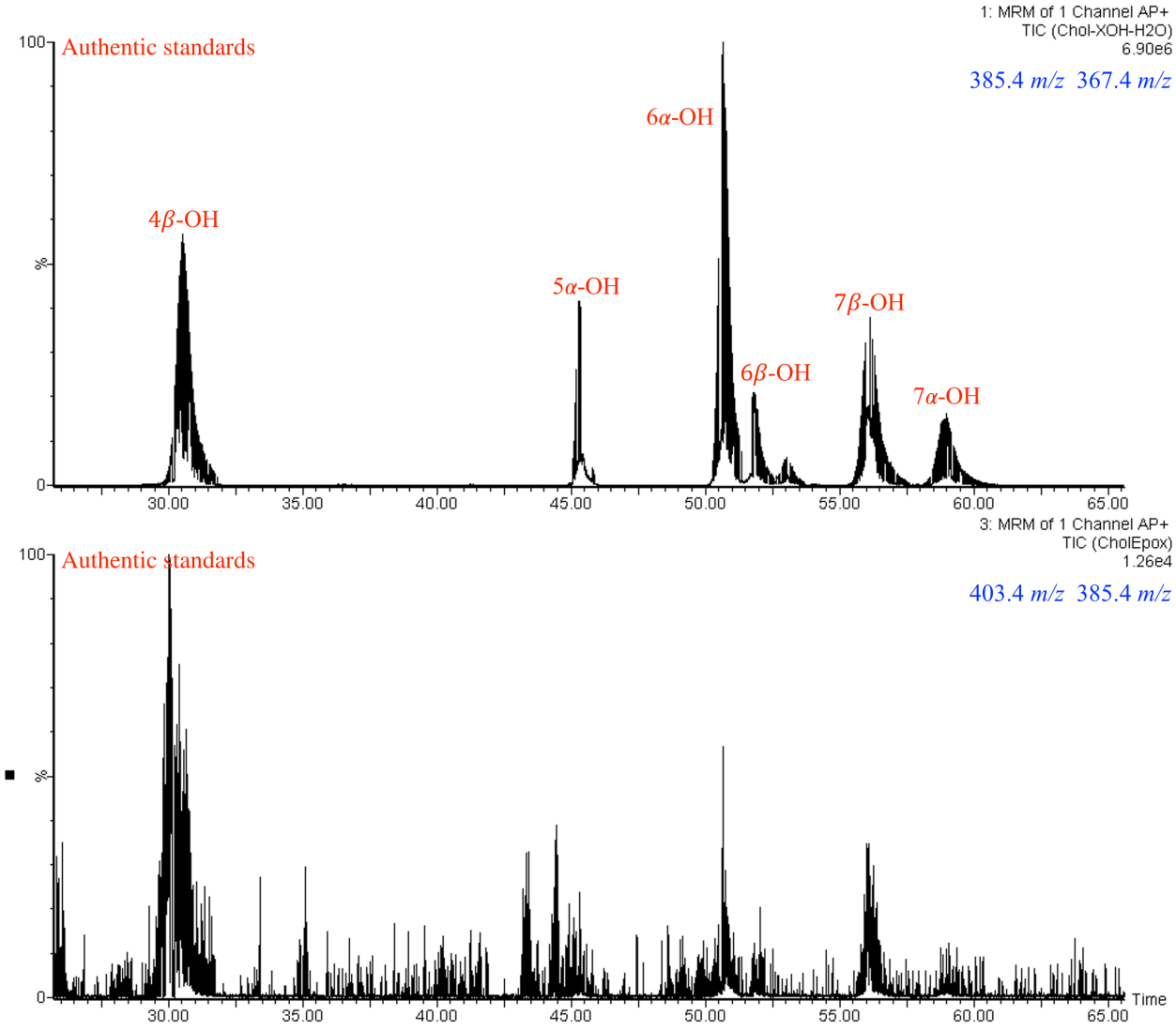

Figure 3.9. HPLC-APCI$^+$-MS/MS chromatograms for authentic standards of chol 4β-OH, 5α-OH, 6α-OH, 6β-OH, 7α-OH, and 7β-OH, for MS/MS transitions corresponding to 385.4 *m/z* → 367.4 *m/z* (top) and 403.4 *m/z* → 385.4 *m/z* (bottom). Data were obtained using the conditions outlined in the experimental section 3.6.

Figure 3.10 shows the chromatograms for authentic standards of chol α- and β-epoxide (mixture), as well as chol 4α-OH, and a co-injection of chol 4α-OH and 4β-OH. For each sample, two MS/MS transitions are shown 385.4 *m/z* → 367.4 *m/z* (top) and 403.4 *m/z* → 385.4 *m/z* (bottom). The chol epoxides have strong signals in each channel, *vide supra*. The chol 4-Ohs have a strong signal in the former channel and a weak one in the latter. The epoxides were quantified relative to authentic cholesterol-5,6-epoxide-17,20,21,21,21,22-d_6 (d_6-chol epoxides) – chol α-epoxide relative to d_6-chol α-epoxide and chol β-epoxide relative to d_6-chol β-epoxide. Chol 4α-OH was quantified relative to d_6-chol β-epoxide, though due to its co-elution with chol β-epoxide its quantification was slightly more complicated, as discussed below.

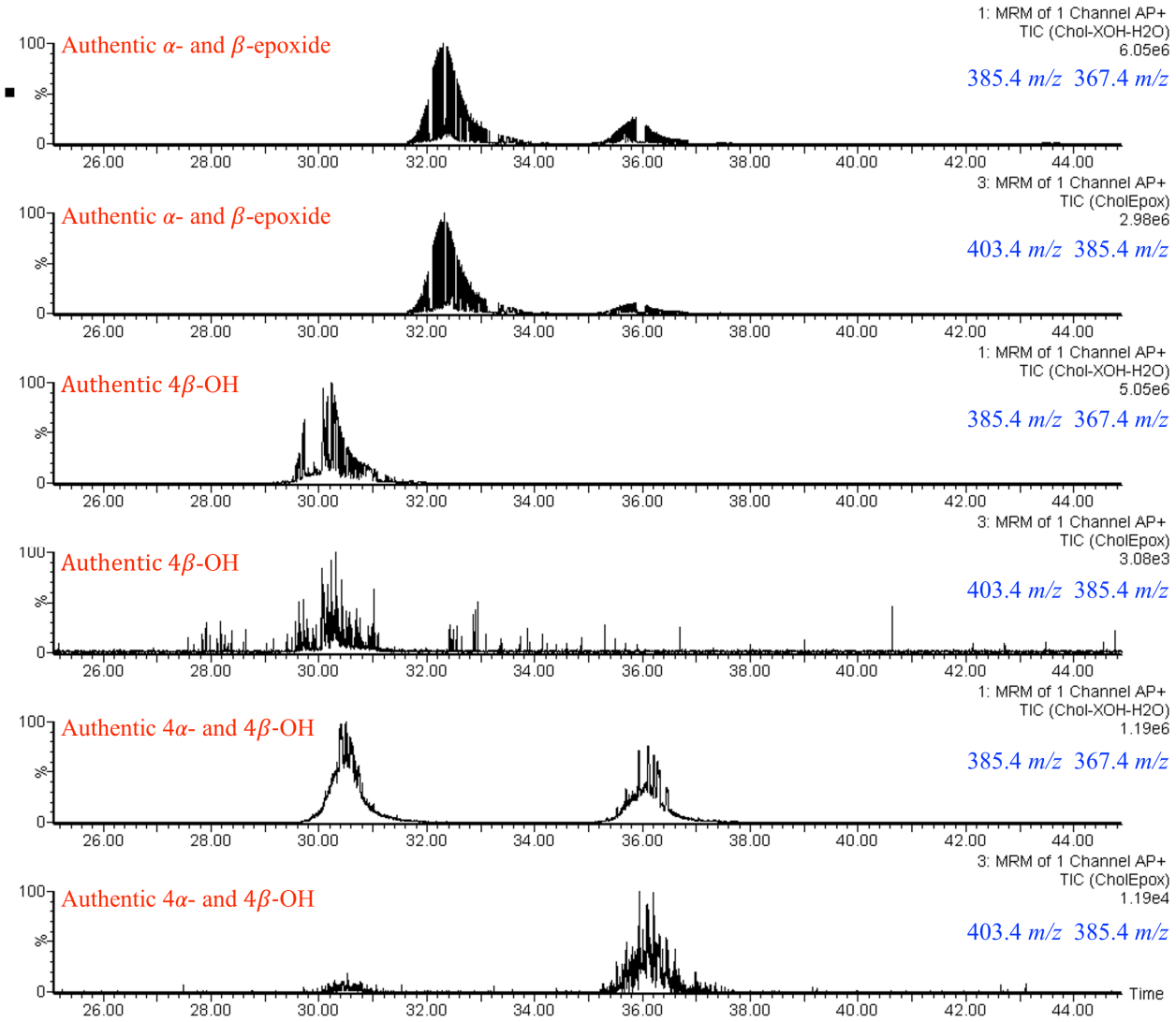

Figure 3.10. HPLC-APCI$^+$-MS/MS chromatograms for authentic standards chol α- and β-epoxide (mixture), as well as chol 4β-OH, and a co-injection of chol 4α-OH and 4β-OH. For each sample, two MS/MS transitions are shown 385.4 *m/z* → 367.4 *m/z* (top) and 403.4 *m/z* → 385.4 *m/z* (bottom). Data were obtained using the conditions outlined in the experimental section 3.6.

As discussed in section 3.3, UV detection was required for 6- and 7-ketochol. Figure 3.11 shows their authentic standards in the presence of 4-nitrophenol (UV internal standard), as well as the authentic standard for triphenylphosphine oxide, which was observed in the autoxidation samples since PPh_3 was added to reduce the chol hydroperoxides to their corresponding alcohols.

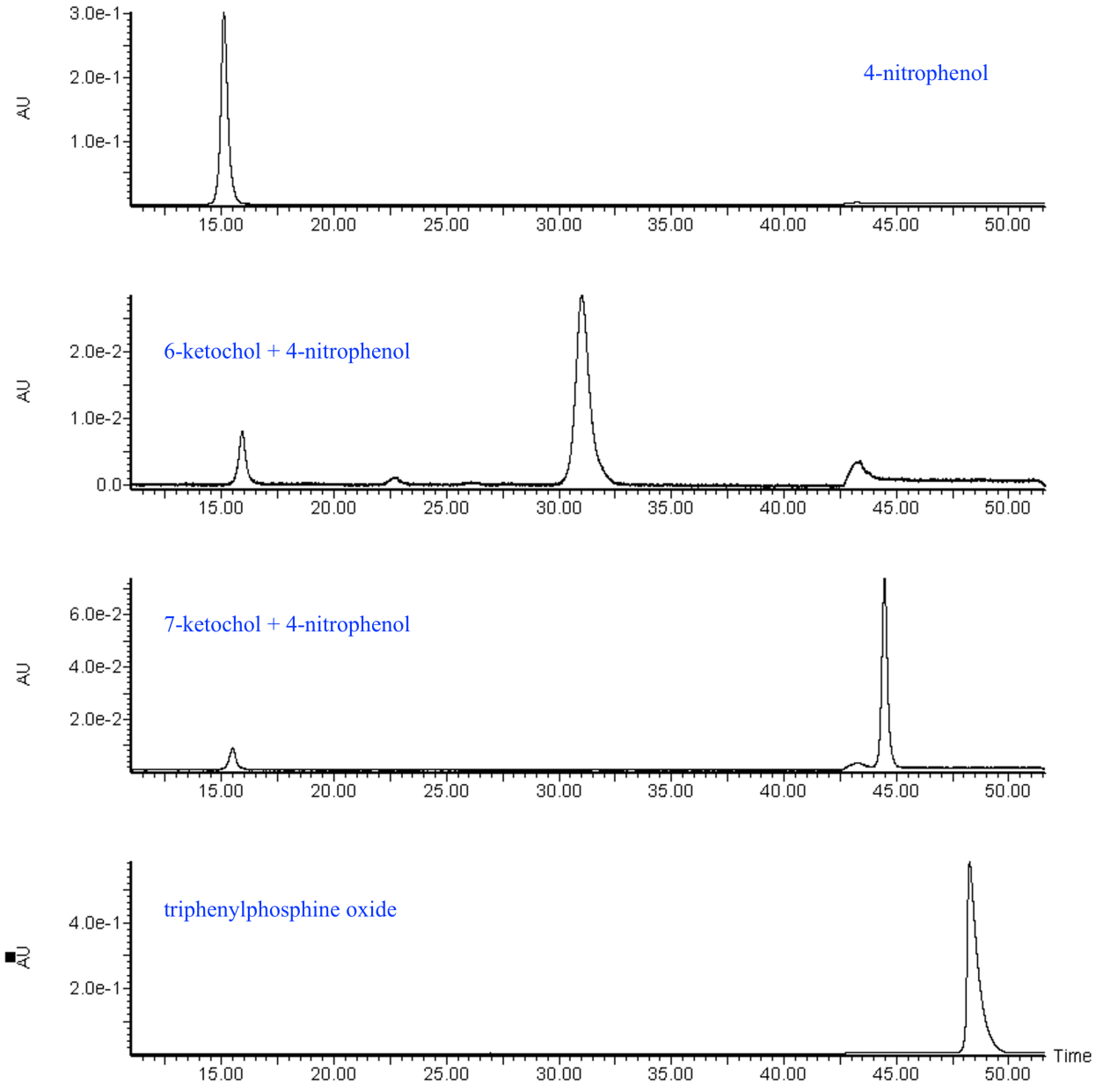

Figure 3.11. HPLC-UV chromatograms at 234 nm for the compounds indicated. Data were obtained using the conditions outlined in the experimental section 3.6.

Figure 3.12 shows an example of a chol autoxidation sample (without added H-atom donor), for which the four key MS/MS transitions are shown. First, 385.4 *m/z* → 367.4 *m/z* was used to quantify the hydroxychol compounds (chol 4α-OH, 4β-OH, 5α-OH, 6α-OH, 6β-OH, 7α-OH, and 7β-OH). Second, 403.4 *m/z* → 385.4 *m/z* was used to quantify the chol epoxides. Third, 391.4 *m/z* → 373.4 *m/z* shows the d_6-internal standards indicated. Fourth, 409.4 *m/z* → 391.4 *m/z* shows the d_6-epoxide internal standards.

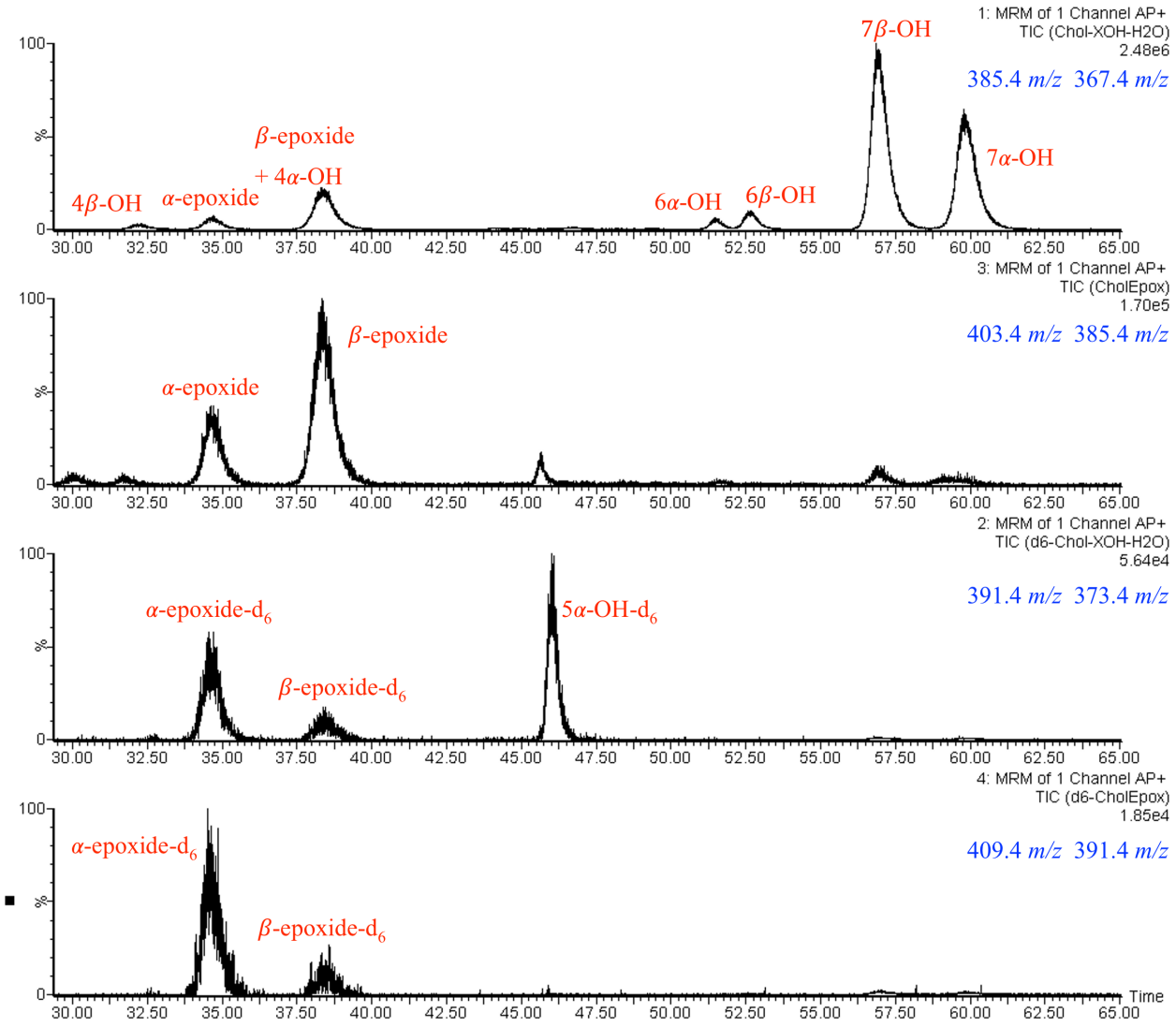

Figure 3.12. HPLC-APCI$^+$-MS/MS chromatograms for a single chol autoxidation sample (without added H-atom donor) showing the four key MS/MS transition channels, indicated in blue. Data were obtained using the conditions outlined in the experimental section 3.6.

Figure 3.13 shows the chromatograms for four different autoxidation samples, showing the same MS/MS transition 385.4 *m/z* → 367.4 *m/z*, which was used to quantify the hydroxychol compounds (chol 4α-OH, 4β-OH, 5α-OH, 6α-OH, 6β-OH, 7α-OH, and 7β-OH). First is a chol autoxidation without added H-atom donor, then analogous samples with added BDMP are shown below.

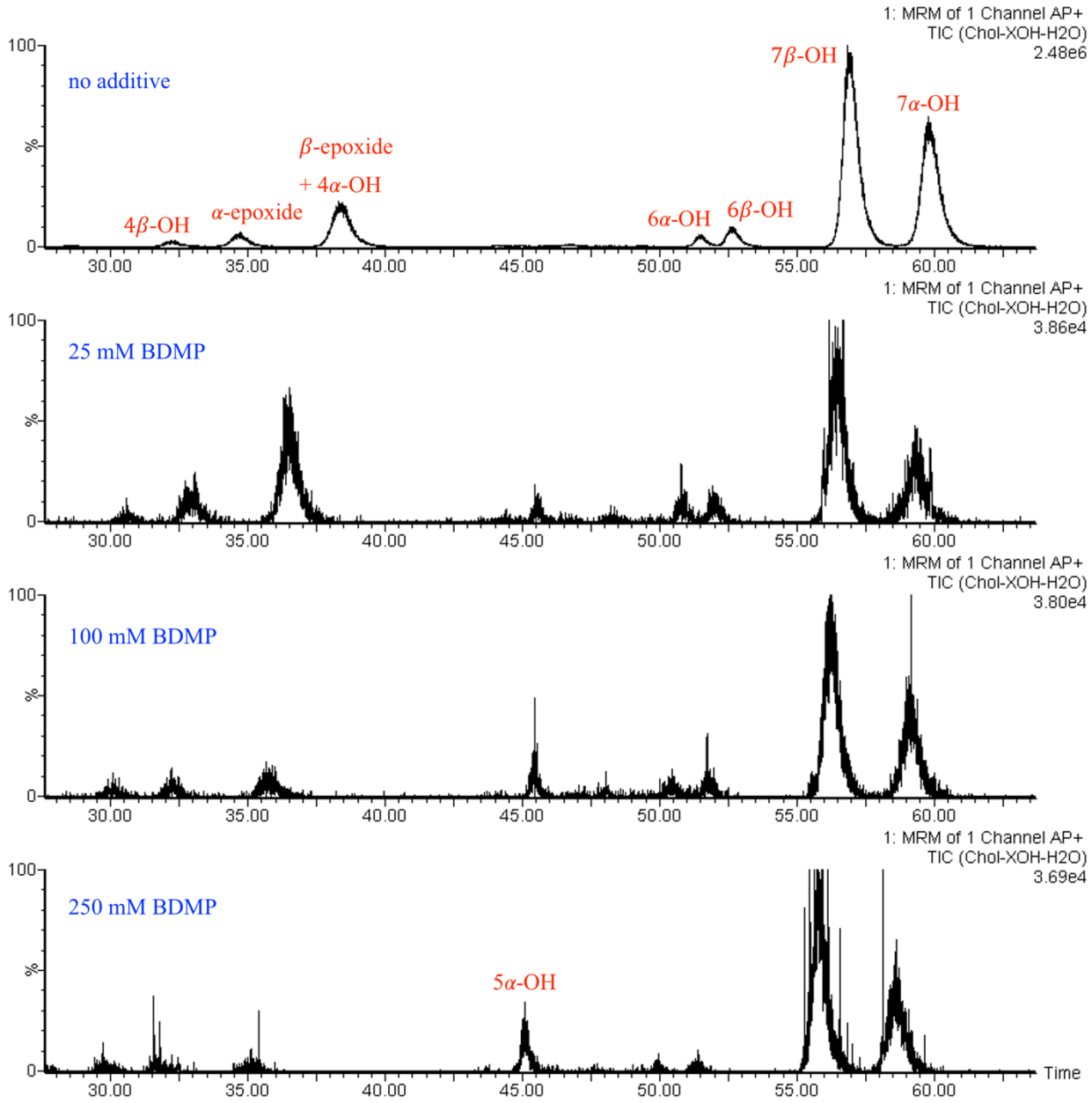

Figure 3.13. HPLC-APCI$^+$-MS/MS chromatograms for 385.4 *m/z* → 367.4 *m/z* of four different chol autoxidation samples – without added H-atom donor, or with varying amounts of added 4-(tert-butyl)-

2,6-dimethylphenol (BDMP, concentration indicated in blue). Data were obtained using the conditions outlined in the experimental section 3.6.

Figure 3.14 shows the same four autoxidation samples as in Figure 3.13 above, except the MS/MS channel 403.4 *m/z* → 385.4 *m/z* of the chol epoxides is shown.

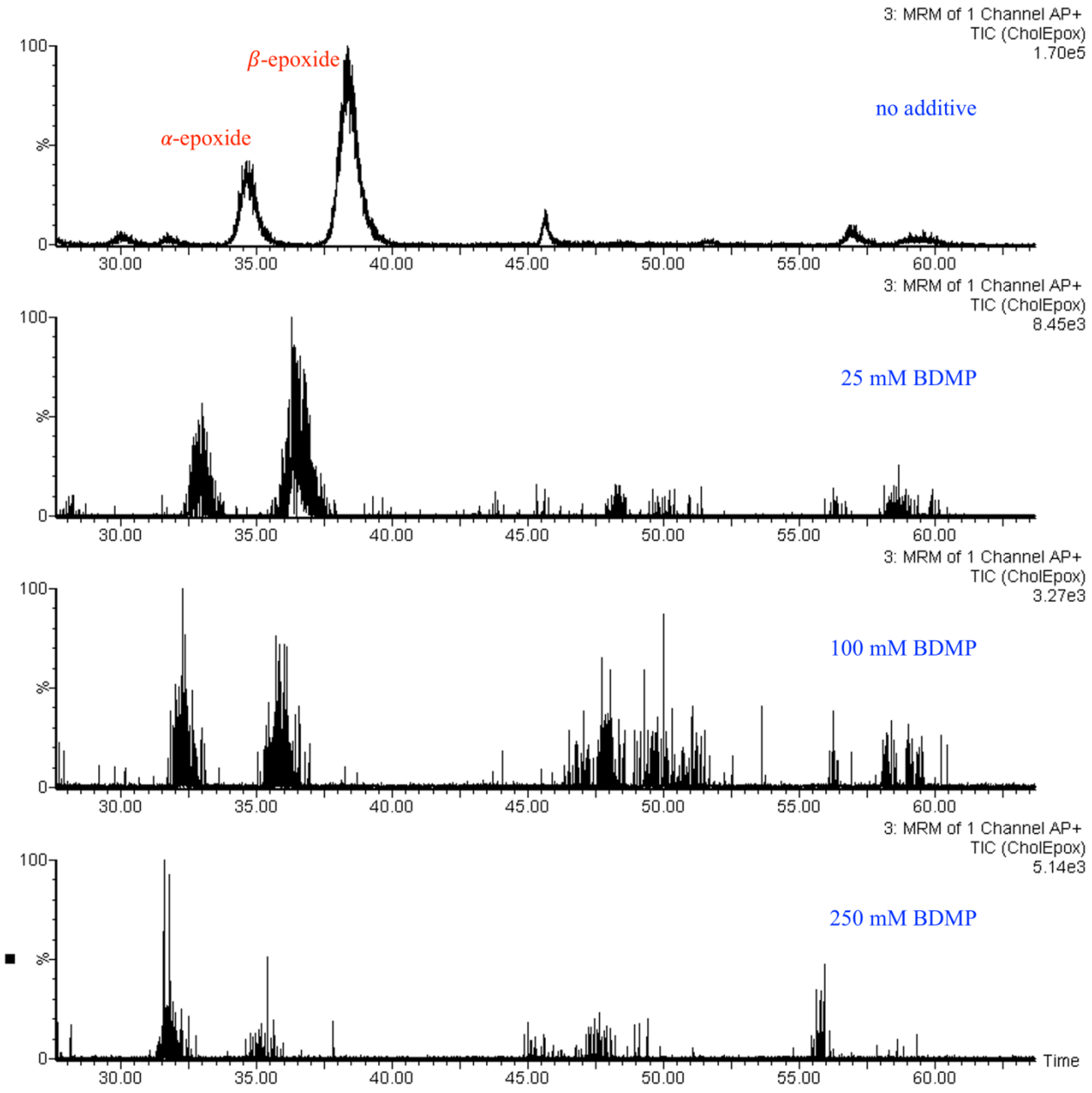

Figure 3.14. HPLC-APCI$^+$-MS/MS chromatograms for 403.4 *m/z* → 385.4 *m/z* of four different chol autoxidation samples – without added H-atom donor, or with varying amounts of added 4-(tert-butyl)-2,6-dimethylphenol (BDMP, concentration indicated in blue). Data were obtained using the conditions outlined in the experimental section 3.6.

Figure 3.15 shows the same four autoxidation samples as in Figures 3.13 and 3.14 above, except the UV absorbance at 234 nm is shown.

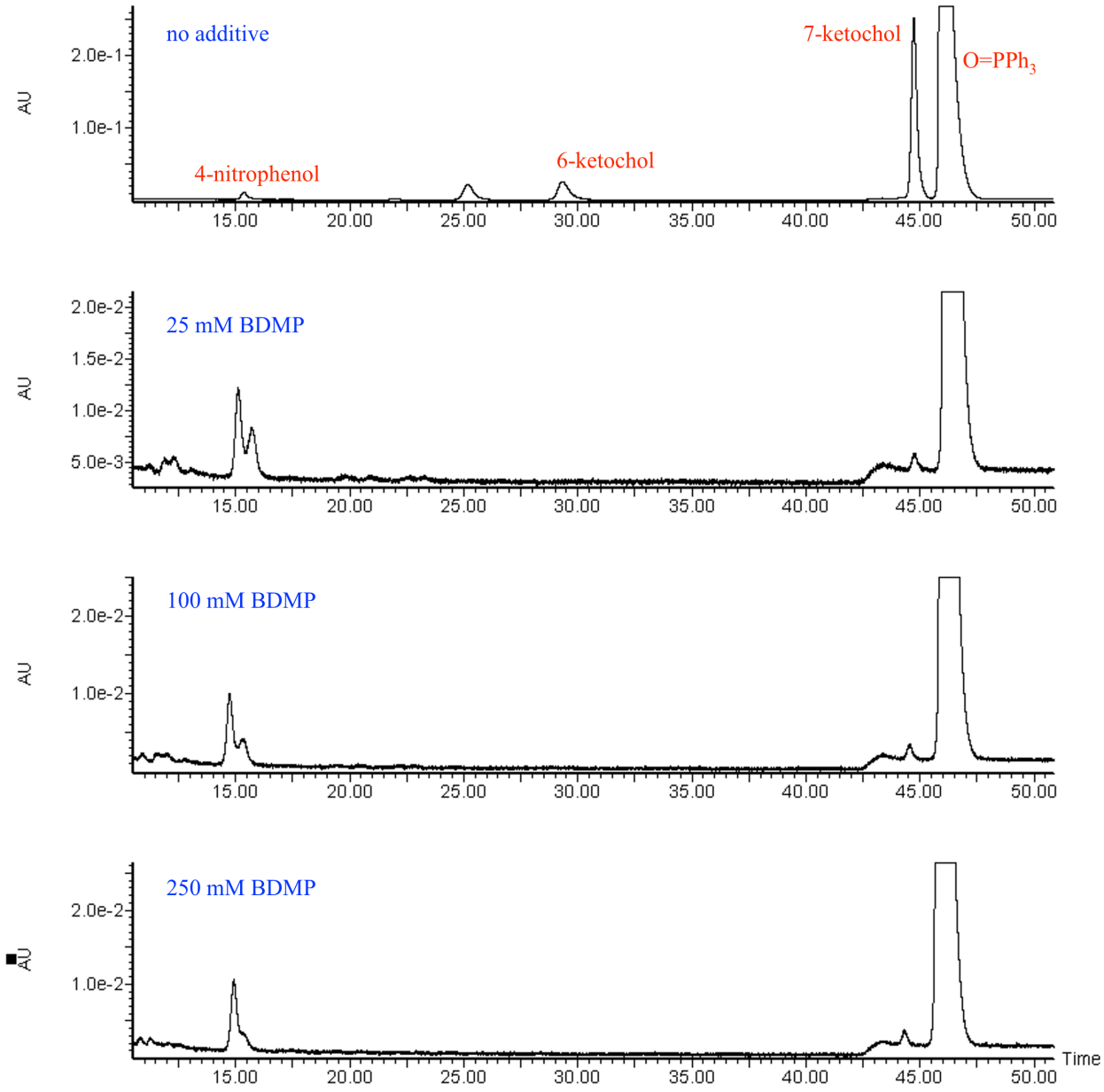

Figure 3.15. HPLC-UV chromatograms at 234 nm of four different chol autoxidation samples – without added H-atom donor, or with varying amounts of added 4-(tert-butyl)-2,6-dimethylphenol (BDMP, concentration indicated in blue). Data were obtained using the conditions outlined in the experimental section 3.6.

The top panel of Figure 3.15 shows an unidentified peak in the UV-spectrum of a chol autoxidation without added H-atom donor. Interestingly, its UV spectrum was similar to 6- and 7-ketochol, and it also had a similar mass spectrum (see the chromatogram of a mass scan in Figure 3.16, and the mass spectra of each peak in Figure 3.17), with a peak at 401.4 *m/z* which, for 6- and 7-ketochol was the $M+H^+$. We initially identified this peak as 4-ketochol; however, upon synthesizing an authentic standard, this was disproven *vide infra*. 3β,5α-dihydroxycholestan-6-one[2,3] can derive from the oxidation of chol triol; however, its retention time and UV trace were not consistent with the unidentified peak in Figure 3.16.

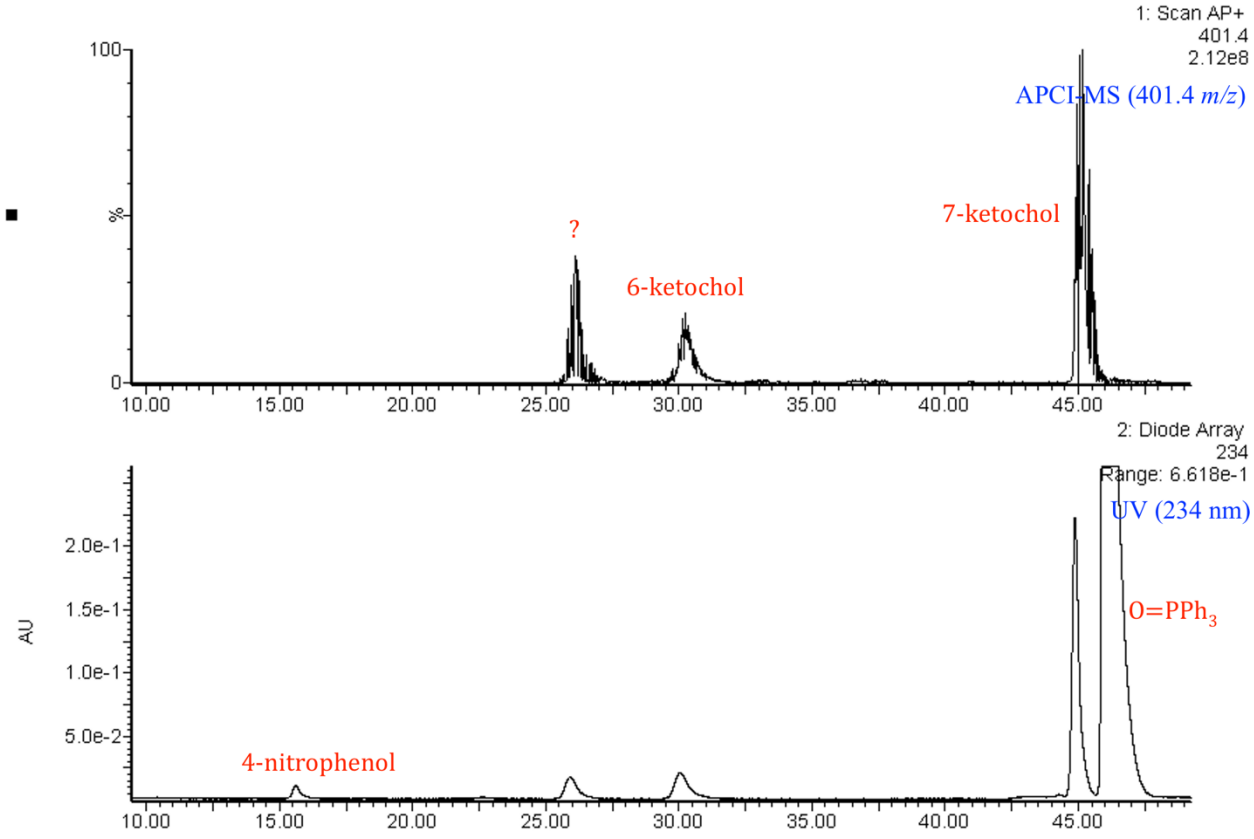

Figure 3.16. HPLC chromatograms of a chol autoxidation (without additive) with detection by $APCI^+$-MS at 401.4 *m/z* (top), UV at 234 nm (bottom). Data were obtained using the conditions outlined in the experimental section 3.6, except a MS scan was performed rather than MS/MS.

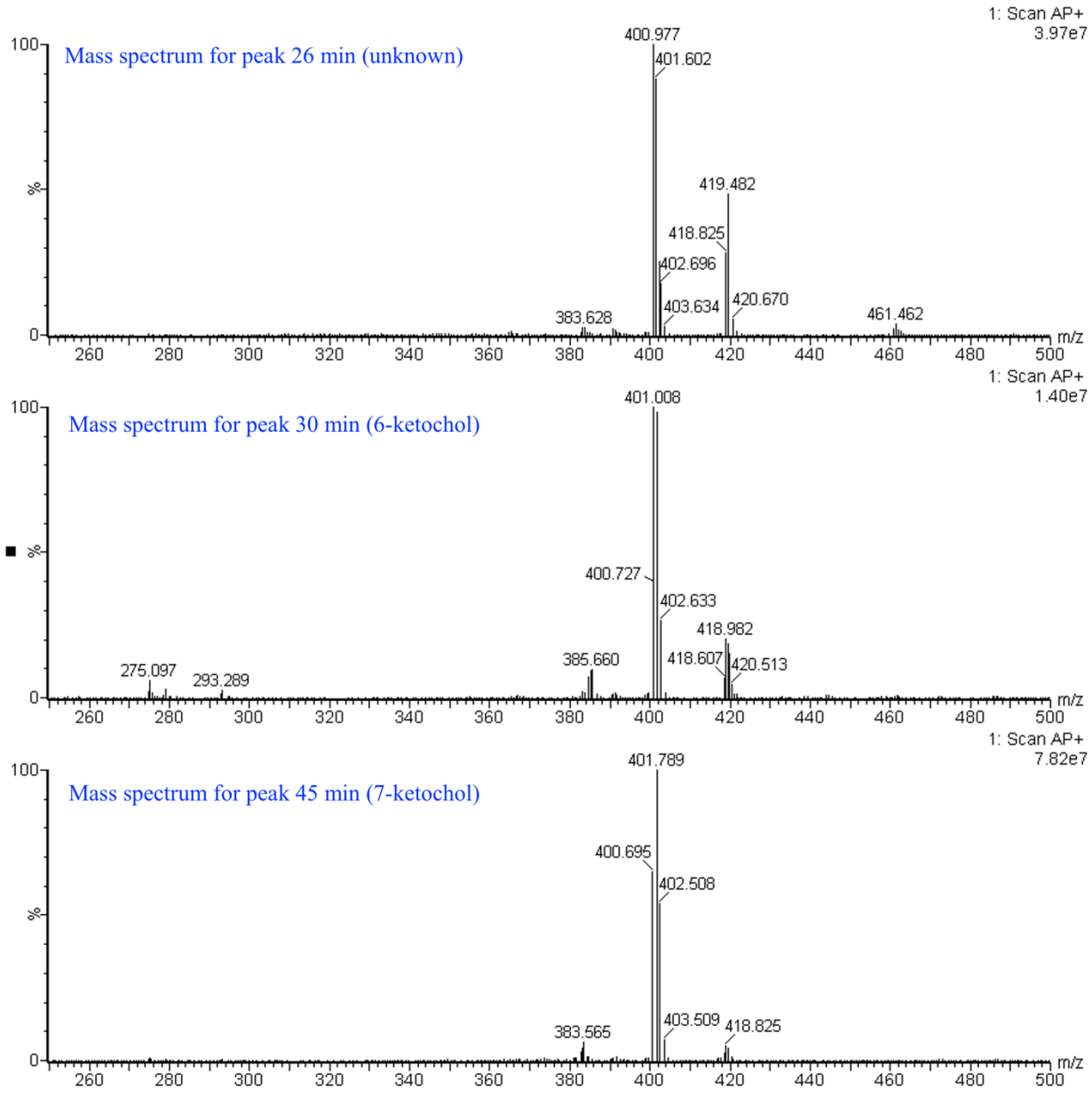

Figure 3.17. Mass spectra corresponding to each of the three peaks in the mass scan chromatogram in Figure 3.16.

Quantification of compounds in Table 3.2: The compounds were quantified as follows:

$$[X] = \frac{Int_x \times [S]}{Int_S \times R_x}$$

where X is the unknown, S is the internal standard, Int is the integration of the peak, and R is the response factor.

The quantification of chol 4α-OH was complicated by its co-elution with chol β-epoxide. Since the β-epoxide could be quantified using its unique MS/MS transition (403.4 *m/z* → 385.4 *m/z*), the shared peak of MS/MS (385.4 *m/z* → 367.4 *m/z*) was integrated and the amount of 4α-OH was quantified as above, except the portion of the peak's integration due to 4α-OH was determined as follows:

$$Int_{4\alpha\mathrm{OH}} = Int_{total} - \frac{[\beta\ \mathrm{epox}] \times \mathrm{Int}_S}{[\mathrm{S}]}$$

The response factors for the compounds in Table 3.2 are the slopes of the standard curves below (or those in ref 1). The apparent concentration (y-axis) is the integrated area of the standard compound divided by the integrated area of its internal standard multiplied by the concentration of the internal standard.

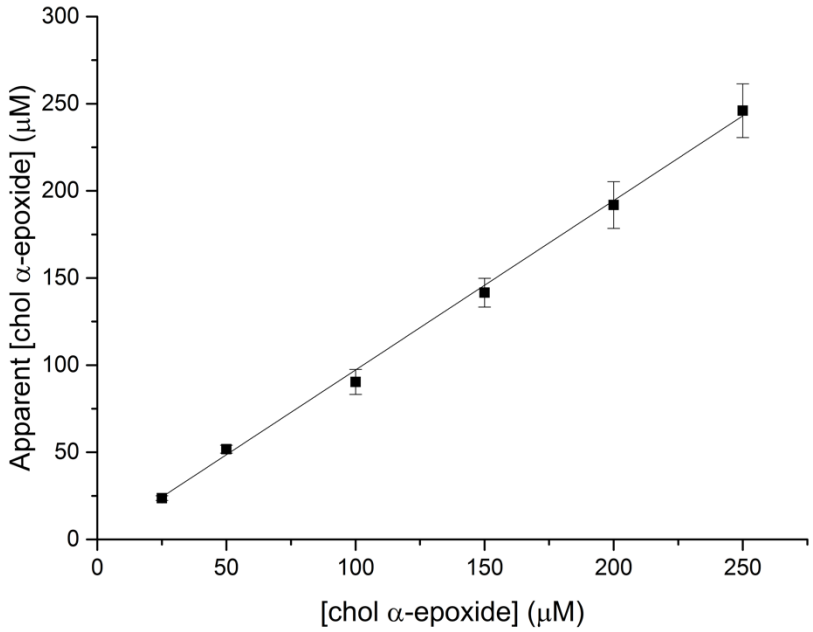

Figure 3.18. Standard curve of cholesterol-5α,6α-epoxide (chol α-epoxide) relative to cholesterol-5α,6α-epoxide-17,20,21,21,21,22-d_6 (d_6-chol α-epoxide) (y=0.9653x; R^2=0.9993).

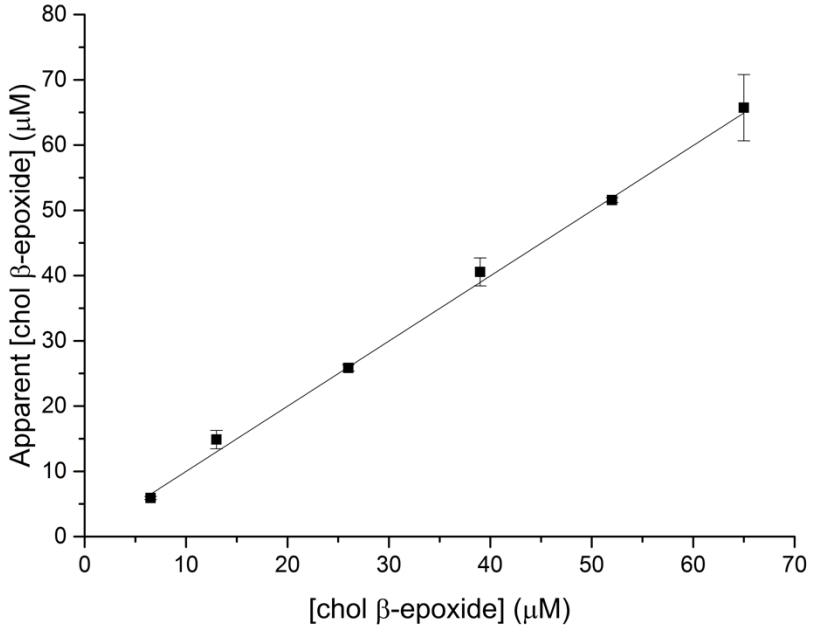

Figure 3.19. Standard curve of cholesterol-5β,6β-epoxide (chol β-epoxide) relative to cholesterol-5β,6β-epoxide-17,20,21,21,21,22-d_6 (d_6-chol β-epoxide) (y=1.011x; R^2=0.9994).

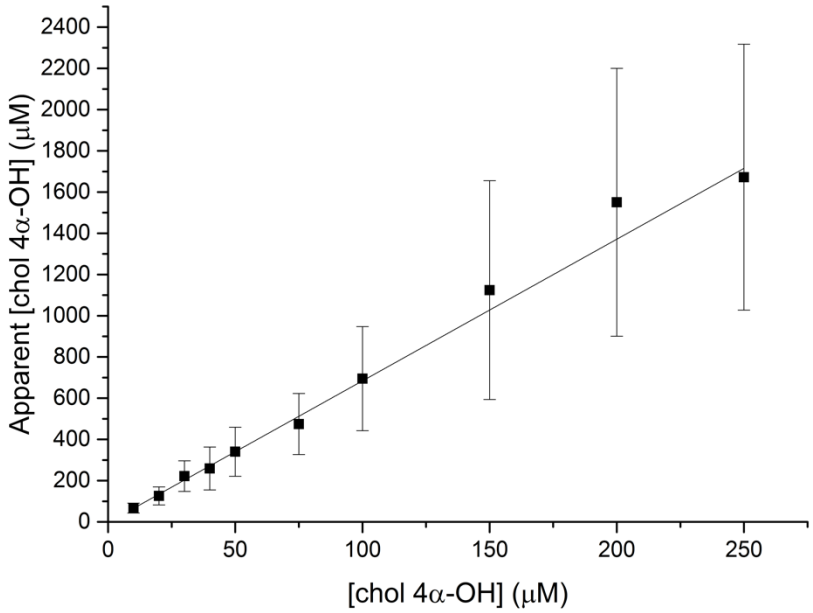

Figure 3.20. Standard curve of 4α-hydroxycholesterol (chol 4α-OH) relative to cholesterol-5β,6β-epoxide-17,20,21,21,21,22-d_6 (d_6-chol β-epoxide) (y=7.1109x; R^2=0.9952).

To test if the co-elution of chol β-epoxide and chol 4α-OH affected the response factor of either compound, or if the slight residual signal of chol 4α-OH in the 403.4 *m/*z -> 385.4 *m/*z channel affected the quantification of chol β-epoxide, standard curves of chol β-epoxide were done in the presence of increasing amounts of chol 4α-OH. Indeed, while the standard curves were all linear, at higher amounts of chol 4α-OH there was a slight suppression of chol β-epoxide ionization. The autoxidation mixtures studied herein were dilute enough in chol 4α-OH (<100 μM) that this would not be an issue.

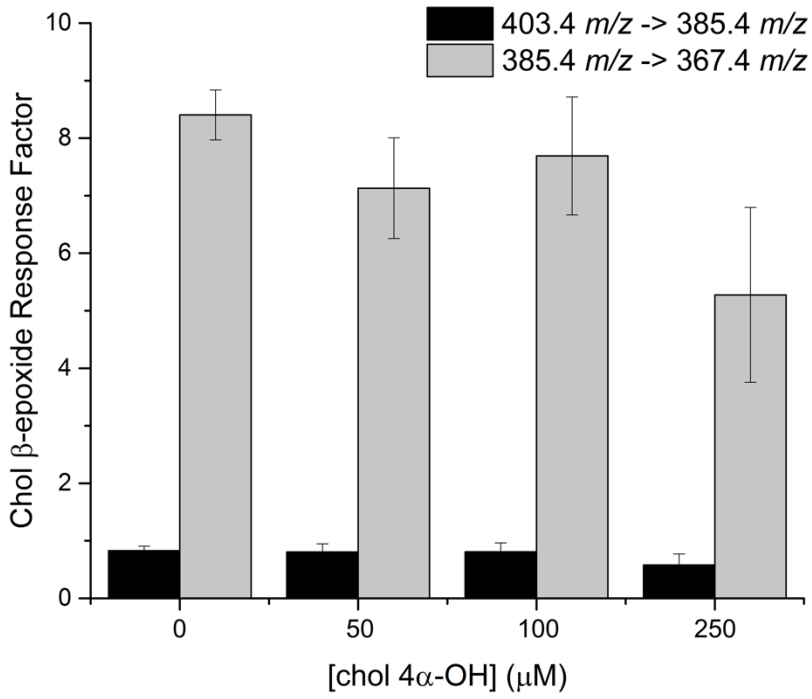

Figure 3.21. Standard curves of cholesterol-5β,6β-epoxide (chol β-epoxide) relative to cholesterol-5β,6β-epoxide-17,20,21,21,21,22-d_6 (d_6-chol β-epoxide) were used to determine its response factor (slope of each standard curve) in the presence of increasing amounts of 4α-hydroxycholesterol (chol 4α-OH).

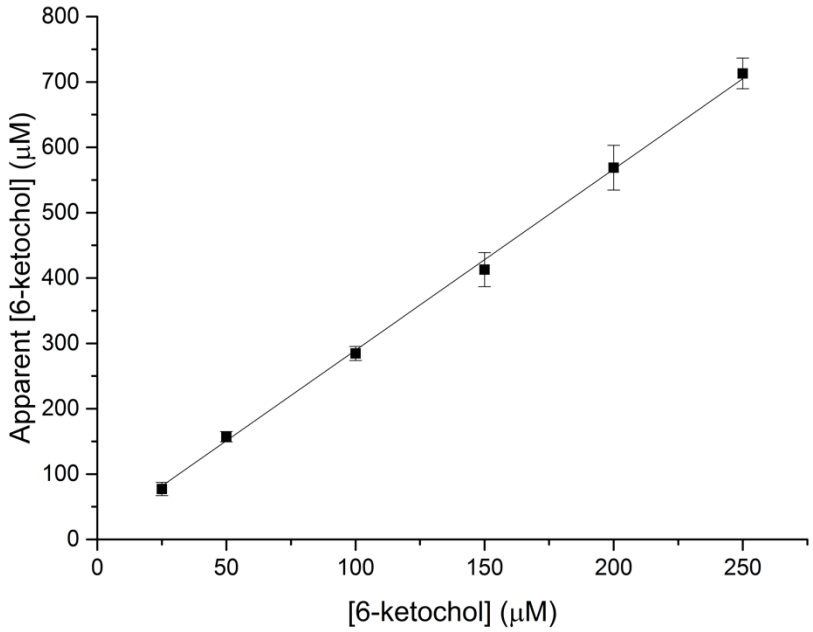

Figure 3.22. Standard curve of 6-ketocholesterol (6-ketochol) relative to 4-nitrophenol (y=2.8392x; R^2=0.9996).

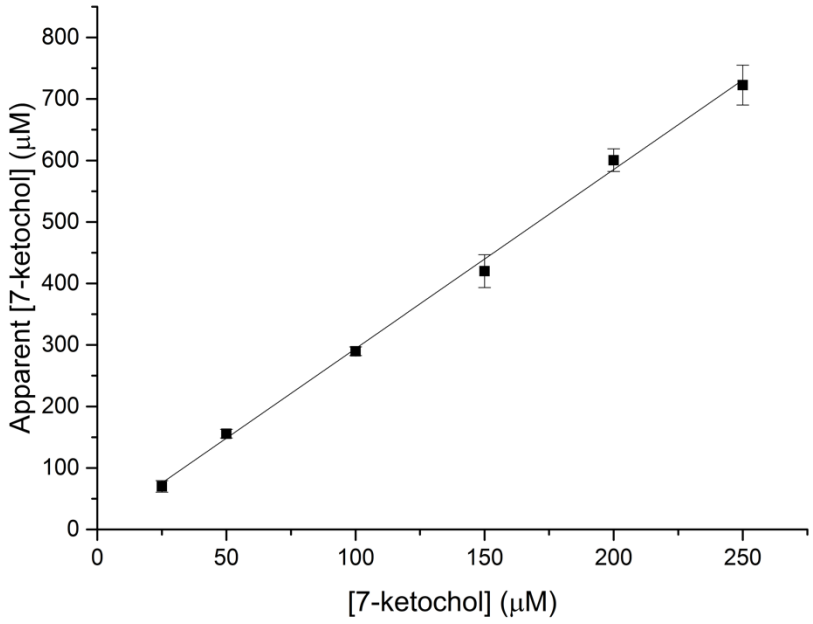

Figure 3.23. Standard curve of 7-ketocholesterol (7-ketochol) relative to 4-nitrophenol (y=2.9124x; R^2=0.9994).

3.9.2 Analysis of 4-Ketochol and Chol Triol

4-ketochol: 4-ketochol was prepared as an inseparable mixture with 4-hydroxycholest-4-ene-3-one (*cf.* NMRs in Figures 3.64-3.68). Both compounds were surprisingly non-polar, presumably due to the hydrogen bonding between the 3- and 4-positions. Like 6- and 7-ketochol, 4-ketochol did not have a measurable MS/MS transition, as the $M+H^+$ ion did not fragment further. 6- and 7-ketochol were therefore quantified by their UV absorption at 234 nm (which could be done simultaneous to MS/MS detection), and while 4-ketochol did have absorbance in the same region, in chol autoxidations it co-eluted with the solvent front containing other absorbing species (*e.g.* PhCl, BHT, PPh_3). Therefore, several chol autoxidation mixtures were re-analyzed by HPLC-APCI-MS to scan for the 4-keto $M+H^+$ ion, however, none was observed in any case (*cf.* Figures 3.24-3.26).

Figure 3.24 shows the mass scans of chol autoxidations with added BDMP. There are the three peaks discussed above (*cf.* Figure 3.16), and additional peaks near the solvent front. However, Figure 3.25 shows a zoom in this region, and compared to the authentic standard of 4-ketochol the larger peaks in the chol autoxidations elute earlier (*ca.* 3 min and 2 min, respectively). Furthermore, Figure 3.26 shows that if authentic 4-ketochol is doped with BHT, PPh_3, and PhCl (all of which are present in the autoxidation mixtures, and are likely to elute early), there is a peak at 2 min and at 3 min, where the 4-ketochol is identified as the latter based on its 401.4 *m/z* ion. Therefore, if any 4-ketochol were present in the chol autoxidations (Figure 3.25), it is likely so minor it is buried in the noise around 3 min.

Coincidentally, when select autoxidation mixtures were re-analyzed by the $APCI^+$-MS scan protocol to detect 4-ketochol (*cf.* Figure 3.24), it was observed that the detection of 6-ketochol was stronger by MS than with UV (detection limit *ca*. 10 μM). We could therefore estimate [6-ketochol] in the higher [BDMP] autoxidations based on relative intensity compared to 7-ketochol. Compared to the amount of chol 6-OH in the analogous samples, the ratio of 6-OH to 6-keto was *ca*. 1:1 regardless of [BDMP].

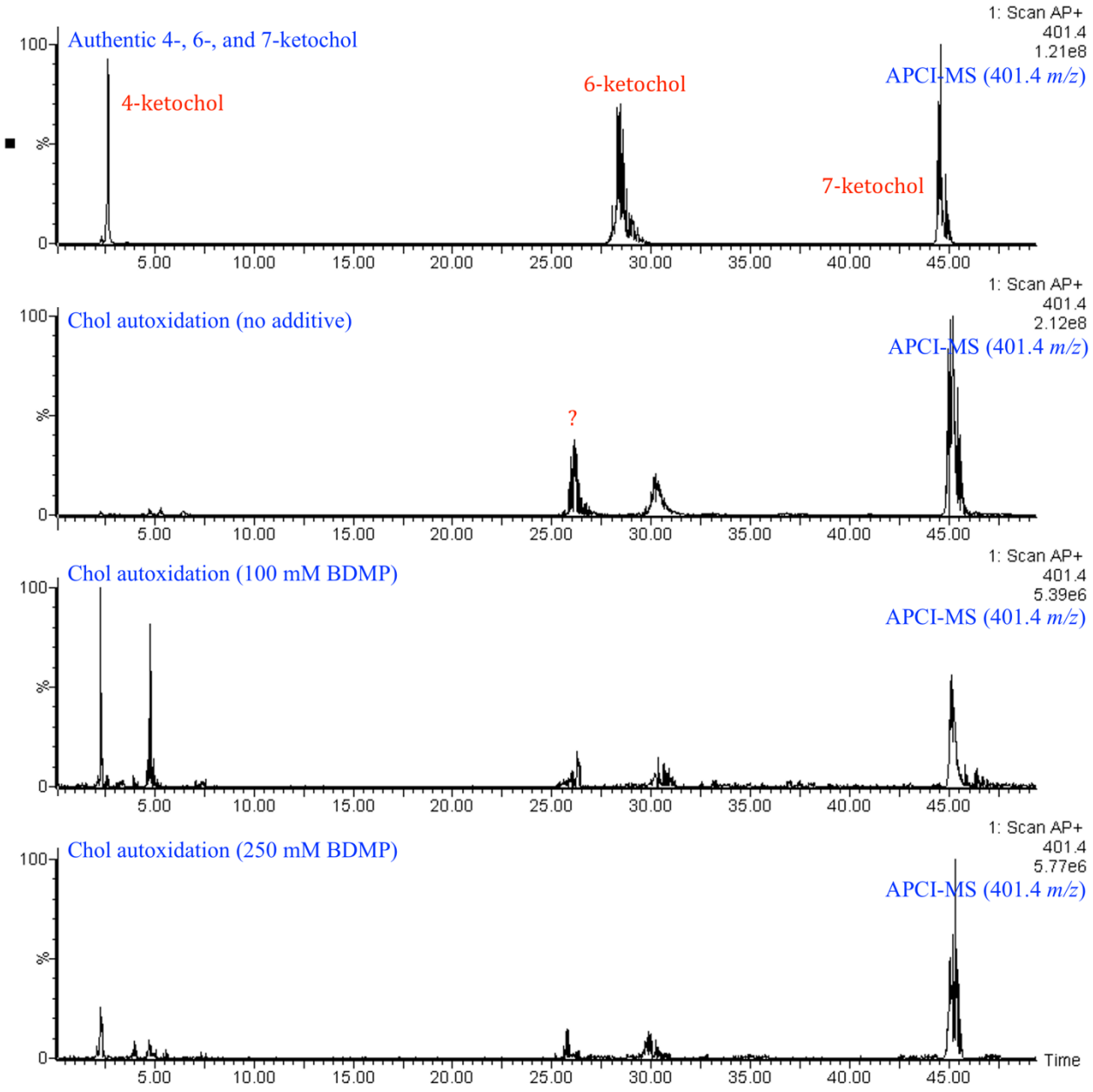

Figure 3.24. HPLC-APCI$^+$-MS chromatograms at 401.4 *m/z* of authentic 4-, 6-, and 7-ketochol, as well as three different chol autoxidation samples – without added H-atom donor, or with varying amounts of added 4-(tert-butyl)-2,6-dimethylphenol (BDMP, concentration indicated in blue). Data were obtained using the conditions outlined in the experimental section 3.6, except that a MS scan was performed rather than MS/MS.

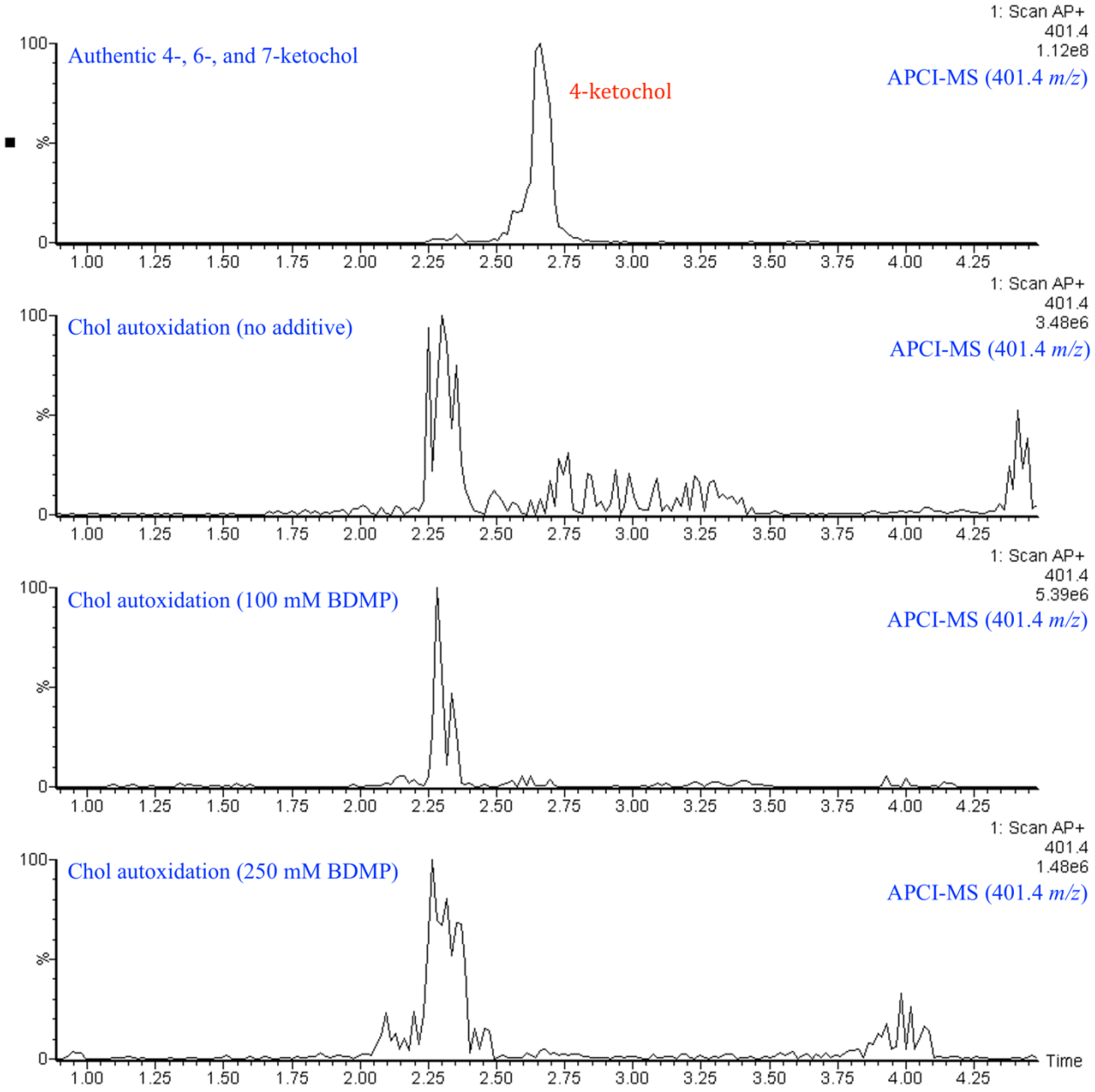

Figure 3.25. The same four chromatograms as in Figure S18, but only the first 1-4 minutes.

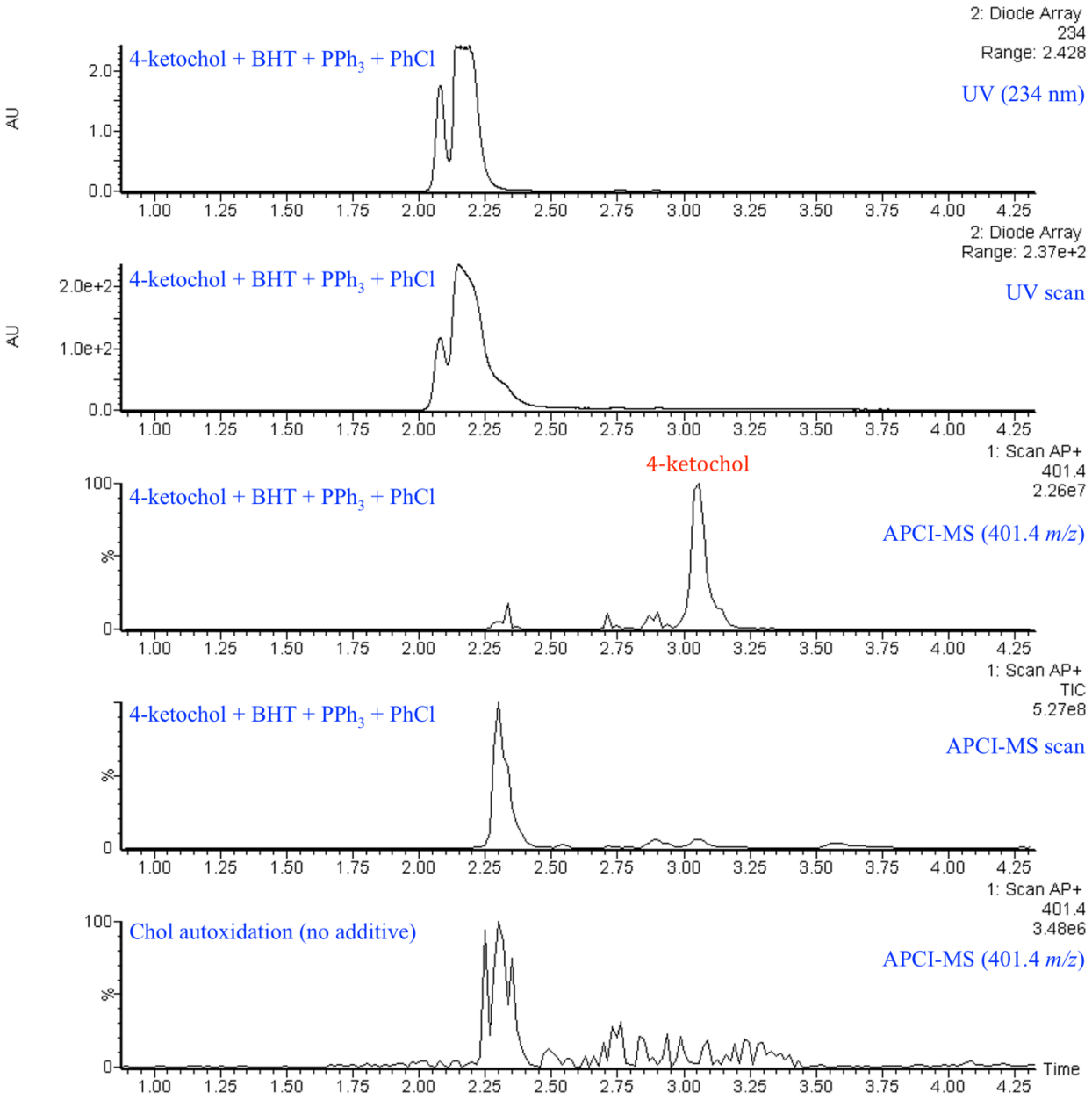

Figure 3.26. HPLC-APCI$^+$-MS or UV chromatograms (either scans or the wavelength/mass indicated) of a chol autoxidation sample without added H-atom donor (bottom) or authentic 4-ketochol doped with BHT, PPh_3, and PhCl. Data were obtained using the conditions outlined in the experimental section, except that MS scans was performed rather than MS/MS.

Chol triol: Cholestane-3β,5α,6β-triol (chol triol) was significantly more polar than the other compounds studied herein, and therefore required modified LC conditions. Rather than the gradient mobile phase (see experimental section 3.6 for details), 9:1 hexanes:iPrOH at 1 mL/min was used. The $APCI^+$-MS/MS protocol used was identical, and chol triol was analyzed by 385.4 *m/z* -> 367.4 *m/z* and compared to authentic cholestane-3β,5α,6β-triol-17,20,21,21,21,22-d_6 (d_6-chol triol) at 391.4 *m/z* -> 373.4 *m/z*. Several chol autoxidation mixtures were re-analyzed by HPLC-APCI-MS/MS with this mobile phase, but trace or no triol was detected (*cf.* Figure 3.27).

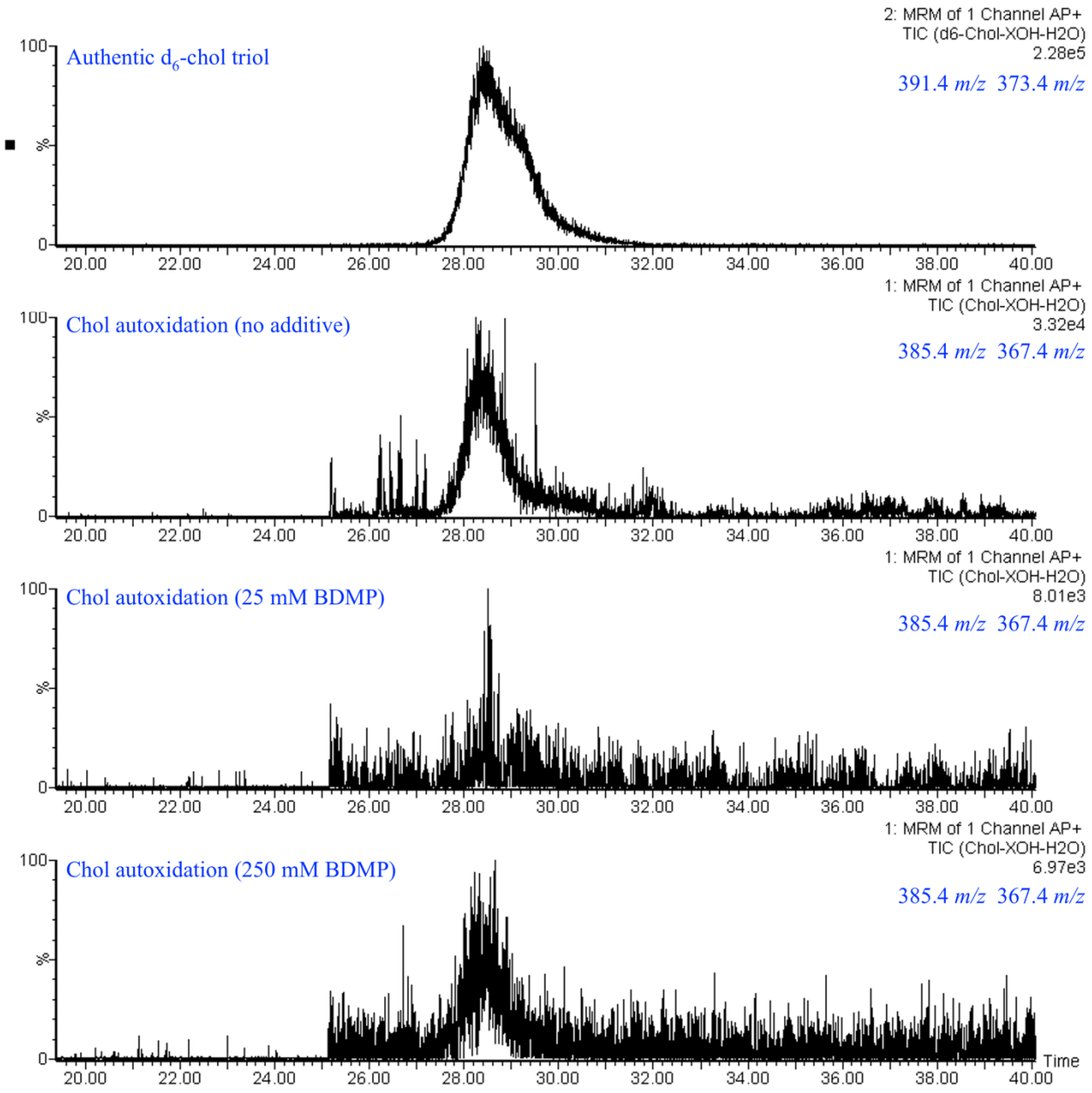

Figure 3.27. HPLC-APCI$^+$-MS/MS chromatograms for four different chol autoxidation samples – without added H-atom donor, or with varying amounts of added 4-(tert-butyl)-2,6-dimethylphenol (BDMP, concentration indicated in blue). Data were obtained using the conditions outlined in the experimental section, except the mobile phase was 9:1 hexanes:iPrOH at 1 mL/min**.**

3.9.3 Additional Data for Cholesterol Autoxidations

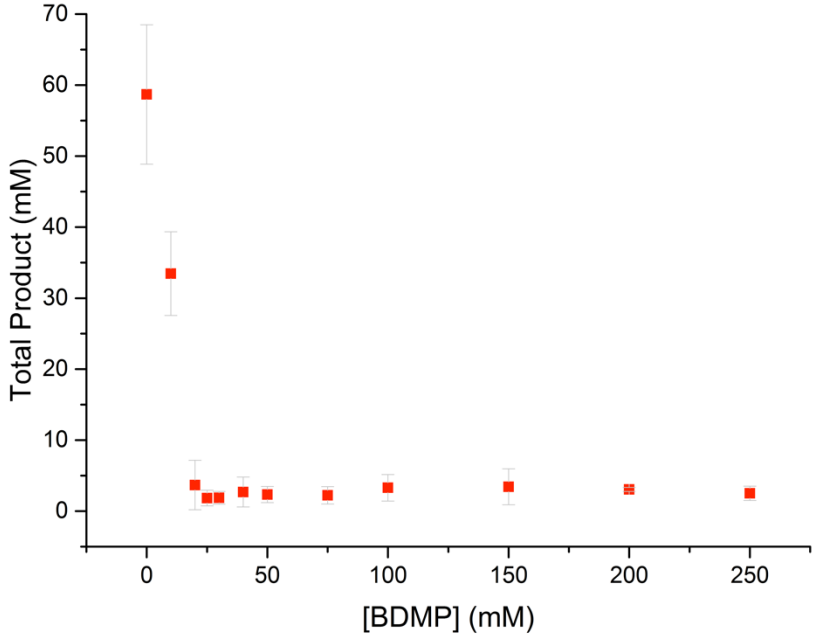

Figure 3.28. For cholesterol autoxidations, the total amount of autoxidation products detected with added [BDMP], based on the initial 100 μL volume which contained 500 mM cholesterol.

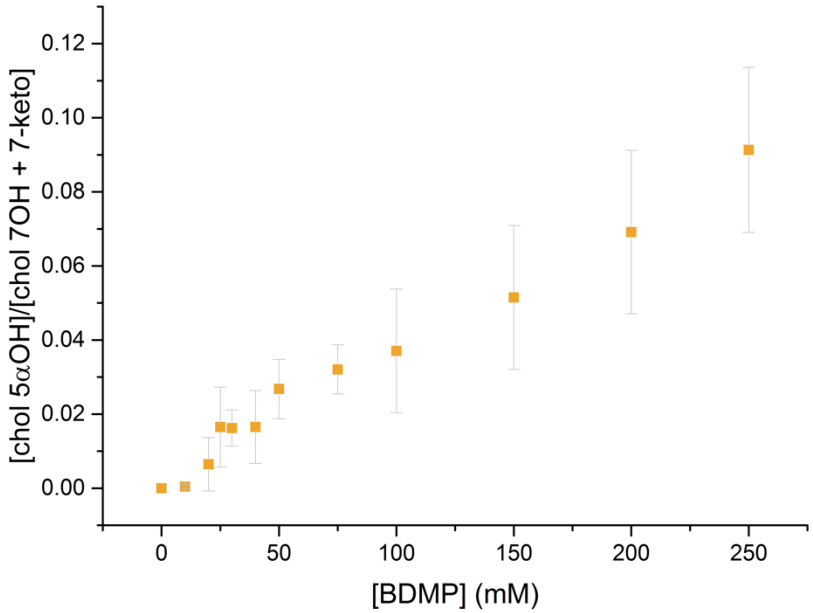

Figure 3.29. Dependence of [chol 5α-OH]/[chol 7-OH + 7-keto] on BDMP concentration in chol autoxidations, where the slope, m = 0.345 M^{-1}. k_β was determined as described previously[1] using k_H of BDMP = (1.3±0.1)×10^5 M^{-1} s^{-1} and $k_\beta = k_H/m$.

PMC-loaded autoxidations: autoxidations were also carried out in the presence of 2,2,5,7,8-pentamethyl-6-chromanol (PMC), which is a more potent H-atom donor than BDMP. Figures 3.30-3.36 show the analogous data for these autoxidations. The lesser amount of autoxidation products as compared to a similar amount of BDMP, coupled with the narrower concentration range wherein the complex interplay between pathways occurs, resulted in larger error in the correlation plots.

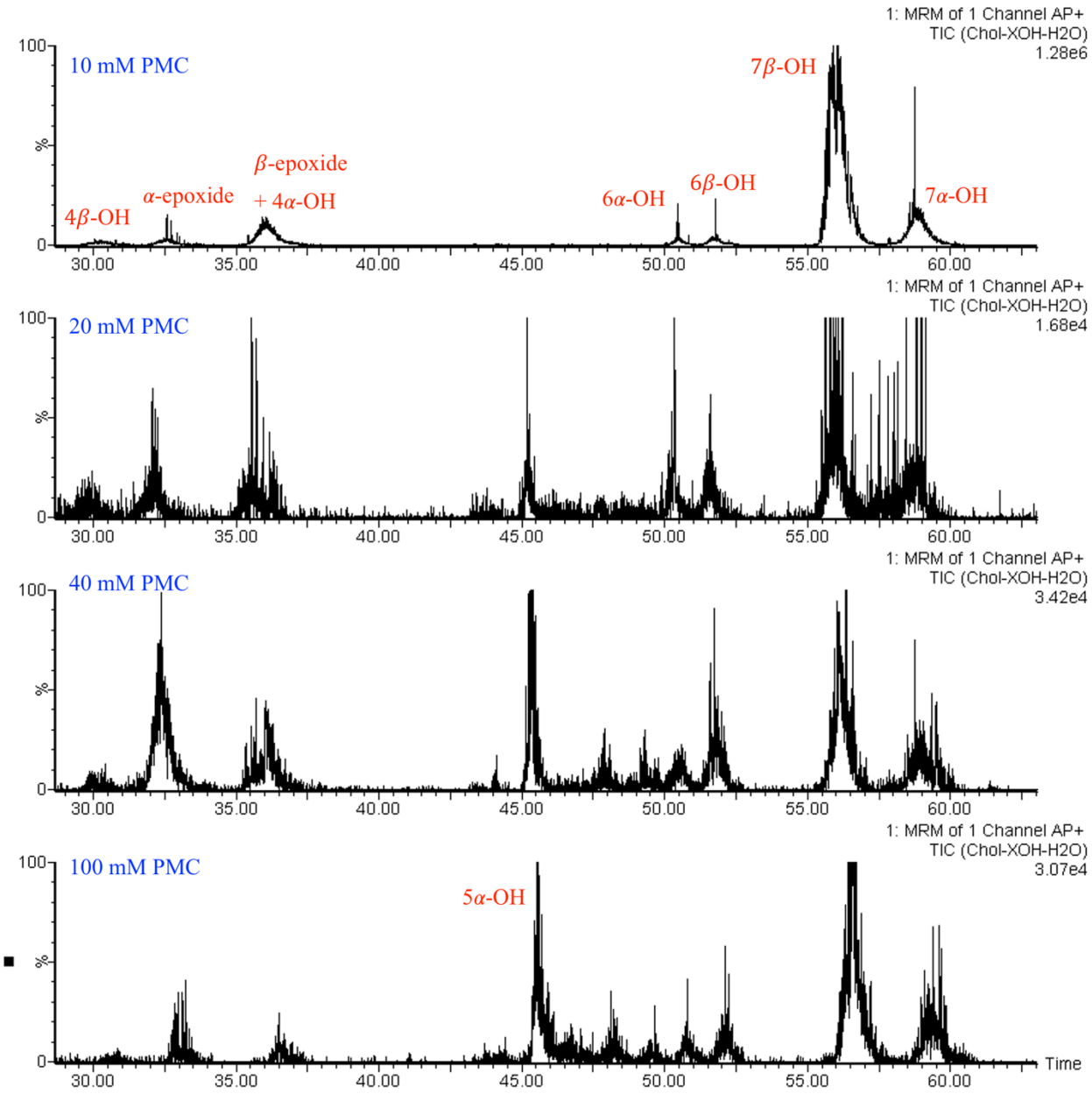

Figure 3.30. HPLC-APCI$^+$-MS/MS chromatograms for 385.4 *m/z* → 367.4 *m/z* of four different chol autoxidation samples – without added H-atom donor, or with varying amounts of added 2,2,5,7,8-pentamethyl-6-chromanol (PMC, concentration indicated in blue). Data were obtained using the conditions outlined in the experimental section 3.6.

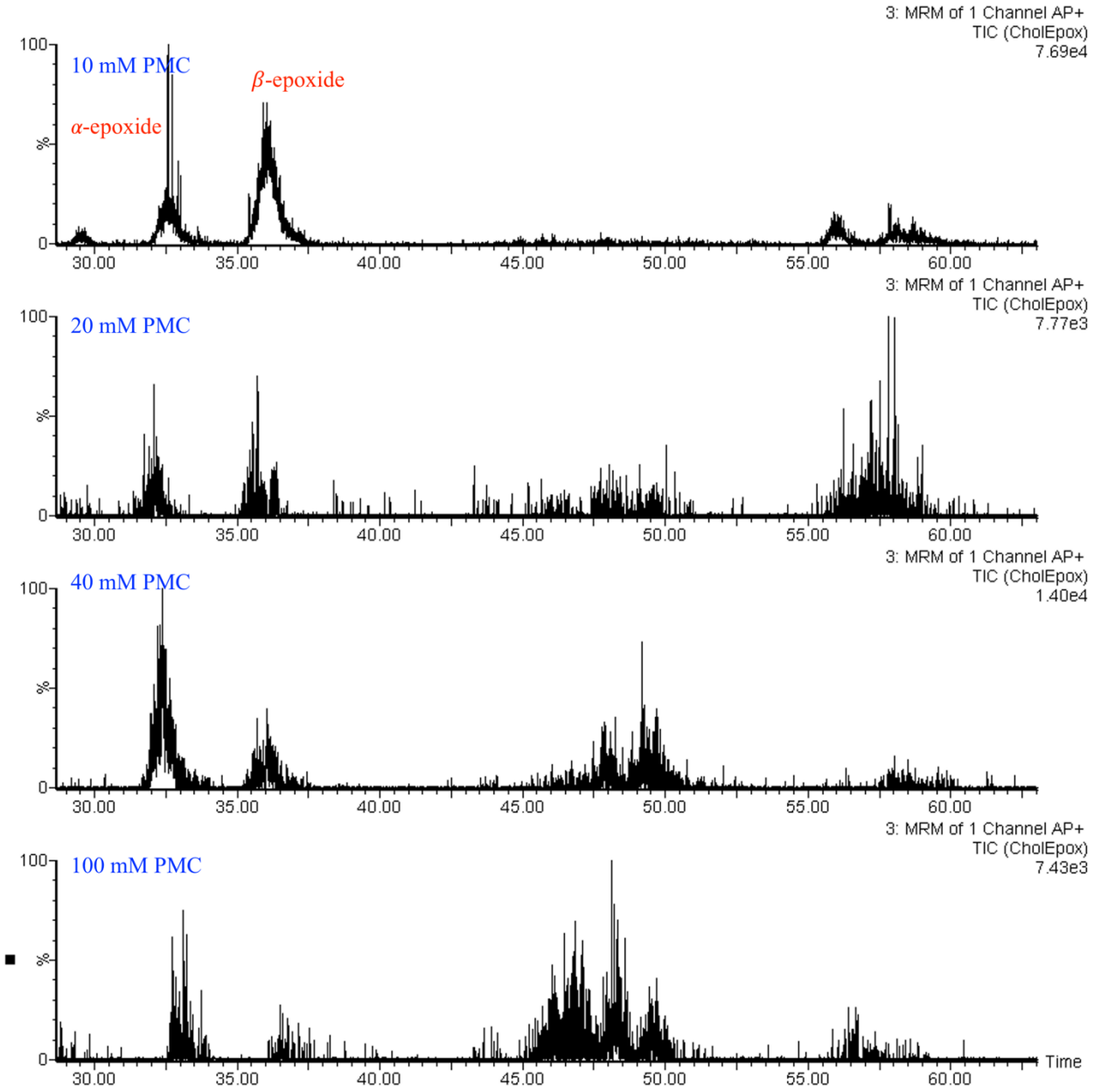

Figure 3.31. HPLC-APCI$^+$-MS/MS chromatograms for 403.4 *m/z* → 385.4 *m/z* of four different chol autoxidation samples – without added H-atom donor, or with varying amounts of added 2,2,5,7,8-pentamethyl-6-chromanol (PMC, concentration indicated in blue). Data were obtained using the conditions outlined in the experimental section 3.6.

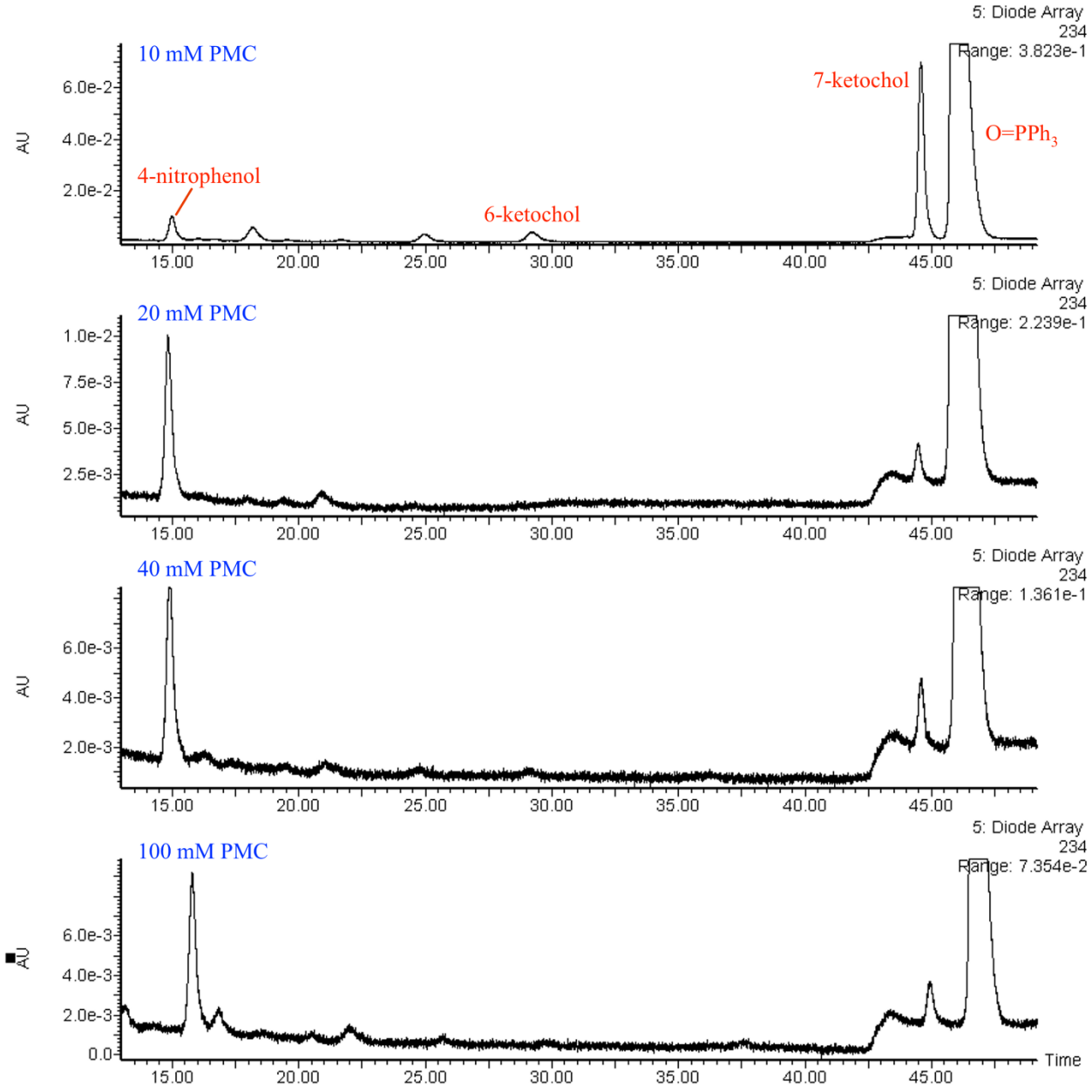

Figure 3.32. HPLC-UV chromatograms at 234 nm of four different chol autoxidation samples – without added H-atom donor, or with varying amounts of added 2,2,5,7,8-pentamethyl-6-chromanol (PMC, concentration indicated in blue). Data were obtained using the conditions outlined in the experimental section 3.6.

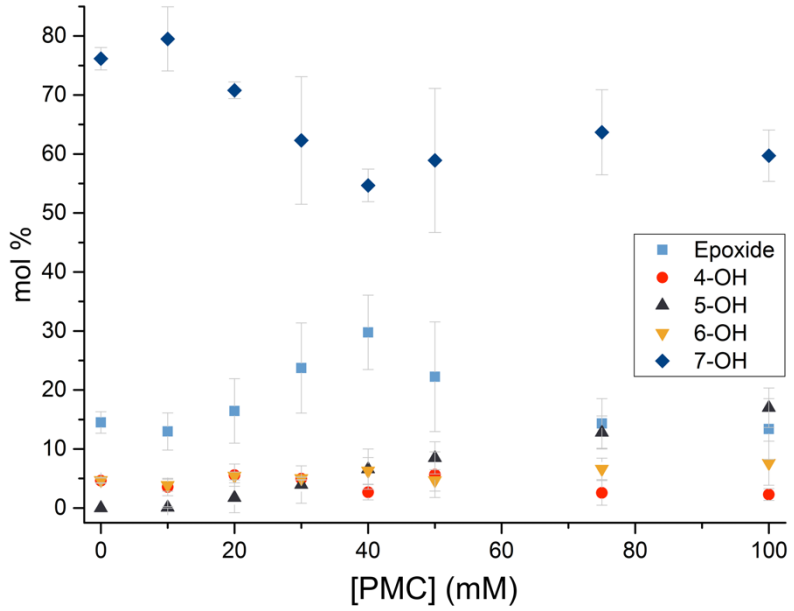

Figure 3.33. Product distribution from chol autoxidations as a function of added PMC.

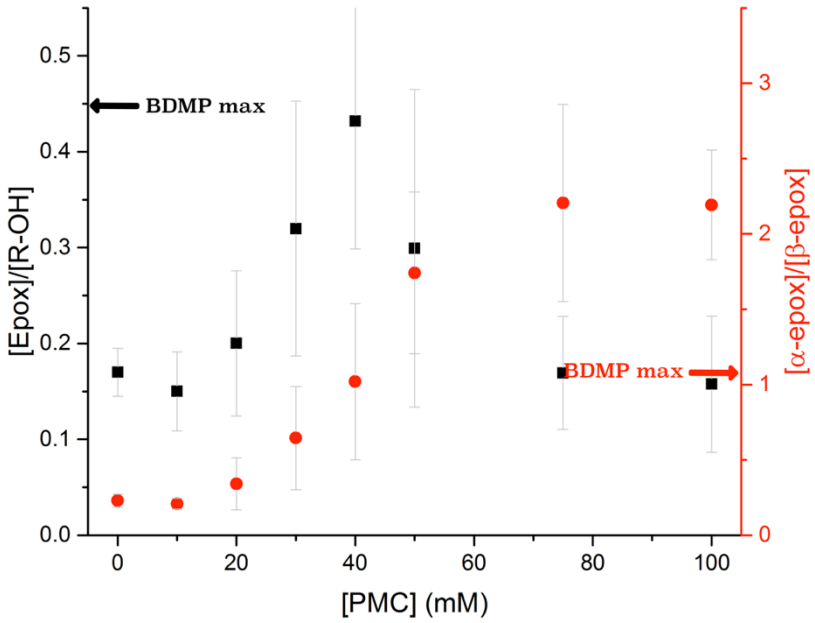

Figure 3.34. Ratio of chol epoxides to chol OH (■), and ratio of α-epoxide to β-epoxide (●) in chol autoxidations as a function of added [PMC].

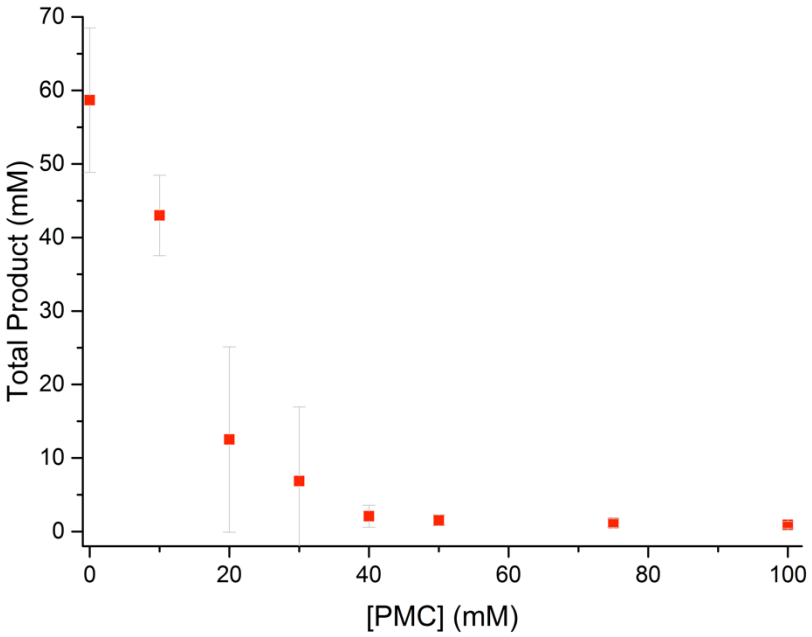

Figure 3.35. For cholesterol autoxidations, the total amount of autoxidation products detected with added [PMC], based on the initial 100 µL volume which contained 500 mM cholesterol.

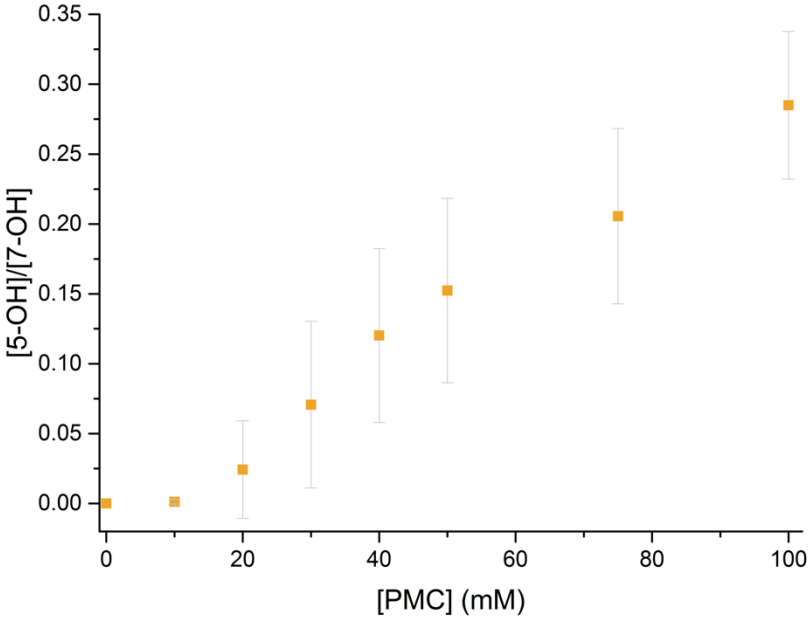

Figure 3.36. Dependence of [chol 5α-OH]/[chol 7-OH + 7-keto] on PMC concentration in chol autoxidations, where the slope = 3.036 M^{-1}.

3.9.4 Additional Data for Cholesteryl Acetate Autoxidations

Control experiments:

To assess the deprotection of cholesteryl acetate, 22 mg cholesteryl acetate (0.05 mmol) and 100 μL chlorobenzene were combined in a vial. 100 μL of 0.2 M BHT and PPh_3 in PhCl, then 2 mL of 1.0 M KOH in MeOH were added and the vial was shaken occasionally over 3 hours. 6 mL CH_2Cl_2 was added and the mixture was washed twice with 6 mL H_2O, dried over $MgSO_4$, concentrated *in vacuo*. The C3-H of chol OAc was completely converted to the C3-H of chol by NMR.

To assess the stability of the chol oxidation products to KOH, as well as their extraction efficiency, 50 mM of each of the authentic standards were subjected to the same procedure as above, then analyzed by HPLC-APCI$^+$-MS/MS as outlined in the experimental section. All compounds were sufficiently recovered (>95%), with the exception of chol triol which had very poor extraction efficiency (~5%).

Figures 3.37-3.39 show the typical chromatograms for chol OAc autoxidations with added BDMP, and Figures 3.40-3.41 show additional trends with added [BDMP]. Figure 3.41 shows the quantification of chol triol in chol OAc autoxidations with is increased relative to chol autoxidations. We suggested this may be due to the KOH workup cleaving compound **3.3.** to form chol triol (as opposed to chol epoxides as in chol autoxidations). Therefore, we treated a set of chol autoxidations to the same KOH workup and noticed an increase in chol triol detected (Figure 3.42).

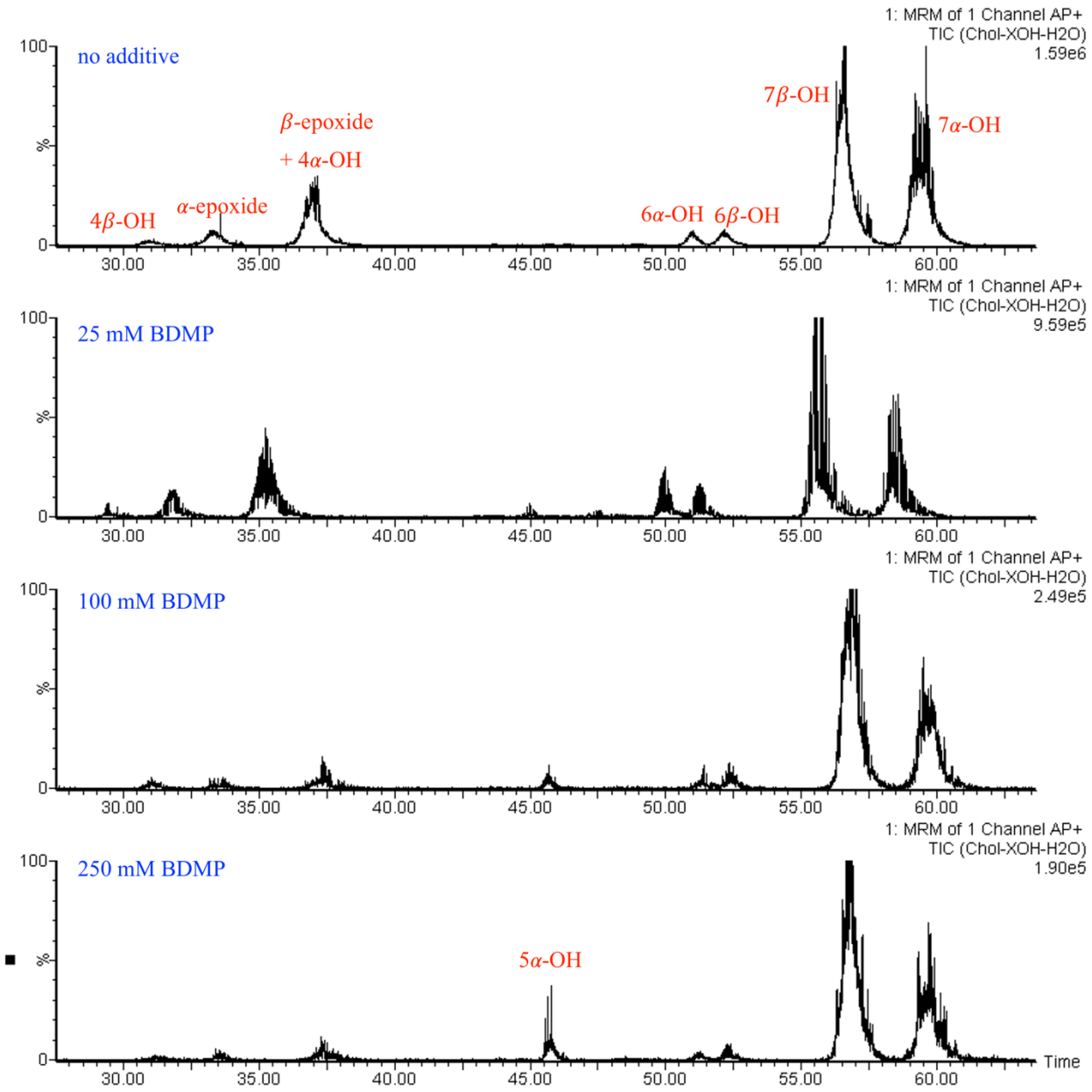

Figure 3.37. HPLC-APCI$^+$-MS/MS chromatograms for 385.4 *m/z* → 367.4 *m/z* of four different chol OAc autoxidation samples – without added H-atom donor, or with varying amounts of added 4-(tert-butyl)-2,6-dimethylphenol (BDMP, concentration indicated in blue). Data were obtained using the conditions outlined in the experimental section 3.6.

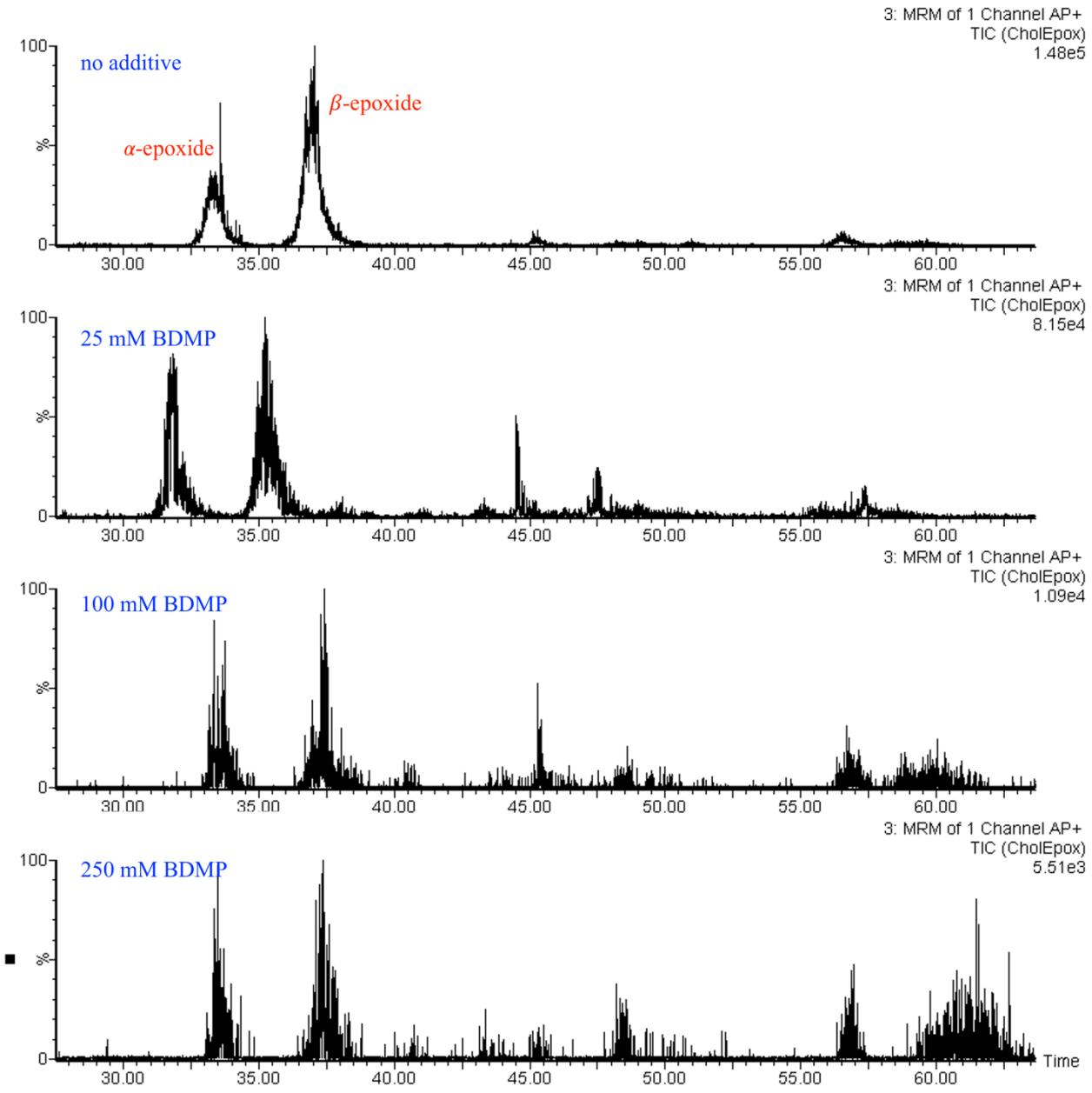

Figure 3.38. HPLC-APCI$^+$-MS/MS chromatograms for 403.4 *m/z* → 385.4 *m/z* of four different chol OAc autoxidation samples – without added H-atom donor, or with varying amounts of added 4-(tert-butyl)-2,6-dimethylphenol (BDMP, concentration indicated in blue). Data were obtained using the conditions outlined in the experimental section 3.6.

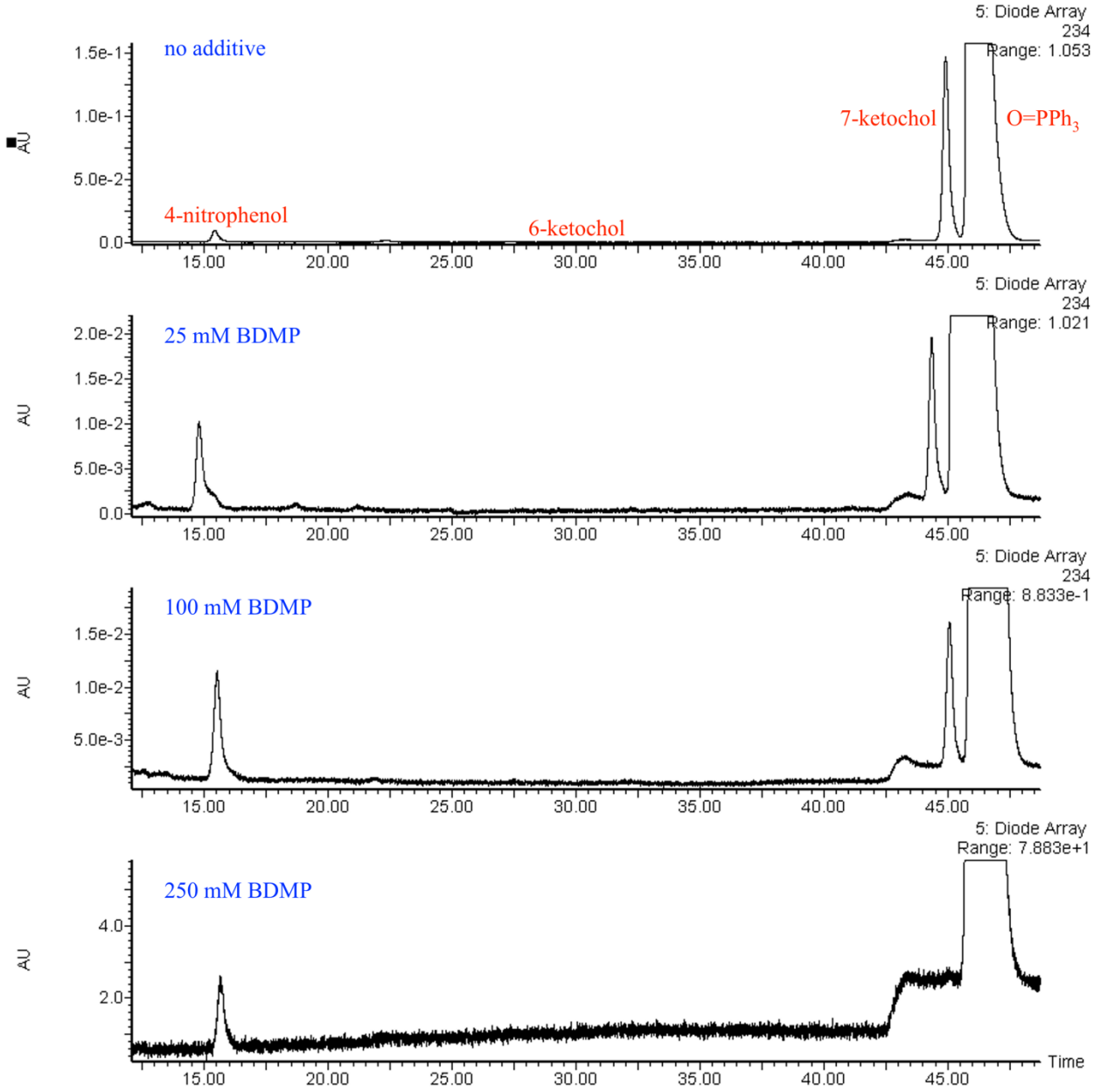

Figure 3.39. HPLC-UV chromatograms at 234 nm of four different chol OAc autoxidation samples – without added H-atom donor, or with varying amounts of added 4-(tert-butyl)-2,6-dimethylphenol (BDMP, concentration indicated in blue). Data were obtained using the conditions outlined in the experimental section 3.6.

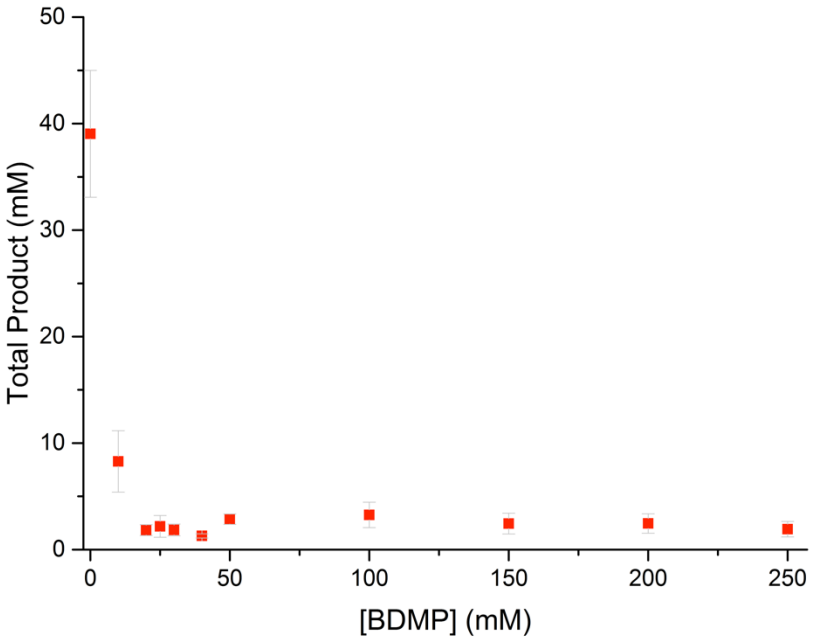

Figure 3.40. For cholesteryl acetate autoxidations, the total amount of autoxidation products detected with added [BDMP], based on the initial 100 μL volume which contained 500 mM cholesteryl acetate.

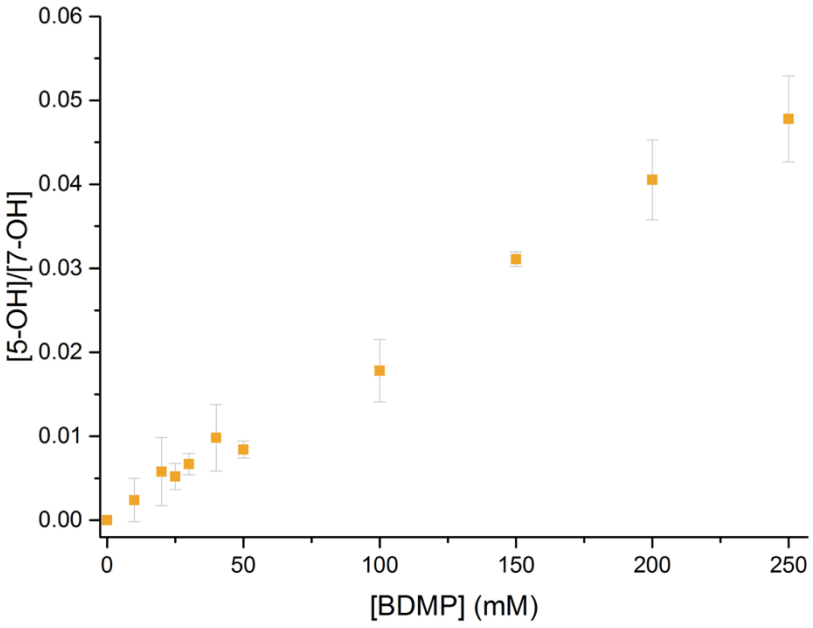

Figure 3.41. Dependence of [chol 5α-OH]/[chol 7-OH + 7-keto] on BDMP concentration in chol OAc autoxidations, where the slope = 0.1932 M^{-1}.

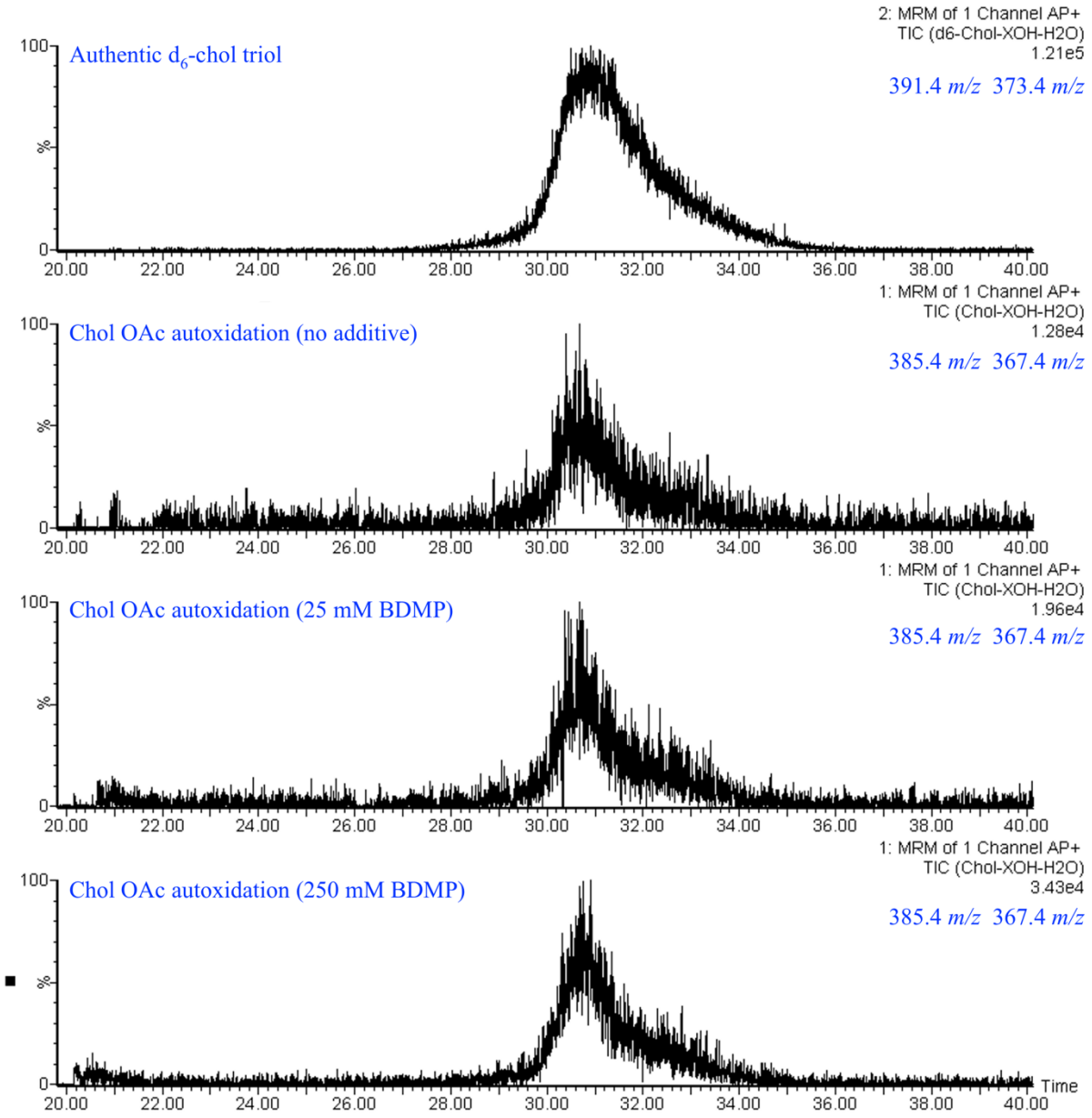

Figure 3.42. HPLC-APCI$^+$-MS/MS chromatograms for four different chol OAc autoxidation samples – without added H-atom donor, or with varying amounts of added 4-(tert-butyl)-2,6-dimethylphenol (BDMP, concentration indicated in blue). Data were obtained using the conditions outlined in the experimental section 3.6, except the mobile phase was 9:1 hexanes:iPrOH at 1 mL/min.

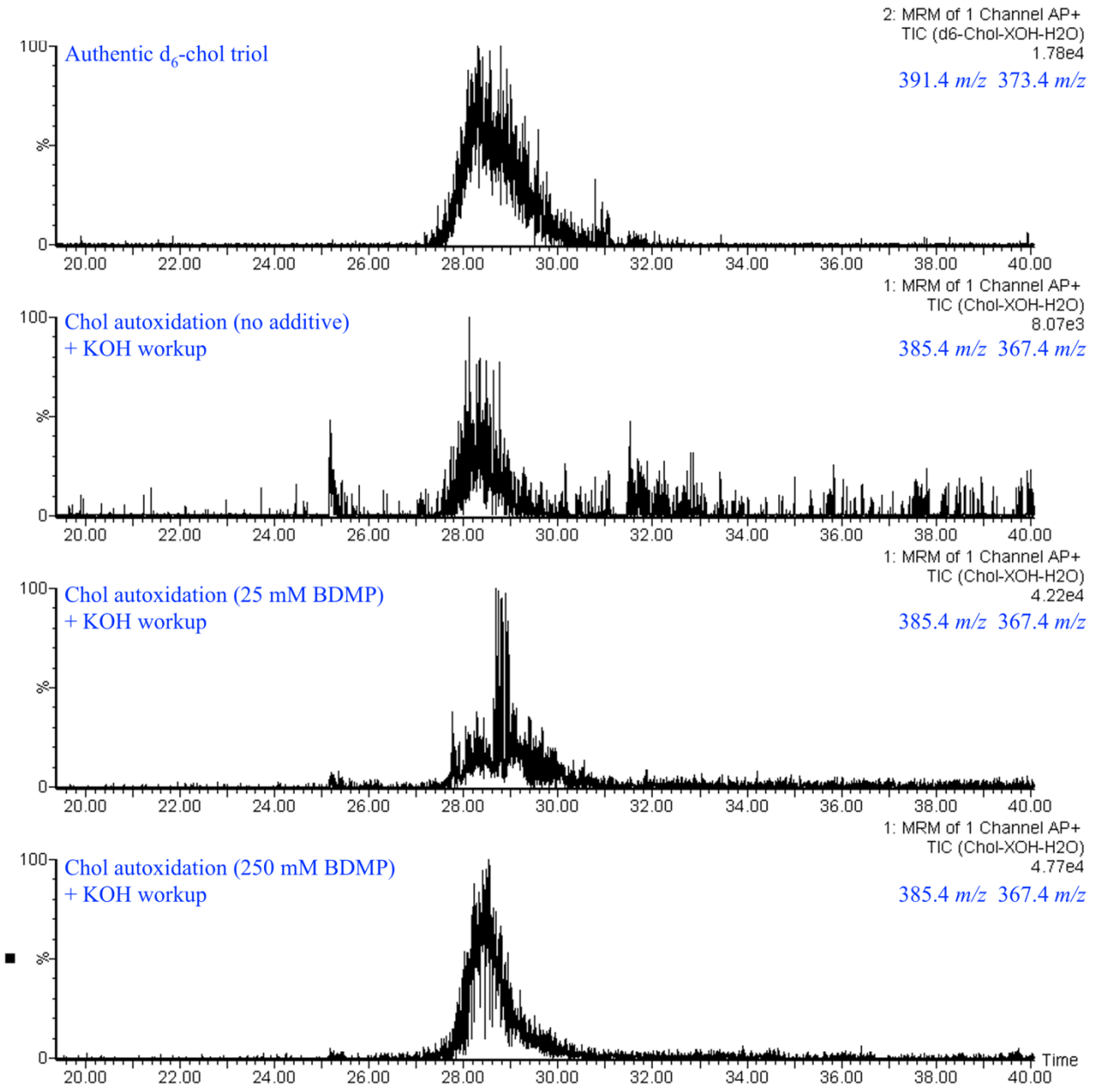

Figure 3.43. HPLC-APCI$^+$-MS/MS chromatograms for four different chol autoxidation samples (treated to the same workup as chol OAc autoxidations) – without added H-atom donor, or with varying amounts of added 4-(tert-butyl)-2,6-dimethylphenol (BDMP, concentration indicated in blue). Data were obtained using the conditions outlined in the experimental section 3.6, except the mobile phase was 9:1 hexanes:iPrOH at 1 mL/min.

\

3.9.5 Chol-2,2,4,4,7,7-d_6 Autoxidations

To assess the contribution of quantum mechanical tunnelling in the H-atom abstraction from chol by a peroxyl radical, we sought to do analogous autoxidations to cholesterol-2,2,4,4,7,7-d_6. This was carried out the same way, instead using (fully protiated) chol 5α-OH and chol epoxides as internal standards for the analogous d_6-autoxidation products (epoxides) or d_5-products in the case of the hydroxychols, which were detected by $APCI^+$-MS/MS at 409.4 *m/z* -> 391.4 *m/z* and 390.4 *m/z* -> 372.4 *m/z*, respectively. The only issue we faced was that since chol β-epoxide-2,2,4,4,6,6-d_6 also had a 391.4 *m/z* -> 373.4 *m/z* transition, there was significant residual signal in the chol 4α-OH-2,2,4,7,7-d_5 390.4 *m/z* -> 372.4 *m/z* channel. We therefore synthesized authentic chol β-epoxide-2,2,4,4,7,7-d_6 to make a standard curve of the residual signal in the 390.4 *m/z* -> 372.4 *m/z* channel (Figures S38). This response factor (0.105) was used to quantify chol 4α-OH-2,2,4,7,7-d_5 analogous to chol autoxidations *vide supra*.

While the full product distribution (as mol%) are presented in sections 3.3-3.4, it is interesting to note that the total amount of epoxide products in the chol-2,2,4,4,7,7-d_6 autoxidation is within error of the amount in a chol autoxidation, the amount of HAT products (chol ROH and keto) are dramatically decreased (*cf.* Figure 3.46). This was fully consistent with the suggestion that the large KIE (20) is due to quantum mechanical tunnelling for H-atom abstraction, which does not affect peroxyl radical addition.

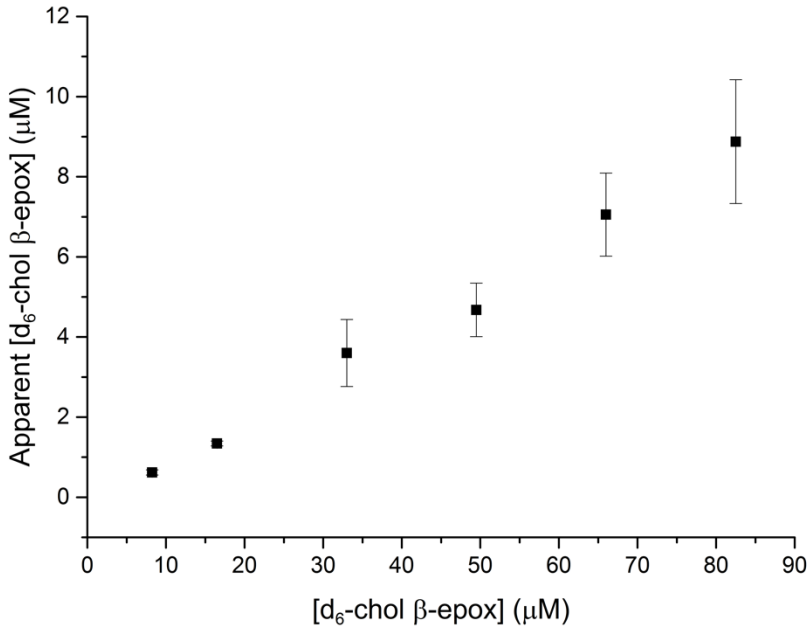

Figure 3.44. Standard curve for the residual signal of chol β-epoxide-2,2,4,4,7,7-d_6 in the channel for $APCI^+$-MS/MS transition corresponding to 390.4 *m/z* -> 372.4 *m/z.*

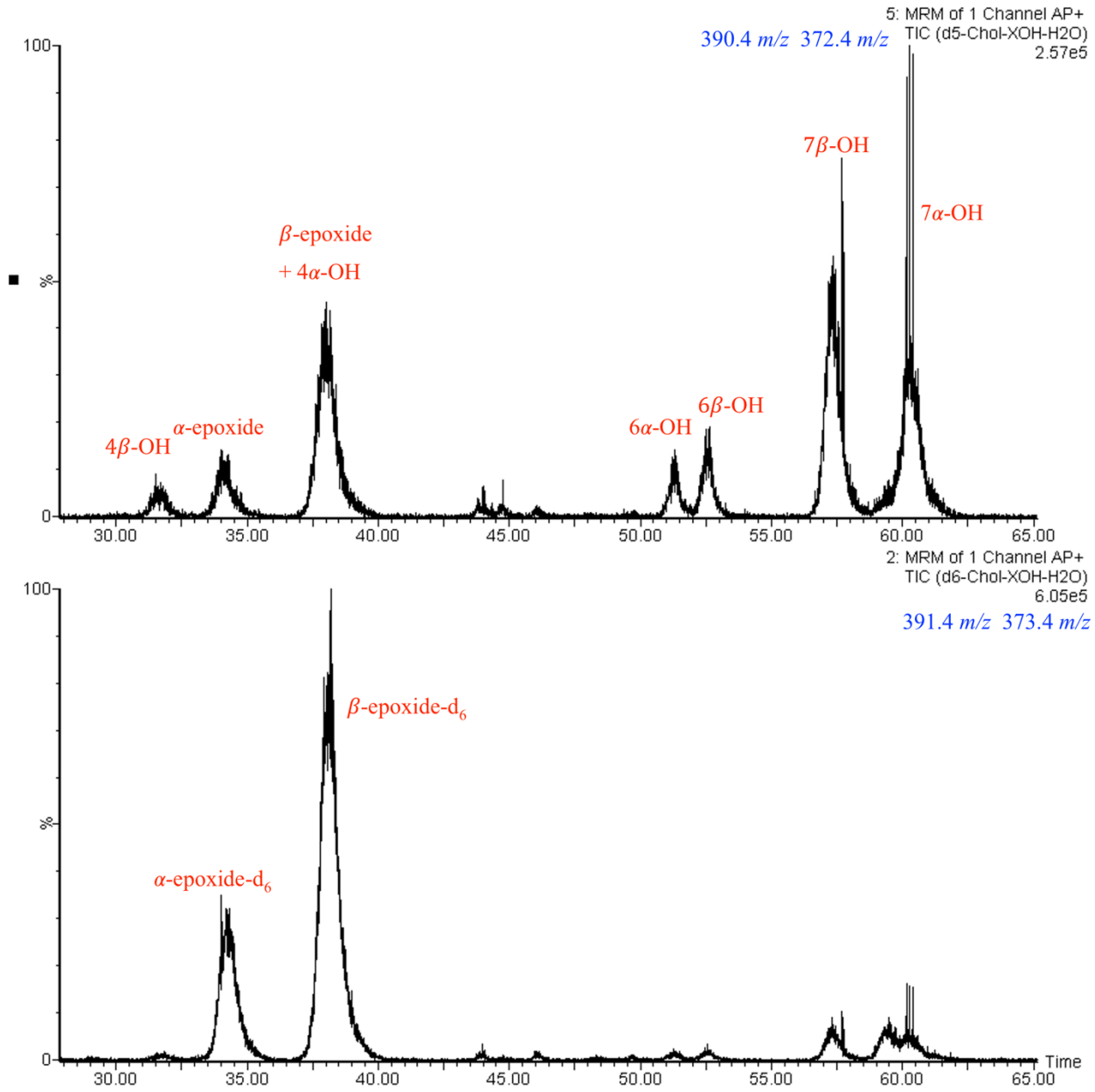

Figure 3.45. HPLC-APCI$^+$-MS/MS chromatograms for 390.4 *m/z* → 372.4 *m/z* (top) and 391.4 *m/z* → 373.4 *m/z* (bottom) of a chol-2,2,4,4,7,7-d$_6$ autoxidation. Data were obtained using the conditions outlined in the experimental section 3.6.

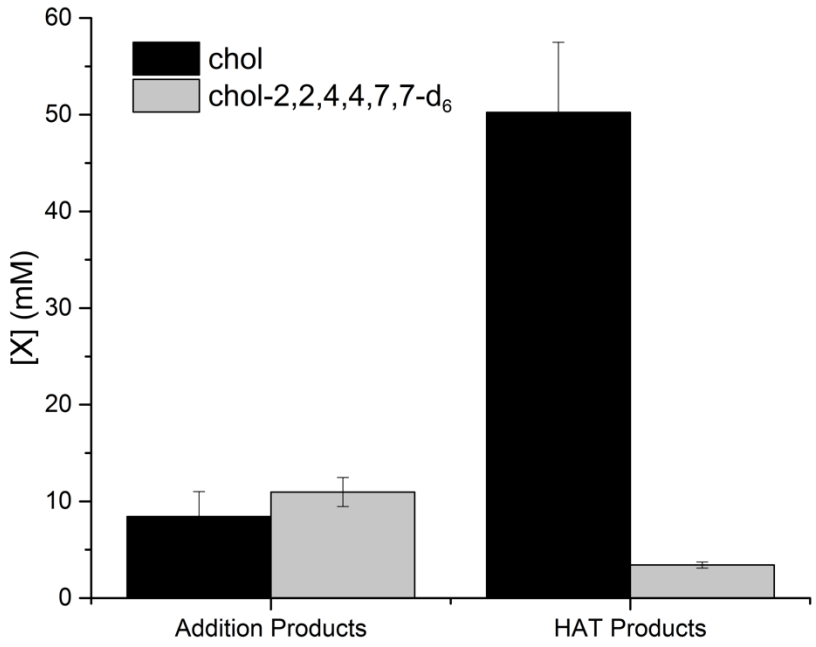

Figure 3.46. The amount of "Addition Products" (chol epoxides which result from initial peroxyl radical addition to chol) and "HAT Products" (hydroxychol or ketochol products which result from initial H-atom abstraction from chol by a peroxyl radical) resulting from the autoxidation of either chol or chol-2,2,4,4,7,7-d_6. Concentrations are based on the initial 100 μL autoxidation mixture which contained 500 mM chol or chol-2,2,4,4,7,7-d_6.

3.9.6 APCI+-MS Infusion of Cholesterol Autoxidations

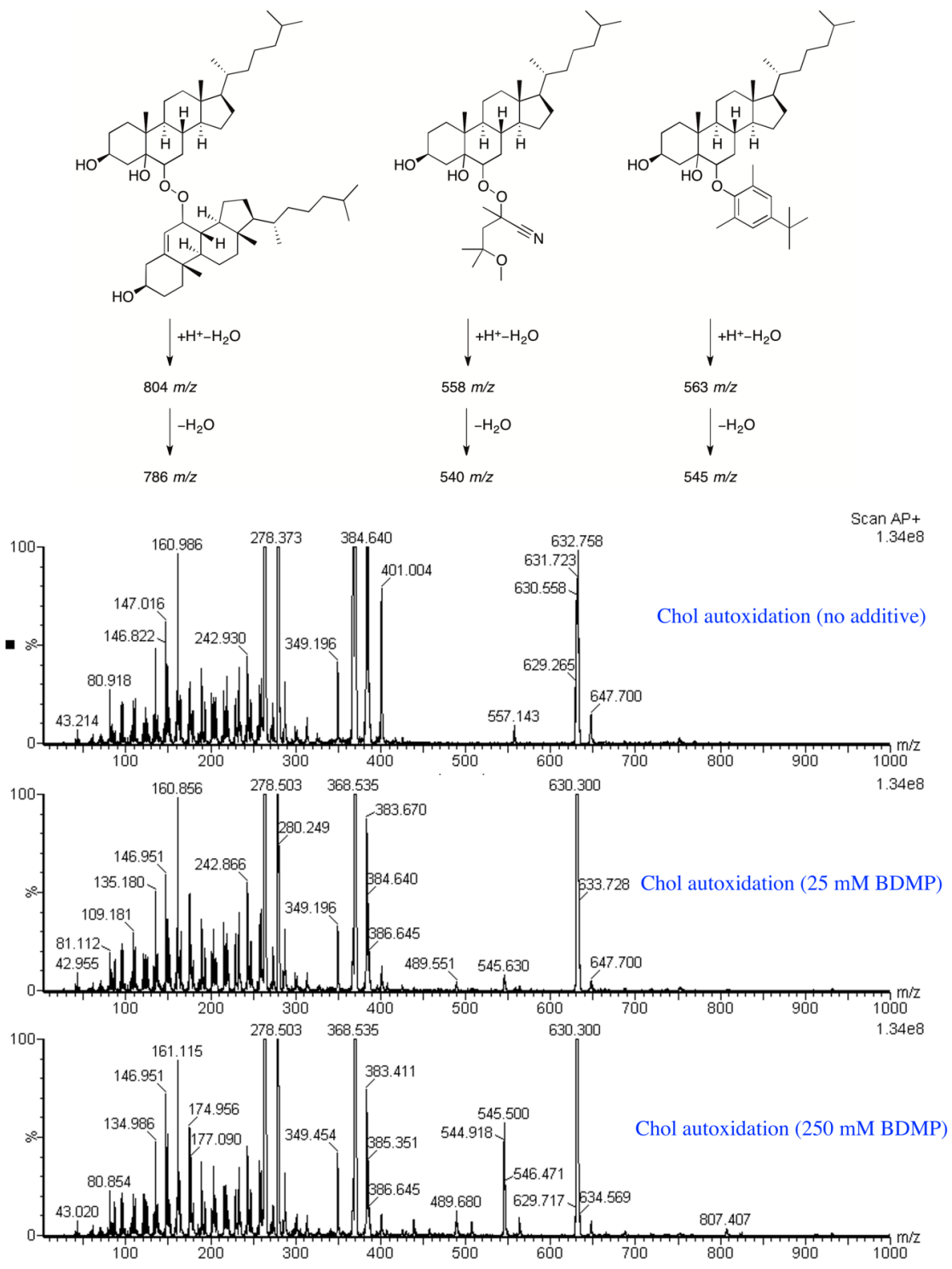

Figure 3.47. Mass spectra for direct APCI+-MS infusions of select chol autoxidation samples, with potential peroxyl (or phenoxyl) radical addition by-products and corresponding ions, above.

3.9.7 Chol Autoxidation Without PPh_3 Workup

As a control for chol XOH and ketochol derived from other reactions (e.g. peroxyl radical termination reactions and from further autoxidation or decomposition of the initially-formed hydroperoxides) a chol autoxidation was carried out without adding PPh_3 (Figure 3.48). The following amounts were detected (mM):

	4a-OH	4b-OH	6a-OH	6b-OH	6-keto	7a-OH	7b-OH	7-keto
No PPh_3:	2	0.4	0.3	1	1	20	20	9
With PPh_3:	0	0	0.1	0.2	0.1	1	4	2

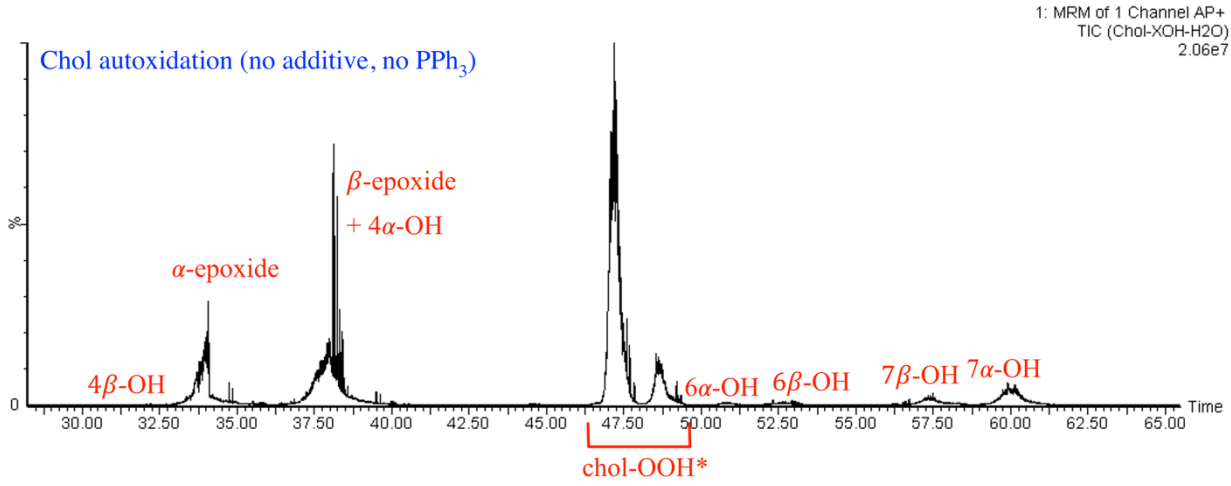

Figure 3.48. HPLC-APCI$^+$-MS/MS chromatogram for 385.4 *m/z* → 367.4 *m/z* of a chol autoxidation samples, without added H-atom donor or added PPh_3. Data were obtained using the conditions outlined in the experimental section 3.6.

The above result, coupled with the fact that in autoxidation samples treated normally: 4-ketochol was not observed; 7-ketochol accounted for ca. 20% of 7-oxysterols; and 6-ketochol accounted for ca. 50% of 6-oxysterols, suggests the aforementioned routes to the ketochol compounds from their corresponding peroxyl radicals or hydroperoxides decrease in efficiency in that order (4-, 7-, and 6-positions).

3.9.8 Chain Lengths

Chain length (x) was determined as follows:

$$x = \frac{[prod]/t}{2ek_d[In]}$$

where the total amount of products ([prod] = [ROH] + [epox] + [keto]) over the autoxidation time period (t) is divided by the concentration of MeOAMVN (In) and the known ek_d value[4] for MeOAMVN at 37°C in benzene.

Table 3.3. Chain lengths for the autoxidation of the compounds indicated, under typical conditions (16 hours, left), and chol autoxidations at various time points (right).

	x		x
Chol	0.9±0.1	Chol – 3 hours	1.1±0.1
Chol + BDMP (> 20 mM)	0.05±0.01	Chol – 6 hours	0.99±0.07
Chol OAc	0.8±0.1	Chol – 9 hours	0.87±0.04
2,2,4,4,7,7-d_6-chol	0.23±0.03	Chol – 12 hours	0.92±0.05

3.9.9 NMR Spectra

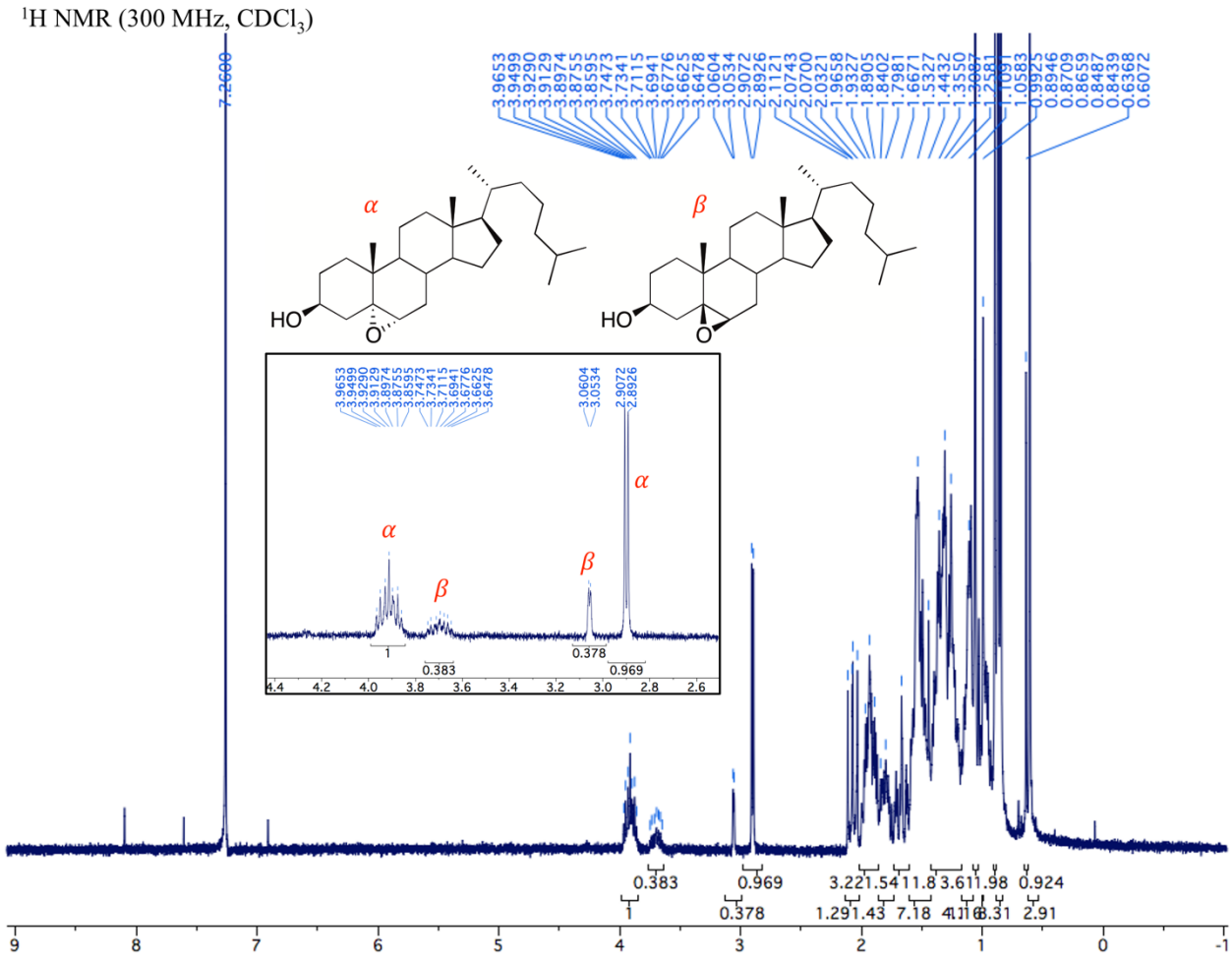

Figure 3.49. ^{1}H NMR spectrum of chol α-epoxide and chol β-epoxide mixture, and zoomed inset.

^{1}H NMR (400 MHz, $CDCl_3$)

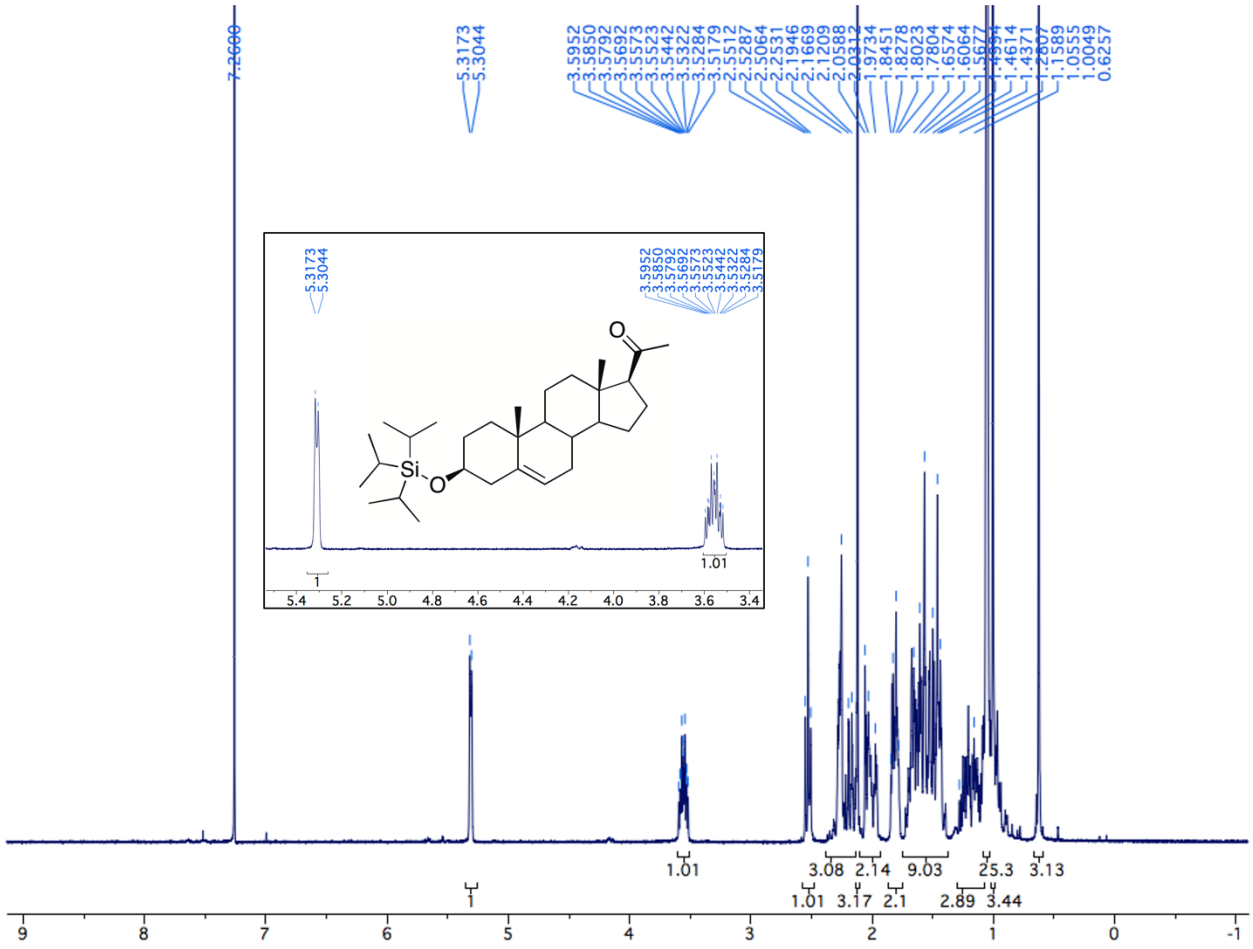

Figure 3.50. ^{1}H NMR spectrum of *3β-((Triisopropylsilyl)oxy)-pregn-5-en-20-one* (4), and zoomed inset.

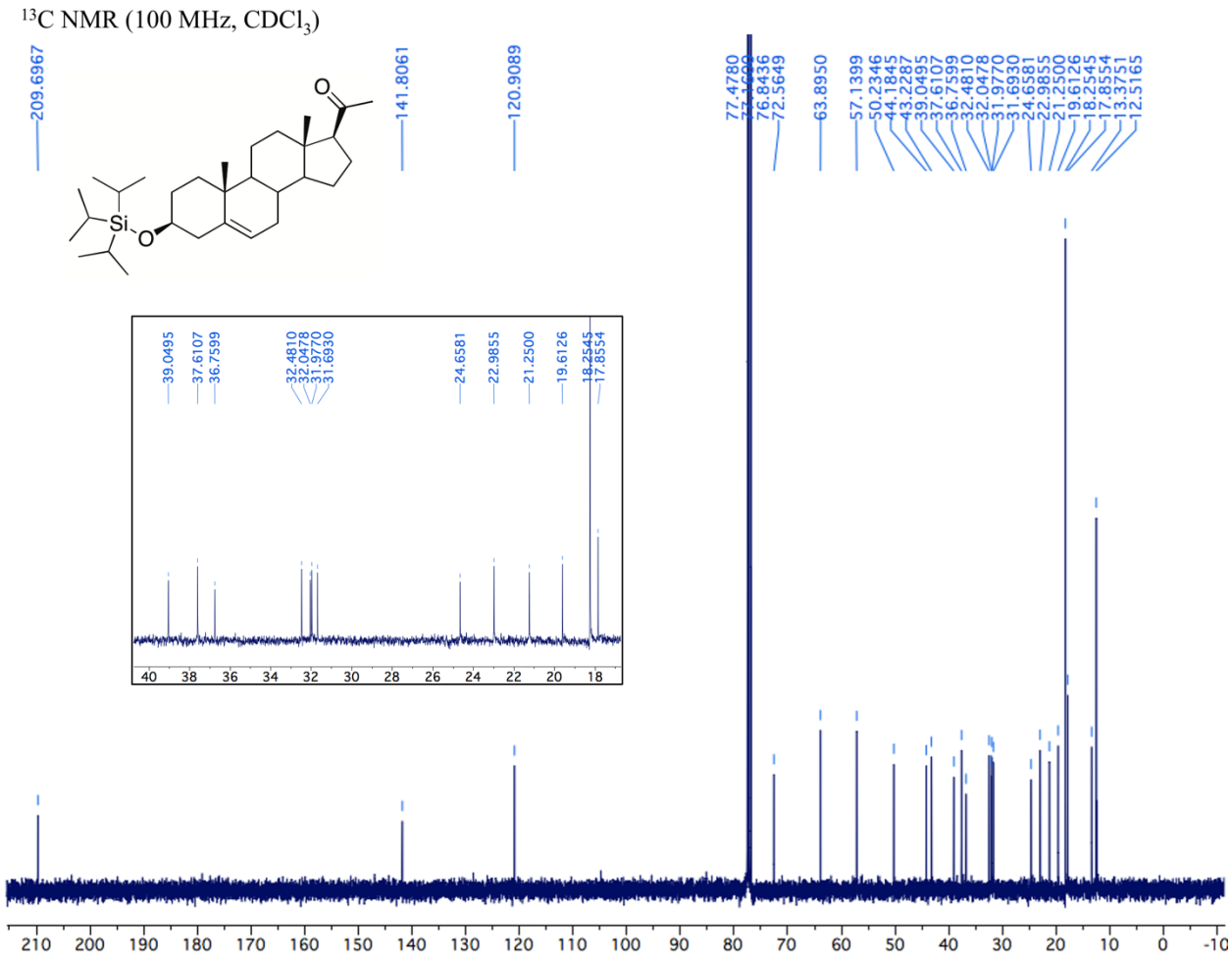

Figure 3.51. ^{13}C NMR spectrum of *3β-((Triisopropylsilyl)oxy)-pregn-5-en-20-one* (4), and zoomed inset.

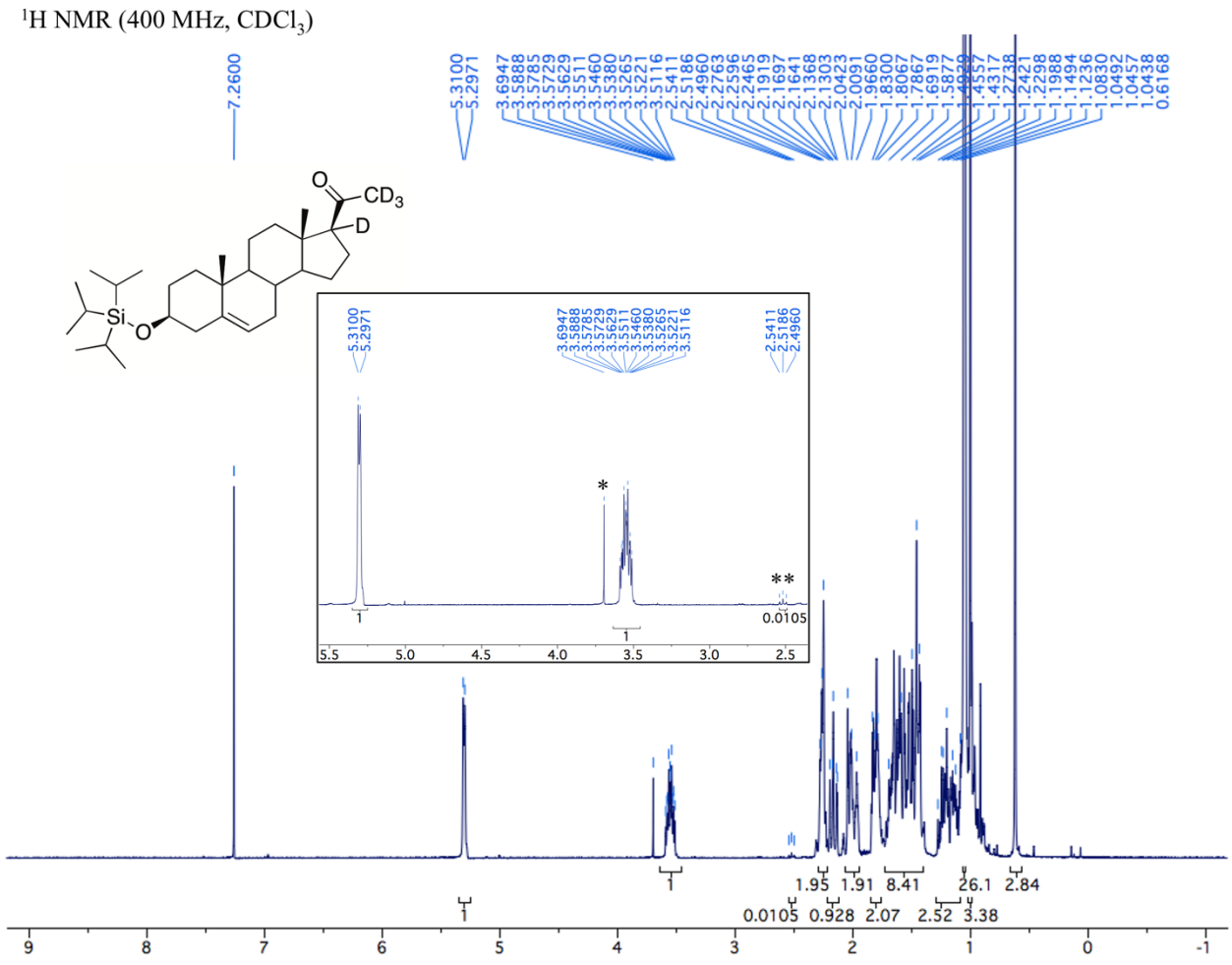

Figure 3.52. ^{1}H NMR spectrum of *3β-((Triisopropylsilyl)oxy)-pregn-5-en-20-one-17,21,21,21-d$_4$ (5)*, and zoomed inset. Note: * indicates residual 1,4-dioxane and ** indicates the nearly completely consumed C17-H, showing ~99% deuterium incorporation at that position.

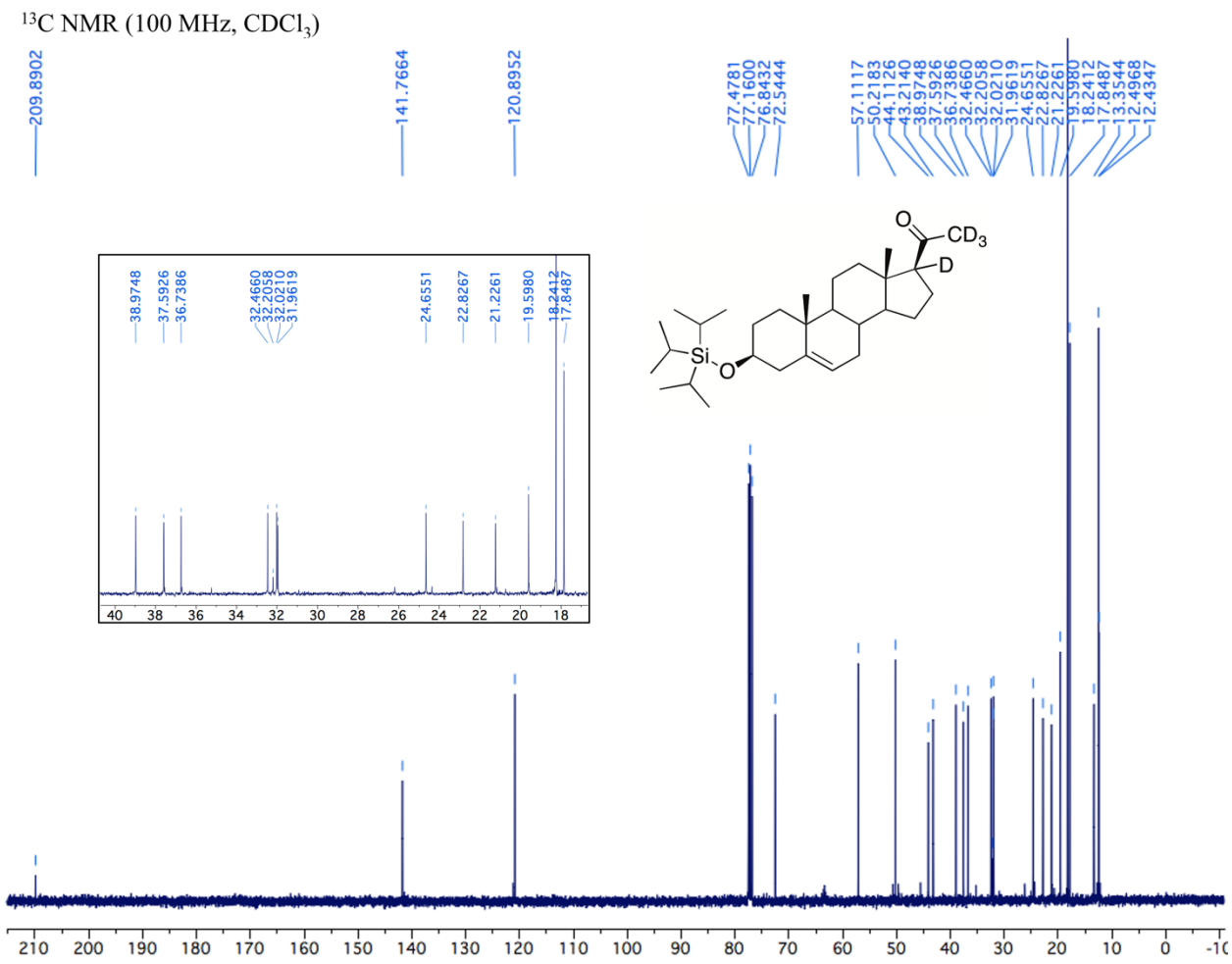

Figure 3.53. ^{13}C NMR spectrum of *3β-((Triisopropylsilyl)oxy)-pregn-5-en-20-one-17,21,21,21-d$_4$ (5)*, and zoomed inset.

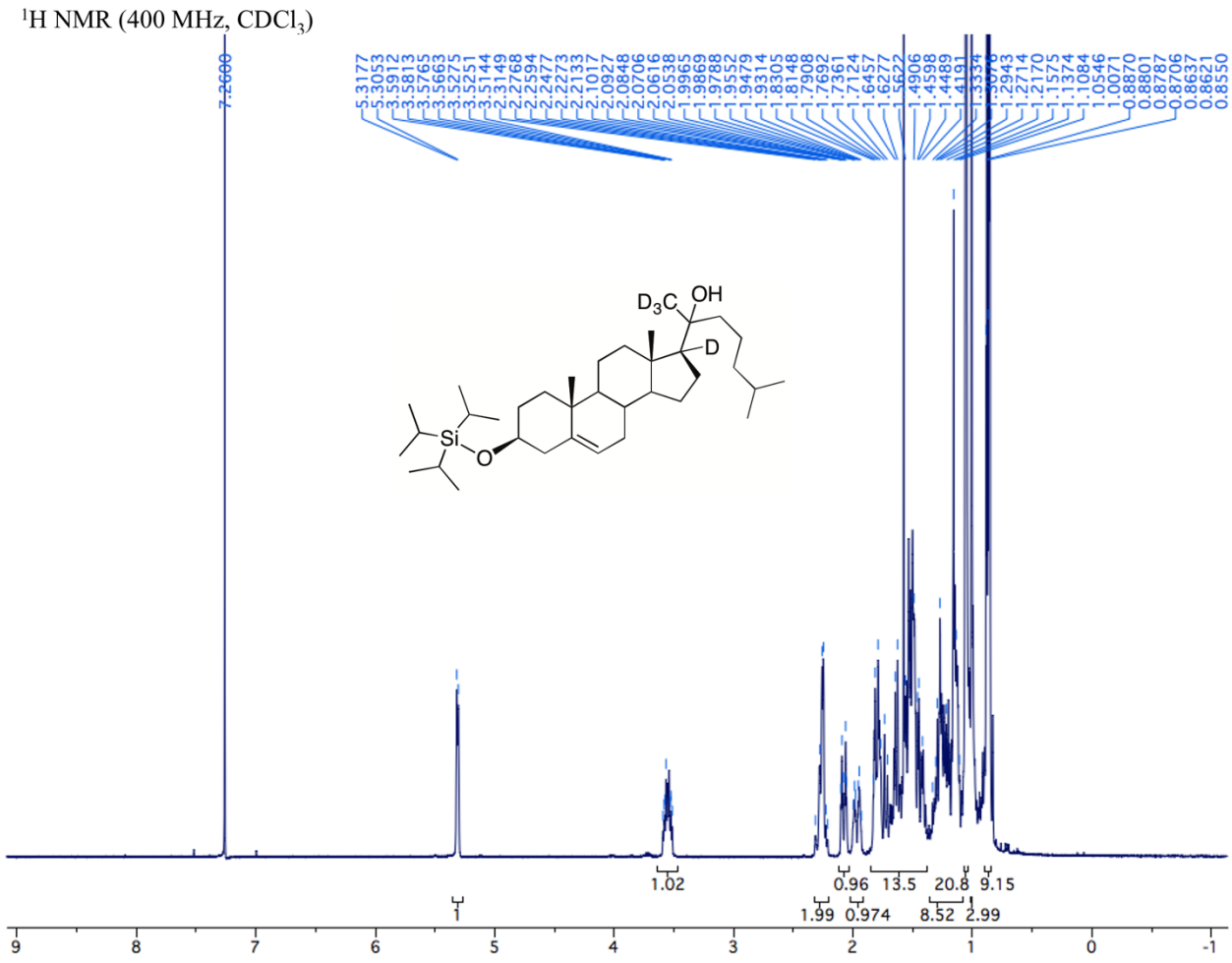

Figure 3.54. ^{1}H NMR spectrum of *3β-((Triisopropylsilyl)oxy)-cholest-5-en-20-ol-17,21,21,21-d_4* (**3.6**).

^{13}C NMR (100 MHz, $CDCl_3$)

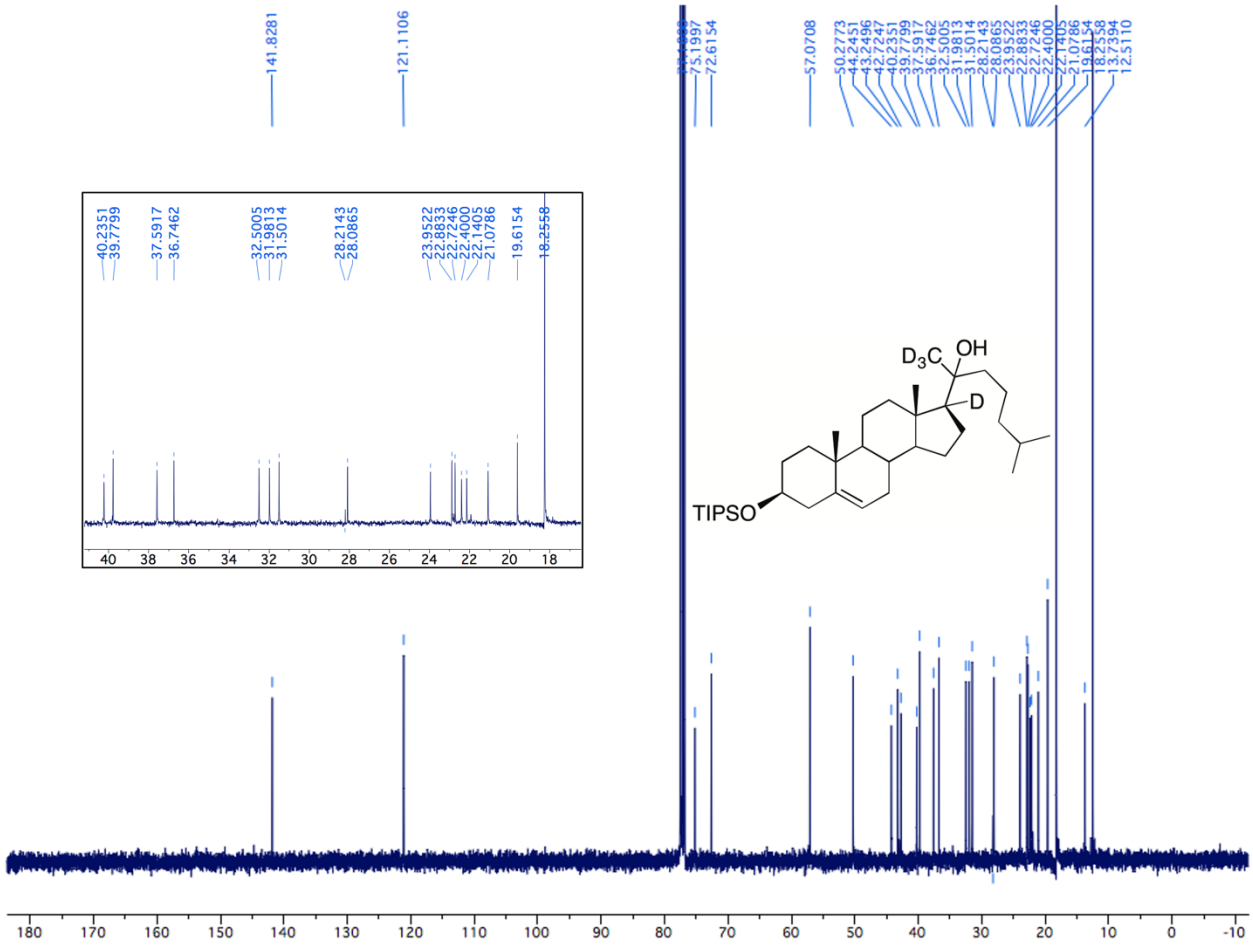

Figure 3.55. ^{13}C NMR spectrum of *3β-((Triisopropylsilyl)oxy)-cholest-5-en-20-ol-17,21,21,21-d_4* (**3.6**), and zoomed insert.

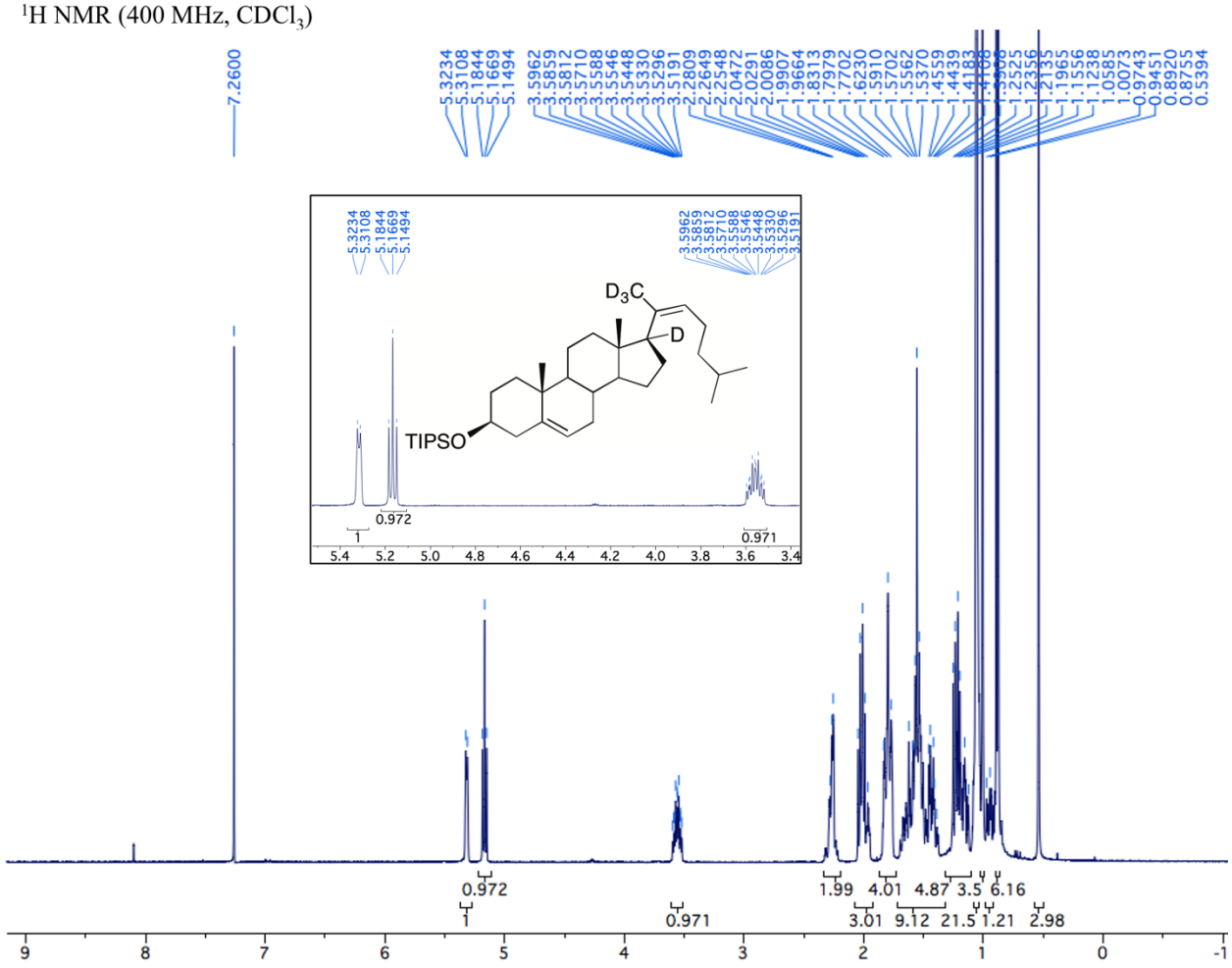

Figure 3.56. ^{1}H NMR spectrum of *3β-((Triisopropylsilyl)oxy)-cholesta-5,20-diene-17,21,21,21-d_4* (**3.7**), and zoomed insert.

^{13}C NMR (100 MHz, $CDCl_3$)

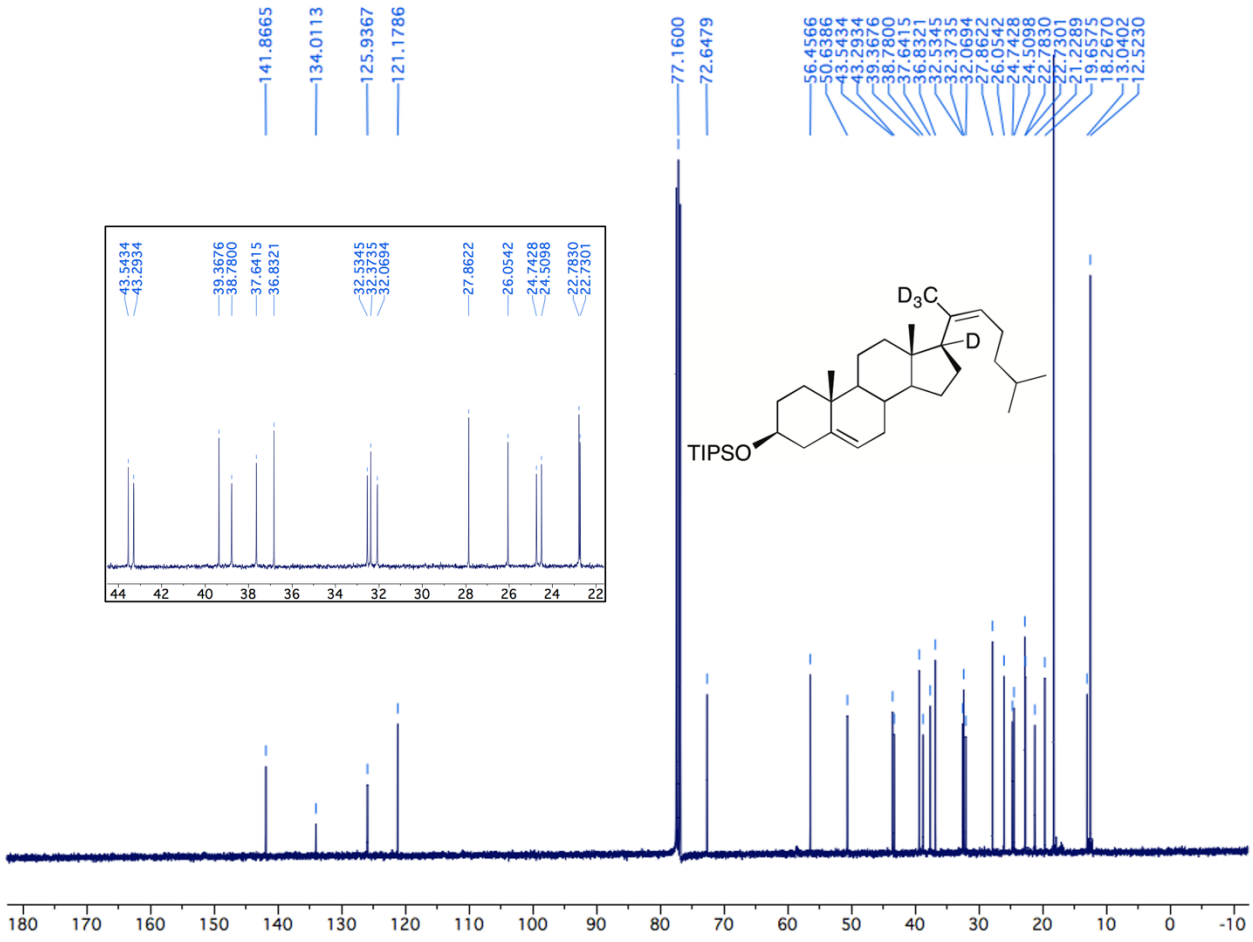

Figure 3.57. ^{13}C NMR spectrum of *3β-((Triisopropylsilyl)oxy)-cholesta-5,20-diene-17,21,21,21-d*$_4$ (**3.7**), and zoomed insert.

^{1}H NMR (400 MHz, $CDCl_3$)

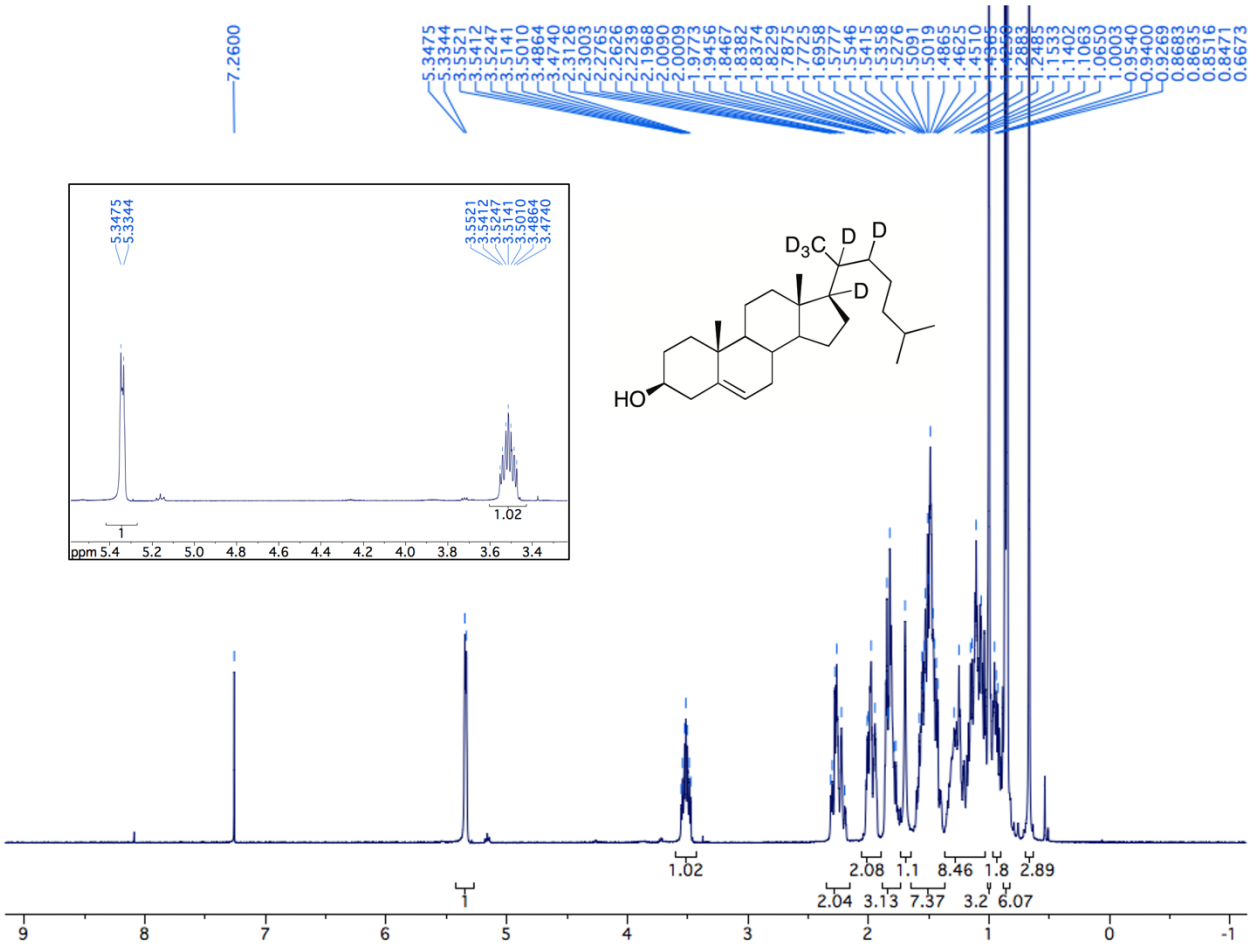

Figure 3.58. ^{1}H NMR spectrum of *cholesterol-17,20,21,21,21,22-d_6 (***3.8***)*, and zoomed insert.

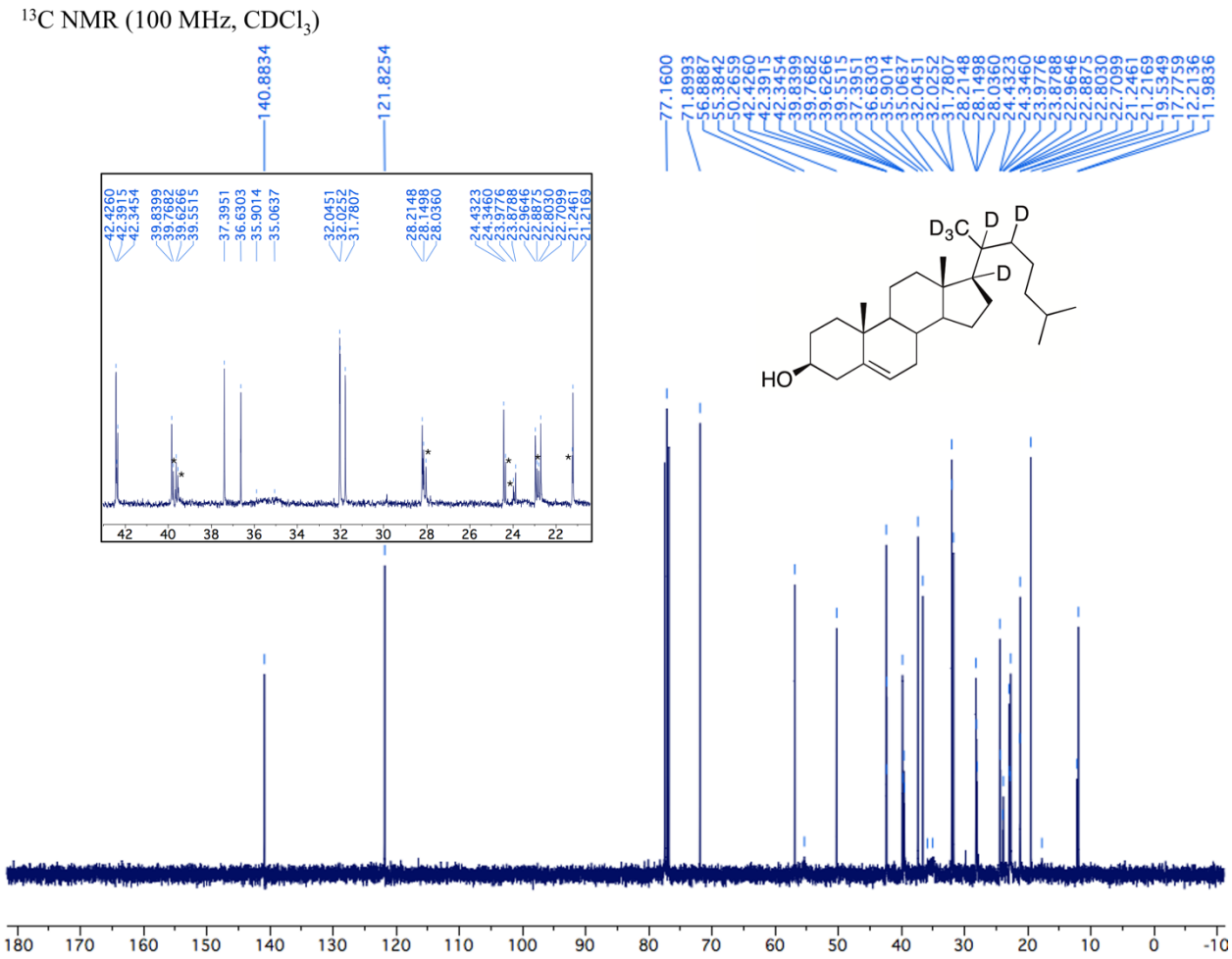

Figure 3.59. ^{13}C NMR spectrum of *cholesterol-17,20,21,21,21,22-d_6* (**3.8**), and zoomed insert. Note * indicates peaks corresponding to the minor stereoisomer.

^{1}H NMR (600 MHz, $CDCl_3$)

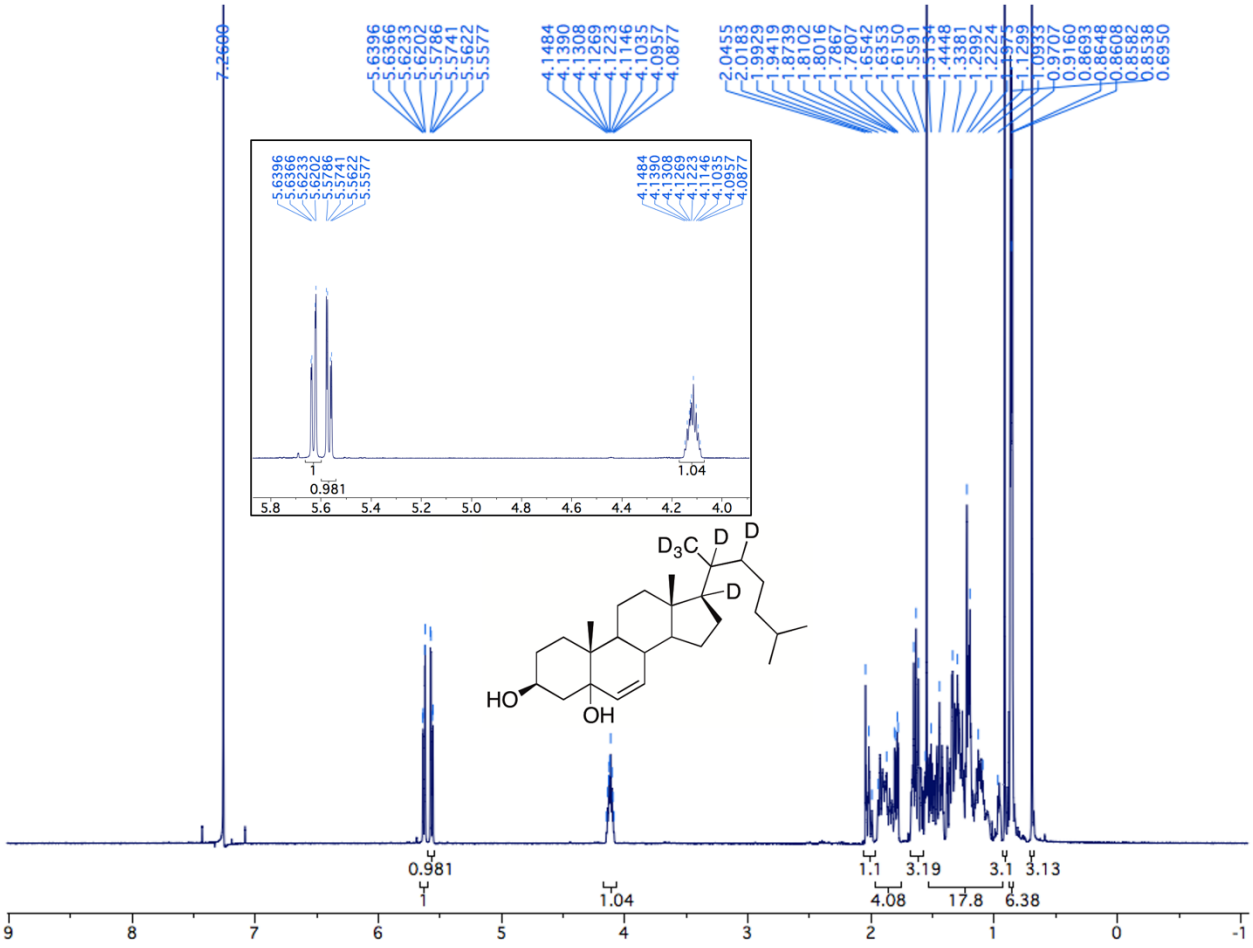

Figure 3.60. ^{1}H NMR spectrum of *5α-hydroxycholesterol-17,20,21,21,21,22-d_6*, and zoomed insert.

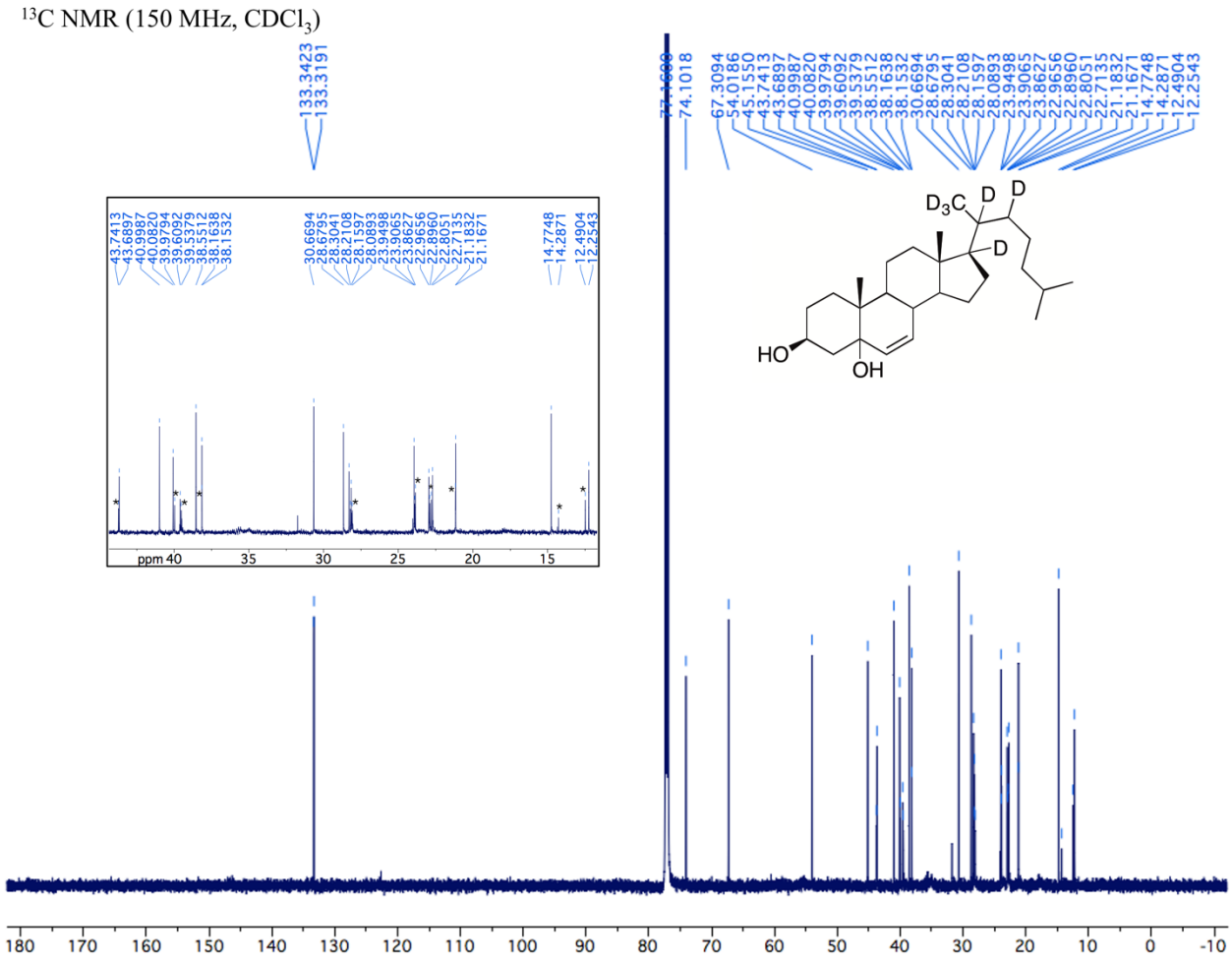

Figure 3.61. ^{13}C NMR spectrum of *5α-hydroxycholesterol-17,20,21,21,21,22-d$_6$*, and zoomed insert.

Note * indicates peaks corresponding to the minor stereoisomer.

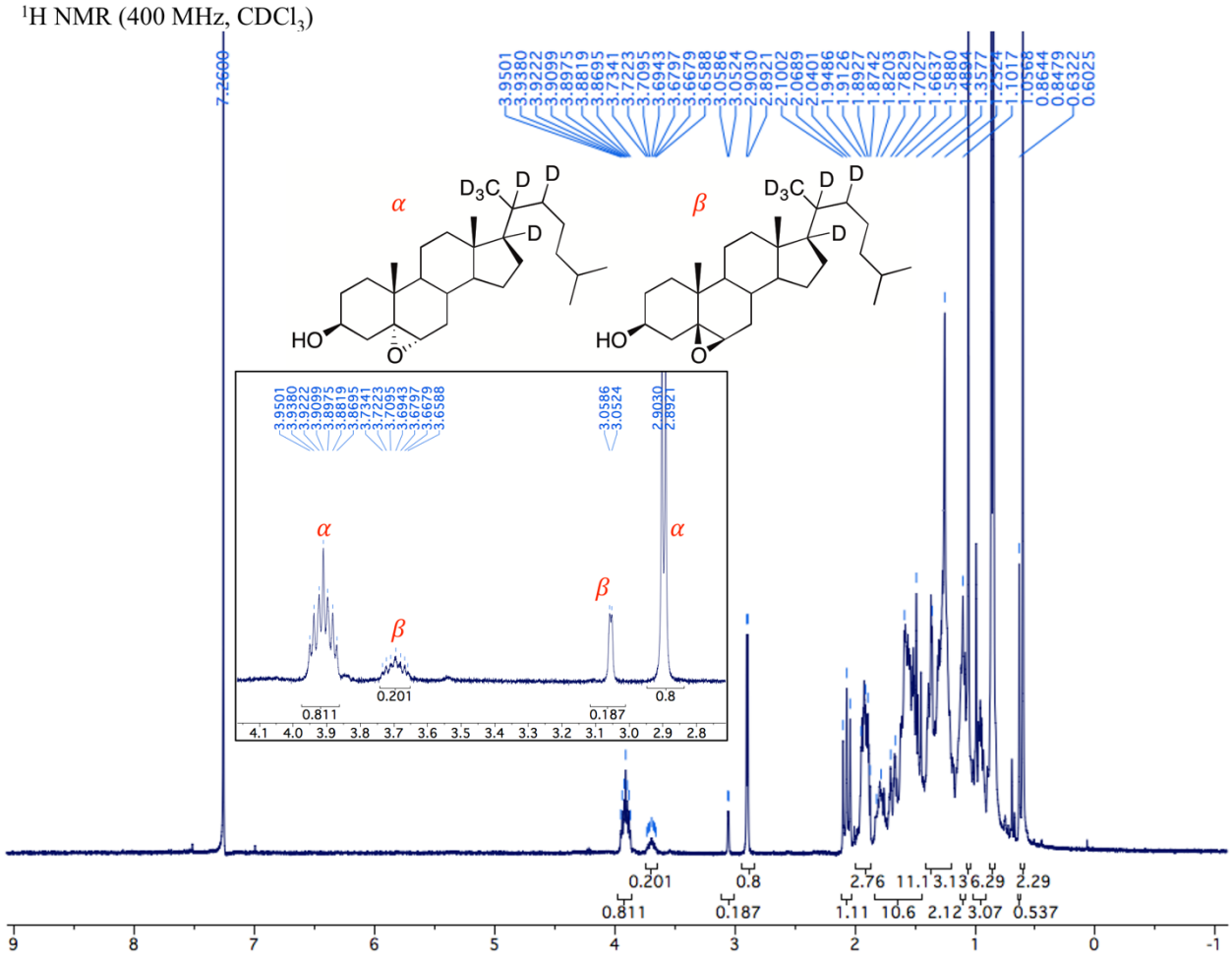

Figure 3.62. ^{1}H NMR spectrum of *cholesterol-5,6-epoxide-17,20,21,21,21,22-d_6*, and zoomed insert.

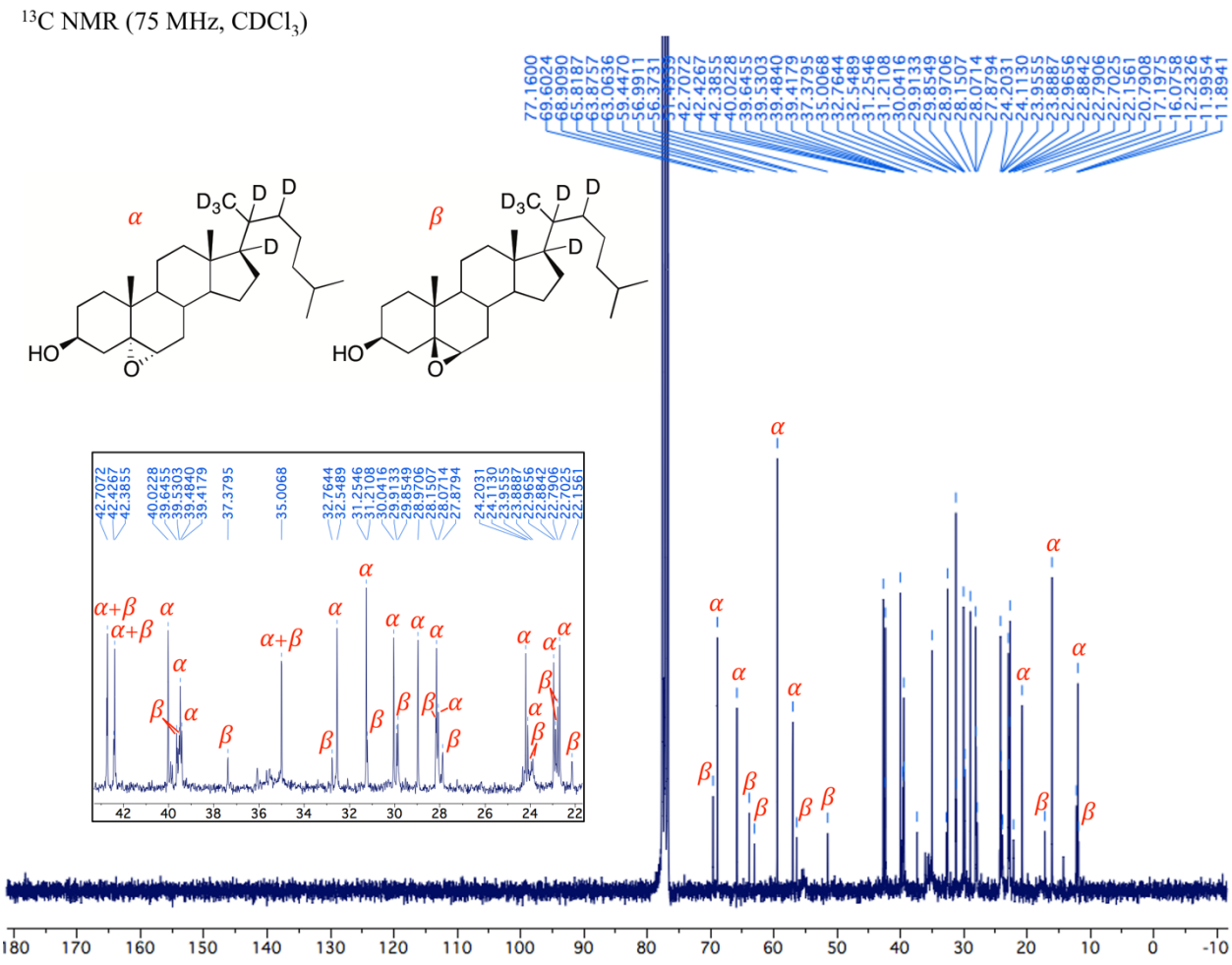

Figure 3.63. ^{13}C NMR spectrum of *cholesterol-5,6-epoxide-17,20,21,21,21,22-d*$_6$, and zoomed insert.

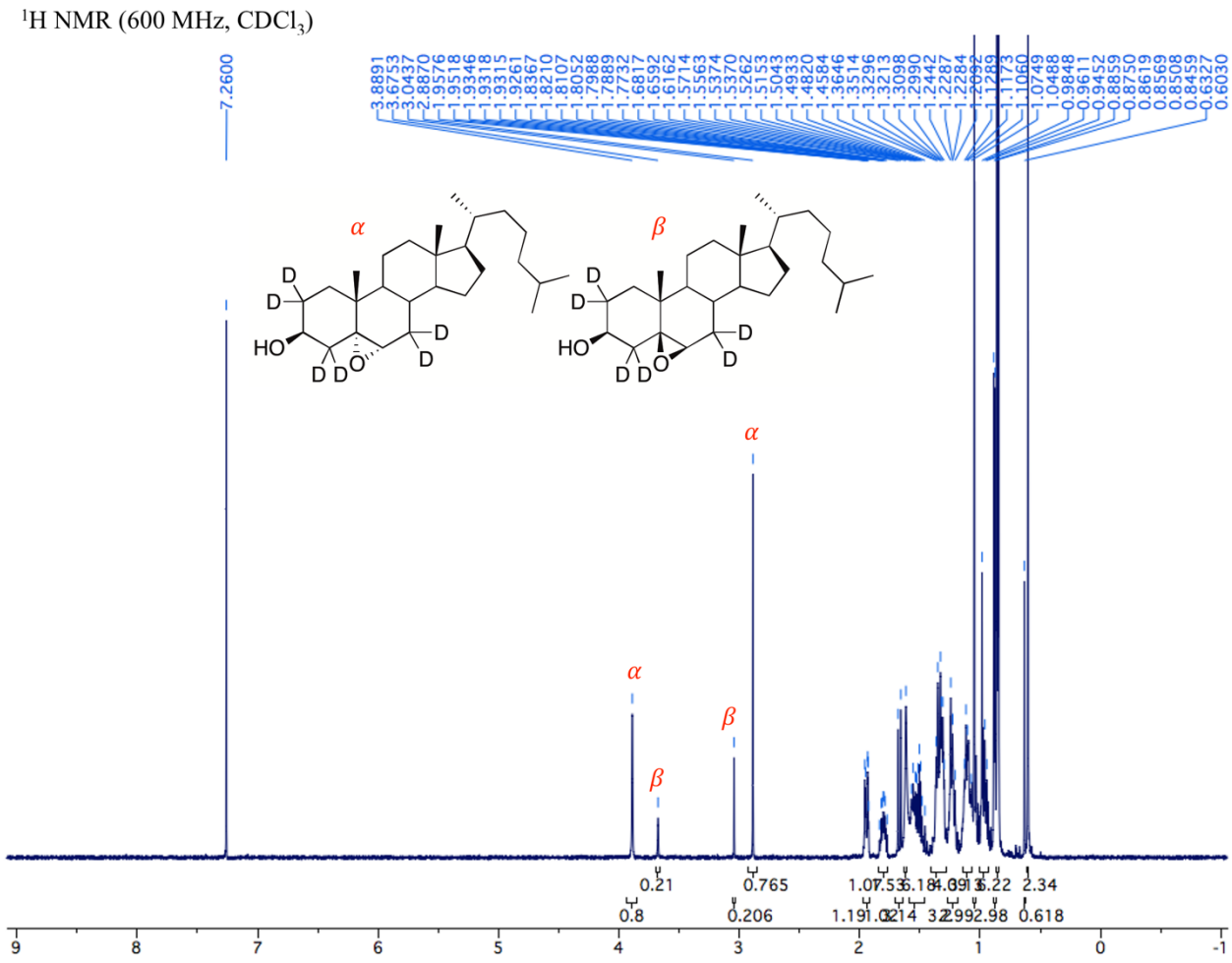

Figure 3.64. [1]H NMR spectrum of *cholesterol-5,6-epoxide-2,2,4,4,7,7-d_6*.

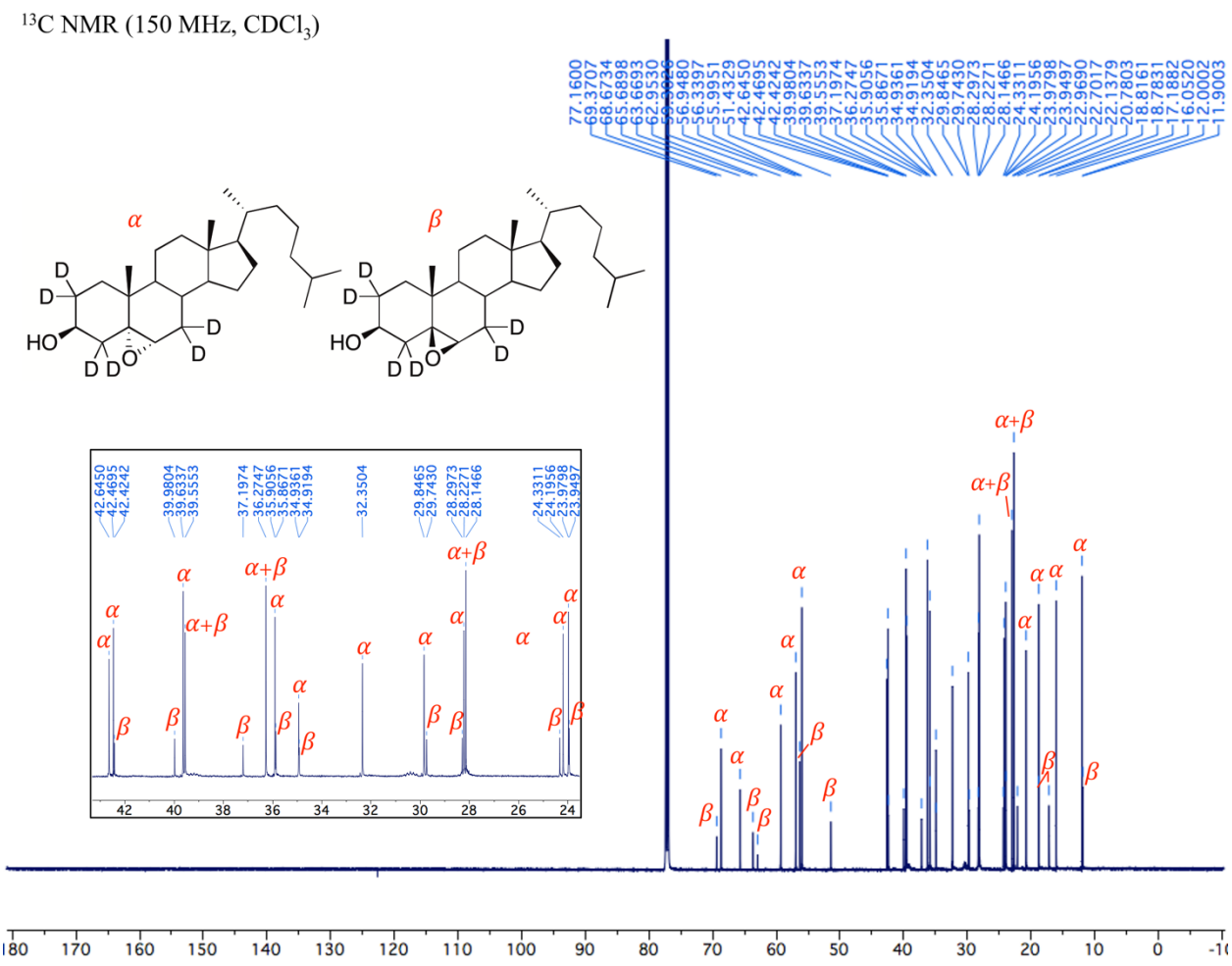

Figure 3.65. ^{13}C NMR spectrum of *cholesterol-5,6-epoxide-2,2,4,4,7,7-d_6*, and zoomed insert.

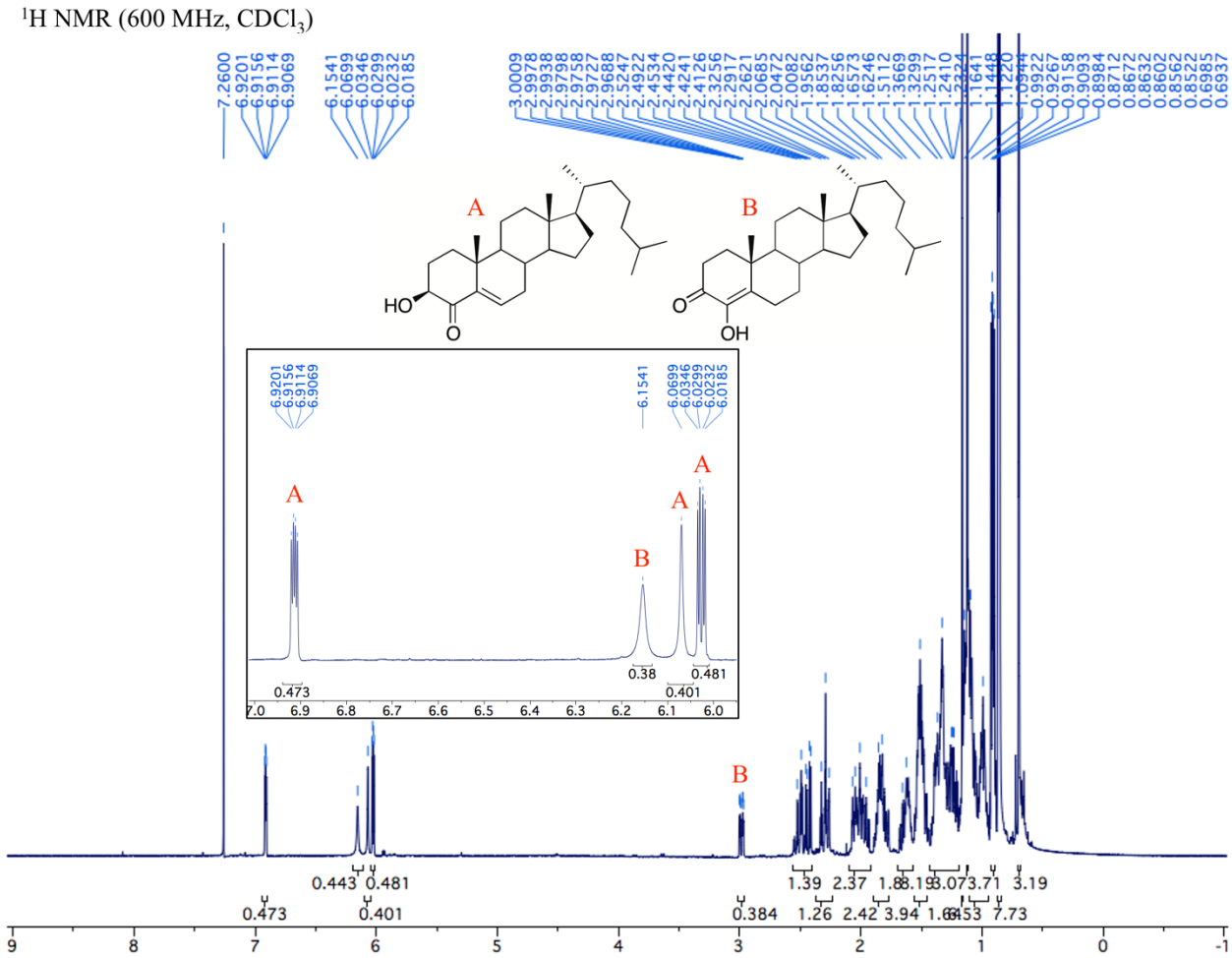

Figure 3.66. ^{1}H NMR spectrum of *4-ketocholesterol* (A) and *4-hydroxycholest-4-ene-3-one* (B) (assignment of the latter based on previous characterization[5]), and zoomed insert.

^{13}C NMR (150 MHz, $CDCl_3$)

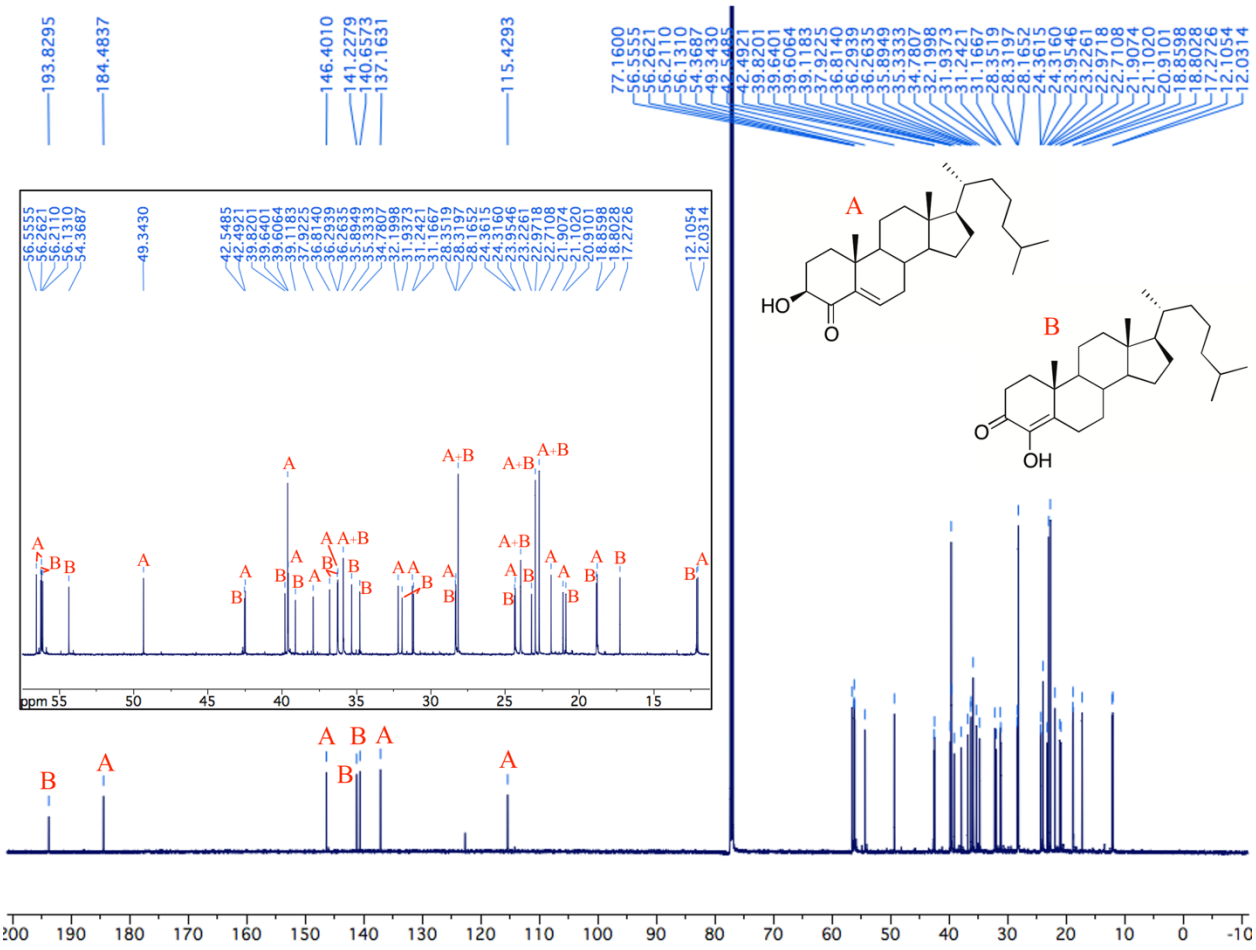

Figure 3.67. ^{13}C NMR spectrum of *4-ketocholesterol* (A) and *4-hydroxycholest-4-ene-3-one* (B) (assignment of the latter based on previous characterization[5]), and zoomed insert.

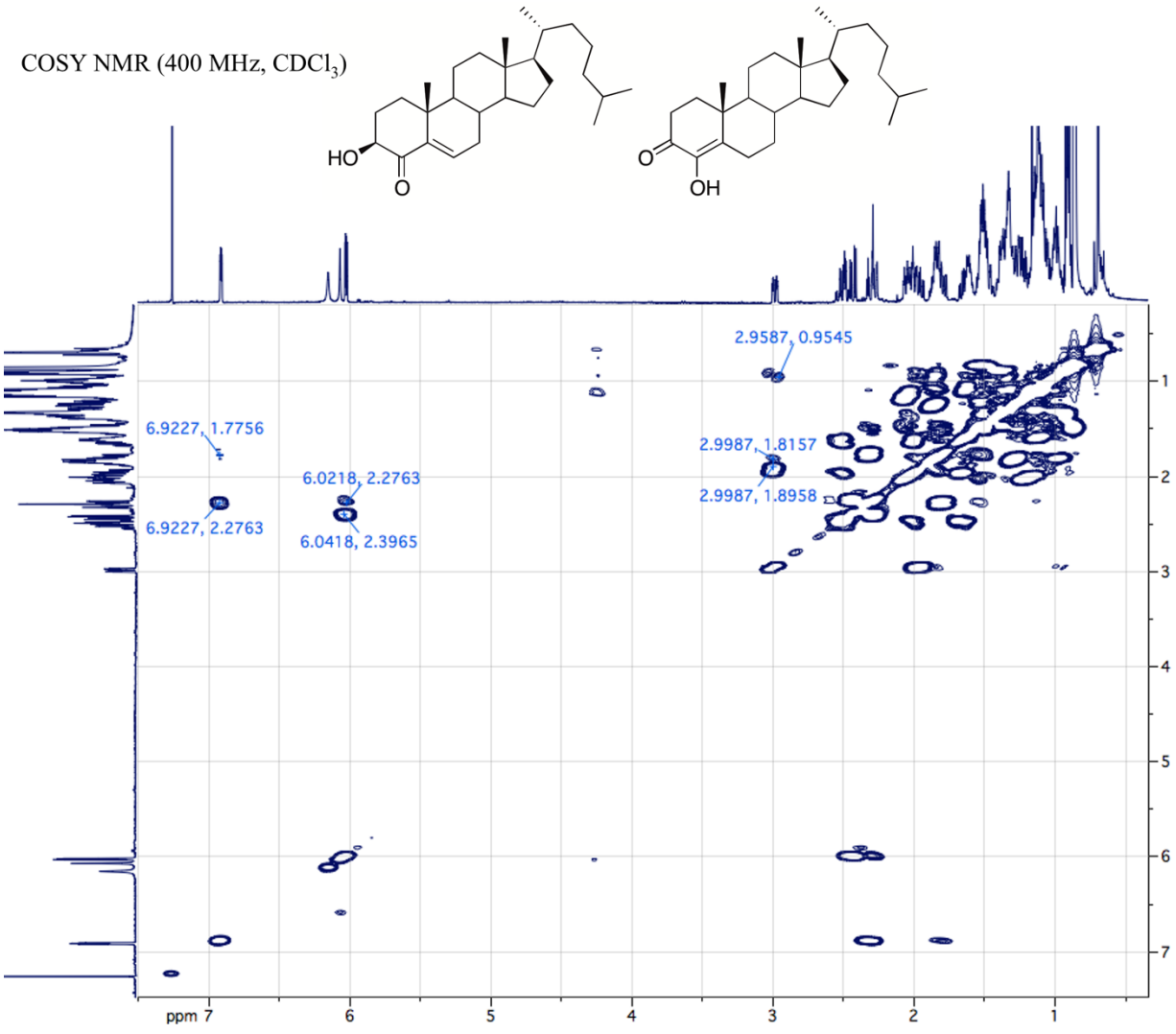

Figure 3.68. COSY NMR spectrum of *4-ketocholesterol* (A) and *4-hydroxycholest-4-ene-3-one* (B).

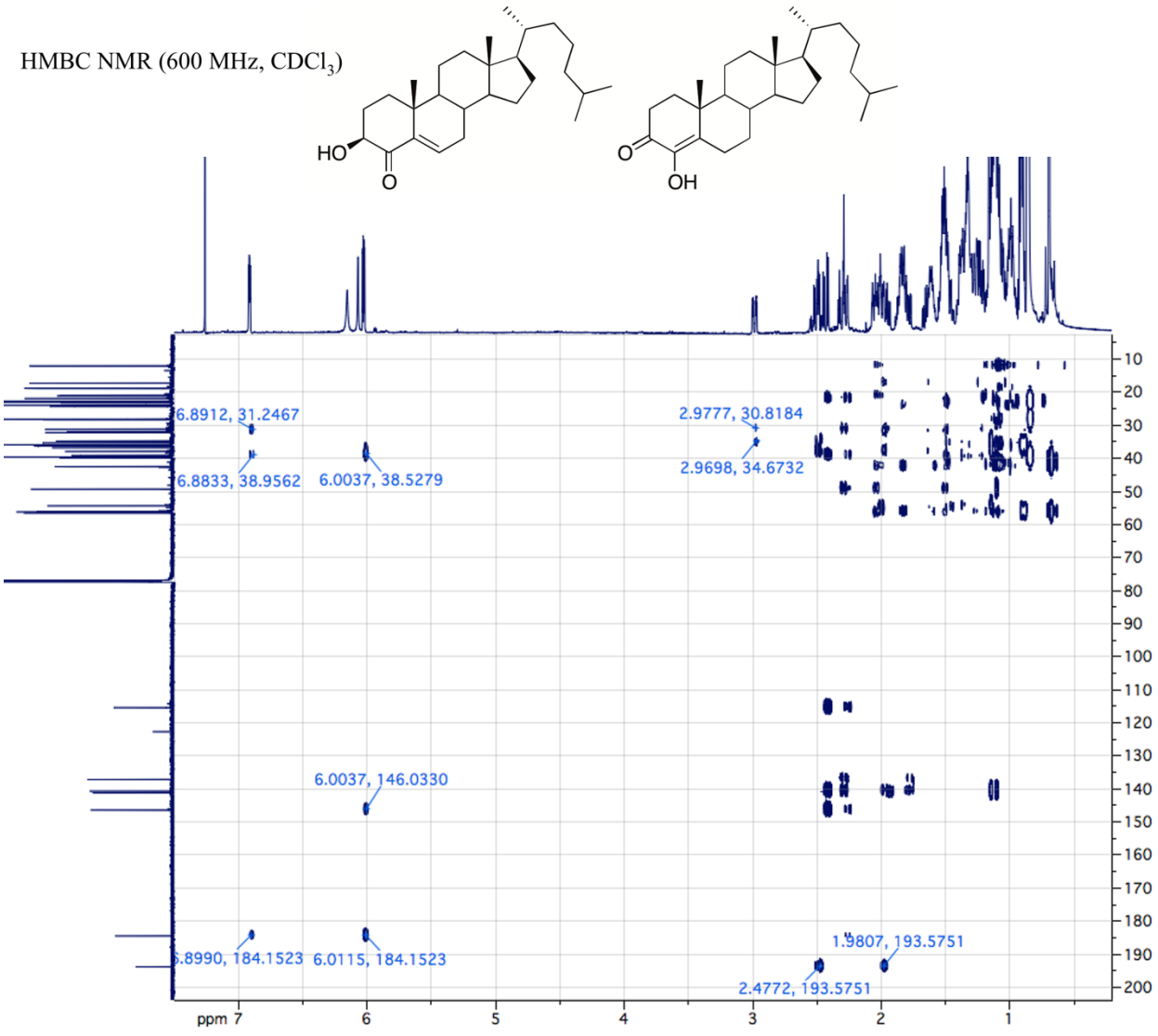

Figure 3.69. HMBC NMR spectrum of *4-ketocholesterol* (A) and *4-hydroxycholest-4-ene-3-one* (B).

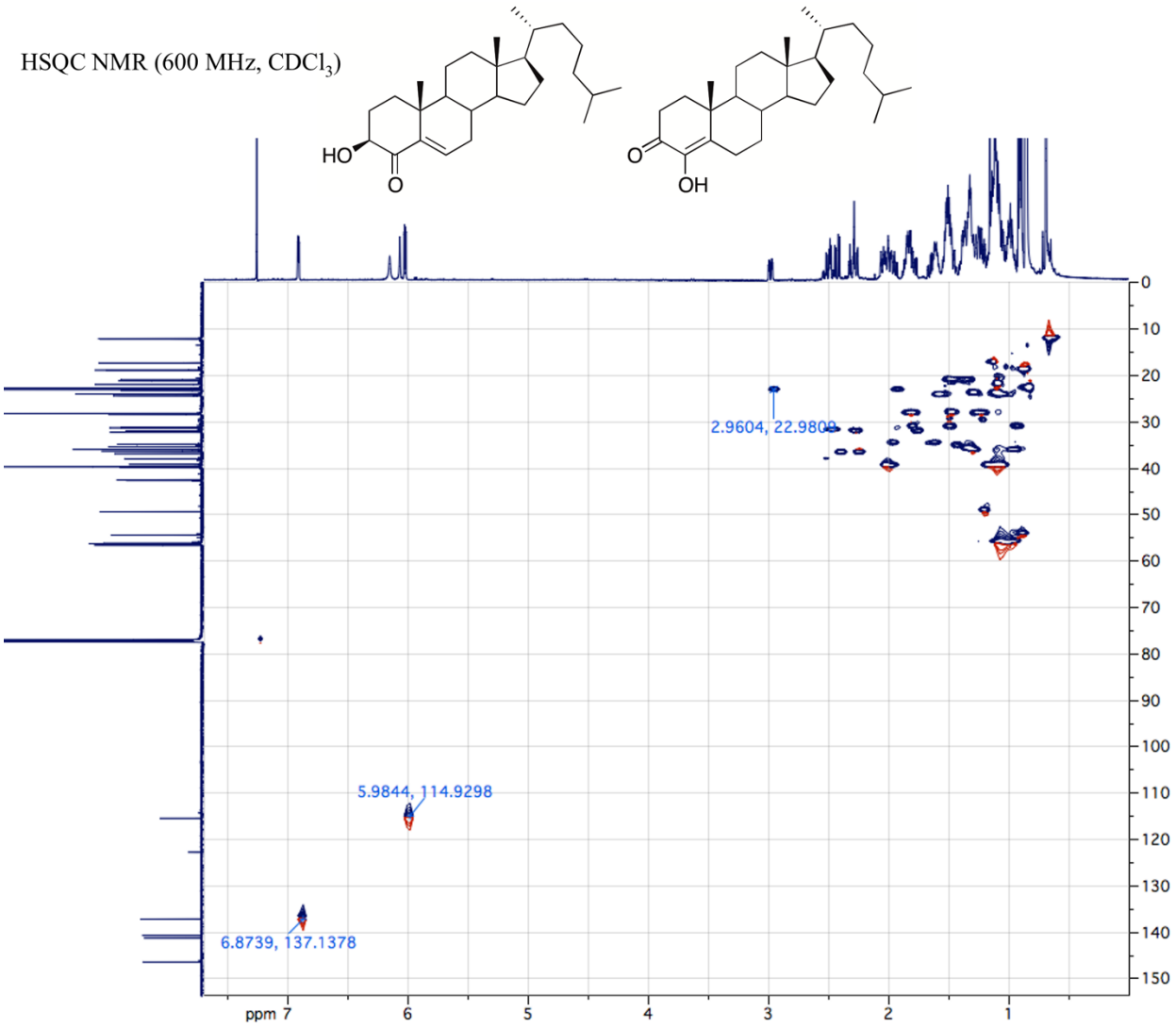

Figure 3.70. HSQC NMR spectrum of *4-ketocholesterol* (A) and *4-hydroxycholest-4-ene-3-one* (B).

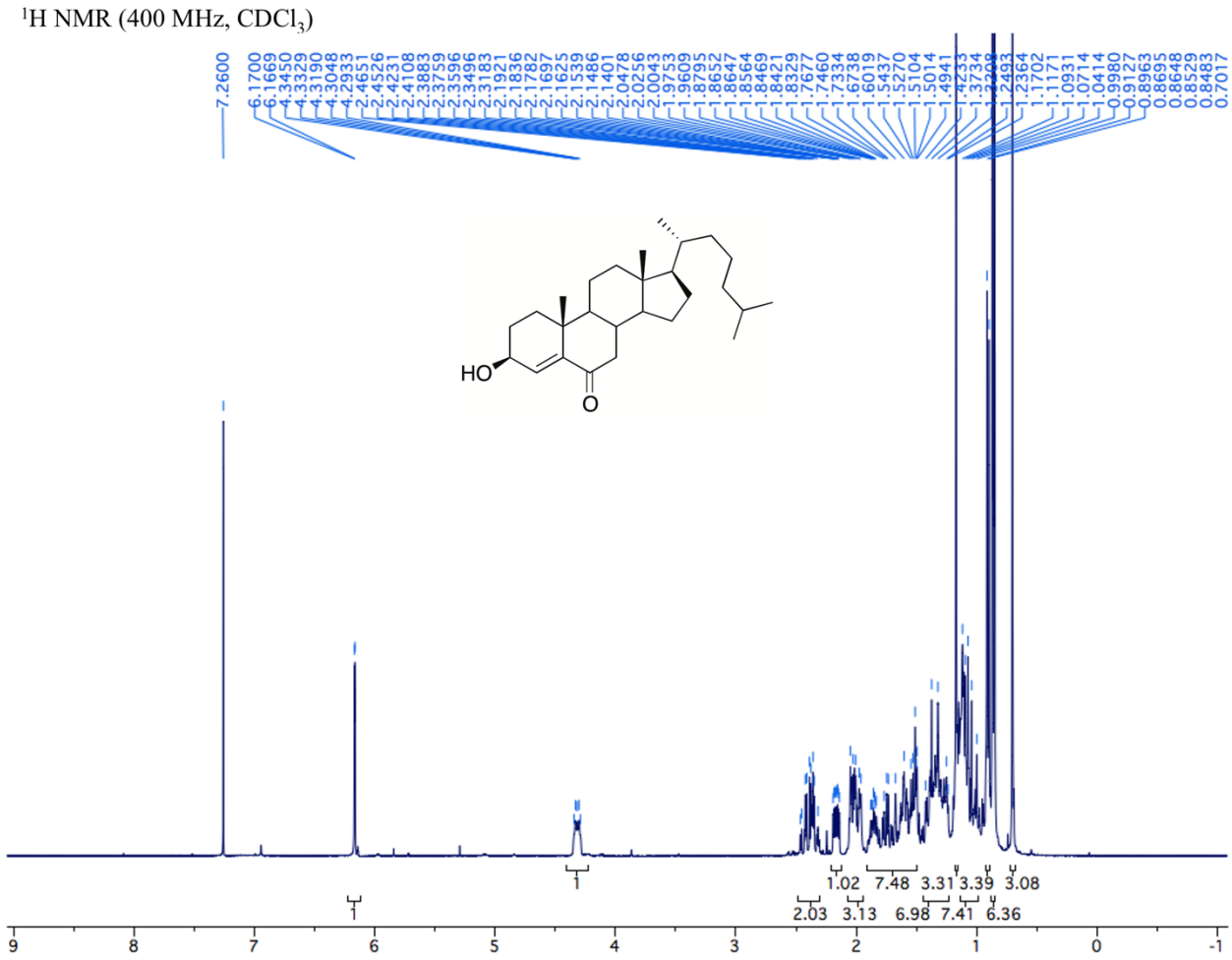

Figure 3.71. ^{1}H NMR spectrum of *6-ketocholesterol*.

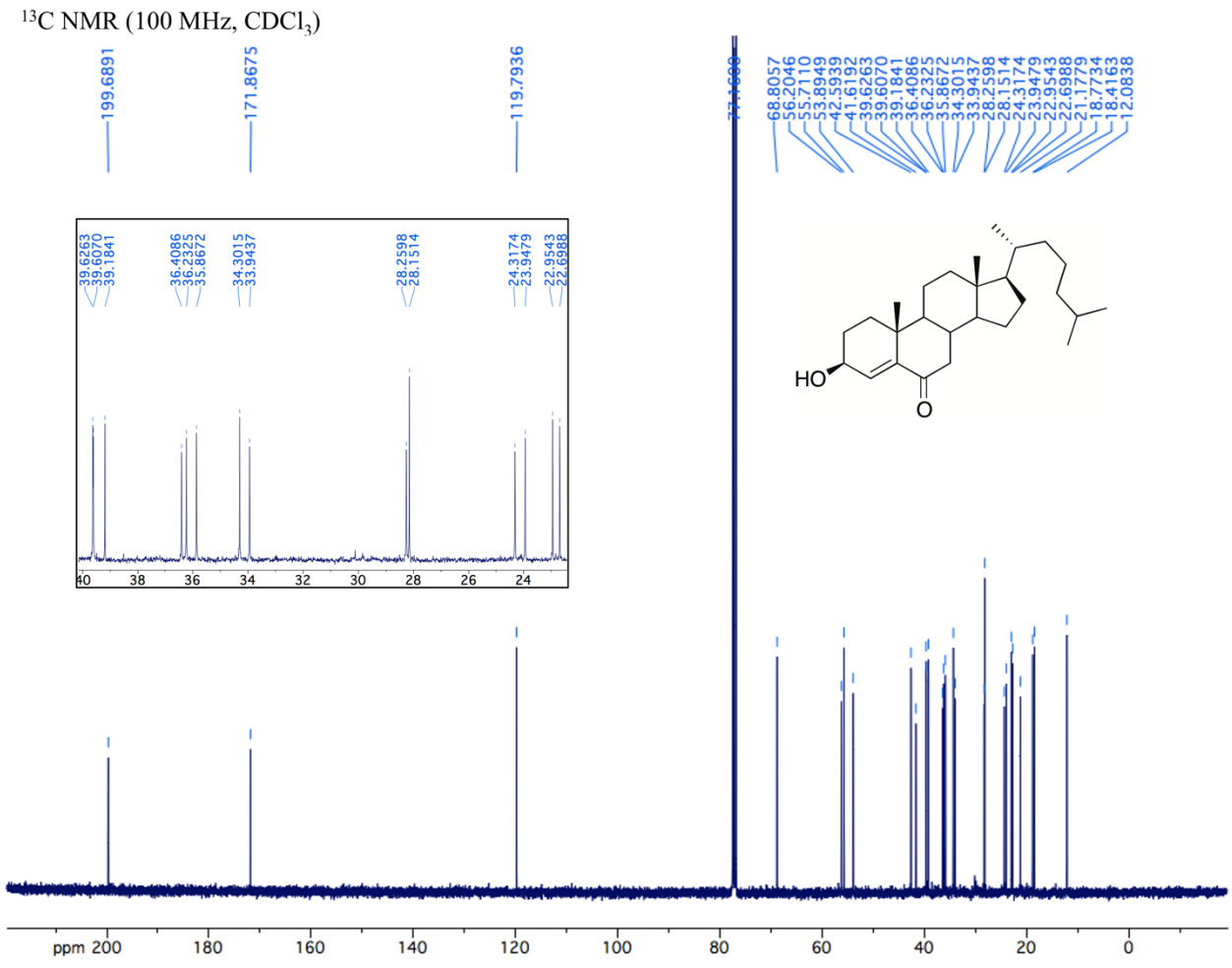

Figure 3.72. ^{13}C NMR spectrum of *6-ketocholesterol*, and zoomed insert.

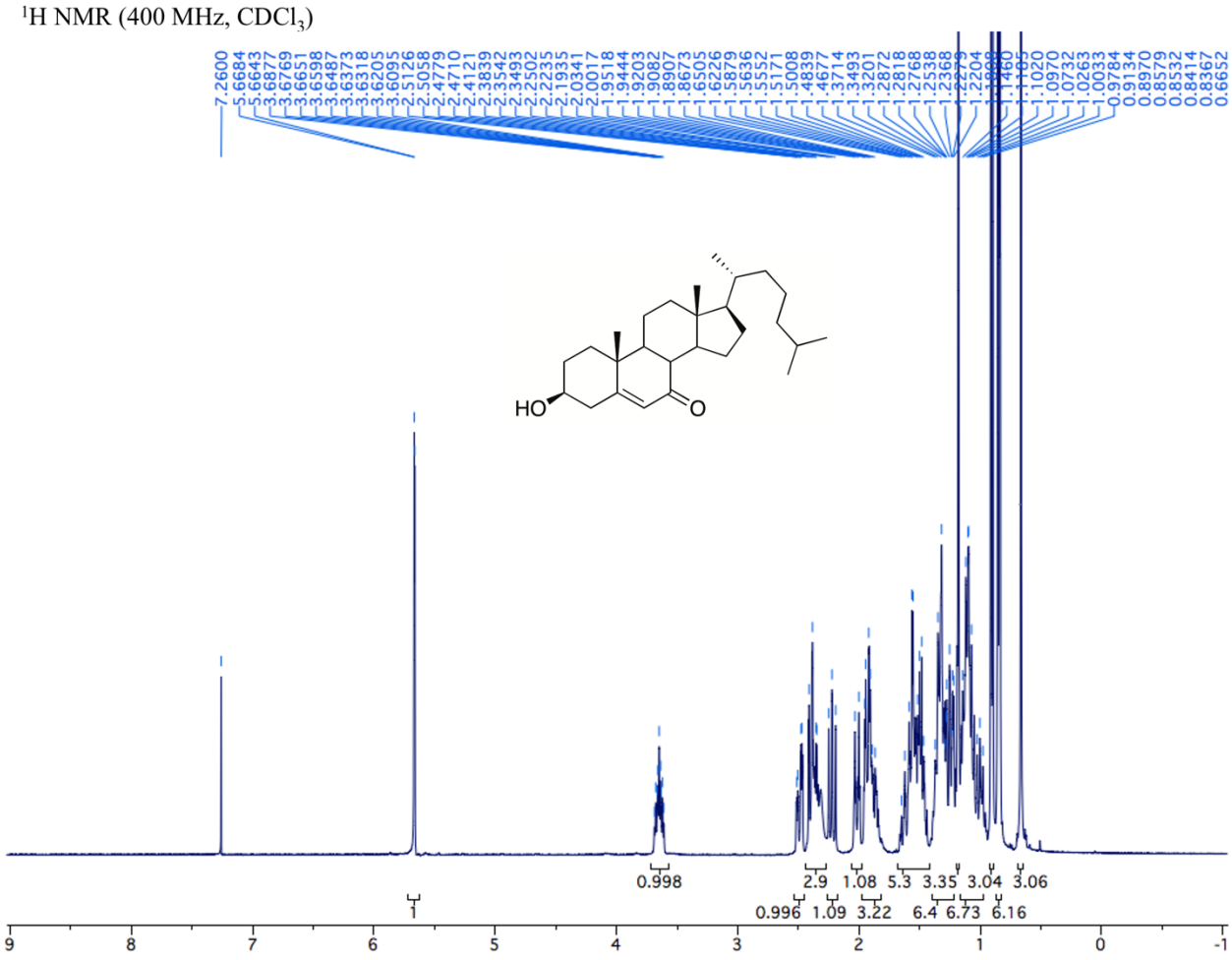

Figure 3.73. ^{1}H NMR spectrum of *7-ketocholesterol*.

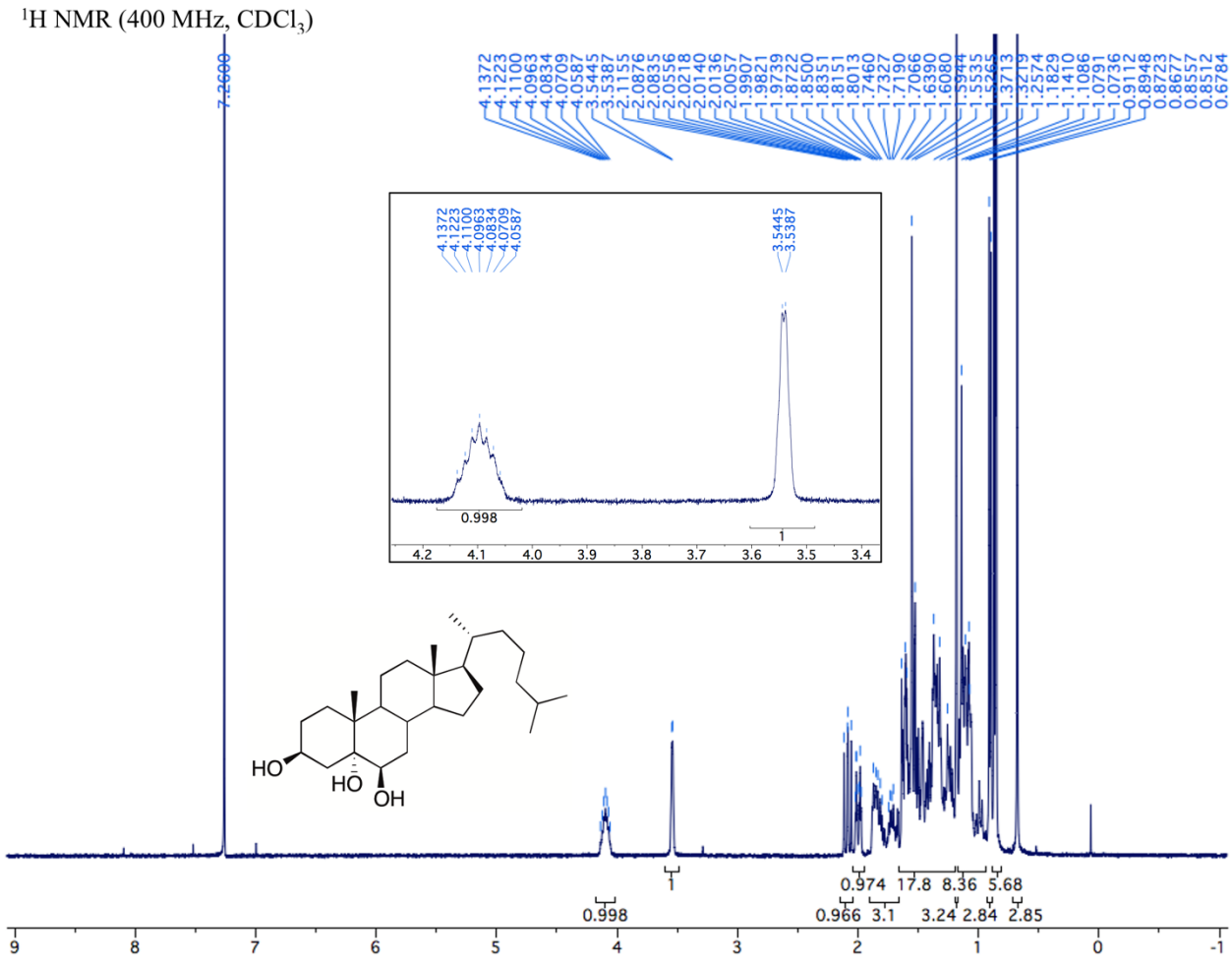

Figure 3.74. ^{1}H NMR spectrum of *cholestane-3β,5α,6β-triol*, and zoomed insert.

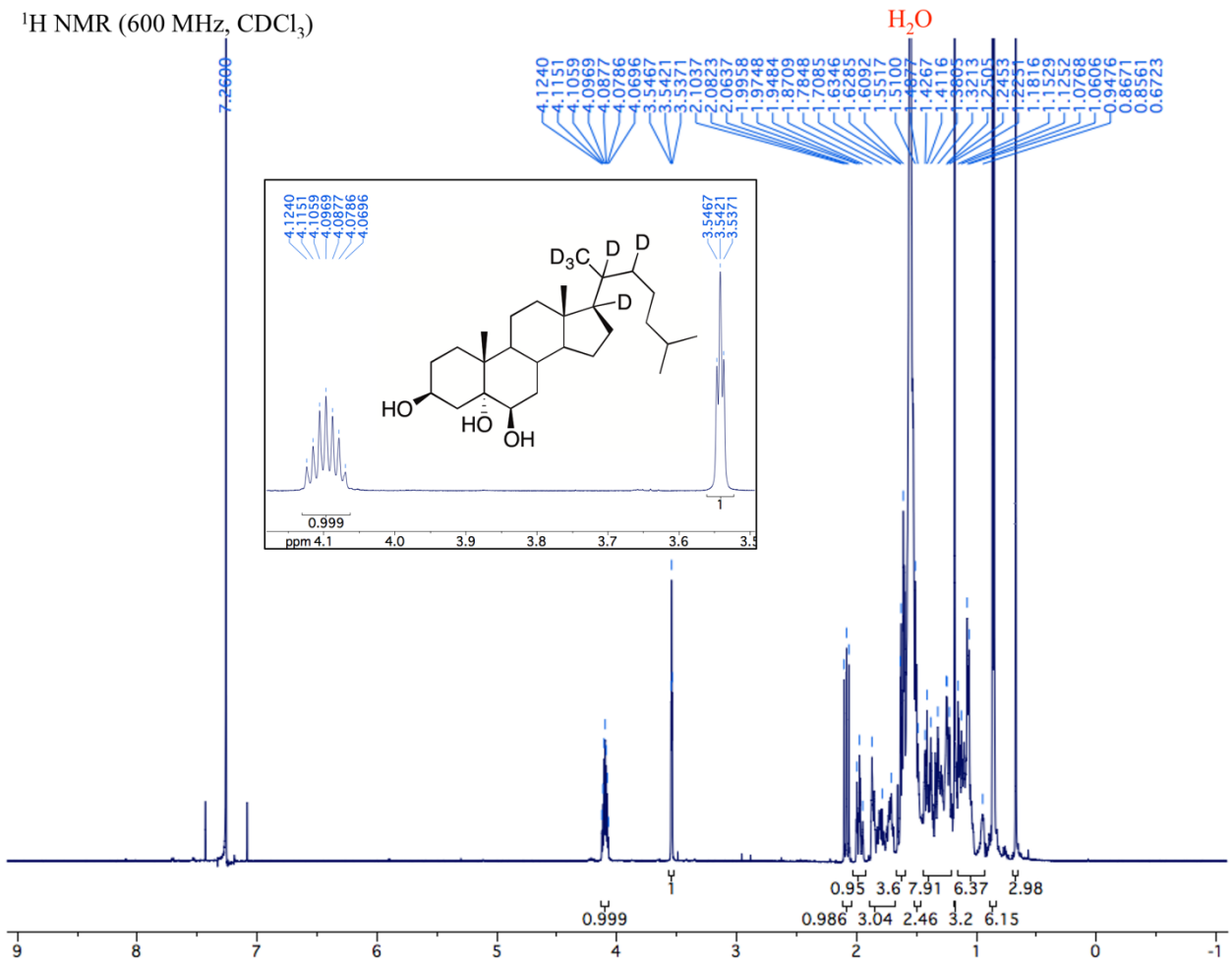

Figure 3.75. ^{1}H NMR spectrum of *cholestane-3β,5α,6β-triol-17,20,21,21,21,22-d_6*, and zoomed insert.

^{13}C NMR (150 MHz, $CDCl_3$)

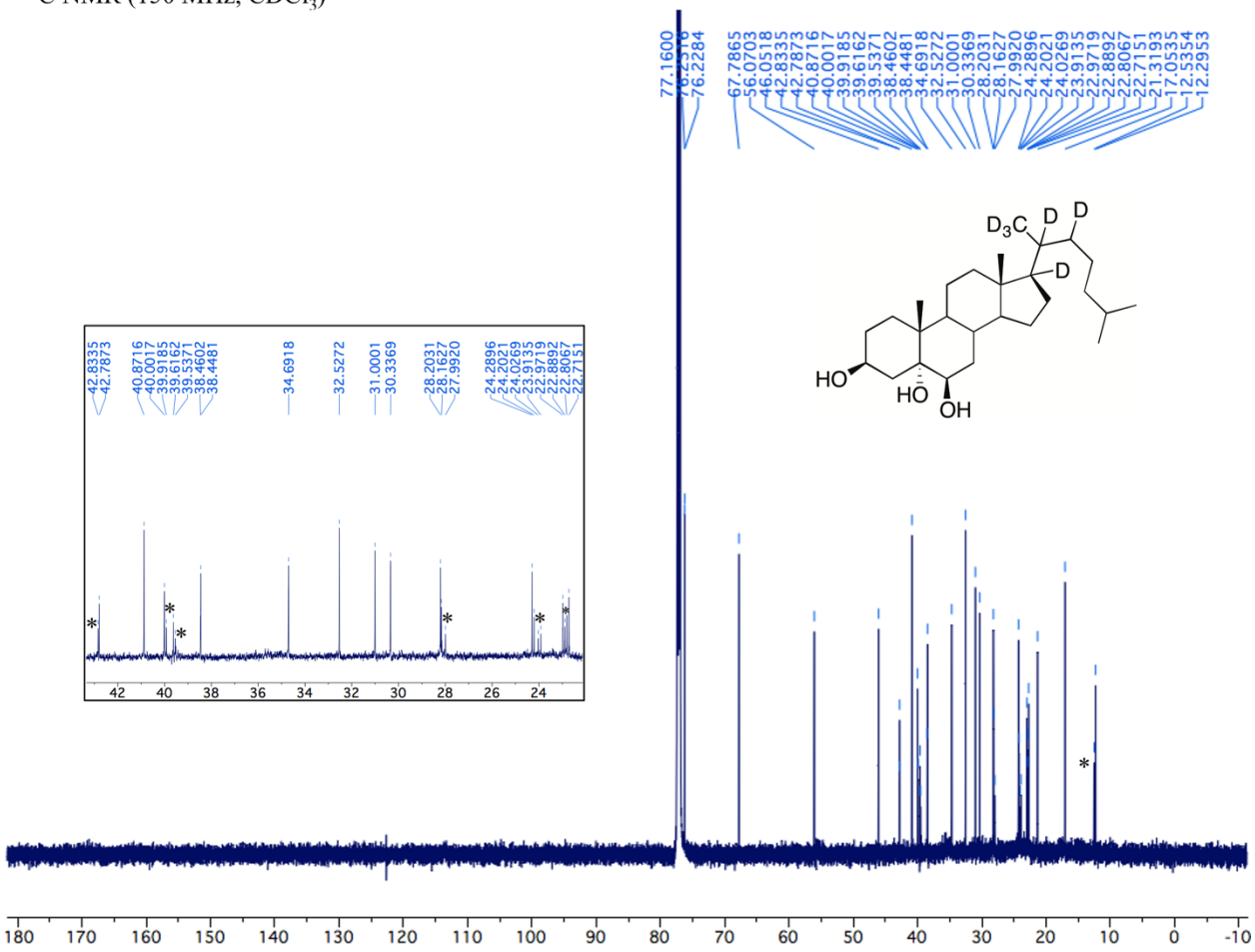

Figure 3.76. ^{13}C NMR spectrum of *cholestane-3β,5α,6β-triol-17,20,21,21,21,22-d*$_6$.

3.9.10 Computational Details

All calculations were carried out using the Gaussian 09 quantum chemistry package[6] using the CBS-QB3 complete basis set approach,[7] with the exception of the calculations for C-O bond length in the protonated chol epoxides (Figure 3.8) which were calculated using only the density functional theory step of CBS-QB3 (B3LYP/CBSB7). To assess the impact of tunnelling in our calculations, the Skodje-Truhlar small-curvature tunnelling approximation for the transmission coefficient[8] was applied as follows:

$$k_{calc} = c_0 \frac{k_B T}{h} e^{\left(-\Delta G^{\ddagger}/RT\right)}$$

$$k_{tunnel} = \kappa(T) \cdot c_0 \frac{k_B T}{h} e^{\left(-\Delta G^{\ddagger}/RT\right)}$$

where k_{calc} is the computed rate constant by transition state theory, and k_{tunnel} incorporates the Skodje-Truhlar tunnelling correction, as follows:

$$\alpha = \frac{2\pi}{h \cdot Im(\nu^{\ddagger})}$$

$$\beta = (k_B T)^{-1}$$

$$if\ \alpha > \beta: \kappa(T) = \frac{\beta\pi/\alpha}{\sin(\beta\pi/\alpha)} - \frac{\beta}{\alpha - \beta} e^{[(\beta-\alpha)(\Delta V^{\ddagger} - V)]}$$

$$if\ \alpha < \beta: \kappa(T) = \frac{\beta}{\beta - \alpha} e^{[(\beta-\alpha)(\Delta V^{\ddagger} - V)]} - 1$$

where h is Planck's constant, $Im(\nu^{\ddagger})$ is the imaginary (negative) frequency of the TS, k_B is Boltzman's constant, T is temperature, and $(\Delta V^{\ddagger} - V)$ is the zero point energy barrier. While we found the addition of the Skodje-Truhlar tunnelling corrections significantly overestimated the computed rate constants, the relative trends of the HAT and peroxyl radical addition pathways, as well as the k_H/k_D values, were much more consistent with the experimental results.

Summary:

Table 3.4. C-H bond strengths.

	BDE (kcal/mol)
Chol C4-H	89.0
Chol C7-H	83.2
Chol OAc C4-H	88.6
Chol OAc C7-H	83.1

Table 3.5. Enthalpy, free energy, and computed rate constant without and with tunnelling correction, for the transition states of H-atom abstraction from chol by a methylperoxyl radical at the positions and with the geometry indicated. All values in kcal/mol.

	$\Delta H^{\ddagger}$	$\Delta G^{\ddagger}$	k_{calc}	k_{tunnel}
4α-H (syn)	13.4	23.9	4.4E-04	2.3E-01
4α-H	14.3	25.0	7.0E-05	6.1E-02
4β-H (H-bond)	7.5	19.4	9.6E-01	6.9E+01
4β-H (syn)	9.7	20.5	1.5E-01	1.3E+02
7α-H (syn)	6.5	17.5	2.4E+01	1.1E+03
7α-H (anti)	8.7	18.9	2.1E+00	2.6E+02
7β-H (syn)	9.1	19.2	1.3E+00	1.9E+02
7β-H (anti)	11.1	21.2	4.4E-02	6.9E+00

Table 3.6. Enthalpy, free energy, and computed rate constant without and with tunnelling correction, for the transition states of H-atom abstraction from chol OAc by a methylperoxyl radical at the positions and with the geometry indicated. All values in kcal/mol.

	$\Delta H^{\ddagger}$	$\Delta G^{\ddagger}$	k_{calc}	k_{tunnel}
4α-H (syn)	12.5	23.3	1.2E-03	5.0E-01
4β-H (syn)	8.7	20.0	3.6E-01	5.4E+01
7α-H (syn)	5.6	16.8	6.9E+01	2.5E+03
7β-H (syn)	9.4	20.1	3.0E-01	4.9E+01

For peroxyl radical addition, given the following scheme:

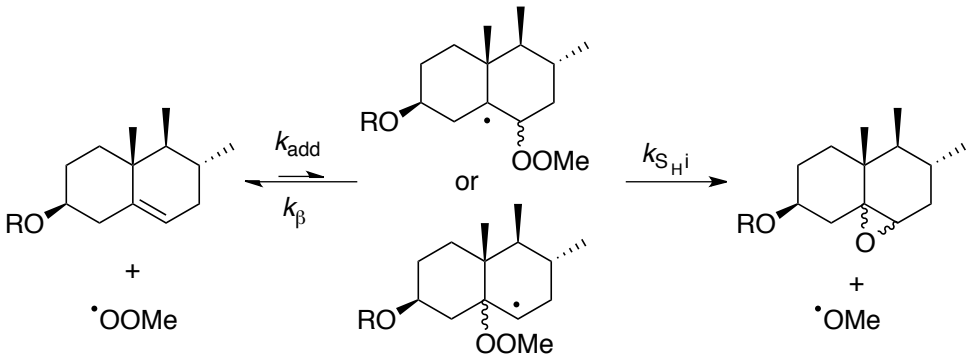

Table 3.7. Free energies (kcal/mol) for the indicated TS, intermediate, or product for the addition of a peroxyl radical to chol or chol OAc. Each value is relative to the starting materials, chol (OAc) + methylperoxyl.

	TS 1	Intermediate	TS 2	Product
5α (chol)	19.3	5.7	15.9	-28.2
5β (chol)	22.0	10.4	18.5	-27.0
6α (chol)	17.9	6.8	13.9	-28.2
6β (chol)	17.6	3.8	13.3	-27.0
6α (chol OAc)	17.6	6.3	14.4	-27.6
6β (chol OAc)	17.9	4.0	13.5	-26.5

Table 3.8. Computed rate constants for peroxyl radical addition to chol or chol OAc (kcal/mol).

	k_{add}	k_{β}	k_{SHi}	k_{calc}
5α (chol)	1.0E+00	1.6E+04	2.2E+05	9.4E-01
5β (chol)	1.0E-02	4.2E+05	7.4E+06	9.9E-03
6α (chol)	1.2E+01	4.7E+04	3.8E+07	1.2E+01
6β (chol)	1.9E+01	4.6E+02	6.6E+05	1.9E+01
6α (chol OAc)	2.0E+01	6.6E+02	8.0E+06	2.0E+01
6β (chol OAc)	1.3E+01	3.8E+02	6.3E+05	1.2E+01

Table 3.9. C-OO• bond strengths for chol-derived peroxyl radicals.

	BDE (kcal/mol)
4α-OO•	26.0
4β-OO•	26.0
5α-OO•	20.4
5β-OO•	17.1
6α-OO•	24.1
6β-OO•	25.2
7α-OO•	21.0
7β-OO•	21.2

Table 3.10. Computed rate constants (M^{-1} s^{-1}) without and with tunnelling corrections (k_{calc} and k_{tunel}, respectively), for the key transition states in H-atom transfer (HAT) from chol to a methylperoxyl, or methylperoxyl addition to chol. The same values for chol-2,2,4,4,7,7-d_6 are included, as well as the corresponding kinetic isotope effects (KIE or k_H/k_D).

	k_{calc} (chol)	k_{calc} (chol-d_6)	KIE (classic)	k_{tunnel} (chol)	k_{tunnel} (chol-d_6)	KIE (tunnelling)
HAT from 4β-H	9.6E-01	1.6E-01	6.1	6.9E+01	1.5E+00	45.7
HAT from 7α-H	2.4E+01	4.2E+00	5.7	1.1E+03	3.7E+01	29.9
Addition to C6 β-face	1.9E+01	1.9E+01	1.0	2.5E+01	2.5E+01	1.0

3.9.11 Supplementary References

(1) Zielinski, Z. A. M.; Pratt, D. A. Cholesterol Autoxidation Revisited: Debunking the Dogma Associated with the Most Vilified of Lipids. *J. Am. Chem. Soc.* **2016**, *138*, 6932.

(2) Carvalho, J. F. S.; Silva, M. M. C.; Moreira, J. N.; Simões, S.; Sá E Melo, M. L. Sterols as Anticancer Agents: Synthesis of Ring-B Oxygenated Steroids, Cytotoxic Profile, and Comprehensive SAR Analysis. *J. Med. Chem.* **2010**, *53*, 7632–7638.

(3) Poirot, M.; Soules, R.; Mallinger, A.; Dalenc, F.; Silvente-Poirot, S. Chemistry, biochemistry, metabolic fate and mechanism of action of 6-oxo-cholestan-3β,5α-diol (OCDO), a tumor promoter and cholesterol metabolite. *Biochimie* **2018**.

(4) Noguchi, N.; Yamashita, H.; Gotoh, N.; Yamamoto, Y.; Numano, R.; Niki, E. 2,2`-Azobis (4-Methoxy-2,4-dimethylvaleronitrile), A New Lipid-Soluble Azo Initiator: Application to Oxidations of Lipids and Low-Density Lipoprotein in Solution and in Aqueous Dispersions. *Free Radic. Biol. Med.* **1998**, *24*, 259.

(5) Thomas, M. G.; Suckling, C. J.; Pitt, A. R.; Suckling, K. E. The synthesis of A- and B-ring fluorinated analogues of cholesterol. *J. Chem. Soc., Perkin Trans. 1* **1999**, 3191–3198.

(6) Frisch, M. J.; Trucks, G. W.; Schlegel, H. B.; Scuseria, G. E.; Robb, M. A.; Cheeseman, J. R.; Scalmani, G.; Barone, V.; Mennucci, B.; Petersson, G. A.; Nakatsuji, H.; Caricato, M.; Li, X.; Hratchian, H. P.; Izmaylov, A. F.; Bloino, J.; Zheng, G.; Sonnenberg, J. L.; Hada, M.; Ehara, M.; Toyota, K.; Fukuda, R.; Hasegawa, J.; Ishida, M.; Nakajima, T.; Honda, Y.; Kitao, O.; Nakai, H.; Vreven, T.; Montgomery, J. A., Jr.; Peralta, J. E.; Ogliaro, F.; Bearpark, M.; Heyd, J. J.; Brothers, E.; Kudin, K. N.; Staroverov, V. N.; Keith, T.; Kobayashi, R.; Normand, J.; Raghavachari, K.; Rendell, A.; Burant, J. C.; Iyengar, S. S.; Tomasi, J.; Cossi, M.; Rega, N.; Millam, J. M.; Klene, M.; Knox, J. E.; Cross, J. B.; Bakken, V.; Adamo, C.; Jaramillo, J.; Gomperts, R.; Stratmann, R. E.; Yazyev, O.; Austin, A. J.; Cammi, R.; Pomelli, C.; Ochterski, J. W.; Martin, R. L.; Morokuma, K.; Zakrzewski, V. G.; Voth, G. A.; Salvador, P.; Dannenberg, J. J.; Dapprich, S.; Daniels, A. D.; Farkas, O.; Foresman, J. B.; Ortiz, J. V.; Cioslowski, J.; Fox, D. J. *Gaussian 09, revision E.01*; Gaussian, Inc.: Wallingford CT, 2009.

(7) Montgomery, J. A.; Ochterski, J. W.; Petersson, G. A. A complete basis set model chemistry. IV. An improved atomic pair natural orbital method. *J. Chem. Phys.* **1994**, *101*, 5900.

(8) Skodje, R. T.; Truhlar, D. G.; Garrett, B. C. A general small-curvature approximation for transition-state-theory transmission coefficients. *J. Phys. Chem.* **2002**, *85*, 3019.

Chapter 4: Tunnelling Underlies the Preference for H-Atom Abstraction in the Reaction of Unsaturated Lipids and Peroxyl Radicals

4.1 Preface

In recent years, there have been a handful of accounts of tunnelling in autoxidations (e.g. tetralin,[1] linoleate,[2,3] and 7-dehydrocholesterol[4]). We have shown (in Chapter 3) that this is the case in H-atom abstraction from cholesterol as well. Herein, we suggest that these reports are likely the rule and not the exception. The key steps in the propagation and inhibition of autoxidation involve the transfer of an H-atom to a peroxyl radical, and this type of transformation is prone to tunnelling; however, it may only be measurable at ambient temperature when the reaction barrier is sufficiently high. To better understand the contribution to tunnelling in hydrocarbon autoxidation and its inhibition, we carried out computations on a series of hydrocarbons , finding that the barrier height is the primary determinant for tunnelling in these reactions. Hence, we anticipated that H-atom abstraction from the simplest unsaturated lipid, oleic acid, would be subject to a large kinetic isotope effect (KIE). Furthermore, given that epoxides derived from peroxyl radical addition have, to our knowledge, never been reported to be products of oleate autoxidation, we wondered if such products may be formed if the labile hydrogens were replaced with deuterium atoms. To test this, we conducted autoxidations on hexadec-8-ene and its deuterated counterpart 7,7,10,10-d_4-hexadec-8-ene, which serves as a model for oleate. The measured KIE on H-atom abstraction was 18±1, suggesting tunnelling does, indeed, underlie the preference for H-atom abstraction vs. addition to the alkene, similar to what we recently reported for cholesterol (cf. Chapter 3). Surprisingly, epoxides were detected under all conditions studied, albeit as minor products. These results helped to solidify the hypothesis presented in Chapter 3 – that quantum mechanical tunnelling is primarily responsible for the susceptibility of lipids and other unsaturated hydrocarbons to autoxidation by H-atom transfer rather than addition.

4.2 Introduction

In the 1880's, Arrhenius was the first to demonstrate that a rate constant, *k,* varies with temperature, but is also proportional to the activation energy, E_a, as outlined in the Arrhenius equation (eq. 4.1). A few decades later Transition State Theory was developed, wherein Eyring related the rate constant, *k*, to thermodynamic quantities by first principles. Thus, the Eyring equation (eq. 4.2) allowed for the calculation of barriers if a rate constant was known, or vice versa. It was later realized that quantum mechanical tunnelling can also impact rate constants, and the so-called "classical" behaviour described by the Eyring equation may not fully capture experimental phenomena. Tunnelling is due to the wave-particle duality of matter; while a particle obeys classical behaviour and must traverse a reaction barrier, a wave can pass through the barrier (cf. Figure 4.1). This quantum mechanical "short-cut" augments the rate constant, which is why in the 1970's Bell proposed including a tunnelling coefficient, *Q*, to the Eyring equation to account for this pathway (eq. 4.3).[5,6]

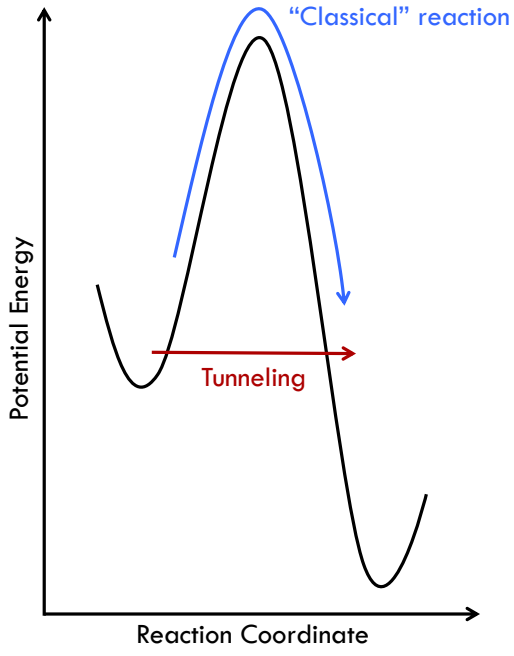

$$k = Ae^{-E_a/RT} \tag{4.1}$$

$$k = \frac{k_B T}{h} e^{-\Delta G^{\ddagger}/RT} \tag{4.2}$$

$$k = Q\frac{k_B T}{h} e^{-\Delta G^{\ddagger}/RT} \tag{4.3}$$

Figure 4.1. A model reaction coordinate diagram showing a classical reaction (blue) or a pathway tunnelling through the barrier (red), and equations 4.1-4.3 (right).

While a deep dive into the physics of tunnelling is beyond the scope of the present study, there are a few factors worth considering. The tunnelling coefficient, Q, is represented by equations 4.4-4.6. The term $2a$ denotes the barrier width, which captures the fact that tunnelling is more facile through a narrower barrier. In other words, since the reaction coordinate (x-axis of a reaction coordinate diagram) is made up of the geometrical coordinates of the reactants and products, tunnelling is more facile when the reactants and products are geometrically similar. Another important factor is the mass of the particle(s) tunnelling, denoted by the term m, which incorporates into equations 4.4-4.6 the concept that heavier particles are less likely to tunnel. While there have been reports of heavy-atom tunnelling (for example, carbon tunnelling[7]), the vast majority of the experimental evidence for tunnelling involves significantly lighter particles, for example, in electron, proton, H-atom, and hydride transfers.[5]

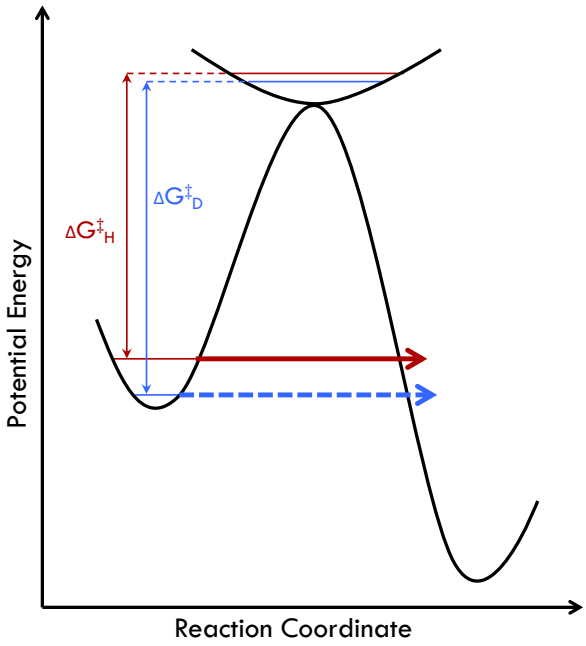

$$Q = \frac{e^{\alpha}}{\beta - \alpha}\left(\beta e^{-\alpha} - \alpha e^{-\beta}\right) \qquad (4.4)$$

$$\alpha = E/RT \qquad (4.5)$$

$$\beta = 2a\pi^2(2mE)^{1/2}/h \qquad (4.6)$$

Figure 4.2. A model reaction coordinate diagram for a H- or D-atom transfer from a C-H or C-D bond, showing that the $\Delta G^{\ddagger}$ for a deuterium atom is greater than the $\Delta G^{\ddagger}$ for the protiated analogue, based on the zero-point vibrational energy difference from the starting materials to the transition state. Furthermore, the H-atom is far more likely to tunnel (red) than the D-atom (blue). Equations 4.4-4.6 are also shown (right).

Kinetic isotope effects are often used to experimentally support whether or not tunnelling plays a role in accelerating a particular reaction. Figure 4.2 shows a model reaction coordinate diagram to a H- or D-atom transfer from a C-H or C-D bond. The classical limit for a deuterium kinetic isotope effect (KIE or k_H/k_D) is ~ 7 at room temperature, which is a result of the differences in zero-point vibrational energies of the two isotopes in the reactants (C-H vs. C-D vibration) compared to in the transition state (TS). In the TS, the C-H and C-D bonds become weaker, and the difference in zero-point vibrational energies is smaller. As a result, the D-atom transfer has a larger activation free energy ($\Delta G^{\ddagger}$), and correspondingly, a smaller rate constant. However, if tunnelling is involved, the above classical explanation is incomplete. A deuterium atom is twice the mass of a hydrogen atom and thus it is significantly less likely to tunnel. Furthermore, the vibrational frequency is lower for deuterium and the barrier is wider, also decreasing the chances of tunnelling. Thus, experimentally determined KIEs wherein the k_H is accelerated due to tunnelling result in KIEs greater than the classical limit. On the other hand, computational models do not explicitly account for tunnelling, so another method used to support whether or not tunnelling plays a role in accelerating a reaction is whether the computed rate constant is significantly altered by the incorporation of tunnelling corrections (which will be discussed in more detail in section 4.3.1).[5,8]

The autoxidation of linoleic acid, the simplest polyunsaturated fatty acid, and its esters have been extensively studied, and the propagation rate constant (k_p) determined to be 62 $M^{-1}s^{-1}$.[9] More recently, the deuterium kinetic isotope effect on the propagation of linoleic acid autoxidation was studied relative to 11,11-d_2-linoleic acid. The KIE was measured to be ca. 13 for abstraction by a chain-carrying linoleate-derived peroxyl radical,[2] and 23 in α-tocopherol-loaded autoxidations[3] where the propagating species is more likely to be a tocopheroxyl radical. The large KIE suggests that tunnelling is involved in the H-atom abstraction. Similarly, the KIE determined for abstraction from the 1-position of tetralin has been measured as ca. 16,[1] albeit the experiments were conducted at 65°C; therefore, the KIE is likely to be significantly greater at lower temperatures (the foregoing

experimental results are summarized in Table 4.1). While KIEs are naturally temperature dependent, this is exacerbated when tunnelling contributes to the reaction of the protiated analogue, as demonstrated in Figure 4.3. Thus tunnelling is most easily observed at low temperatures, or when the reaction barriers are high enough that the over-barrier path does not completely dominate at the given temperature.[8] In other words, reactions with relatively low barriers may involve tunnelling at low temperatures; however, at temperatures wherein the reactants (whether protiated or deuterated) have sufficient energy to easily overcome the reaction barrier, the tunnelling pathway may not be as significant.

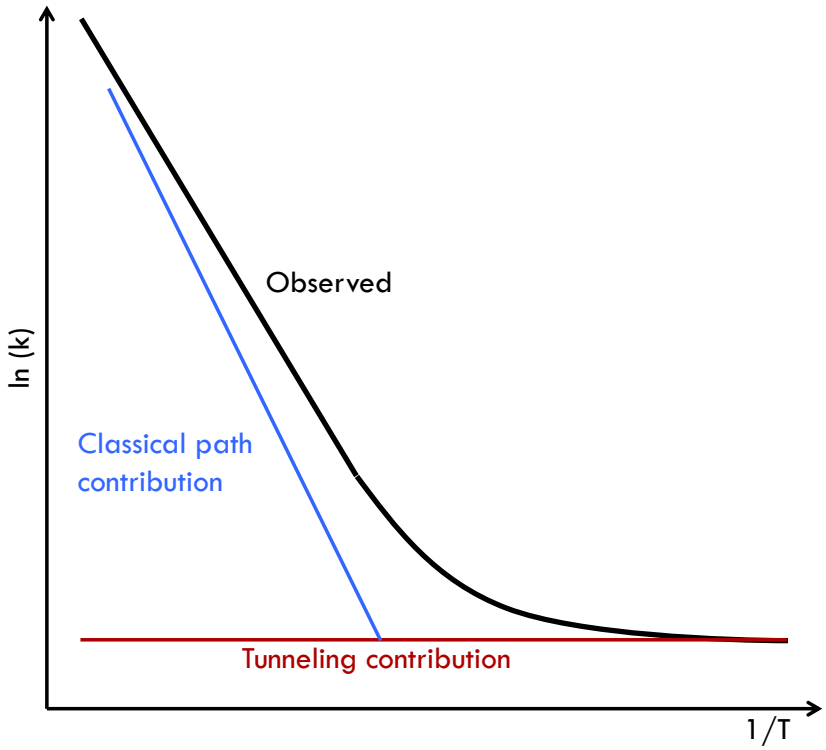

Figure 4.3. A model Eyring plot for a theoretical reaction where tunnelling contributes to the observed rate constant, showing that the classical path dominates at higher temperatures and the tunnelling path dominates at lower temperatures.

In their study of the KIE in tetralin, Porter *et al.* concluded that, as compared to enzymatic transformations:

> "[t]he extent of tunnelling that accompanies hydrogen atom transfer to peroxyls in solution has been the subject of less rigorous experimental and theoretical analyses. The high H(D) KIEs reported here for tetralin autoxidation calls for further examination of structure−reactivity patterns for hydrogen atom transfer from C−H bonds to peroxyl radicals in solution coupled with a theoretical analysis of such transformations." [1]

Other examples of large KIEs in the context of autoxitaions include tocopherol-loaded autoxidations of 11,11,14,14- d_4-α-linolenic acid[3] and 9,14-d_2-7-dehydrocholesterol,[4] which yielded KIEs of 32 and 21, respectively. Furthermore, we recently measured a KIE for cholesterol autoxidation (relative to 2,2,4,4,7,7-d_6-cholesterol) of ca. 20 (cf. Chapter 3).[10] These results piqued our interest in the contribution of tunnelling in H-atom transfer reactions, in particular to peroxyl radicals, in general. Indeed, the foregoing handful of examples begs for an exploration of why tunnelling may occur in these instances – are they surprising outliers (exceptional), or are they "the rule"?

4.3 Results

4.3.1 Modelling Tunnelling Computationally

Following the recent reports of tunnelling in in H-atom abstractions by peroxyl radicals from hydrocarbons, we set out to explore these cases in more detail. As mentioned above, calculations can be done with and without tunnelling corrections, to help support an experimental KIE that suggests tunnelling may occur.[8] To assess the contribution of tunnelling computationally, calculations were carried out on model compounds using the Gaussian 09 quantum chemistry package[11] using the CBS-QB3 complete basis set approach.[12] The rate constants for H- or D-atom abstraction (k_H and k_D) were calculated from the thermochemical data using transition state theory (eq. 4.7), where c_0 is a normalization factor required for a bimolecular reaction such that $c_0 = RT/P$.

$$k_{calc} = c_0 \frac{k_B T}{h} e^{\left(-\Delta G^{\ddagger}/RT\right)} \kappa(T) \qquad (4.7)$$

$$\kappa(T) = \frac{\beta\pi/\alpha}{sin(\beta\pi/\alpha)} - \frac{\beta}{\alpha-\beta} e^{[(\beta-\alpha)(\Delta V^{\ddagger}-V)]}, \text{ if } \alpha \geq \beta \quad (4.8)$$

$$\kappa(T) = \frac{\beta}{\beta-\alpha} e^{[(\beta-\alpha)(\Delta V^{\ddagger}-V)]}, \text{ if } \beta \geq \alpha \quad (4.9)$$

$$\alpha = 2\pi/\mathrm{hIm}\left(v^{\ddagger}\right) \quad (4.10)$$

$$\beta = (k_B T)^{-1} \quad (4.11)$$

Tunnelling was accounted for in the computed rate constants using Skodje-Truhlar tunnelling corrections, κ(T),[13,14] as in equations 4.8-4.11. This is a parabolic approximation to the minimum energy path, where $(\Delta V^{\ddagger} - V)$ is the reaction energy barrier and $\mathrm{Im}\left(v^{\ddagger}\right)$ is the (negative) frequency of the vibrational mode in the transition state that corresponds to the H- or D-atom transfer. It is worth noting that κ(T) is merely an approximation of the tunnelling coefficient, *Q*, described in equations 4.3-4.6, and while more sophisticated approximations exist, the Skodje-Truhlar method offers what we deemed to be an acceptable compromise between accuracy[13] and computational feasibility.

Calculations were carried out on: a model of non-conjugated polyunsaturated fatty acids such as linoleic and linolenic acids (1,4-pentadiene); a cholesterol model; and tetralin, for the relevant H- and D-atom abstractions by a methylperoxyl radical (cf. Table 4.1). The KIE for abstraction of a bis-allylic H-atom at room temperature for 1,4-pentadiene was computed to be 23.5 with tunnelling corrections (compared to 3.1 without). This agrees well with the experimental value of 13 at 37°C, and underscores the contribution of tunnelling in the H-atom abstraction. We recently reported that the KIE for cholesterol autoxidation (relative to 2,2,4,4,7,7-d_6-cholesterol) was measured to be ca. 20 at 37°C (cf. Chapter 3).[10] Therein we discussed that H-atom abstraction occurs from both the C4-H and C7-H, though for simplicity we discuss only the most preferred C7α-H abstraction here. Similar to linoleate, the computed cholesterol model agrees well with experiment: the computed KIE at room temperature of 29.9 supports the experimental evidence for tunnelling in the H-atom abstraction, as compared to a computed KIE of 5.7 without tunnelling corrections. The KIE determined for

abstraction from the 1-position of tetralin has been measured as ca. 16,[1] though this value is expected to be greater at temperatures lower than 65°C, *vide supra*. Indeed the computed KIE at room temperature is predicted to be 4-fold larger (a value of 63).

In all three cases set forth in Table 4.1, the experimental evidence of tunnelling is supported by the computed KIEs when tunnelling corrections are included; thus this computational approach appears to corroborate the notion that tunnelling is important in these reactions. We note that the barrier for linoleate should be lower than that for cholesterol, based on the 6-fold increase in the experimentally determined k_p, and this is not reflected in the computational results. We suspect the truncated computational model 1,4-pentadiene lacks the hyperconjugative effect of the alkyl groups present in linoleate; thus the barrier is likely overestimated for this reason. Furthermore, as mentioned above, the computed barrier for the cholesterol model in Table 4.1 is for the most favourable 7α-H abstraction. As demonstrated experimentally in Chapter 3, C-H abstraction also occurs from the 4-position; therefore, the effective barrier is likely higher when considering abstraction may occur at either position, on the α- or β-face of the sterol framework.

The computed transition state (TS) structures for the systems of Table 4.1 are shown in Figure 4.4. The HAT TS in each instance adopts the preferred syn-geometry, which allows the internal peroxyl oxygen to participate in a secondary orbital interaction with the π-system in 1,4-pentadiene, tetralin, or cholesterol. This interaction is evident in the highest (fully) occupied molecular orbitals (HOMOs) which have in-phase overlaps, whereas the singly occupied molecular orbitals (SOMOs) have out-of-phase interactions about the plane of the H-atom transfer. The significance of this interaction will be discussed in more detail in Chapters 5 and 6.

Table 4.1. Experimental propagation rate constants (k_p), computed reaction barriers ($\Delta \boldsymbol{G}^{\ddagger}_{\boldsymbol{calc}}$), as well as experimental and computed deuterium kinetic isotope effects (KIE or k_H/k_D) for linoleate, cholesterol, and tetralin H- or D-atom abstraction by a methylperoxyl radical. The abstracted H- or D-atoms are indicated in the computational models.

Experimental			**Computational**		
substrate	k_p (M^{-1} s^{-1})	k_H/k_D	model	$\Delta G^{\ddagger}_{calc}$ (kcal/mol)	$(k_H/k_D)_{calc}$ (at 25°C)
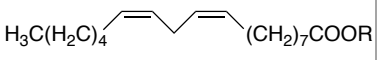 linoleate	62	13 (at 37°C)	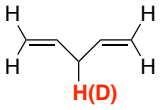	18.8	23.5
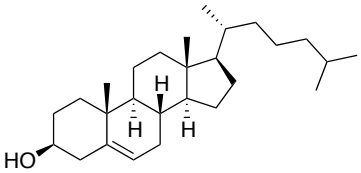 cholesterol	11	20 (at 37°C)	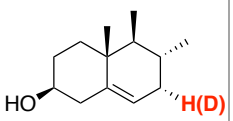	17.5	29.9
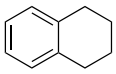 tetralin	6	16 (at 65°C)	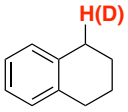	20.0	62.7

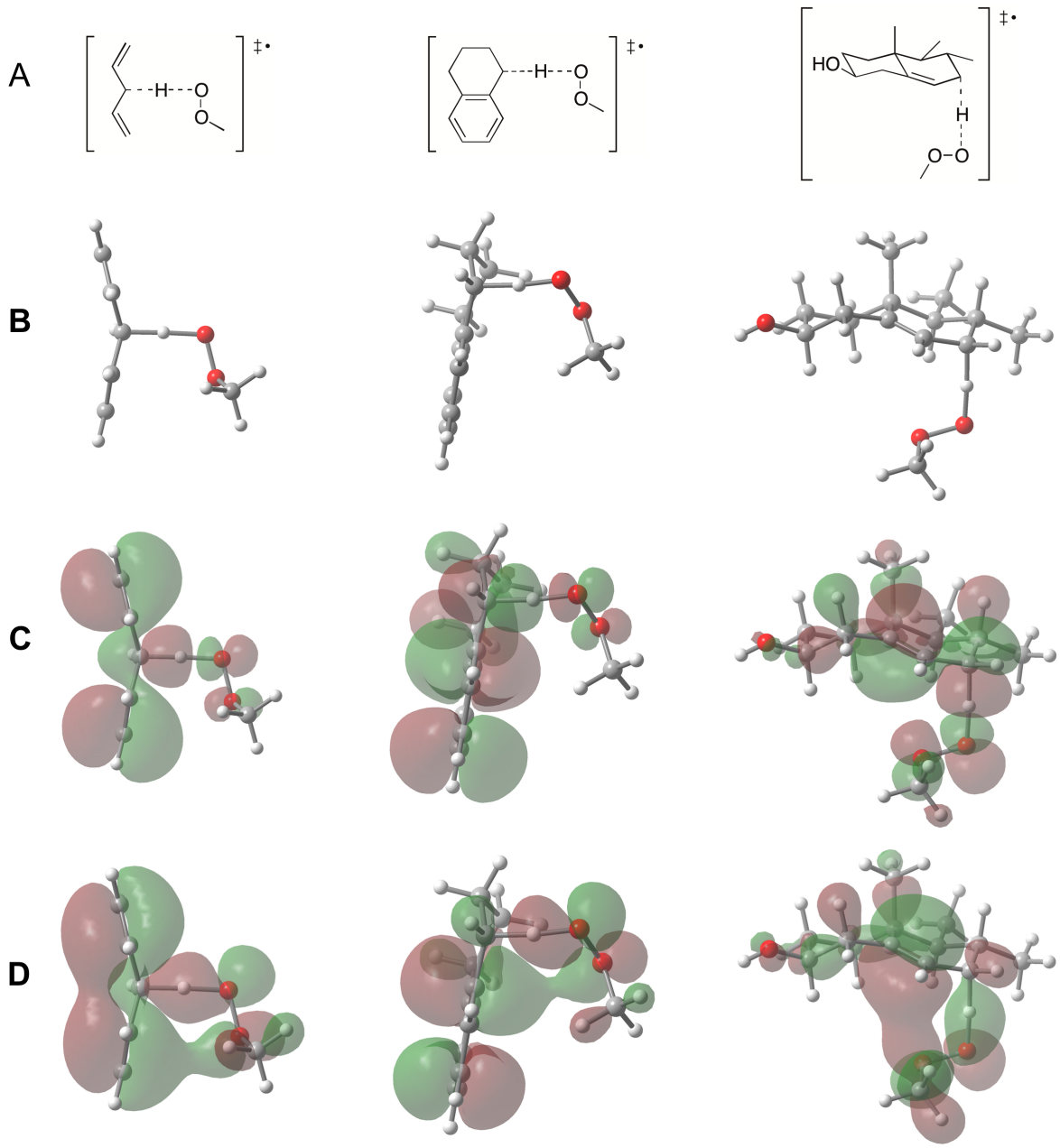

Figure 4.4. ChemDraw (A) and CBS-QB3 computed (B) transition state structures for H-atom transfer to a methylperoxyl radical from 1,4-pentadiene (linoleate model), tetralin, or a cholesterol model. The singly occupied molecular orbitals (C) and highest (fully) occupied molecular orbitals (D) are included for the computed structures.

Figure 4.4 shows the reaction barriers for these H-atom transfer reactions. Recalling equations 4.4-4.6 defining the tunnelling coefficient, *Q*, the key factors to efficient tunnelling are the barrier shape and mass of the particle tunnelling. The barrier shape is important for two main reasons:

first, the barrier width (i.e. geometries of the reactants as compared to the products) is important as particles are more likely to tunnel through a narrow barrier (i.e. one requiring little reorganization in geometry); and second, the barrier height is important as tunnelling is more likely to be observed at temperatures where the reactants do not have enough energy to easily overcome the barrier. In the reactions shown in Figure 4.3, the transfer of an H-atom from a C-H bond to a peroxyl radical involves little geometrical reorganization apart from the transfer of the H-atom itself; thus they involve a light particle and a narrow barrier. These factors make these HAT reactions prime candidates for tunnelling. As demonstrated in Figure 4.3, tunnelling is typically observed at temperatures where the over-barrier path remains slow. Therefore, the fact that tunnelling has been observed at 37°C for linoleate and cholesterol, and at 65°C for tetralin, may be due to the fact that their barriers are also particularly high.

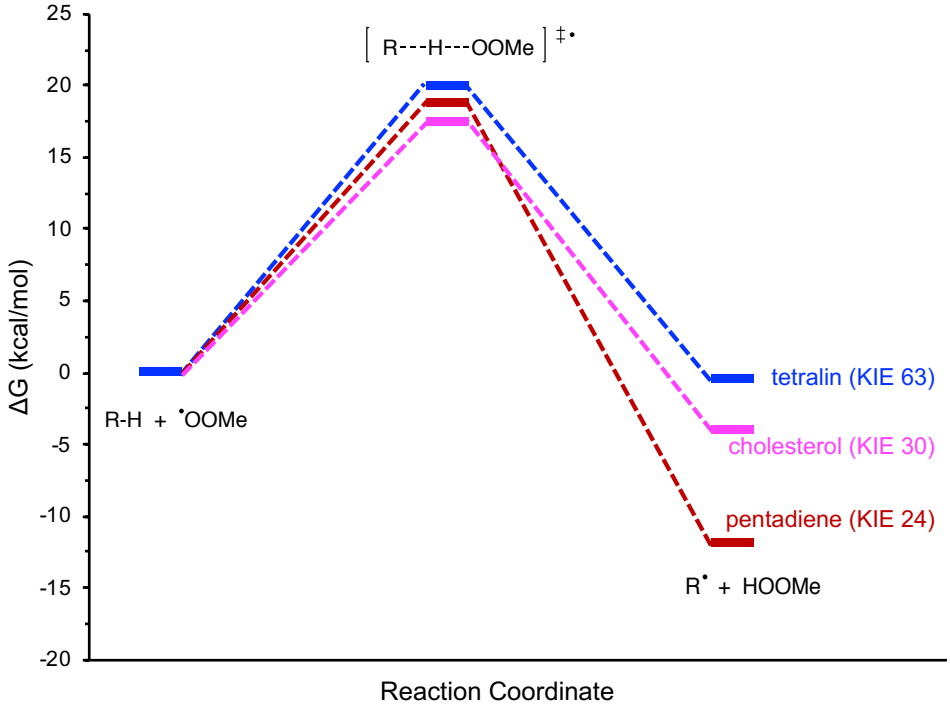

Figure 4.5. The computed free energy barriers for H-atom abstraction from tetralin, cholesterol, or 1,4-pentadiene (linoleate model) by a methylperoxyl radical, and the computed kinetic isotope effect (KIE or k_H/k_D) for each at room temperature.

To investigate whether the foregoing systems are unique, we calculated the H-atom transfer to a peroxyl radical for another series of hydrocarbons. Figure 4.6 shows the reaction barriers for propane, toluene, propene, and cyclopentane. These systems have even higher barriers, and correspondingly, their KIEs are predicted to be even larger still! However, the trends in KIE do not align completely with barrier height. The Skodje-Truhlar tunnelling corrections additionally incorporate the (negative) frequency of the vibrational mode associated with the H- or D-atom transfer, as an estimate for the barrier shape (i.e. width) in the parabolic approximation. Interestingly, toluene and propene each have more negative vibrational modes (-1786 and -1795 cm^{-1}, respectively) than propane and cyclopentane (-1610 and -1675 cm^{-1}, respectively). In the case of toluene and propene, the D-atom transfer is predicted to have a significant tunnelling contribution as well (accelerating the rate constant for D-atom abstraction, k_D, ca. 70-fold in both instances), decreasing the predicted KIE; whereas D-atom tunnelling in propane and cyclopentane is minor (ca. 10-fold acceleration in k_D).

It is worth noting that a more sophisticated tunnelling correction method might yield differing results. The Skodje-Truhlar method does not consider the reaction products, and may therefore overestimate the tunnelling contribution for endothermic systems; for effective tunnelling in such a system, the reactants must first travel along the reaction pathway to a point where tunnelling through the barrier to the products would be more likely. Nevertheless, the computational approach used herein was able to adequately support the experimental results for the systems where such data exists. Furthermore, it suggests that C-H abstraction by peroxyl radicals is generally susceptible to acceleration by quantum mechanical tunnelling, which is influenced by a number of factors – the most significant being the barrier height.

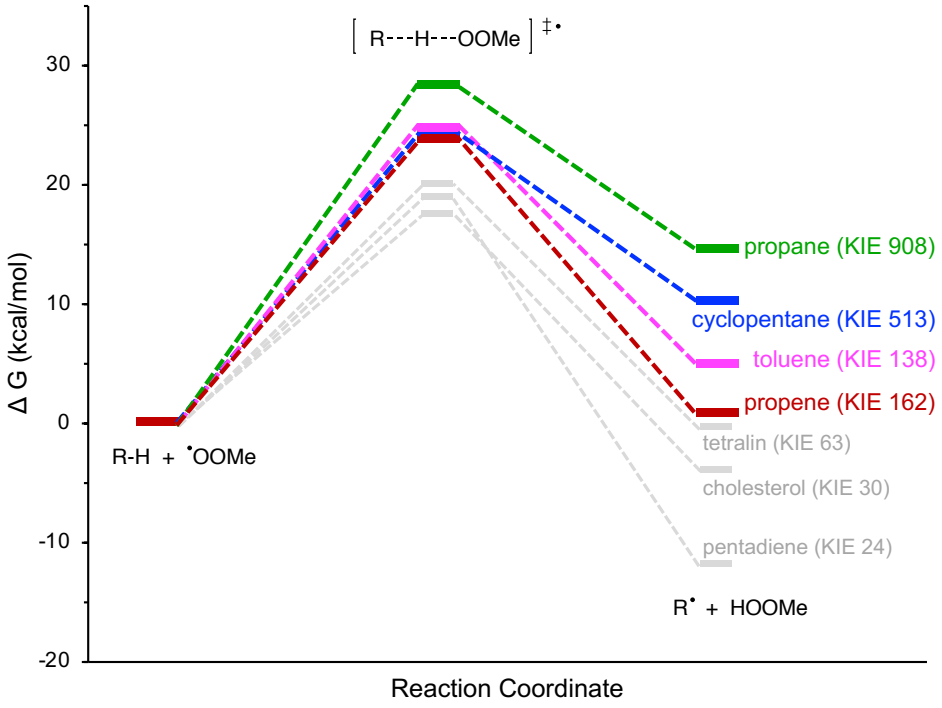

Figure 4.6. The computed free energy barriers for H-atom abstraction from propane, cyclopentane, toluene, or propene by a methylperoxyl radical, and the computed kinetic isotope effect (KIE or k_H/k_D) for each. The plots of Figure 4.5 are included in grey for reference.

4.3.2 Experimental and Computational Study of an Oleate Model

Given the foregoing and our interest in lipid peroxidation, we surmised that the monounsaturated fatty acid oleic acid would have an even larger KIE than linoleate. Propene can be considered a model for oleate (cf. Table 4.2), though the barrier is likely overestimated since propene lacks the hyperconjugative effects of the additional alkyl groups (e.g. H-atom abstraction from the 2-position of hex-3-ene has a barrier of 19.3 kcal/mol). To our knowledge, no KIE has been reported for the reaction of oleate with a peroxyl radical. Interestingly, as a monounsaturated lipid, one can envision oleate might have similar reactivity to cholesterol. As has been previously demonstrated[10] (cf. Chapter 3), peroxyl radical addition readily occurs in cholesterol autoxidation, and the corresponding cholesterol epoxides constitute 10-30 mol% of the product mixture, depending on the amount of H-atom donor present. Other hydrocarbons are known to autoxidize via peroxyl radical addition,

including styrene and 7-dehydrocholesterol; however in those instances the intermediate alkyl radical is in a stabilized benzylic or allylic position, respectively (cf. Scheme 4.1).

Table 4.2. Experimental propagation rate constant (k_p), computed reaction barrier ($\Delta \boldsymbol{G}^{\ddagger}_{\boldsymbol{calc}}$), as well as experimental and computed deuterium kinetic isotope effects (KIE or k_H/k_D) for oleate H- or D-atom abstraction by a methylperoxyl radical. The abstracted H- or D-atoms are indicated in the computational model.

Experimental			**Computational**		
substrate	k_p (M^{-1} s^{-1})	k_H/k_D	model	$\Delta G^{\ddagger}_{calc}$ (kcal/mol)	$(k_H/k_D)_{calc}$ (at 25°C)
$H_3C(H_2C)_7$ $(CH_2)_7COOR$ oleate	0.9	?	H H H(D)	23.8	162

Scheme 4.1. Peroxyl radical addition to various hydrocarbons.

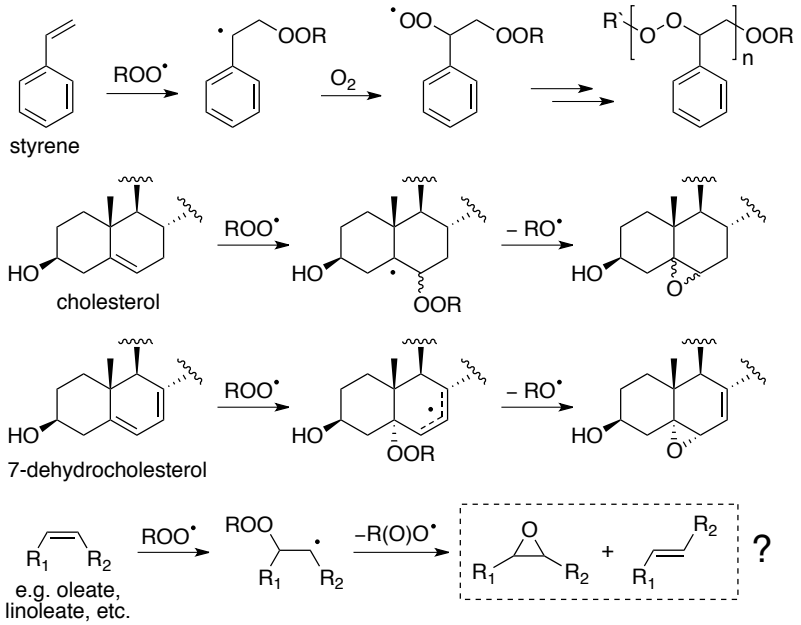

Oleate autoxidation had previously been studied by Porter et al. [14] using normal-phase HPLC. Six primary hydroperoxide products were detected: **4.1a, 4.1b, 4.2a, 4.2b, 4.3a**, and **4.3b**, from H-atom abstraction from either of the allylic positions, and subsequent addition of oxygen to either end of the intermediate radicals (Scheme 4.2). As H-atom donor was added to the autoxidation medium, the amount of **4.3a** and **4.3b** decreased, due to the reversible addition of oxygen ($k_\beta \sim 0.5$ to 8 s^{-1}). Thus **4.1** and **4.2** were deemed the kinetic products, and **4.3** the thermodynamic products, of oleate autoxidation. No oleate-derived epoxides were detected; however, it is possible this was an artifact of the LC-MS method Porter et al. used. It is worth noting that linoleate-derived epoxides were only recently identified as products of linoleate autoxidation.[15] We therefore were interested in revisiting the autoxidation of a simple monounsaturated hydrocarbon, to determine whether peroxyl radical addition occurs in the natural substrate, and what the effect of deuterating the allylic positions might be. We opted to use *cis*-hexadec-8-ene as a model for oleate, on the basis that $R_1 = R_2 = (CH_2)_5CH_3$ would provide a simpler product distribution (cf. Scheme 4.2 and Scheme 4.3).

Scheme 4.2. Oleate autoxidation.

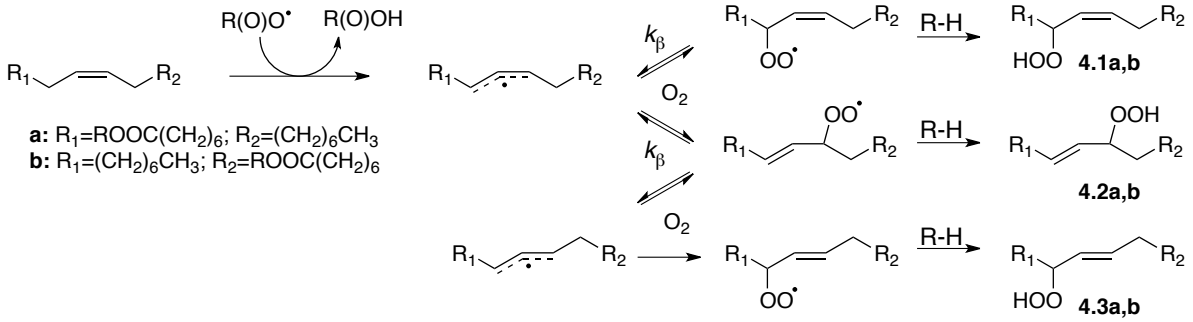

Cis-hexadec-8-ene is commercially available, but was synthesized, since we planned to employ the same methodology to prepare the deuterated analog, *vide infra*. Authentic standards were

prepared for the expected autoxidation products, in order to develop an analytical method for their detection. As it is common to reduce the hydroperoxide products to their corresponding alcohols prior to analysis, authentic standards for *cis*- and *trans*-hexadec-8-en-7-ol (*cis*-7-OH and *trans*-7-OH), and *trans*-hexadec-9-en-8-ol (*trans*-8-OH) were prepared, as well as the corresponding α,β-unsaturated ketones (*cis*-7-keto, *trans*-7-keto, and *trans*-8-keto), and *cis*-and *trans*-2,3-diheptyloxirane (*cis*- and *trans*-epox). In principle, the KIE on the autoxidation of oleate could be measured by consumption of starting material alone. In practice, due to the complex kinetics (as outlined in Chapter 1) it can be challenging to adequately quantify the consumption of starting material when, ideally, observing only the first few percent of the reaction. Furthermore, given that a large KIE was observed in cholesterol for the H-atom abstraction mechanism and not the peroxyl radical addition, and given that the same would be expected of oleate (and the model *cis*-hexadec-8-ene), such an approach would result in an underestimated KIE for the H-atom transfer pathway(s). Thus, quantification of the autoxidation products was deemed a more ideal approach, to determine the KIE on each pathway individually.

Scheme 4.3. Potential products of *cis*-hexadec-8-ene autoxidation, derivatized for GC-FID detection.

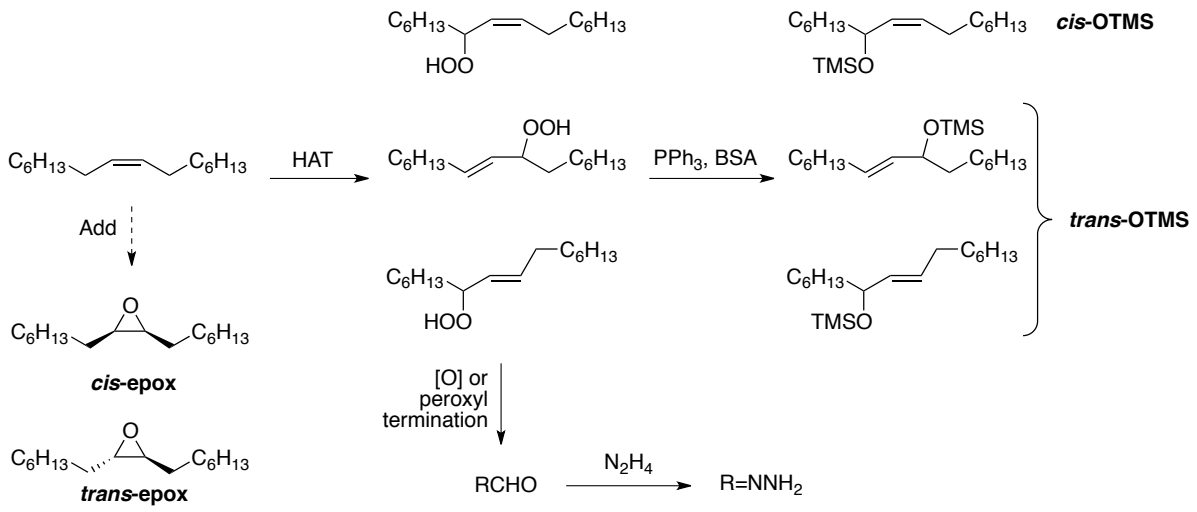

The authentic standards were used to optimize a GC-FID protocol. Co-elution was an issue, therefore the ketones were derivatized to their corresponding hydrazones upon treatment with hydrazine hydrate, and the alcohols were silylated with N,O-bis(trimethylsilyl)acetamide (BSA), as outlined in Scheme 4.3. The optimized conditions could not resolve *trans*-7-OTMS and *trans*-8-OTMS; however, the relative amounts of the hydroperoxide products is well known for oleate autoxidation, and their quantification relative to the epoxides was the current goal. *Cis*-hexadec-8-ene autoxidations were carried out under the same conditions used by Porter et al.[14] to study oleate autoxidation; specifically, using di-tert-butyl hyponitrite (DTBN) as the initiator, with and without *t*-BuOOH, for 6 hours (cf. Figure 4.7A and B, and see Experimental Section 4.6.2 for more details). Recall, it was with the addition of H-atom donor (*t*-BuOOH) that the kinetic products of oleate autoxidation were identified. To our surprise, the epoxide products were present, albeit in small quantities, under both sets of conditions: they constituted 9 mol% of the product mixture in the absence of H-atom donor, and 5 mol% with *t*-BuOOH.

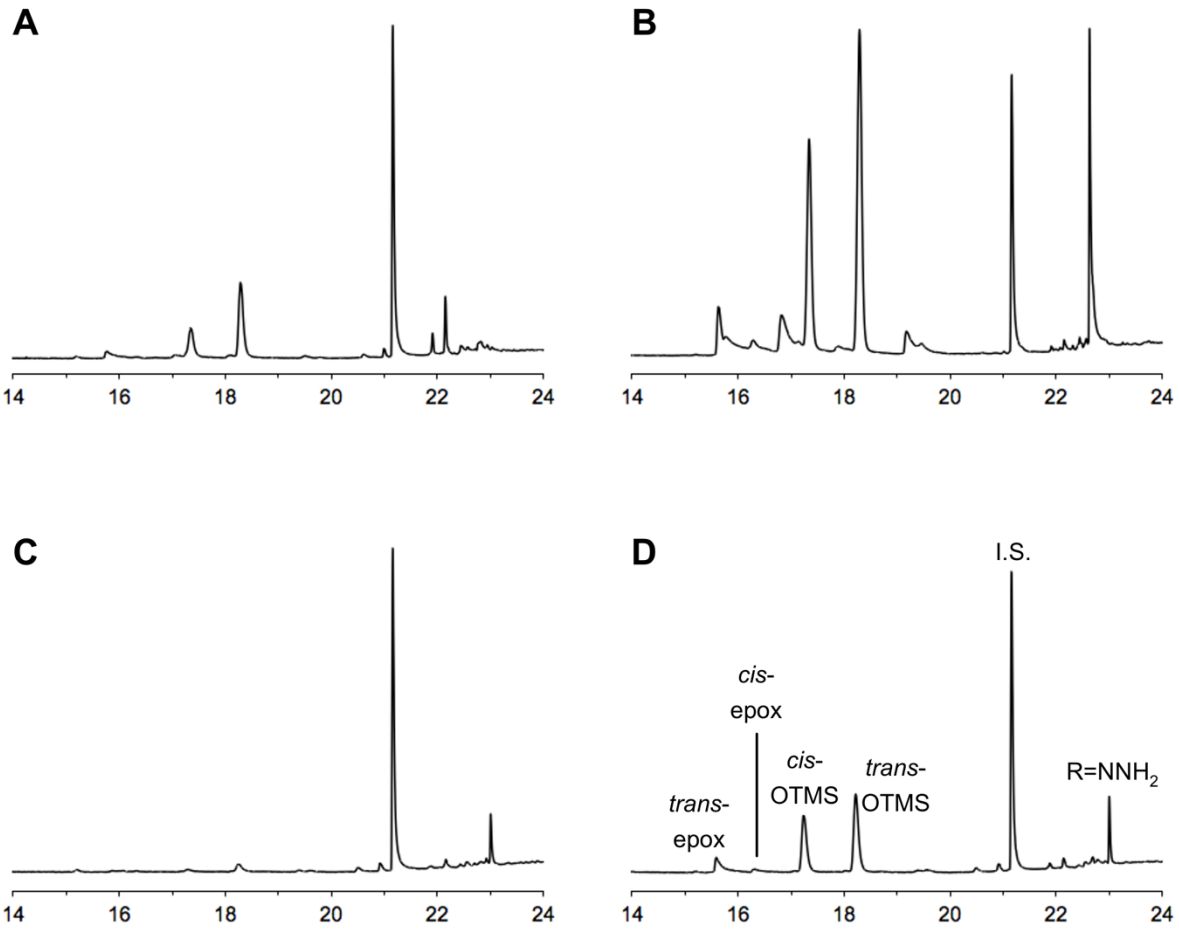

Figure 4.7. GC-FID chromatograms (FID response over time) for 6 hour DTBN-initiated autoxidations of: (A) cis-hexadec-8-ene; (B) cis-hexadec-8-ene + *t*-BuOOH; (C) 7,7,10,10-d_4-cis-hexadec-8-ene; (D) 7,7,10,10-d_4-cis-hexadec-8-ene + *t*-BuOOH. The peaks are labelled as outlined in Scheme 4.3, and dodecyl benzene was used as the internal standard (I.S.).

As a comparison to the cholesterol autoxidations of Chapters 2 and 3, autoxidations were also carried out with 2,2'-azobis(4-methoxy-2,4-dimethylvaleronitrile) (MeOAMVN) as the initiator. This method is generally considered to be a better model for lipid autoxidation; however, the initiator was developed[16] after the seminal work[14] on oleate autoxidation. The autoxidations were again carried out with and without added *t*-BuOOH, for 6 hours (cf. Figure 4.8A and B). The epoxide products were again present in both cases, constituting 15 mol% of the product distribution in the absence of *t*-BuOOH, and 4 mol% in its presence.

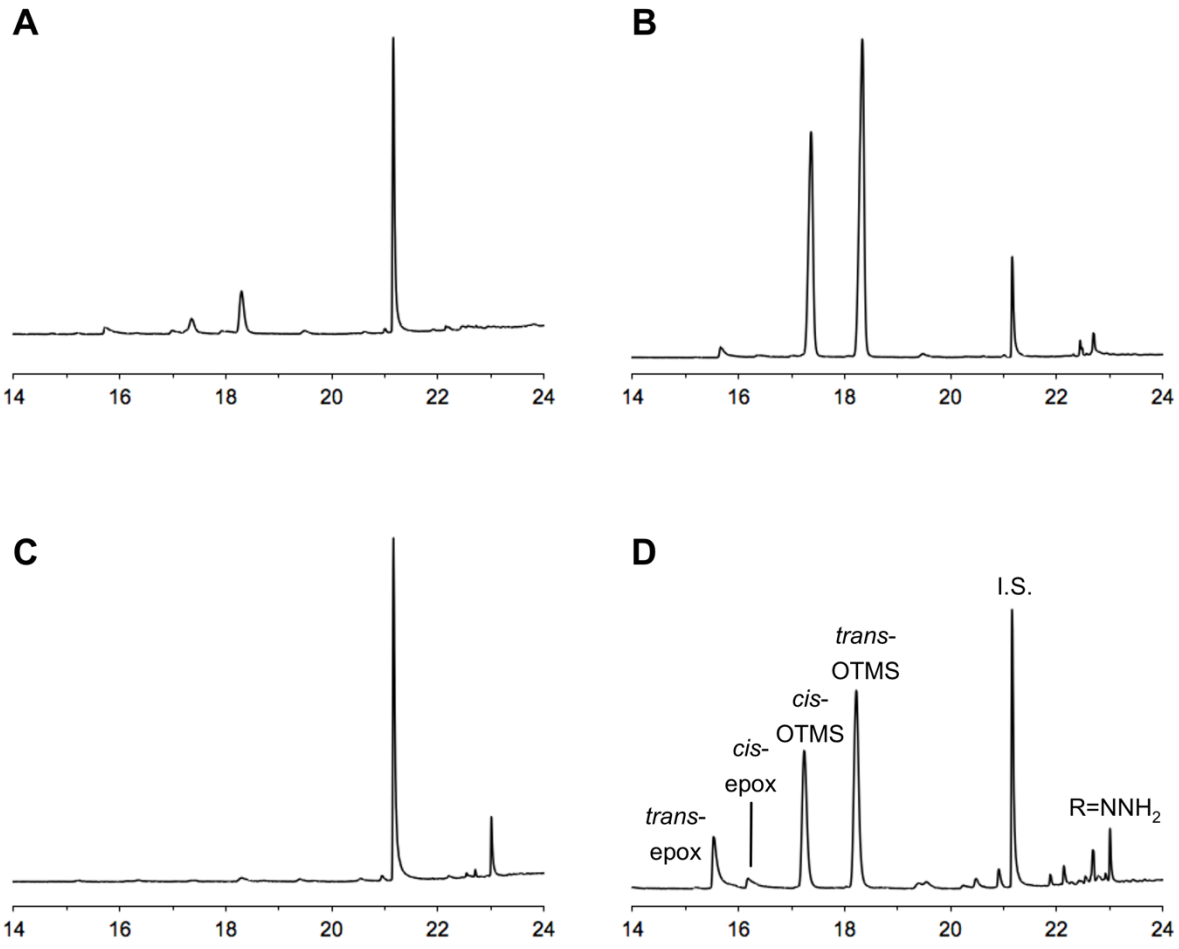

Figure 4.8. GC-FID chromatograms (FID response over time) for 6 hour MeOAMVN-initiated autoxidations of: (A) cis-hexadec-8-ene; (B) cis-hexadec-8-ene + *t*-BuOOH; (C) 7,7,10,10-d_4-cis-hexadec-8-ene; (D) 7,7,10,10-d_4-cis-hexadec-8-ene + *t*-BuOOH. The peaks are labelled as outlined in Scheme 4.3, and dodecyl benzene was used as the internal standard (I.S.).

We then sought to examine whether tunnelling may be the reason for the dominance of the H-atom abstraction products, as was the case in cholesterol autoxidation. We therefore synthesized 7,7,10,10-d_4-*cis*-hexadec-8-ene according to Scheme 4.4, which was inspired by the work of Dejarlais & Emken[17] using the deuteration protocol of Ariza et al.[18] Once optimized in this way, the synthesis was straightforward, except that the final step Wittig reaction yielded a mixture of *cis*- and *trans*-hexadec-8-ene that was inseparable by normal phase chromatography. Silver-impregnated silica gel

chromatography was therefore carried out to separate the two isomers, albeit the separation was still challenging, and each column resulted in only a few fractions of pure 7,7,10,10-d_4-*cis*-hexadec-8-ene, with the remainder co-eluting with the *trans*-isomer. Nevertheless, with some 7,7,10,10-d_4-*cis*-hexadec-8-ene in hand, we carried out autoxidations under the four sets of conditions described above for the protiated analogue (cf. Figure 4.7C and D, and Figure 4.8C and D). To our surprise, in the absence of *t*-BuOOH, the deuterated substrate appeared immune to autoxidation, as only trace product formed in the 6 hour autoxidation! This was entirely in contrast to the results observed with cholesterol (cf. Chapter 3), where the deuterated analogue had a KIE of ca. 20 on its H-atom abstraction, but underwent peroxyl radical addition to yield cholesterol-epoxides at the same rate as the protiated substrate. In the presence of *t*-BuOOH, deuterated hexadec-8-ene yielded 21 and 18 mol% epoxide products for DTBN- and MeOAMVN-loaded autoxidations, respectively. Similar to cholesterol, in these cases the total amount of epoxide products was roughly the same as the analogous hexadec-8-ene autoxidations, whereas the amount of H-atom abstraction products (RO(O)H and R=O, detected as R-OTMS and R=NNH_2, respectively) decreased.

Scheme 4.4. Synthesis of 7,7,10,10-d_4-hexadec-8-ene.

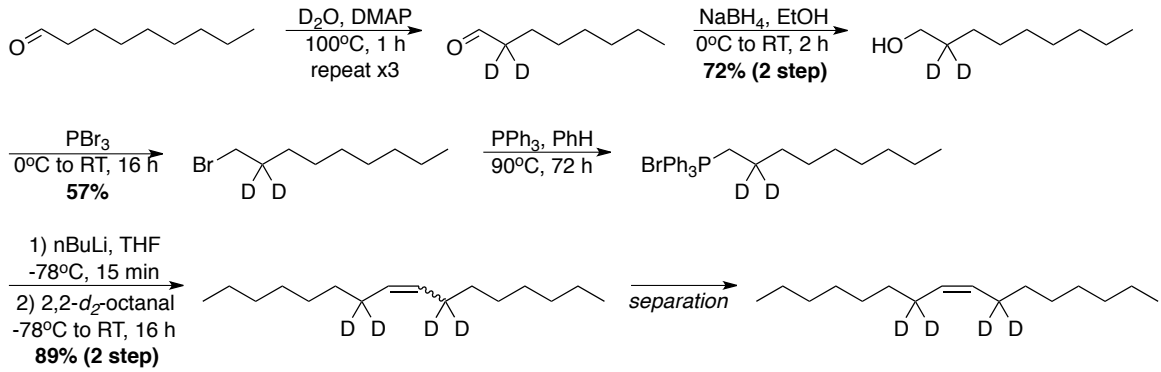

Perplexed by the foregoing results, we wondered if the deuterated hexadec-8-ene autoxidations would yield a detectable amount of product(s) if left for a longer period of time. We therefore carried out autoxidations under the same four sets of conditions, for both the protiated and deuterated analogues of *cis*-hexadec-8-ene, for 24 hours (the half-life of MeOAMVN is 6h at 37ºC, and DTBN's is 55h at 30ºC, based on their decomposition rate constants, *vide infra*). Gratifyingly, while the deuterated analogues yielded ca. 10-fold less autoxidation products than the protiated systems at 24 hours, it was enough to analyze the corresponding product distributions (cf. Figure 4.9 and Figure 4.10). In the absence of *t*-BuOOH, the epoxide products accounted for 37 and 50 mol% of the product distribution for DTBN- and MeOAMVN-loaded autoxidations, respectively. The product distribution of the *t*-BuOOH-loaded autoxidations were essentially the same at 6 and 24 hours, except that the proportion of keto products increased relative to the hydroperoxide products. The keto products may be formed from peroxyl-peroxyl termination reactions, or from the degradation of hydroperoxides (cf. Scheme 1.11A in Chapter 1) over time – the latter being a reasonable explanation for the foregoing observation.

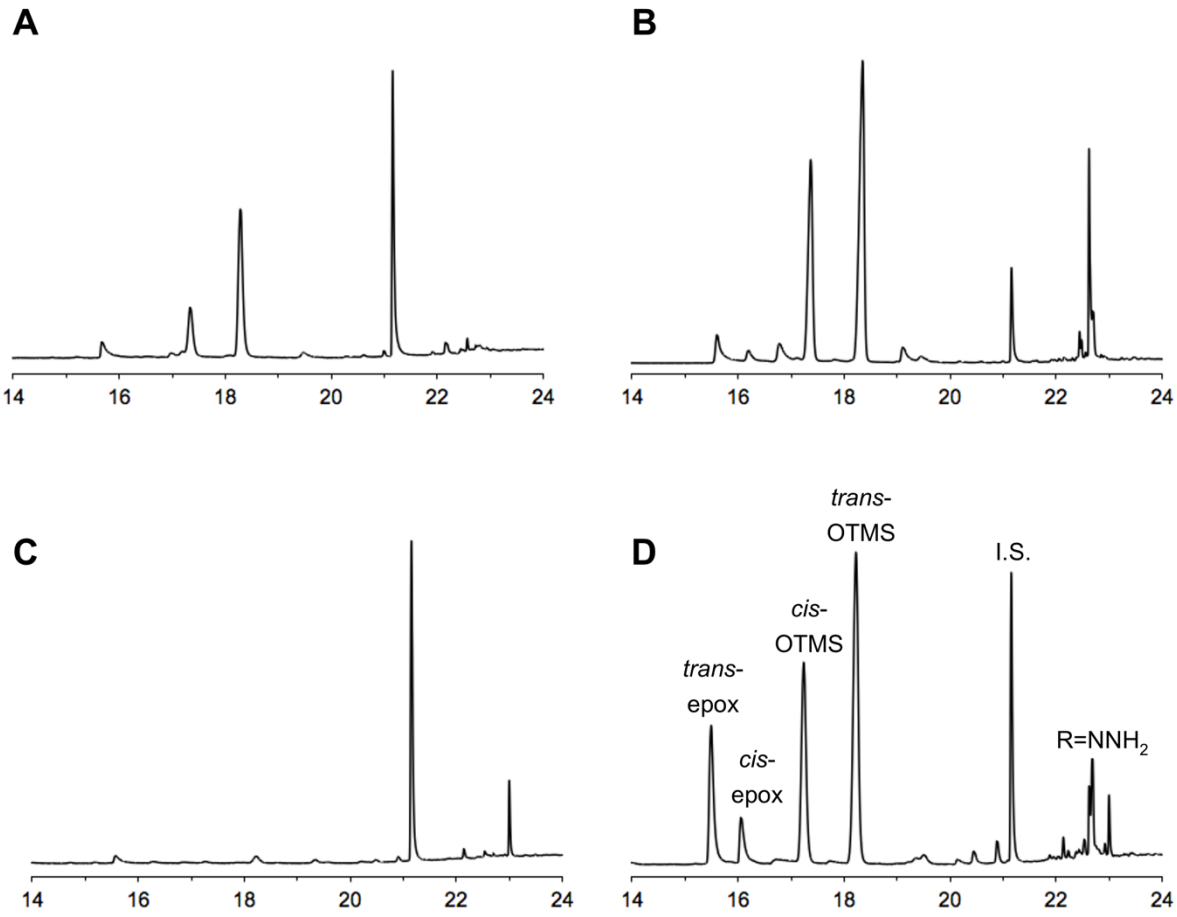

Figure 4.9. GC-FID chromatograms (FID response over time) for 24 hour MeOAMVN-initiated autoxidations of: (A) cis-hexadec-8-ene; (B) cis-hexadec-8-ene + tBuOOH; (C) 7,7,10,10-d_4-cis-hexadec-8-ene; (D) 7,7,10,10-d_4-cis-hexadec-8-ene + tBuOOH. The peaks are labelled as outlined in Scheme 4.3, and dodecyl benzene was used as the internal standard (I.S.).

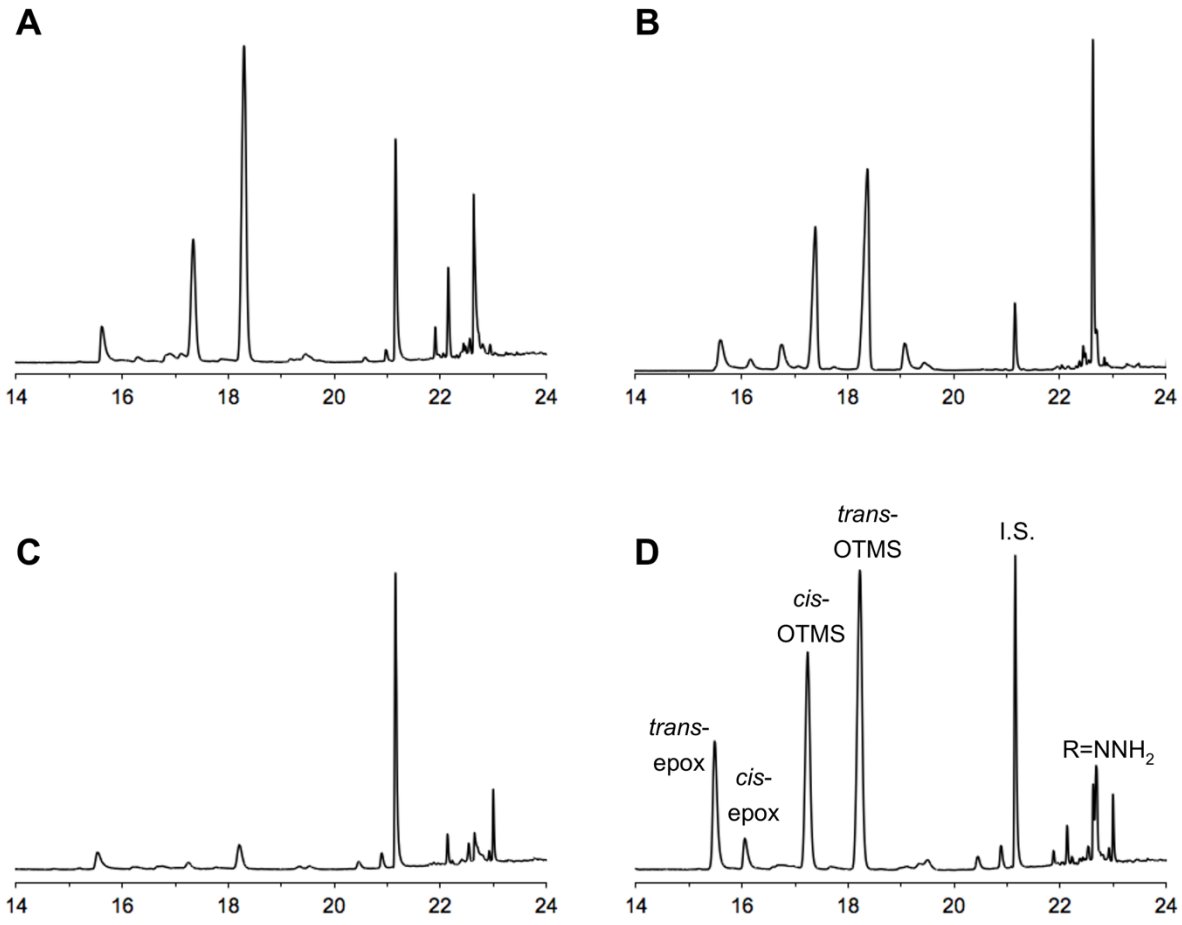

Figure 4.10. GC-FID chromatograms (FID response over time) for 24 hour DTBN-initiated autoxidations of: (A) cis-hexadec-8-ene; (B) cis-hexadec-8-ene + tBuOOH; (C) 7,7,10,10-d_4-cis-hexadec-8-ene; (D) 7,7,10,10-d_4-cis-hexadec-8-ene + tBuOOH. The peaks are labelled as outlined in Scheme 4.3, and dodecyl benzene was used as the internal standard (I.S.).

The KIE on H-atom abstraction in the autoxidation of (d_4-)*cis*-hexadec-8-ene with MeOAMVN was 18 ± 1. This suggests that tunnelling does indeed dictate the preference for the H-atom abstraction pathway over peroxyl radical addition. This value was also quite similar to that in cholesterol (20 ± 1), which also bears a single unsaturation. Interestingly, the KIE was slightly lower in DTBN-initiated autoxidations (11.5 ± 0.2). This difference is perhaps due to the initiation by alkoxyl radicals with DTBN rather than peroxyl radicals with MeOAMVN, and that H-atom abstraction by the much more reactive alkoxyl radicals will be subject to a much smaller KIE. Given

the short chain lengths under these conditions, *vide infra*, the significance of initiator-substrate reactions relative to substrate-substrate reactions is consistent with the foregoing assertion.

Interestingly, there was a small, but measurable, KIE on epoxide formation of 2.3 ± 0.5 with MeOAMVN (1.8 ± 0.3 with DTBN), which was non-existent in the analogous cholesterol study in Chapter 3. Furthermore, the KIE on epoxide formation disappeared in the presence of *t*-BuOOH to 0.9 ± 0.2 with MeOAMVN (1.0 ± 0.3 with DTBN). The addition of *t*-BuOOH also affected the KIE on HAT, reducing it to 5.5 ± 0.5 with MeOAMVN (6 ± 1 with DTBN). The significance of the KIE on epoxide formation will be discussed in more detail below from a mechanistic perspective. The reduced KIE on HAT in the presence of *t*-BuOOH is a little more difficult to reconcile. We suggest this is perhaps due to the intermediate alkyl radical abstracting an H-atom from *t*-BuOOH rather than reacting with oxygen, effectively exchanging the deuterium for a hydrogen. While the rate of the former reaction is significantly slower than the latter (ca. 10^3 $M^{-1}s^{-1}$ vs. diffusion-controlled), it is well known that a residual protio effect can have a significant impact on the observed k_H/k_D. [19] In other words, even if a small proportion of the intermediate alkyl radicals abstracted an H-atom from *t*-BuOOH rather than reacting with O_2, the corresponding generation of protiated starting material could result in a significant underestimation of the KIE.

Table 4.3. Experimentally-determined kinetic isotope effect (KIE) on H-atom transfer (HAT) from, or peroxyl radical addition (epoxidation) to, *cis*-hexadec-8-ene relative to d_4-*cis*-hexadec-8-ene under the indicated conditions.

Initiator	**HAT** (no additive)	**Epoxidation** (no additive)	**HAT** (with tBuOOH)	**Epoxidation** (with tBuOOH)
MeOAMVN	18 +/- 1	2.3 +/- 0.5	5.5 +/- 0.5	0.9 +/- 0.2
DTBN	11.5 +/- 0.2	1.8 +/- 0.3	6 +/- 1	1.0 +/- 0.3

Another experimental detail useful in elucidating mechanistic insight is the chain length (x), which is determined according to eq. 4.12:

$$x = \frac{[prod]/t}{2ek_d[In]} \qquad (4.12)$$

where the total amount of products ([prod] = [ROH] + [epox] + [keto]) over the autoxidation time period (t) is divided by the concentration of MeOAMVN or DTBN (In) and the known ek_d values for MeOAMVN at 37°C (benzene)[16] and DTBN at 30°C (chlorobenzene). [20] The chain lengths were independent (within error) of initiator, and the values were significantly lower than 1 without added *t*-BuOOH. This may suggest that either the propagation of the chain reaction is ineffective, or alternatively, that there are additional undetected products of the autoxidation which artificially lowers the [prod] term, and consequently the chain length (x). These possibilities will be considered from a mechanistic perspective, *vide infra*. Though it is worth noting here that this is not entirely surprising, given the reason for adding *t*-BuOOH in the first place is to suppress termination.

Table 4.4. Chain lengths (x) for MeOAMVN-loaded autoxidations of *cis*-hexadec-8-ene and d_4-*cis*-hexadec-8-ene under various conditions.

	cis-hexadec-8-ene + MeOAMVN	*cis*-hexadec-8-ene + DTBN	d_4-*cis*-hexadec-8-ene + MeOAMVN	d_4-*cis*-hexadec-8-ene + DTBN
6 hours	0.14 ± 0.08	0.12 ± 0.08	0.013 ± 0.006	0.02 ± 0.01
24 hours	0.10 ± 0.05	0.10 ± 0.03	0.009 ± 0.004	0.012 ± 0.004
6 hours + t-BuOOH	3 ± 1	3 ± 2	0.6 ± 0.2	0.5 ± 0.3
24 hours + t-BuOOH	1.3 ± 0.5	2 ± 1	0.3 ± 0.1	0.5 ± 0.2

Given that *cis*-hexadec-8-ene autoxidations appeared to behave differently than cholesterol experimentally, we sought to explore whether the experimental evidence was supported by computations. Hex-3-ene was used as a computational model, which gave a computed rate constant for H-atom abstraction of 1.0 M^{-1} s^{-1} without any tunnelling corrections, and 150 M^{-1} s^{-1} using Skodje-Truhlar tunnelling corrections. It is worth noting that the experimental k_p value is 0.9 M^{-1} s^{-1}, and the over-estimation of tunnelling-corrected rate constants was a common theme in our (gas phase) computational results. The value in such calculations, however, is in determining whether or not tunnelling is likely to occur in a given transformation. While the KIE was not explicitly calculated for this system (this may be the focus of future work), the fact that the computed k_p was accelerated 150-fold with Skodje-Truhlar tunnelling corrections suggesting tunnelling is important in the H-atom abstraction (i.e. an upper limit for the computed KIE is 150, provided there is no tunnelling in the D-atom abstraction). As outlined in Figure 4.3, the overall rate constant for epoxidation is also computed to be 1.0 M^{-1} s^{-1}, and tunnelling is not predicted therein. Interestingly, the second step for epoxide formation is 10x slower than for the corresponding TS in cholesterol, likely due to the added degrees of freedom in hex-3-ene as compared to the conformationally rigid backbone in cholesterol ($\Delta S^{\ddagger}$ of -0.46 cal/°K for the hex-3-ene intermediate, compared to +0.71 and +1.4 cal/°K for the 6α and 6β peroxide intermediates, respectively, for the cholesterol model).

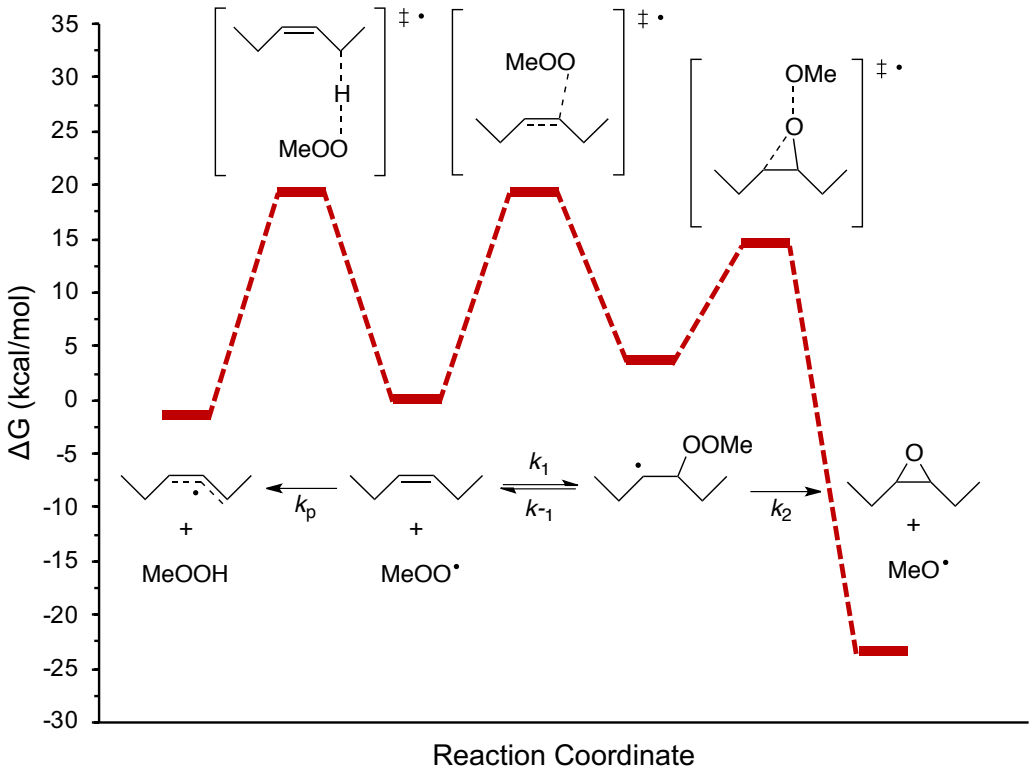

$$k_p = 1.0\ \mathrm{M^{-1}s^{-1}}$$

$$k_{add} = \frac{k_1 k_2}{(k_{-1} + k_2)} = \frac{(1.0\ \mathrm{M^{-1}s^{-1}})(6.4 \times 10^4\ \mathrm{s^{-1}})}{(18.9\ \mathrm{s^{-1}} + 6.4 \times 10^4\ \mathrm{s^{-1}})} = 1.0\ \mathrm{M^{-1}s^{-1}}$$

Figure 4.11. CBS-QB3 computed reaction barriers for H-atom abstraction from, or addition to, hex-3-ene by a methylperoxyl radical.

4.4 Discussion

The overall rate constant for peroxyl radical addition to the oleate model is computed to be 1.0 M^{-1} s^{-1}, which is identical to the computed rate constant for H-atom abstraction without tunnelling corrections. This suggests that the ratio of addition to abstraction products should be 1:1, if tunnelling were not a factor. However, experimentally, the epoxides only constitute ca. 5-15 mol% of the

product mixture, depending on the conditions. This suggests tunnelling may be involved in accelerating the H-atom abstraction, and indeed this is supported by the experimentally-determined KIE of 18 ± 1 in MeOAMVN-initiated autoxidations without additive. However, the surprising result that, under the same conditions, epoxide formation had a KIE of 2.3 ± 0.5 was not consistent with what was observed in cholesterol autoxidations (Chapter 3). This led us to consider if there were mechanistic differences between the oleate model and cholesterol. To summarize, we suggest the mechanism for *cis*-hexadec-8-ene autoxidation in Scheme 4.5 below, which appears consistent with the various pieces of computational and experimental evidence reported herein.

Scheme 4.5. Proposed mechanism of *cis*-hexadec-8-ene autoxidation.

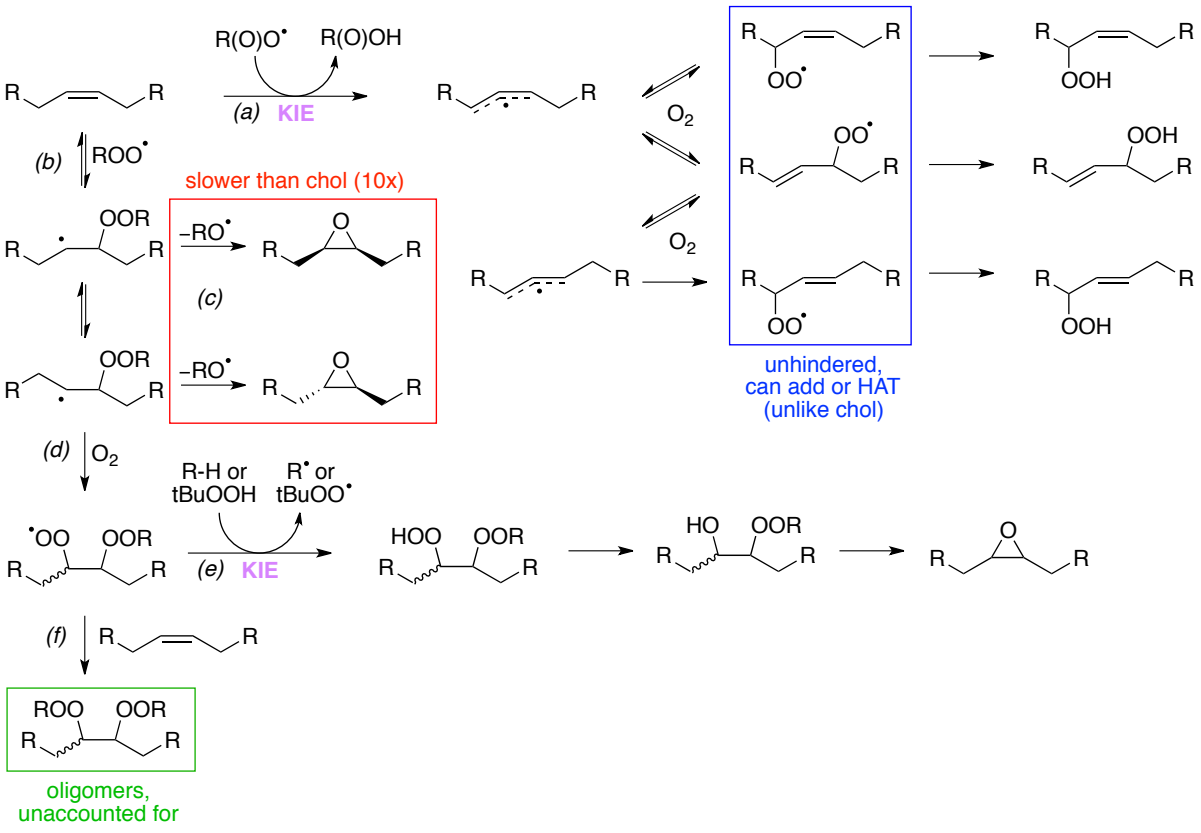

Given that the substrate-derived peroxyl radical in the oleate model is less hindered than that in cholesterol autoxidation, we predict it would more easily carry the chain, i.e. abstract an H-atom from, or add to, another *cis*-hexadec-8-ene molecule. However, this is not supported by the experimental k_p values nor the chain length calculations in each case: MeOAMVN-initiated cholesterol autoxidation has a chain length of approximately 1, whereas the oleate model chain length was 10-fold lower under the same conditions. Casting this aside for a moment, if we assume both H-atom abstraction from (pathway (a)), and addition to (pathway (b)), the oleate model are possible, the alkyl radical formed upon peroxyl radical addition has two fates: (c) intramolecular homolytic substitution (S_Hi) to yield an epoxide; or (d) addition of oxygen to yield a peroxide-peroxyl radical intermediate. As demonstrated in the computational results, the rate of pathway (c) is 10-fold slower than the corresponding reaction in cholesterol; therefore suggesting pathway (d) is more prevalent in the oleate model. Thus the resultant peroxyl radical is similarly faced with two options: (e) abstract a labile H-atom from another equivalent of *cis*-hexadec-8-ene to form a hydroperoxide; or (f) add to another *cis*-hexadec-8-ene to form an oligomer. Note that any of the peroxyl radicals in Scheme 4.5 may alternatively undergo termination, to form the corresponding alcohol or ketone.

As was suggested in Chapter 3, the hydroperoxide product of pathway (e) may form an epoxide, following a displacement of the added peroxide fragment. Interestingly, this pathway would involve a KIE if the H-atom is abstracted from another equivalent of (d_4)-*cis*-hexadec-8-ene. This is consistent with the KIE measured for epoxide formation in the absence of any additive, suggesting at least a portion of the epoxide detected is the result of pathway (e). The fact that the KIE disappeared in the presence of *t*-BuOOH is also consistent with this proposed mechanism, as *t*-BuOOH would be much more likely to provide the labile H-atom for pathway (e) than (d_4)-*cis*-hexadec-8-ene itself. Attempts to quantify the pathway (e) products were unsuccessful. We were unable to synthesize the α-hydroxy peroxide through attempts to open 2,3-diheptyloxirane with a hydroperoxide. Hexadecane-8,9-diol was prepared, but was not present in any of the autoxidations. This is not entirely surprising

as PPh_3 may not decompose the pathway (e) peroxide product. As was mentioned in Chapter 3, other means of cleaving the peroxidic bond (e.g. Zn or Mg) also leads to the hydrolysis of the epoxide products, thus the presence of the diol in such a product mixture could not be used to quantify the pathway (e) products.

Given that the experimental evidence supports pathway (d) as being a significant contributor to the mechanism, the surprisingly low chain length (x) can now be addressed. Since the calculation of chain length includes the total amount of products ([prod]), the chain length would be artificially low if not all autoxidation products were detected in the analysis. The oligomers formed from pathway (f) were not detected in our analysis, and it is also possible that the displacement of a peroxide to form an epoxide from pathway (e) does not go to completion. Thus the products of the peroxyl radical addition pathway (b) may be underestimated as compared to the products of H-atom abstraction pathway (a), which is also consistent with the fact that d_4-*cis*-hexadec-8-ene appeared immune to autoxidation without added *t*-BuOOH, after only 6 hours.

Our study on the mechanism of oleate autoxidation (via the model compound hexadec-8-ene) prompted us to consider future work on other related substrates. One such example is plasmenyl-glycerophospholipids, or plasmalogens, which have a general structure **4.4**, with a vinyl ether linkage at the sn-1 position and an ester linking the sn-2 position. The sn-1 position is typically derived from a saturated or mono-unsaturated C16 or C18 fatty alcohol, whereas the sn-2 position is derived from a polyunsaturated fatty acid, namely docosahexaenoic or arachidonic acid. The headgroup R^3 is generally choline or ethanolamine.

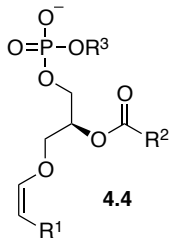

4.4

Plasmalogens are particularly prevalent in the nervous system, comprising 20% of the glycerophospholipids in human brain tissue, and in particular, ca. 80% of the ethanolamine glycerophospholipids in myelin-rich white matter are plasmalogens. Plasmalogens are also prevalent in heart, kidney, and skeletal muscle tissue, where they constitue 20-30% of the total phospholipid content.[21]

A complete understanding of the function of plasmenyl-phospholipids remains elusive, though their unique structure is known to be important in maintaining membrane structure, decreasing membrane fluidity, and assisting in the function of membrane proteins. Individuals with peroxisome biogenesis disorders, which lead to plasmalogen deficiencies, show abnormal neurological and skeletal development, impaired respiration, and development of cataracts. There are also some links to lower levels of plasmalogens and the onset of neurodegenative disorders; however, no causal link has been identified.[21] Plasmalogens have also been studied in the context of oxidative stress, and it is believed that the vinyl-ether functionality makes them sacrificial oxidants. Plasmalogens are reported to react 1 to 2 orders of magnitude faster with singlet oxygen ($^1O_2$) than cholesterol or phospholipids containing oleate or arachidonate.[22] They have also been found to protect polyunsaturated fatty acids from peroxidation (both iron-induced and when initiated by water- or lipid-soluble azo-compounds), wherein the plasmalogens decrease the rate of peroxidation and are consumed in the process.[23] It has been shown that oxidation of plasmalogens by $^1O_2$ or R(O)O$^\bullet$ causes cleavage of the vinyl-ether moiety to release long chain aldehydes and α-hydroxy aldehydes, respectively; the latter are reported to be derived from the hydrolysis of intermediate plasmalogen epoxides (cf. Scheme 4.6). [21,24] To our knowledge, the hydroperoxide that would be derived from H-atom abstraction at the allylic position of a plasmalogen has not been reported. [24] The release of long chain aldehydes upon plasmalogen autoxidation is particularly intriguing, given that they are reported to have antioxidant effects *in vivo*; however, other lipid-derived aldehydes, such as 9-hydroxynonenal, are associated with the pathogenic/degenerative effects of lipid autoxidation.

Scheme 4.6. Proposed formation of a long chain α-hydroxy aldehyde from plasmenyl-lipid autoxidation.

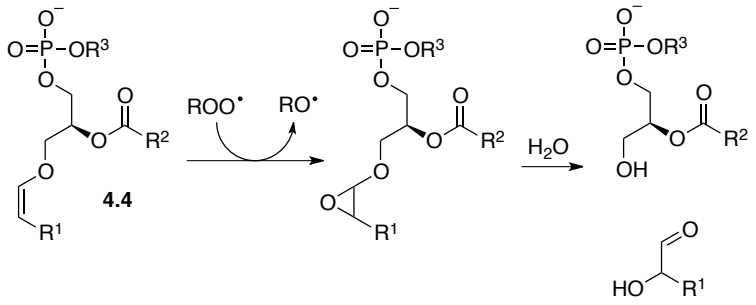

As a comparison for the vinyl ether moiety in plasmenyl lipids, computations were carried out on *cis*-methoxybut-1-ene. The computed rate constant for H-atom abstraction from the plasmenyl lipid model was 0.6 M^{-1} s^{-1}, which is slightly slower than the value computed for the oleate model of 1.0 M^{-1} s^{-1}. While the KIE was not explicitly calculated, the computed k_p was accelerated 100-fold with Skodje-Truhlar tunnelling corrections, suggesting tunnelling is important, but is not quite as significant a contributor as was the case in the oleate model (recall, the computed k_p was 150-fold higher with tunnelling corrections). As outlined in $k_p = 0.6\ M^{-1}s^{-1}$

$$k_{add} = \frac{k_1 k_2}{(k_{-1} + k_2)} = \frac{(16.4\ M^{-1}s^{-1})(9.5 \times 10^5\ s^{-1})}{(252\ s^{-1} + 9.5 \times 10^5\ s^{-1})} = 16\ M^{-1}s^{-1}$$

Figure **4.12**, the overall rate constant for epoxidation is computed to be 16 M^{-1} s^{-1}, which is significantly higher than the rate of H-atom abstraction. Furthermore, the computed rate constant for epoxidation in methoxybut-1-ene is also accelerated relative to the same transformation in hex-3-ene (1.0 M^{-1} s^{-1}, *vide supra*). In particular, the transition states for the first and second steps of epoxidation (peroxyl radical addition and S_Hi) are lowered in methoxybut-1-ene by 1.6 and 1.7 kcal/mol, respectively; however, the alkyl radical intermediate therebetween is only lowered by 0.1 kcal/mol. This suggests that the influence of the α-heteroatom is more stabilizing in the transition states than in

the intermediate radical, likely due to the formation of a partial positive charge on the carbon atom adjacent the heteroatom in the TSs.

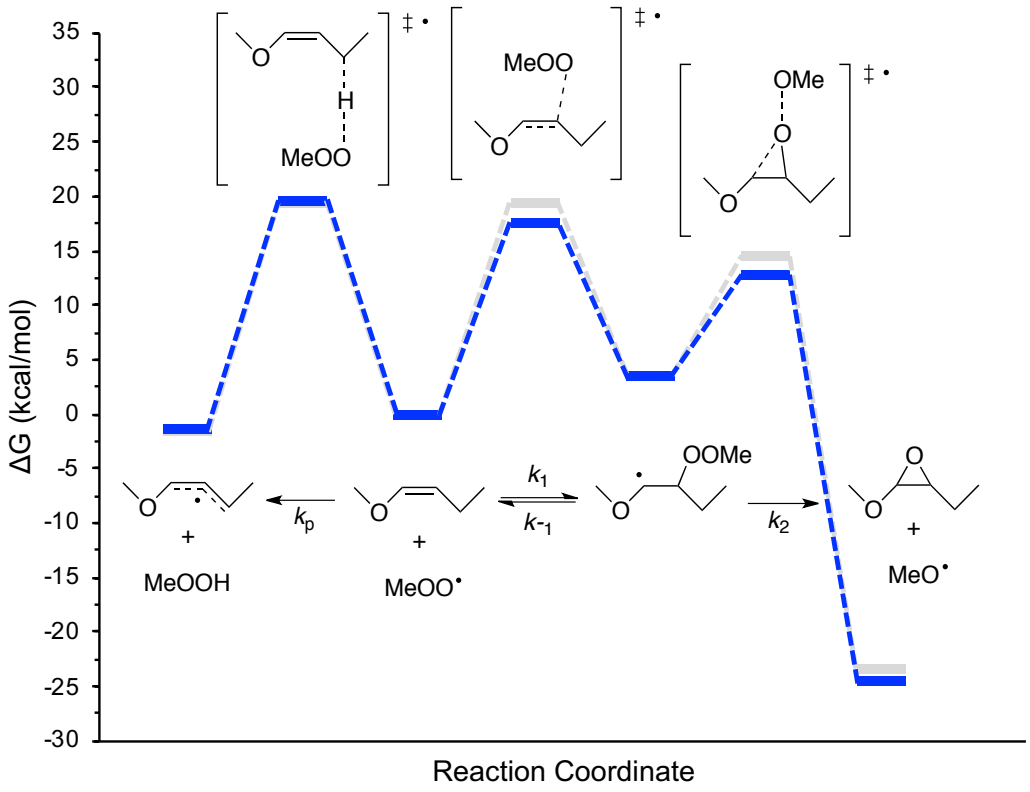

$$k_p = 0.6\ \mathrm{M^{-1}s^{-1}}$$

$$k_{add} = \frac{k_1 k_2}{(k_{-1} + k_2)} = \frac{(16.4\ \mathrm{M^{-1}s^{-1}})(9.5 \times 10^5\ \mathrm{s^{-1}})}{(252\ \mathrm{s^{-1}} + 9.5 \times 10^5\ \mathrm{s^{-1}})} = 16\ \mathrm{M^{-1}s^{-1}}$$

Figure 4.12. CBS-QB3 computed reaction barriers for H-atom abstraction from, or addition to, cis-methoxybut-1-ene by a peroxyl radical. The analogous values for hex-3-ene, as presented in Figure 4.11, are also provided in grey.

The computational results suggest the peroxyl radical addition pathway may be more competitive with the H-atom abstraction pathway in plasmenyl lipids, as compared to their

monounsaturated fatty acid counterparts. The computations on hex-3-ene demonstrated that, without correcting for tunnelling, the H-atom abstraction and peroxyl radical addition pathways were predicted to be equally fast (1.0 M^{-1} s^{-1}). Tunnelling was both predicted computationally, and observed in hexadec-8-ene autoxidations experimentally, accelerating the H-atom abstraction pathway such that the hydroperoxide products produced therefrom outnumbered the epoxide products by 85:15 (in MeOAMVN-initiated autoxidations without additive). On the other hand, computations on methoxybut-1-ene predicted the peroxyl radical addition pathway is 25-fold faster than H-atom abstraction in the absence of tunnelling. However, tunnelling is predicted to accelerate the H-atom abstraction in the methoxybut-1-ene model, suggesting both the H-atom abstraction and peroxyl radical addition pathways may be accessible in plasmenyl lipid autoxidation. The experimental exploration of this hypothesis is worthy of further exploration.

4.5 Conclusions and Perspective

The foregoing results suggest tunnelling is more prevalent in H-atom abstractions by peroxyl radicals than was previously appreciated. This suggests tunnelling serves to accelerate the H-atom abstraction pathway relative to the peroxyl radical addition pathway in monounsaturated lipids such as oleate and cholesterol. This is fully consistent with the fact that tunnelling is most facile when a reaction has a narrow barrier and involves the transfer of a light particle, as is the case in both the propagation and inhibiton steps of hydrocarbon autoxidation. We demonstrated this experimentally with hexadec-8-ene, which serves as a model for oleate. Not only did we measure a KIE of 18, supporting the importance of tunnelling in the H-atom abstraction, but we also observed epoxide products derived from the peroxyl radical addition pathway which was previously unreported in oleate autoxidation. While epoxides were also detected in cholesterol autoxidation, the peroxyl radical addition pathway in the oleate model was complicated, presumably by the fact that the latter substrate is less hindered. Finally, some preliminary calculations suggest the peroxyl radical addition pathway may be even

more significant in plasmenyl lipids, which may help to explain their perplexing biochemistry. A more complete study of plasmenyl lipid autoxidation is needed and will be the focus of future work in our group.

4.6 Experimental Details

4.6.1 Syntheses

2,2-d_2-octanal: Prepared as previously reported:[18] to octanal (8 mL, 51 mmol) was added D_2O (8 mL) and DMAP (625 mg, 5.1 mmol) in a flask and heated to 100°C for 1 hour. CH_2Cl_2 (150 mL) was added and the mixture was washed with 40 mL 1M HCl, 40 mL $NaHCO_3$ (aq. sat.), and 40 mL brine, then dried over $MgSO_4$ and concentrated. This was repeated twice more, until the amount of deuteration was >95% by ^{1}H NMR (based on the decrease in the multiplet at 2.4 ppm). The product was carried on crude to the next step. ^{1}H-NMR (400 MHz; $CDCl_3$): δ 9.76 (s, 1H), 1.61 (m, 2H), 1.29 (m, 9H), 0.88 (m, 3H).

2,2-d_2-octan-1-ol**:** To octanal-d_2 (3.5 g, 26.9 mmol) in dry EtOH (125 mL) at 0°C was added $NaBH_4$ (1.07 g, 28.2 mmol) in portions. The mixture was allowed to come to room temperature for 1 hour. Water was slowly added to quench the reaction. The EtOH was removed in vacuo and DCM was added. The organic layer was seprated and dried over $MgSO_4$ and concentrated. The product was purified by silica gel column 10:1 hexanes:EtOAc. 72% yield (2 step). ^{1}H-NMR (400 MHz; $CDCl_3$): δ 3.63 (s, 1H), 1.28 (m, 12H), 0.88 (t, J = 6.9 Hz, 3H).

2,2,-d_2-1-bromooctane: To octanol-d_2 (neat, 800 mg, 6.1 mmol) was slowly added PBr_3 (285 μL, 3.0 mmol) at 0°C, then the reaction was stirred at room temperature overnight. The reaction was taken up in ether, washed with H_2O, $NaHCO_3$ (aq. sat.), then brine, and the organic layer was dried over $MgSO_4$ and concentrated. The crude oil was passed through a plug of silica with approximately 3

column volumes of 10% EtOAc in hexanes. 57% yield. ^{1}H-NMR (400 MHz; $CDCl_3$): δ 3.39 (s, 2H), 1.41 (m, 2H), 1.28 (m, 10H), 0.88 (t, J = 6.9 Hz, 3H).

7,7,10,10-d_4-*cis*-hexadec-8-ene: 1-bromooctane-d_2 (660 mg, 3.38 mmol) was dissolved in 5 mL dry benzene and PPh_3 (892 mg, 3.4 mmol) was added. A reflux condenser was affixed to the flask and the reaction was heated to 90ºC for 3 days. The crude mixture was triturated with ether, the ether decanted, and the residual solvent was removed in vacuo. The crude solid (1.5 g, 3.4 mmol) was taken up in 50 mL dry THF, cooled to -78ºC, and nBuLi (2.5 M in hexane, 1.35 mL, 3.4 mmol) was added dropwise. The solution turned deep orange, and was stirred for 15 minutes. Octanal-d_2 (433 mg, 3.4 mmol) was added dropwise in 5 mL THF at -78ºC, then the reaction was allowed to come to room temperature and stirred overnight. The crude product was purified by silica gel column (hexanes) to yield a mixture of cis- and trans-isomers in a ratio of *ca*. 4:1, 89% yield. The cis-isomer was isolated by 5 mol% Ag-impregnated silica gel column (hexanes). ^{1}H-NMR (400 MHz; $CDCl_3$): δ 5.35 (s, 2H), 1.28 (m, 20H), 0.88 (t, J = 6.9 Hz, 6H); ^{13}C-NMR (100 MHz; $CDCl_3$): δ 130.0, 32.1, 29.41, 29.39, 26.7 (m), 22.8, 14.3.

cis-hexadec-8-ene: 1-iodoooctane (2.80 g, 11.7 mmol) was dissolved in 15 mL dry benzene and PPh_3 (3.06 g, 11.7 mmol) was added. A reflux condenser was affixed to the flask and the reaction was heated to 90ºC overnight. The crude mixture was triturated with ether, the ether decanted, and the residual solvent was removed in vacuo. The crude solid (3.5 g, 6.9 mmol) was taken up in 150 mL dry THF, cooled to -78ºC, and nBuLi (2.5 M in hexane, 2.77 mL, 6.9 mmol) was added dropwise. The solution turned deep orange, and was stirred for 15 minutes. Octanal (1.1 mL, 6.9 mmol) was added dropwise in 15 mL THF at -78ºC, then the reaction was allowed to come to room temperature and stirred overnight. The crude product was purified by silica gel column (hexanes) to yield a mixture of cis- and trans-isomers in a ratio of *ca*. 4:1, 56% yield. The cis-isomer was isolated by Ag-impregnated silica gel column (hexanes). ^{1}H-NMR (400 MHz; $CDCl_3$): δ 5.35 (m, 2H), 2.01 (dd, J =

6.4, 6.8 Hz, 4H), 1.28 (m, 20H), 0.88 (t, J = 6.9 Hz, 6H); ^{13}C-NMR (100 MHz; $CDCl_3$): δ 130.1, 32.0, 29.9, 29.44, 29.39, 27.4, 22.8, 14.3.

2,3-diheptyloxirane: Hexadec-8-ene (200 mg, 0.89 mmol) and mCPBA (171 mg, 0.99 mmol) were stirred in 5.0 mL DCM overnight. Aqueous $NaCO_3$ was added and the mixture stirred for 15 min. The aqueous layer was separated and the organic phase was washed with water then brine, dried over $MgSO_4$, then concentrated. The crude product was purified by silica gel column (hexanes). *cis-2,3-diheptyloxirane:* ^{1}H-NMR (400 MHz; $CDCl_3$): δ 2.90 (m, 2H), 1-51-1.28 (m, 24H), 0.88 (t, J = 6.9 Hz, 6H); *trans-2,3-diheptyloxirane:* ^{1}H-NMR (400 MHz; $CDCl_3$): δ 2.65 (m, 2H), 1-51-1.28 (m, 24H), 0.88 (t, J = 6.9 Hz, 6H).

trans-hexadec-9-en-8-ol: Hexadec-8-ene (200 mg, 0.89 mmol) and Rose Bengal (4 mg, 0.0045 mmol) were dissolved in 5.0 mL pyridine. O_2 was bubbled through the solution while irradiating with a 400W sodium lamp at a distance of ~ 5 cm, and while cooling in a circulating bath (~10ºC) for 6 hours. PPh_3 (236 mg, 0.9 mmol) was added to reduce the hydroperoxide product to the corresponding alcohol, and the solvent was removed in vacuo. The crude product was purified by silica gel column (hexanes). ^{1}H-NMR (400 MHz; $CDCl_3$): δ 5.63 (dt, J = 15.16, 6.95 Hz, 1H), 5.45 (ddt, J = 15.36, 7.13, 1.32 Hz, 1H), 4.03 (q, J = 6.65 Hz, 1H), 2.02 (q, J = 6.97 Hz, 2H), 1-52-1.22 (m, 22H), 0.88 (m, 6H).

trans-hexadec-9-en-8-one: Pyridinium chlorochromate (PCC, 91 mg, 0.42 mmol) was added to (E)-hexadec-9-en-8-ol (50 mg, 0.21 mmol) and 4Å molecular sieves (100 mg) in 2 mL DCM. The mixture was stirred overnight, during which it turned from orange to brown. The mixture was passed through a pad of Celite over a plug of silica, washed through with DCM, and concentrated. The crude product was purified by silica gel column (hexanes). ^{1}H-NMR (400 MHz; $CDCl_3$): δ 6.80 (dt, J = 15.85, 6.93 Hz, 1H), 6.06 (dt, J = 15.86, 1.52 Hz, 1H), 2.50 (t, J = 7.49 Hz, 2H), 2.32 (t, J = 7.53 Hz, 2H), 2.18 (m, 2H) 1.64-1.22 (m, 16H), 0.86 (m, 6H).

hexadec-8-yn-7-ol: 1-Nonyne (500 uL, 3.05 mmol) in dry THF was cooled to -78ºC. n-BuLi (2.5M in hexane, 1.32 mL, 3.3 mmol) was added dropwise and stirred 30 minutes. Heptanal (426 uL, 3.05 mmol) was added dropwise in THF. The solution was warmed to room temperature and stirred for 2 hours. NH_4Cl (aq.) was added and the solution was extracted twice with ether, and the combined ether layers were washed with brine, dried over $MgSO_4$ and concentrated. The crude product was purified by silica gel column (hexanes). ^{1}H-NMR (400 MHz; $CDCl_3$): δ 4.37-4.32 (m, 1H), 2.20 (td, *J* = 7.06, 1.97 Hz, 2H), 1.70-1.27 (m, 24H), 0.88 (t, *J* = 6.78, 6H).

cis-hexadec-8-en-7-ol: Hexadec-8-yn-7-ol (100 mg, 0.42 mmol) was dissolved in 2 mL hexane, with quinoline (50 uL, 0.42 mmol) and 10 mg Lindlar's catalyst. The mixture was stirred under H_2 for 3 hours, filtered over Celite and washed through with EtOAc, and the eluate was concentrated. ^{1}H-NMR (400 MHz; $CDCl_3$): δ 5.48 (dtd, *J* = 10.92, 7.38, 0.82 Hz, 1H), 5.36 (ddt, *J* = 10.75, 8.97, 1.62 Hz, 1H), 4.43 (q, *J* = 7.34 Hz, 1H), 2.12-2.03 (m, 2H), 1.43-1.26 (m, 22H), 0.88 (t, *J* = 6.89, 6H).

trans-hexadec-8-en-7-ol: Hexadec-8-yn-7-ol (100 mg, 0.42 mmol) was added dropwise to $LiAlH_4$ (32 mg, 0.84 mmol) in 2 mL THF at 0ºC. The mixture was then warmed, and refluxed overnight. Water was added dropwise to quench the reaction. The solution was extracted with ether, washed with brine, dried over $MgSO_4$, and concentrated. ^{1}H-NMR (400 MHz; $CDCl_3$): δ 5.63 (dtd, *J* = 15.41, 6.72, 0.69 Hz, 1H), 5.44 (ddt, *J* = 15.35, 7.11, 1.35 Hz, 1H), 4.03 (q, *J* = 6.72 Hz, 1H), 2.02 (dd, *J* = 13.63, 6.77 Hz, 2H), 1.41-1.22 (m, 22H), 0.88 (t, *J* = 6.84, 6H).

cis-hexadec-8-en-7-one: cis-hexadec-8-en-7-ol (20 mg, 0.083 mmol) and Dess-Martin periodinane (53 mg, 0.125 mmol) were stirred in 1 mL DCM for 1 hour. Na_2SO_3 (aq. sat.) and $NaHCO_3$ (aq. sat.) were added and the mixture stirred 30 minutes. The solution was extracted with EtOAc three times. The organic phase washed with $NaHCO_3$ then brine, dried over $MgSO_4$, and concentrated. ^{1}H-NMR (400 MHz; $CDCl_3$): δ 6.80 (dt, *J* = 15.85, 6.93 Hz, 1H), 6.06 (dt, *J* = 15.86, 1.52 Hz, 1H), 2.50 (t, *J* = 7.49 Hz, 2H), 2.32 (t, *J* = 7.53 Hz, 2H), 2.18 (m, 2H) 1.64-1.22 (m, 16H), 0.86 (m, 6H).

trans-hexadec-8-en-7-one: trans-hexadec-8-en-7-ol (20 mg, 0.083 mmol) and Dess-Martin periodinane (53 mg, 0.125 mmol) were stirred in 1 mL DCM for 1 hour. Na_2SO_3 (aq. sat.) and $NaHCO_3$ (aq. sat.) were added and the mixture stirred 30 minutes. The solution was extracted with EtOAc three times. The organic phase washed with $NaHCO_3$ then brine, dried over $MgSO_4$, and concentrated. ^{1}H-NMR (400 MHz; $CDCl_3$): δ 6.80 (dt, *J* = 15.85, 6.93 Hz, 1H), 6.06 (dt, *J* = 15.86, 1.52 Hz, 1H), 2.50 (t, *J* = 7.49 Hz, 2H), 2.32 (t, *J* = 7.53 Hz, 2H), 2.18 (m, 2H) 1.64-1.22 (m, 16H), 0.86 (m, 6H).

hexadecane-8,9-diol: 2,3-diheptyloxirane was stirred for 2 hours in 1 mL acetone, 100 uL water, and 10 uL of 70% perchloric acid. Ether was added, and the solution was washed once with $NaHCO_3$ (aq.), twice with brine, then dried over $MgSO_4$ and concentrated. ^{1}H-NMR (400 MHz; $CDCl_3$): δ 3.61-3.55 (m, 2H), 1.53-1.25 (m, 24H), 0.88 (t, *J* = 6.90, 6H).

4.6.2 Autoxidations

DTBN-initiated autoxidations are based on Porter *et. al. J. Am. Chem. Soc.* **1994**, *116*, 6690.

The autoxidations were scaled down to conserve *d*$_4$-hexadec-8-ene, and care was taken to ensure proper mixing of the substrate and initiator in the small HPLC vials. BDMP was used to quench the reaction in place of BHT, as it eluted earlier in the GC chromatogram, and treatment with BSA and hydrazine hydrate was to derivatize the alcohols to O-TMS, and the ketones to hydrazones, respectively, for better separation by GC.

DTBN-initiated hexadec-8-ene autoxidations: A stock solution of DTBN (77.5 mg/mL in hexane) was prepared and 5 μL was added to hexadec-8-ene (10 mg, 0.045 mmol) in a small vial, such that DTBN was 5 mol% relative to hexadec-8-ene. The vial was heated to 30°C and after 6 hours, half the mixture was transferred to a separate vial and quenched with 160 μL of a solution of 25.1 mg/mL BDMP and 36.8 mg/mL PPh_3 in ACN. 75 μL of BSA was added and the solution heated to 70°C for 5

minutes, then 6.25 μL hydrazine hydrate was added and the solution was left at 70ºC a further 30 minutes. 5 μL of internal standard solution (20 mM dodecyl benzene in PhCl) was added, and the solution was topped to 0.5 mL with 250 μL ACN. The other half of the autoxidation mixture was treated in the same way after 24 hours at 30ºC.

Hydroperoxide-loaded, DTBN-initiated hexadec-8-ene autoxidations: A stock solution of DTBN (77.5 mg/mL in hexane) was prepared and 5 μL was added to hexadec-8-ene (10 mg, 0.045 mmol) and 50 μL of t-BuOOH (5-6 M in decane) in a small vial, such that DTBN was 5 mol% relative to hexadec-8-ene. The vial was heated to 30ºC and after 6 hours, half the mixture was transferred to a separate vial and the t-BuOOH was removed *in vacuo*. 160 μL of a solution of 25.1 mg/mL BDMP and 36.8 mg/mL PPh_3 in ACN was added. 75 μL of BSA was added and the solution heated to 70ºC for 5 minutes, then 6.25 μL hydrazine hydrate was added and the solution was left at 70ºC a further 30 minutes. 5 μL of internal standard solution (20 mM dodecyl benzene in PhCl) was added, and the solution was topped to 0.5 mL with 250 μL ACN. The other half of the autoxidation mixture was treated in the same way after 24 hours at 30ºC.

MeOAMVN-initiated hexadec-8-ene autoxidations: A stock solution of MeOAMVN (5.4 mg/mL in benzene) was prepared and 5 μL was added to hexadec-8-ene (10 mg, 0.045 mmol) in a small vial, such that the final concentration of MeOAMVN was 5 mM. The vial was heated to 37ºC and after 6 hours, half the mixture was transferred to a separate vial and quenched with 160 μL of a solution of 25.1 mg/mL BDMP and 36.8 mg/mL PPh_3 in ACN. 75 μL of BSA was added and the solution heated to 70ºC for 5 minutes, then 6.25 μL hydrazine hydrate was added and the solution was left at 70ºC a further 30 minutes. 5 μL of internal standard solution (20 mM dodecyl benzene in PhCl) was added, and the solution was topped to 0.5 mL with 250 μL ACN. The other half of the autoxidation mixture was treated in the same way after 24 hours at 37ºC.

Hydroperoxide-loaded, MeOAMVN-initiated hexadec-8-ene autoxidations: A stock solution of MeOAMVN (8.0 mg/mL in benzene) was prepared and 15 μL was added to hexadec-8-ene (10 mg, 0.045 mmol) and 50 μL t-BuOOH (5-6 M in decane) in a small vial, such that the final concentration of MeOAMVN was 5 mM. The vial was heated to 37ºC and after 6 hours, half the mixture was transferred to a separate vial and the t-BuOOH was removed *in vacuo*. 160 μL of a solution of 25.1 mg/mL BDMP and 36.8 mg/mL PPh_3 in ACN was added. 75 μL of BSA was added and the solution heated to 70ºC for 5 minutes, then 6.25 μL hydrazine hydrate was added and the solution was left at 70ºC a further 30 minutes. 5 μL of internal standard solution (20 mM dodecyl benzene in PhCl) was added, and the solution was topped to 0.5 mL with 250 μL ACN. The other half of the autoxidation mixture was treated in the same way after 24 hours at 37ºC.

7,7,10,10-d_4-hexadec-8-ene autoxidations: Each of the above was also carried out with 7,7,10,10-d_4-hexadec-8-ene.

4.6.3 GC-FID Analysis

An Agilent GC 7890 was used with the following instrument control parameters:

Front SS Inlet He

Mode	Split
Heater	On 300 ∞C
Pressure	On 11.553 psi
Total Flow	On 92.574 mL/min
Septum Purge Flow	On 3 mL/min
Split Ratio	50 :1
Split Flow	87.817 mL/min
Injection Volume	3 μL

Column #1

Pressure	
Setpoint	On
(Initial)	11.553 psi
Hold Time	14 min
Post Run	5.2264 psi

Agilent 19091J-413: 1

HP-5 5% Phenyl Methyl Siloxan

-60 ∞Có325 ∞C (325 ∞C): 30 m x 320 µm x 0.25 µm

In	Front SS Inlet He
Out	Front Detector FID
(Initial)	130 ∞C
Pressure	11.553 psi
Flow	1.7563 mL/min
Average Velocity	34.524 cm/sec
Holdup Time	1.4483 min

GC

Oven

Temperature

Setpoint	On
(Initial)	130 ∞C
Hold Time	0 min
Post Run	45 ∞C
Program	
#1 Rate	1.5 ∞C/min
#1 Value	160 ∞C
#1 Hold Time	0 min
#2 Rate	28 ∞C/min
#2 Value	300 ∞C
#2 Hold Time	5 min
#3 Rate	34 ∞C/min

#3 Value	130 ∞C
#3 Hold Time	0 min
Front Detector FID	
Heater	On 300 ∞C
H2 Flow	On 50 mL/min
Air Flow	On 400 mL/min
Makeup Flow	On 25 mL/min

4.6.4 Computational Methods

All calculations were carried out using the Gaussian 09 quantum chemistry package[11] using the CBS-QB3 complete basis set approach.[12] The Skodje-Truhlar small-curvature tunnelling approximation[13,14] was used to estimate the transmission coefficient, as outlined in Eqs 4.8-4.11. Hindered internal rotor corrections have been found to be negligible for H-atom abstraction at these temperatures, and were thus ignored.[13]

4.7 References

(1) Muchalski, H.; Levonyak, A. J.; Xu, L.; Ingold, K. U.; Porter, N. A. *J. Am. Chem. Soc.* **2015**, *137*, 94.

(2) Hill, S.; Lamberson, C. R.; Xu, L.; To, R.; Tsui, H. S.; Shmanai, V. V.; Bekish, A. V.; Awad, A. M.; Marbois, B. N.; Cantor, C. R.; Porter, N. A.; Clarke, C. F.; Shchepinov, M. S. *Free Radic. Biol. Med.* **2012**, *53*, 893.

(3) Lamberson, C. R.; Xu, L.; Muchalski, H.; Montenegro-Burke, J. R.; Shmanai, V. V.; Bekish, A. V.; McLean, J. A.; Clarke, C. F.; Shchepinov, M. S.; Porter, N. A. *J. Am. Chem. Soc.* **2014**, *136*, 838.

(4) Muchalski, H.; Xu, L.; Porter, N. A. *Org. Biomol. Chem.* **2015**, *13*, 1249.

(5) Anslyn, E. V.; Dougherty, D. A. *Modern Physical Organic Chemistry*; Sausalito, CA: University Science, 2006.

(6) Bell, R. P. *Chem. Soc. Rev.* **1974**, *3*, 513.

(7) Zuev, P. S.; Sheridan, R. S.; Albu, T. V.; Truhlar, D. G.; Hrovat, D. A.; Borden, W. T. *Science* **2003**, *299*, 867.

(8) Ley, D.; Gerbig, D.; Schreiner, P. R. *Org. Biomol. Chem.* **2012**, *10*, 3781.

(9) Xu, L.; Davis, T. A.; Porter, N. A. *J. Am. Chem. Soc.* **2009**, *131*, 13037.

(10) Zielinski, Z. A. M.; Pratt, D. A. *J. Am. Chem. Soc.* **2019**, *141*, 3037.

(11) Frisch, M. J. *et. al. Gaussian 09, revision B.01*; Gaussian, Inc.: Wallingford CT, 2009.

(12) Montgomery, J. A.; Ochterski, J. W.; Petersson, G. A. *J. Chem. Phys.* **1994**, *101*, 5900.

(13) Vandeputte, A. G.; Sabbe, M. K.; Reyniers, M.-F.; Van Speybroeck, V.; Waroquier, M.; Marin, G. B. *J. Phys. Chem. A* **2007**, *111*, 11771.

(14) Porter, N. A.; Mills, K. A.; Carter, R. L. *J. Am. Chem. Soc.* **1994**, *116*, 6690.

(15) Aliwarga, T.; Raccor, B. S.; Lemaitre, R. N.; Sotoodehnia, N.; Gharib, S. A.; Xu, L.; Totah, R. A. *Free Radic. Biol. Med.* **2017**, *112*, 131.

(16) Noguchi, N.; Yamashita, H.; Gotoh, N.; Yamamoto, Y.; Numano, R.; Niki, E. *Free Radic. Biol. Med.* **1998**, *24*, 259.

(17) Dejarlais, W. J.; Emken, E. A. *Lipids* **1976**, *11*, 594.

(18) Ariza, X.; Asins, G.; Garcia, J.; Hegardt, F. G.; Makowski, K.; Serra, D.; Velasco, J. *J. Label. Compd. Radiopharm.* **2010**, *53*, 556.

(19) Wu, A.; Mader, E. A.; Datta, A.; Hrovat, D. A.; Borden, W. T.; Mayer, J. M. *J. Am. Chem. Soc.* **2009**, *131*, 11985.

(20) Barclay, L. R. C.; Ingold, K. U. *J. Am. Chem. Soc.* **1981**, *103*, 6478.

(21) Braverman, N. E.; Moser, A. B. *Biochim. Biophys. Acta* **2012**, *1822*, 1442.

(22) Broniec, A.; Klosinski, R.; Pawlak, A.; Wrona-Krol, M.; Thompson, D.; Sarna, T. *Free Radic. Biol. Med.* **2011**, *50*, 892.

(23) Sindelar, P. J.; Guan, Z.; Dallner, G.; Ernster, L. *Free Radic. Biol. Med.* **1999**, *26*, 318.

(24) Loidl-Stahlhofen, A.; Hannemann, K.; Felde, R.; Spiteller, G. *Biochem. J.* **1995**, *309*, 807.

(25) Broniec, A.; Żądło, A.; Pawlak, A.; Fuchs, B.; Kłosiński, R.; Thompson, D.; Sarna, T. *Free Radic. Biol. Med.* **2017**, *106*, 368.

4.8 Supporting Information

4.8.1 NMR Spectra

All compounds have been previously reported, and their characterizations match the literature. ^{1}H NMR are shown below for the intermediates in the synthesis of 7,7,10,10-d_4-hexadec-8-ene, to demonstrate the successful deuteration of the indicated positions. Due to the volatility of the intermediates, they were not left under high vacuum for long and therefore residual solvent was present (indicated on the spectra).

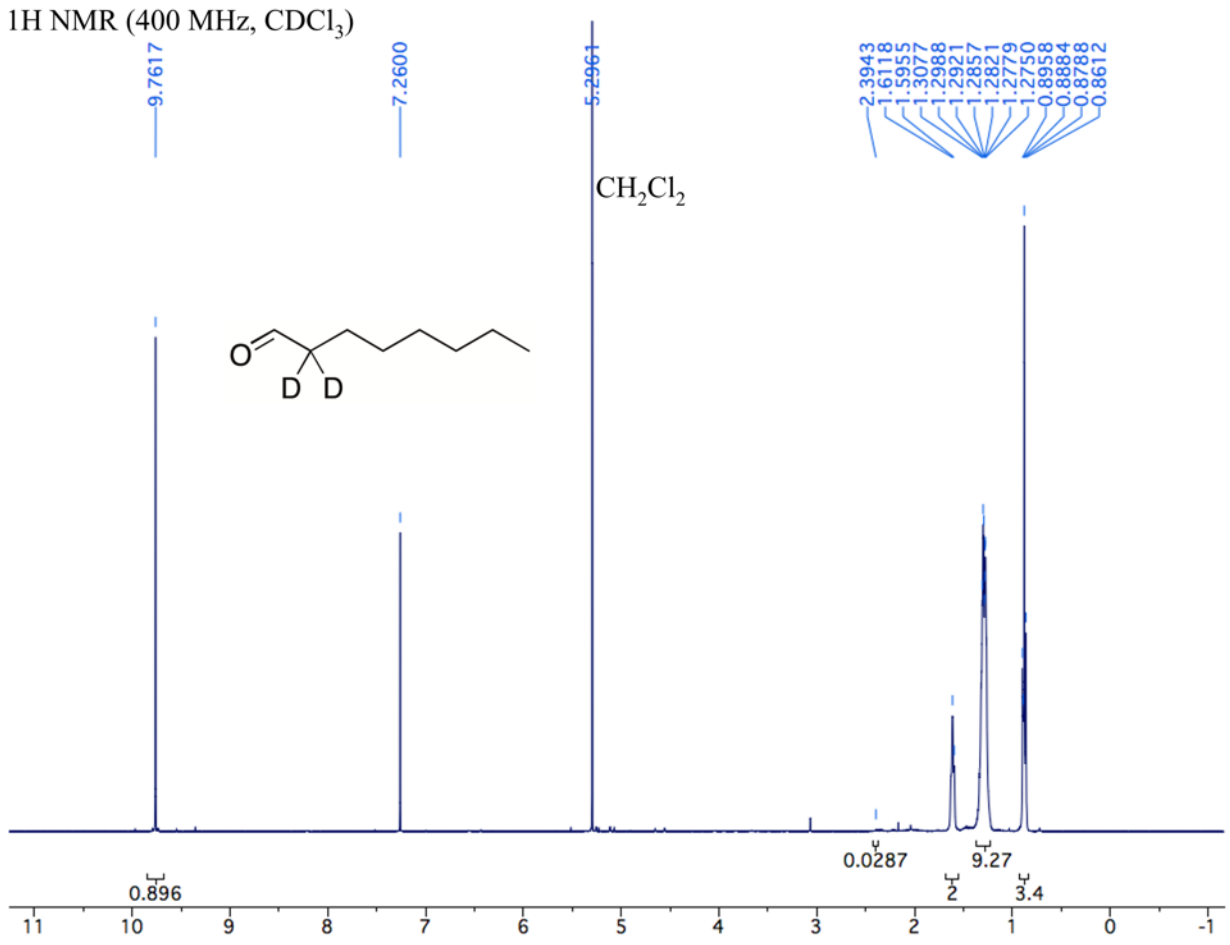

1H NMR (400 MHz, $CDCl_3$)

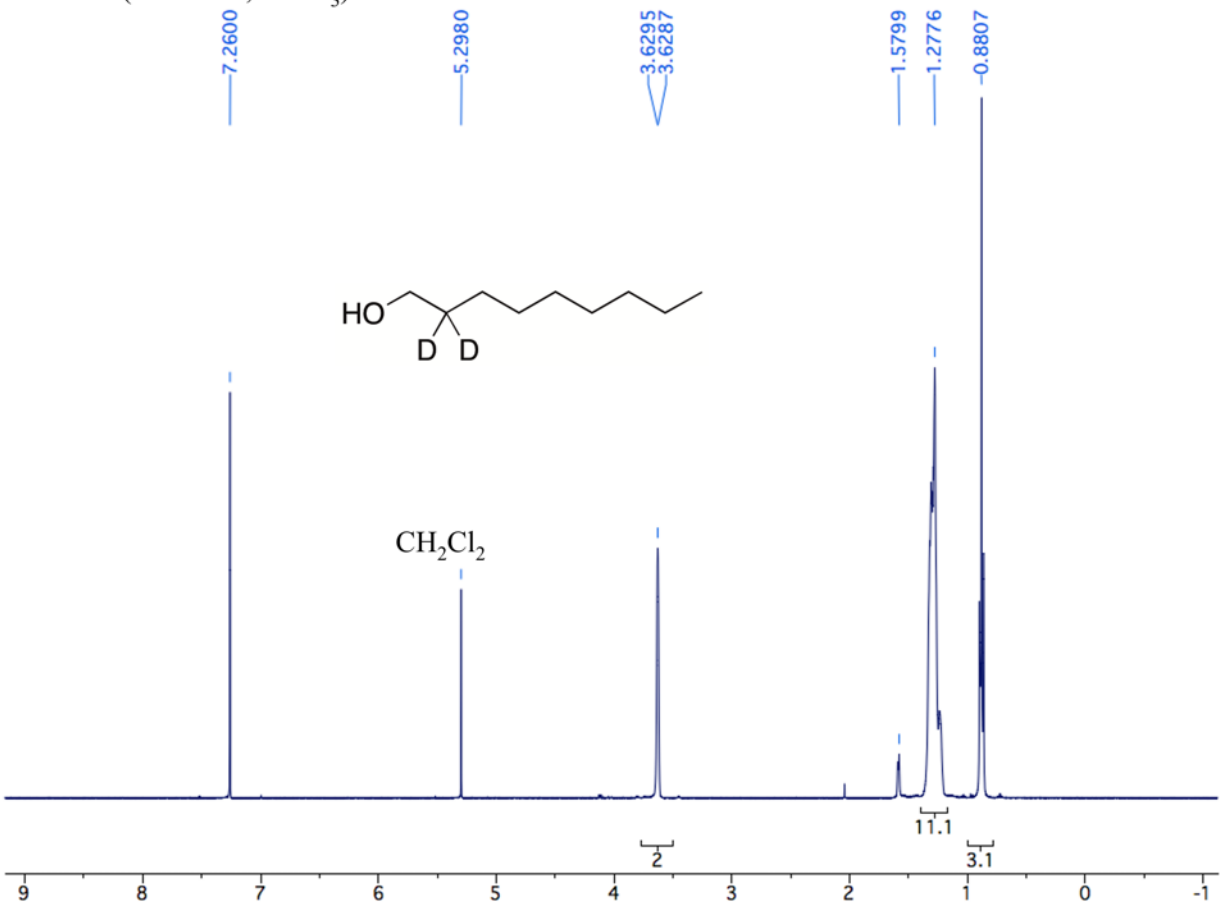

1H NMR (400 MHz, $CDCl_3$)

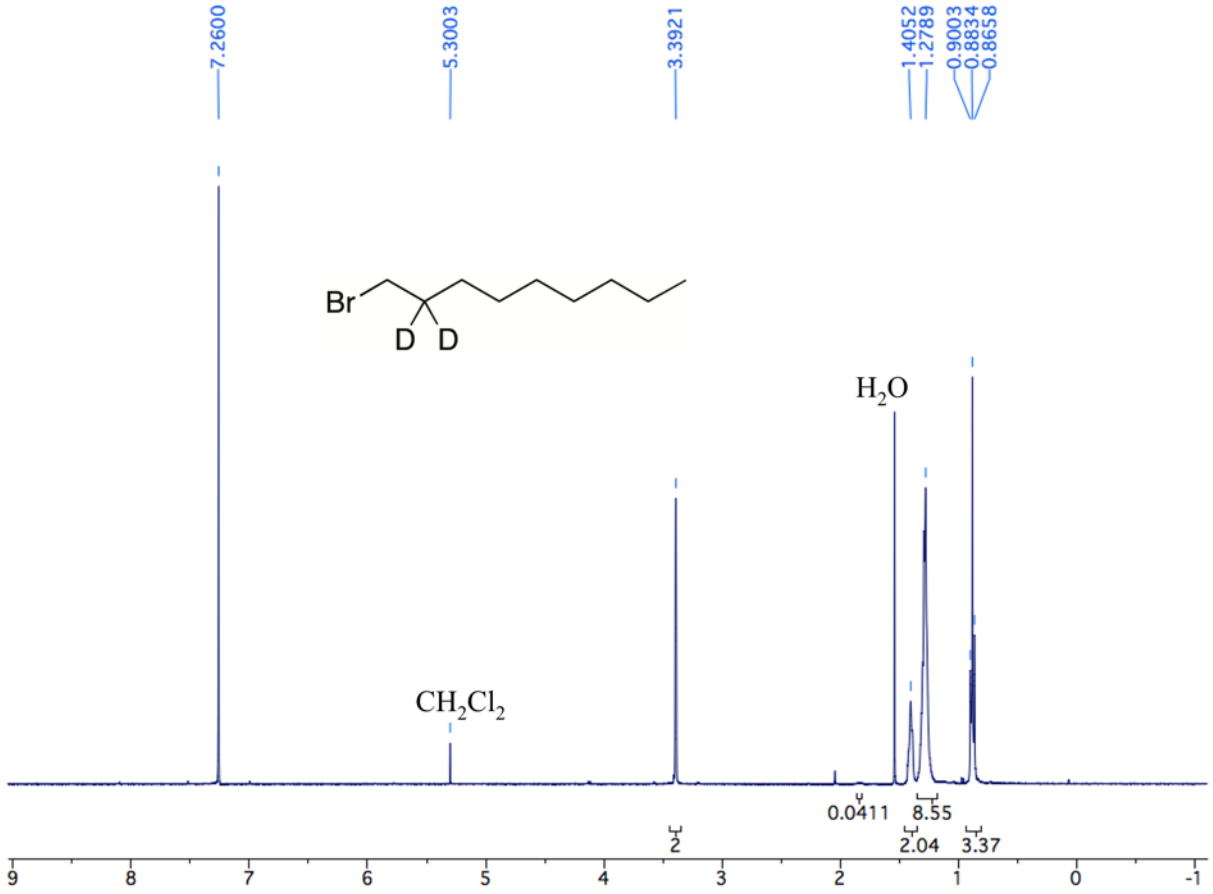

1H NMR (400 MHz, $CDCl_3$)

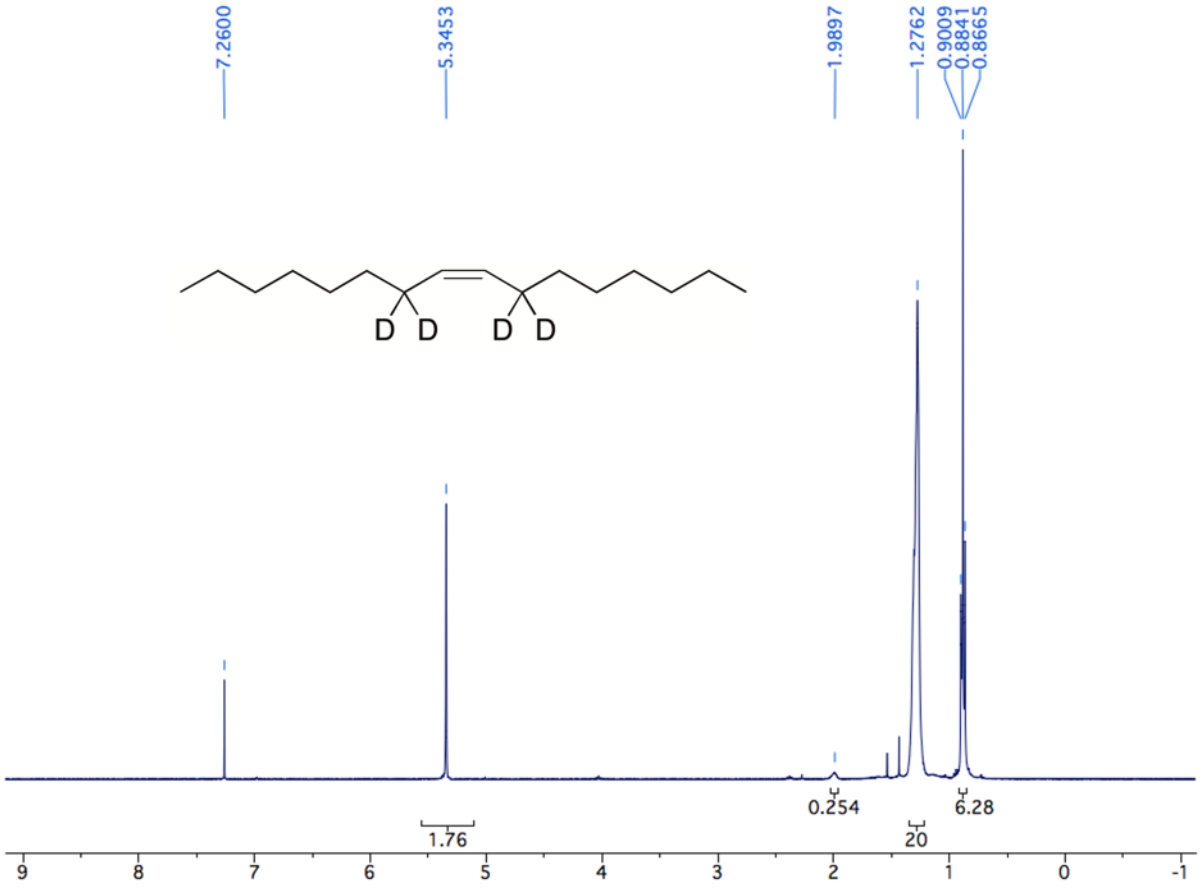

13C NMR (100 MHz, $CDCl_3$)

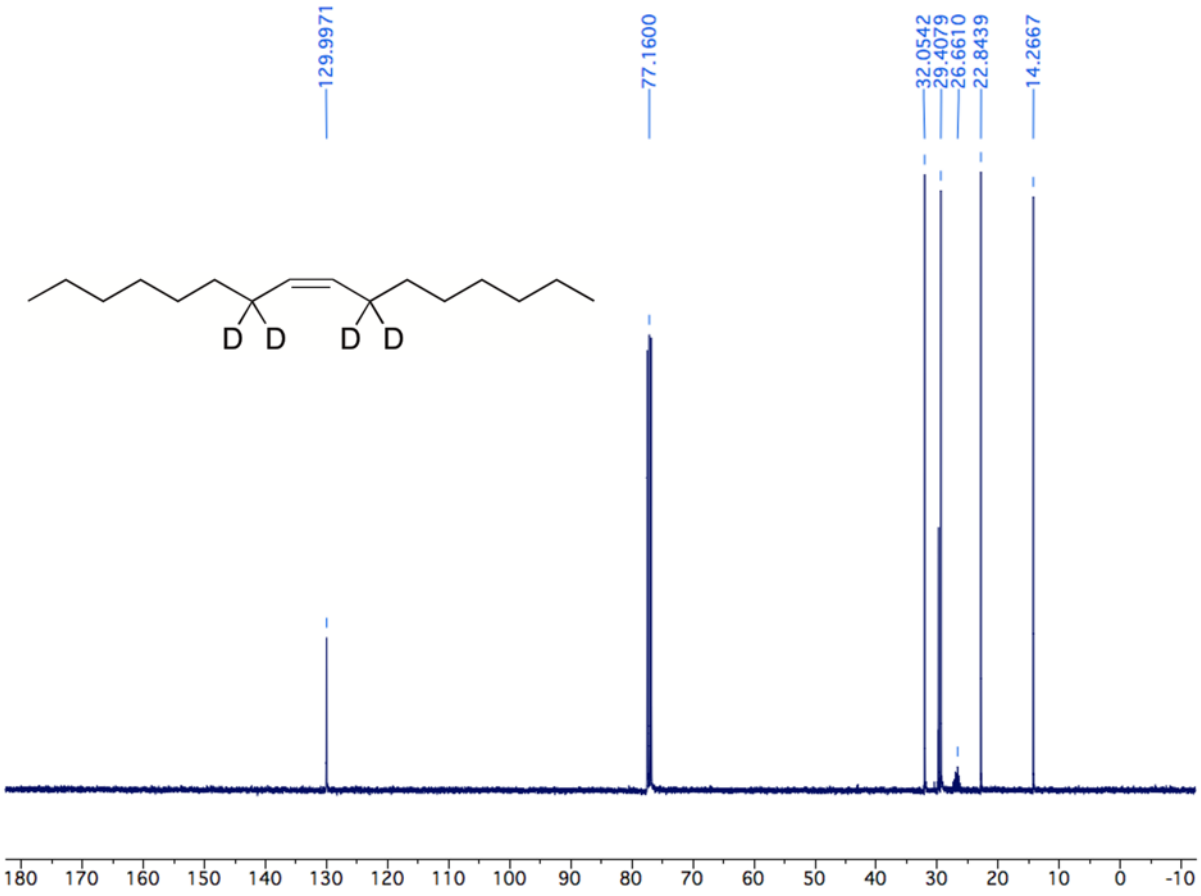

1H NMR (400 MHz, $CDCl_3$)

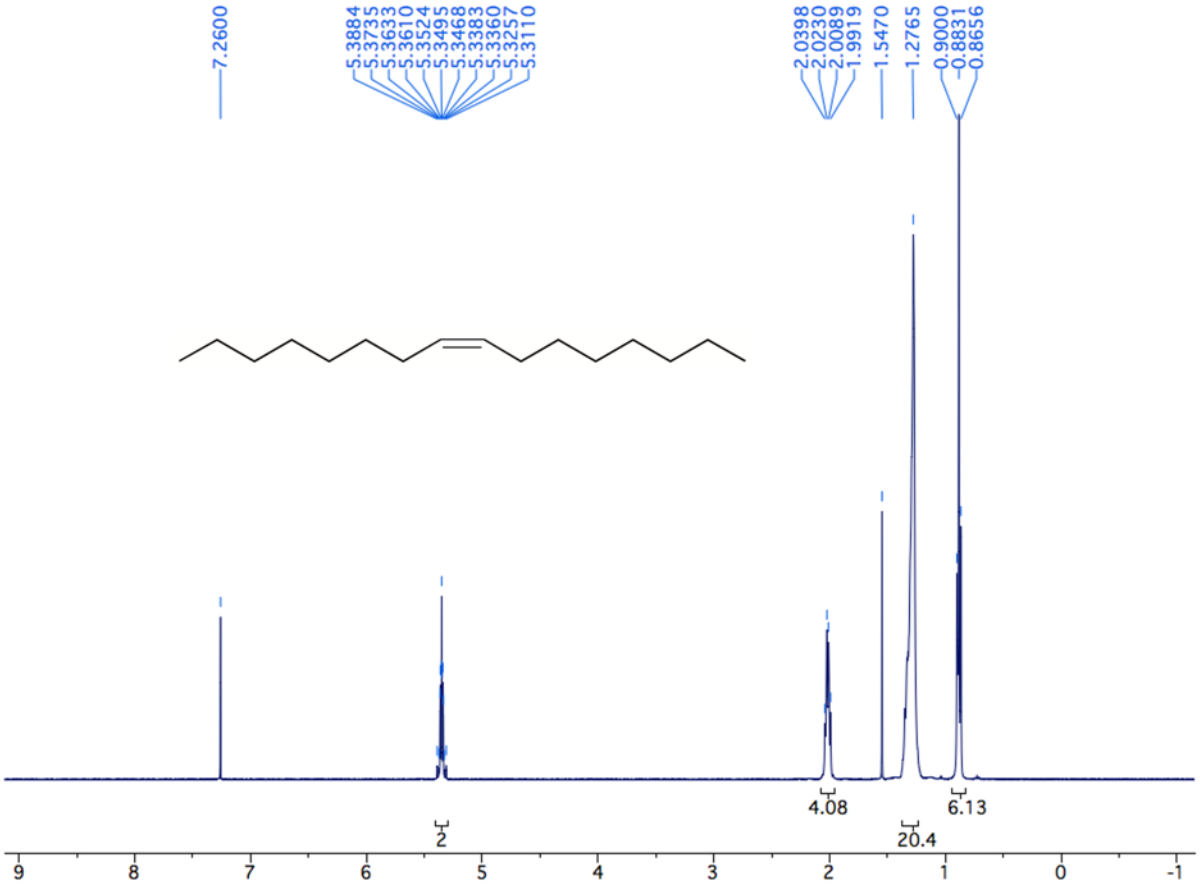

13C NMR (100 MHz, $CDCl_3$)

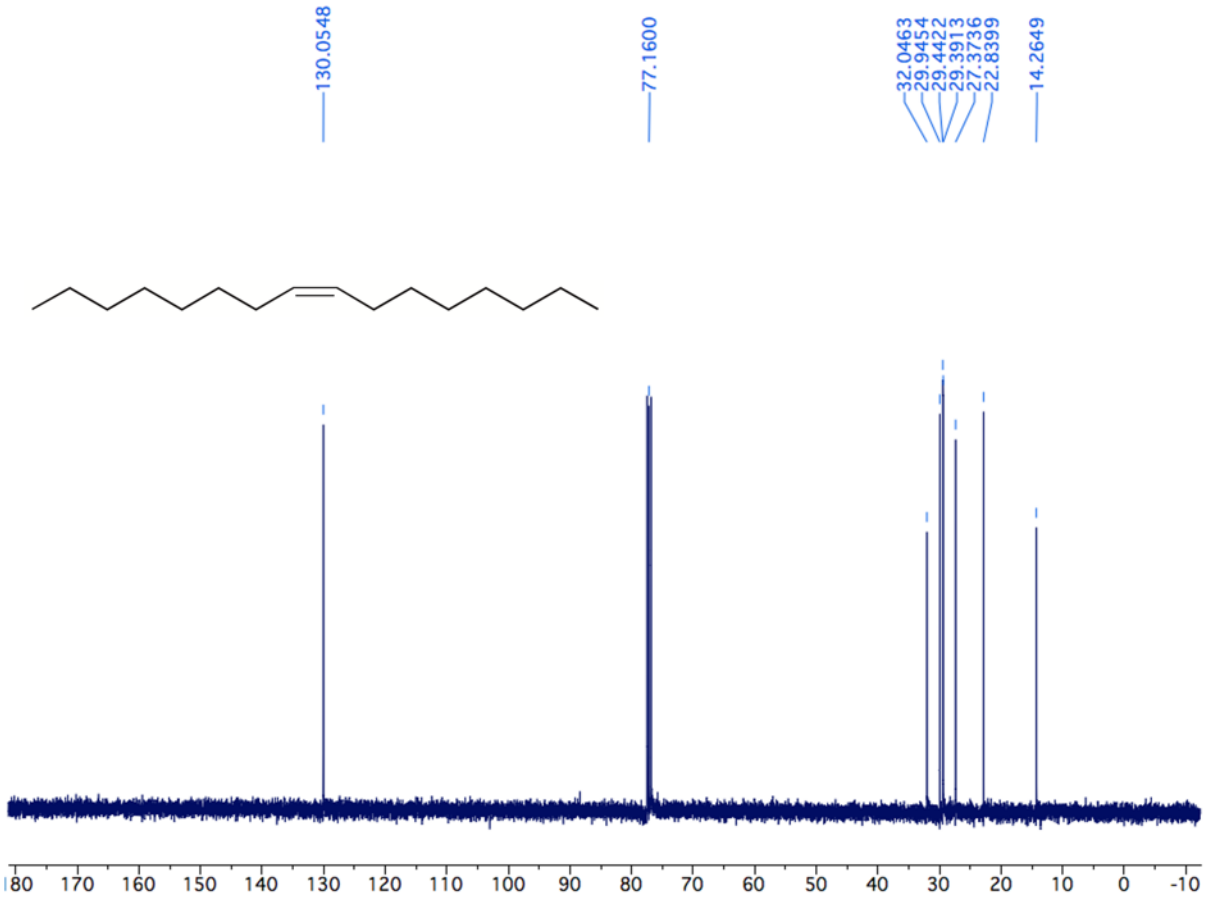

4.8.2 Supplementary GC-FID Data

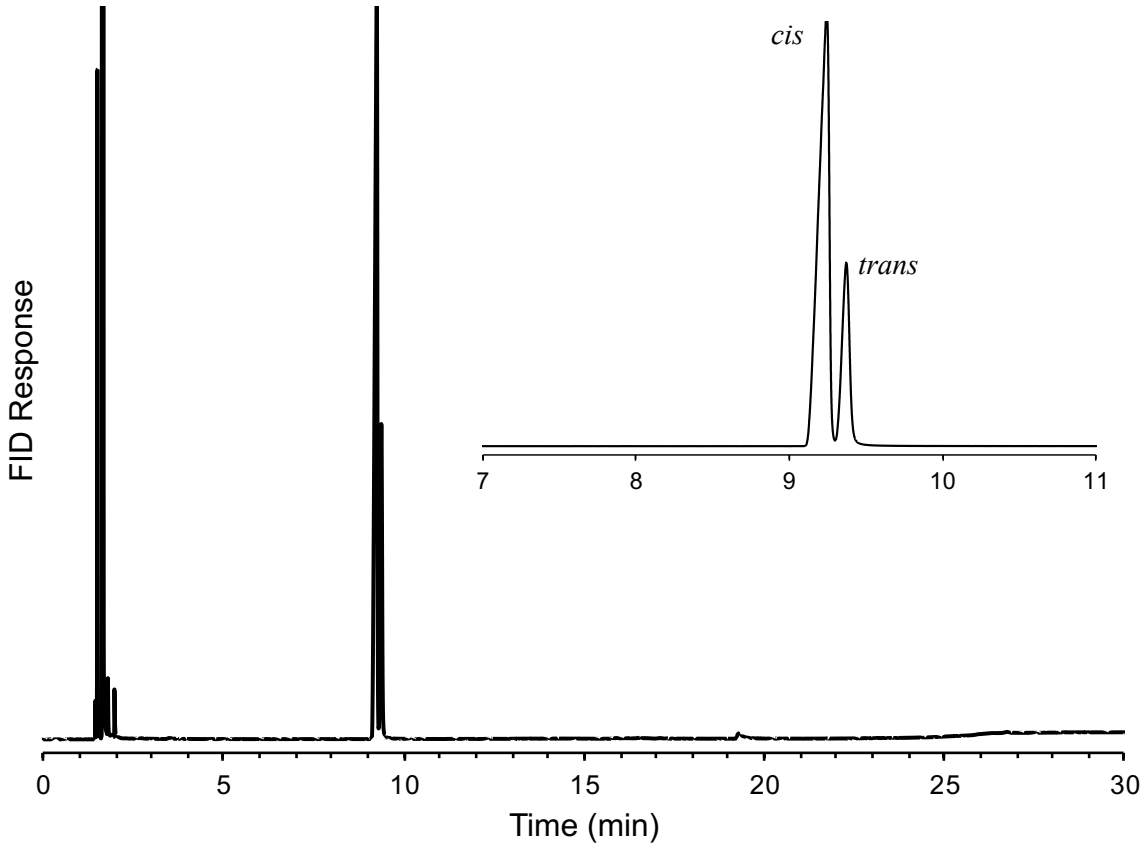

Figure 4.13. GC-FID chromatogram of hexadec-8-ene as a mixture of ca. 4:1 *cis:trans*.

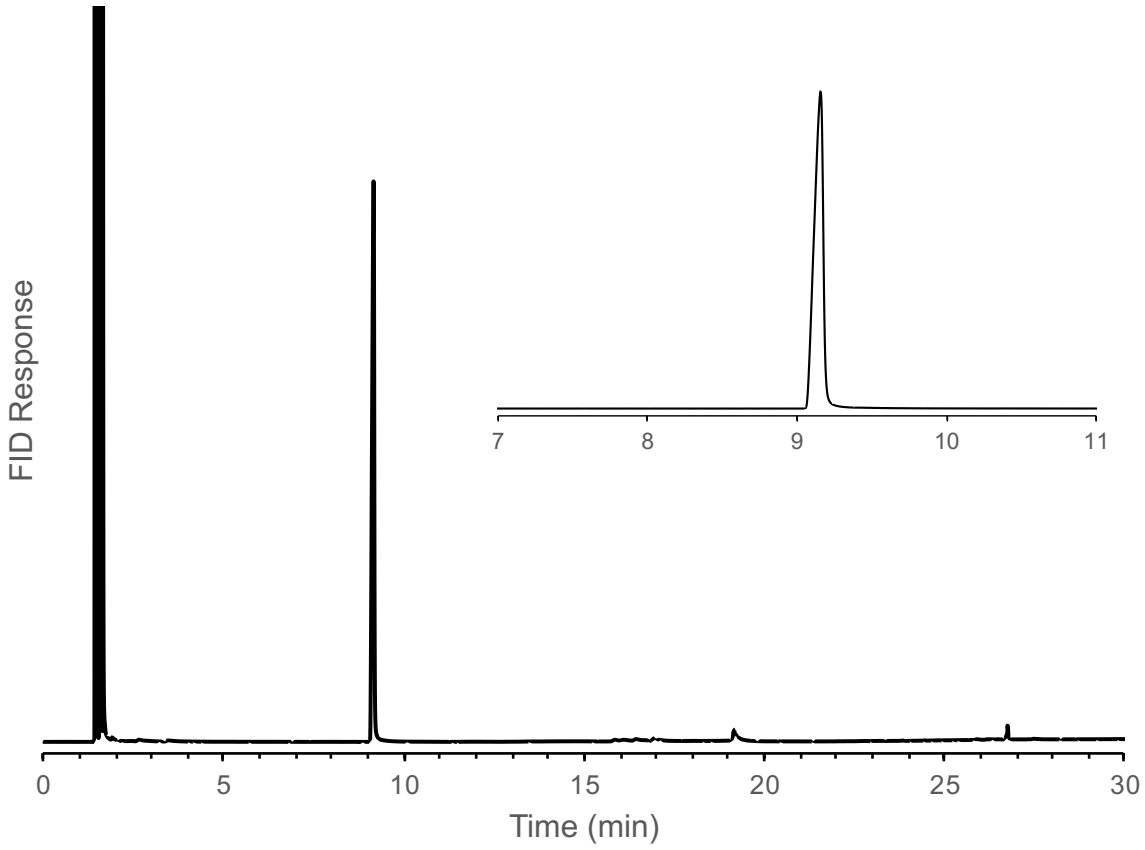

Figure 4.14. GC-FID chromatogram of *cis*-hexadec-8-ene after purification by Ag-impregnated silica gel column.

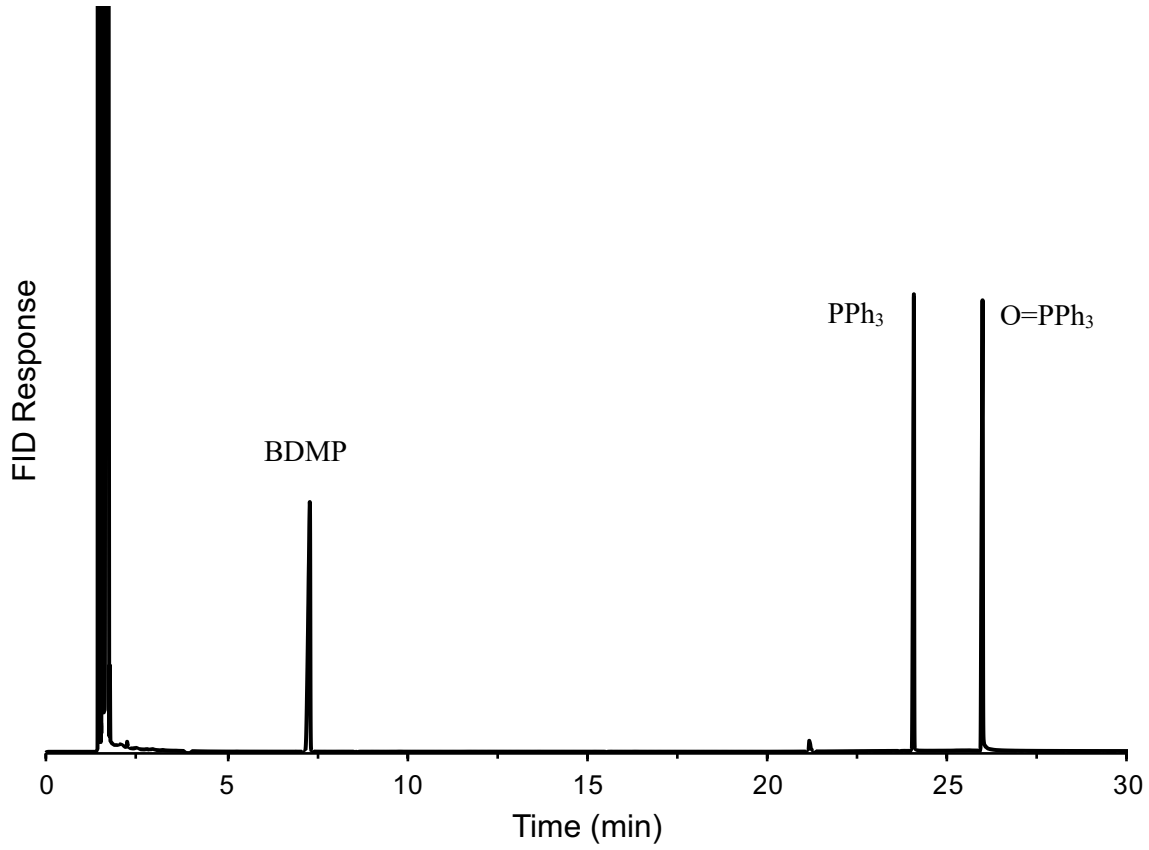

Figure 4.15. GC-FID chromatogram of 4-*tert*-butyl-2,6-dimethylphenol (BDMP), triphenylphosphine (PPh_3), and triphenylphosphine oxide ($O=PPH_3$) as a co-injection (independently assigned).

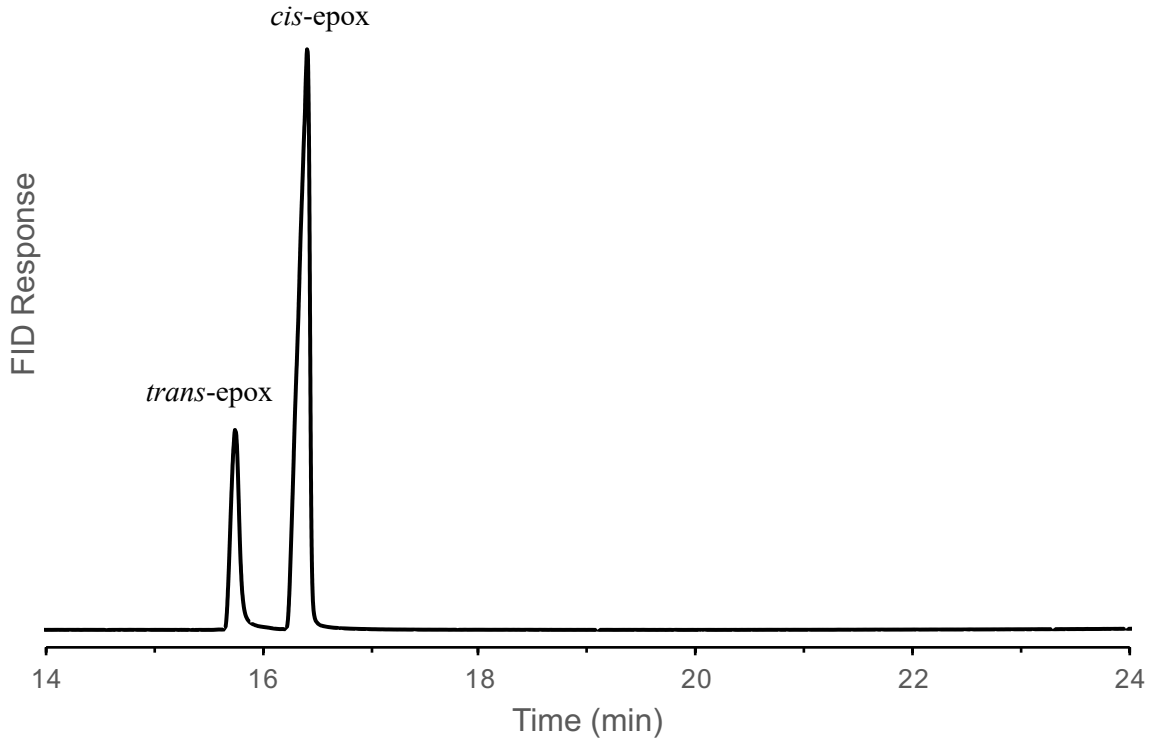

Figure 4.16. GC-FIC chromatogram of 2,3-diheptyloxirane (*cis*- and *trans*-epox), assigned based on ratio by NMR.

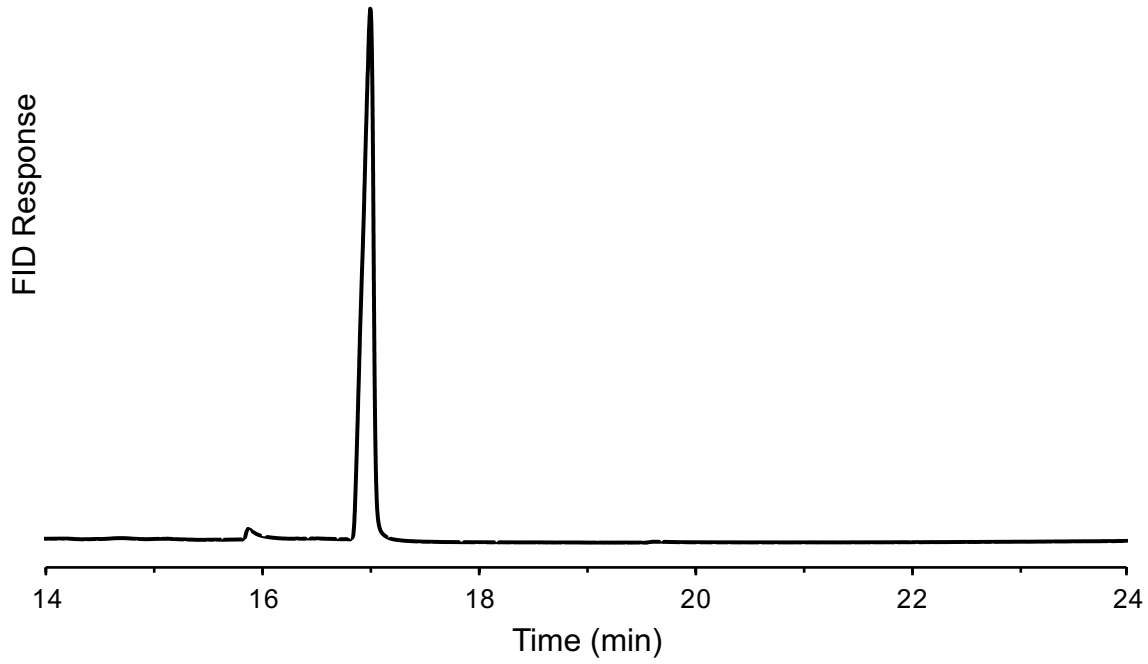

Figure 4.17. GC-FID chromatogram of *trans*-hexadec-9-en-8-ol (*trans*-8OH).

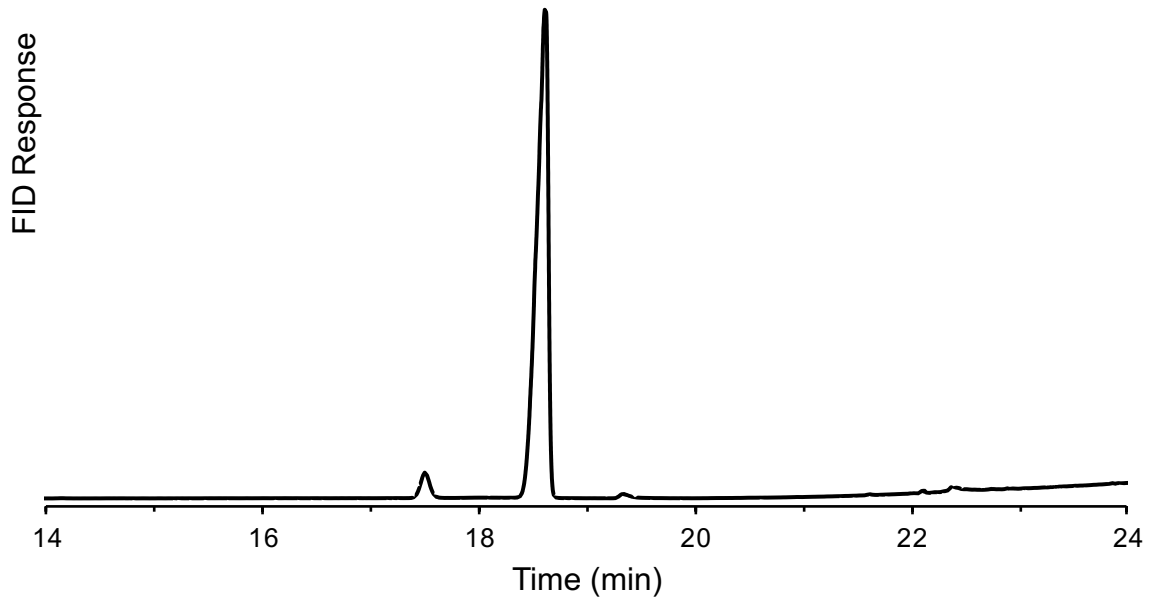

Figure 4.18. GC-FID chromatogram of *trans*-hexadec-9-en-8-ol treated with BSA to derivatize the alcohol with TMS (*trans*-8-OTMS).

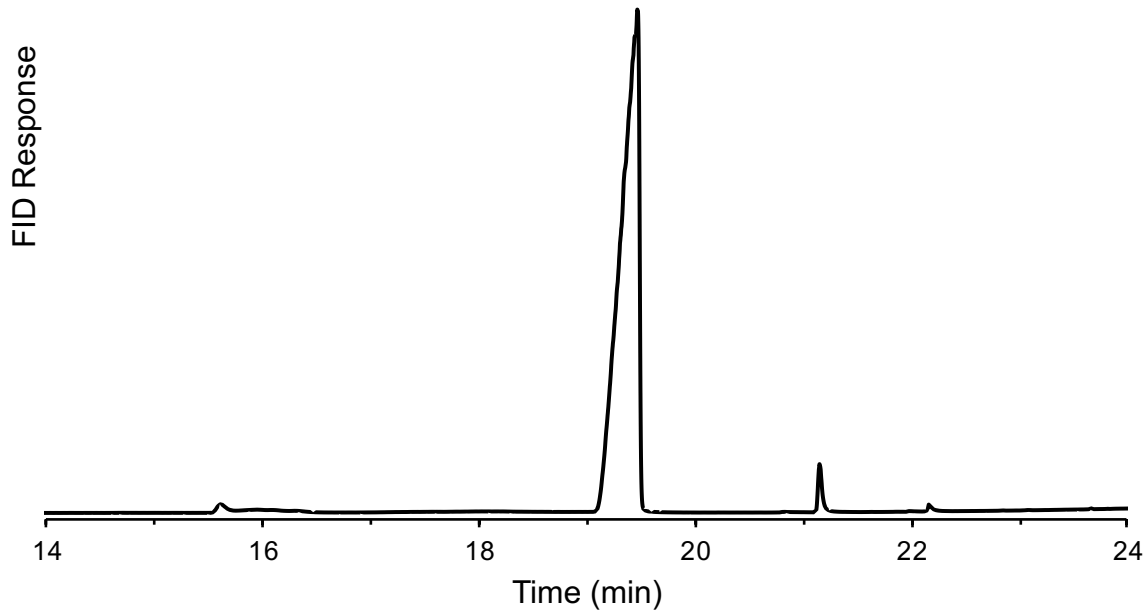

Figure 4.19. GC-FID chromatogram of *trans*-hexadec-9-en-8-one (*trans*-8-keto*)*; the sample contained dodecyl benzene as internal standard (21.2 min).

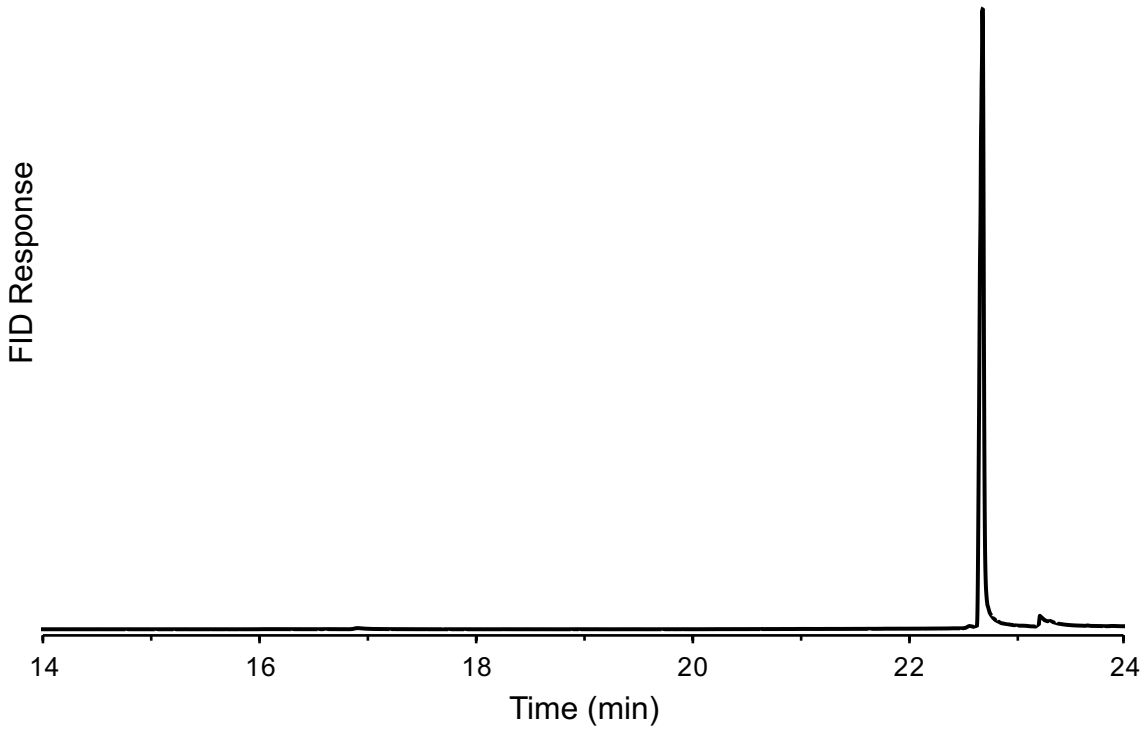

Figure 4.20. GC-FID chromatogram of *trans*-hexadec-9-en-8-one treated with hydrazine hydrate to derivatize the ketone to a hydrazone (*trans*-8-NNH_2).

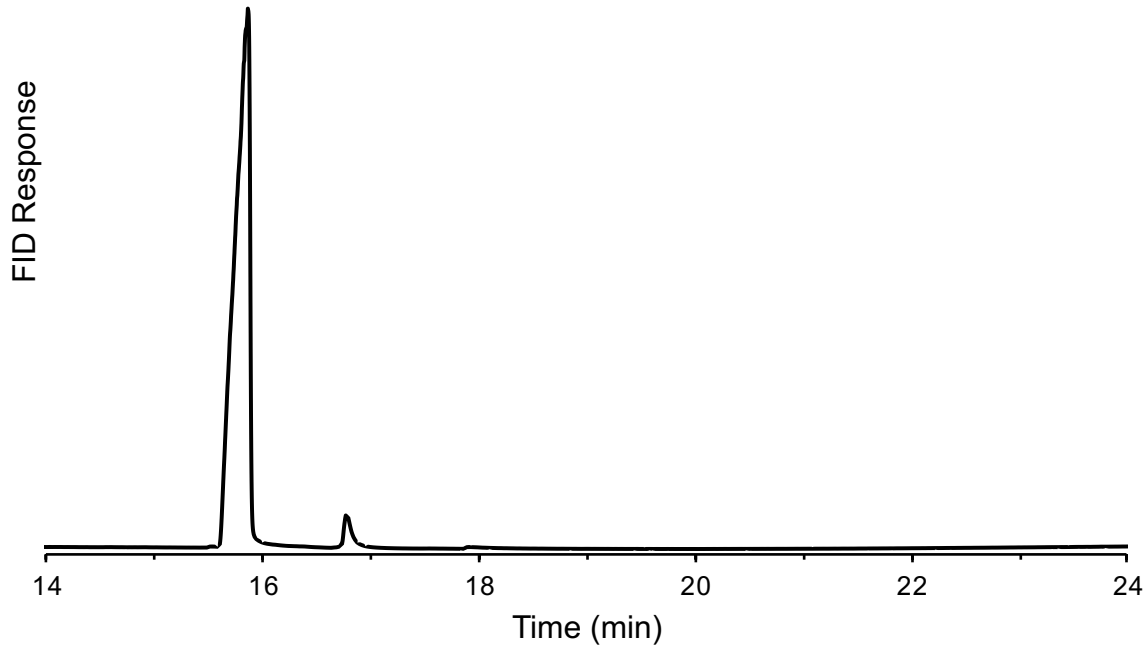

Figure 4.21. GC-FID chromatogram of *cis*-hexadec-8-en-7-ol (*cis*-7OH); the impurity at 16.8 min is *trans*-hexadec-8-en-7-ol (supported by NMR).

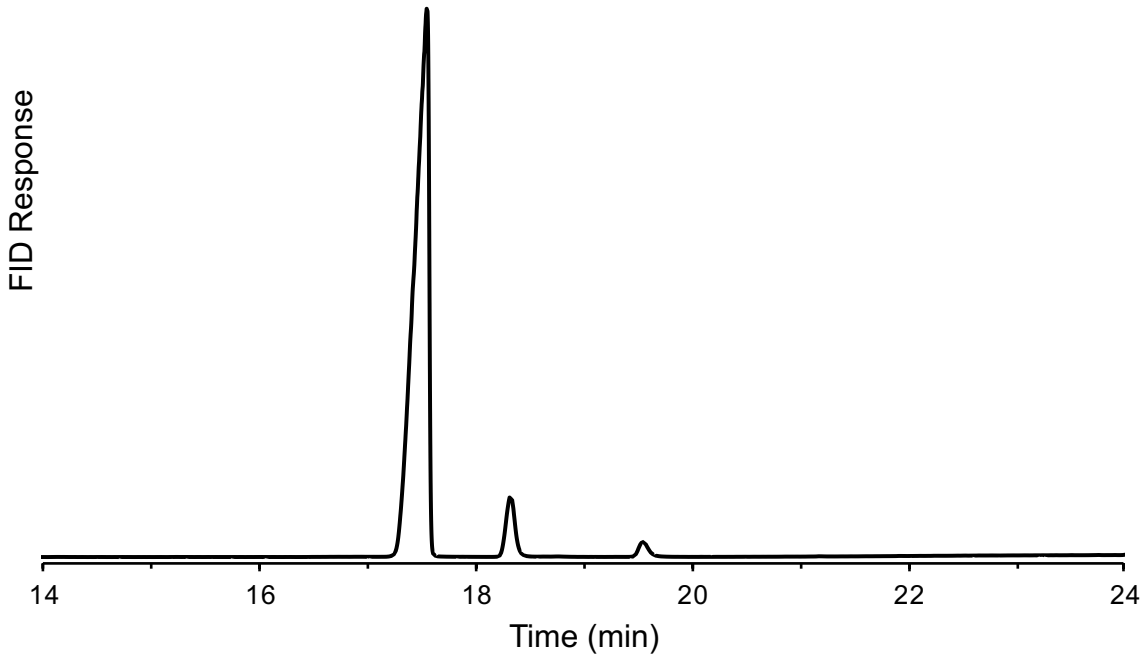

Figure 4.22. GC-FID chromatogram of *cis*-hexadec-8-en-7-ol treated with BSA to derivatize the alcohol with TMS (*cis*-7-OTMS); the impurity at 18.4 min is *trans*-7-OTMS (cf. Figure 4.21).

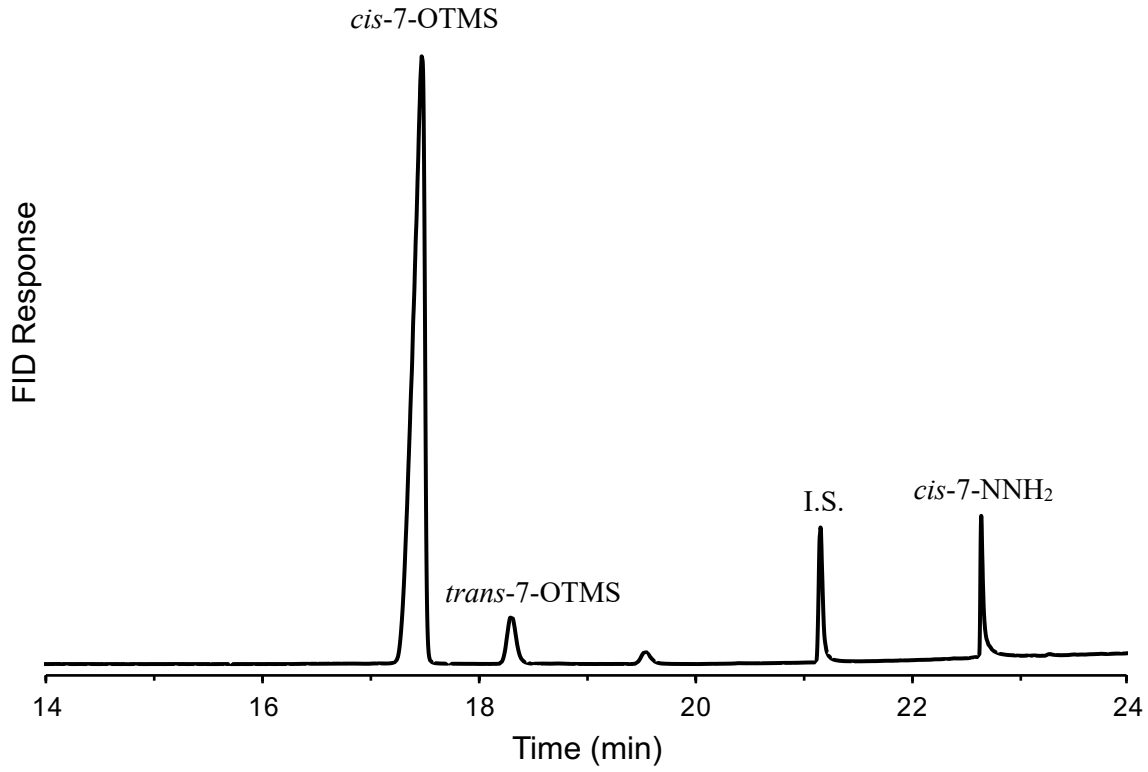

Figure 4.23. GC-FID chromatogram of *cis*-hexadec-8-en-7-one treated with hydrazine hydrate to derivatize the ketone to a hydrazone (*cis*-7-NNH_2*)*. Note: *cis*-hexadec-8-en-7-ol was oxidized (incomplete) and then treated with BSA, hydrazine hydrate, and internal standard (dodecyl benzene).

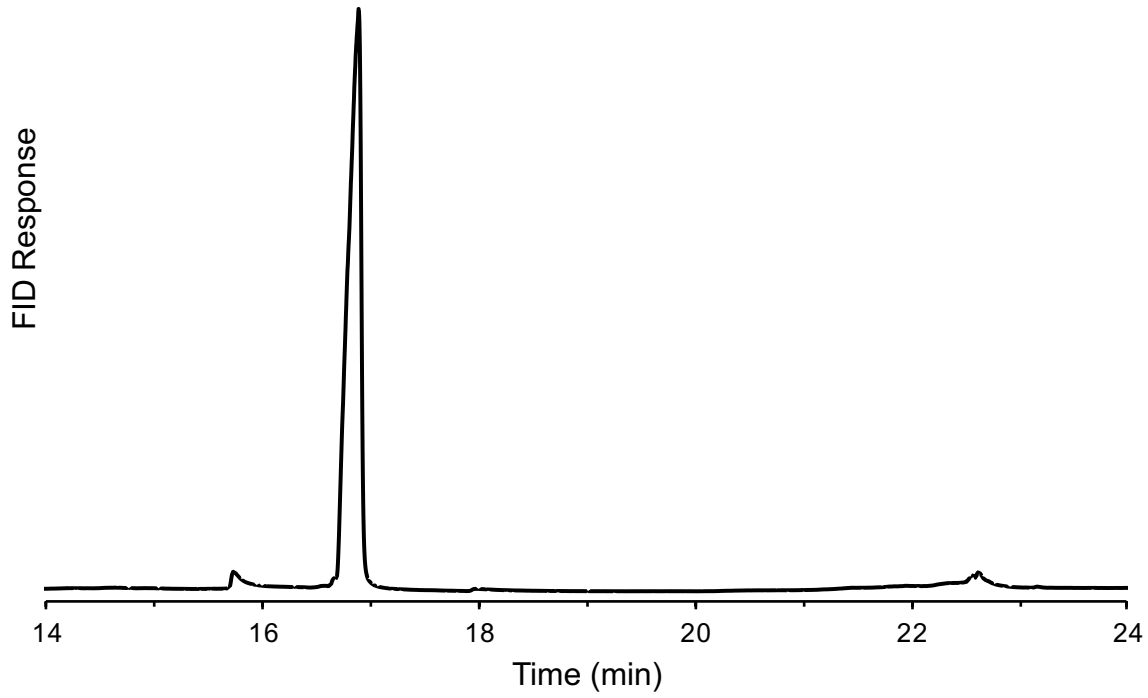

Figure 4.24. GC-FID chromatogram of *trans*-hexadec-8-en-7-ol (*trans*-7OH); the impurity at 15.9 min is *cis*-hexadec-8-en-7-ol (supported by NMR).

.

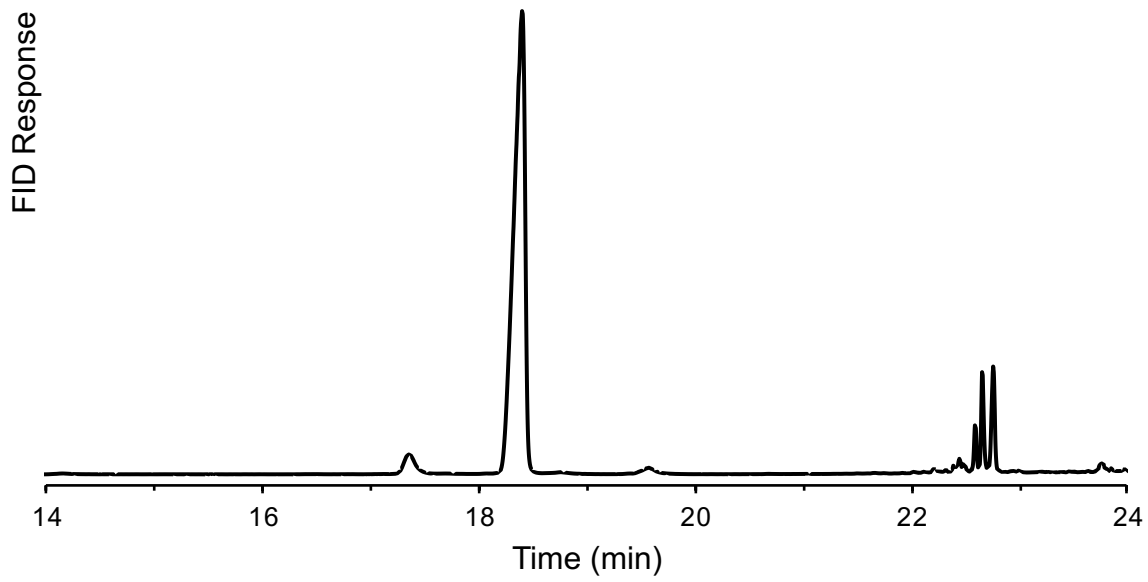

Figure 4.25. GC-FID chromatogram of *trans*-hexadec-8-en-7-ol treated with BSA to derivatize the alcohol with TMS (*transs*-7-OTMS); the impurity at 17.4 min is *cis*-7-OTMS (cf. Figure 4.24).

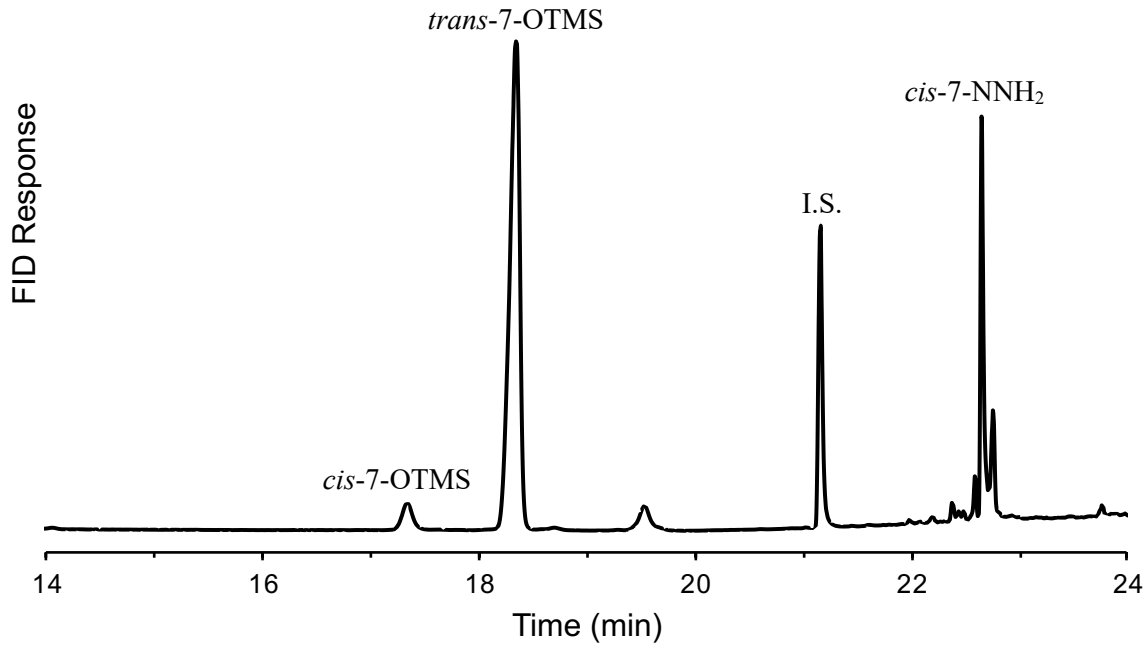

Figure 4.26. GC-FID chromatogram of *trans*-hexadec-8-en-7-one treated with hydrazine hydrate to derivatize the ketone to a hydrazone (*trans*-7-NNH_2). Note: *trans*-hexadec-8-en-7-ol was oxidized (incomplete) and then treated with BSA, hydrazine hydrate, and internal standard (dodecyl benzene).

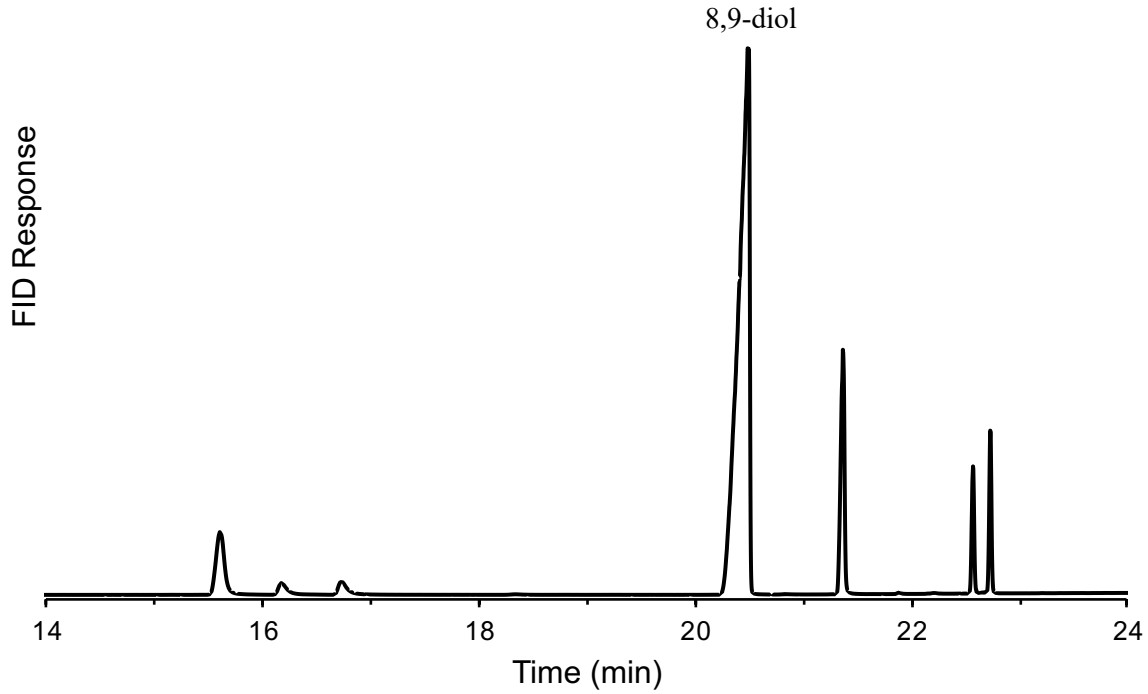

Figure 4.27. GC-FID chromatogram of hexadecane-8,9-diol treated with BSA, hydrazine hydrate, and internal standard (dodecyl benzene), thus derivatizing the diol with TMS.

The compounds were quantified as follows:

$$[X] = \frac{Int_x \times [S]}{Int_S \times R_x}$$

where X is the unknown, S is the internal standard, Int is the integration of the peak, and R is the response factor. The response factors are the slopes of the standard curves below. The apparent concentration (y-axis) is the integrated area of the standard compound divided by the integrated area of its internal standard multiplied by the concentration of the internal standard.

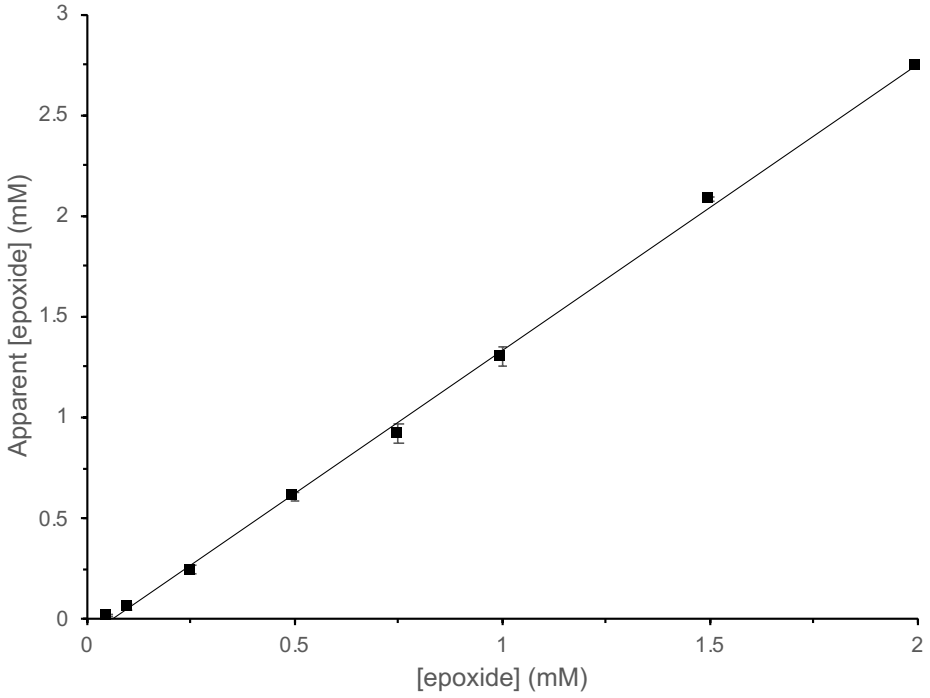

Figure 4.28. Standard curve of cis-2,3-diheptyloxirane relative to internal standard dodecyl benzene (y=1.3495x; R^2=0.9974). Both cis- and trans-2,3-diheptyloxirane showed responses within error of eachother; therefore, this value was used for both compounds. Control experiments were conducted to ensure the experimental derivatization conditions did not degrade these compounds.

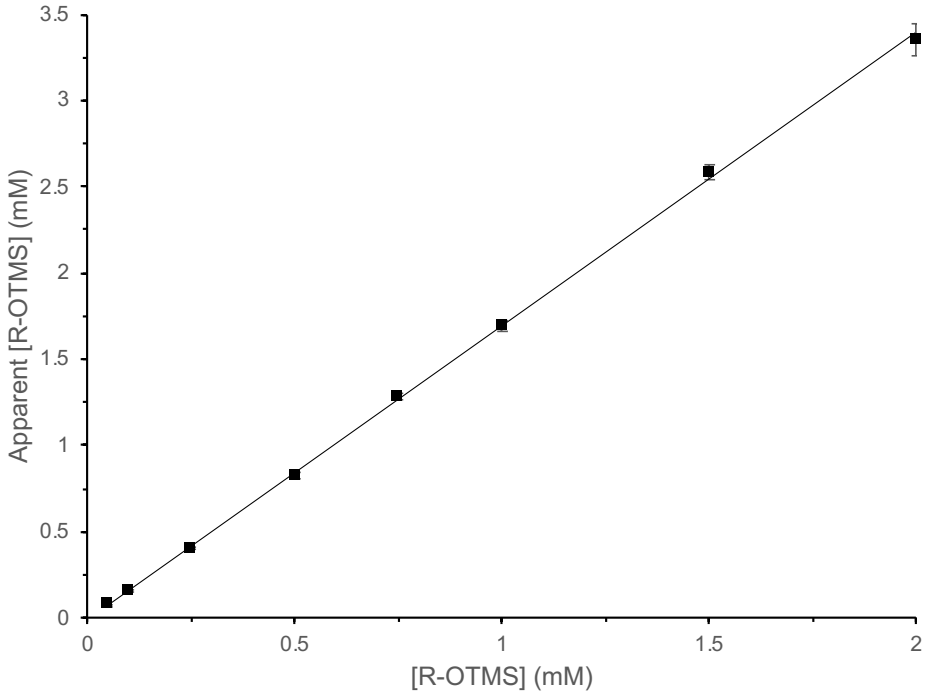

Figure 4.29. Standard curve of trans-(hexadec-9-en-8-yloxy)trimethylsilane relative to internal standard dodecyl benzene (y=1.6929x; R^2=0.9998). Cis- and trans-(hexadec-8-en-7-yloxy)trimethylsilane showed responses within error of this; therefore, this value was used for all three compounds. To prepare the standard curve, trans-hexadec-9-en-8-ol was treated with BSA at 70°C for 5 minutes. Control experiments were conducted to ensure the experimental derivatization conditions did not degrade these compounds, and to ensure complete derivatization of the free ROH to ROTMS.

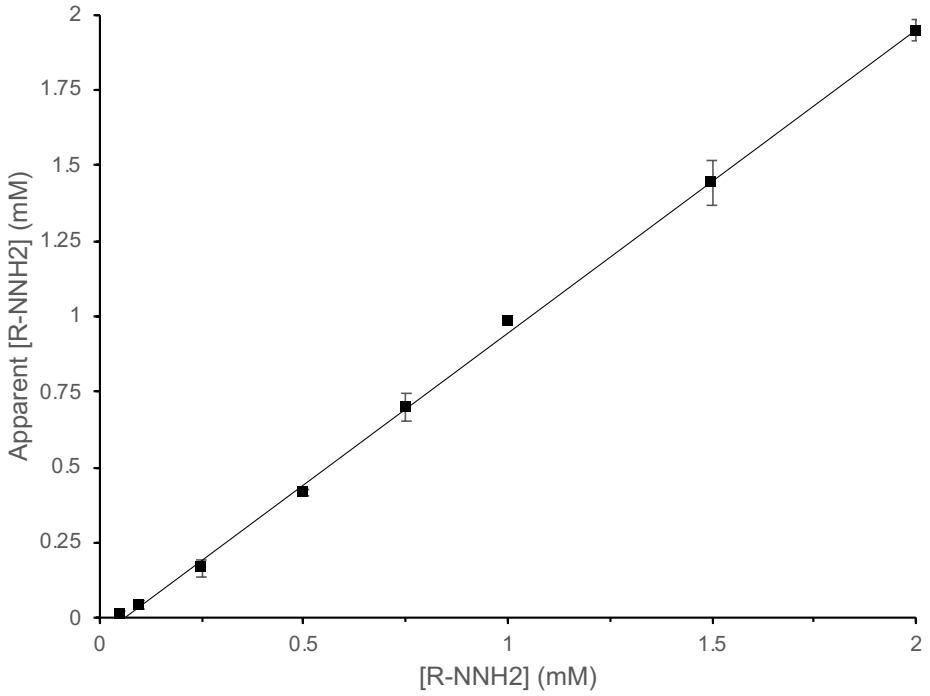

Figure 4.30. Standard curve of (trans-hexadec-9-en-8-ylidene)hydrazine relative to internal standard dodecyl benzene (y=0.9592x; R^2=0.9979). (Cis-hexadec-8-en-7-ylidene)hydrazine and (trans-hexadec-8-en-7-ylidene)hydrazine showed responses within error of this; therefore, this value was used for all three compounds. To prepare the standard curve, trans-hexadec-9-en-8-one was treated with hydrazine hydrate at 70°C for 30 minutes. Control experiments were conducted to ensure the experimental derivatization conditions did not degrade these compounds, and to ensure complete derivatization of the free RCHO to $RNNH_2$.

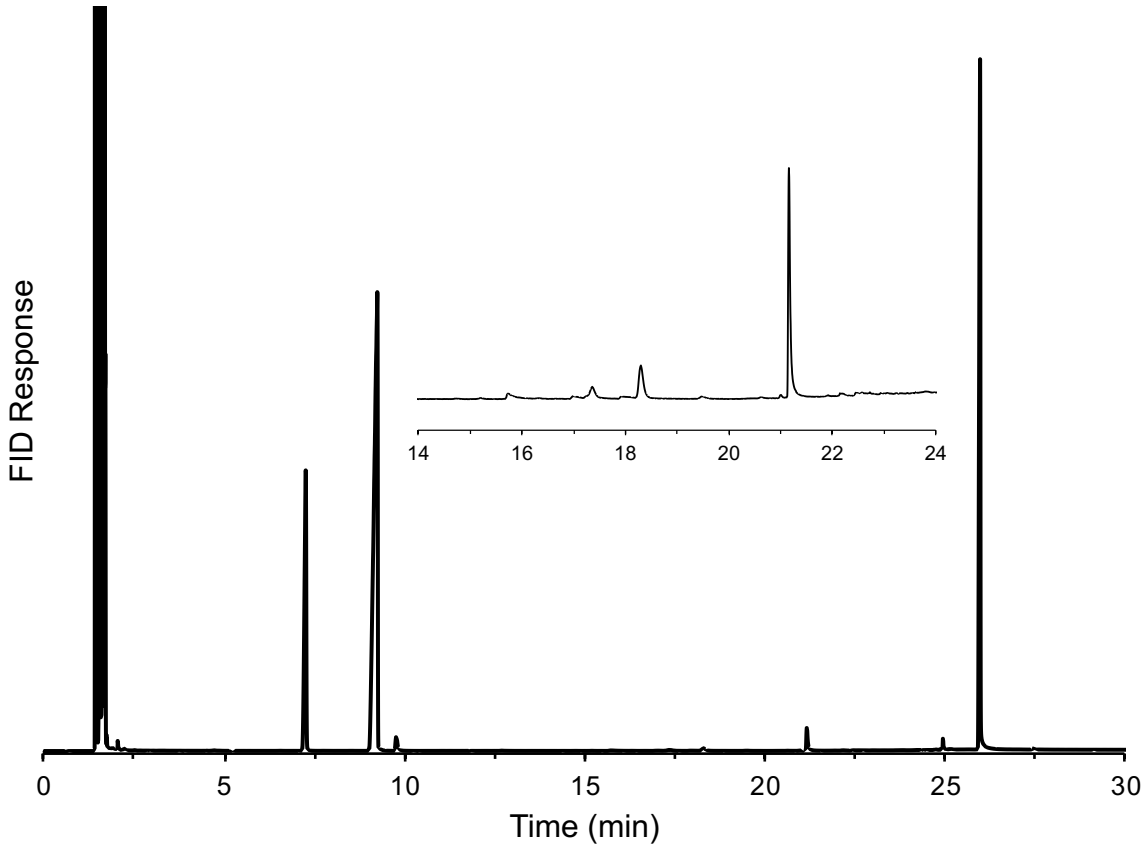

Figure 4.31. GC-FID chromatogram of 6 hour MeOAMVN-initiated autoxidation of cis-hexadec-8-ene.

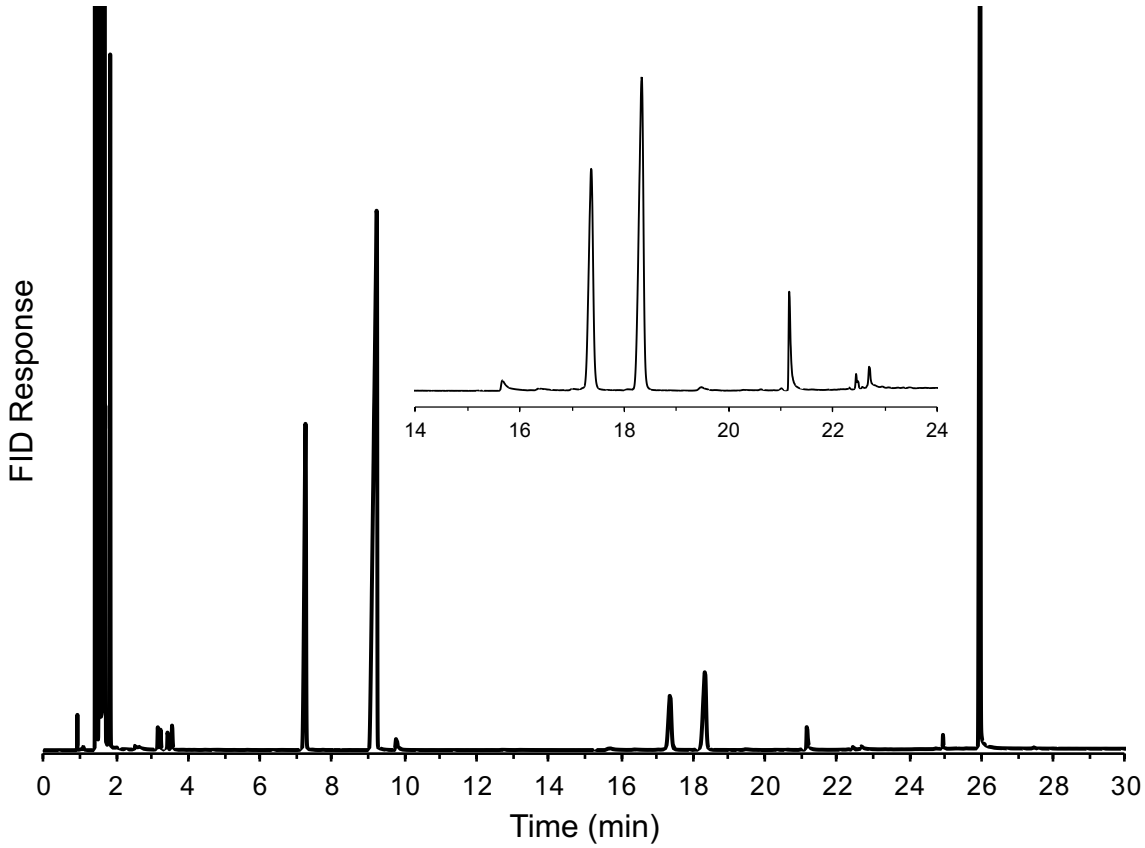

Figure 4.32. GC-FID chromatogram of 6 hour MeOAMVN-initiated, t-BuOOH-loaded autoxidation of cis-hexadec-8-ene.

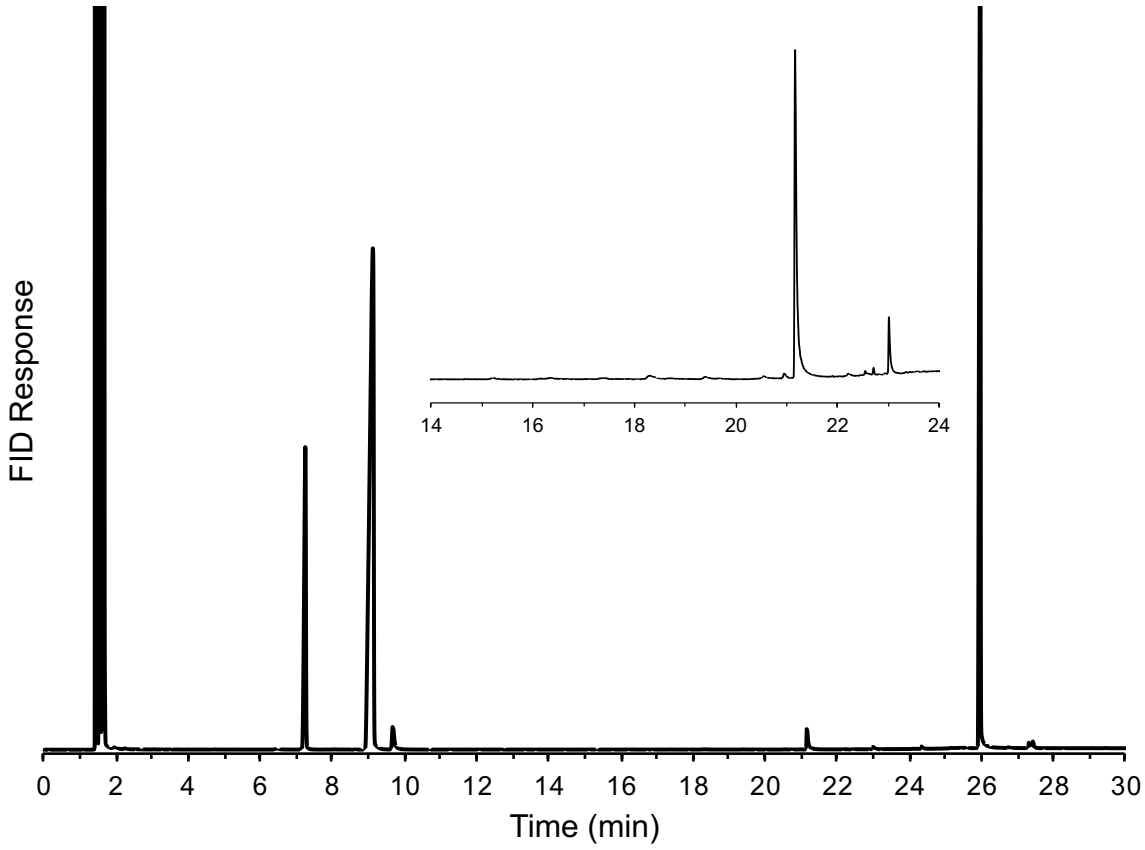

Figure 4.33. GC-FID chromatogram of 6 hour MeOAMVN-initiated autoxidation of 7,7,10,10-d_4-cis-hexadec-8-ene.

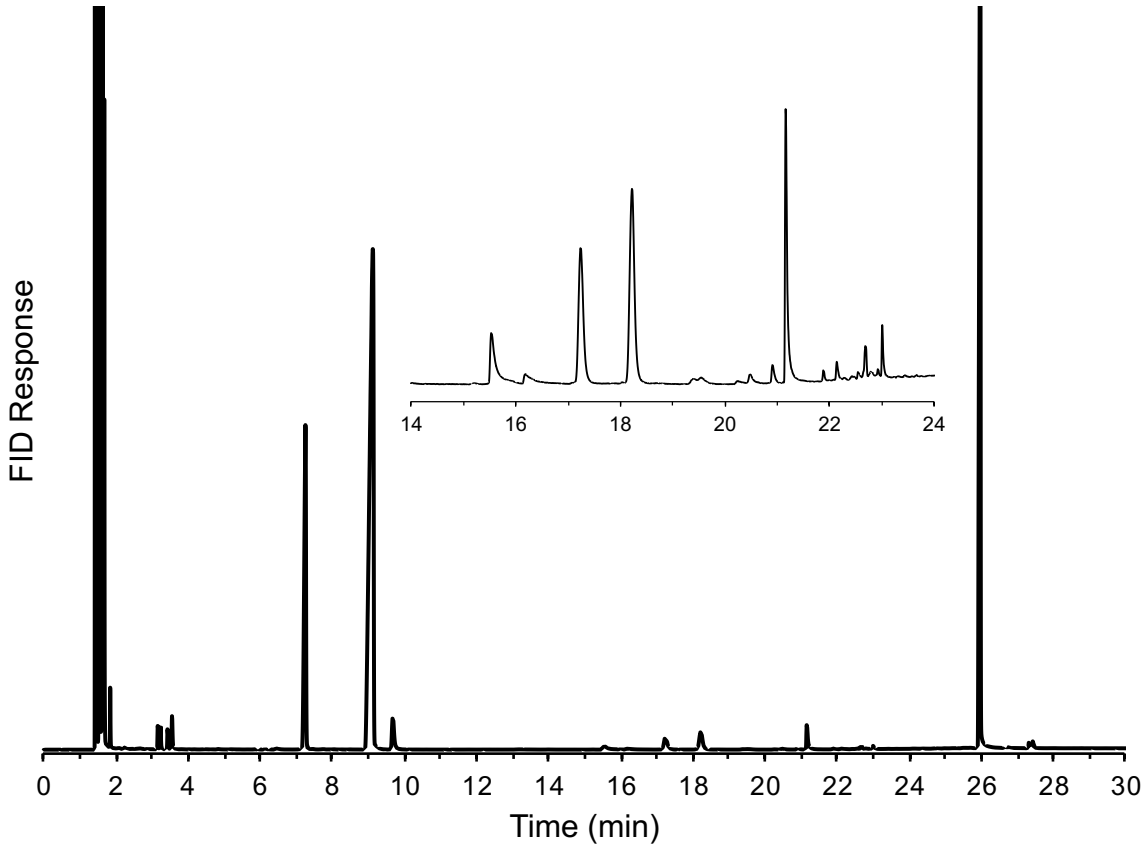

Figure 4.34. GC-FID chromatogram of 6 hour MeOAMVN-initiated, t-BuOOH-loaded autoxidation of 7,7,10,10-d_4-cis-hexadec-8-ene.

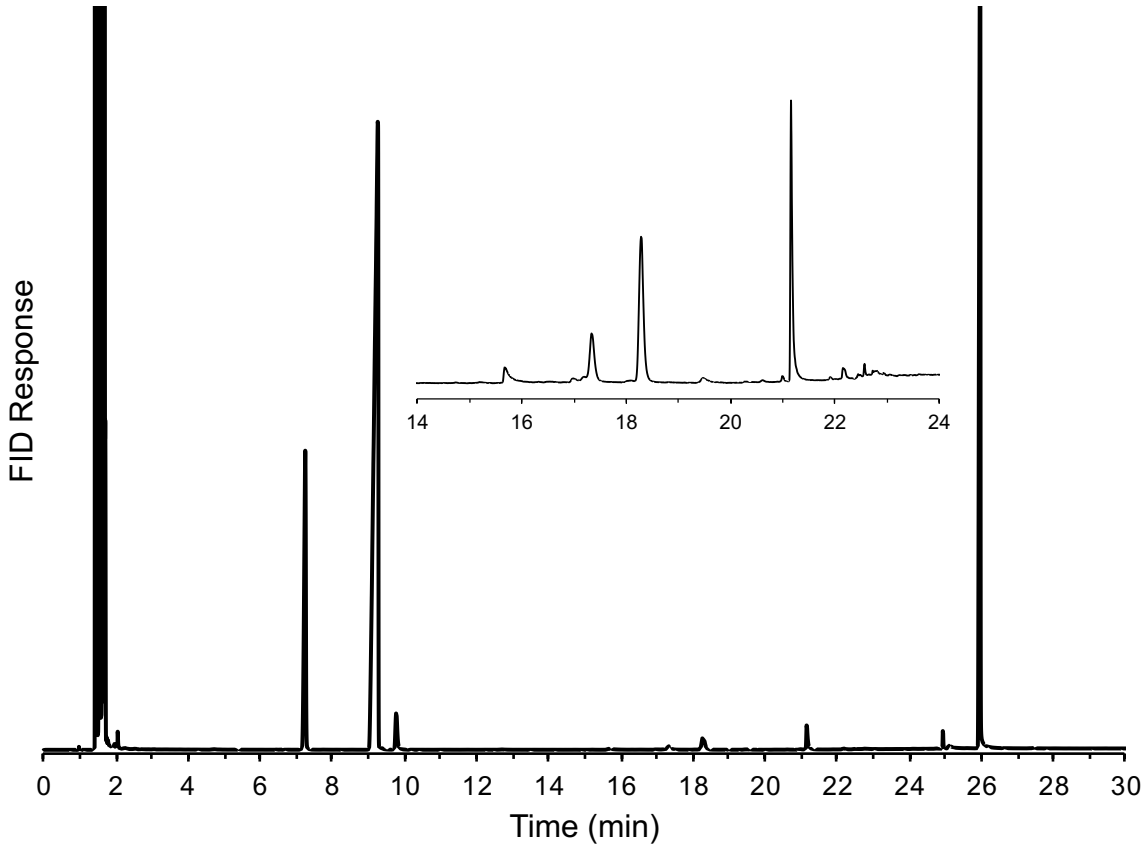

Figure 4.35. GC-FID chromatogram of 24 hour MeOAMVN-initiated autoxidation of cis-hexadec-8-ene.

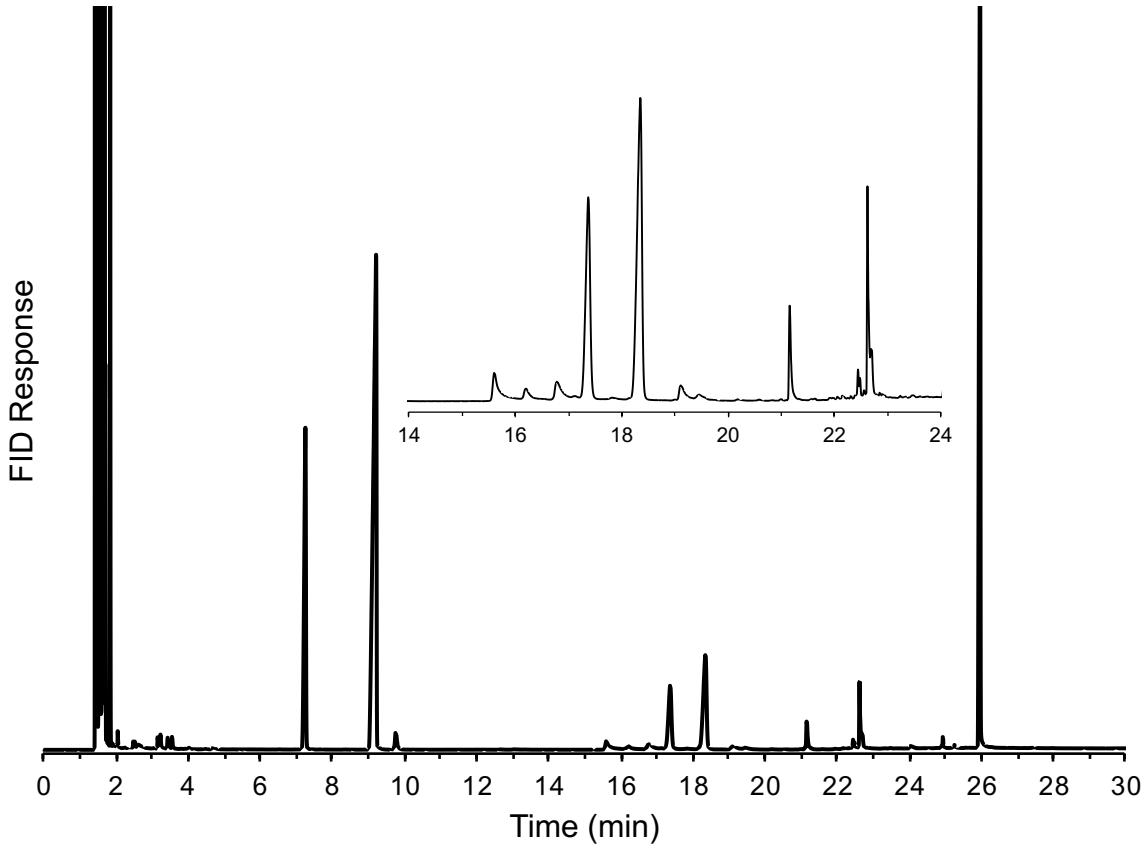

Figure 4.36. GC-FID chromatogram of 24 hour MeOAMVN-initiated, t-BuOOH-loaded autoxidation of cis-hexadec-8-ene.

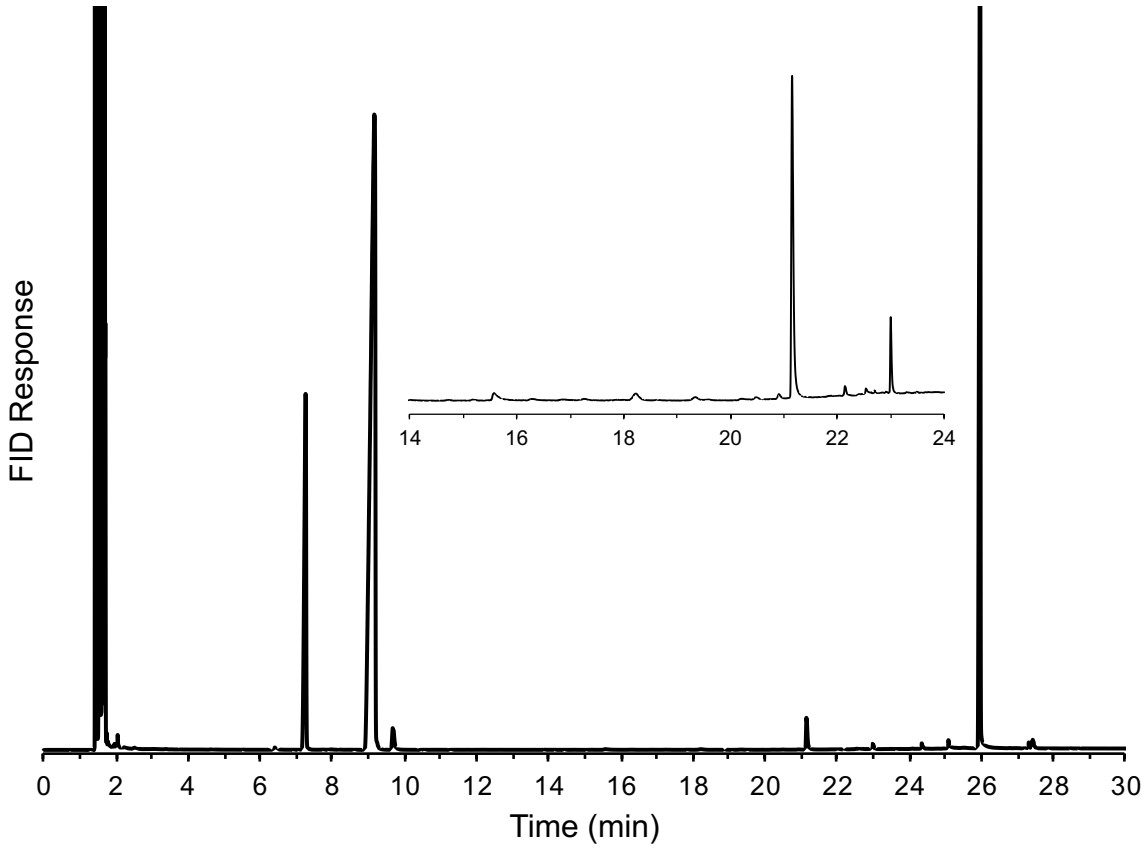

Figure 4.37. GC-FID chromatogram of 24 hour MeOAMVN-initiated autoxidation of 7,7,10,10-d_4-cis-hexadec-8-ene.

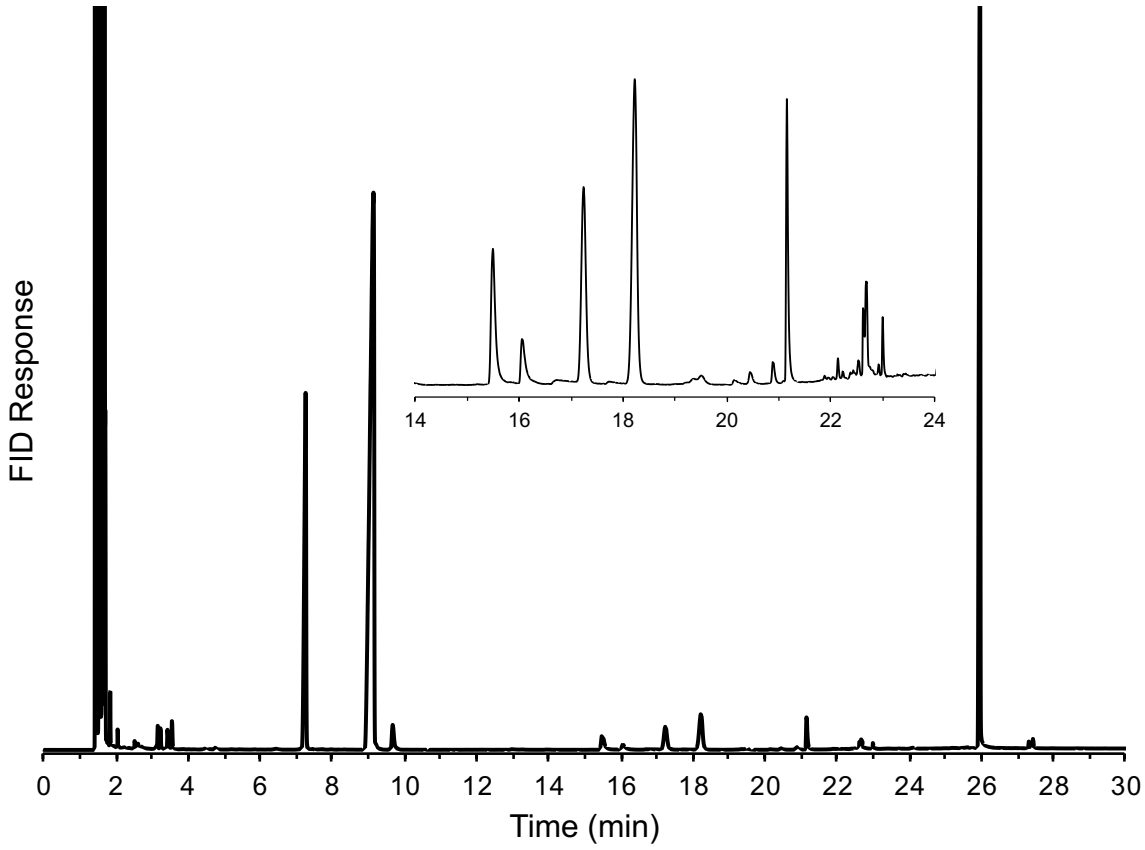

Figure 4.38. GC-FID chromatogram of 24 hour MeOAMVN-initiated, t-BuOOH-loaded autoxidation of 7,7,10,10-d_4-cis-hexadec-8-ene.

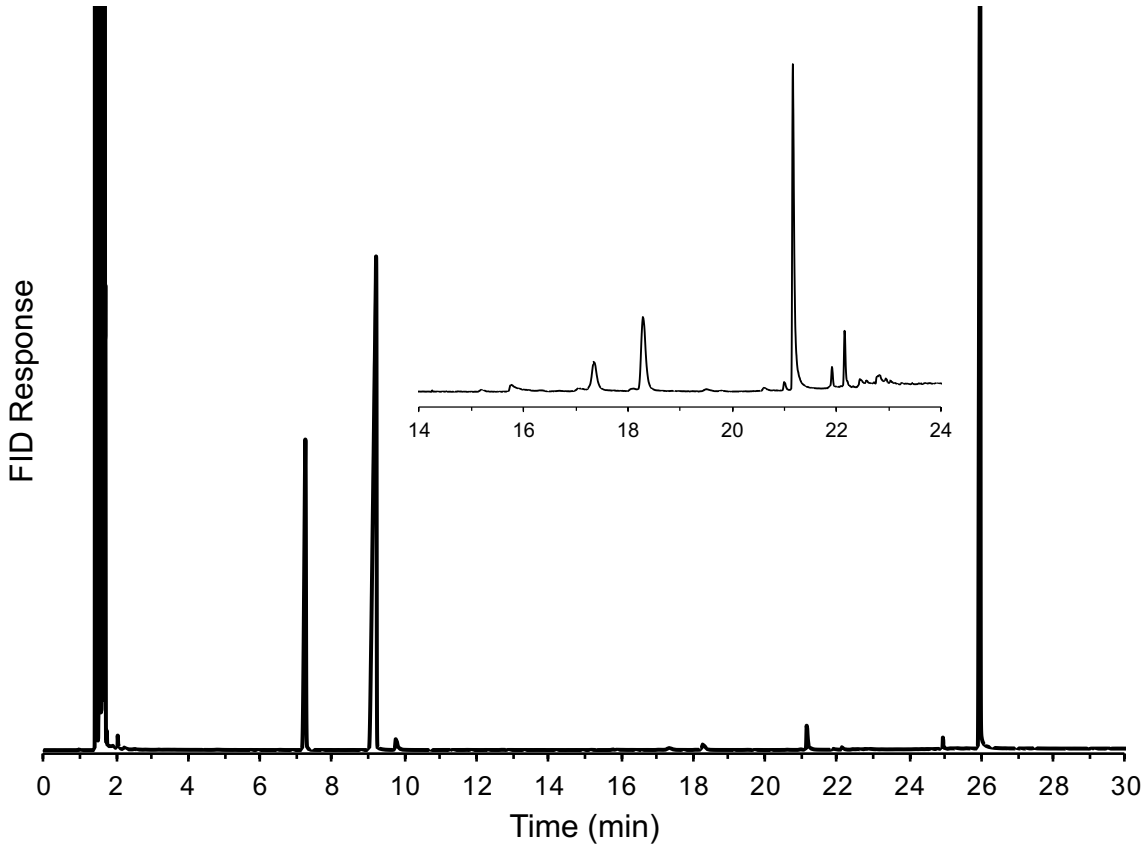

Figure 4.39. GC-FID chromatogram of 6 hour DTBN-initiated autoxidation of cis-hexadec-8-ene.

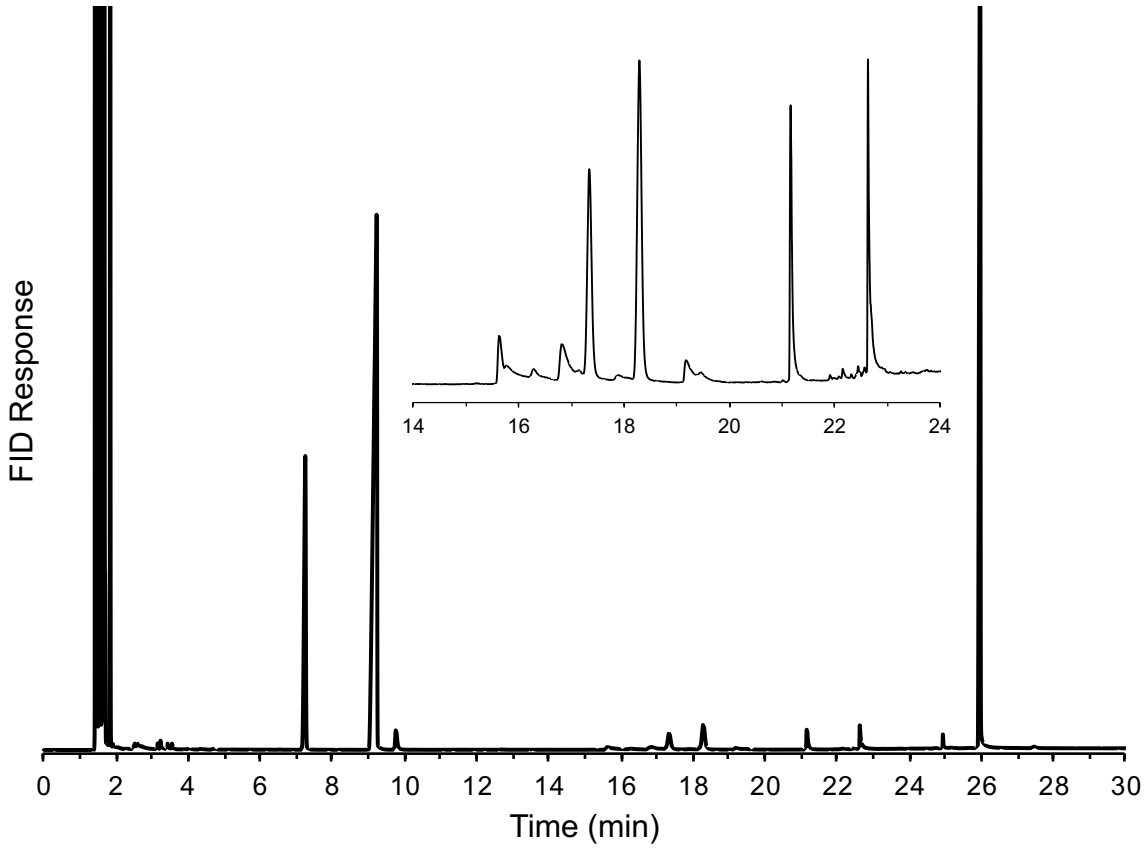

Figure 4.40. GC-FID chromatogram of 6 hour DTBN-initiated, t-BuOOH-loaded autoxidation of cis-hexadec-8-ene.

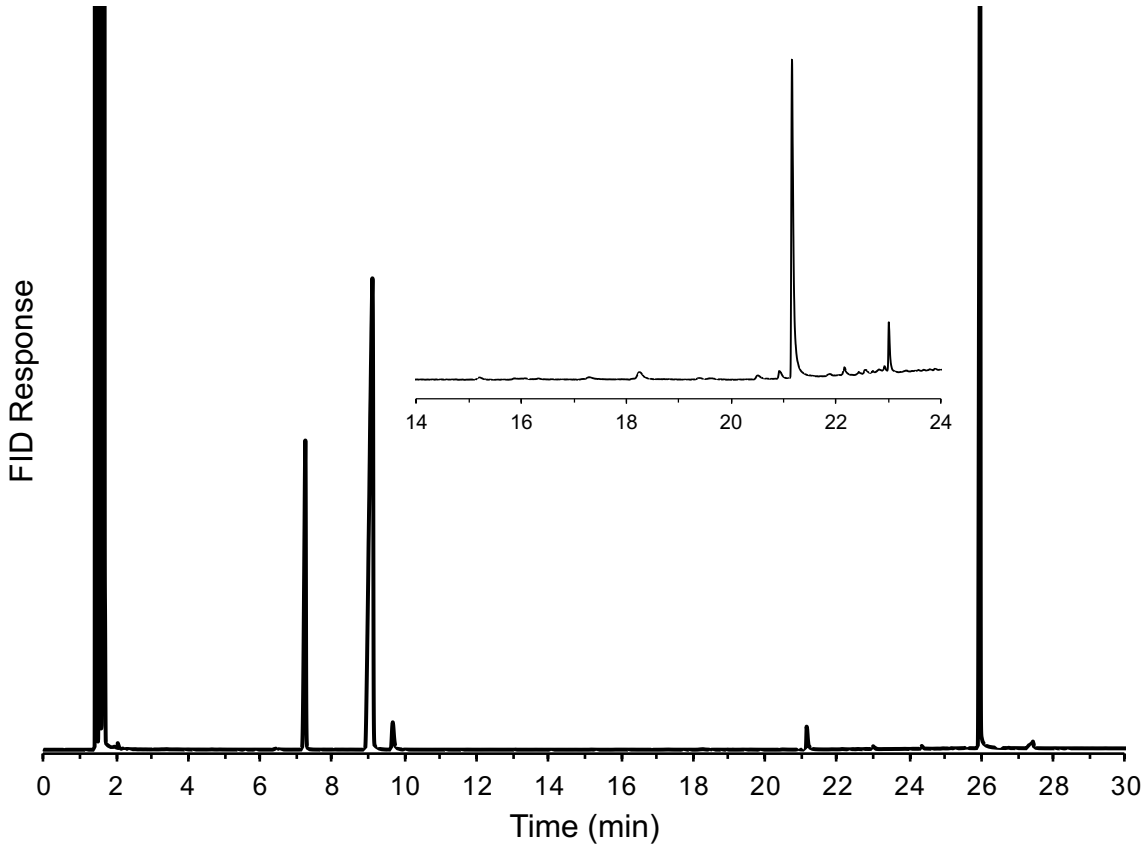

Figure 4.41. GC-FID chromatogram of 6 hour DTBN-initiated autoxidation of 7,7,10,10-d_4-cis-hexadec-8-ene.

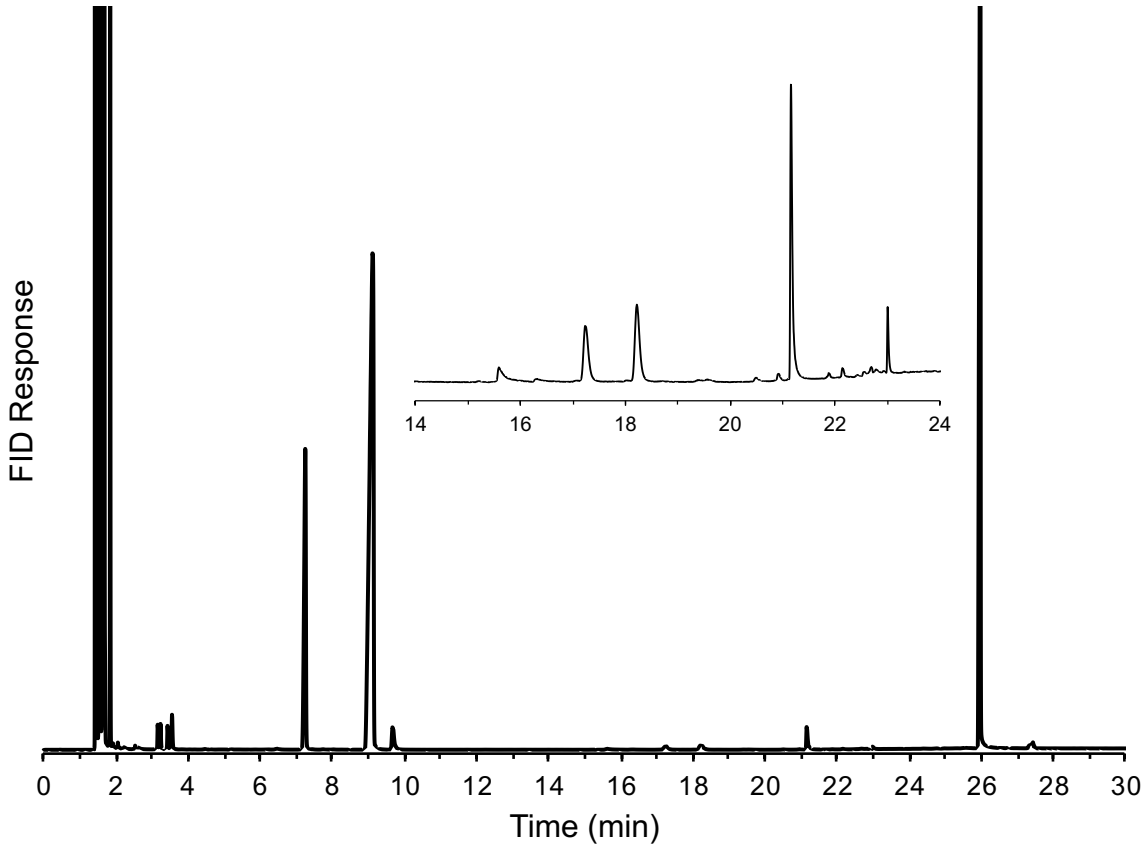

Figure 4.42. GC-FID chromatogram of 6 hour DTBN-initiated, t-BuOOH-loaded autoxidation of 7,7,10,10-d_4-cis-hexadec-8-ene.

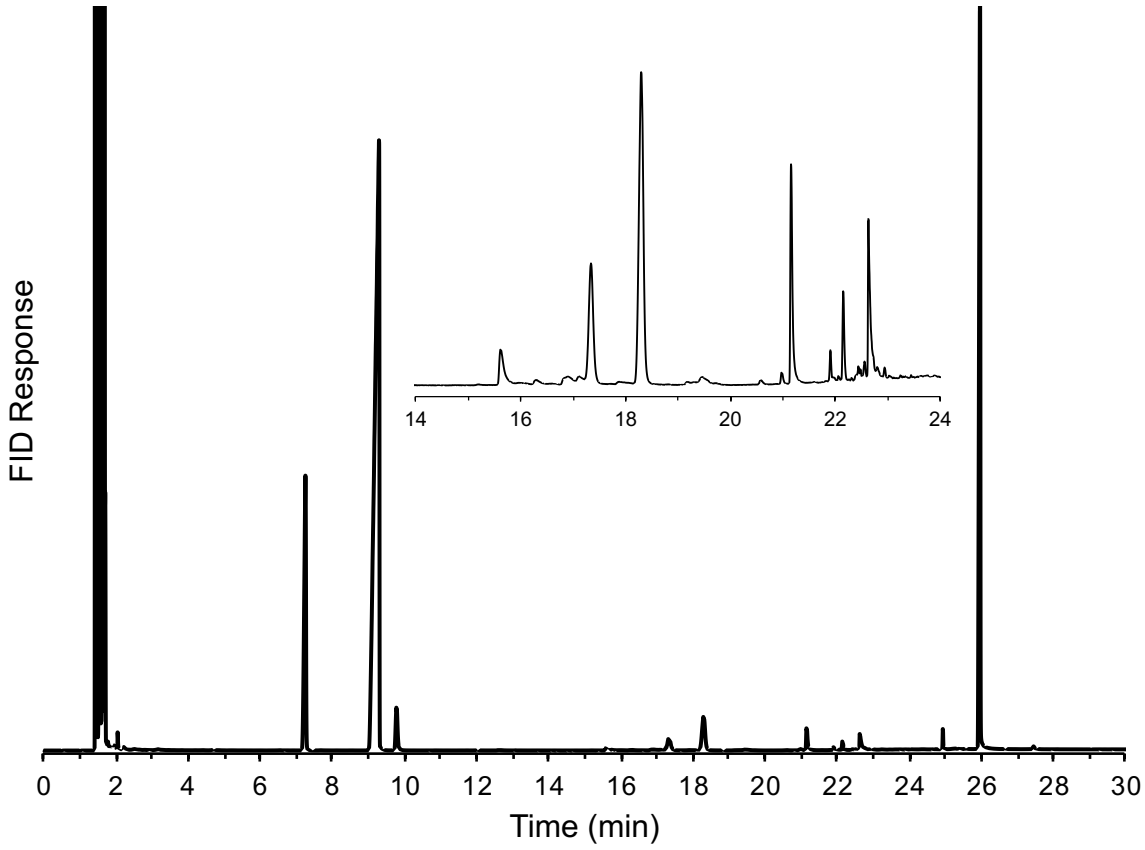

Figure 4.43. GC-FID chromatogram of 24 hour DTBN-initiated autoxidation of cis-hexadec-8-ene.

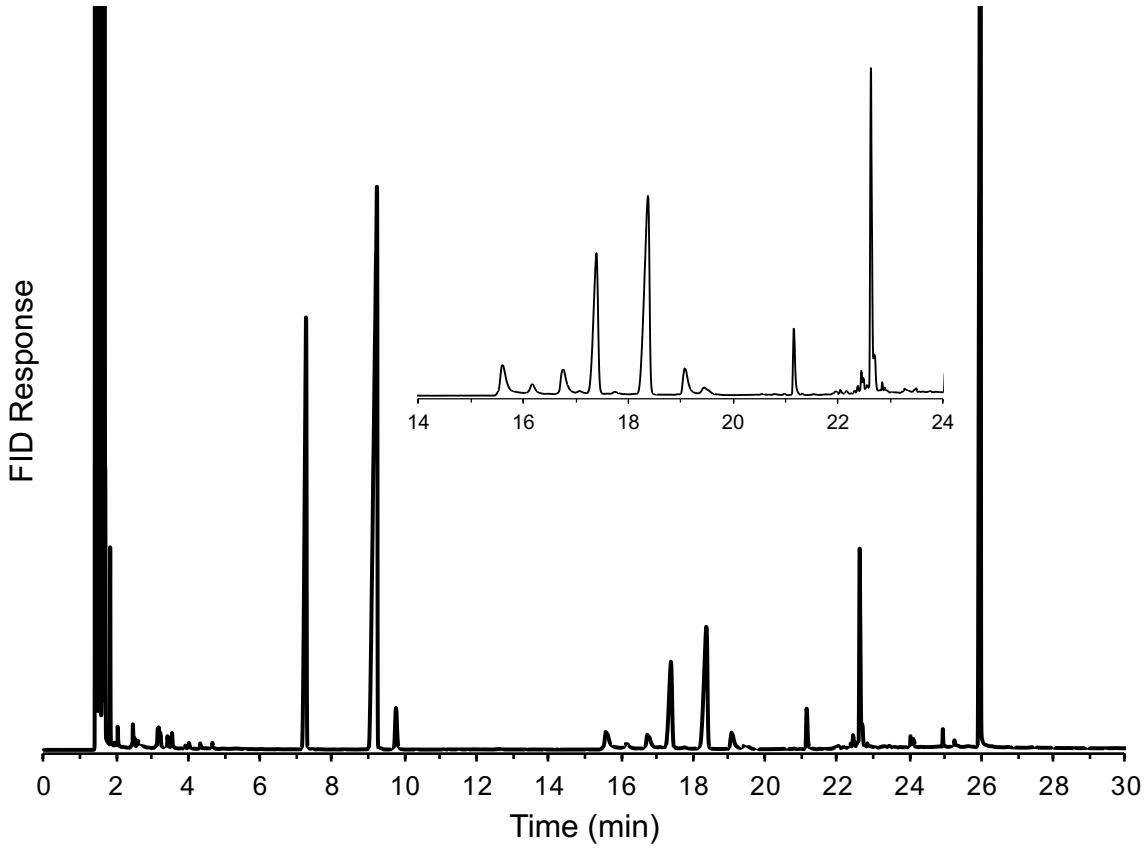

Figure 4.44. GC-FID chromatogram of 24 hour DTBN-initiated, t-BuOOH-loaded autoxidation of cis-hexadec-8-ene.

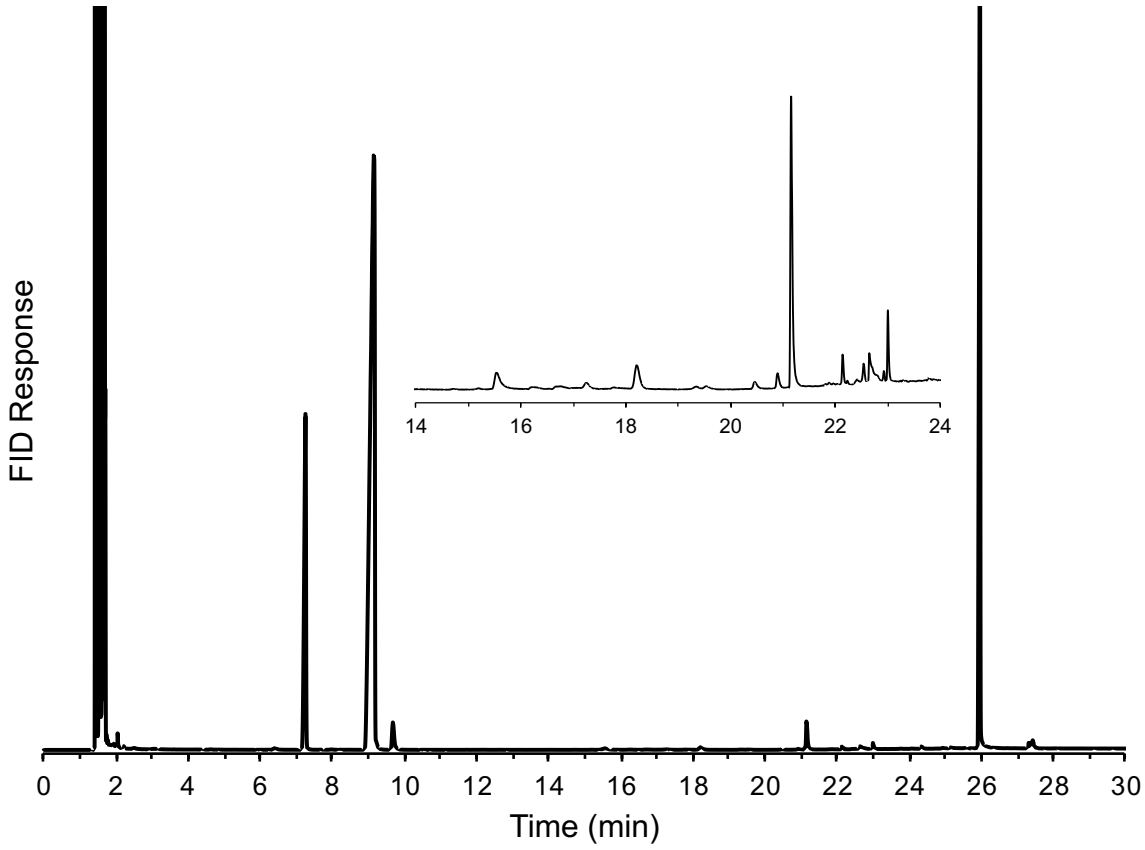

Figure 4.45. GC-FID chromatogram of 24 hour DTBN-initiated autoxidation of 7,7,10,10-d_4-cis-hexadec-8-ene.

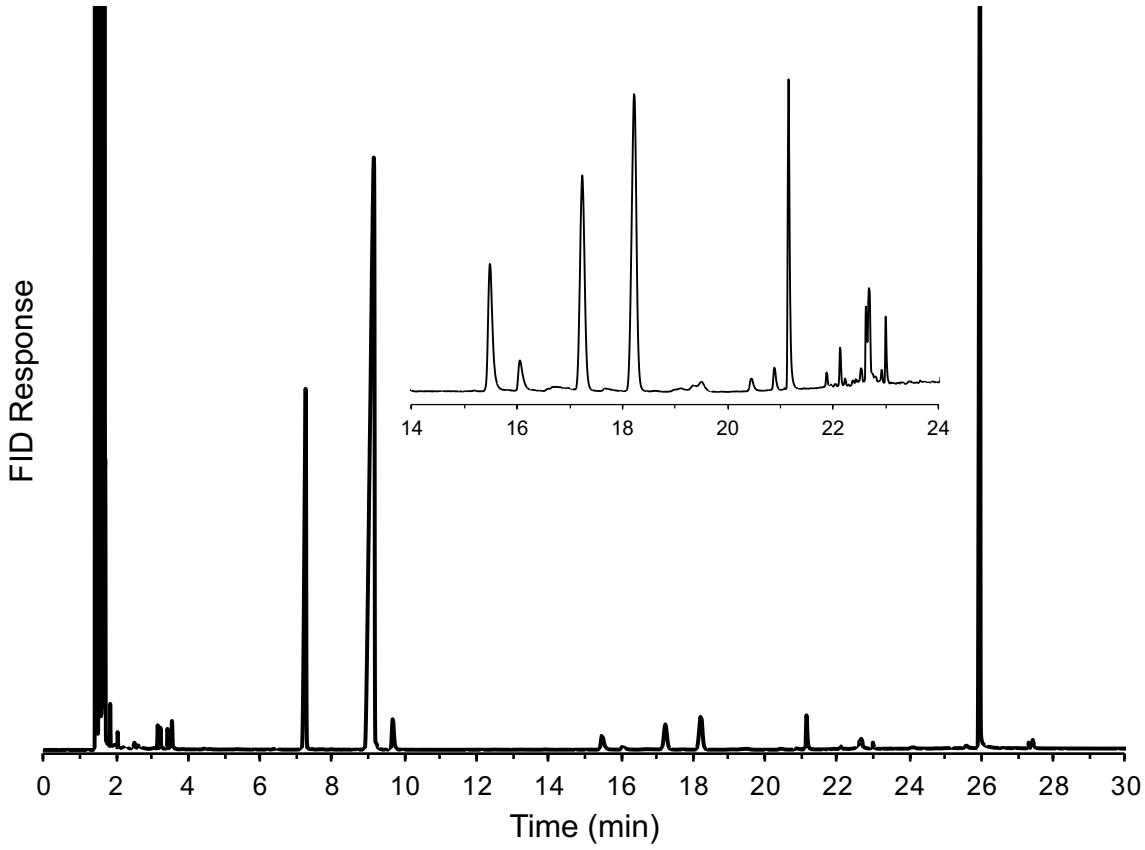

Figure 4.46. GC-FID chromatogram of 24 hour DTBN-initiated, t-BuOOH-loaded autoxidation of 7,7,10,10-d_4-cis-hexadec-8-ene.

Chapter 5. Redox Chemistry of Selenenic Acids and the Insight It Brings on Transition State Geometry in the Reactions of Peroxyl Radicals*

5.1 Preface

The redox chemistry of selenenic acids has been explored for the first time using a persistent selenenic acid, 9-triptyceneselenenic acid (RSeOH), and the results have been compared with those we recently obtained with its lighter chalcogen analogue, 9-triptycenesulfenic acid (RSOH). Specifically, the selenenyl radical was characterized by EPR spectroscopy and equilibrated with a phenoxyl radical of known stability in order to determine the O–H bond dissociation enthalpy of RSeOH (80.9 ± 0.8 kcal/mol): ca. 9 kcal/mol stronger than in RSOH. Kinetic measurements of the reactions of RSeOH with peroxyl radicals demonstrate that it readily undergoes H-atom transfer reactions (e.g., $k = 1.7 \times 10^5$ M^{-1} s^{-1} in PhCl), which are subject to kinetic solvent effects and kinetic isotope effects similar to RSOH and other good H-atom donors. Interestingly, the rate constants for these reactions are only 18- and 5-fold smaller than those measured for RSOH in PhCl and CH_3CN, respectively, despite being 9 kcal/mol less exothermic for RSeOH. IR spectroscopic studies demonstrate that RSeOH is less H-bond acidic than RSOH, accounting for these solvent effects and enabling estimates of the pK_as in RSeOH and RSOH of ca. 15 and 10, respectively. Calculations suggest that the TS structures for these reactions have significant charge transfer between the chalcogen atom and the internal oxygen atom of the peroxyl radical, which is nominally better for the more polarizable selenenic acid. The higher than expected reactivity of RSeOH toward peroxyl radicals is the strongest experimental evidence to date for charge transfer/secondary orbital interactions in the reactions of peroxyl radicals with good H-atom donors.

---

* This chapter is reproduced with permission from Zielinski, Z.A.; Presseau, N.; Amorati, R.; Valgimigli, L.; Pratt, D.A. *J. Am. Chem. Soc.* **2014**, *136*, 1570. Copyright 2014 American Chemical Society.

This chapter is presented as it was published in the *Journal of the American Chemical Society* (Zielinski, Z.A.; Presseau, N.; Amorati, R.; Valgimigli, L.; Pratt, D.A. *J. Am. Chem. Soc.* **2014**, *136*, 1570), with the exception of Section 5.5, which adds a perspective in the context of this Thesis. This work was performed with our collaborators at the University of Bologna, Ricardo Amorati and Luca Valgimigli, who carried out the EPR experiments, autoxidations, and IR measurements. The synthesis (cf. Scheme 5.1) was initially carried out by a Nathalie Presseau, with limited success in obtaining pure **5.2** from **5.5**. Therefore, using **5.3** obtained by Nathalie, the synthesis was repeated to obtain sufficient amounts of **5.5,** and the conditions for obtaining **5.2** were optimized.

5.2 Introduction

Selenenic acids (RSeOH) are the selenium analogues of sulfenic acids (RSOH), both being the heavier (valence) isoelectronic cousins to the more commonly encountered hydroperoxides (ROOH). Selenenic acids are believed to be transient intermediates in a number of redox reactions involving organoselenium compounds, inferred largely from the analogous chemistry exhibited by sulfenic acids derived from organosulfur compounds.[1,2] The two most important reactions that lead to selenenic acids are the oxidation of a selenol (e.g. with H_2O_2 as in Eq. 5.1), first demonstrated directly in 2001,[3] and *syn* elimination from a selenoxide (e.g. Eq. 5.2), a common synthetic transformation for late-stage introduction of an alkene.[4-6] The former reaction is believed to be key to the essential antioxidant enzyme glutathione peroxidase,[7,8] whose active site selenocysteine residue is responsible for the reduction of hydroperoxides and H_2O_2 to alcohols and water, respectively, prompting the widespread pursuit of small molecule mimics for therapeutic and/or chemopreventive purposes against disease wherein oxidative stress has been implicated.[9]

$$RSeH + H_2O_2 \rightarrow RSeOH + H_2O \qquad (5.1)$$

$$RSe(=O)CH_2CH_2R' \rightarrow RSeOH + H_2C=CH\text{-}R' \qquad (5.2)$$

Despite their prominence in these (and other[1]) roles, the properties of selenenic acids have been elusive owing to the ease with which they self-condense, disproportionate and/or oxidize. While the synthesis of isolable selenenic acids has been pursued for some time,[10] with a handful of examples of sterically-hindered areneselenenic acids being reported,[3,11] as well as a single alkaneselenenic acid,[12] essentially no investigation of their physicochemical properties has accompanied them. Of particular interest are their redox characteristics, which are expected to figure prominently in their chemistry.

We recently reported the results of detailed studies on the redox chemistry of a persistent sulfenic acid, 9-triptycenesulfenic acid (**5.1**), in order to provide a thermodynamic[13] and kinetic[14] rationale for the involvement of sulfenic acids in the radical-trapping antioxidant activity of natural product organosulfur compounds, such as the garlic-derived allicin[15] and anamu-derived petivericin,[16] as well as sulfenic acid mediated processes, including cysteine-mediated redox cell signaling.[17] In an effort to shed light on the redox chemistry of selenenic acids, and provide a basis for a direct comparison of their electronic properties with those of sulfenic acids (and hydroperoxides), we report here the results of corresponding studies on the selenium analogue of **5.1**: 9-triptyceneselenenic acid (**5.2**).[12] The studies described herein provide important fundamental insights into the thermodynamics and kinetics of radical reactions of selenenic acids, in particular, and provide a unique perspective on the importance of transition state geometry in formal H-atom transfer reactions to autoxidation chain-carrying peroxyl radicals, in general.

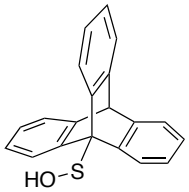

5.1

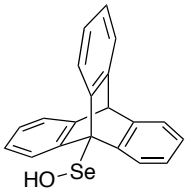

5.2

5.3 Results and Discussion

9-Triptyceneselenenic acid (**5.2**) was prepared as shown in Scheme 5.1. Briefly, 9-bromotriptycene was subjected to lithium-halogen exchange, and the resultant organolithium was quenched with *bis*(phenethyl)diselenide **5.3**, which was prepared from phenethyl bromide as suggested by Thompson and Boudjouk.[36] The resultant selenide **5.4** was then oxidized with MCPBA to yield the selenoxide **5.5**, which underwent Cope-type elimination at room temperature to give **5.2**. The successful isolation of pure **5.2** required the solid-state decomposition of the precursor selenoxide under high vacuum over a 2 week period to minimize the self-condensation of **5.2** to give the corresponding selenoseleninate **5.6**. As such, solutions of **5.2** were prepared immediately prior to use in the experiments reported below.

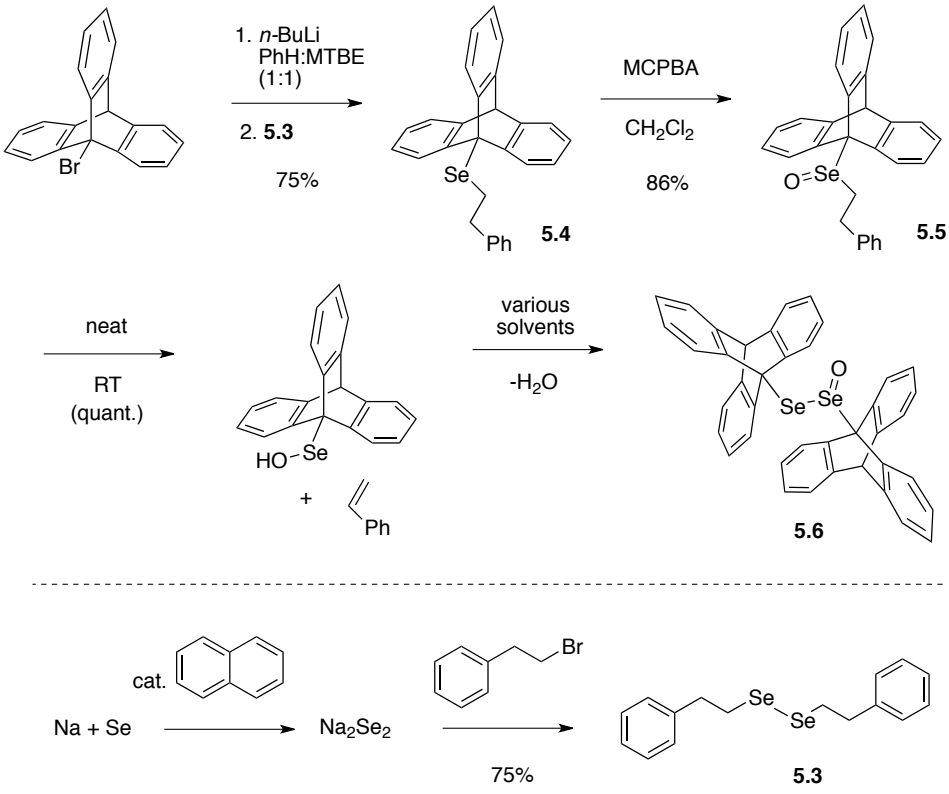

Scheme 5.1. Synthesis of 9-triptyceneselenenic acid **5.2** (and the corresponding selenoseleninate 5.**6**).

A deoxygenated solution of the selenenic acid in benzene was photolyzed in the presence of 10% (by volume) di-*tert*-butyl peroxide in the cavity of an X-band EPR spectrometer, affording the noisy spectrum shown in Figure 5.1. The field center of the broad singlet (2.4 G line width) is g = 2.0191, consistent with an oxygen-centered radical with spin delocalization onto a heavier atom, and slightly larger than that of the corresponding sulfinyl radical derived from the analogous sulfenic acid **5.1** for which we had measured g = 2.0114.[13] Continuous photolysis was necessary as the resultant selenenyl radical decayed on the time scale of the acquisition, yielding only the weak signal shown which prevented resolution of the coupling with ^{77}Se (which has a nuclear spin of I = +1/2 and is 7.6% at natural abundance).

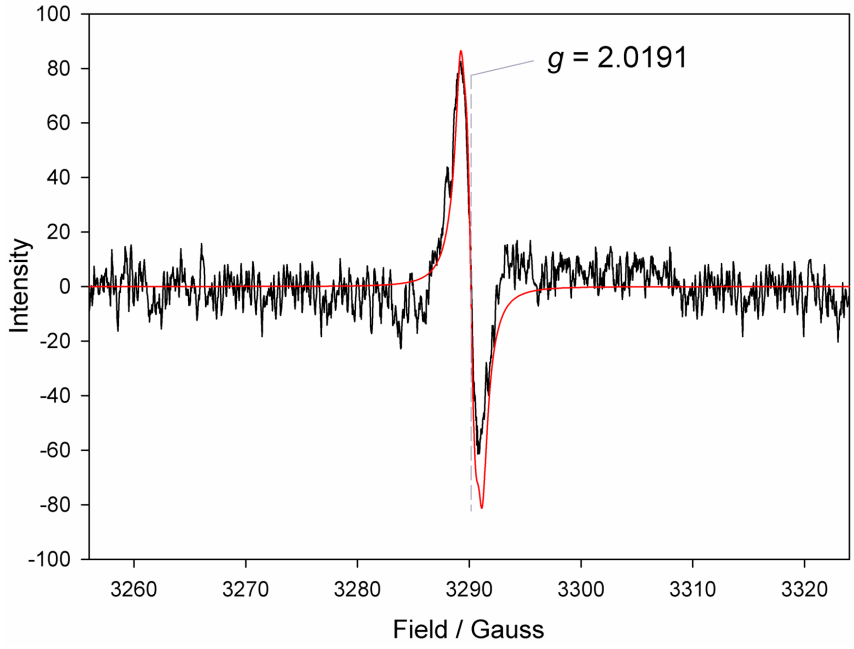

Figure 5.1. EPR spectrum of **5.2•** from continuous photolysis of a solution of **5.2** in benzene containing 10% di-*tert*-butylperoxide. The simulated spectrum is shown in red.

While the selenenyl radical was not particularly persistent, we hoped that its rapid equilibration with a compound of known O-H BDE[13,18,19] would allow the determination of the O-H BDE of a selenenic acid for the first time. To provide guidance on which compound to use in the

equilibration experiment, we carried out computations on a model selenenic acid (t-BuSeOH), for which CBS-QB3[30] calculations predicted an O-H BDE of 81.2 kcal/mol. On the basis of this result, we chose 2,4,6-tri-*tert*-butylphenol (TTBP) as the reference compound for the equilibriation experiment, as it has an O-H BDE of 80.1 kcal/mol[19] and yields a persistent phenoxyl radical upon H-atom abstraction. Gratifyingly, continuous photolysis of mixtures of selenenic acid and TTBP in benzene containing 10% di-*tert*-butyl peroxide (by volume) afforded spectra showing both the selenenyl and phenoxyl radicals (*cf.* Figure 5.2). Equilibrium constants of $K = 4.0 \pm 2.1$ were obtained from simulation of the spectra, which afford $\Delta H = 0.8 \pm 0.4$ kcal/mol assuming a negligible entropy change for the formal H-atom transfer process, and therefore an O-H BDE of 80.9 ± 0.8 kcal/mol for **5.2**.

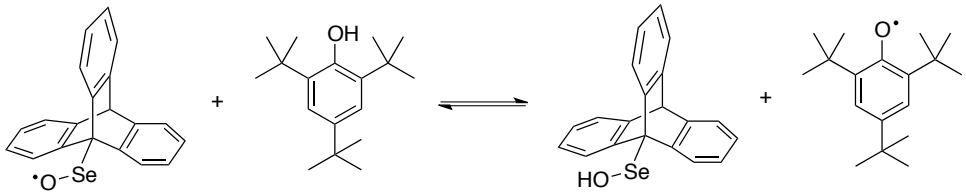

The increased strength of the O-H bond in the selenenic acid in comparison to the sulfenic acid (71.9 ± 0.3 kcal/mol, also measured by the radical equilibration EPR approach; for comparison CBS-QB3 predicts an O-H BDE of 68.6 kcal/mol in *t*-BuSOH)[13,42] can be rationalized by the longer Se-O bond in the selenenyl radical as compared to the S-O bond in the sulfinyl radical. The calculated minimum energy structures of the *tert*-butyl selenenyl and sulfinyl radicals from the CBS-QB3 calculations are shown in Figure 5.3, wherein the Se-O and S-O bond distances are 1.68 and 1.51 Å, respectively. The associated spin delocalization in the selenenyl radical is predicted to be ca. 20% on the selenium atom and 80% on the oxygen atom as compared to ca. 40% on the sulfur atom and 60% on the oxygen atom in the sulfinyl radical.[43]

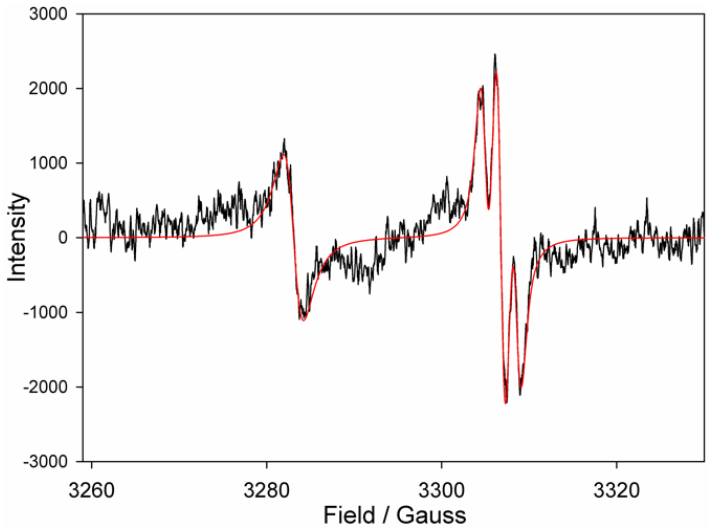

Figure 5.2. Representative EPR spectrum obtained from continuous photolysis of a 1:1 mixture of **5.2** and 2,4,6-tri-*tert*-butylphenol in benzene containing 10% di-*tert*-butylperoxide. The simulated spectrum for a 4:1 mixture of the 2,4,6-tri-*tert*-butylphenoxyl and selenenyl radicals is shown in red.

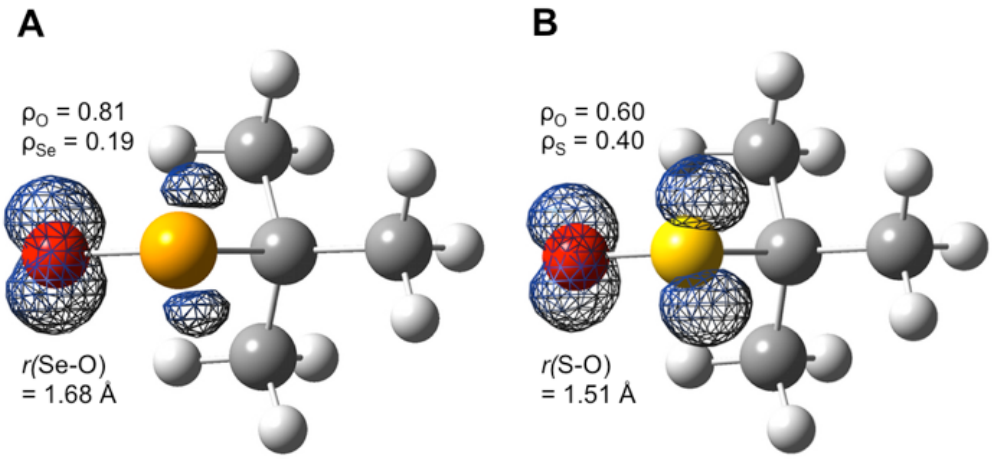

Figure 5.3. Calculated structures and spin density distributions in *t*-BuSeO$^{\bullet}$ (A) and *t*-BuSO$^{\bullet}$ (B).

It is of interest to compare the O-H BDE in a selenenic acid to the Se-H BDE in a selenol – often its direct precursor in redox reactions, such as in the catalytic cycle of glutathione peroxidase (as in Eq. 5.1). Since, to the best of our knowledge, no experimental value is available for the Se-H

BDE of an alkaneselenol (the Se-H BDEs for HSeH and PhSeH are reported to be 79.0 ± 0.2[21] and 78 ± 4[22] kcal/mol, respectively), we calculated it for *t*-BuSeH using CBS-QB3 to allow for direct comparison to the foregoing calculations on *t*-BuSeOH. These calculations reveal that the O-H bond in *t*-BuSeOH (81.2 kcal/mol) is *slightly stronger* than the Se-H bond in *t*-BuSeH (78.9 kcal/mol). This result is particularly interesting because the trend is completely different from that observed for the lighter chalcogen: the O-H bond in *t*-BuSOH (68.6 kcal/mol) is *much weaker* than the S-H bond in *t*-BuSH (87.6 kcal/mol).[23] This fundamentally different trend – which is rooted in the very high stability of the sulfinyl radical[13] – underscores the need for caution when rationalizing the reactivity of selenium-containing compounds simply on the basis of their similarity to sulfur-containing compounds.

Electrochemical experiments also suggest that selenenic acids are more difficult to oxidize than sulfenic acids. Cyclic voltammograms, which were irreversible at scan rates ranging from 1 to 1000 mV/s, consistently showed anodic (oxidation) peaks at potentials that were ca. 200 mV more oxidizing than for the sulfenic acid under identical conditions (representative voltammograms are given in the Supporting Information, Section 5.7). Attempts to obtain reversible voltammograms by addition of acid to suppress deprotonation of the resultant radical cation (and subsequent rapid reactions of the selenenyl radical; *vide supra*) led to no observable signal in the potential window, presumably due to acid catalysis of the self-condensation of the selenenic acid to yield the selenoseleninate (**5.6**). Likewise, addition of base to yield the selenenate anion in the hopes of obtaining a reversible $RSeO^{\bullet}/RSeO^{-}$ couple also led to no observable signal in the potential window, again due to base-catalyzed formation of the selenoseleninate (**5.6**).

The H-atom transfer reactivity of the selenenic acid was probed in studies of the kinetics of its reactions with peroxyl radicals, the results of which could be compared to the results of analogous experiments we previously carried out on the corresponding sulfenic acid.[14] These measurements were made using the well-established inhibited autoxidation of styrene approach using O_2

consumption to monitor reaction progress (*cf.* Figure 5.4), from which rate constants could be determined for the formal H-atom transfer (k_{inh}) from the initial rates (Table 5.1).[24] In chlorobenzene, a rate constant of $(1.7 \pm 0.3) \times 10^5$ $M^{-1}s^{-1}$ was obtained, indicating that selenenic acids are indeed very reactive in H-atom transfer reactions. For comparison, the analogous sulfenic acid reacts with a rate constant of $(3.0 \pm 0.3) \times 10^6$ $M^{-1}s^{-1}$ under identical conditions,[14] a reactivity that is identical with that of α-tocopherol, nature's premier lipid-soluble radical-trapping antioxidant, under equivalent conditions.[24] A kinetic solvent effect diminishes the reactivity of **5.2** by a factor of 4.9 on moving from chlorobenzene to acetonitrile, in comparison to a factor of 19 for **5.1**. As in our previous studies with sulfenic acid **5.1**,[14] a large primary deuterium kinetic isotope effect was determined for the reaction of **5.2** with peroxyls, consistent with a formal H-atom transfer mechanism.

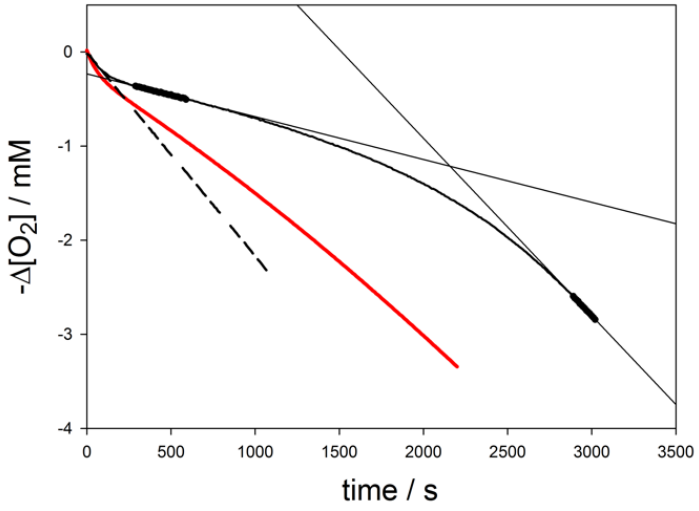

Figure 5.4. Oxygen consumption during the autoxidation of styrene (50% by volume) initiated by AIBN (0.05 M) at 303 K without inhibitor (dashed line), or in the presence of **5.2** (7.6 μM) in PhCl + 0.5% CH_3OH (black line) or PhCl + 0.5% CH_3OD (red line). The resultant k_H/k_D is 2.9.

Ingold has shown that the rates of H-atom transfer reactions vary in different solvents (S) according to a model that assumes the H-atom donor (H-A) is unreactive when its labile H-atom is

involved in an H-bond with the solvent.[25,26] As a result, the kinetics can be accurately described only using a model that involves a predissociation of this H-bonded complex:

$$\text{S---H-A} \leftrightarrows \text{S + H-A + X}^{\bullet} \rightarrow \text{S + A}^{\bullet} + \text{H-X} \qquad (5.3)$$

Ingold went on to show that the solvent effects could be quantitated using an empirical linear free energy relationship based on the H-bond donating strength of the H-atom donor (α_2^H) and the H-bond accepting strength of the solvent (β_2^H):

$$\log k^S = -8.3\alpha_2^H\beta_2^H + \log k^0 \qquad (5.4)$$

As such, the larger kinetic solvent effect on the reaction of the sulfenic acid in comparison to the selenenic acid implies that the former is a better H-bond donor than the latter.

Table 5.1. Rate constants (k_{inh}) for the reactions of selenenic acid 5.2 with peroxyl radicals at 303 K.[a]

Conditions	k_{inh} *for* **5.2** ($M^{-1}s^{-1}$)	k_{inh} *for* **5.1** ($M^{-1}s^{-1}$)[c]
Styrene/PhCl	$(1.7\pm0.3)\times10^5$	$(3.0\pm0.3)\times10^6$
Styrene/CH_3CN	$(3.5\pm0.4)\times10^4$	$(1.6\pm0.3)\times10^5$
Styrene/CH_3CN/H_2O[b]	$(3.4\pm0.3)\times10^4$	$(1.1\pm0.2)\times10^5$
Styrene/CH_3CN/D_2O[b]	$(5.1\pm0.6)\times10^3$	$(1.8\pm0.2)\times10^4$
k_H/k_D	6.7±0.9	6.1±0.4

[a]Literature data for the reactions of sulfenic acid **5.1** obtained under the same conditions are presented for comparison.[b]H_2O or D_2O added in 1% v/v. [c]Taken from ref 13.

Indeed, FT-IR spectra of **5.1** and **5.2** obtained in the non-H-bond accepting solvent CCl_4 in the presence of increasing amounts of acetonitrile reveal trends that are consistent with the observed kinetic solvent effects. From these spectra, the equilibrium constants corresponding to H-bond formation between **5.1** or **5.2** and acetonitrile can be derived from the integration of the peak corresponding to the free O-H stretch as a function of acetonitrile concentration (vide infra) to give 2.78 ± 0.45 M^{-1} and 0.92 ± 0.20 M^{-1}, respectively. Using Abraham's equation, these equilibrium constants yield values of α_2^H of 0.54 and 0.37 for **5.1** and **5.2**, respectively. On the basis of these values of α_2^H, we would expect the rate constants for H-atom transfer from **5.1** and **5.2** to peroxyl radicals to drop 22- and 8-fold on moving from chlorobenzene (β_2^H = 0.09)[27] to acetonitrile (β_2^H = 0.39),[27,44] from Ingold's equation 5.4,[25] in excellent agreement with the experimental results of 19 and 4.9, respectively.[45]

It should be pointed out that the values of α_2^H derived from the FT-IR measurements also provide some insight into the relative acidities of **5.1** and **5.2**. Since the H-bond donating ability generally correlates with the pK_a of the donor, it can be expected that **5.1** has a pK_a similar to that of phenol (pK_a = 10, α_2^H = 0.60),[10] while **5.2** has a pK_a similar to that of methanol (α_2^H = 0.37, pK_a = 15).[10] We had previously measured a pK_a value of 12.5 for **5.1** in 4/1 CH_3CN/H_2O, which would undoubtedly be slightly lower in water, but attempts to measure the pK_a of **5.2** under similar conditions were unsuccessful owing to selenoseleninate formation under the conditions of the potentiometric titration.

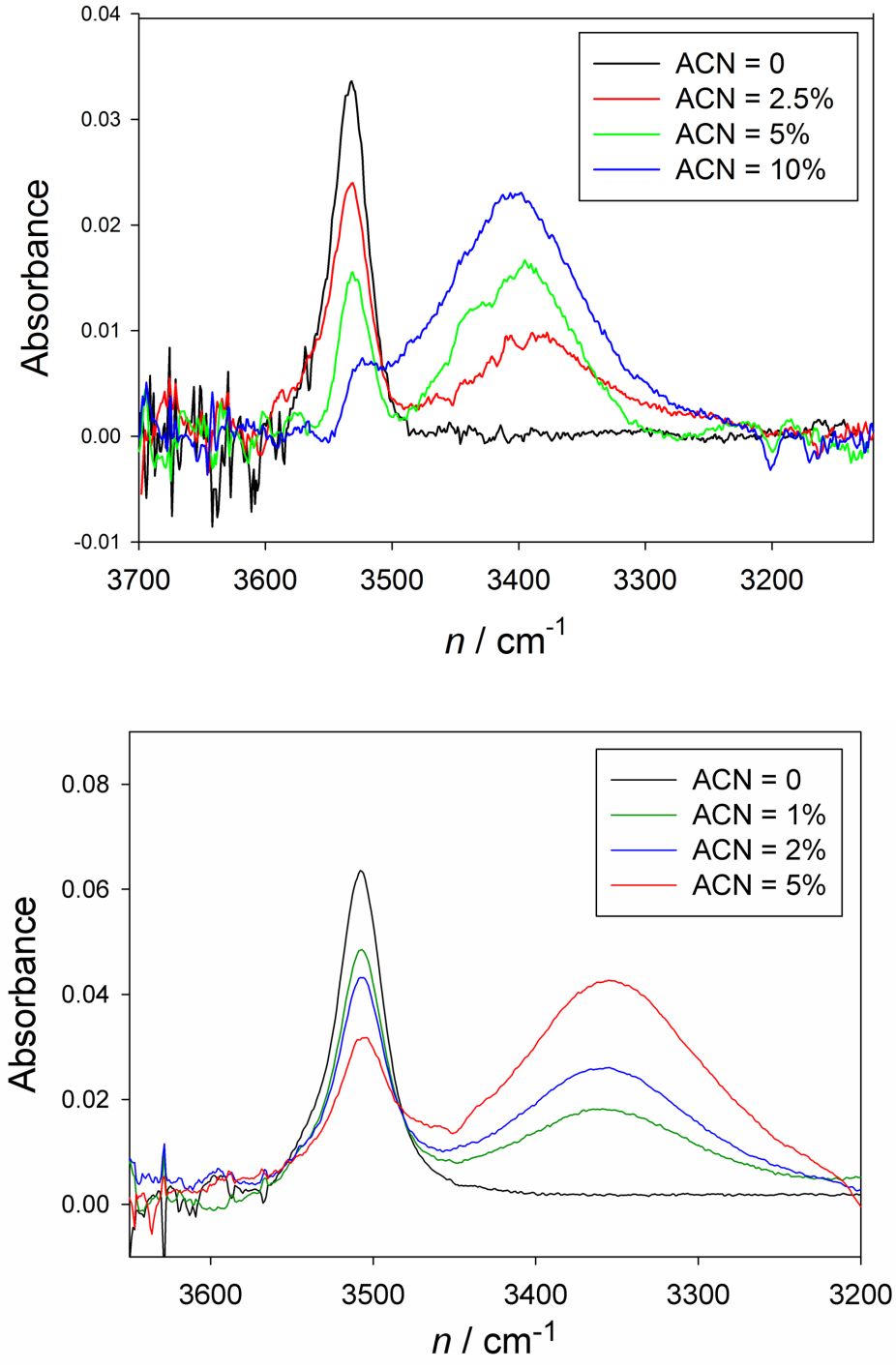

Figure 5.5. Representative FT-IR spectra of the O-H stretching region of **5.2** (1 mM, top) and **5.1** (10 mM, bottom) in CCl_4 containing increasing amounts of acetonitrile as cosolvent.

At first glance, the slower reaction of the selenenic acid with peroxyl radicals relative to the sulfenic acid appears fully consistent with the fact that the selenenic acid has a stronger O-H bond. However, Evans-Polanyi relationships between rate constants for the reactions of H-atom donors with peroxyl radicals (k_{inh}) and the X-H BDEs of the H-atom donors imply that a much larger reactivity difference should exist between the selenenic and sulfenic acids given the 9 kcal/mol difference in their O-H BDEs. For instance, the Evans-Polanyi correlations in Figure 5.6 for 4-substituted phenols, 4-substituted 2,6-dimethylphenols and 4-substituted 2,6-di-*tert*-butylphenols predict differences of *3 orders of magnitude* in k_{inh} for an O-H BDE difference of 9 kcal/mol.[28] Interestingly, including the data for **5.1** and **5.2** in these correlations finds them on the lines of best fit for the 2,6-di-*tert*-butylated phenols and the unsubstituted phenols, respectively. The data for substituted phenols have long been assumed to lie on different lines owing to the differing steric demands on the reactions, which increases the entropy of activation for the more hindered substrates, decreasing the pre-exponential factor for their reactions.[28] This implies that the sulfenic and selenenic acids also have different steric requirements. Indeed, the longer C-Se and Se-O bonds in the selenenic acid (1.956 and 1,866 Å, respectivelt)[12] relative to the C-S and S-O bonds in the sulfenic acid (1.833 and 1.622 Å, respectively)[29] should minimize steric interactions between the triptycene moiety and the substituent on the peroxyl radical to which the H-atom is being transferred.

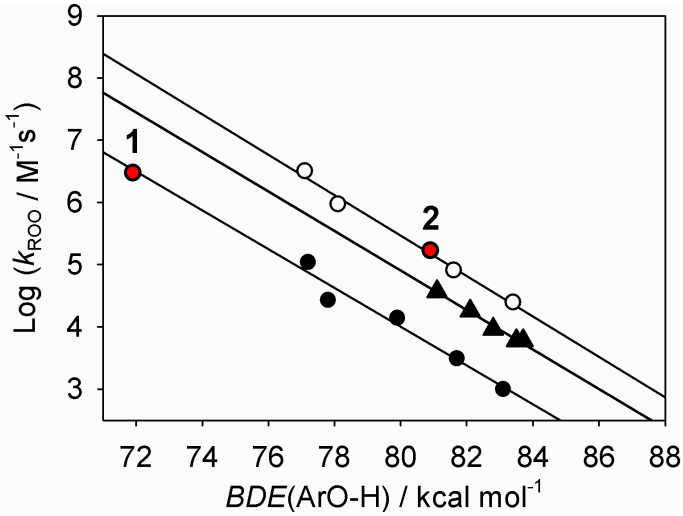

Figure 5.6. Evans-Polanyi correlations for the reactions of peroxyl radicals with 4-substituted phenols (○), 2,6-dimethyl-4-substituted phenols (▲) and 2,6-di-*tert*-butyl-4-substituted phenols (●). Also shown are the corresponding data for **5.1 (1)** and **5.2 (2)**.

To provide insight into the transition state (TS) structures by which these reactions proceed, and the extent to which they are impeded by steric interactions, we again turned to computation. Since TS calculations of reactions of **5.1** and **5.2** with peroxyl radicals are far too large to be carried out with the high-accuracy CBS-QB3 approach used for the BDE calculations above, we turned to density functional theory using B3LYP and the dispersion-correcting potentials (DCPs) of DiLabio and Torres.[30] The calculated minimum energy TS structures are shown in Figure 5.7, and alongside are the corresponding thermokinetic parameters. While the calculated rate constants (from transition state theory) are overestimated relative to experiment by roughly 1 order of magnitude,[46] they are consistent with the experimental results in that they indicate that the selenenic acid **5.2** reacts more slowly with peroxyl radicals than the sulfenic acid **5.1**. Indeed, the calculated ratio k (**5.1**) / k (**5.2**) = 33 is in very good agreement with the experimental value of k_{inh} (**5.1**) / k_{inh} (**5.2**) = 18.

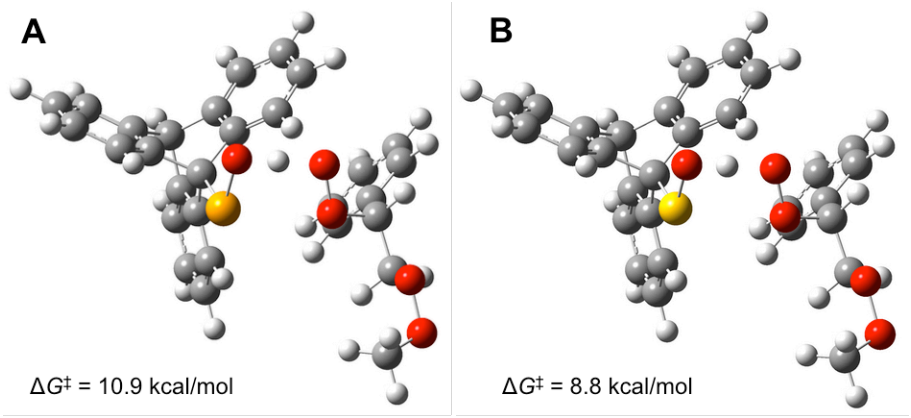

Figure 5.7. DCP-B3LYP/6-31+G(2d,2p)-calculated transition state structures for the reactions of selenenic acid **5.2** (A) and sulfenic acid **5.1** (B) with a styrylperoxyl radical (representative of the chain-carrying peroxyl radicals in styrene autoxidations).

Somewhat surprisingly, the TS structures in Figure 5.7 feature a syn relationship of the substituents on the oxygen atoms between which the H-atom is being transferred. While previous CBS-QB3 calculations on less sterically encumbered sulfenic acids (e.g., *t*-BuSOH) and peroxyl radicals (MeOO•) indicated that this conformation is preferred by a significant margin over a TS structure wherein the substituents on the oxygen atoms adopt an anti conformation ($\Delta G_{syn}^{\ddagger}$ = 10.1 kcal/mol and $\Delta G_{anti}^{\ddagger}$ = 14.9 kcal/mol, Figure 5.8B,D),[15] we anticipated that the larger substituents would alter this preference.[14] In order to provide a corresponding unhindered comparison for the selenenic acid, we carried out CBS-QB3 calculations on the reaction of *t*-BuSeOH and MeOO•. Indeed, the same geometric preference is predicted for this reaction (Figure 5.8A,C), with the syn TS being preferred by an even greater margin over the anti TS ($\Delta G_{syn}^{\ddagger}$ = 7.9 kcal/mol and $\Delta G_{anti}^{\ddagger}$ = 19.8 kcal/mol). However, most interestingly, the order of reactivity is predicted to be different in the smaller models than in the larger models: that is, the *t*-BuSeOH/•OOMe reaction is predicted to be *faster* than the corresponding *t*-BuSOH/•OOMe reaction.[47] This is particularly surprising, given that the strength of the O−H bond in *t*-BuSeOH is predicted to be 12.6 kcal/mol stronger than the O−H bond in *t*-BuSOH!

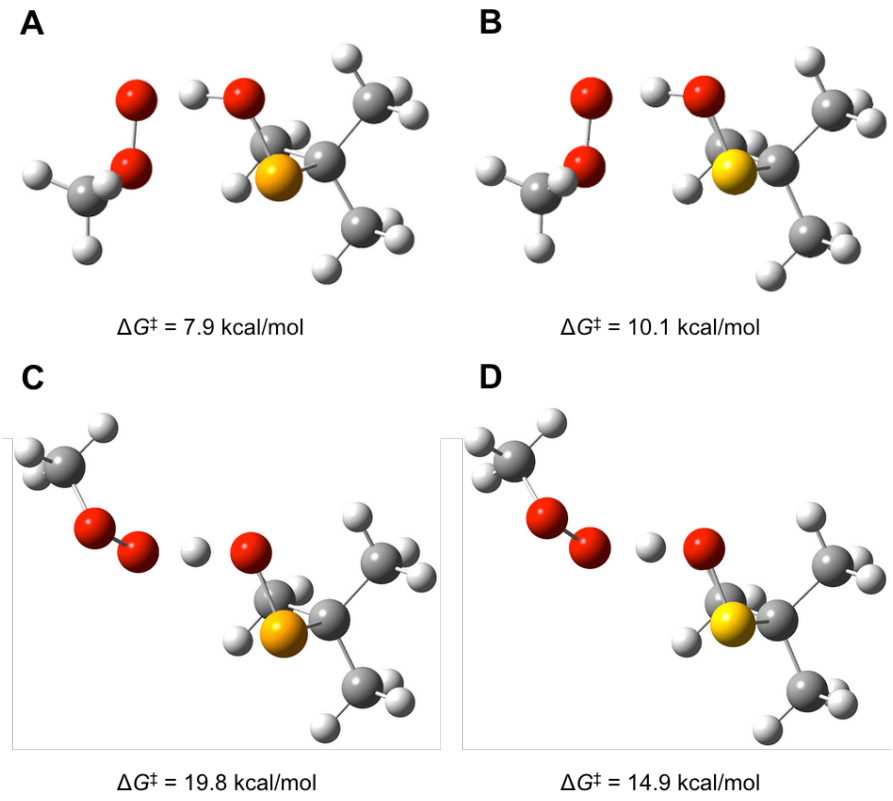

Figure 5.8. CBS-QB3-Calculated *syn* (A,B) and *anti* (C,D) transition state structures for the reactions of *t*-BuSeOH (A,C) and *t*-BuSOH (B,D) with a model alkylperoxyl radical (MeOO•).

The reactions of sulfenic acids with peroxyl radicals have been described as taking place by proton-coupled electron transfer,[15,31] facilitated by the overlap between orbitals based on the sulfenic acid sulfur atom and the inner oxygen atom of the peroxyl radical - seen clearly in the three highest (doubly) occupied MOs shown in Figure 5.9 - accounting for the preference for the *syn* TS in the formal H-atom transfer.[48] This description would appear to be appropriate for the reactions of selenenic acids with peroxyl radicals as well, as the same interactions are evident in the corresponding MOs shown on the left in Figure 5.9. The lower barrier for the *t*-BuSeOH/•OOMe reaction in comparison to that for *t*-BuSOH/•OOMe via the low-energy *syn* pathway can therefore be understood on the basis of improved charge transfer between the larger, less electronegative selenium atom and the internal oxygen atom of the peroxyl radical in comparison to the smaller, more

electronegative sulfur atom. Indeed, bond order analysis of the structures in Figure 5.8 (and Figure 5.9) reveals a much larger bonding interaction between the selenium atom and the internal oxygen atom of the peroxyl radical in the selenenic acid *syn* TS (0.229) in comparison to the sulfur and corresponding oxygen atom in the sulfenic acid *syn* TS (0.180).[49]

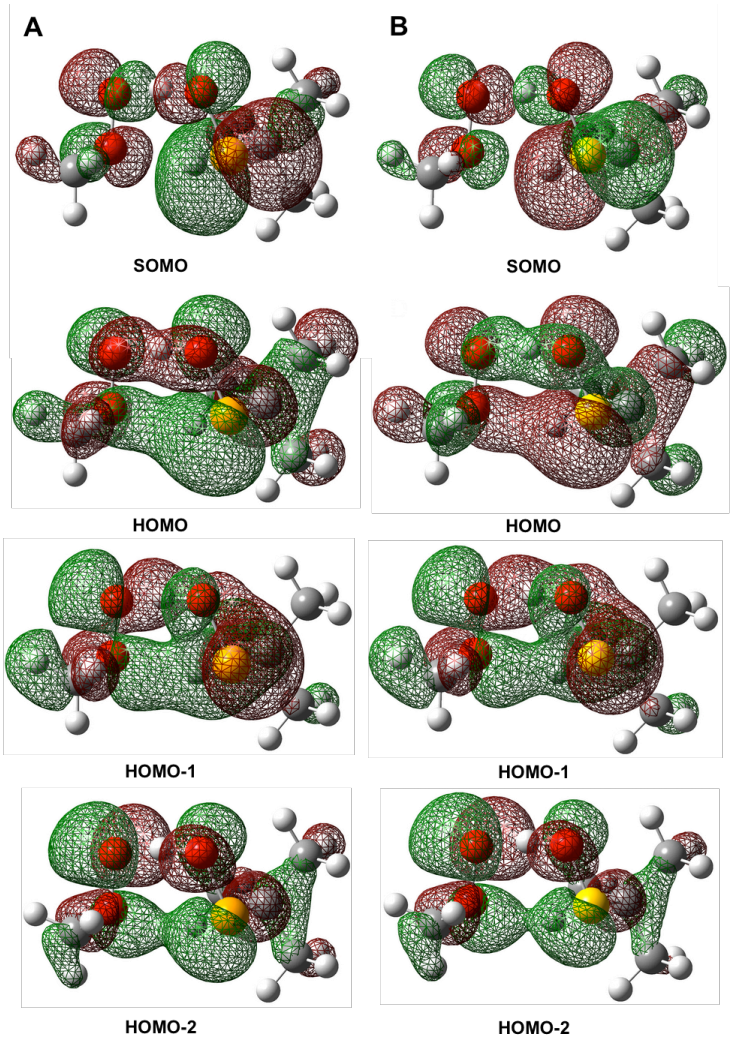

Figure 5.9. The four highest energy occupied molecular orbitals corresponding to the *syn* transition state structures for the reactions of *t*-BuSeOH (A) and *t*-BuSOH (B) with MeOO$^{\bullet}$ obtained from the UB3LYP/CBSB7 step of the CBS-QB3 calculation.

Since the high reactivity of selenenic acids toward peroxyl radicals appears to be driven by charge transfer from the selenium to the internal oxygen atom of the peroxyl radical, the barrier of the

reaction should be highly dependent on the extent to which orbitals centered on these atoms overlap. To illustrate this point, we calculated the $\Delta G^{\ddagger}$ value for the reactions of *t*-BuSeOH with MeOO• as a function of the Se-O/O-O torsion angle in the TS structure. The results are shown in Figure 5.10, revealing a substantial dependence of the barrier height on the torsion angle: rising from ca. 8 kcal/mol to ca. 20 kcal/mol upon going from the *syn* structure to the orthogonal structure. We carried out analogous calculations for the reactions of *t*-BuSOH with MeOO•, which reavealed a similar, but less severe angular dependence; the barrier rises from ca. 10 kcal/mol to ca. 15 kcal/mol in the orthogonal structure (see also Figure 5.10).[50] Thus, while selenenic acids may be more reactive toward peroxyl radicals than sulfenic acids at the "ideal" TS geometry, they become less reactive as the geometry is distorted to reduce the Se/O overlap in the TS. It seems reasonable to suggest that the triptycene moieties necessary to make the sulfenic and selenenic acids persistent and amenable to experimental study also make it difficult for them to achieve "ideal" TS geometries in reactions with peroxyl radicals. Indeed, while the calculated TS structures in Figures 5.7 (full model) and 5.8 (smaller model) feature similar overall geometries, the distances between the chalcogen atom and the inner oxygen atom of the peroxyl radical are significantly longer in the former in comparison to the latter (3.12 and 3.14 Å vs 3.01 and 3.00 Å), and the Se-O/O-O and S-O/O-O torsion angles have opened up to 17 and 20° from 9 and 10°, respectively,[43] diminishing overlap between the orbitals on the chalcogen atom and the internal oxygen atom of the peroxyl.

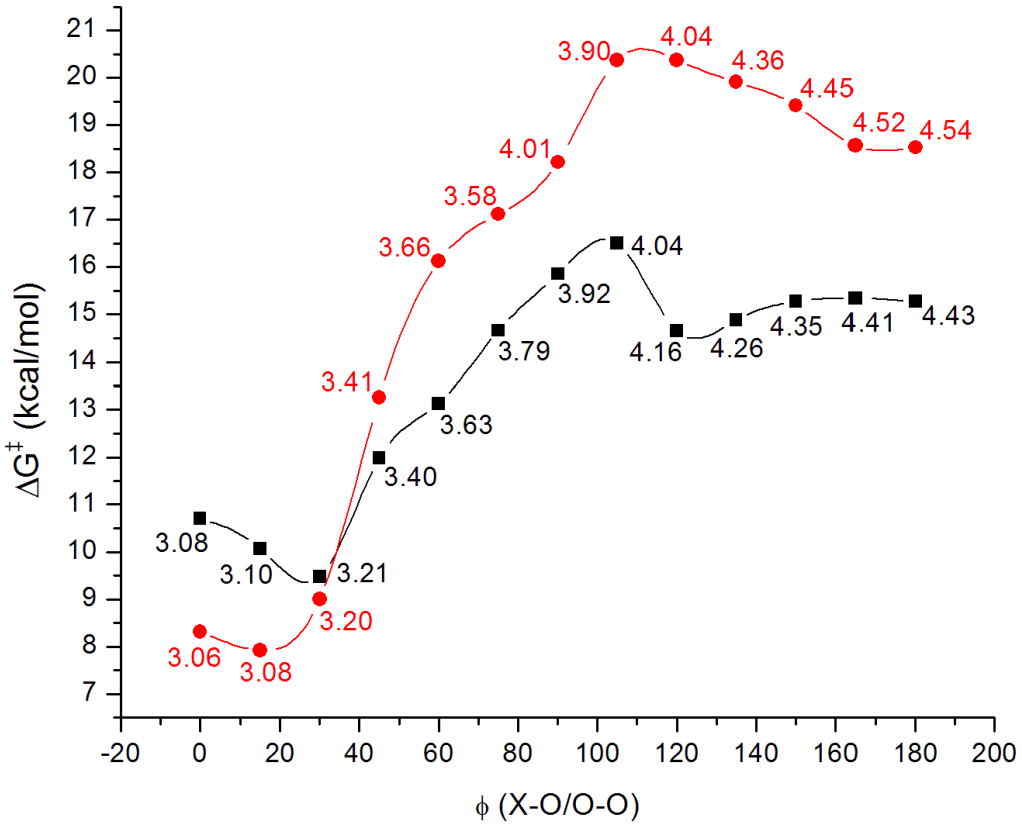

Figure 5.10. Dependence of the CBS-QB3-calculated $\Delta G^{\ddagger}$ values for the reactions of *t*-BuSeOH (red ●) and *t*-BuSOH (black ■) with MeOO• on the Se-O/O-O and S-O/O-O torsion angles in the transition state structures, respectively. The points are labeled with the distance between the chalcogen atom and the inner oxygen atom of the peroxyl radical in the corresponding structures.

The higher than expected reactivity of the persistent selenenic acid **5.2** toward peroxyl radicals (relative to the persistent sulfenic acid **5.1**) is the strongest evidence to date for charge transfer/secondary orbital interactions in the reactions of good H-atom donors with peroxyl radicals. While this has been suggested to be key to the reactions of ubiquitous radical- trapping antioxidants, such as phenols[31,32] and diaryl- amines,[33,34] as well as related compounds,[15,35] it is yet to be firmly supported by experiment. Given that these reactions underlie the preservation of virtually all hydrocarbon materials (including us!), we trust the foregoing insights will help clarify

structure−reactivity trends already established or yet to be uncovered with the design of new compounds.

5.4 Conclusions

A persistent selenenic acid bearing a triptycene moiety has been used to characterize the redox chemistry of selenenic acids for the first time. The strength of the O-H bond in the selenenic acid is ca. 81 kcal/mol, making it weaker than the corresponding O-H bond in a hydroperoxide (ca. 86 kcal/mol), but much stronger than in a sulfenic acid (ca. 70 kcal/mol).[13,15] Insights from theoretical calculations indicate that the lack of any periodic trend in the BDEs is the result of lesser spin delocalization in the selenenyl radical relative to the sulfinyl radical, owing to the longer Se-O bond. As such, selenenic acids are unusual among the three (valence) isoelectronic species in that the O-H bond is stronger than the Se-H bond in the selenol (from which it is often derived). This trend is in contrast with those established for sulfenic acids and hydroperoxides, which are characterized by significantly weaker bonds (by ca. 20 kcal/mol) to hydrogen than in the corresponding thiols and alcohols, respectively. These insights serve as a cautionary note on rationalizing the reactivity of selenium-containing compounds simply on the basis of their structural similarity to sulfur-containing compounds.

The kinetics of formal H-atom transfer reactions from the persistent selenenic acid were evaluated using peroxyl radicals as a model oxidant, revealing very high reactivity ($k_{inh} = 1.7 \times 10^5$ $M^{-1}s^{-1}$) relative to the strength of the O-H bond. CBS-QB3 calculations on a model system wherein the triptycene is replaced with a *tert*-butyl group and a methylperoxyl radical is used as the oxidant reveal that these reactions proceed with a negligible enthalpic barrier via a transition state stabilized greatly by interactions between orbitals with significant contributions from the selenium atom and the internal oxygen atom of the peroxyl radical. The calculations also indicate that these interactions are

highly sensitive to the transition state geometry; even small perturbations in the structure that diminish these interactions significantly increase $\Delta G^{\ddagger}$, and account for the lower observed reactivity of the hindered 9-triptyceneselenenic acid in comparison to that expected on the basis of the model calculations. These insights reveal the dramatic impact of small perturbations on the transition state geometries for formal H-atom transfer reactions facilitated by secondary orbital interactions (e.g. in proton-coupled electron transfer reactions). That is, steric arguments for the rationalization of reactivity trends must be considered carefully in light of the impact they have not only on potential approach trajectories of the reactants, but also in their abilities to maximize secondary orbital overlap in the transition state.

The foregoing results indicate that unhindered selenenic acids are likely to be among the most reactive H-atom donors toward radical centers that have an adjacent high-lying electron-pair, such as in peroxyl or phenoxyl radicals, which facilitate the reaction via interaction with orbitals centered on the selenium atom. As such, the formation of a selenenic acid either by oxidation of a selenol or by Cope elimination from a selenoxide may serve to convert a relatively poor H-atom donor into an excellent one and may present a complementary mechanism for the reducing activities of selenium compounds beyond the two-electron chemistry that is most commonly observed and/or assumed.

5.5 Perspective

The initial objective of the foregoing work was to explore the redox chemistry of selenenic acids (RSeOH) as compared to sulfenic acids (RSOH), by utilizing methods we had successfully employed on the latter – namely, preparing the more bulky and persistent triptycene derivative. The experimental results, as supported by the theoretical calculations, revealed a surprisingly significant effect of the selenium atom as a secondary orbital donor. This effect accelerated the H-atom transfer reactivity of RSeOH with peroxyl radicals far greater than would be predicted, based on its O-H

BDE. As outlined in Chapter 1 (Section 1.2), several explanations have been advanced for such deviations in Evans-Polanyi relationships. We were therefore interested in seeing if the influence of secondary orbital interactions could help explain outliers to such relationships, and further, if computations could be used to quantify or predict trends in H-atom transfer reactivity. The results of this computational study are presented in Chapter 6.

5.6 Experimental Section

5.6.1 Synthesis

Bis(2-phenethyl) diselenide **(5.3).** Dry selenium powder (3.5 g, 44 mmol), sodium chips (1.06 g, 44 mmol), and naphthalene (0.57 g, 4.5 mmol) were stirred in dry THF (100 mL) under argon for 12 h. To the dark purple mixture was added 2-bromo-ethylbenzene (5.88 mL 44 mmol) dropwise. The mixture was stirred for 1 h, during which the color changed to light orange. A tan salt was removed by filtration, and the filtrate was concentrated *in vacuo*. The resulting orange oil was loaded on a silica gel flash column and eluted first with hexanes and then with benzene to give an orange oil (7.77 g, 48% yield). ^{1}H NMR (400 MHz, $CDCl_3$) δ 3.03-3.07 (m, 4H), 3.14-3.18 (m, 4H), 7.20-7.24 (m, 6H), 7.29-7.33 (m, 4H); ^{13}C NMR ($CDCl_3$, 300 MHz) δ30.7 37.5, 126.3, 128.4, 128.5, 140.7; HRMS (EI+) calculated for $C_{16}H_{18}Se_2$ 369.6739, observed 369.6735. The ^{1}H NMR spectrum is in good agreement with that presented in the literature;[36] the ^{13}C NMR spectrum has not been reported to date.

9-Triptycene(phenethyl)selenide **(5.4).** 9-Bromotriptycene[13] (1.8 g, 5.4 mmol) was dissolved in dry benzene (100 mL) and dry methyl *tert*-butyl ether (70 mL), cooled to -18°C, and n-butyllithium (3.8 mL, 5.4 mmol) were added dropwise. Bis-(phenethyl) diselenide **5.3** (2.1 g, 5.4 mmol) was suspended in a minimum amount of dry benzene and added slowly to the reaction mixture at 0°C. The reaction mixture was stirred at room temperature for 12 h, before it was quenched with water and extracted with ether. The organic phase was washed with brine and then dried over $MgSO_4$, filtered and

concentrated *in vacuo*. The resulting oily yellow solid was loaded on a silica gel flash column and eluted with 5% dichloromethane in hexanes to yield an off-white solid which was recrystallized from benzene/ethanol (1.77 g, 75% yield). ^{1}H NMR (400 MHz, $CDCl_3$) δ3.16-3.21 (m, 2H), 3.28-3.33 (m, 2H), 5.38 (s, 1H), 7.02-7.05 (m, 6H), 7.27-7.31 (m, 1H), 7.35-7.41 (m, 7H), 7.56-7.59 (m, 3H); ^{13}C NMR (400 MHz, $CDCl_3$) δ25.7 36.8, 54.1, 60.3, 123.4, 124.0, 125.0, 125.6, 126.6, 128.5, 128.6, 140.6, 145.1, 145.6; HRMS (EI+) calculated for $C_{28}H_{22}Se$ 438.0887, observed 438.0876.

9-Triptycene phenethyl selenoxide **(5.5).** A solution of **5.4** (94 mg, 0.21 mmol) in dry dichloromethane (18 mL) was cooled to -78°C. mCPBA (77%, 48 mg, 0.21 mmol) was added slowly in 5 mL of dry dichloromethane. The reaction mixture was worked up immediately by washing twice with 20 mL of cold 0.7 M aqueous KOH, followed by 20 mL of ice water, then 20 mL of cold brine. The organic phase was dried over $MgSO_4$, filtered and concentrated *in vacuo* at -78°C. A white solid was obtained (84 mg, 86% yield). The 9-triptycene phenethyl selenoxide was generally obtained as a mixture with 9- triptyceneselenenic acid and styrene due to Cope elimination *in situ*. ^{1}H NMR (300 MHz, $CDCl_3$) δ3.47- 3.64 (m, 2H), 3.83-3.93 (m, 1H), 4.00-4.09 (m, 1H), 5.37 (s, 1H), 7.02-7.05 (m, 6H), 7.28-7.37 (m, 9H) 7.93-8.02 (m, 1H), 8.31-8.39 (m, 1H); ^{13}C NMR (300 MHz, $CDCl_3$) δ29.7, 30.5, 48.7, 68.1, 121.6, 123.0, 123.6, 125.3, 125.7, 127.1, 128.8, 129.0, 144.3, 145.7. No molecular ion could be observed by MS due to its ready fragmentation to the selenenic acid.

9-Triptyceneselenenic acid **(5.2).** Selenoxide **5.5** was left under high vacuum for 2 weeks at room temperature. ^{1}H NMR (300 MHz, $CDCl_3$) δ 5.42 (s, 1H), 7.02-7.05 (m, 6H), 7.41-7.44 (m, 6H); ^{13}C NMR (300 MHz, $CDCl_3$) δ 54.1, 64.1 123.0, 123.7, 125.3, 125.7, 144.3, 145.7; HRMS (ES-) calculated for $C_{20}H_{14}OSe$ 349.0132, observed 349.0104. The spectral characteristics are in good agreement with those presented in the literature.[12]

5.6.2 EPR experiments

Spectra were recorded at 298K by irradiating deoxygenated benzene solutions of **5.2** containing di-*tert*-butyl peroxide (10% v/v) with a 500W high-pressure Hg lamp in the spectrometer cavity. The

measured *g* factor was corrected with respect to the known value of 2,2,6,6-tetramethylpiperidine-N-oxyl radical in benzene (g = 2.0064). Equilibration studies were performed by irradiating mixtures of **5.2** and 2,4,6-tri-*tert*-butylphenol[19] in different ratios.[18,33,37,38] The relative amount of the corresponding radicals was determined by fitting the experimental spectrum with computer simulations using WinESR software, developed by Prof. Marco Lucarini (Univ. Bologna), based on the Monte Carlo method.[37] Different irradiation intensities were compared to make sure that equilibrium was established. The equilibrium constant K was determined according to eq. 5.5, which yielded ΔH for equilibration by eq. 5.6 under the assumption that $\Delta S \approx 0$.[33,37,38]

$$K = ([\text{TripSeOH}]/[\text{TTBP}]) \times ([\text{TTBP}^{\bullet}]/[\text{TripSeO}^{\bullet}]) \qquad (5.5)$$

$$\Delta G = \Delta H - \text{T}\Delta S = -R\text{T} \times \ln K \qquad (5.6)$$

5.6.3 Autoxidations

Rate constants (k_{inh}) for the reactions of **5.2** with peroxyl radicals were dermined by kinetic analysis of inhibited autoxidations of styrene (50% v/v) in air saturated chlorobenzene or acetonitrile solution at 303K.[24] The reaction was thermally initiated at constant rate R_i (determined experimentally, in the range $(2–9) \times 10^{-9}$ M s^{-1}) by the decomposition of 2,2'-azodiisobutyronitrile (AIBN, $(1–5) \times 10^{-2}$ M) and the oxygen consumption was monitored in a two-channel oxygen-uptake apparatus already described elsewhere.[39,40] 2,2,5,7,8-Pentamethyl-6-chromanol (PMHC) was used as reference antioxidant.[39,40] From the slope of the oxygen consumption during the inhibited period (R_{inh}), k_{inh} values were obtained by using eq. 5.7 where R_0 is the rate of oxygen consumption in the absence of antioxidants, $2k_t$ is the bimolecular termination rate constant of styrene (4.2×10^7 $M^{-1}s^{-1}$) and n is the stoichiometric coefficient of the antioxidant, which was determined experimentally from the length of the inhibited period (τ) by eq. 5.8.[39,40] When the inhibited period was not clearly visible kinetic data were confirmed by fitting the experimental traces with numerical simulations using Gepasi 3.0 software, as previously described.[41]

$$(R_0/R_{inh}) - (R_{inh}/R_0) = nk_{inh}[AH]/\sqrt{(2k_tR_i)} \qquad (5.7)$$

$$n = \tau\ R_i/[AH] \qquad (5.8)$$

Deuterium kinetic isotope effects were determined by comparing inhibited autoxidations recorded upon addition of 1% v/v H_2O or D_2O.[39,40]

5.6.4 IR Measurements

Spectra of **5.1** and **5.2** were recorded at 298 K in a FT-IR spectrometer under a nitrogen atmosphere using a sealed KBr cell with an optical path of 0.5 mm. Solutions of the test compound (1–10 mM) in CCl_4 and in CCl_4/CH_3CN mixtures were analyzed in absorbance mode referenced to the blank spectrum of the corresponding solvent mixture. The integrated signal of the "free" O-H stretching mode at ca. 3530 cm^{-1} obtained after manual baseline correction, was plotted *vs.* the concentration of acetonitrile and fit to eq. 5.9.

$$[\mathbf{5.1}\text{ or }\mathbf{5.2}]_{free} = [\mathbf{5.1}\text{ or }\mathbf{5.2}]_{tot} / (1 + K_{solv} \times [Solv]) \qquad (5.9)$$

From the measured equilibrium constant K_{solv}, the corresponding α_2^H values were obtained by Abraham's equation 5.10,[27] using the revised value of $\beta_2^H = 0.39$ for acetonitrile.[44]

$$\log (K_{solv} / M^{-1}) = 7.354\ \alpha_2^H\beta_2^H - 1.094 \qquad (5.10)$$

5.6.5 Computations

All calculations were carried out using the Gaussian 09 quantum chemistry package[51] using the CBS-QB3 complete basis set approach,[20] except for the calculated transition state structures shown in Figure 5.10, which were obtained using B3LYP and a 6-31+G(2d,2p) basis set including the

dispersion correcting potentials of DiLabio and Torres.[30] Wiberg bond order analysis[52] was carried out using the AOMix software developed by Gorelsky.[53]

5.7 References

(1) Rappoport, Z. *The Chemistry of Organic Selenium and Tellurium Compounds*; Wiley, 2012.

(2) Mugesh, G.; Mont, du, W.-W.; Sies, H. *Chem. Rev.* **2001**, *101*, 2125–2180.

(3) Goto, K.; Nagahama, M.; Mizushima, T.; Shimada, K.; Kawashima, T.; Okazaki, R. *Org. Lett.* **2001**, *3*, 3569–3572.

(4) Jones, D. N.; Mundy, D.; Whitehouse, R. D. *J. Chem. Soc. D* **1970**, 86.

(5) Sharpless, K. B.; Lauer, R. F. *J. Am. Chem. Soc.* **1973**, *95*, 2697–2699.

(6) Reich, H. J.; Renga, J. M.; Reich, I. L. *J. Am. Chem. Soc.* **1975**, *97*, 5434–5447.

(7) Flohe, L.; Gunzler, W. A.; Schock, H. H. *FEBS Letters* **1973**, *32*, 132–134.

(8) Rotruck, J. T.; Pope, A. L.; Ganther, H. E.; Swanson, A. B.; Hafeman, D. G.; Hoekstra, W. G. *Science* **1973**, *179*, 588–590.

(9) Bhabak, K. P.; Mugesh, G. *Acc. Chem. Res.* **2010**, *43*, 1408–1419.

(10) Reich, H. J.; Jasperse, C. P. *J. Org. Chem.* **1988**, *53*, 2389–2390.

(11) Saiki, T.; Goto, K.; Okazaki, R. *Angew. Chem. Int. Ed. Engl.* **1997**, *36*, 2223–2224.

(12) Ishii, A.; Matsubayashi, S.; Takahashi, T.; Nakayama, J. *J. Org. Chem.* **1999**, *64*, 1084–1085.

(13) McGrath, A. J.; Garrett, G. E.; Valgimigli, L.; Pratt, D. A. *J. Am. Chem. Soc.* **2010**, *132*, 16759–16761.

(14) Amorati, R.; Lynett, P. T.; Valgimigli, L.; Pratt, D. A. *Chem. Eur. J.* **2012**, *18*, 6370–6379.

(15) Vaidya, V.; Ingold, K. U.; Pratt, D. A. *Angew. Chem. Int. Ed.* **2009**, *48*, 157–160.

(16) Lynett, P. T.; Butts, K.; Vaidya, V.; Garrett, G. E.; Pratt, D. A. *Org. Biomol. Chem.* **2011**, *9*, 3320–3330.

(17) Paulsen, C. E.; Carroll, K. S. *Chem. Rev.* **2013**, *113*, 4633−4679.

(18) Lucarini, M.; Pedulli, G. F.; Cipollone, M. *J. Org. Chem.* **1994**, *59*, 5063–5070.

(19) Mulder, P.; Korth, H.-G.; Pratt, D. A.; DiLabio, G. A.; Valgimigli, L.; Pedulli, G. F.; Ingold, K. U. *J. Phys. Chem. A* **2005**, *109*, 2647–2655.

(20) Montgomery, J. A.; Frisch, M. J.; Ochterski, J. W.; Petersson, G. A. *J. Chem. Phys.* **1999**, *110*, 2822.

(21) Gibson, S. T. *J. Chem. Phys.* **1986**, *85*, 4815–4824.

(22) Leeck, D. T.; Li, R.; Chyall, L. J.; Kenttämaa, H. I. *J. Phys. Chem.* **1996**, *100*, 6608–6611.

(23) Janousek, B. K.; Reed, K. J.; Brauman, J. I. *J. Am. Chem. Soc.* **1980**, *102*, 3125–3129.

(24) Burton, G. W.; Doba, T.; Gabe, E.; Hughes, L.; Lee, F. L.; Prasad, L.; Ingold, K. U. *J. Am. Chem. Soc.* **1985**, *107*, 7053–7065.

(25) Snelgrove, D. W.; Lusztyk, J.; Banks, J. T.; Mulder, P.; Ingold, K. U. *J. Am. Chem. Soc.* **2001**, *123*, 469–477.

(26) Litwinienko, G.; Ingold, K. U. *Acc. Chem. Res.* **2007**, *40*, 222–230.

(27) Abraham, M. H.; Grellier, P. L.; Prior, D. V.; Morris, J. J.; Taylor, P. J. *J. Chem. Soc., Perkin Trans. 2* **1990**, 521.

(28) Valgimigli, L.; Pratt, D. A. In *Encyclopedia of Radicals in Chemistry, Biology and Materials*; John Wiley & Sons, Ltd: Chichester, UK, 2011.

(29) Ishii, A.; Komiya, K.; Nakayama, J. *J. Am. Chem. Soc.* **1996**, *118*, 12836−12837.

(30) Torres, E.; DiLabio, G. A. *J. Phys. Chem. Lett.* **2012**, *3*, 1738− 1744.

(31) DiLabio, G. A.; Johnson, E. R. *J. Am. Chem. Soc.* **2007**, *129*, 6199−6203.

(32) Valgimigli, L.; Amorati, R.; Petrucci, S.; Pedulli, G. F.; Hu, D.; Hanthorn, J. J.; Pratt, D. A. *Angew. Chem., Int. Ed.* **2009**, *48*, 8348− 8351.

(33) Hanthorn, J. J.; Valgimigli, L.; Pratt, D. A. *J. Am. Chem. Soc.* **2012**, *134*, 8306−8309.

(34) Hanthorn, J. J.; Amorati, R.; Valgimigli, L.; Pratt, D. A. *J. Org. Chem.* **2012**, *77*, 6895−6907.

(35) Amorati, R.; Pedulli, G. F.; Pratt, D. A.; Valgimigli, L. *Chem. Commun.* **2010**, *46*, 5139.

(36) Thompson, D. P.; Boudjouk, P. *J. Org. Chem.* **1988**, *53*, 2109–2112.

(37) Lucarini, M.; Pedrielli, P.; Pedulli, G. F.; Cabiddu, S.; Fattuoni, C. *J. Org. Chem.* **1996**, *61*, 9259–9263.

(38) Shanks, D.; Amorati, R.; Fumo, M. G.; Pedulli, G. F.; Valgimigli, L.; Engman, L. *J. Org. Chem.* **2006**, *71*, 1033–1038.

(39) Lucarini, M.; Pedulli, G. F.; Valgimigli, L.; Amorati, R.; Minisci, F. *J. Org. Chem.* **2001**, *66*, 5456–5462.

(40) Amorati, R.; Pedulli, G. F.; Valgimigli, L. *Org. Biomol. Chem.* **2011**, *9*, 3792–3800.

(41) Valgimigli, L.; Amorati, R.; Fumo, M. G.; DiLabio, G. A.; Pedulli, G. F.; Ingold, K. U.; Pratt, D. A. *J. Org. Chem.* **2008**, *73*, 1830–1841.

(42) The increased O−H BDE in **5.1** in comparison to t-BuSOH is likely the result of the three sp^2 carbons bound to the quaternary carbon in the former being more inductively withdrawing than the sp^3 carbons in the latter, stabilizing the starting material and destabilizing the radical from **5.1** relative to t-BuSOH.

(43) The CCSD(T), MP2, and MP4 steps of the CBS-QB3 calculation each predict a spin distribution of ca. 0.2/0.8 (Se/O) in the selenenyl radical and ca. 0.4/0.6 (S/O) in the sulfinyl radical, whereas B3LYP predicts roughly 0.5/0.5 in both. The inclusion of effective core potentials in these calculations did not change the spin distributions to any significant extent.

(44) Valgimigli, L.; Bartolomei, D.; Amorati, R.; Haidasz, E.; Hanthorn, J. J.; Nara, S. J.; Brinkhorst, J.; Pratt, D. A. *Beilstein J. Org. Chem.* **2013**, *9*, 2781−2792.

(45) Ingold's equation refers to the KSE in pure solvents, while kinetics were measured in 50% v/v styrene/solvent mixtures.

(46) This is unsurprising, given that the calculations are of isolated molecules and the experiments were carried out in chlorobenzene, which would slow the reaction slightly due to H bonding; see refs 25 and 26.

(47) It must be pointed out that the DCP-B3LYP approach used to calculate the TS structures for the reactions of **5.1** and **5.2** with styrylperoxyl radicals also predicts a lower free energy barrier (by 1.2 kcal/mol) for the t-BuSeOH/•OOMe reaction in comparison to the t- BuSOH/•OOMe reaction, in good agreement with the CBS-QB3 calculations.

(48) This can also be described simply as an H-atom transfer reaction facilitated by a secondary orbital interaction, which lowers the energy of the syn TS relative to the anti TS. For a related example, see: Hu, D.; Pratt, D. A. *Chem. Commun.* **2010**, *46*, 3711−3713.

(49) In contrast, the anti TS structures have essentially the same bond order between the chalcogen atom and the internal oxygen atom of the peroxyl radical (S/O, 0.096; Se/O, 0.101).

(50) The optimal TS structure is calculated for a Se−O/O−O or S− O/O−O torsion angle of roughly 20° due to the orbital overlap between the chalcogen atom and inner peroxyl atom in the HOMO, which is impossible at a torsion angle of 0°.

(51) Frisch, M. J.; Trucks, G. W.; Schlegel, H. B.; Scuseria, G. E.; Robb, M. A.; Cheeseman, J. R.; Scalmani, G.; Barone, V.; Mennucci, B.; Petersson, G. A.; Nakatsuji, H.; Caricato, M.; Li, X.; Hratchian, H. P.; Izmaylov, A. F.; Bloino, J.; Zheng, G.; Sonnenberg, J. L.; Hada, M.; Ehara, M.; Toyota, K.; Fukuda, R.; Hasegawa, J.; Ishida, M.; Nakajima, T.; Honda, Y.; Kitao, O.; Nakai, H.; Vreven, T.; Montgomery, J. A., Jr.; Peralta, J. E.; Ogliaro, F.; Bearpark, M.; Heyd, J. J.; Brothers, E.; Kudin, K. N.; Staroverov, V. N.; Keith, T.; Kobayashi, R.; Normand, J.; Raghavachari, K.; Rendell, A.; Burant, J. C.; Iyengar, S. S.; Tomasi, J.; Cossi, M.; Rega, N.; Millam, J. M.; Klene, M.; Knox, J. E.; Cross, J. B.; Bakken, V.; Adamo, C.; Jaramillo, J.; Gomperts, R.; Stratmann, R. E.; Yazyev, O.; Austin, A. J.; Cammi, R.; Pomelli, C.; Ochterski, J. W.; Martin, R. L.; Morokuma, K.; Zakrzewski, V. G.; Voth, G. A.; Salvador, P.; Dannenberg, J. J.; Dapprich, S.; Daniels, A. D.; Farkas, O.; Foresman, J. B.; Ortiz, J. V.; Cioslowski, J.; Fox, D. J. *Gaussian 09, revision B.01*; Gaussian, Inc., Wallingford, CT, 2009.

(52) Mayer, I. *Chem. Phys. Lett.* **1983**, *97*, 270−274. Wiberg, K. B. *Tetrahedron* **1968**, *24*, 1083−1096.

(53) Gorelsky, S. I. *AOMix: Program for Molecular Orbital Analysis, version 6.82*, 2013; http://www.sg-chem.net/. Gorelsky, S. I.; Lever, A. B. P. *J. Organomet. Chem.* **2001**, *635*, 187−196.

5.8 Supporting Information

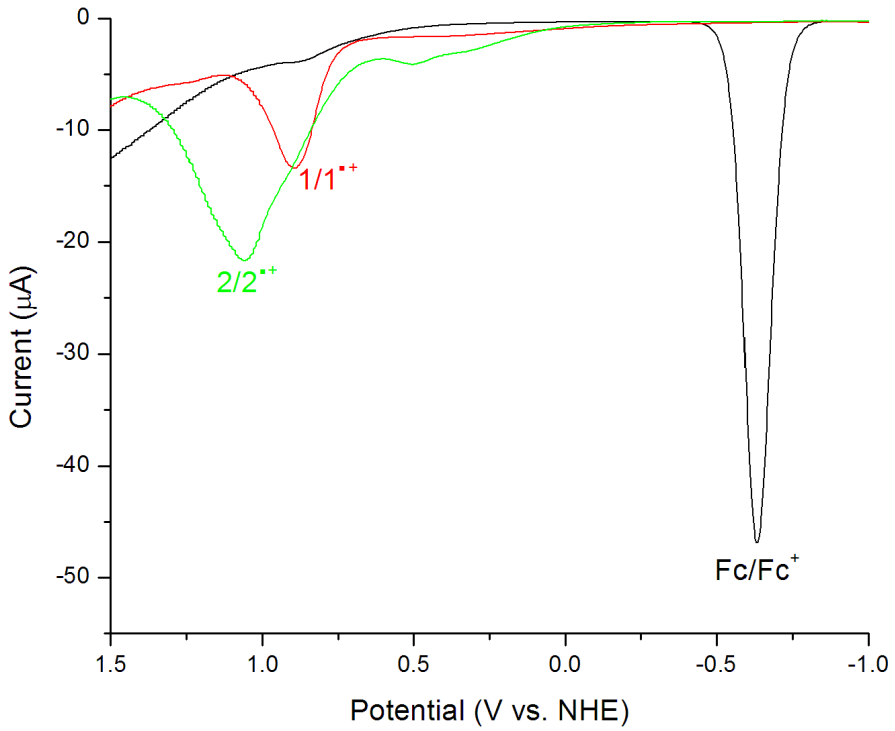

Figure 5.11. Overlay of representative differential pulse voltammograms of **5.1** and **5.2** recorded in dry acetonitrile containing 0.1 M $Bu_4N{\cdot}PF_6$ at 25°C. Voltammograms were recorded using a potentiostat with a glassy-carbon working electrode, a platinum counter electrode, and a Ag/ $AgNO_3$ (0.005 M) reference electrode calibrated using the ferrocene/ferrocenium couple. The experimental parameters were as follows: scan rate - 20 mV/s, pulse width - 0.05 s, pulse period - 0.2 s.

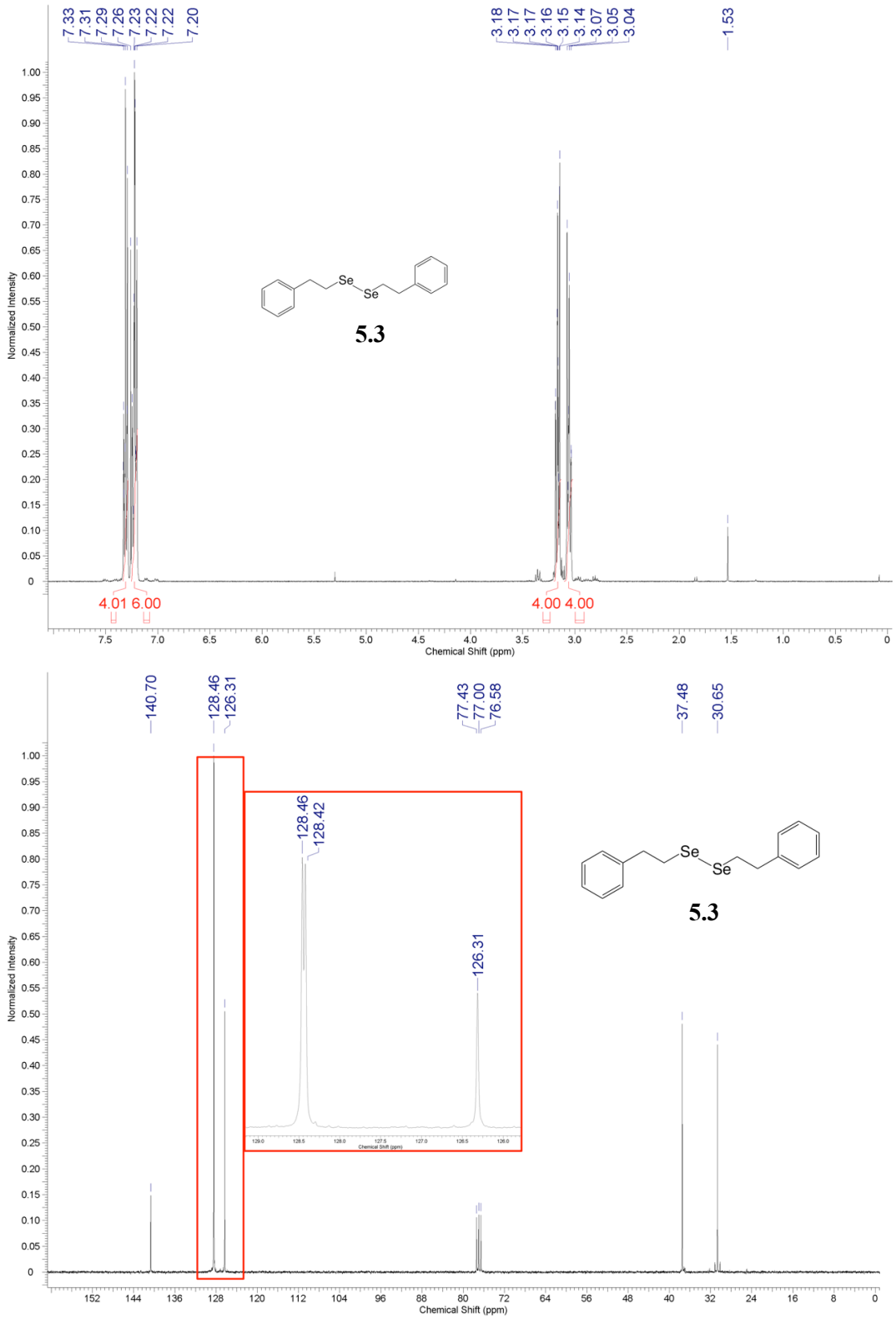

Figure 5.12. ^{1}H and ^{13}C NMR spectra of diselenide **5.3** in $CDCl_3$ at 400 MHz and 75 MHz, respectively.

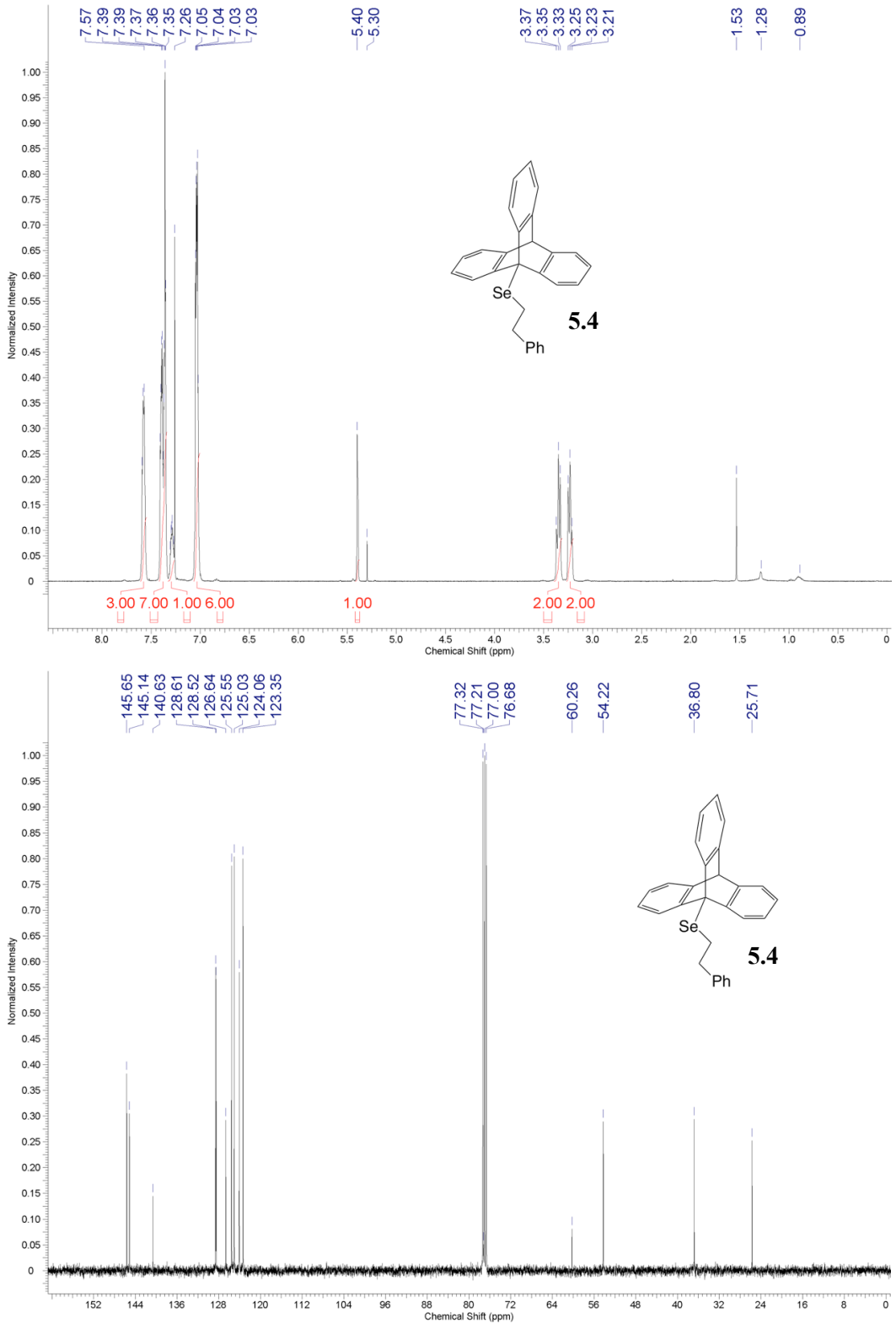

Figure 5.13. ^{1}H and ^{13}C NMR spectra of selenide 5.4 in $CDCl_3$ at 400 MHz and 100 MHz, respectively.

Working with the selenoxide was difficult owing to the rapid elimination of styrene from the selenoxide and the rapid self-condensation of the selenenic acid to form selenoseleninate. As such, the selenoxide was always isolated crude as a mixture containing selenenic acid and styrene. The spectra below are representative.

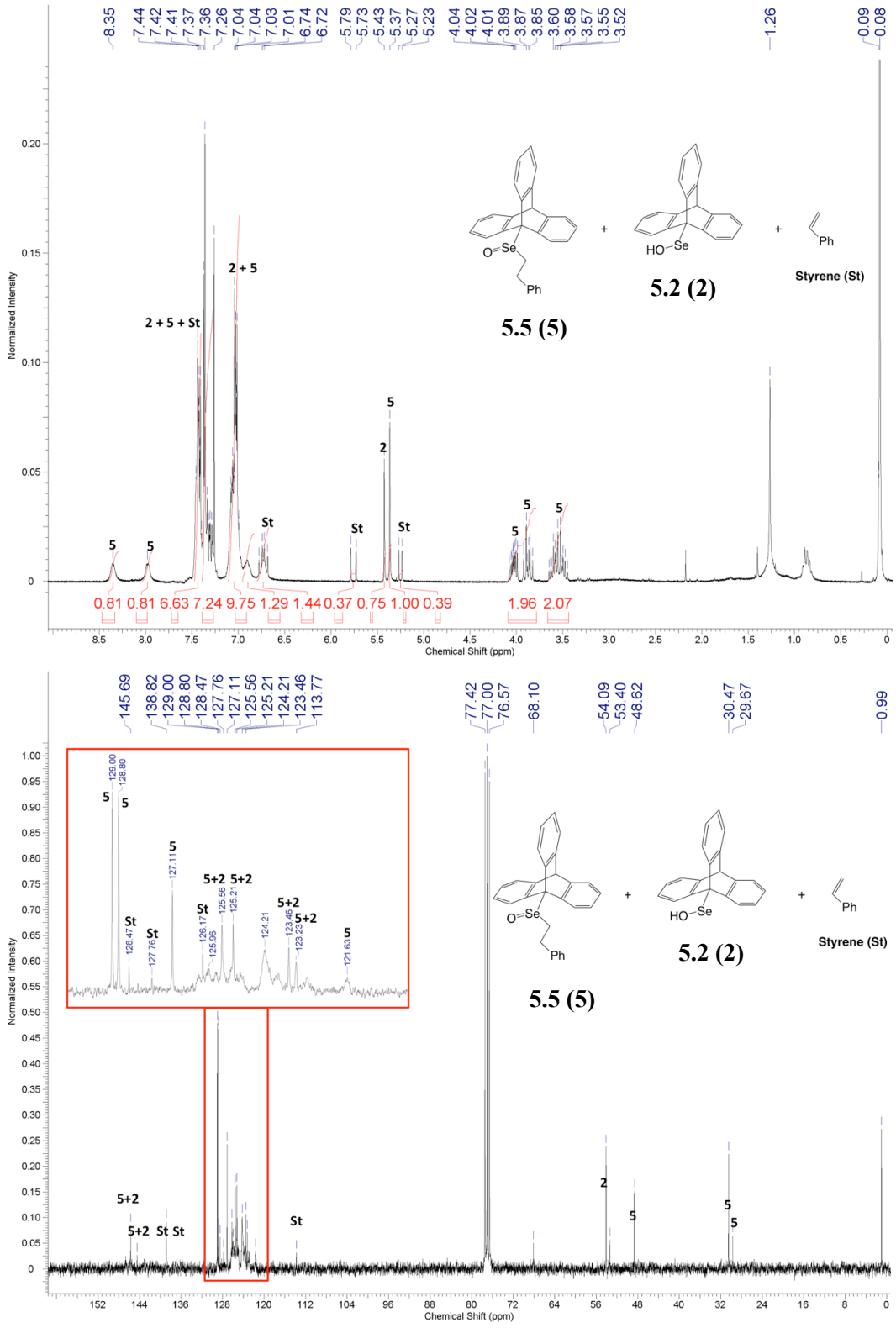

Figure 5.14. ^{1}H and ^{13}C NMR spectra of selenoxide **5.5** in $CDCl_3$ at 300 MHz and 75 MHz, respectively. For simplicity in peak assignment **5.5** is referred to as **5**, and **5.2** is referred to as **2**.

Chapter 6: On the Role of Secondary Orbital Interactions in H-Atom Transfer Reactions

6.1 Preface

Secondary orbital interactions have provided a rationale for seemingly anomalous trends in H-atom transfer (HAT) reactivity, the best experimental evidence[1] of which, to our knowledge, was presented in Chapter 5. Herein we explore secondary orbital interactions computationally across a larger set of compounds with several types of secondary orbital donors. While the results presented herein do underscore the importance of secondary orbital interactions in H-atom abstractions by peroxyl radicals, it also highlights the challenges in studying these types of reactions. Efforts to quantify or predict rate constants in HAT reactions is complicated by the many confounding stereoelectronic effects present in the associated transition states. Furthermore, the mechanism of HAT may be one in which the proton and electron are transferred together, as $H^{\bullet}$, or separately in a proton-coupled electron transfer.

6.2 Introduction

The Evans-Polanyi Principle implies a correlation between H-atom transfer reactivity (k_{HAT}) and the strength of the X-H bond from which the H-atom is being abstracted. Several theories have been advanced to explain outliers to the correlation, as summarized in Figure 6.1. Briefly, the concept of triplet-repulsion[2,3] is based on the eletronegativies of the atoms between which the H-atom is exchanged; since they each must bear unpaired electron density of the same spin in the transition state (TS), the repulsion therebetween is decreased as the electronegativies of the atoms increase. Polar effects[4-6] are also related to the electronegativities of the atoms between which the H-atom is exchanged, or the effect of substituents, which stabilize the dipole created in the TS. It is worth noting that the foregoing theories were advanced before computations revealed insight into the transition state (TS) geometry of H-atom transfers to peroxyl radicals. Indeed, the assumption had been that the

TS in such a reaction would be the *anti* configuration which minimized steric interactions. However, it has since been demonstrated that secondary orbital interactions can have a stabilizing effect on the *syn* transition state geometry, outweighing any associated steric hindrance, and can have a remarkable effect on accelerating H-atom transfer reactivity. As outlined in Section 1.2, this was first demonstrated in simple self-exchange reactions such as the hydrogen peroxide/hydroperoxyl radical couple. [7] Since then, there have been a number of publications discussing secondary orbital interactions in H-atom transfers to peroxyl radicals, such as from an allylic C-H, [8] the diarylamine N-H, [9] and O-H abstractions in phenols, [10] hydroxylamines, [11] and sulfenic[12] and selenenic acids. [1] We have therefore been interested in exploring these stereoelectronic effects computationally, across more diverse sets of substrates and different types of secondary orbital donors.

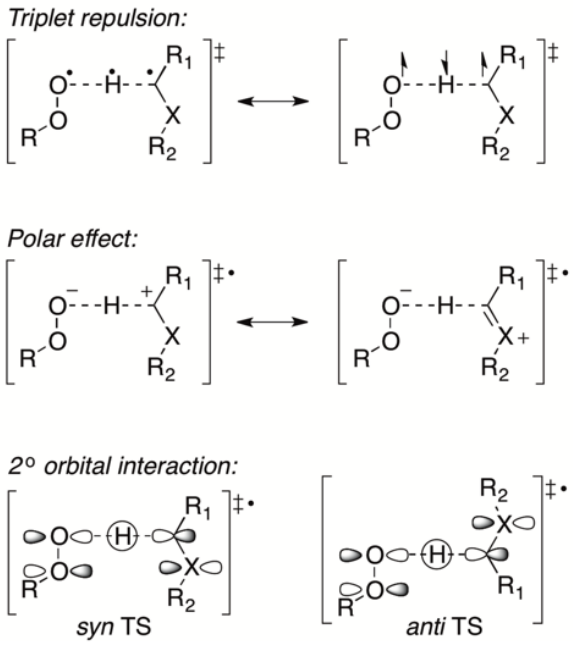

Figure 6.1. Stereoelectronic factors affecting the HAT transition state.

Herein the formal H-atom transfer of a labile H-atom to a peroxyl radical has largely been generalized as "HAT", the mechanism whereby H• is abstracted by a peroxyl radical (*cf.* Figure 6.2, top). However, in reality, a formal H-atom transfer may also occur wherein the proton and electron are transferred separately, by a so-called proton-coupled electron transfer (PCET) mechanism (*cf.* Figure 6.2, bottom). For simplicity in this analysis, we will discuss mechanistic differences between HAT and PCET, though there are other nuanced mechanisms discussed in the more recent literature, such as sequential proton loss electron transfer (SPLET), or electron transfer followed by proton transfer (ET-PT). The nuance between these various mechanisms is subtle and can be difficult to study experimentally.

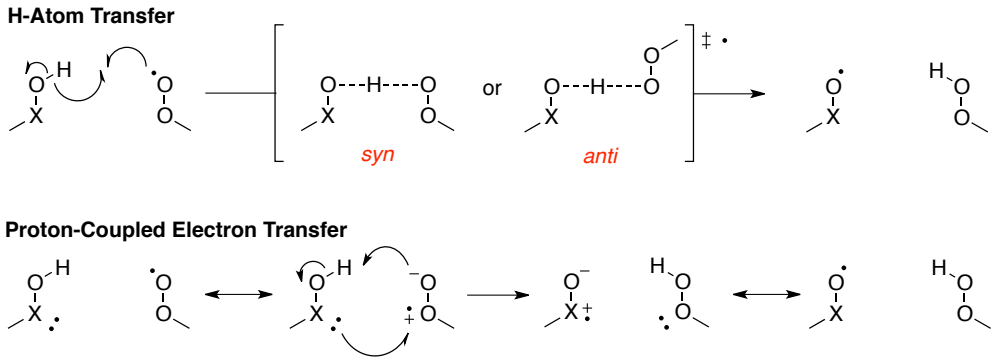

Figure 6.2. HAT vs. PCET in a model system.

As discussed in the introductory chapter (Section 1.2), a formal HAT to a peroxyl radical can theoretically occur with the reactants at any dihedral angle, though when a secondary orbital interaction is accessible, the preferred geometry is a *syn* TS, provided the secondary orbital interaction provides sufficient stabilization to the TS to overcome any destabilization due to steric interactions. For PCET, it may be more beneficial to first consider the molecular orbitals involved rather than the geometry of the reactants. For example, PCET, too, can occur via any dihedral angle;

however, the electron is transferred through a different set of orbitals (orthogonally) as compared to the proton transfer.

A seminal study in this field was conducted by Mayer et al. [13] who compared benzyl/toluene and phenoxyl/phenol self-reactions. They showed that the formal H-atom transfer reaction between a benzyl radical and toluene has a TS structure wherein the 2p-π orbital of the radical approaches the toluene C-H with C_{2h} symmetry (cf. Figure 6.3, left). The main contributors to the singly occupied molecular orbital (SOMO) of the benzyl/toluene TS are in the plane of the H-atom transfer and localized on the two CH_2 groups, with a node at the hydrogen. This is deemed characteristic of a HAT mechanism. On the contrary, the optimal TS for the phenoxyl/phenol self-reaction has nearly planar C_2 geometry (cf. Figure 6.3, right). The main contributors to the SOMO are the σ orbitals of the lone pairs on the two oxygen atoms, between which a *proton* (rather than a hydrogen atom) are exchanged. The electron is transferred separately (orthogonally) from the highest (fully) occupied molecular orbital in this PCET TS. Thus the work by Mayer et al. [13] suggests that the SOMO orbital can be an indicator in delineating HAT and PCET mechanisms, whereby the former involves orbitals lying in the plane of the H-atom transfer, and the latter involves orbitals orthogonal to the plane of H-atom transfer.

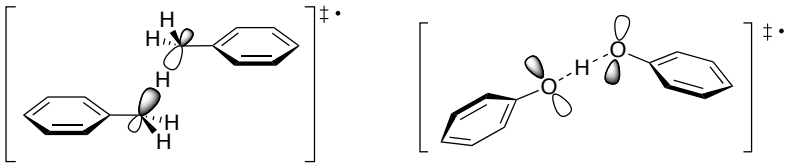

Figure 6.3. An H-atom transfer mechanism operates in the benzyl/toluene self-reaction (left), whereas a proton-coupled electron transfer mechanism operates in the phenoxyl/phenol self-reaction (right). Models of the transition state structures are shown with the major contributing orbitals to the singly occupied molecular orbital, where additional minor contribution from the aromatic rings is omitted for simplicity (see Mayer et al. **[13]** for the associated computational models).

6.3 Results and Discussion

6.3.1 Deviations in Evans-Polanyi Correlations

The correlation presented in Figure 1.2A (Chapter 1) offers an interesting case-study, in that there is a series of H-atom transfers from C-H bonds that do not lie on the same correlation line in the Evans-Polanyi plot. Figure 1.2A was based on experimentally-determined BDEs and HAT rate constants from the literature; however, the computed CBS-QB3 BDEs and HAT rate constants with tunnelling corrections (as outlined in Chapter 4, and in the Computational Methods Section 6.5) correlate well for a series of C-H abstractions from hydrocarbons or C-H bonds α to a heteroatom, as compared to the experimental data, where available (*cf.* Figure 6.4). For the hydrocarbons, the cases where a π-orbital exists α to the C-H bond being abstracted (propene, 1,4-pentadiene, and toluene), the resulting TS geometry is a syn orientation. Likewise, for the abstraction of C-H bonds α to a heteroatom, the cases where the heteroatom is N, S, and O (but not Se), the syn TS geometry is preferred over the anti, suggesting a secondary orbital interaction contributes to the overall stereoelectronics. However, a similar argument can be made for the heteroatom introducing a polar effect. When the Evans-Polanyi plot is overlaid with the corresponding rate constants for abstraction by an alkoxyl radical – which lacks the acceptor for a secondary orbital interaction – tetrahydrofuran, pyrrolidine, and tetrahydrothiophene no longer lie on the same line, suggesting a secondary orbital interaction accelerates their reaction with peroxyl radicals, whereas a polar effect likely effects the reaction of tetrahydroselenophene with peroxyl and alkoxyl radicals alike.

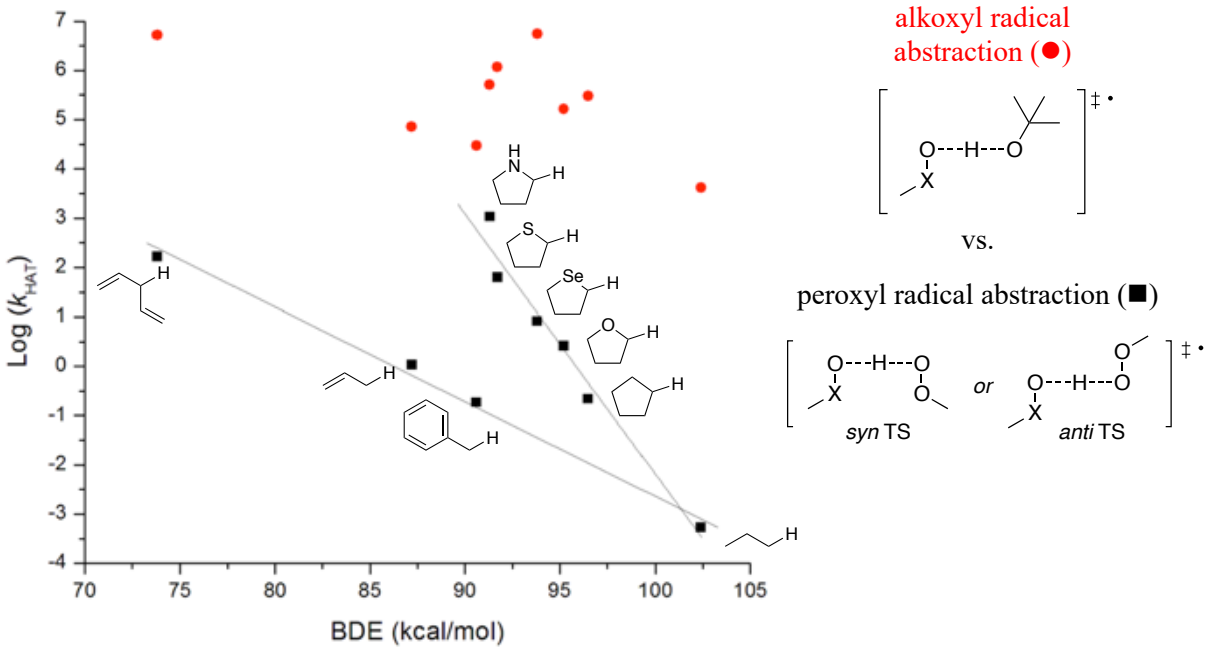

Figure 6.4. Evans-Polanyi correlation of CBS-QB3 computed bond dissociation enthalpies (BDEs) and hydrogen atom transfer (HAT) rate constants (k, M^{-1} s^{-1}) for C-H abstractions by a methylperoxyl radical (■) or t-butoxyl radical (●).

We have sought to determine a metric to quantify the strength of a secondary orbital interaction, and one approach is to consider the free energy difference between the *syn* and *anti* TS geometries. Thus $\Delta\Delta G^{\ddagger}_{(syn\text{-}anti)}$ is a value (in kcal/mol) of how stable the *syn* TS is relative to the *anti* TS, where a negative value suggests a secondary orbital interaction stabilizes the *syn* TS, the strength of which is reflected in the magnitude of the $\Delta\Delta G^{\ddagger}_{(syn\text{-}anti)}$ term. For example, as discussed for the cases outlined in Figure 6.4, when the α heteroatom was N, S, or O (but not Se) the *syn* TS was preferred over the *anti*, and indeed, Table 6.1 shows this is reflected in the associated $\Delta\Delta G^{\ddagger}_{(syn\text{-}anti)}$ values. ROOH dihedral angles are also included for reference, as the significance of this metric will be discussed *vide infra*. For X = Se, a stationary point was located for the *syn* TS geometry, but the

anti-geometry is preferred; whereas for X = C, the *syn*-geometry was evidently so disfavoured, a stationary point could not be located.

Table 6.1. CBS-QB3 computed $\Delta\Delta G^{\ddagger}_{(syn\text{-}anti)}$ and ROOH dihedral angles for H-atom abstraction by a methylperoxyl radical for various substrates having a heteroatom α to the C-H bond being abstracted, and propene for comparison.

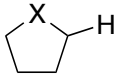	$\Delta\Delta G^{\ddagger}_{(syn\text{-}anti)}$ (kcal/mol)	Me-O-O-H dihedral angle (*syn*)	Me-O-O-H dihedral angle (*anti*)
X = N	-1.2	101°	98°
X = S	-0.20	102°	98°
X = Se	0.27	101°	98°
X = O	-0.24	93°	97°
X = C	--	--	97°
propene	-0.87	99°	98°

6.3.2 HAT vs PCET Mechanisms

The HAT reactions of Figure 6.4 were all C-H abstractions with varying secondary orbital donors. In contrast, Figure 6.5 shows a series of ArX-H abstractions by peroxyl radicals, where X= CH_2, NH, O, S, or Se. PhOH is notoriously erroneous in *ab initio* calculations. [14] For example, in the computed system used herein the PhOH-OOMe barrier was vastly overestimated and the SOMO/HOMO were incorrectly assigned, suggesting an error in the computed electronic structure; therefore, MePhOH (p-cresol) was used instead. As demonstrated in Figure 6.5, H-atom abstraction from toluene involves orbital alignment akin to what Mayer et al. observed for the HAT mechanism: the SOMO orbital is in the plane of the H-atom transfer. On the other hand, H-atom abstraction from p-cresol adopts more PCET character: the SOMO orbital is skewed out-of-plane relative to the H-

atom transfer, though not as drastically as was observed for the phenoxyl/phenol self-reaction. Also indicated in Figure 6.5 is the H-O-O-Me dihedral angle for each transformation, which we consider a good metric for the degree of planarity in the TS, where toluene-OOMe (99°) is closer to the right angle that would be expected for a "true" HAT mechanism, and p-cresol-OOMe (138°) is more opened, consistent with a PCET mechanism. In each case, the HOMO orbital shows a favourable secondary orbital overlap, and the *syn* TS geometry is preferred over an *anti*-configuration. Interestingly, while Mayer et al. observed drastically different TS geometry for the HAT (benzyl/toluene) and PCET (phenoxyl/phenol) reactions, the reaction of toluene and phenol with peroxyl radicals operates with only subtly different TS geometry (based on the H-O-O-Me dihedral). Thus, the orbital analysis suggests toluene reacts with a peroxyl radical by a HAT mechanism and p-cresol reacts with a peroxyl radical by a PCET mechanism, but *both* involve a secondary orbital interaction in the preferred *syn* geometry, which is evident in the HOMO orbitals.

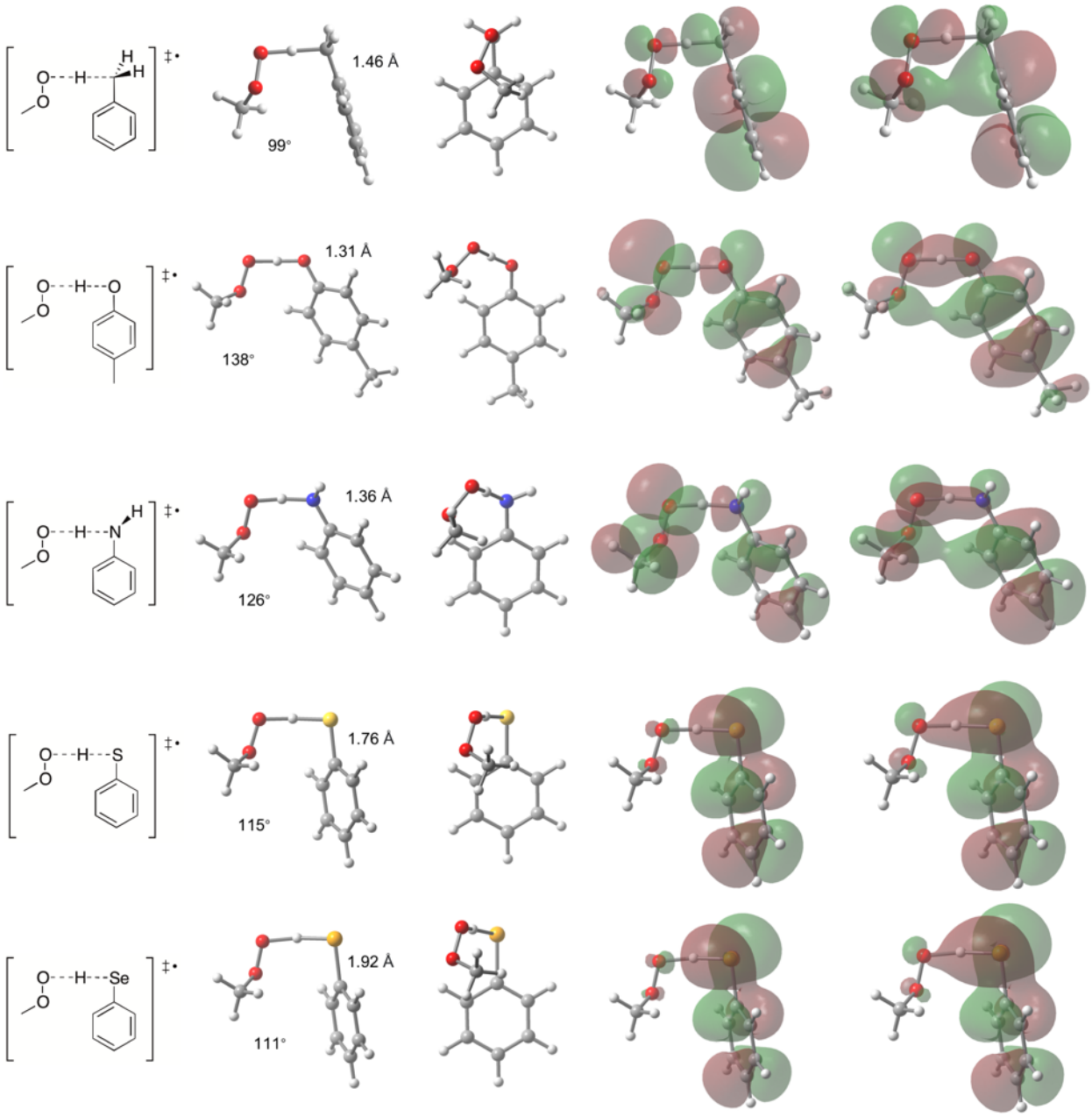

Figure 6.5. CBS-QB3 computed transition state structures for H-atom transfer to a methylperoxyl radical from toluene, p-cresol, aniline, thiophenol, or selenophenol, and the associated singly occupied molecular orbitals (SOMOs) and highest (fully) occupied molecular orbitals (HOMOs), where the orbitals are from the UB3LYP/CBSB7 step of the CBS-QB3 calculation. The Ar-X bond lengths and H-O-O-Me dihedral angles are indicated for each structure.

Expanding to other systems, aniline, thiophenol, and selenophenol (X = N, S, Se) all appear to be "somewhere between" HAT and PCET. That's to say that their H-O-O-Me dihedral angles are 126°, 115°, and 111°, respectively. Thus, it remains unclear to us if an exact boundary can be placed between HAT and PCET mechanisms. Furthermore, one might envision the acidity of the systems being associated with the propensity for PCET, yet the trends in pK_a (*cf.* Table 6.2) do not align with the trends in H-O-O-Me dihedral angles for the HAT/PCET orbital analysis. Thus the orbital/geometrical analysis provided in the SOMO orbitals and H-O-O-Me dihedral angles seems to provide a qualitative picture of HAT vs. PCET mechanisms, yet the trends in Figure 6.5 and Table 6.2 fail to, from our analysis, provide an answer as to *why* one mechanism may operate over the other. Interestingly, for all of the ArX-H systems presented in Figure 6.5, the H-O-O-Me dihedral angles were essentially identical whether in the preferred *syn,* or the higher energy *anti,* TS geometry (± 1° for all cases but X = S, which was 4° greater), suggesting the preference for HAT vs. PCET is unaffected by the secondary orbital interaction. This is consistent with the fact that the electron transfer in a PCET reaction is known to occur in the *syn* or *anti* TS, as long as the orbitals are aligned (e.g. the phenoxyl/phenol case referred to in Figure 6.3). On the other hand, the cases in Table 6.1 all had H-O-O-Me dihedral angles of 97-98° in the *anti* TS geometry, whereas the angles differed (albeit to a less significant extent than the aromatic systems) when in the *syn* TS, where a secondary orbital interaction exists. This is likely due to the fact that the lone pair on the α-heteroatom (or π-system in the case of propene) cannot be delocalized through the C-H bond and onto the abstracting peroxyl, as is the case in the aromatic systems for X-H atom abstractions when the X-atom has a lone pair.

It is also worth pointing out that, as the Ar-X bond lengthens (as indicated in Figure 6.5), the secondary orbital overlap appears to decrease in the HOMO orbitals for thiophenol-OOMe and selenophenol-OOMe, though the interaction is still strong enough to favour the *syn* TS geometry over the *anti*. Indeed, the $\Delta\Delta G^{\ddagger}_{(syn\text{-}anti)}$ for these reactions are all negative, as outlined in Table 6.2; however, the absolute values of these terms are difficult to correlate to any trend. The *syn* TS is

significantly more favourable than the *anti* TS for p-cresol as compared to the other systems ($\Delta\Delta G^{\ddagger}_{(syn\text{-}anti)}$ = -4.2). Initially, one might assume this could be due the p-methyl group (introduced for computational feasibility) increasing the energy of the secondary orbital donor (i.e. the ArX-H HOMO); however Table 6.2 demonstrates that this is not the case. Thus, our best guess is that the geometrical alignment of the orbitals may be the determining factor, though this is a tough metric to quantify. For example, the Ar-X bond is shortest in p-cresol, which may facilitate a better overlap between the internal peroxyl oxygen atom and the aromatic ring's π-system. However, this trend does not continue when comparing X = NH, S, and Se, where thiophenol evidently benefits from a greater secondary orbital interaction than aniline. Indeed, in thiophenol the H-O-O-Me dihedral angle is smaller than in aniline (indicating more HAT than PCET character for the former, as compared to the latter), which may also mean the former has a more beneficial geometry for the secondary orbital overlap than the latter (which also has a *slightly* lower secondary orbital donor HOMO energy). From our perspective, this analysis underscores the difficulty in truly *quantifying* secondary orbital interactions, as one metric is often contradicted by at least two others.

Table 6.2. CBS-QB3 computed $\Delta\Delta G^{\ddagger}_{(syn\text{-}anti)}$ and secondary orbital energy for the ArX-H HOMO for various ArX-H substrates, as well as their corresponding literature pK_a values.

ArX-H	$\Delta\Delta G^{\ddagger}_{(syn\text{-}anti)}$ (kcal/mol)	2° orbital energy (A.U.)	pK_a
toluene	-1.2	-0.32	41
p-cresol	-4.2	-0.31	10.3
aniline	-1.0	-0.29	30.6
thiophenol	-1.9	-0.31	6.6
selenophenol	-1.1	-0.31	5.9

Figure 1.2 and Figure 6.4, and the associated analyses in Section 1.2 and *vide supra* showed that secondary orbital interactions may provide a better explanation than triplet repulsion for deviations in linearity in the Evans-Polanyi correlations in certain systems. However, the Evans-Polanyi correlation for the ArX-H systems is shown in Figure 6.6, in which toluene falls well below the line the other systems lie on. Unlike the correlation in Figure 6.4, the deviation in linearity for toluene is rather best explained through triplet repulsion. Thus, not only are secondary orbital interactions difficult to quantify due to the various contradicting geometrical and stereoelectronic effects, the presence or absence of a secondary orbital interaction is, evidently, *not always* the best explanation for deviations in linearity in Evans-Polanyi correlations: the case of tetrahydroselenophene in Figure 6.4 was best explained through polar effects, and the case of toluene in Figure 6.6 was best explained by triplet repulsion. Thus, a thorough analysis of each of the various factors may be necessary to fully understand trends in reactivity in H-atom abstractions by peroxyl radicals. It is also worth noting that the effect of secondary orbital interactions may be better quantified using dispersion corrections[15] in the computed transition states, which may be worthy of investigation in future works.

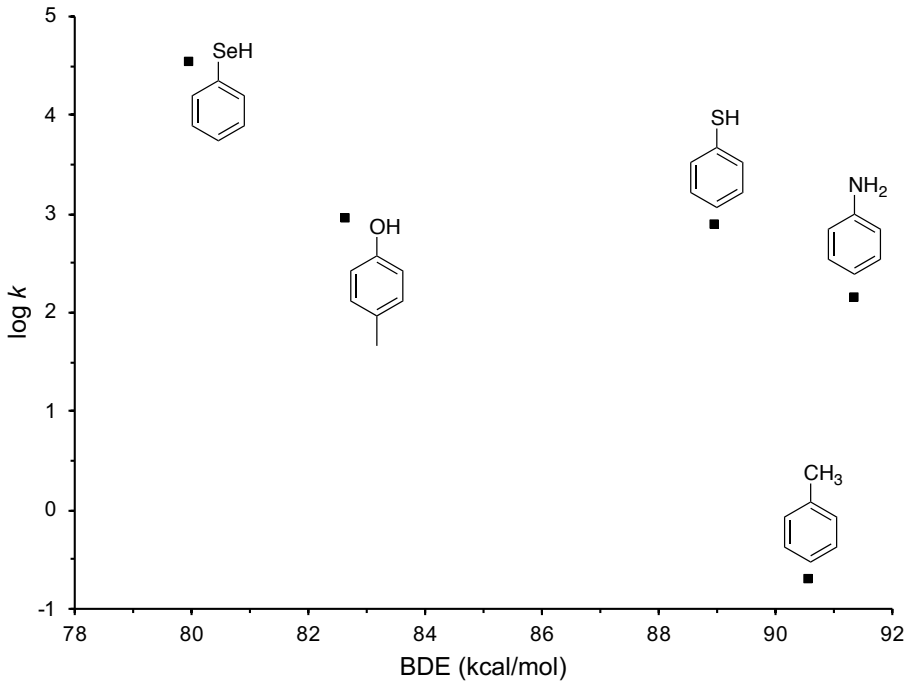

Figure 6.6. Evans-Polanyi correlation of CBS-QB3 computed bond dissociation enthalpies (BDEs) and tunnelling-corrected hydrogen atom transfer (HAT) rate constants (k, M^{-1} s^{-1}) for ArX-H abstractions by a methylperoxyl radical for the indicated compounds.

To further underscore the above-discussed geometrical and orbital analyses in relation to HAT vs. PCET mechanisms, Figure 6.7 shows that similar trends exist when comparing propene to vinyl alcohol. Like toluene, the SOMO and HOMO orbitals, as well as H-O-O-Me dihedral angle in the propene-OOMe H-atom abstraction TS are indicative of a HAT mechanism. In contrast, the analysis of vinyl alcohol, like ArOH, is indicative of a PCET mechanism. Furthermore, vinyl alcohol is vastly accelerated in *syn* geometry as compared to *anti*, having a $\Delta\Delta G^{\ddagger}_{\text{(syn-anti)}}$ of -7.6 kcal/mol (compared to -0.87 kcal/mol in propene), which is an absolute value greater than any of the systems shown to this point in the present chapter. However, in the previous chapter (Chapter 5) we illustrated a system with an even more significant secondary orbital interaction, which deserves to be revisited.

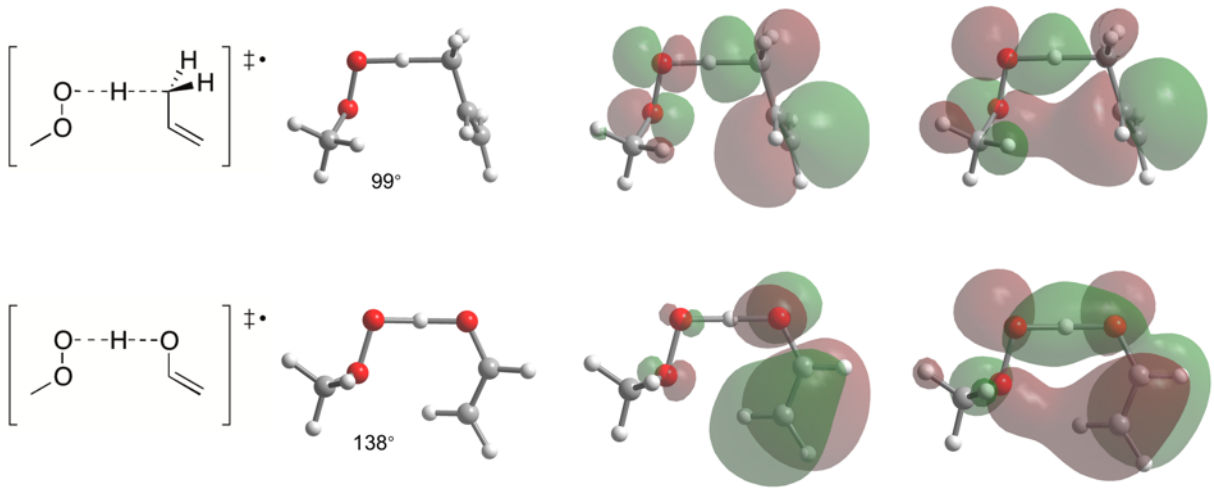

Figure 6.7. CBS-QB3 computed transition state structures for H-atom transfer to a methylperoxyl radical from propene or vinyl alcohol, and the associated singly occupied molecular orbitals (SOMOs) and highest (fully) occupied molecular orbitals (HOMOs), where the orbitals are from the UB3LYP/CBSB7 step of the CBS-QB3 calculation. The H-O-O-Me dihedral angles are indicated for each structure.

6.3.3 A Study in Chalcogens

As was demonstrated in Chapter 5, our study of the redox chemistry of 9-triptyceneselenenic acid (RSeOH) was the best experimental evidence to date for the influence of secondary orbital interactions in H-atom abstractions by peroxyl radicals, as its HAT rate constant was only 18-fold smaller than that in the corresponding 9-triptycenesulfenic acid (RSO-H), despite its O-H BDE being 9 kcal stronger. Furthermore, the calculations therein predicted an unhindered selenenic acid would be even more reactive to HAT with a peroxyl radical than the sulfenic acid analogue, due to said interaction. Indeed the $\Delta\Delta G^{\ddagger}_{(\text{syn-anti})}$ for *t*-BuSeOH is computed to be far greater than any other system studied herein, with a value of -12 kcal/mol. Thus we revisit these systems here in the context of the above computational analysis, and expand the comparison to include the structurally-related hydroperoxides (ROOH) and hydropersulfides (RSSH).

The $\Delta\Delta G^{\ddagger}_{(syn\text{-}anti)}$ for each system is overlaid on the Evans-Polanyi correlation presented in Figure 6.8, for which *t*-BuSeOH, unsurprisingly, has a significantly greater absolute value than the others. Correspondingly, its (formal) H-atom transfer rate constant is significantly accelerated compared to the others, which essentially lie on one line (albeit a only a three-point line).

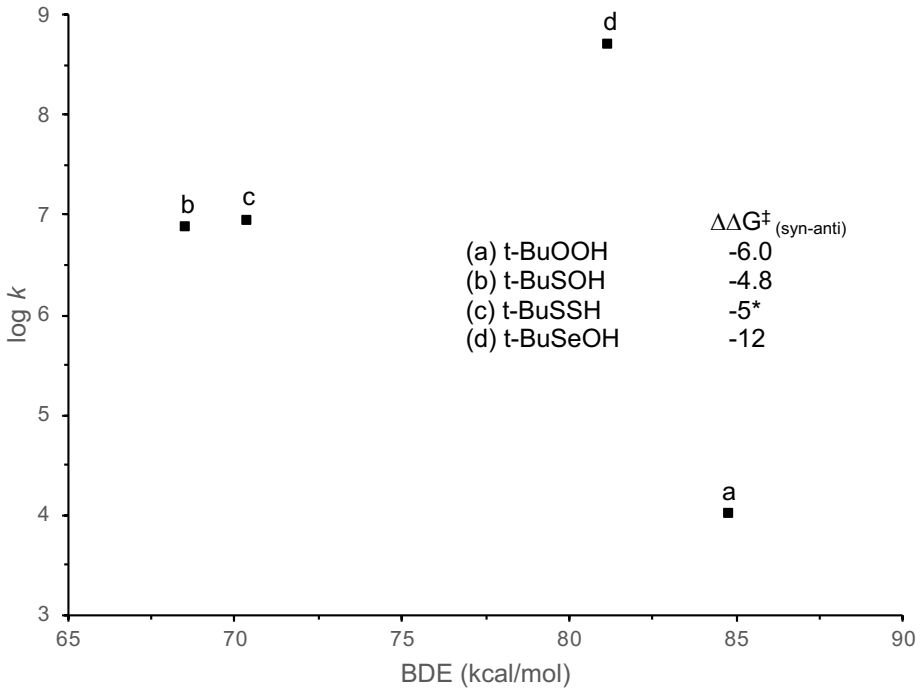

Figure 6.8. Evans-Polanyi correlation of CBS-QB3 computed bond dissociation enthalpies (BDEs) and hydrogen atom transfer (HAT) rate constants (k, M^{-1} s^{-1}) for H-atom abstractions by a methylperoxyl radical for *t*-BuSOH, *t*-BuSSH*, *t*-BuSeOH, and *t*-BuOOH.

Figure 6.9 shows the CBS-QB3 computed TS structures for H-atom abstraction by a methylperoxyl radical for *t*-BuOOH, *t*-BuSOH, *t*-BuSeOH, and *t*-BuSSH. As compared to the ArX-H cases studied in Figure 6.5, the orbital analysis and geometries suggest these cases have more HAT character, with *t*-BuSOH and *t*-BuSeOH perhaps showing slight PCET character, based on the H-O-

* We were unable to locate a stationary point for the *anti* TS geometry in *t*-BuSSH; therefore this value is an estimation based on a calculation where the geometry about the O-O/S-S dihedral angle was restricted.

O-Me dihedral angles. Interestingly, unlike the ArX-H systems above, the chalcogen series each showed more PCET character in the *anti* TS relative to the preferred *syn* TS, in that the H-O-O-Me dihedral angles were 118°, 123°, 117°, and 106° for *t*-BuOOH, *t*-BuSOH, *t*-BuSeOH, and *t*-BuSSH[*], respectively, in the *anti*-geometry. We had previously calculated the H-atom abstraction barrier's dependence on the X-O/O-O dihedral angle (i.e. at various points between the *syn* and *anti* TS geometries) for *t*-BuSOH and *t*-BuSeOH. We include here the analogous plots for *t*-BuOOH and *t*-BuSSH, and include the H-O-O-Me dihedral angles as our proposed metric for HAT vs. PCET mechanisms in Figure 6.10. In all cases, the TS structures have the most PCET character when in the *syn* and *anti* geometries, and more HAT character when the TS geometry is somewhere therebetween (i.e. *ca*. 35-90°). Interestingly, this appears to have no effect on the reaction barrier, which is more closely associated with the strength of the secondary orbital interaction. This further underscores the fact that there are several different geometrical considerations, stereoelectronic effects, and orbital analyses required to fully understand the reactivity of these formal HAT reactions. When it comes to delineating the HAT mechanism from the PCET mechanism, it appears the assignment is non-binary; indeed, there is a significant "grey area" lying between the two. What's more is that, whether the electron and proton are transferred together (HAT) or orthogonally (PCET), it appears to have a negligible effect on the barrier to the transformation.

[*] We were unable to locate a stationary point for the *anti* TS geometry in *t*-BuSSH; therefore this value is an estimation based on a calculation where the geometry about the O-O/S-S dihedral angle was restricted.

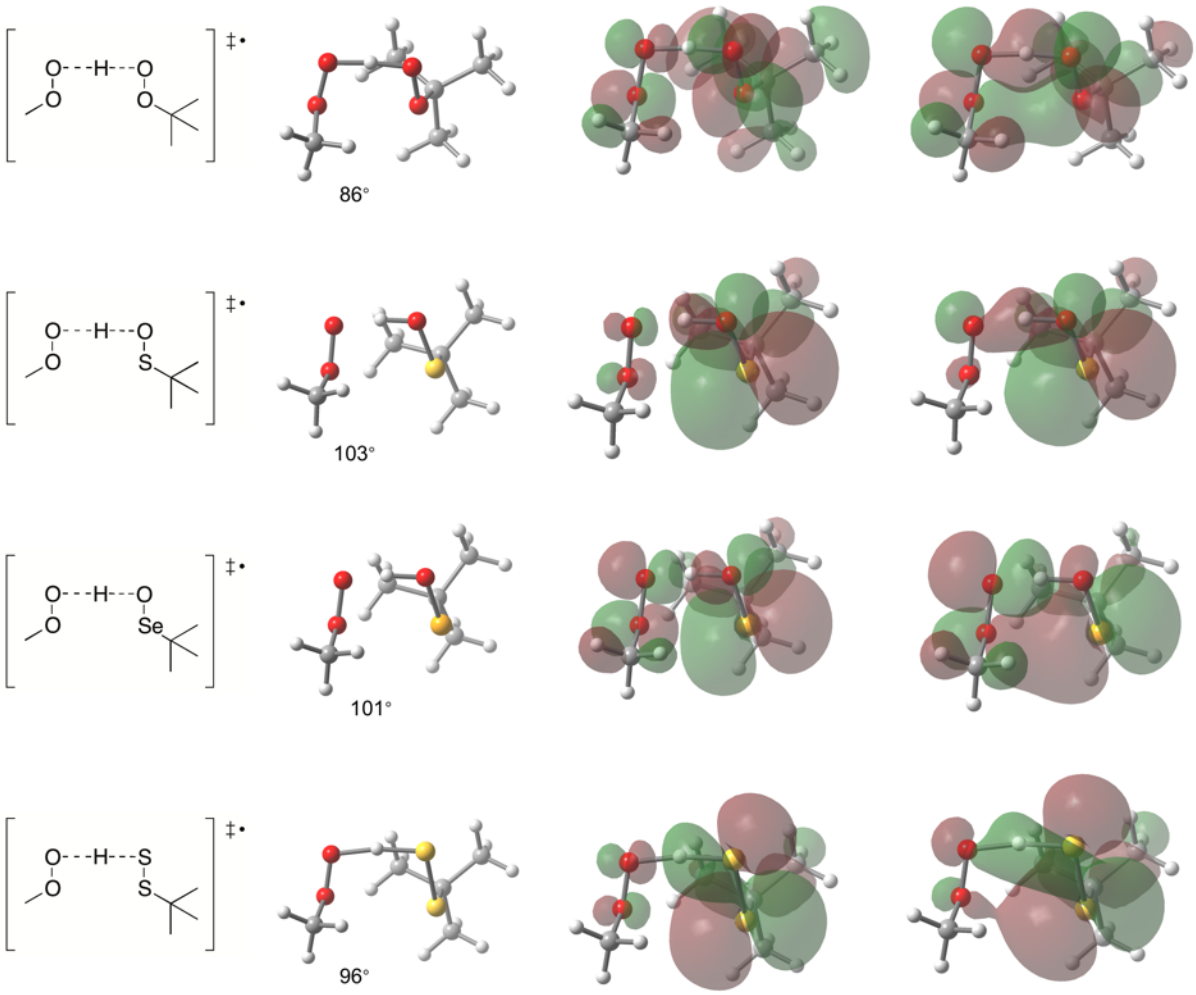

Figure 6.9. CBS-QB3 computed transition state structures for H-atom transfer to a methylperoxyl radical from *t*-BuOOH, *t*-BuSOH, *t*-BuSeOH, and *t*-BuSSH, and the associated singly occupied molecular orbitals (SOMOs) and highest (fully) occupied molecular orbitals (HOMOs), where the orbitals are from the UB3LYP/CBSB7 step of the CBS-QB3 calculation. The H-O-O-Me dihedral angles are indicated for each structure.

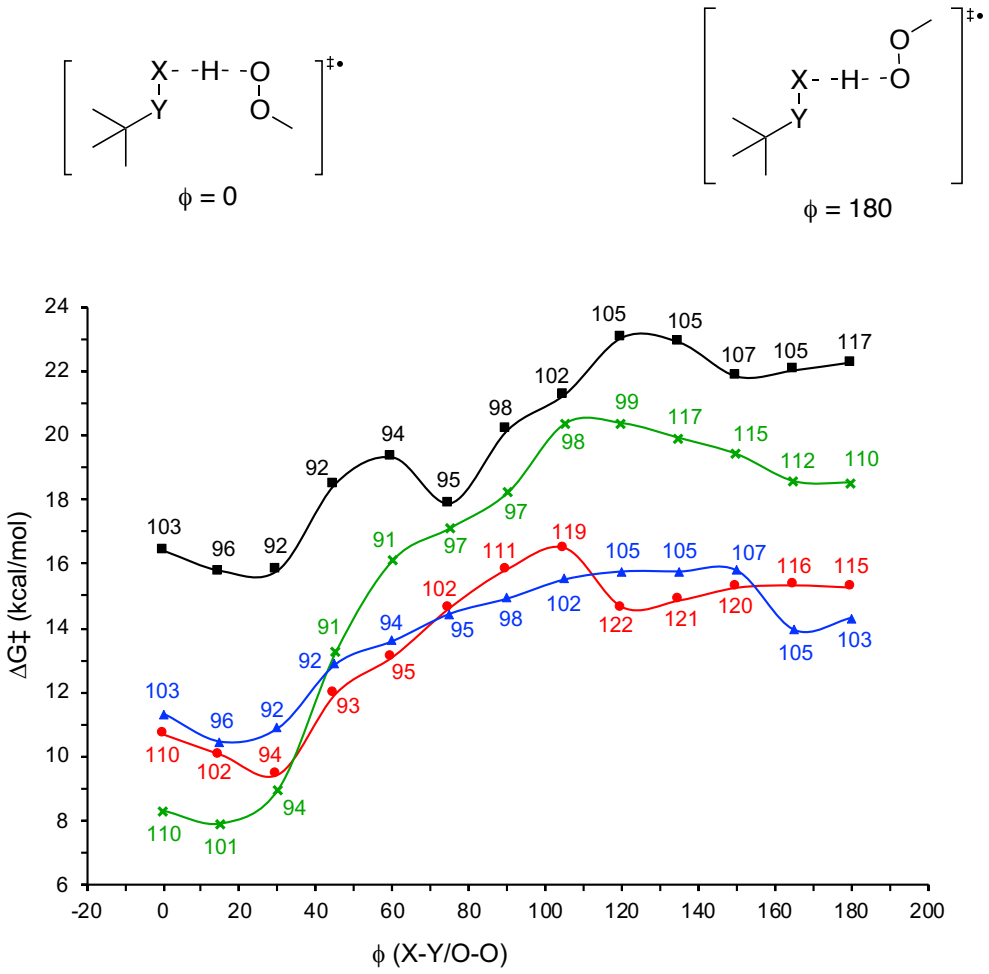

Figure 6.10. Dependence of the CBS-QB3-calculated $\Delta G^{\ddagger}$ values for the reactions of *t*-BuOOH (black ■), *t*-BuSOH (red ●), *t*-BuSSH (blue ▲), and *t*-BuSeOH (green ×) with MeOO• on the O-O/O-O, S-O/O-O, S-S/O-O, and Se-O/O-O torsion angles in the transition state structures, respectively. The points are labeled with the H-O-O-Me dihedral angle of the peroxyl radical in the corresponding structures.

6.3.4 Can the Effect of Secondary Orbital Interactions be Predicted?

While the H-atom abstraction by a peroxyl radical for each discrete set of substrates studied herein offered some clues to the trends in reactivity, kinetics, and mechanisms, the overall message appears to be that these types of systems are extremely difficult to quantify and predict. Indeed, our initial goal was to attempt to explain larger data sets, which resulted in the poor correlation shown in Figure 6.11. It appears a closer look at a number of different metrics (geometry, donor orbital energy, PCET

vs. HAT mechanism, polar effects, triplet repulsion, and perhaps others we have not even considered, such as the effect of early vs. late TS) is required when comparing the (formal) H-atom transfer reactivity of a particular substrate with peroxyl radicals.

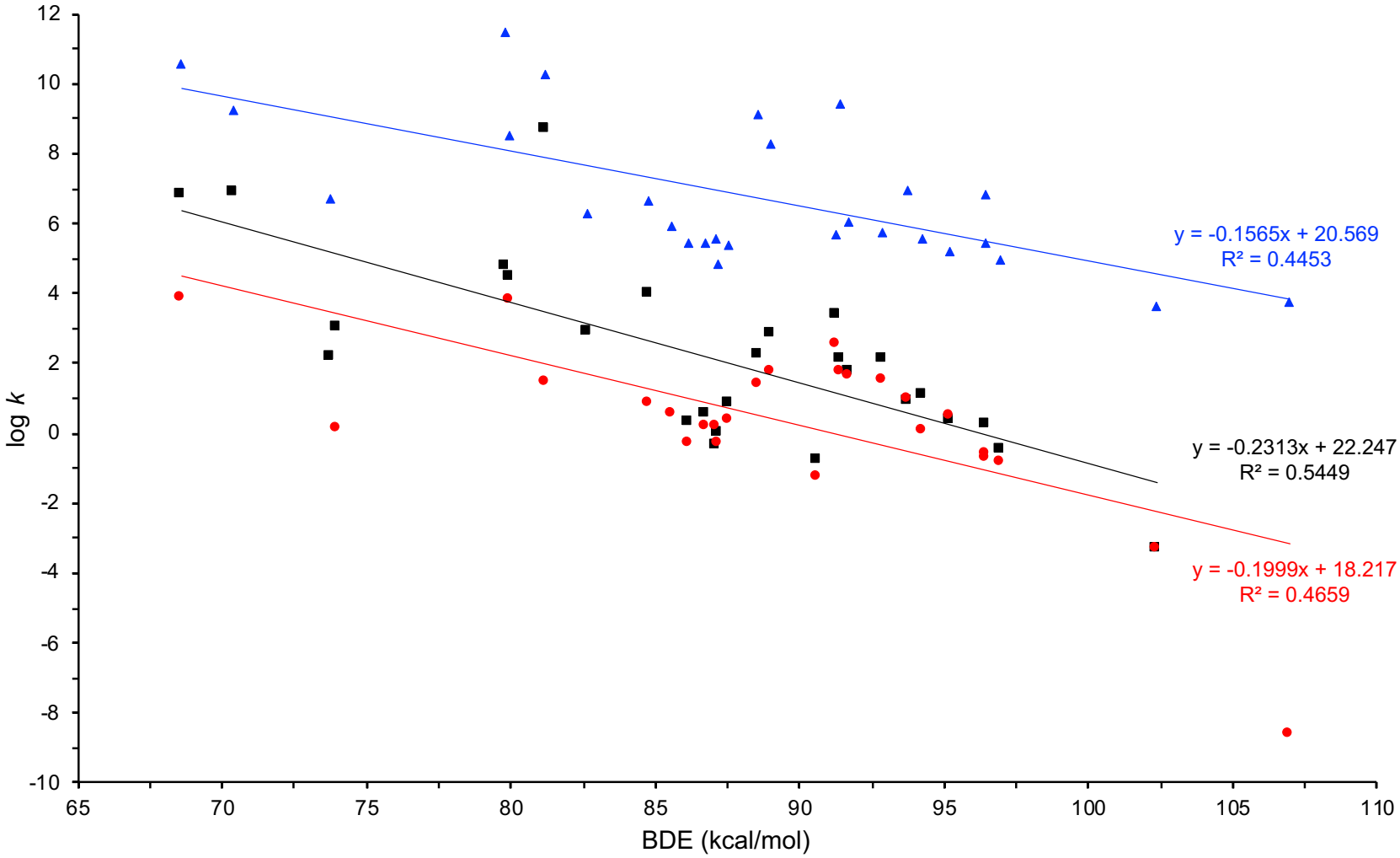

Figure 6.11. Evans-Polanyi plot for abstraction by MeOO• in the syn-geometry (black ■) or anti-geometry (red ●), or abstraction by *t*-BuO• (blue ▲), for various substrates studied, as outlined in Table 6.3.

Table 6.3. List of compounds, and their respective bond dissociation enthalpies (BDEs), from Figure 6.11.

Compound	BDE (kcal/mol)
t-BuSOH	68.6
t-BuSSH	70.4
1,4-pentadiene	73.8
N,N-dimethylhydroxylamine	74.0
divinylamine	79.8
selenophenol	80.0
t-BuSeOH	81.2
p-cresol	82.7
t-BuOOH	84.8
2-methylbut-2-ene (C4-H)	85.6
cis-butene	86.2
trans-butene	86.8
phenol	87.1
propene	87.2
2-methylbut-2-ene (C1-H)	87.6
vinyl amine	88.6
thiophenol	89.0
toluene	90.6
pyrrolidine	91.3
aniline	91.4
tetrahydrothiophene	91.7
dimethylamine	92.9
tetrahydrofuran	93.8
dimethylsulfane	94.3
tetrahydroselenophene	95.2
cyclopentane	96.5
dimethylselane	96.5
dimethylether	97.0
propane	102.4
t-BuOH	107.0

6.4 Conclusions and Perspective

The computational results presented herein underscore the complexity of the stereoelectronic effects present in the TS of H-atom abstractions by peroxyl radicals – the key step in both the propagation, and inhibition of autoxidation. Secondary orbital interactions have been used to explain some anomalous trends in HAT reactivity, such as the comparison between RSOH and RSeOH presented in Chapter 5, and the related recent report of the drastic effect oxidation of the RSOH sulfur to RSO_2H has on its HAT reactivity with peroxyl radicals – reducing it by 7 orders of magnitude. [16] While we were unable to determine a single metric to explain deviations in linearity in Evans-Polanyi relationships across diverse types of compounds (cf. Figure 6.11), we were able to examine several subsets of compounds to assess the factors influencing their HAT reactivity. The examples presented herein demonstrate that while secondary orbital interactions can lead to a preference for the *syn* TS geometry, they alone cannot account for trends in reactivity. Certain outliers to Evans-Polanyi correlations are better explained by invoking triplet-repulsion and/or polar effects. Furthermore, we have demonstrated that an analysis of the TS geometry and molecular orbitals can have some insight into the mechanism of the formal HAT, though it is difficult to outright delineate between HAT and PCET. While the results herein hardly offer a quantitative or predictive model for the influence of any given stereoelectronic effect on the H-atom transfer ability of a give substrate, we believe such computational modelling remains a powerful tool in helping to understand and explain seemingly anomalous experimental results (as has been done throughout this Thesis).

6.5 Computational Methods

All calculations were carried out using the Gaussian 09 quantum chemistry package[17] using the CBS-QB3 complete basis set approach.[18] The Skodje-Truhlar small-curvature tunnelling approximation[19] was used to estimate the transmission coefficient, as outlined in Eqs 4.8-4.11. Hindered internal rotor

corrections have been found to be negligible for H-atom abstraction at these temperatures, and were thus ignored.[20]

6.6 References

(1) Zielinski, Z.; Presseau, N.; Amorati, R.; Valgimigli, L.; Pratt, D. A. *J. Am. Chem. Soc.* **2014**, *136*, 1570.

(2) Zavitsas, A. A. *J. Am. Chem. Soc.* **1972**, *94*, 2779.

(3) Zavitsas, A. A.; Chatgilialoglu, C. *J. Am. Chem. Soc.* **1995**, *117*, 10645.

(4) Beckwith, A. L. J. *Chem. Soc. Rev.* **1993**, *22*, 143.

(5) Giese, B. *Angew. Chem. Int. Ed. 22*, 753.

(6) Kaushal, P.; Mok, P. L. H.; Roberts, B. P. *J. Chem. Soc., Perkin Trans. 2* **1990**, 1663.

(7) Isborn, C.; Hrovat, D. A.; Borden, W. T.; Mayer, J. M.; Carpenter, B. K. *J. Am. Chem. Soc.* **2005**, *127*, 5794.

(8) Hu, D.; Pratt, D. A. *Chem. Commun.* **2010**, *46*, 3711.

(9) Hanthorn, J. J.; Valgimigli, L.; Pratt, D. A. *J. Am. Chem. Soc.* **2012**, *134*, 8306.

(10) DiLabio, G. A.; Johnson, E. R. *J. Am. Chem. Soc.* **2007**, *129*, 6199.

(11) Amorati, R.; Pedulli, G. F.; Pratt, D. A.; Valgimigli, L. *Chem. Commun.* **2010**, *46*, 5139.

(12) Vaidya, V.; Ingold, K. U.; Pratt, D. A. *Angew. Chem. Int. Ed.* **2008**, *48*, 157.

(13) Mayer, J. M.; Hrovat, D. A.; Thomas, J. L.; Borden, W. T. *J. Am. Chem. Soc.* **2002**, *124*, 11142.

(14) Tishchenko, O.; Truhlar, D. G. *J. Phys. Chem. Lett.* **2012**, *3*, 2834.

(15) Torres, E.; DiLabio, G. A. *J. Phys. Chem. Lett.* **2012**, *3*, 1738.

(16) Griesser, M.; Chauvin, J.-P. R.; Pratt, D. A. *Chem. Sci.* **2018**, *9*, 7218.

(17) Frisch, M. J. *et. al. Gaussian 09, revision B.01*; Gaussian, Inc.: Wallingford CT, 2009.

(18) Montgomery, J. A.; Ochterski, J. W.; Petersson, G. A. *J. Chem. Phys.* **1994**, *101*, 5900.

(19) Skodje, R. T.; Truhlar, D. G.; Garrett, B. C. *J. Phys. Chem.* **2002**, *85*, 3019.

(20) Vandeputte, A. G.; Sabbe, M. K.; Reyniers, M.-F.; Van Speybroeck, V.; Waroquier, M.; Marin, G. B. *J. Phys. Chem. A* **2007**, *111*, 11771.

Chapter 7: Summary and Perspective

The work presented herein underscores that complexity of the radical reactions involved in autoxidation can make them challenging to study from a kinetic and mechanistic perspective.[1] Indeed, the mechanism of cholesterol autoxidation, which was believed to be well understood decades ago, has been shown to be far more complex than previously appreciated. Furthermore, complex quantum mechanical and stereoelectronic effects need to be invoked in order to fully understand the experimental phenomena among the H-atom transfer reactions key to both the propagation and inhibition of autoxidation. This work has demonstrated that a thorough mechanistic study in this area can benefit from a combination of experimental techniques and computational analysis.

The revisitation of cholesterol autoxidation was initially prompted by the suggestion that the presence of the secosterol ozonolysis products of cholesterol in atherosclerotic heart tissue was due to an endogenous mechanism of ozone production.[2] The demonstration that these compounds could also form from the (acid catalyzed) Hock fragmentation of cholesterol 5-hydroperoxide from our group,[3] offered an alternative mechanism of secosterol formation through cholesterol oxidation by singlet oxygen. We have since shown[4] that, not only can cholesterol 5-hydroperoxide be produced in the autoxidation of cholesterol in the presence of an H-atom donor, but cholesterol 4- and 6-hydroperoxide are also detected in cholesterol autoxidation in the presence or absence of H-atom donor. While cholesterol 4- and 6-hydroperoxides are minor autoxidation products, as compared to cholesterol 7-hydroperoxide, they have heretofore been overlooked. In Chapter 2, we demonstrated that Hock fragmentation of cholesterol 6-hydroperoxide yields the same secosterol products that have been linked to cardiovascular disease,[5] cancer,[6] and neurodegeneration (including Alzheimer's,[7] Parkinson's[8] and multiple sclerosis[9]), though previously attributed to endogenous ozone. Thus, our work not only provided a more reasonable route to these secosterols, invoking molecular oxygen rather than high-energy oxidants ($^1O_2$ or O_3), but it also provided a link between autoxidation and degenerative disease, akin to the well-studied[10-12] link between polyunsaturated fatty acid autoxidation

and Hock fragmentation to yield pathogenic compounds like 4-hydroxynonenal. The significance of the differing physical properties (e.g. solubility) of such electrophilic species remains to be appreciated, as it is likely any selectivity in targeting cellular nucleophiles could lead to differing pathological effects.

Our study on cholesterol autoxidation was greatly facilitated by the synthesis of the novel 17,20,21,21,21,22-d_6-cholesterol to be used as a standard in HPLC-APCI$^+$-MS/MS analysis, as outlined in Chapter 3.[13] Therein, we studied the interplay between two mechanistic pathways possible for cholesterol and a peroxyl radical: abstraction of cholesterol's C4-H or C7-H by the peroxyl to yield hydroperoxide products; or peroxyl radical addition to the C5=C6 unsaturation in cholesterol to yield epoxide products. While both pathways operate in cholesterol autoxidations under any of the studied conditions, the preference for the former is due to the influence of quantum mechanical tunnelling, as evidenced by a kinetic isotope effect (k_H/k_D) of 20 on the H-atom abstraction. The variability in product distributions based on the addition of H-atom donor, or by the surprising substituent effect when cholesterol is esterified, underscores that caution should be taken when using certain oxysterol products, or ratios thereof, as biomarkers. What remains to be explored in this area is the significance of the various oxysterols in the pathogenesis of disease. Indeed, the aforementioned pathogenic potential of the secosterols derived from cholesterol ozonolysis, or the Hock fragmentation of cholesterol 5- or 6-hydroperoxide, is so well understood simply because Wentworth and coworkers[2] went looking for them to support their mechanistic proposal. It is therefore possible that analogous compounds derived from cholesterol 4- or 7-hydroperoxide could be similarly significant in the link between cholesterol autoxidation and degenerative disease. Indeed, our group has already demonstrated that unique secosterols with similar chromatographic and spectroscopic properties as the cholesterol ozonolysis products are derived from Hock fragmentation of cholesterol 7-hydroperoxide.[14] An analogous study on cholesterol 4-hydroperoxide is warranted, though complicated due to the difficulty in synthesizing this regioisomer cleanly.

In Chapter 4, we further explored the interplay between the H-atom abstraction and peroxyl radical addition pathways, and the significance of tunnelling on the former. We demonstrated the ability to predict the significance of tunnelling computationally, and suggest that the handful of reports of tunnelling in C-H abstractions by peroxyl radicals are likely the rule and not the exception when it comes to large deuterium kinetic isotope effects. We demonstrated that, analogous to cholesterol, the H-atom abstraction in an oleate model is accelerated due to tunnelling experimentally, though peroxyl radical addition still occurs to a minor extent. The latter result was surprising, given that, to our knowledge, oleate-derived epoxides have never been identified as autoxidation products, though this could be an artifact of the analytical techniques used in previous studies. [15] Based on an analogous computational modelling of a vinyl ether, we suggest that both H-atom abstraction and peroxyl radical addition pathways should also operate in the autoxidation of plasmalogen lipids, wherein the epoxide products of the latter pathway may be more prevalent. Future work exploring the autoxidation of such compounds is warranted, to determine if the interplay between these two pathways could be related to the perplexing biochemistry associated with this class of lipids.

Chapter 5 moved from studying the kinetics and mechanisms of lipid autoxidation to the study of much more reactive H-atom donors. The redox chemistry of selenenic acids was explored for the first time using the persistent 9-triptyceneselenenic acid (TrpSeOH),[16] as had been recently done for the analogous 9-triptycenesulfenic acid (TrpSOH).[17] The O-H bond dissociation enthalpy of the former was determined to be 80.9 ± 0.8 kcal/mol, as compared to 71.9 ± 0.3 kcal/mol in the latter, due to a longer chalcogen-oxygen bond in the former, resulting in less delocalization of the unpaired spin in the resulting radical. Surprisingly though, H-atom transfer to a peroxyl radical from TrpSeOH was only 18-fold slower than TrpSOH in PhCl (1.7×10^5 and 3.0×10^6 M^{-1} s^{-1}, respectively), which was unexpected based on the ca. 9 kcal/mol difference in their bond strengths. The experimental results were supported by computational modelling, which further predicted than an unhindered selenenic acid would be *even more reactive* than the corresponding sulfenic acid. This was due to the

significant effect of a secondary orbital interaction between the selenium atom and the internal peroxyl oxygen, suggesting that unhindered selenenic acids are likely among the most reactive H-atom donors to peroxyl radicals. Unfortunately the study of such compounds directly is complicated by their propensity to self-condense, disproportionate and/or oxidize.

The effect of secondary orbital interactions was further explored computationally in Chapter 6, where their effects were studied among a broader class of compounds. While several trends in Evans-Polanyi correlations were explained in analyzing the effects of secondary orbital interactions, certain cases were better explained by invoking other stereoelectronic effects like triplet-repulsion or polar effects. Interestingly, a geometrical analysis of (formal) H-atom transfer transition states offered some insight into the delineation between HAT and PCET mechanisms: in the case of ArX-H bonds, the mechanism was seemingly independent of the TS geometry, whereas the chalcogen series (ROOH, RSOH, RSSH, and RSeOH) showed some variability between HAT or PCET that was dependent upon the TS geometry. These results underscored that it is challenging to use any single metric to quantify or predict H-atom transfer reactivity, but the influence of secondary orbital interactions can have a huge impact on the kinetics and mechanism of these reactions.

Taken together, these results offer a thorough analysis of the factors influencing H-atom transfer reactions to peroxyl radicals, and the alternative pathway by which they add to unsaturated substrates. These reactions are ubiquitous, and are the key step in the autoxidation process that degrades virtually all petroleum products, and in many ways degrades us humans as well. These reactions are also key to the performance of the antioxidants that slow the autoxidation process, whether they be natural enzymes, the vitamins or nutrients found in healthy foods, or the chemical additives found in everything from plastics to engine oil. This alone, notwithstanding the fact that we have brought into question several widely-accepted theories herein, proves that this will be an interesting area of research for some time to come.

7.1 References

(1) Zielinski, Z. A. M.; Pratt, D. A. *J. Org. Chem.* **2017**, *82*, 2817.

(2) Wentworth, P.; Nieva, J.; Takeuchi, C.; Galvé, R.; wentworth, A. D.; Dilley, R. B.; DeLaria, G. A.; Saven, A.; Babior, B. M.; Janda, K. D.; Eschenmooser, A.; Lerner, R. A. *Science* **2003**, *302*, 1053.

(3) Brinkhorst, J.; Nara, S. J.; Pratt, D. A. *J. Am. Chem. Soc.* **2008**, *130*, 12224.

(4) Zielinski, Z. A. M.; Pratt, D. A. *J. Am. Chem. Soc.* **2016**, *138*, 6932.

(5) Takeuchi, C.; Galvé, R.; Nieva, J.; Witter, D. P.; wentworth, A. D.; Troseth, R. P.; Lerner, R. A.; Wentworth, P. *Biochemistry* **2006**, *45*, 7162.

(6) Nieva, J.; Song, B.-D.; Rogel, J. K.; Kujawara, D.; Altobel, L., III; Izharrudin, A.; Boldt, G. E.; Grover, R. K.; wentworth, A. D.; Wentworth, P., Jr. *Chem. Biol.* **2011**, *18*, 920.

(7) Usui, K.; Hulleman, J. D.; Paulsson, J. F.; Siegel, S. J.; Powers, E. T.; Kelly, J. W. *Proc. Natl. Acad. Sci. USA* **2009**, *106*, 18563.

(8) Bosco, D. A.; Fowler, D. M.; Zhang, Q. H.; Nieva, J.; Powers, E. T.; Wentworth, P.; Lerner, R. A.; Kelly, J. W. *Nat. Chem. Biol.* **2006**, *2*, 249.

(9) Cygan, N. K.; Scheinost, J. C.; Butters, T. D.; Wentworth, P., Jr. *Biochemistry* **2011**, *50*, 2092.

(10) Esterbauer, H.; Schaur, R. J.; Zollner, H. *Free Radic. Biol. Med.* **1991**, *11*, 81.

(11) Ullery, J. C.; Marnett, L. J. *Biochim. Biophys. Acta, Biomembr.* **2012**, *1818*, 2424.

(12) Codreanu, S. G.; Ullery, J. C.; Zhu, J.; Tallman, K. A.; Beavers, W. N.; Porter, N. A.; Marnett, L. J.; Zhang, B.; Liebler, D. C. *Mol. Cell. Proteomics* **2014**, *13*, 849.

(13) Zielinski, Z. A. M.; Pratt, D. A. *J. Am. Chem. Soc.* **2019**, *141*, 3037.

(14) Schaefer, E. L.; Zopyrus, N.; Zielinski, Z. A. M.; Facey, G. A.; Pratt, D. A. *Angew. Chem. Int. Ed.* **2020**, *59*, 2089.

(15) Porter, N. A.; Mills, K. A.; Carter, R. L. *J. Am. Chem. Soc.* **1994**, *116*, 6690.

(16) Zielinski, Z.; Presseau, N.; Amorati, R.; Valgimigli, L.; Pratt, D. A. *J. Am. Chem. Soc.* **2014**, *136*, 1570.

(17) McGrath, A. J.; Garrett, G. E.; Valgimigli, L.; Pratt, D. A. *J. Am. Chem. Soc.* **2010**, *132*, 16759.